University of Rochester
Laboratory for Laser Energetics

DOE/NA/28302-1092
January 2013

LLE 2012 Annual Report

October 2011 – September 2012


1850
MELIORA
UNIVERSITY of
ROCHESTER

University of Rochester
Laboratory for Laser Energetics

DOE/NA/28302-1092
January 2013

LLE 2012 Annual Report

UR LLE

October 2011 – September 2012

Inertial Fusion Program and National Laser Users' Facility Program

Contents

Executive Summary

The fiscal year ending September 2012 (FY12) concluded the fifth year of the third five-year renewal of Cooperative Agreement DE-FC52-08NA28302 with the U.S. Department of Energy (DOE). This annual report serves as the final report for the Agreement and summarizes progress in inertial fusion research at the Laboratory for Laser Energetics (LLE) during the past fiscal year including work on the National Ignition Campaign (NIC). It also reports on LLE's progress on laboratory basic science research; laser, optical materials, and advanced technology development; operation of OMEGA and OMEGA EP for the NIC and high-energy-density (HED) campaigns, the National Laser Users' Facility (NLUF), and other external users; and programs focusing on the education of high school, undergraduate, and graduate students during the year.

Progress in Inertial Confinement Fusion (ICF) Research

One of LLE's principal missions is to conduct research in inertial confinement fusion (ICF) with particular emphasis on supporting the goal of achieving ignition on the National Ignition Facility (NIF). This program uses the Omega Laser Facility. During FY12, a total of 1920 target shots were taken at the Omega Laser Facility (including the 60-beam UV laser OMEGA and the four-beam, high-energy petawatt laser OMEGA EP. More than 43% of the facility's target shots in FY12 were designated as NIC experiments or experiments in support of NIC. During the last five years of the current Cooperative Agreement, 8204 target shots were taken on the Omega Laser Facility in support of the National Nuclear Security Administration (NNSA) missions. The OMEGA and OMEGA EP lasers attained average experimental effectiveness of 96.7% and 95.5%, respectively, in FY12.

LLE plays a lead role in the validation of the performance of cryogenic target implosions, essential to all forms of ICF ignition. LLE is responsible for a number of critical elements within the Integrated Experimental Teams (IET's) supporting the demonstration of indirect-drive ignition on the NIF and is the lead laboratory for the validation of the polar-drive approach to ignition on the NIF. LLE has also developed, tested, and constructed a number of diagnostics that are being used on the NIF for the NIC. During this past year, progress in the inertial fusion research program continued in three principal areas: NIC experiments and experiments in support of NIC; development of diagnostics for experiments on the NIF, OMEGA, and OMEGA EP; and theoretical analysis and design efforts aimed at improving direct-drive–ignition capsule designs (including polar-drive–ignition designs) and advanced ignition concepts such as shock ignition and fast ignition.

1. National Ignition Campaign Experiments in FY12

In this volume we report (p. 1) on direct-drive implosion experiments performed on the OMEGA laser that have shown a reduction in measured laser-to-capsule coupling efficiency of 10% to 20% compared to simulations. This reduction is attributed to cross-beam-energy transfer (CBET). CBET scatters energy via stimulated Brillouin scattering from the central portion of an incoming laser beam to an outgoing laser beam. One-dimensional hydrodynamic simulations including CBET show good agreement with all observables in the OMEGA implosion experiments. Three strategies to mitigate CBET are identified: the use of narrow beams, multicolor lasers, and higher-Z ablators. Experiments on OMEGA using narrow laser beams have demonstrated improvements in implosion performance.

Measurements of the hot-electron generation by the two-plasmon–decay (TPD) instability under plasma conditions relevant to direct-drive inertial confinement fusion are reported (p. 20). Density scale lengths of ~400 μm at quarter-critical electron density in planar CH targets allow the TPD instability to be driven to saturation for laser intensities greater than $\sim 3.5 \times 10^{14}$ W/cm^2. In the saturated regime, ~1% of the laser energy is converted to hot electrons. The hot-electron temperature is observed to increase rapidly from 25 keV to 90 keV as the laser intensity is increased from 2 to 7×10^{14} W/cm^2. This increase in hot-electron temperature is compared to predictions from nonlinear Zakharov models.

Time-resolved K_α spectroscopy was used in an experiment conducted on the OMEGA EP laser (p. 15) to infer the hot-electron equilibration dynamics in high-intensity laser interac-

tions with thin-foil solid targets. The measured K_α-emission pulse width increases from ~3 to 6 ps for laser intensities from ~10^{18} to 10^{19} W/cm^2. Collisional energy-transfer model calculations suggest that hot electrons with mean energies from ~0.8 to 2 MeV are contained inside the target. The inferred mean hot-electron energies are broadly consistent with ponderomotive scaling over the relevant intensity range.

The thermal conductivity of solid D_2 was measured by the 3ω method, in which a wire embedded in the medium serves as both a heater and a temperature sensor (p. 48). Accurate values of conductivity were obtained for solid D_2 in the temperature range of 13.4 K to 18.6 K. In this temperature range, normal and ortho D_2 are found to have the same conductivity.

A comprehensive review of the cryogenic-deuterium and deuterium–tritium implosions that have been performed on the OMEGA Laser System over the last decade is presented (p. 72). The success of ignition target designs in inertial confinement fusion (ICF) experiments critically depends on the ability to maintain the main fuel entropy at a low level while accelerating the shell to ignition-relevant velocities of $V_{\text{imp}} > 3 \times 10^7$ cm/s. The fuel entropy is inferred from the experiments by measuring fuel areal density near peak compression. Measured areal densities up to $\langle \rho R \rangle_{\text{n}} = 300$ mg/cm^2 (larger than 85% of predicted values) have been demonstrated in the cryogenic implosion with V_{imp} approaching 3×10^7 cm/s and peak laser intensities of 8×10^{14} W/cm^2. Scaled to the laser energies available at the National Ignition Facility, implosions hydrodynamically equivalent to these OMEGA designs are predicted to achieve $\langle \rho R \rangle_{\text{n}} = 1.2$ g/cm^2, sufficient for ignition demonstration in direct-drive ICF experiments.

A study of the effect of medium-Z doping of plastic ablators on laser imprinting and Rayleigh–Taylor instability growth in direct-drive implosions on the OMEGA Laser System is presented (p. 103). The targets were spherical plastic (CH) shells that were volume doped with a varied concentration of Si (4.3% and 7.4%) and Ge (3.9%). The targets were imploded by 48 beams with a low-adiabat, triple-picket laser shape pulse with a peak intensity of 4×10^{14} W/cm^2 and x-ray radiographed through a 400-nm opening in the side of the target. The results show that volumetric impurity doping strongly reduces the shell's density modulation and instability growth rate. Simulations using the two-dimensional (2-D), radiation–hydrodynamics code *DRACO* show good agreement with the measurements.

A technique to measure a shell's trajectory in direct-drive inertial confinement fusion implosions is presented (p. 109). The x-ray self-emission of the target was measured with an x-ray framing camera. Optimized filtering limited the x-ray emission from the corona plasma, isolating a sharp intensity gradient to the ablation surface. This technique enables one to measure the radius of the imploding shell with an accuracy of better than 1 nm and to determine a 200-ps average velocity to better than 2%.

The results of collaborative (LLE, University of Bordeaux, France, CEA, CNRS, CELIA, MIT, and LLNL) OMEGA shock-ignition experiments that use a novel beam configuration with separate low-intensity compression beams and high-intensity spike beams are discussed (p. 113). Significant improvements in the performance of plastic-shell, D_2 implosions were observed with repointed beams. The analysis of the coupling of the high-intensity spike beam's energy into the imploding capsule indicates that absorbed hot-electron energy contributes to the coupling. The backscattering of the laser energy was measured to reach 36% at single-beam intensities of ~8×10^{15} W/cm^2. Hard x-ray measurements revealed a relatively low hot-electron temperature of ~30 keV independent of intensity and timing. At the highest intensity, stimulated Brillouin scattering occurs near and above the quarter-critical density and the two-plasmon–decay instability is suppressed.

Measurements of strong-shock generation in the presence of pre-plasmas with relevance to shock ignition are reported (p. 137). A planar target was irradiated with a laser pulse consisting of a pre-plasma–generating foot followed by a high-intensity spike, driving a strong shock into the target. The observed shock dynamics inferred from velocity interferometer for any reflector (VISAR) and streaked optical pyrometer (SOP) measurements are reproduced well using 2-D *DRACO* simulations, indicating that plastic-ablator shocks of up to 70-Mbar strength have been generated.

The first x-ray Thomson-scattering (XRTS) measurement of shock-compressed liquid deuterium performed at the Omega Laser Facility is reported (p. 143). The noncollective, spectrally resolved, inelastic XRTS employs 2.96-keV Cl Ly_α line emission. Microscopic property measurements of shocked deuterium show an inferred spatially averaged electron temperature of 8±5 eV, an electron density of 2.2×10^{23} cm^{-3}, and an ionization of 0.8 (–0.25, +0.15). Two-dimensional hydrody-

namic simulations using equation-of-state models suited for the extreme parameters also occurring in ICF research and planetary interiors are consistent with the experimental results.

The measurement of magnetic fields induced by the Rayleigh–Taylor (RT) instability in planar plastic foil with ultrafast proton radiography is presented (p. 159). Thin plastic foils were irradiated with ~4-kJ, 2.5-ns laser pulses focused to an intensity of $\sim 10^{14}$ W/cm^2. Target modulations were seeded by laser nonuniformities and amplified during target acceleration by the RT instability. The experimental data show the hydrodynamic evolution of the target and the generated MG-level magnetic fields in the broken foil, which are in good agreement with predictions from 2-D magneto-hydrodynamic simulations.

The two-plasmon–decay common-wave process has been demonstrated at the Omega Laser Facility (p. 172). The total energy in hot electrons produced in a planar target is measured to be the same when using one or two laser beams and significantly reduced with four beams for a constant overlapped intensity. This is caused by multiple beams sharing the same common electron plasma wave in the two-plasmon–decay (TPD) instability. A model, consistent with the experimental results, predicts that multiple laser beams can only drive a resonant common TPD electron plasma wave in the region of wave numbers bisecting the beams. In this region, the gain is proportional to the overlapped laser-beam intensity.

The current understanding of multibeam laser–plasma instabilities including CBET and TPD for direct-drive ignition is reviewed (p. 181). CBET is driven by multiple laser beams and can significantly reduce the hydrodynamic efficiency in direct-drive experiments on OMEGA. Reducing the radii of the laser beams significantly increases the hydrodynamic efficiency at the cost of an increase in low-mode nonuniformities. The combination of zooming and dynamic bandwidth reduction will provide a 30%-effective increase in the drive energy on OMEGA direct-drive implosions. TPD instability can also be driven by multiple laser beams. Both planar and spherical experiments were performed to study the hot electrons generated by TPD at the Omega Laser Facility. The fraction of laser energy converted to hot electrons scales with the hot-electron temperature for all geometries and over a wide range of intensities. At ignition-relevant intensities, the fraction of laser energy converted to hot electrons is measured to decrease by an order of magnitude when the ablator material is changed from carbon–hydrogen to aluminum. The TPD results are compared with a multibeam linear theory and a nonlinear Zakharov model.

We report on investigations of stress-radiation–induced swelling in plastic capsules (p. 191). The process of filling targets with DT for cryogenic experiments on the OMEGA laser induces small-scale features on the inner surface of the plastic capsules. Each feature was a cluster of low-level domes (<0.1 nm high) with individual lateral dimensions smaller than 5 nm that collectively covered lateral dimensions of up to 300 nm^2. These features were observed only when a high-radiation dose was combined with high stress in the plastic wall, as occurs when the capsules are permeation filled and transferred at cryogenic temperatures. No porosity or void structure was observed in or below these domes. It is speculated that the domes' swelling is caused by a radiation-induced bond scission and chemical restructuring that reduces the plastic density in localized regions.

Measurements carried out as a collaboration among scientists from LLE, MIT, and General Atomics (GA) of energetic protons in cone-in-shell fast-ignitor experiments on OMEGA are presented (p. 204). In these experiments, charged-particle spectrometers were used to measure a significant population ($>10^{13}$) of energetic protons (7.5 MeV maximum), indicating the presence of strong electric fields. These energetic protons, observed in directions both transverse and forward relative to the direction of the short-pulse laser beam, have been used to study aspects of coupling efficiency of the fast ignitor. Forward-going protons were less energetic and showed no dependence on laser intensity or whether the cone tip was intact when the short-pulse laser was fired. Maximum proton energies transverse to the cone-in-shell target scale with incident on-target laser intensity (2 to 6×10^{18} W/cm^2), as described by the ponderomotive scaling ($\sim I^{1/2}$). It is shown that these protons are accelerated from the entire cone surface, possibly due to return currents, rather than from the cone tip alone. The proton-inferred lower bound on the hot-electron temperature was hotter than the ponderomotive scaling by a factor of 2 to 3.

2. Theoretical Design and Analysis

A description of low-adiabat, cryogenic deuterium–tritium, and warm-plastic-shell polar-drive (PD)–implosion designs for the OMEGA laser begins on p. 57. The designs are at two differ-

ent on-target laser intensities, each at a different in-flight aspect ratio (IFAR). The first design permits one to study implosion energetics and target performance closer to ignition-relevant intensities (7×10^{14} W/cm^2 at the quarter-critical surface), where nonlocal heat conduction and laser–plasma interactions can play an important role, but at lower values of IFAR (~22). The second design permits one to study implosion energetics and target performance at a lower intensity (3×10^{14} W/cm^2) but at higher IFAR (~32), where the shell instability can play an important role. The higher-IFAR designs are accessible on the existing OMEGA Laser System, only at lower intensities. Implosions at ignition-relevant intensities can be obtained only by reducing target radius, although only at smaller values of IFAR. Polar-drive geometry requires that the laser beams be repointed to improve shell symmetry. The higher-intensity designs optimize target performance by repointing beams to a lesser extent and compensate for the reduced equatorial drive by increasing beam energies for the repointed beams and using custom beam profiles that improve equatorial illumination at the expense of irradiation at higher latitudes. These designs will be studied when new phase plates for OMEGA, corresponding to the smaller target radii and custom beam profiles, are obtained. Implosion results from the combined set of high-intensity and high-IFAR implosions should yield valuable data to validate models of laser-energy deposition, heat conduction, nonuniformity growth, and fuel assembly in PD geometry.

3. Diagnostics

We report on the design and implementation of a narrow-band x-ray imager for a Cu K_α line at ~8 keV using a spherically bent quartz crystal for the OMEGA EP laser (p. 34). The quartz crystal is cut along the 2131 (211) planes for a $2d$ spacing of 0.3082 nm, resulting in a Bragg angle of 88.7°, very close to normal incidence. An optical system is used to remotely align the spherical crystal without breaking the vacuum of the target chamber. The images show a high signal-to-background ratio of typically >100:1 with laser energies ≥1 kJ at a 10-ps pulse duration and a spatial resolution of less than 10 nm.

A single-shot, electro-optic data-acquisition system with a 600:1 dynamic range for the NIF Dante instrument has been demonstrated (p. 129). The prototype system uses multiple optical wavelengths to allow for the multiplexing of up to eight signals onto one photodetector and provides optical isolation and a bandwidth of 6 GHz.

The high-resolution spectroscopy used to measure ICF neutron spectra to infer the areal density (ρR) of cryogenic DT implosions on OMEGA is described in detail in an article starting on p. 165. Neutron time-of-flight (nTOF) techniques are used to measure the spectrum of neutrons that elastically scatter off the dense deuterium (D) and tritium (T) fuel. High signal-to-background data have been recorded on cryogenic DT implosions using a well-collimated 13.4-m line of sight and an nTOF detector with an advanced liquid scintillator compound. An innovative method to analyze the elastically scattered neutron spectra was developed using well-known cross sections of the DT nuclear reactions. The measured areal densities are consistent with alternative ρR measurements and 1-D simulations.

A reflective optical transport system has been built for ultraviolet Thomson scattering from electron plasma waves on OMEGA (p. 178). A Schwarzschild objective that uses two concentric spherical mirrors coupled to a Pfund objective provides diffraction-limited imaging across all reflected wavelengths. This enables the operator to perform Thomson-scattering measurements of ultraviolet (0.263-μm) light scattered from electron plasma waves.

Lasers, Optical Materials, and Advanced Technology

The design of an ultra-intense optical parametric chirped-pulse–amplification (OPCPA) system at 910 nm is presented in an article starting on p. 30. Technologies are being developed for large-scale systems based on deuterated potassium dihydrogen phosphate (DKDP) optical parametric amplifiers that could be pumped by kilojoule-class Nd:glass lasers such as OMEGA EP. Results from a prototype white-light–seeded chain of noncollinear optical parametric amplifiers (NOPA's) are reviewed. The development of a cylindrical Öffner stretcher that has advantages over standard stretchers for ultra-intense, high-contrast systems is described. Development of the laser's front end will result in the demonstration of a mid-scale optical parametric amplifier line (OPAL) that will use scalable technologies to produce 7.5-J, 15-fs pulses with a temporal contrast exceeding 10^{10}.

A new operation regime of NbN superconducting single-photon detectors (SSPD's) by integrating them with a low-noise, cryogenic, high-electron-mobility transistor and a high-load resistor is proposed (p. 39). The new SSPD operating scheme makes it possible to distinguish dark pulses from actual photon pulses in SSPD's and therefore gain a better understanding of the origin of dark counts generated by the detector. A statistical analysis of amplitude distributions of recorded trains of the SSPD photoresponse transients is used to obtain informa-

tion on the spectral characteristics of incident photons and demonstrates that meander-type SSPD's exhibit some photon-number–resolving capability.

A low-temperature chemical cleaning approach has been developed (p. 149) to remove manufacturing residue from multilayer dielectric (MLD) pulse-compressor gratings to be used in the OMEGA EP Laser System. The method strips baked-on photoresist, metal contaminants, and debris without damaging the grating's delicate surface structure. Because targeted cleaning steps remove specific families of contaminants (heavy organics, light organics, metals, and oxides), the process can be adjusted to strip known quantities and types of material. After cleaning, grating samples showed excellent performance in short-pulse (10-ps) laser-damage testing at 1054 nm. Average in-air damage thresholds were 4.06±0.19 J/cm^2 and 3.32±0.22 J/cm^2 (beam normal) in the 1-on-1 and *N*-on-1 regimes, respectively, for a set of nine gratings cleaned at processing temperatures in the range of 40°C to 70°C. Post-cleaning diffraction efficiencies were consistently above 96%.

National Laser Users' Facility and External Users' Programs

Under the facility governance plan that was implemented in FY08 to formalize the scheduling of the Omega Laser Facility as an NNSA User Facility, Omega Facility shots are allocated by campaign. The majority (67.6%) of the FY12 target shots were allocated to the National Ignition Campaign (NIC) conducted by integrated teams from the national laboratories and LLE and to the high-energy-density campaigns conducted by teams led by scientists from the national laboratories. Nearly 29% of the facility shots in FY12 were allocated to basic science experiments. Half of these were dedicated to university basic science under the National Laser Users' Facility (NLUF) Program, and the remaining shots were allotted to the Laboratory Basic Science (LBS) Program, comprising peer-reviewed basic science experiments conducted by the national laboratories and by LLE including the Fusion Science Center (FSC). The Omega Facility is also being used for several campaigns by teams from the Commissariat à l'Énergie Atomique (CEA) of France and the Atomic Weapons Establishment (AWE) of the United Kingdom. These programs are conducted on the facility on the basis of special agreements put in place by the DOE/NNSA and the participating institutions.

During FY12 the facility users included 11 collaborative teams participating in the NLUF Program; 12 teams led by LLNL and LLE scientists participating in the LBS Program; many collaborative teams from the national laboratories conducting experiments for the NIC; investigators from LLNL and LANL conducting experiments for high-energy-density–physics programs; scientists and engineers from CEA, AWE, and the Center for Radiative Shock Hydrodynamics (CRASH) of the University of Michigan.

1. NLUF Programs

In FY12, the Department of Energy (DOE) issued a solicitation for NLUF grants for the period FY13–FY14. A record of 23 proposals were submitted to DOE for the NLUF FY13–FY14 program. These proposals requested a total of ~62 shot days of Omega Facility time in each of the two fiscal years. An independent DOE Technical Evaluation Panel reviewed the proposals on 11 July 2012 and recommended that 11 proposals receive DOE funding and 28 days of shot time on OMEGA in both FY13 and FY14. Table I lists the successful NLUF proposals for FY13–FY14. FY12 was the second of a two-year period of performance for the NLUF projects approved for the FY11–FY12 funding and OMEGA shots. Eleven NLUF projects were allotted Omega Laser Facility shot time and conducted a total of 277 target shots on the facility. The work of the NLUF programs in FY12 is summarized beginning on p. 224.

2. Laboratory Basic Science Program (LBS)

In FY12, LLE issued a solicitation for LBS proposals to be conducted in FY13. A total of 32 proposals were submitted with requests for a total of 68 shot days of Omega Facility time in FY13 for these proposed experiments. An independent review committee reviewed the proposals and recommended that 16 proposals receive 28 shot days at the Omega Laser Facility in FY13. Table II lists the successful LBS proposals. Fifteen LBS projects were allotted Omega Facility shot time and conducted a total of 273 target shots at the facility in FY12. This work is summarized beginning on p. 244.

3. FY12 LLNL Omega Facility Programs

In FY12, LLNL conducted several campaigns on the OMEGA and OMEGA EP Laser Systems, as well as campaigns that used the OMEGA and OMEGA EP beams jointly. Overall, LLNL led 335 target shots involving OMEGA and 121 target shots involving OMEGA EP. Approximately 38% of the total number of shots (124 OMEGA shots and 39 OMEGA EP shots) supported the NIC. The remaining 211 OMEGA shots and 82 OMEGA EP shots were dedicated to experiments for HED physics.

Table I: NLUF proposals approved for shots at the Omega Laser Facility for FY13–FY14.

Principal Investigator	Institution	Project Title
F. N. Beg	University of California, San Diego	Systematic Study of Fast-Electron Energy Deposition in Imploded Plasmas with Enhanced OMEGA EP Laser Contrast and Intensity
R. P. Drake	University of Michigan	Experimental Astrophysics on the OMEGA Laser
T. Duffy	Princeton University	Dynamic Compression of Earth and Planetary Materials Using OMEGA
W. Fox	University of New Hampshire	Dynamics and Instabilities of Magnetic Reconnection Current Sheets in High-Energy-Density Plasmas
P. Hartigan	Rice University	Astrophysical Dynamics in the Laboratory: Mach Stems and Magnetized Shocks
R. Jeanloz	University of California, Berkeley	Journey to the Center of Jupiter, Recreating Jupiter's Core on OMEGA
H. Ji	Princeton University	Study of Particle Acceleration and Fine-Scale Structures of Collisionless Magnetic Reconnection Driven by High-Energy Petawatt Lasers
B. Qiao	University of California, San Diego	Dynamics of High-Energy Proton Beam Focusing and Transition into Solid Targets of Different Materials
R. D. Petrasso	Massachusetts Institute of Technology	Studies of Laboratory Astrophysics, Inertial Confinement Fusion, and High-Energy-Density Physics with Nuclear Diagnostics
A. Spitkovsky	Princeton University	Generation of Collisionless Shocks in Laser-Produced Plasmas
R. B. Stephens	General Atomics	Investigation of the Dependence of Fast-Electron Generation and Transport on Laser Pulse Length and Plasma Materials

The objectives of the LLNL-led NIC campaigns conducted on the Omega Facility included the following:

- *Thermal Conductivity Study of CH/Be and CH/D_2 Interfaces by Refraction-Enhanced X-Ray Radiography*
- *High-Resolution Measurements of Velocity Nonuniformities Created by Microscopic Perturbations in NIF Ablator Materials*
- *Measuring the Adiabatic Index of Polystyrene Using Counter-Propagating Shocks and X-Ray Thomson Scattering*
- *Ablator Opacity Measurements*
- *Multipump Stimulated Raman Scattering*
- *Comparison of Plastic and High-Density Carbon Ablator Performance*
- *Shock Release of ICF-Relevant Materials*

The LLNL-led HED campaigns included the following research:

1. *Material Dynamics and Equation of State*
   a. *Tantalum Rayleigh–Taylor Experiments*
   b. *Iron Rayleigh–Taylor Experiments*
   c. *Double-Pulse Radiography Development*
   d. *Diffraction Studies on Shocked Tantalum*
   e. *Ta X-Ray Diffraction*
   f. *Hydrogen Equation of State*
   g. *XAFS Study of Ramp-Compressed Fe, Ta, and Mo*
   h. *Tin Melt*
   i. *Gigabar Equation of State*
   j. *Equation of State for Foams Using OMEGA EP*
   k. *Advanced X-Ray Diffraction Techniques*

2. *Radiation Transport*
   a. *Heated Wall*
   b. *Crystal Window*

3. *High-Temperature Plasma Opacity*
   a. *High-Temperature Plasma Opacity Experiments on OMEGA and OMEGA EP*

4. *Burn Physics*
   a. *Non-LTE Transport and Nuclear Lifetimes*

Table II: Approved FY13 LBS proposals.

Principal Investigator	Affiliation	Project Title
P. M. Celliers	LLNL	Equation of State and Optical Properties of Dense Silica: Shock Study of Coesite and Stishovite
H. Chen	LLNL	Exploring Pair Plasma and Their Applications Using OMEGA EP
J. R. Davies	LLE	Fast-Electron Control with Magnetic Field in Hohlraum
J. H. Eggert	LLNL	HED Condensed Matter: Magnesium and Aluminum
G. Fiksel	LLE	Magnetic Reconnection and Particle Energization in High-Energy-Density Plasmas in the Presence of an External Magnetic Field
G. Fiksel	LLE	Magnetized ICF Implosions on OMEGA
R. F. Heeter	LLNL	"Gattling Gun" Long-Duration Radiation Sources on OMEGA EP for Sustained-Drive Hydrodynamics and Low-Density Atomic Physics Applications on OMEGA EP and the NIF
B. R. Maddox	LLNL	Direct Measurements of Dislocation-Based Plastic Flow in Quasi-Isentropically Compressed bcc Metals
H.-S. Park	LLNL	Astrophysical Collisionless Shock Generation by Laser-Driven Experiments
P. K. Patel	LLNL	Areal-Density Measurements of Cone-in-Shell Implosions Using Compton Radiography for Fast Ignition
Y. Ping	LLNL	Long-Term Dynamics of Hole Boring and Target Heating at Fast-Ignition-Relevant Conditions
S. P. Regan	LLE	Collective X-Ray Scattering from Shocked Liquid Deuterium
J. R. Rygg	LLNL	Extreme Chemistry, Equation of State, and Optical Properties of Dense Water at Terapascal Pressure
A. A. Solodov	LLE	Fast-Ignition Integrated Experiments with Low-*Z* Cone-Tip Targets
C. Stoeckl	LLNL	Spectroscopy of Neutrons Generated Through Nuclear Reactions with Light Ions in Short-Pulse Laser-Interaction Experiments
W. Theobald	LLE	Laser Channeling in Long-Scale-Length, Overdense Plasmas

5. *Hydrodynamics*
   a. *Short-Pulse, UV Backlighting Development for the NIF*

6. *X-Ray Source Development and Application*
   a. *X-Ray Source Development with Nanostructured Materials*
   b. *Solar Cell Electrostatic Discharge*

4. FY12 LANL OMEGA Facility Programs

In FY12, Los Alamos National Laboratory (LANL) executed 244 total shots on OMEGA. LANL experiments contributed to the National Ignition campaign (NIC) in the following ways:

- *Measured the x-ray ablative Richtmyer–Meshkov growth of isolated defects on plastic ablators*
- *Studied branching ratios in DT fusion plasmas*
- *Continued neutron imaging and radchem scintillator development for the NIF*

High-energy-density (HED) campaigns included the following:

- *Studies of shear in a counter-propagating flow geometry and reshock-driven turbulent mixing*
- *Backlit defect implosion experiments to study effect of trench defect and polar direct drive*
- *Measurements of the effect of capsule asymmetries on neutron yield and ion temperature*
- *Imaging x-ray Thomson scattering platform development for dense plasmas and warm-dense-matter equation of state*
- *Measurement of a supersonic radiation wave and foam aerogel EOS*

OMEGA Laser Facility Users Group (OLUG)

A capacity gathering of 115 researchers from over 25 universities and laboratories and 9 countries met at the Laboratory for Laser Energetics (LLE) for the Fourth Omega Laser Facility

Users Group (OLUG) Workshop in April 2012. The purpose of the 2.5-day workshop was to facilitate communications and exchanges among individual Omega users and between users and the LLE management; to present ongoing and proposed research; to encourage research opportunities and collaborations that could be undertaken at the Omega Laser Facility and in a complementary fashion at other facilities [such as the National Ignition Facility (NIF) or the Laboratoire pour l'Utilisation des Lasers Intenses (LULI)]; to provide an opportunity for students, postdoctoral fellows, and young researchers to present their research in an informal setting; and to provide feedback to LLE management from the users about ways to improve the facility and future experimental campaigns.

The interactions were wide ranging and lively, as illustrated in the workshop report (p. 213). OLUG consists of 304 members from 33 universities and 25 centers and national laboratories; their names and affiliations can be found at www.lle.rochester.edu/media/about/docu-ments/OLUGMEMBERS.pdf. OLUG is by far the largest users group in the world in the field of high-energy-density (HED) physics and certainly one of the most active. During the first two mornings of the workshop, seven science and facility talks were presented. The facility talks proved especially useful for those not familiar with the art and complexities of performing experiments at the Omega Facility. But since the facility is constantly changing and improving, even experienced users significantly benefited from these updates.

The overview science talks, given by leading world authorities, described the breadth and excitement of HED science undertaken at the Omega Laser Facility. Approximately 50 students and postdoctoral fellows participated in the workshop; 42 of these participants were supported by travel grants from the National Nuclear Security Administration (NNSA). The content of their presentations ranged from target fabrication to simulating aspects of supernovae; the presentations generated spirited discussions, probing questions, and friendly suggestions. In total, there were 75 contributed posters, including 11 that focused on the Omega Facility. The invited and facility presentations, as well as OLUG's Findings and Recommendations, can be found at www.lle.rochester.edu/about/omega_laser_users_group.php.

FY12 Omega Facility Report

During FY12, the Omega Facility conducted 1494 target shots on OMEGA and 426 target shots on OMEGA EP for a record total of 1920 target shots (see Tables 132.V and 132.VI). OMEGA averaged 11.2 target shots per operating day with availability and experimental effectiveness averages for FY12 of 94.2% and 96.7%, respectively. OMEGA EP was operated extensively in FY12 for a variety of internal and external users. A total of 356 target shots were taken into the OMEGA EP target chamber and 70 joint target shots into the OMEGA target chamber. OMEGA EP averaged 6.1 target shots per operating day with Availability and Experimental Effectiveness averages for FY12 of 88.0% and 95.5%, respectively. Highlights of achievements in FY12 are detailed starting on p. 221 and include the following:

- Multi-FM Beam Smoothing on OMEGA EP
- Equivalent-Target-Plane Diagnostics on OMEGA EP
- OMEGA EP Short-Pulse Contrast Improvement
- OMEGA EP Spatial Profile Improvements on Beamlines 3 and 4
- OMEGA Pulse-Shape-Measurement Capabilities
- 4ω Probe Laser System
- Thomson-Scattering Spectrometer System on OMEGA

1. Experimental Operations and Diagnostics

In FY12, 26 new target diagnostics were commissioned on OMEGA and 8 on OMEGA EP. These included a suite of TIM-based scattered-energy calorimeters, the SXS crystal spectrometer for x-ray streak cameras, the first of the new PJX-2 streak cameras, a new high-speed video target viewing system, and an additional x-ray pinhole camera. The streaked optical pyrometer diagnostic measures the time-resolved laser-driven shocks on OMEGA. This system has been upgraded with a ROSS streak camera system and improved optical relay for higher resolution in increased signal strength. As in previous years, many of the new instruments were developed by or in collaboration with other laboratories, including LLNL, LANL, CEA, and General Atomics. Experimental facility improvements included the introduction of an image plate scanning capability on OMEGA, the addition of a second image plate scanner on OMEGA EP, and the commissioning of a set of fully integrated TIM-based target positioning systems on both OMEGA and OMEGA EP. Two of the OMEGA TIM's were retrofit with new EMI-resistant, OMEGA EP–type control systems, and updated TIM vacuum system operating software was installed on both OMEGA and OMEGA EP.

Education

As the only major university participant in the National ICF Program, education continues to be an important mission for the Laboratory. Laboratory education programs span the range of high school (p. 219) to graduate education.

1. High School Program

During the summer of 2012, 16 students from Rochester-area high schools participated in the Laboratory for Laser Energetics' Summer High School Research Program. The goal of this program is to excite a group of high school students about careers in the areas of science and technology by exposing them to research in a state-of-the-art environment. Too often, students are exposed to "research" only through classroom laboratories, which have prescribed procedures and predictable results. In LLE's summer program, the students experience many of the trials, tribulations, and rewards of scientific research. By participating in research in a real environment, the students often become more excited about careers in science and technology. In addition, LLE gains from the contributions of the many highly talented students who are attracted to the program. The students spent most of their time working on their individual research projects with members of LLE's technical staff. The projects were related to current research activities at LLE and covered a broad range of areas of interest including experimental concept development and diagnostics modeling, computational modeling of implosion physics, materials science, laser system development and diagnostics, isotope separation, and database development (see Table 132.IV).

Two-hundred and ninety-seven high school students have now participated in the program since it began in 1989. Thirty of the participating students have gone on to gain semi-finalist status at the Intel Science Talent Search national competition and four of the students have gained finalist status at this competition.

At a symposium conducted at the end of the summer program, LLE presented its 16th annual William D. Ryan Inspirational Teacher Award to Ms. Sage Miller, a mathematics and computer science teacher at Webster Schroeder and Webster Thomas High Schools. This award is presented to a teacher who motivated one of the participants in LLE's Summer High School Research Program to study science, mathematics, or technology and includes a $1000 cash prize. Teachers are nominated by alumni of the summer program. Ms. Miller was nominated by Troy Thomas and Avery Gnolek, participants in the 2011 program, both of whom credit her for their decisions to major in computer science.

2. Undergraduate Students Program

Forty-two undergraduate students participated in work or research projects at LLE this past year. Student projects include operational maintenance of the Omega Laser Facility; work in laser development, materials, and optical-thin-film-coating laboratories; computer programming; image processing; and diagnostics development. This is a unique opportunity for students, many of whom will go on to pursue a higher degree in the area in which they gained experience at the Laboratory.

3. Graduate Student Programs

Graduate students are using the OMEGA Facility as well as other LLE facilities for fusion and HED physics research and technology development activities. These students are making significant contributions to LLE's research program. Twenty-six faculty from five University academic departments collaborate with LLE scientists and engineers. Presently, 74 graduate students are involved in research projects at LLE, and LLE directly sponsors 38 students pursuing Ph.D. degrees via the NNSA-supported Frank Horton Fellowship Program in Laser Energetics. Their research includes theoretical and experimental plasma physics, HED physics, x-ray and atomic physics, nuclear fusion, ultrafast optoelectronics, high-power-laser development and applications, nonlinear optics, optical materials and optical fabrication technology, and target fabrication. In addition, LLE directly funds research programs within the MIT Plasma Science and Fusion Center, the State University of New York (SUNY) at Geneseo, and the University of Wisconsin. These programs involve a total of approximately 6 graduate students, 25 to 30 undergraduate students, and 10 faculty members.

Over 300 graduate students have now conducted their graduate research work at LLE since the graduate research program began at the Laboratory. In addition, one-hundred-twenty graduate students and post-graduate fellows from other universities have conducted research at the LLE laser facilities as part of the NLUF program. Some 29 graduate students and 29 undergraduate students were involved in research on the Omega Facility as part of NLUF teams in FY12.

Robert L. McCrory
Director, Laboratory for Laser Energetics
Vice President, University of Rochester

Crossed-Beam Energy Transfer in Direct-Drive Implosions

Introduction

The direct-drive approach to inertial confinement fusion (ICF)[1,2] is based on the implosion, compression, and subsequent ignition of millimeter-diameter cryogenic deuterium–tritium (DT) ice shell targets using high-intensity ($I \sim 10^{14}$ to 10^{15} W/cm^2) laser irradiation [Fig. 129.1(a)]. Direct drive offers the possibility of higher gain than from indirect-drive implosions of the same laser energy.[4] [Reference 3 is cited in the caption of Fig. 129.1(a) below.] To validate physics effects in direct-drive–ignition experiments planned for the National Ignition Facility (NIF),[5] the experiments are carried out on the OMEGA Laser System,[6] which employs 60 laser beams with a total energy of up to 30 kJ [Figs. 129.1(b) and 129.1(c)]. Experiments to study ignition-relevant conditions require a laser energy of ~1 MJ and will be conducted on the NIF in the polar-drive configuration.[7]

High-intensity incident light is absorbed in the corona of direct-drive targets, and the released heat drives the implosions by ablating the outer target surface. The dominant absorption mechanism on the OMEGA and NIF lasers, which operate on a wavelength λ_L = 351 nm, is inverse bremsstrahlung, or "collisional absorption."[8] Laser light is absorbed in a relatively narrow radial region with electron densities n_e from ~0.5 to 1 n_{cr}, where $n_{cr} = \pi c^2 m_e / \lambda_L^2 e^2$ is the critical density, m_e is the electron mass, e is the electron charge, and c is the speed of light. The symmetric illumination of targets with many laser beams, crossing each other at different angles and directions, creates conditions for transferring energy among beams because of electromagnetically seeded, low-gain stimulated Brillouin scattering (SBS).[9] Figure 129.2 illustrates the geometry of crossing rays when the most-efficient energy transfer occurs at the radii outside the highest-absorption region with n_e from ~0.1 to 0.5 n_{cr}. The outgoing edge-beam light in Beam 1 seeds perturbations to the incoming center-beam light in Beam 2 (Fig. 129.2), scattering this light outward. Because of this scattering, the incoming light fails to penetrate into the most-absorbing region of the corona (where $n_e \sim n_{cr}$) and

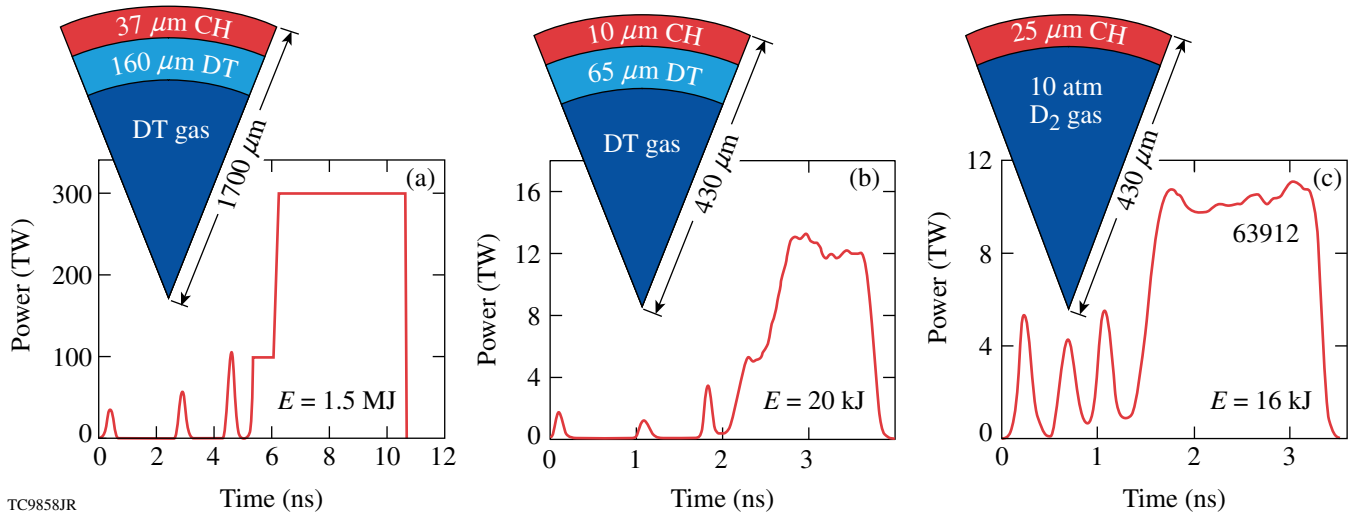

Figure 129.1
(a) A 1.5-MJ direct-drive NIF ignition design.[3] This design utilizes a triple-picket pulse and obtains an energy gain of about 50. (b) Typical cryogenic OMEGA target. This target is a scaled-down version of the design in (a) and is optimized for a laser energy of up to 25 kJ. (c) Example of a warm OMEGA target (shot 63912). Such targets are a less-expensive alternative to cryogenic OMEGA targets. The warm targets are used to study laser coupling, hydrodynamic stability, hot-spot formation, and other aspects of implosion physics.

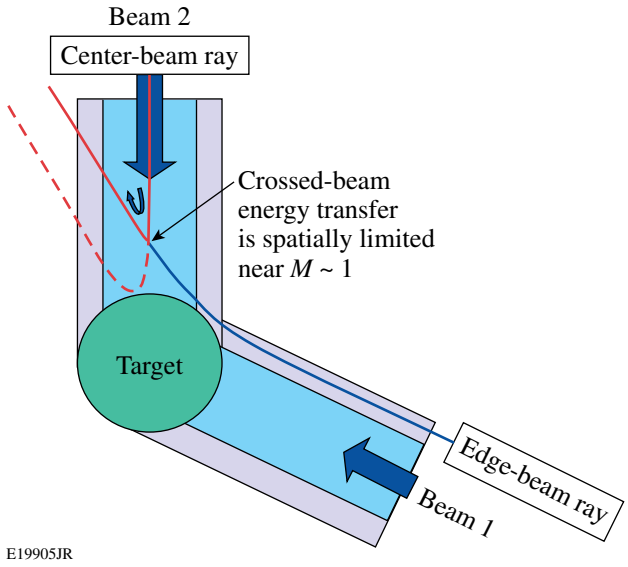

Figure 129.2
Schematic illustration of a laser-ray geometry with the most energetically efficient crossed-beam energy transfer (CBET) in the corona of an implosion target. An incident edge-beam ray (shown in blue) in Beam 1 is refracted and turned outward above the critical radius. On its outgoing trajectory, this ray seeds perturbations to an incoming center-beam ray (shown in red) in Beam 2 that results in energy transfer from the latter ray to the outgoing ray (also shown in red). The energy transfer occurs near the Mach 1 radius, which is typically located at n_e from 0.2 to 0.3 n_{cr}. As the result of CBET, center-beam rays deliver less energy to the maximum absorption region near the critical radius.

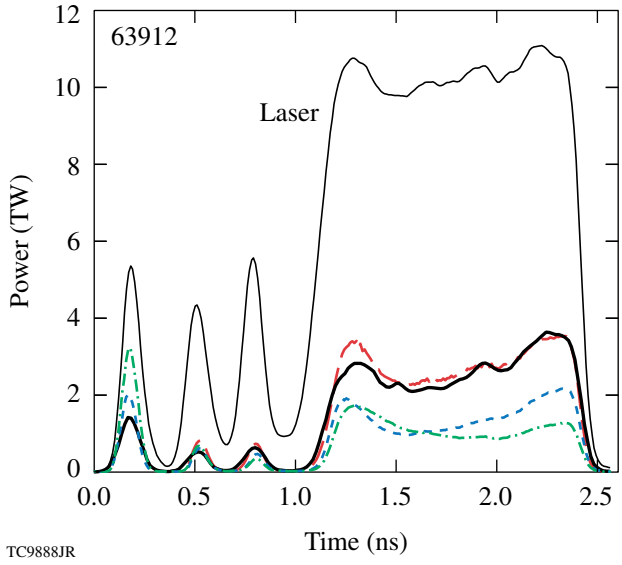

Figure 129.3
Reflected light power history measured (thick black line) and simulated using flux-limited transport (green dashed–dotted line), nonlocal transport (blue dashed line), and nonlocal transport with CBET (red dashed line). The thin black line shows the incident laser power. Note good agreement between the measured power history and the simulated one with CBET.

deposits its energy there, as it does without scattering, reducing laser coupling. Calculations show that crossed-beam energy transfer (CBET) becomes important in OMEGA implosions at intensities $I > 10^{14}$ W/cm^2.

Figure 129.3 illustrates the discrepancy between the modeled scattered-light power without CBET in a plastic-shell (CH) implosion driven at $I = 4.5 \times 10^{14}$ W/cm^2 and experimental observations. The green dashed–dotted and blue dashed lines in Fig. 129.3 show simulated powers using flux-limited (with the flux-limiter parameter $f = 0.06$)[10] and nonlocal[11] heat transport models, respectively. These simulations significantly underestimate and are not able to correctly reproduce the measured power[12] shown by the thick solid black line in Fig. 129.3. The simulations overpredict the measured absorption by about 10%. Simulations of the same implosion but including CBET accurately reproduce the measurements (compare red dashed and solid black lines in Fig. 129.3). Simulations including CBET show good agreement with all observables in implosion experiments using different laser energies, pulse shapes, and targets. Examples of these simulations are discussed in Ref. 13 with more examples discussed below. Good agreement with measurements is obtained only in simulations using CBET and nonlocal transport. Simulations using flux-limited transport with or without CBET fail to consistently reproduce experiments.

The performance of implosions can be improved by mitigating CBET.[13] This article considers three mitigation techniques: One technique uses a laser-beam (or focal-spot) diameter smaller than the target diameter. This can be very efficient in reducing CBET and increasing laser coupling, but on the downside the narrow beams introduce beam-overlap nonuniformities, which can degrade the implosion performance. Experiments on OMEGA have been performed to investigate the optimum beam diameters by balancing CBET with the effects of nonuniformity in low-adiabat implosions. This is discussed below in detail. The second technique employs multicolored laser light, which modifies resonance coupling between beams. Using, for example, a two-color split, CBET can be reduced by a factor of 1/2 for the wavelength separation $\Delta\lambda > 5$ Å of the two wavelengths (for 351-nm light). The third technique uses targets with plastic ablators doped with high-Z elements (e.g., Ge).

The following sections describe the simulation technique for modeling CBET (with details described in Appendices A,

B, and C); discuss CBET in OMEGA implosions, comparing simulations and measurements; and consider the three techniques for mitigating CBET: narrow beams, multicolored lasers, and Ge-doped plastic ablators. The conclusions are presented in the final section.

Modeling CBET

The numerical algorithm for CBET considers pairwise interactions of pump light rays (denoted with index j) with probe light rays (denoted with index i). All possible crossings of the pump rays with the probe light on the path ℓ in a target corona are taken into account. The path ℓ is calculated using Snell's law. The intensity of the probe light along ℓ obeys the equation

$$\frac{\mathrm{d}I_i}{\mathrm{d}\ell} = \xi I_i \sum_j L_{ij}^{-1}, \tag{1}$$

where L_{ij} is the SBS gain length for the rays i and j and ξ is a limiting parameter,[13] $0 < \xi \leq 1$ (see the next section). The spatial gain L_{ij} is estimated in the strong damping limit,[8] which is well satisfied in direct-drive implosions,[14] and given in Appendices A and B for the fluid [Eq. (A2)] and kinetic [Eq. (B8)] models, respectively. A random polarization of the illuminating beams in implosions is accounted for in Eq. (1) by increasing L_{ij} by a factor of 2.

The algorithm uses a simplified assumption of spherical symmetry for both the implosion hydrodynamics and laser illumination. Intensity profiles for laser beams can take an arbitrary shape (e.g., super-Gaussian $n = 4$ in the standard OMEGA setup). The algorithm is incorporated into the laser-absorption package of the one-dimensional (1-D) hydrodynamic code *LILAC*,[15] allowing for a self-consistent calculation of laser deposition with CBET.

Simulations of implosions with $I \gtrsim 4 \times 10^{14}$ W/cm^2 show that the CBET model overpredicts scattered power, indicating the possible presence of additional mechanisms that increase laser coupling. This discrepancy is resolved by introducing a simple model for clamping the ion-acoustic waves.[16] The clamp model was incorporated in *LILAC* and is discussed in Appendix C.

CBET in OMEGA Implosions

OMEGA implosions are used to validate the accuracy of the CBET model, comparing simulations with observables. Laser coupling is characterized by the time-dependent absorption fraction, inferred from scattered-light measurements and scattered-frequency spectra.[12] The hydrodynamic efficiency of simulated implosions can be constrained by bang time (time of rising of the neutron rate)[17] and shell trajectory measurements (inferred from x-ray self-emission images of implosion targets).[18]

Simulations of implosions at $I \gtrsim 4 \times 10^{14}$ W/cm^2 indicate that the CBET model overpredicts measured scattered light and, as a result, shows earlier bang times. The agreement with experiments can be improved by reducing CBET in simulations. This is accomplished by clamping ion-acoustic waves with the clamp parameter $\left(\tilde{n}_\mathrm{e}/n_\mathrm{e}\right)_\mathrm{cl}$ (Appendix C).[16] Simulations using a single clamp value show good agreement for implosions with different pulse shapes and intensities up to $I \approx 6 \times 10^{14}$ W/cm^2 (for higher intensities, see below). Targets with different ablators, however, require different clamping. For example, it was found that $\left(\tilde{n}_\mathrm{e}/n_\mathrm{e}\right)_\mathrm{cl} \approx 0.1\%$ fits data for plastic and 10% fits data for glass (SiO_2) ablators. In the previous study,[13] CBET was reduced assuming $\xi < 1$ in Eq. (1). This approach is less universal, however, because it requires different ξ depending on the laser energy, pulse shapes, and targets.

The fluid and kinetic versions of the CBET model (Appendices A and B, respectively) were compared using implosions of plastic- and glass-shell targets. Small differences between the results of these versions were observed. The differences are typically smaller than deviations of simulations from measurements. The majority of simulation results discussed here were obtained using the fluid version, which is less computationally expensive.

Figure 129.3 compares measured and simulated scattered-light powers for a triple-picket, warm plastic-shell implosion with a main pulse intensity $I = 4.5 \times 10^{14}$ W/cm^2 (OMEGA shot 63912).[19] The simulations employing the fluid CBET model with $\left(\tilde{n}_\mathrm{e}/n_\mathrm{e}\right)_\mathrm{cl} = 0.1\%$ (red dashed line) accurately reproduce the measured time-dependent scattered power (thick solid line).

Figure 129.4 compares measured [Fig. 129.4(a)] and simulated scattered-light spectra with [Fig. 129.4(b)] and without CBET [Figs. 129.4(c) and 129.4(d)] for the same implosion as in Fig. 129.3. The simulated spectra reproduce all basic features of the measured spectrum: time-dependent frequency shifts during pickets and an initial blue shift and later red shift of scattered light during the main pulse. The details and accuracy of reproduction of the measured spectrum depend, however, on the heat-transport model used and the presence of CBET.[20] The simulations using flux-limited transport [Fig. 129.4(c)] underestimate the blue shifts during the first picket and initial part of the main pulse, indicating that the density and velocity

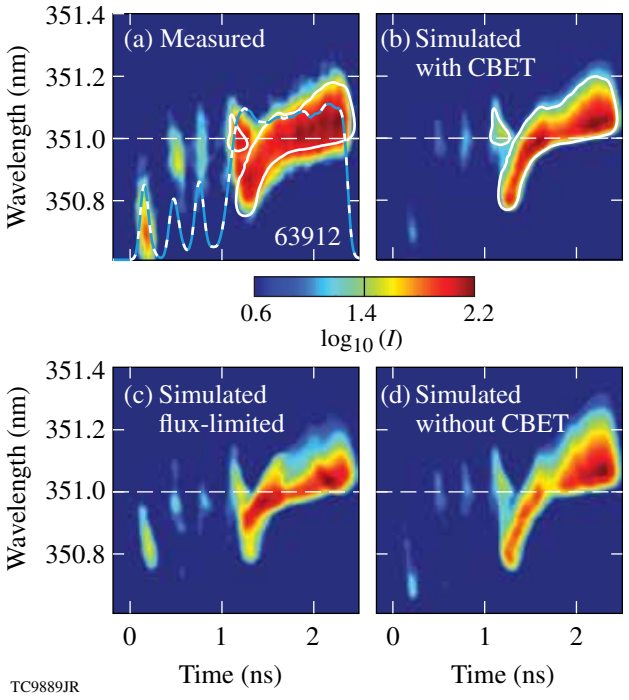

Figure 129.4
(a) Measured and [(b)–(d)] simulated scattered-light spectra for a warm plastic-shell implosion (OMEGA shot 63912). *LILAC* predictions using nonlocal transport and CBET are shown in (b) and simulations without CBET using flux-limited and nonlocal transports are shown in (c) and (d), respectively. The white contours in (a) indicate the shape of the simulated spectrum in (b). The incident light wavelength is represented by the dashed line.

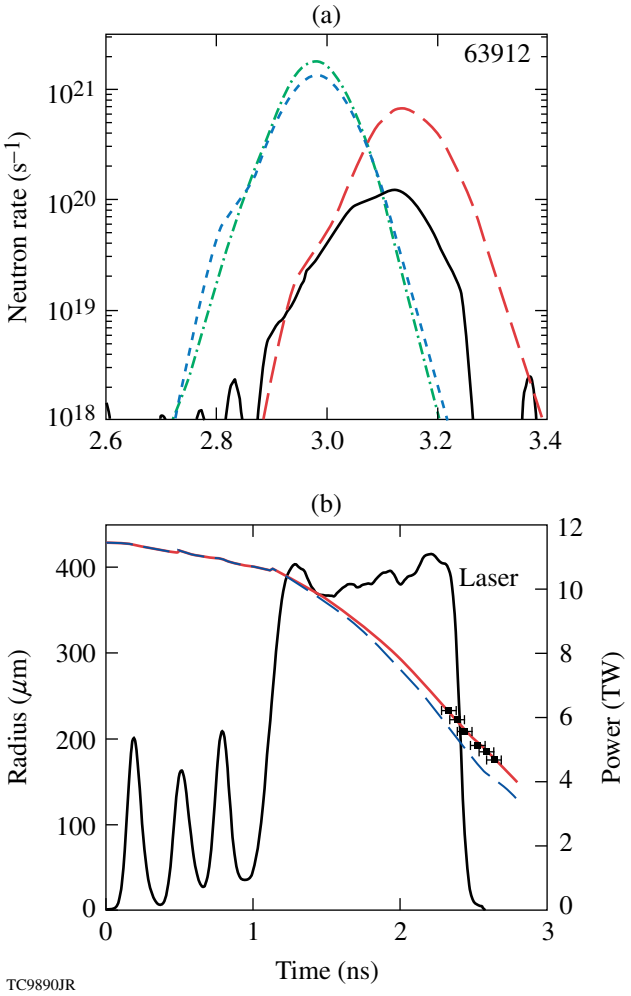

Figure 129.5
(a) Neutron-production history measured (black solid line) and simulated with flux-limited transport (green dashed–dotted line), nonlocal transport (blue dashed line), and nonlocal transport and CBET (red dashed line). The measurements and simulations with CBET show good agreement between bang times, which are estimated as the rise time of the neutron rate. (b) Ablation-front trajectory inferred from x-ray framing camera images[18] (black dots) and the trajectories simulated using nonlocal transport with and without CBET (red solid and blue dashed lines, respectively). The simulations with CBET show good agreement with measurements.

distributions in the target corona are not accurately predicted. The simulations using nonlocal transport without CBET [Fig. 129.4(d)] overestimate the late-time red shift during the main pulse; those with CBET [Fig. 129.4(b)] agree best with the measurements.

The predicted hydrodynamic efficiency of implosions can be verified using measured bang-time and ablation-front trajectories. Figure 129.5(a) shows the measured (solid line) and simulated (blue dashed, green dashed–dotted, and red dashed lines) neutron-production histories for the same implosion as in Fig. 129.3. The experimental bang time for this implosion is about 2.95 ns. The simulations using nonlocal transport and CBET (red dashed line) show bang time coinciding with the measured time within experimental uncertainty. The simulations without CBET, using both flux-limited (green dashed–dotted line) and nonlocal transport (blue dashed line), predict bang times ~200 ps earlier than measured. This is consistent with the higher predicted absorption (or underpredicted scattered-light power) shown in Fig. 129.3.

Figure 129.5(b) shows the measured (squares) and simulated ablation-front trajectories, where the simulations use nonlocal transport with and without CBET (red solid and blue dashed lines, respectively). The trajectory simulated using CBET agrees well with the measured trajectory. The simulations without CBET predict a faster implosion.

Neutron yield is perhaps the most important characteristic of implosions; however, it cannot be directly used to validate the CBET model. This is because the neutron-production

rate strongly depends on temperature and density distributions inside the hot spot.[1] Low-adiabat, warm implosions on OMEGA typically produce yields that are 20% to 25% of *LILAC*-simulated yields. This approximately factor-of-4 yield reduction is unlikely due to inaccuracies in the CBET model and more likely due to asymmetry of implosions. Relative yields, however, are used to study the mitigation of CBET in the **Narrow Beams** section below.

The CBET model was validated using different targets, laser energies, and pulse shapes and shows good and consistent agreement with measurements (see other examples in Ref. 13) up to intensities $I \approx 6 \times 10^{14}$ W/cm^2. At higher intensities of $I \sim 10^{15}$ W/cm^2, the CBET model predicts more scattered light than measured, indicating the presence of an additional absorption mechanism that increases laser coupling. Possible candidates for this mechanism include two-plasmon-decay instability (TPD),[21] which converts incident light into plasma waves with a subsequent dissipation of these waves,[22] and saturation of SBS in intense laser speckles.[23]

Glass-shell implosions were not studied as thoroughly as the plastic-shell implosions discussed above. Only a few implosions were analyzed and were in good agreement with simulations using an appropriate clamp parameter. Figure 129.6 presents an example of a glass-shell implosion that used an 860-μm-diam, 20-μm-thick glass shell filled with 20 atm of D_2 gas. A shaped pulse [the thin solid line in Fig. 129.6(a)] with 26 kJ of energy was used to provide an on-target intensity of $I \approx 10^{15}$ W/cm^2. The best agreement between measured and predicted scattered-light and neutron-production histories [see Figs. 129.6(a) and 129.6(b), respectively] was obtained using simulations with nonlocal transport and CBET, in which $\left(\tilde{n}_e/n_e\right)_{cl} = 10\%$ (compare thick solid and red dashed lines). Simulations without CBET using flux-limited and nonlocal transports [the dashed–dotted and short-dashed lines in Figs. 129.6(a) and 129.6(b)] show significant disagreement with measurements.

Mitigation of CBET

CBET significantly reduces laser coupling in direct-drive implosions. While the laser absorption in a typical OMEGA implosion is reduced by ~10%, the implosion hydrodynamic efficiency is reduced by ~20%. This can be attributed to the laser-deposition area moving outward from the critical surface when CBET is present.[13] Laser coupling can be partially or, in some cases, completely recovered by employing different mitigation techniques for CBET. Three such techniques are considered below. One technique uses narrow laser beams and is extensively tested in OMEGA experiments and simulations. The other two techniques use multicolored lasers and high-Z dopant ablators.

1. Narrow Beams

The idea of using narrow beams to mitigate CBET is illustrated in Fig. 129.2, which shows a ray geometry with the most-efficient energy transfer. By narrowing the beams, one can eliminate edge-beam rays that seed CBET. Figure 129.7 quantitatively illustrates the contribution of different parts of

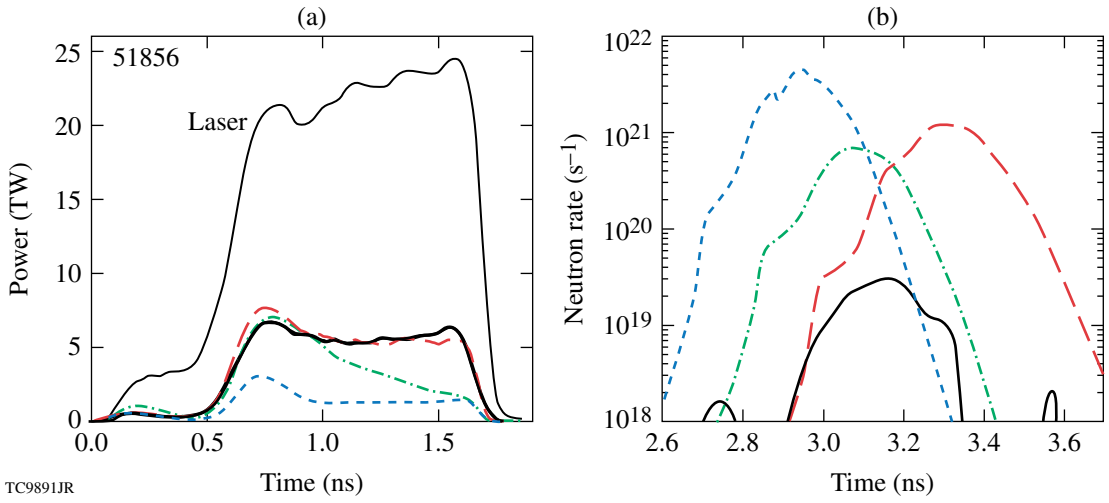

Figure 129.6
(a) Reflected-light power history in a glass-shell implosion (OMEGA shot 51856). (For notations see Fig. 129.3.) (b) Neutron-production history measured and simulated. [For notations see Fig. 129.5(a).] Note good agreement of the measured scattered light and bang time in (a) and (b) with the simulations with CBET and poor agreement with the simulations without CBET.

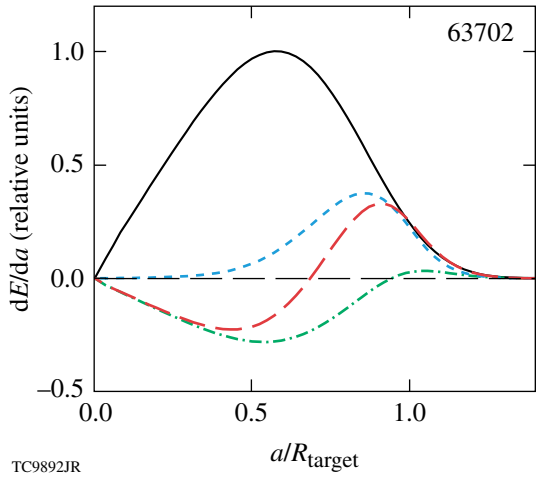

Figure 129.7
Distributions of time-integrated energy transferred between crossing beams as functions of the relative ray impact parameter a/R_{target} in a plastic-shell implosion (OMEGA shot 63702). Distribution of the incident energy is shown by the black solid line. Distribution of the transferred energy for the incoming trajectories is shown by the green dashed–dotted line, for the outgoing trajectories by the blue dashed line, and for whole trajectories (including the incoming and out-going parts) by the red dashed line. The negative dE/da corresponds to energy losses and the positive one to energy gains.

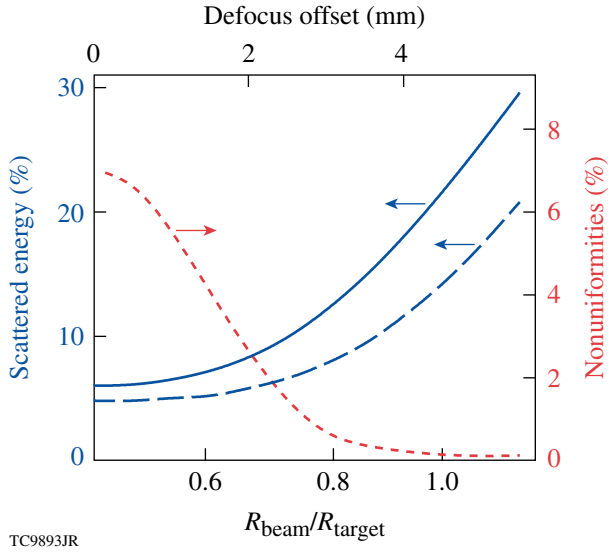

Figure 129.8
Predicted scattered energy and deposition nonuniformities (rms) as functions of R_{beam}/R_{target} in plastic-shell implosions. The scattered energy is normalized to the incident energy. The simulated energies with and without CBET are shown by the blue solid and dashed lines, respectively. The deposition nonuniformities (red dashed line) are calculated using the OMEGA beam-port geometry and time averaging over the whole laser pulse.

beams to CBET. This figure shows the simulated distributions of energy transferred to (when the sign of dE/da is positive) or from (when the sign is negative) light rays with an impact parameter a. The outgoing rays (blue dashed line) always gain energy, and the gain reaches the maximum for rays with a/R_{target} from ~0.7 to 1.1. The incoming rays (green dashed–dotted line) mostly lose energy, transferring it to outgoing rays. This loss takes place for a/R_{target} from 0 to ~0.9 and is peaked at $a/R_{target} \sim 0.5$. The incoming rays with $a/R_{target} \gtrsim 0.9$ gain some energy, but this gain is not significant. The rays with $0.5 \lesssim a/R_{target} \sim 0.9$ lose energy as they travel toward the target and gain it on the way out. The cumulative effect of CBET for the whole ray trajectory (including the incoming and outgoing parts) is shown by the red dashed line in Fig. 129.7. The rays with $a/R_{target} < 0.7$ overall lose energy and the rays with $a/R_{target} > 0.7$ gain energy. This suggests that by eliminating rays with $a/R_{target} > 0.7$, one can completely suppress CBET.

Figure 129.8 shows simulation results for implosions at the same conditions [similar to the one shown in Fig. 129.1(c)] except using different beam radii R_{beam}, which are defined to encircle 95% energy. The beam radius is changed by defocusing beams with an assumed profile $I(r) \sim \exp\left[-\left(r/r_0\right)^{2.1}\right]$, where $r_0 = 135\ \mu$m. The ratio R_{beam}/R_{target} is varied from 0.5 to 1.1. The simulations including CBET (solid line) show a decrease in scattered energy when R_{beam}/R_{target} is decreased. The scattered energy in the simulations without CBET (blue dashed line) is reduced as well. This is because smaller beams provide illumination of the target surface by more-normal incident light. Such light penetrates deeper into the target corona and is absorbed more efficiently. Therefore, the benefits of using smaller beams include two aspects: reducing CBET and increasing absorption as a result of more-normal incident light.

The smaller beams can have a negative effect on implosion performance because of increasing beam-overlap nonuniformities. Two-dimensional (2-D) hydrodynamic simulations using the code *DRACO*[24] predict nearly symmetric implosions and small reduction in neutron yield for R_{beam}/R_{target} from ~1 to 0.8 [see Figs. 129.9(a) and 129.9(b)]. Simulations assuming $R_{beam}/R_{target} \lesssim 0.7$ show significantly distorted targets at maximum compression and reduced neutron yields [by a factor of 2 or more, see Fig. 129.9(c)]. These 2-D results agree with the simple calculations of deposition nonuniformities presented in Fig. 129.8 (red dashed line). The calculations predict a significant increase in the nonuniformities in the range of R_{beam}/R_{target} from 0.8 to 0.7. Therefore, these results suggest

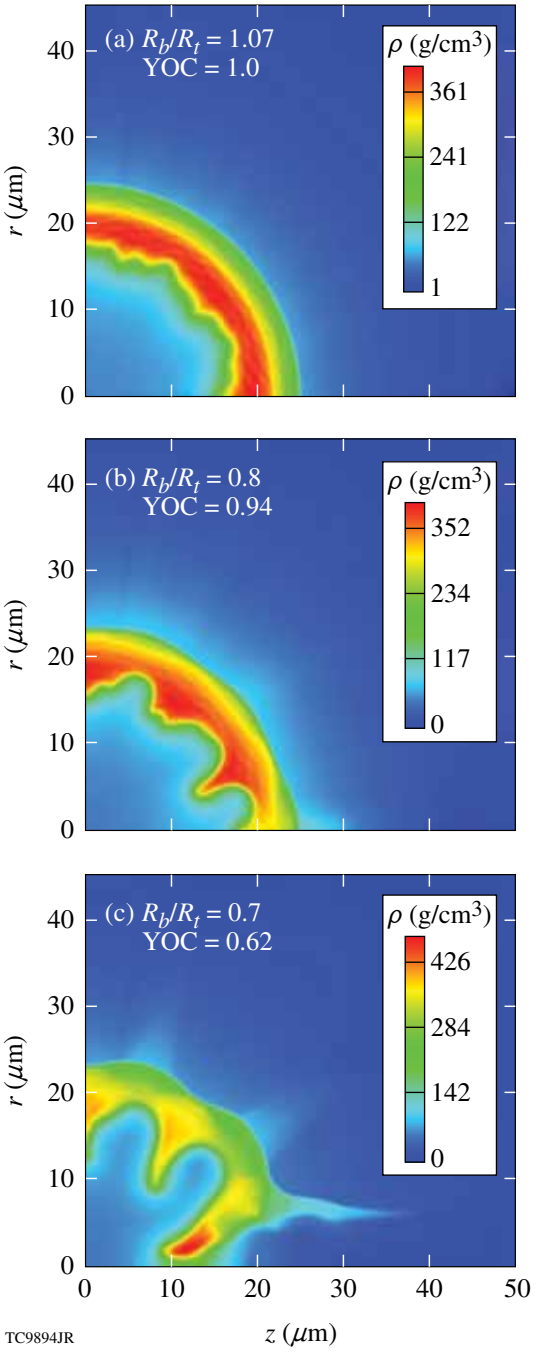

Figure 129.9
Density distributions at maximum compression from 2-D hydrodynamic simulations of implosion targets illuminated by different-sized laser beams: (a) $R_{beam}/R_{target} = 1.07$, (b) 0.8, and (c) 0.7. Beam-overlap nonuniformities in the case of small R_{beam}/R_{target} result in asymmetric implosions and degradation of neutron yield. Each simulation shows yield over clean (YOC, which is the 2-D yield normalized to the 1-D yield).

an optimum $R_{beam}/R_{target} \sim 0.8$ that balances the reduction of CBET and increase of beam-overlap nonuniformities.

Two sets of implosion experiments on OMEGA were performed to investigate the effects of narrow beams. These experiments used triple-picket pulses with a peak overlap intensity $I \approx 4.5 \times 10^{14}$ W/cm^2 that drive targets with an adiabat[a] $\alpha \approx 4$. The primary goal of the first set of experiments is to demonstrate enhanced laser coupling in implosions with narrow-beam illumination.[25] The experiments use fixed-diameter (860-μm) nominal OMEGA targets and variable-diameter beams. The beam diameters are varied by defocusing beams obtained using small distributed phase plates (DPP's).[26] Figure 129.10 shows the measured beam profiles for different defocus offsets corresponding to different R_{beam}/R_{target}.

The experiments with variable beams use a range of R_{beam}/R_{target} from 0.5 to 1.09. Figure 129.11 compares measured and simulated scattered-light spectra for wide and narrow beams ($R_{beam}/R_{target} = 1.0$ and 0.5, respectively). Note the good agreement between the simulated and measured spectra. The implosion with narrow beams and reduced CBET shows the presence of the red-shifted part of the spectrum, which corresponds to light that deeply penetrates inside the target corona.

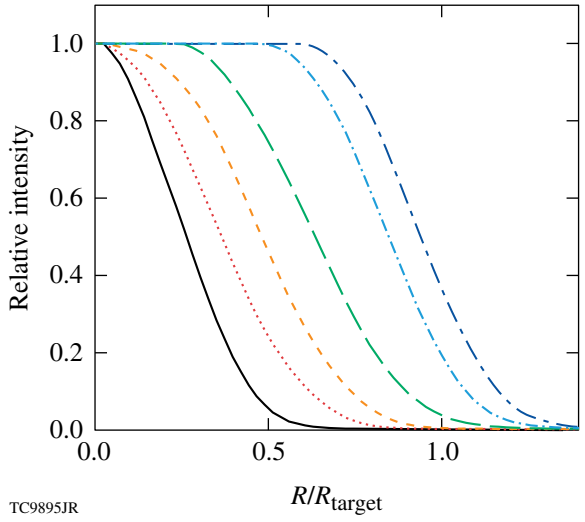

Figure 129.10
Measured profiles of beams with small distributed phase plates (DPP's) at different defocus offsets. The beam profile at best focus is shown by the solid line and wider beams have increasing defocus offsets. These profiles correspond to $R_{beam}/R_{target} = 0.5, 0.65, 0.74, 0.88, 1.0$, and 1.09 (from narrow to wide, respectively).

[a]The ratio of the pressure in an imploding shell to the Fermi-degenerate pressure.

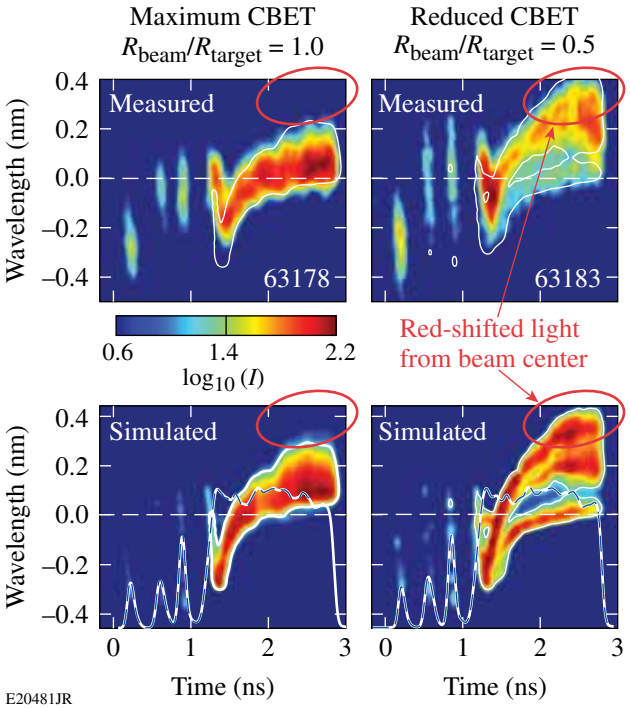

Figure 129.11
Measured and simulated scattered-light spectra for plastic-shell implosions using wide and narrow laser beams (R_{beam}/R_{target}=1.0 and 0.5, respectively). The implosion with narrow beams recovers the red-shifted part of the spectrum (shown by the red ovals), which corresponds to rays that deeply penetrate into the target corona. These rays are not present in the implosion with wide beams $\left(R_{beam}/R_{target} = 1.0\right)$ because of CBET. Note good agreement between measured and simulated spectra.

The implosions with wide beams $\left(R_{beam}/R_{target} = 1.0\right)$ do not show such red-shifted parts, indicating that deeply penetrated light has been scattered.

Figure 129.12 shows the scattered-light fractions in implosions with different R_{beam}/R_{target}. The measured fractions (solid red circles with error bars) are reduced in implosions with narrower beams, in agreement with simulations that include CBET (triangles and solid line). The reduction in scattered light and corresponding increase in absorption result in earlier bang times in implosions with narrow beams. Figure 129.13 summarizes the bang-time measurements and shows good agreement between the measurements (solid circles) and simulations with CBET (triangles).

The earlier bang times correspond to higher-velocity implosions in agreement with the results of the ablation-front trajectory measurements. Figure 129.14(a) shows two examples of trajectories both measured (squares) and simulated with CBET (lines), for R_{beam}/R_{target}=1.0 and 0.75. The targets illuminated with smaller beams clearly demonstrate higher velocity. Figure 129.14(b) compares the implosion velocities inferred from the measured trajectories (squares) and those simulated with and without CBET (triangle and diamonds, respectively).

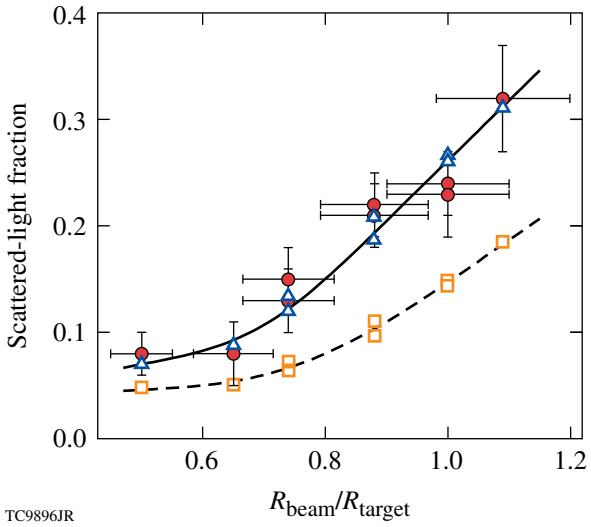

Figure 129.12
Scattered-light fractions in implosion experiments using variable-diameter beams. Measurements corresponding to implosions with different R_{beam}/R_{target} are shown by the solid red circles with error bars. Simulation results with and without CBET are shown by the blue open triangles and orange open squares and approximated by the solid and dashed lines, respectively. The measured fractions are in good agreement with the simulated ones including CBET.

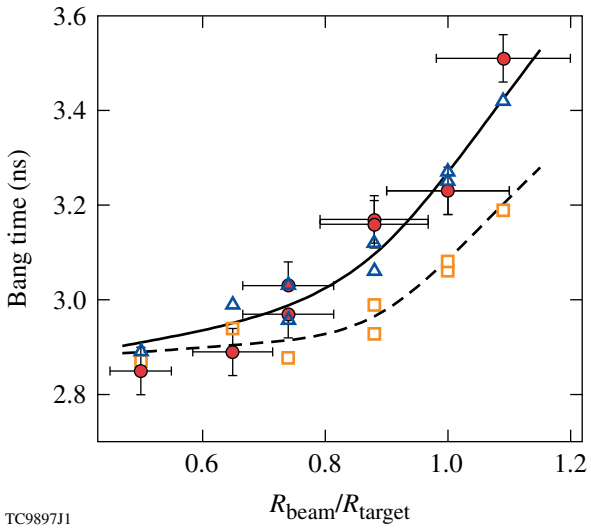

Figure 129.13
Bang times in implosion experiments using variable-diameter beams. (For notations see Fig. 129.12.) The measured bang times are in good agreement with the simulated ones including CBET.

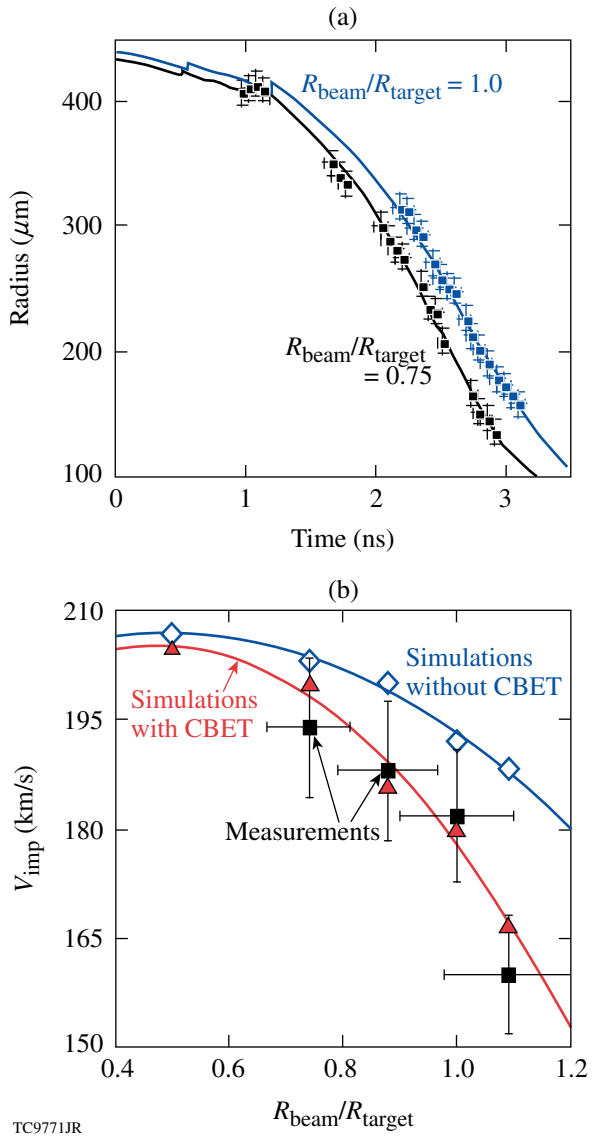

Figure 129.14
(a) Ablation-front trajectories inferred from x-ray framing camera images (squares) and simulated (lines) in implosions with wide and narrow beams (R_{beam}/R_{target} = 1.0 and 0.75, respectively). (b) Measured (squares) and simulated with (red line and triangles) and without (blue line and diamonds) CBET implosion velocities as functions of R_{beam}/R_{target}. Higher implosion velocities are achieved with smaller beams in both measurements and simulations.

Higher implosion velocities are achieved with smaller beams in both measurements and simulations, and the simulations with CBET show good agreement with the measured data (triangles and squares).

The described experiments cannot, however, be used to demonstrate improvements in neutron yield because of the significant level of single-beam nonuniformity (imprint) when using beams smaller than target diameters. As a result, measured neutron yields are reduced by a factor of 5 to 10 with respect to the yields in similar implosions but illuminated with best uniformity. To address the issue of yield improvement, additional experiments employing uniform beams with standard OMEGA SG4 DPP's, polarization smoothing (PS),[27] and smoothing by spectral dispersion (SSD)[28] were performed. The SG4 DPP's with PS and SSD are optimized for the on-target uniformity in the case of 860-μm-diam targets. These experiments vary R_{beam}/R_{target} by changing the target size. The three target diameters used—860, 950, and 1000 μm—correspond to R_{beam}/R_{target} = 0.97, 0.88, and 0.83, respectively. This range of R_{beam}/R_{target} was narrower than that used in the previous set of experiments but covers the important region around $R_{beam}/R_{target} \sim 0.8$, where significant changes in neutron yield are expected because of beam-overlap nonuniformities. To reduce the effects of small-scale single-beam imprinting, the implosions were designed to be robust to Rayleigh–Taylor instability,[29] having relatively low in-flight aspect ratio[1] IFAR ≈ 30, which was about the same for all targets.

Figure 129.15(a) shows measured neutron yields that were normalized to simulations including CBET (circles) as a function of R_{beam}/R_{target}. If all nonuniformity sources are kept constant for different R_{beam}/R_{target}, then expected measured yields normalized to predicted yields should be independent of R_{beam}/R_{target}. This is shown in Fig. 129.15(a) by the dashed line. The data follow this line down to $R_{beam}/R_{target} \approx 0.86$. For smaller R_{beam}/R_{target}, the relative yields drop because of enhanced beam-overlap nonuniformity. Figure 129.15(b) demonstrates the benefit of using narrow beams, showing the same measurements as in Fig. 129.15(a) but normalized to simulations without CBET and assuming R_{beam}/R_{target} = 1. Such a normalization uses "clean" yields without both beneficial effects of narrow beams: reduced CBET and more-normal light illumination. The relative yields in Fig. 129.15(b) show an increase by a factor of ~1.5 for smaller beams with the maximum yield at $R_{beam}/R_{target} \approx 0.88$. Further reduction of R_{beam}/R_{target} results in a reduction in yields, indicating that beam-overlap nonuniformities dominate the target performance. These data demonstrate the beneficial effects of reducing R_{beam}/R_{target} from ~1 down to ≈0.85.

2. Multicolored Lasers

The efficiency of CBET is determined by the SBS gain, which is resonant and sensitive to a wavelength separation $\Delta\lambda$ between interacting beams [see Eqs. (A2) and (B8) in Appendices A and B]. Changing the wavelengths of beams affects the SBS gain and, therefore, increases or decreases CBET. Benefits of a wavelength separation technique were recently demon-

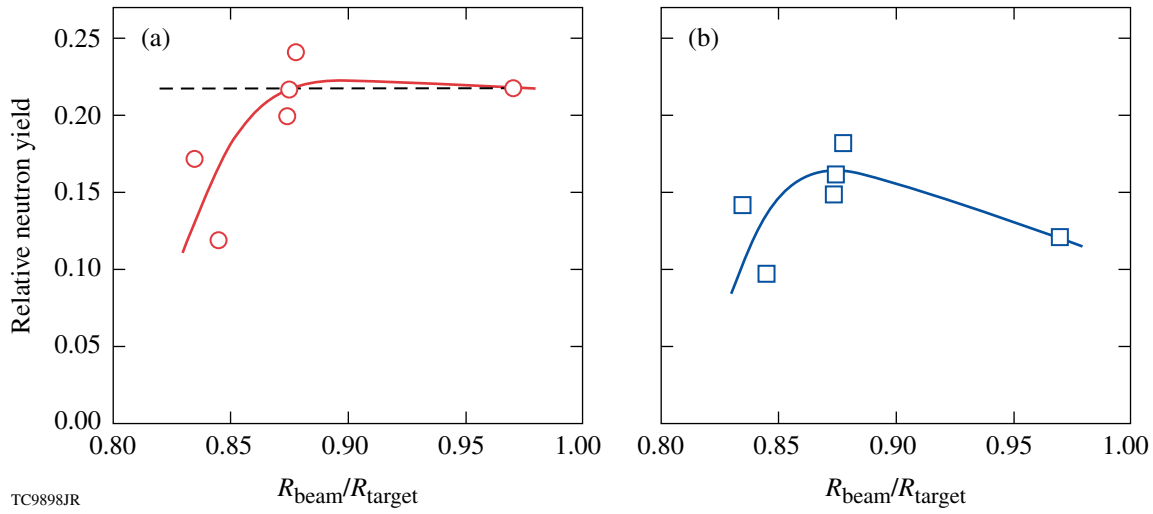

Figure 129.15
Relative neutron yields in experiments using uniform beams and variable-diameter targets. (a) Measured yields normalized to simulations with CBET (circles). (b) The same yields as in (a) but normalized to simulations without CBET and having $R_{beam}/R_{target} = 1$ (squares). The solid lines in (a) and (b) approximate the data points. The dashed line in (a) shows an expected constant relative yield in the case of similar uniformity. The drop of relative yields at $R_{beam}/R_{target} < 0.86$ is due to an increase in beam-overlap nonuniformities at small R_{beam}/R_{target}.

strated in indirect-drive implosions on the NIF.[30] The applied $\Delta\lambda$ in these implosions is relatively small (up to ~3 Å in UV light). Mitigation of CBET in direct-drive implosions requires a larger $\Delta\lambda$ among beams to eliminate the coupling resonances.[13]

To illustrate the CBET mitigation effect in direct-drive experiments, consider the simplest case of a laser system operating on two subsets of lasers with wavelengths separated by $\Delta\lambda$. These wavelengths can be distributed among different beams, or each beam can include both wavelengths (e.g., as a uniform mix, or one wavelength at the center and the other at the edge of a beam). For a large separation,

$$\Delta\lambda \gg \lambda_L\left(c_a/c\right) \sim 5\,\text{Å}, \tag{2}$$

one subset does not "see" the presence of the other and there is no interaction between them [i.e., gain length L_{ij} becomes large, see Eq. (1)]. Here, $c_a = \sqrt{\left(ZT_e + 3T_i\right)/M_i}$ is the ion-acoustic sound speed, Z is the ionization, M_i is the ion mass, and T_e and T_i are the electron and ion temperatures, respectively. In this case of large $\Delta\lambda$, CBET occurs only within each subset and, therefore, the total CBET is reduced by 1/2 with respect to the case of $\Delta\lambda = 0$. [This reduction is equivalent to assuming $\xi = 1/2$ in Eq. (1)]. Figure 129.16 shows simulated absorption fractions (solid line) for a plastic-shell implosion driven by two-color illumination as a function of $\Delta\lambda$. The absorption fraction changes very little for $\Delta\lambda < 3$ Å and increases significantly (by up to 10%) for $\Delta\lambda > 5$ Å. The dashed line in Fig. 129.16 shows the asymptotic limit of 1/2 CBET. In general, an N-color separation can result in the asymptotic reduction of CBET by a factor of $1/N$.

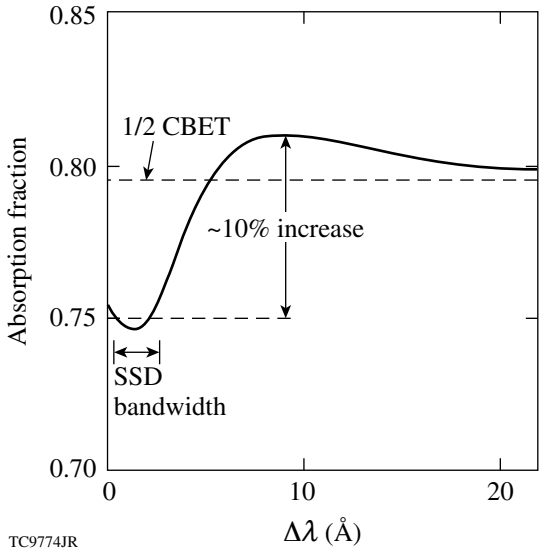

Figure 129.16
Simulated absorption fraction (solid line) as a function of the wavelength separation $\Delta\lambda$ in a plastic-shell implosion using two-color light. The upper dashed line corresponds to 50%-reduced CBET using one-color light.

As a practical application of laser drive using two or more colors distributed among different beams, a uniform spatial mix of these beams is suggested. More beams will provide a better

mixing uniformity, and using more colors is more beneficial in reducing CBET.

The results discussed in this section neglect the effects of TPD instability and laser speckles. The presence of speckles and anomalous absorption resulting from TPD can significantly modify the results shown in Fig. 129.16 that were obtained using a simple linear theory and the planar wave approximation [Eq. (1)]. Implosion experiments on OMEGA suggest that both these mechanisms, TPD and speckles, are not important at intensities $I \lesssim 6 \times 10^{14}$ W/cm^2 (see **CBET in OMEGA Implosions**, p. 3). One can expect that the multicolored technique can work in implosions within this range of intensities, and more theoretical study is required to accurately predict laser coupling at higher intensities.

3. High-Z Dopants

The dependence of CBET on plasma ion charge Z is complex (see Appendices A and B). Ion charge also affects other aspects of implosion physics: in particular, heat transport and hydrodynamics.

Figure 129.17 presents simulation results for implosion plastic shells with the varied dopant concentration of Ge: 0%, 1%, and 4%. The absorption fraction grows with increased Ge concentration in simulations both including (circles) and not including (triangles) CBET. The simulations including CBET show an ~6% larger increase in absorption for 4%-Ge doping. These indicate a reduction of CBET in implosions with doped ablators, which is mainly caused by increased coronal electron temperature in these implosions. On the other hand, because of less-effective heat transport in a higher-Z coronal plasma, the hydrodynamic efficiency of these implosions is reduced. The simulations show that 4%-Ge dopant reduces the hydrodynamic efficiency by ~5% (see diamonds in Fig. 129.17), reducing the overall benefit of using high-Z dopants in direct-drive implosions.

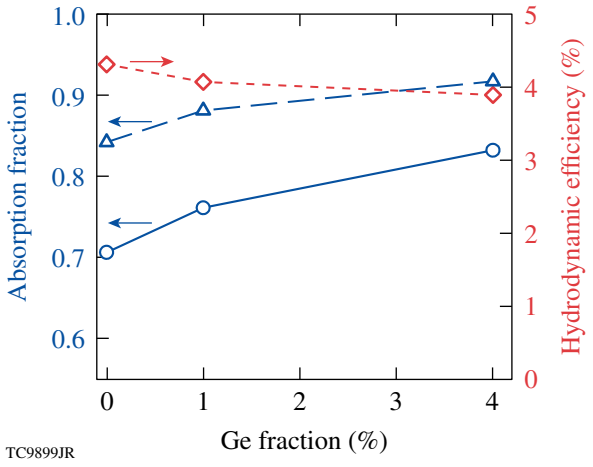

Figure 129.17
Simulated absorption fractions with (solid line and circles) and without (blue dashed line and triangles) CBET for imploded plastic shells with different fractions of doped Ge. The effect of CBET is reduced in implosions with a higher-Ge dopant. Hydrodynamic efficiency in implosions with CBET (red dashed line and diamonds) is decreased with increasing-Ge dopant.

Conclusions

CBET can significantly reduce the performance of direct-drive ICF implosions. It is responsible for about 10% reduction of laser absorption and about 20% reduction of hydrodynamic efficiency in implosion experiments on OMEGA. CBET is observed in time-resolved, scattered-light spectra as a suppression of red-shifted light during the main laser drive. This light is present in simulations without CBET, indicating that CBET mostly scatters the center-beam incoming light, which otherwise would penetrate to higher-density corona regions, where it is reflected with the maximum red shift.

Two models of CBET have been developed and implemented into the laser-absorption package of the 1-D hydrodynamic code *LILAC*: a fluid model (Appendix A) and a kinetic model (Appendix B), assuming spherically symmetric laser illumination of implosion targets. Both models were extensively tested using different OMEGA implosions with varied laser energies, pulse shapes, and target structure and composition. These demonstrated good agreement between model predictions and observables, which include scattered-light spectra and power, bang times, shell trajectories, and neutron yields (see **CBET in OMEGA Implosions**, p. 3). The fluid and kinetic models show quite similar results between each other.

The performance of direct-drive targets can be improved by mitigating CBET. This article considered three mitigation techniques: using narrow beams, using multicolored lasers, and high-Z–doped ablators. The first technique is efficient in improving laser coupling. The implosion experiments on OMEGA show a significant decrease of scattered-light power, earlier bang times, and an increase in implosion velocity (see Figs. 129.12–129.14) when reducing the beam radius. The small beams introduce more beam-overlap nonuniformities that reduce implosion performance by decreasing neutron yields. The experiments on OMEGA suggest an optimum $R_{\text{beam}}/R_{\text{target}} \sim 0.85$ that maximizes the performance by balancing CBET with the effects of beam-overlap nonuniformities (see Fig. 129.15).

Simulations suggest that using multicolored lasers can be another efficient technique to mitigate CBET. By splitting light into N separate colors, CBET can be reduced by a factor of ~1/N. This technique requires, however, relatively large wavelength separations $\Delta\lambda$ [Eq. (2)], which probably cannot be achieved on the OMEGA and NIF lasers. To utilize the multicolored split technique, future direct-drive laser systems should be designed to use subsets of lasers operating at different wavelengths. Such systems can benefit from using the narrow-beam technique discussed above and using many separate beams to reduce beam-overlap nonuniformity.

Test simulations of imploded plastic shells doped with high-Z elements reveal no advantages to using this technique. Unless the simulations show a relative reduction in CBET and improvement in laser coupling in the case of Ge-doped targets, the overall implosion performance suffers because of the reduction in heat transport in a higher-Z coronal plasma (see Fig. 129.17).

ACKNOWLEDGMENT

This work was supported by the US DOE Office of Inertial Confinement Fusion under Cooperative Agreement No. DE-FC52-08NA28302, the University of Rochester, and the New York State Energy Research and Development Authority. The support of DOE does not constitute an endorsement by DOE of the views expressed in this article.

Appendix A: Fluid Equations

The fluid approach for the CBET model is based on the electron-density equation, the equation of motion for ions, and the wave equation for laser light.[8] The steady-state interaction of two light waves of the same linear polarization and an ion-acoustic wave is considered in the strong damping limit. Details of derivation of the equation for the probe-light intensity I_{probe} are given in Ref. 9; this equation can be written as

$$\frac{\mathrm{d}I_{\text{probe}}}{\mathrm{d}\ell} = \frac{I_{\text{probe}}}{L}, \tag{A1}$$

where ℓ is the probe-light path,

$$L^{-1} = \frac{\pi}{\lambda_L}\frac{n_e/n_{cr}}{\sqrt{1-n_e/n_{cr}}} \times \frac{1}{\left[\tilde{\nu}_a^2\eta^2+\left(1-\eta^2\right)^2\right]^{1/2}}\left(\frac{I_{\text{pump}}}{I_{\text{probe}}}\right)^{1/2}\left|\frac{\tilde{n}_e}{n_e}\right| \tag{A2}$$

is the SBS spatial gain rate,

$$\left|\frac{\tilde{n}_e}{n_e}\right| = \frac{e^2\lambda_L^2}{\pi m_e^2 c^3}\frac{Z}{c_a^2}\left(\frac{m_e}{M_i}\right)\frac{\left(I_{\text{probe}}I_{\text{pump}}\right)^{1/2}}{\left[\tilde{\nu}_a^2\eta^2+\left(1-\eta^2\right)^2\right]^{1/2}} \tag{A3}$$

is the relative amplitude of electron-density perturbations in the ion-acoustic wave, and I_{pump} is the pump-light intensity. In Eqs. (A2) and (A3), $\tilde{\nu}_a = \nu_a/k_a c_a$ is the dimensionless damping of ion-acoustic waves.[31] The variable η includes the dependency on geometry and frequency of the interacting waves,

$$\eta = \frac{\left(\mathbf{k}_a\cdot\mathbf{u}\right)}{k_a c_a} - \frac{\omega_a}{k_a c_a}, \tag{A4}$$

where $\mathbf{u}$ is the flow velocity and ω_a and $\mathbf{k}_a$ are the ion-acoustic wave frequency and wave vector, respectively. The interacting waves satisfy the following three-wave matching conditions:

$$\omega_a = \omega_{\text{probe}} - \omega_{\text{pump}} \tag{A5}$$

and

$$\mathbf{k}_a = \mathbf{k}_{\text{probe}} - \mathbf{k}_{\text{pump}}. \tag{A6}$$

The frequency changes in probe and pump light are calculated considering the plasma expansion and Doppler effects.[32] More details of implementation of Eq. (A1) into *LILAC* can be found in Ref. 13.

Appendix B: Kinetic Equations

The electron-density perturbation $\tilde{n}_e$ in an ion-acoustic wave is calculated using the linearized Vlasov equations for electrons and ions and the Poisson equation for the self-consistent electrostatic potential. One gets[33]

$$\tilde{n}_e = \frac{k_a^2\phi_p}{4\pi e}\frac{\chi_e\left(1+\Sigma_i\chi_i\right)}{1+\chi_e+\Sigma_i\chi_i}, \tag{B1}$$

where the summation is taken over all ion species, ϕ_p is the beat ponderomotive potential of interacting light waves, χ_e and χ_i are the electron and ion linear susceptibilities, respectively, which can be written as follows:

$$\chi_e \approx \omega_{pe}^2/k_a^2 v_{T_e}^2, \tag{B2}$$

$$\chi_{\mathrm{i}} = \frac{\omega_{\mathrm{pi}}^2}{k_{\mathrm{a}}^2 v_{\mathrm{T_i}}^2}\left(1 + \frac{x}{\sqrt{\pi}}\int_{-\infty}^{\infty}\frac{e^{-z^2}}{z-x}\mathrm{d}z\right), \tag{B3}$$

and

$$x = \frac{\omega_{\mathrm{a}} + i\nu_{\mathrm{ie}} - \left(\mathbf{k}_{\mathrm{a}}\cdot\mathbf{u}\right)}{\sqrt{2}\,k_{\mathrm{a}} v_{\mathrm{T_i}}}. \tag{B4}$$

In the above equations, $v_{\mathrm{T_e}} = \left(T_{\mathrm{e}}/m_{\mathrm{e}}\right)^{1/2}$ and $v_{\mathrm{T_i}} = \left(T_{\mathrm{i}}/M_{\mathrm{i}}\right)^{1/2}$ are the electron and ion thermal velocities, respectively; ν_{ie} is the ion–electron collisional frequency; and $\omega_{\mathrm{pe}} = \left(4\pi \mathrm{e}^2 n_{\mathrm{e}}/m_{\mathrm{e}}\right)^{1/2}$ and $\omega_{\mathrm{pi}} = \left(4\pi \mathrm{e}^2 Z n_{\mathrm{e}}/M_{\mathrm{i}}\right)^{1/2}$ are the electron and ion plasma frequencies, respectively.

The equation for light waves is

$$\frac{\partial^2 \mathbf{A}}{\partial t^2} - c^2\Delta\mathbf{A} + \omega_{\mathrm{pe}}^2\left(1 + \frac{\tilde{n}_{\mathrm{e}}}{n_{\mathrm{e}}}\right)\mathbf{A} = 0. \tag{B5}$$

Assuming that the probe and pump waves are *s*-polarized, the corresponding component of the vector potential **A** can be expressed as

$$A(\mathbf{r},t) = \frac{1}{2}\Big[A_{\mathrm{probe}}\exp\left(-i\omega_{\mathrm{probe}}t + i\mathbf{k}_{\mathrm{probe}}\mathbf{r}\right) + A_{\mathrm{pump}}\exp\left(-i\omega_{\mathrm{probe}}t + i\mathbf{k}_{\mathrm{probe}}\mathbf{r}\right) + \mathrm{c.c.}\Big]. \tag{B6}$$

Then the potential ϕ_{p} takes the form

$$\phi_{\mathrm{p}} = -\frac{\mathrm{e}}{2m_{\mathrm{e}}c^2}A_{\mathrm{probe}}A_{\mathrm{pump}}^{*}. \tag{B7}$$

Substituting Eq. (B1) into Eq. (B5), and using Eqs. (B6) and (B7), and the definition $A^2 = 8\pi cI/\omega_{\mathrm{L}}^2$, where ω_{L} in the laser frequency, one obtains the equation for the probe light-intensity I_{probe}, similar in form to Eq. (A1), in which

$$L^{-1} = \frac{\pi}{\lambda_L}\frac{n_{\mathrm{e}}/n_{\mathrm{cr}}}{\sqrt{1 - n_{\mathrm{e}}/n_{\mathrm{cr}}}}\frac{\mathrm{Im}(B)}{|B|}\left(\frac{I_{\mathrm{pump}}}{I_{\mathrm{probe}}}\right)^{1/2}\left|\frac{\tilde{n}_{\mathrm{e}}}{n_{\mathrm{e}}}\right|, \tag{B8}$$

$$\left|\frac{\tilde{n}_{\mathrm{e}}}{n_{\mathrm{e}}}\right| = \frac{\mathrm{e}^2\lambda_L^2}{\pi m_{\mathrm{e}}^2 c^3}\frac{k_{\mathrm{a}}^2}{\omega_{\mathrm{pe}}^2}\frac{\left(I_{\mathrm{probe}}I_{\mathrm{pump}}\right)^{1/2}}{|B|}, \tag{B9}$$

and

$$B = \frac{1 + \chi_{\mathrm{e}} + \Sigma_{\mathrm{i}}\chi_{\mathrm{i}}}{\chi_{\mathrm{e}}\left(1 + \chi_{\mathrm{i}}\right)}. \tag{B10}$$

The interacting ion-acoustic and light waves satisfy the matching conditions given by Eqs. (A5) and (A6). Equations (B8) and (B9) substitute the fluid approach equations [Eqs. (A2) and (A3)] in the numerical procedure when the kinetic option is chosen.

Appendix C: The Clamp Model

The amplitude of ion-acoustic waves can experience a nonlinear saturation, depending on the laser intensities and ion composition of a plasma. This saturation can reduce an energy transfer predicted by the CBET model. A simple model for clamping of ion-acoustic waves was proposed[16] that limits the amplitude of electron-density perturbations $\left|\tilde{n}_e/n_e\right|$ defined by Eqs. (A3) and (B9) for the fluid and kinetic models, respectively. Specifically, the corresponding values of $\left|\tilde{n}_e/n_e\right|$ in Eqs. (A2) and (B8) are substituted by

$$\left\langle\frac{\tilde{n}_{\mathrm{e}}}{n_{\mathrm{e}}}\right\rangle = \min\left[\left|\frac{\tilde{n}_{\mathrm{e}}}{n_{\mathrm{e}}}\right|, \left(\frac{\tilde{n}_{\mathrm{e}}}{n_{\mathrm{e}}}\right)_{\mathrm{cl}}\right]. \tag{C1}$$

The clamping parameter $\left(\tilde{n}_{\mathrm{e}}/n_{\mathrm{e}}\right)_{\mathrm{cl}}$ is determined from experiments.

REFERENCES

1. J. D. Lindl, *Inertial Confinement Fusion: The Quest for Ignition and Energy Gain Using Indirect Drive* (Springer-Verlag, New York, 1998). pp. 39 and 61.
2. R. L. McCrory, D. D. Meyerhofer, R. Betti, R. S. Craxton, J. A. Delettrez, D. H. Edgell, V. Yu Glebov, V. N. Goncharov, D. R. Harding, D. W. Jacobs-Perkins, J. P. Knauer, F. J. Marshall, P. W. McKenty, P. B. Radha, S. P. Regan, T. C. Sangster, W. Seka, R. W. Short, S. Skupsky, V. A. Smalyuk, J. M. Soures, C. Stoeckl, B. Yaakobi, D. Shvarts, J. A. Frenje, C. K. Li, R. D. Petrasso, and F. H. Séguin, Phys. Plasmas **15**, 055503 (2008).
3. V. N. Goncharov, T. C. Sangster, T. R. Boehly, S. X. Hu, I. V. Igumenshchev, F. J. Marshall, R. L. McCrory, D. D. Meyerhofer, P. B. Radha, W. Seka, S. Skupsky, C. Stoeckl, D. T. Casey, J. A. Frenje, and R. D. Petrasso, Phys. Rev. Lett. **104**, 165001 (2010).
4. S. Atzeni and J. Meyer-ter-Vehn, *The Physics of Inertial Fusion: Beam Plasma Interaction, Hydrodynamics, Hot Dense Matter*, International Series of Monographs on Physics (Clarendon Press, Oxford, 2004), p. 4750.

5. J. Paisner *et al.*, Laser Focus World **30**, 75 (1994).

6. T. R. Boehly, D. L. Brown, R. S. Craxton, R. L. Keck, J. P. Knauer, J. H. Kelly, T. J. Kessler, S. A. Kumpan, S. J. Loucks, S. A. Letzring, F. J. Marshall, R. L. McCrory, S. F. B. Morse, W. Seka, J. M. Soures, and C. P. Verdon, Opt. Commun. **133**, 495 (1997).

7. S. Skupsky, J. A. Marozas, R. S. Craxton, R. Betti, T. J. B. Collins, J. A. Delettrez, V. N. Goncharov, P. W. McKenty, P. B. Radha, T. R. Boehly, J. P. Knauer, F. J. Marshall, D. R. Harding, J. D. Kilkenny, D. D. Meyerhofer, T. C. Sangster, and R. L. McCrory, Phys. Plasmas **11**, 2763 (2004).

8. W. L. Kruer, *The Physics of Laser-Plasma Interactions*, Frontiers in Physics, Vol. 73, edited by D. Pines (Addison-Wesley, Redwood City, CA, 1988), pp. 46 and 88.

9. C. J. Randall, J. R. Albritton, and J. J. Thomson, Phys. Fluids **24**, 1474 (1981).

10. R. C. Malone, R. L. McCrory, and R. L. Morse, Phys. Rev. Lett. **34**, 721 (1975).

11. V. N. Goncharov, T. C. Sangster, P. B. Radha, R. Betti, T. R. Boehly, T. J. B. Collins, R. S. Craxton, J. A. Delettrez, R. Epstein, V. Yu. Glebov, S. X. Hu, I. V. Igumenshchev, J. P. Knauer, S. J. Loucks, J. A. Marozas, F. J. Marshall, R. L. McCrory, P. W. McKenty, D. D. Meyerhofer, S. P. Regan, W. Seka, S. Skupsky, V. A. Smalyuk, J. M. Soures, C. Stoeckl, D. Shvarts, J. A. Frenje, R. D. Petrasso, C. K. Li, F. Séguin, W. Manheimer, and D. G. Colombant, Phys. Plasmas **15**, 056310 (2008).

12. W. Seka, D. H. Edgell, J. P. Knauer, J. F. Myatt, A. V. Maximov, R. W. Short, T. C. Sangster, C. Stoeckl, R. E. Bahr, R. S. Craxton, J. A. Delettrez, V. N. Goncharov, I. V. Igumenshchev, and D. Shvarts, Phys. Plasmas **15**, 056312 (2008).

13. I. V. Igumenshchev, D. H. Edgell, V. N. Goncharov, J. A. Delettrez, A. V. Maximov, J. F. Myatt, W. Seka, A. Shvydky, S. Skupsky, and C. Stoeckl, Phys. Plasmas **17**, 122708 (2010).

14. J. Myatt, A. V. Maximov, W. Seka, R. S. Craxton, and R. W. Short, Phys. Plasmas **11**, 3394 (2004).

15. J. Delettrez, R. Epstein, M. C. Richardson, P. A. Jaanimagi, and B. L. Henke, Phys. Rev. A **36**, 3926 (1987).

16. P. Michel *et al.*, Phys. Rev. Lett. **102**, 025004 (2009).

17. R. A. Lerche, D. W. Phillion, and G. L. Tietbohl, Rev. Sci. Instrum. **66**, 933 (1995).

18. D. T. Michel, C. Sorce, R. Epstein, N. Whiting, I. V. Igumenshchev, R. Jungquist, and D. H. Froula, "Shell Trajectory Measurements from Direct-Drive Experiments," submitted to Review of Scientific Instruments.

19. P. B. Radha, C. Stoeckl, V. N. Goncharov, J. A. Delettrez, D. H. Edgell, J. A. Frenje, I. V. Igumenshchev, J. P. Knauer, J. A. Marozas, R. L. McCrory, D. D. Meyerhofer, R. D. Petrasso, S. P. Regan, T. C. Sangster, W. Seka, and S. Skupsky, Phys. Plasmas **18**, 012705 (2011).

20. D. H. Edgell, W. Seka, J. A. Delettrez, R. S. Craxton, V. N. Goncharov, I. V. Igumenshchev, J. Myatt, A. V. Maximov, R. W. Short, T. C. Sangster, and R. E. Bahr, Bull. Am. Phys. Soc. **52**, 195 (2007); *ibid.* **53**, 168 (2008); *ibid*. **54**, 145 (2009).

21. W. Seka, D. H. Froula, D. H. Edgell, J. F. Myatt, R. W. Short, I. V. Igumenshchev, V. N. Goncharov, and A. V. Maximov, Bull. Am. Phys. Soc. **56**, 327 (2011).

22. V. N. Goncharov, T. C. Sangster, R. Epstein, S. X. Hu, I. V. Igumenshchev, D. H. Froula, R. L. McCrory, D. D. Meyerhofer, P. B. Radha, W. Seka, S. Skupsky, C. Stoeckl, D. T. Casey, J. A. Frenje, and R. D. Petrasso, Bull. Am. Phys. Soc. **56**, 240 (2011).

23. A. V. Maximov, J. F. Myatt, R. W. Short, I. V. Igumenshchev, D. H. Edgell, and W. Seka, Bull. Am. Phys. Soc. **56**, 328 (2011).

24. D. Keller, T. J. B. Collins, J. A. Delettrez, P. W. McKenty, P. B. Radha, B. Whitney, and G. A. Moses, Bull. Am. Phys. Soc. **44**, 37 (1999).

25. D. H. Froula, I. V. Igumenshchev, D. T. Michel, D. H. Edgell, R. Follett, V. Yu. Glebov, V. N. Goncharov, J. Kwiatkowski, F. J. Marshall, P. B. Radha, W. Seka, C. Sorce, S. Stagnitto, C. Stoeckl, and T. C. Sangster, "Increasing Hydrodynamic Efficiency by Reducing Cross-Beam Energy Transfer in Direct-Drive Implosion Experiments," submitted to Physical Review Letters.

26. Y. Lin, T. J. Kessler, and G. N. Lawrence, Opt. Lett. **20**, 764 (1995).

27. T. R. Boehly, V. A. Smalyuk, D. D. Meyerhofer, J. P. Knauer, D. K. Bradley, R. S. Craxton, M. J. Guardalben, S. Skupsky, and T. J. Kessler, J. Appl. Phys. **85**, 3444 (1999).

28. S. P. Regan, J. A. Marozas, J. H. Kelly, T. R. Boehly, W. R. Donaldson, P. A. Jaanimagi, R. L. Keck, T. J. Kessler, D. D. Meyerhofer, W. Seka, S. Skupsky, and V. A. Smalyuk, J. Opt. Soc. Am. B **17**, 1483 (2000).

29. S. Chandrasekhar, *Hydrodynamic and Hydromagnetic Stability*, International Series of Monographs on Physics (Dover Publications, New York, 1981), p. 428.

30. P. Michel *et al.*, Phys. Plasmas **17**, 056305 (2010).

31. E. A. Williams, R. L. Berger, R. P. Drake, A. M. Rubenchik, B. S. Bauer, D. D. Meyerhofer, A. C. Gaeris, and T. W. Johnston, Phys. Plasmas **2**, 129 (1995).

32. T. Dewandre, J. R. Albritton, and E. A. Williams, Phys. Fluids **24**, 528 (1981).

33. E. A. Williams, B. I. Cohen, L. Divol, M. R. Dorr, J. A. Hittinger, D. E. Hinkel, A. B. Langdon, R. K. Kirkwood, D. H. Froula, and S. H. Glenzer, Phys. Plasmas **11**, 231 (2004).

Time-Resolved Measurements of Hot-Electron Equilibration Dynamics in High-Intensity Laser Interactions with Thin-Foil Solid Targets

High-intensity laser interactions with solid targets generate extreme states of matter[1] with unique energy-transport properties.[2,3] At laser intensities above 10^{18} W/cm^2, high-current electron beams with ~MeV energies are generated,[4–7] heating matter to high thermal temperatures over picosecond time scales.[2,3,8] Understanding the energy partition and its evolution in these highly nonequilibrium plasmas is an important open issue, underpinning applications in high-energy-density science,[1] plasma-based particle acceleration,[9] warm, dense matter,[10] high-peak-power γ-ray generation,[11] and advanced inertial fusion energy concepts, including fast ignition.[12] In these conditions, the hot-electron equilibration dynamics are not completely understood, and accurate time-resolved measurements are required to test energy partition and temperature equilibration models.

The only previous hot-electron equilibration data in this regime are the time-resolved K_α-emission data of Chen *et al.*[13] In these experiments thin-foil targets were irradiated with ~0.5-ps pulses focused to intensities up to 10^{19} W/cm^2, and the K_α-emission pulse width was used to characterize the time scale for energy thermalization ("relaxation") between hot and cold electrons. The data showed K_α-emission pulse widths from ~12 to 16 ps. The data were compared to an electron-energy–transfer model that included ion-front expansion and collisional electron-energy transfer based on the Landau–Spitzer theory.[14] With increasing laser intensity, the model did not reproduce the rise time (~10 ps) or the duration of the measured K_α signals, revealing an incomplete picture of the hot-electron equilibration dynamics.

In this article, ultrafast measurements of the hot-electron relaxation time in high-intensity laser–solid interactions are reported. Thin-foil targets were irradiated with 0.5- to 1-ps pulses focused to intensities from ~10^{18} to 10^{19} W/cm^2 and the hot-electron equilibration dynamics studied with time-resolved K_α spectroscopy. In these interactions, the full width at half maximum (FWHM) of the K_α signal increased with laser intensity from ~3 to 6 ps. These are the first experiments at relativistic laser intensities to show rapid hot-electron relaxation times with K_α-emission pulse widths up to a factor of 4× shorter than in previously reported experiments.[13] To provide insight into the mean energy of the hot electrons contained inside the target, the duration of the measured K_α signals were compared to predictions from a collisional energy-transfer model. Assuming collisional energy transfer dominates, the data suggest that hot electrons with mean energies from ~0.8 to 2 MeV are contained inside the target. The inferred mean hot-electron energies are broadly consistent with ponderomotive scaling[6] over the relevant intensity range.

The experiments were carried out with LLE's Multi-Terawatt (MTW) laser.[15] Figure 129.18 shows a schematic of the experimental setup. The MTW laser delivered 1- to 10-J, 0.5- to 1-ps pulses at a wavelength of 1.053 μm that were focused by an f/3 off-axis parabolic mirror to a spot with a FWHM of ~5 μm, providing vacuum-focused intensities from ~10^{18} to 10^{19} W/cm^2. The laser-intensity contrast was ~10^8 at 100 ps before the peak of the main laser pulse.[16] The laser was focused at normal incidence on 500 × 500 × 20-μm^3 Cu-foil targets mounted on 17-μm-diam silicon carbide stalks.

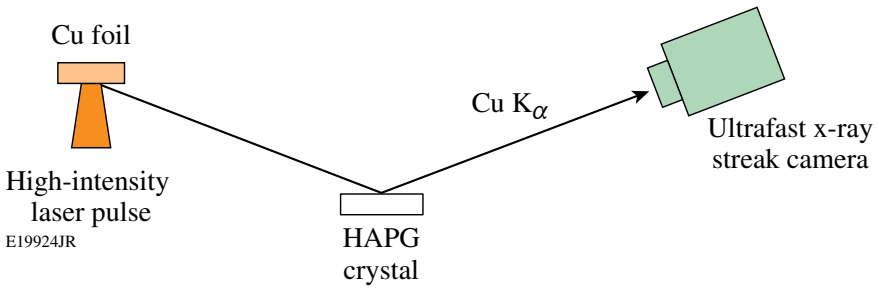

Figure 129.18
Experimental setup. HAPG: highly annealed pyrolytic graphite.

Time resolving the K_α radiation generated in these experiments is a direct technique for inferring the hot-electron relaxation time.[13] K_α radiation emitted from the target was measured with a 2-ps time-resolution x-ray streak camera[17] coupled to a HAPG (highly annealed pyrolytic graphite) crystal spectrometer. The HAPG crystal was toroidally curved and collected radiation from 7.8 to 8.5 keV. This spectral range covers the $2p \rightarrow 1s$ transition in Cu, allowing for time-resolved Cu K_α measurements at 8.05 keV.

The streak camera was independently characterized by direct illumination of the photocathode with a 10-mJ, 0.5-ps pulse of 263-nm light. Figure 129.19 shows a schematic of the setup. By passing half of the UV beam through a quartz plate of known thickness, two pulses were generated, providing a sweep-speed calibration. Figure 129.19(b) shows a typical streak-camera trace for these two pulses. The pulse widths (FWHM) are 1.8±0.1 and 1.9±0.1 ps. Temporal dispersion in the streak camera gives a slightly different impulse response for x-ray illumination. Monte Carlo modeling of the electron optics inside the streak tube shows that this offset is ~0.2 ps, giving an impulse response for x rays of ~2 ps.

Figure 129.20 shows an example of time-resolved plasma x-ray emission data for different high-intensity laser irradiation conditions. Figure 129.20(a) shows the time-resolved K_α emission from a $500 \times 500 \times 20$-μm^3 Cu foil irradiated with a 0.9-J, 0.6-ps pulse focused to 3.6×10^{18} W/cm^2. The pulse width is 3.0±0.2 ps. Figure 129.20(b) shows the K_α emission from a similar target irradiated with an 8.5-J, 0.8-ps pulse focused to 2.9×10^{19} W/cm^2. The pulse width is 5.5±0.1 ps. The K_α emission from these targets was measured as a peaked signal with a sharp rise and a slower decay. The signal rise time did not vary with laser intensity and was determined by the experimental resolution. The signal decay time increased with laser intensity and was sensitive to the hot-electron equilibration dynamics.

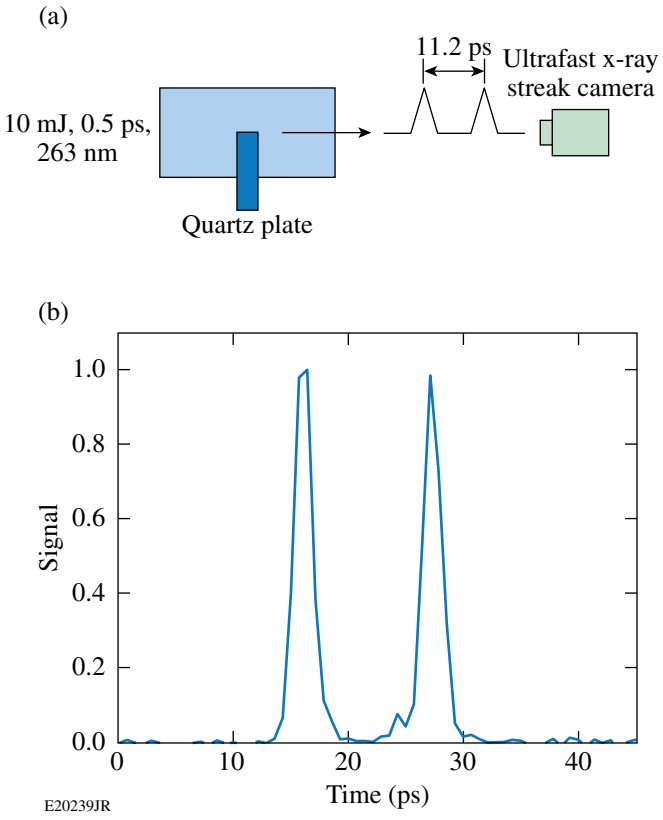

Figure 129.19
(a) Streak-camera calibration setup. (b) Streak-camera response measurement with 0.5-ps, 263-nm pulses showing pulse widths of 1.8±0.1 and 1.9±0.1 ps.

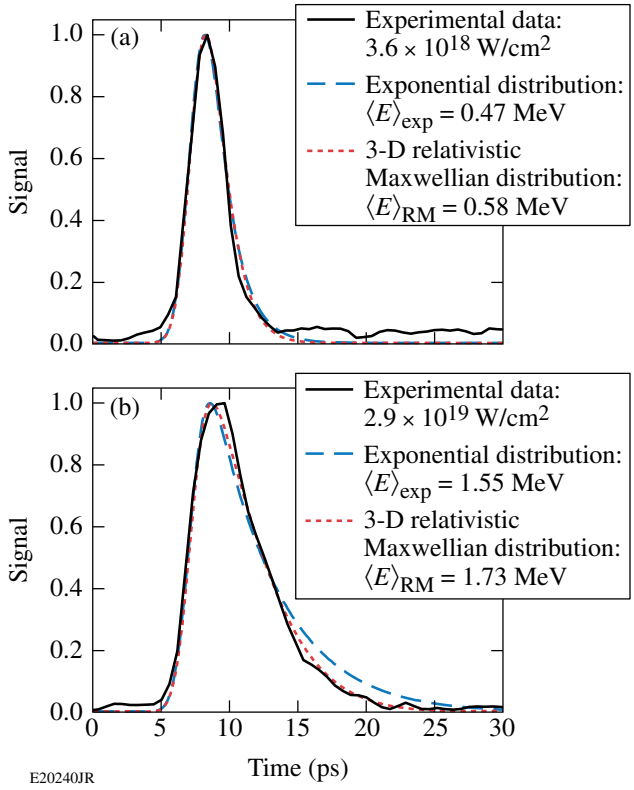

Figure 129.20
Experimental time-resolved K_α emission data from $500 \times 500 \times 20$-μm^3 Cu foils. The targets were irradiated with (a) a 0.9-J, 0.6-ps pulse and (b) an 8.7-J, 0.8-ps pulse. The data are shown with theoretical fits based on a collisional energy-loss model with exponential (blue dashed line) and 3-D relativistic Maxwellian (red dashed line) hot-electron energy distributions.

K_α radiation was generated in these experiments by hot electrons that were confined by target charging.[7,18,19] The thin-foil targets rapidly charge because of the electrostatic potential that develops after the initial loss of a small fraction of high-energy electrons.[18] The remaining hot electrons (>90% of the total laser-accelerated population) make multiple round-trips of the target as they recirculate (reflux) because their collisional range is several hundred microns at solid density.[20]

A collisional energy-loss model for understanding hot-electron relaxation and the time dependence of K_α emission in these targets has been developed. The model calculates the K_α emission rate for a given hot-electron energy distribution, assuming that all of the electrons are trapped inside the foil. The hot-electron energy loss rate is given by[20]

$$\frac{\mathrm{d}E}{\mathrm{d}t} = -\frac{n_\mathrm{e} e^4 L_\mathrm{d}}{4\pi\epsilon_0^2 m_\mathrm{e} v}, \tag{1}$$

where n_e is the electron density for solid Cu (2.46×10^{24} cm^{-3}), E is the hot-electron energy, m_e is the electron rest mass, v is the hot-electron velocity, e is the electron charge, and ϵ_0 is the permittivity of free space. The stopping number L_d (or "log Λ") depends weakly on material and the hot-electron energy, with values for Cu taken from Ref. 21. The time spent by hot electrons outside the target during recirculation is assumed negligible, and energy losses to ion acceleration and self-generated electric fields are not considered in this model.[7,18,19]

K_α-emission pulse widths have been calculated for hot electrons with exponential

$$\left(f_\mathrm{h} \propto e^{-\gamma m_\mathrm{e} c^2 / k_\mathrm{B} T_\mathrm{h}}\right)$$

and three-dimensional relativistic Maxwellian

$$\left[f_\mathrm{h} \propto \gamma\left(\gamma^2 - 1\right)^{1/2} e^{-\gamma m_\mathrm{e} c^2 / k_\mathrm{B} T_\mathrm{h}}\right]$$

energy distributions, where k_B is Boltzmann's constant, T_h is the hot-electron temperature, and γ is the Lorentz factor. Isochoric energy transfer to solid matter in these calculations is assumed. The K_α-emission rate is proportional to the Cu ion density, the time-varying number of hot electrons, and the parameter $\langle \sigma_\mathrm{K} v \rangle$ averaged over the hot-electron energy distribution, where σ_K is the K-shell ionization cross section and v is the hot-electron velocity. The cross section for ionization of K-shell electrons was taken from Ref. 21.

Figure 129.20 shows synthetic K_α streaks that were calculated from this model. The synthetic pulse widths represent a convolution of the calculated K_α-emission rate with the laser pulse duration and the temporal resolution of the x-ray streak camera. In the low-intensity case [Fig. 129.20(a)], the model predicts well the K_α emission pulse shape, independent of the hot-electron energy distribution that was used. The best fit of the experimental data was obtained with the parameters $\langle E \rangle_\mathrm{exp} = 0.47$ MeV for the exponential energy distribution and $\langle E \rangle_\mathrm{RM} = 0.58$ MeV for the three-dimensional (3-D) relativistic Maxwellian energy distribution. In the high-intensity case [Fig. 129.20(b)], the best fit was obtained with the parameters $\langle E \rangle_\mathrm{exp} = 1.55$ MeV and $\langle E \rangle_\mathrm{RM} = 1.73$ MeV. In this case, the K_α-emission pulse shape was better reproduced by model calculations with a 3-D relativistic Maxwellian energy distribution.

Figure 129.21 shows the variation with increasing laser intensity of the measured K_α emission pulse width. An upper estimate of the true K_α-emission pulse width was obtained by accounting for instrumental effects, subtracting the FWHM of the impulse response function from the streak-camera trace in quadrature. Gaussian pulse shapes are assumed. For laser intensities between 2.7×10^{18} and 3.4×10^{19} W/cm^2, the duration of the measured K_α signal increases from ~3 to 6 ps. Over this intensity range, the K_α-emission pulse width increases with

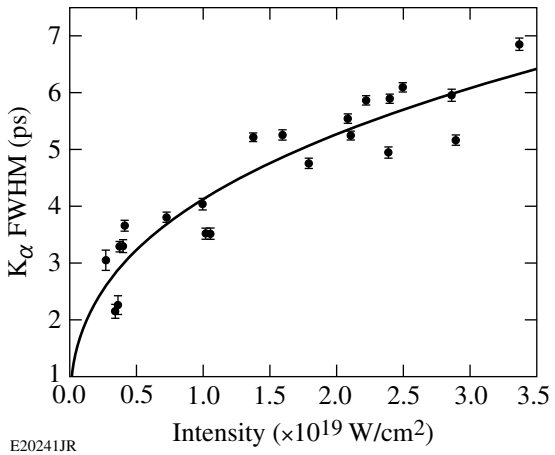

Figure 129.21
Experimental K_α-emission pulse width as a function of laser intensity. The pulse widths have been adjusted to account for the impulse response of the streak camera.

laser intensity and is given by $\tau_{K_\alpha}[\text{ps}] = (4.1 + 0.3) I_{19}^{0.35\pm0.07}$, where I_{19} is the laser intensity in units of 10^{19} W/cm^2.

To obtain a mean hot-electron energy scaling, these data are compared with the collisional energy-loss model. Figure 129.22(a) shows the relationship between the calculated K_α-emission pulse width and the mean hot-electron energy for exponential and 3-D relativistic Maxwellian energy distributions. In these calculations, the K_α-emission rate was convolved with a 0.8-ps FWHM Gaussian pulse that approximated the range of laser pulse durations that were used in these experiments. The synthetic pulse was convolved with a 2-ps FWHM Gaussian instrument response that was removed in quadrature for comparison with the experimental data (Fig. 129.21). Figure 129.22(a) shows that calculations with a 3-D relativistic Maxwellian energy distribution have slightly higher mean hot-electron energies than with an exponential energy distribution for a given K_α-emission pulse width. This offset is ~100 to 200 keV.

Figure 129.22(b) shows the mean hot-electron energies that are inferred from the experimental data based on this model. Two scaling laws were obtained: For an exponential energy distribution, $\langle E \rangle_{\text{exp}}[\text{MeV}] = (1.12\pm0.11) I_{19}^{0.51\pm0.11}$. For a 3-D relativistic Maxwellian energy distribution, $\langle E \rangle_{\text{RM}} = [\text{MeV}] = (1.19\pm0.11) I_{19}^{0.46\pm0.10}$. Assuming collisional energy transfer dominates, these results show that mean hot-electron energies from ~0.8 to 2 MeV are required to generate K_α-emission pulse widths consistent with the experimental observations.

Figure 129.22(c) compares these inferred mean hot-electron energies with ponderomotive scaling.[6] Ponderomotive scaling gives

$$\langle E \rangle = m_e c^2 \left[1 + \left(2U_p / m_e c^2 \right) \right]^{1/2},$$

where $U_p = 9.33 \times 10^{-14} I\,[\text{W/cm}^2]\,(\lambda\,[\mu\text{m}])^2$ is the ponderomotive potential. In general, good agreement was found. The best agreement was found for calculations with an exponential energy distribution. A similar scaling predicting ~100- to 200-keV-higher mean hot-electron energies was found with calculations using the 3-D relativistic Maxwellian energy distribution.

Including the energy-transfer model energy loss to self-generated fields and ion acceleration would increase the inferred mean hot-electron energy and lead to a faster increase in the K_α-emission pulse width with laser intensity since these effects are expected to be greater at higher intensities. In the limit of isochoric energy transfer, additional energy loss mechanisms will increase the mean hot-electron energy required to gen-

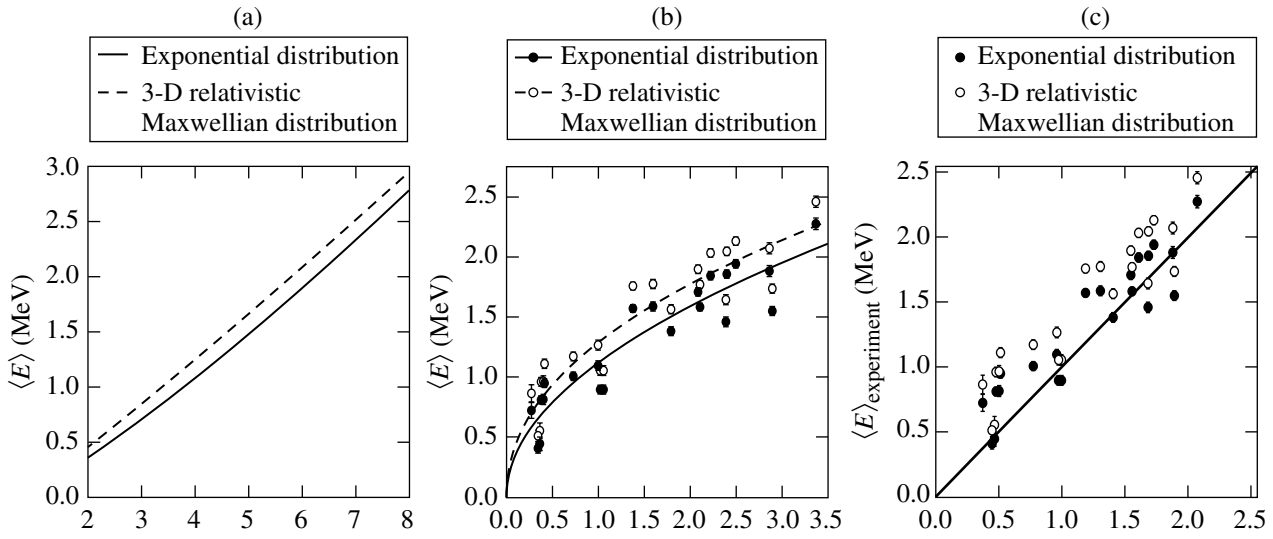

Figure 129.22
(a) Calculated mean hot-electron energy $\langle E \rangle$ as a function of K_α-emission pulse width based on a 0.8-ps laser-pulse duration. (b) Inferred $\langle E \rangle$ as a function of laser intensity, assuming exponential (solid line) and 3-D relativistic Maxwellian (dashed line) hot-electron energy distributions. (c) Comparison of the experimentally inferred $\langle E \rangle$ with ponderomotive scaling.[6]

erate the experimentally observed K_α emission. These results represent a minimum value for the inferred mean hot-electron energy required to generate the experimentally observed K_α-emission pulse widths.

In summary, the hot-electron equilibration dynamics in thin-foil solid targets irradiated with high-intensity laser pulses have been studied. Time-resolved K_α spectroscopy measurements show K_α-emission pulse widths from ~3 to 6 ps for laser intensities between ~10^{18} and 10^{19} W/cm^2. Assuming collisional energy transfer dominates, the experimental data suggest that hot electrons with mean energies from ~0.8 to 2 MeV are contained inside the target. The inferred mean hot-electron energy scaling with laser intensity is broadly consistent with ponderomotive scaling. These findings are important for the understanding of a wide range of high-energy-density physics applications that require a large and fast energy input into matter.

ACKNOWLEDGMENT

This work was supported by the U.S. Department of Energy Office of Inertial Confinement Fusion under Cooperative Agreement No. DE-FC52-08NA28302, the University of Rochester, and the New York State Energy Research and Development Authority. The support of DOE does not constitute an endorsement by DOE of the views expressed in this article.

REFERENCES

1. B. A. Remington *et al.*, Science **284**, 1488 (1999).
2. J. A. Koch *et al.*, Phys. Rev. E **65**, 016410 (2001); K. Eidmann *et al.*, J. Quant. Spectrosc. Radiat. Transf. **81**, 133 (2003); P. Audebert *et al.*, Phys. Rev. Lett. **94**, 025004 (2005).
3. C. R. D. Brown *et al.*, Phys. Rev. Lett. **106**, 185003 (2011).
4. D. F. Price *et al.*, Phys. Rev. Lett. **75**, 252 (1995); H. Chen, B. Soom, B. Yaakobi, S. Uchida, and D. D. Meyerhofer, Phys. Rev. Lett. **70**, 3431 (1993); K. B. Wharton *et al.*, Phys. Rev. Lett. **81**, 822 (1998); K. Yasuike *et al.*, Rev. Sci. Instrum. **72**, 1236 (2001); S. P. Hatchett *et al.*, Phys. Plasmas **7**, 2076 (2000).
5. F. N. Beg *et al.*, Phys. Plasmas **4**, 447 (1997).
6. S. C. Wilks *et al.*, Phys. Rev. Lett. **69**, 1383 (1992).
7. P. M. Nilson, A. A. Solodov, J. F. Myatt, W. Theobald, P. A. Jaanimagi, L. Gao, C. Stoeckl, R. S. Craxton, J. A. Delettrez, B. Yaakobi, J. D. Zuegel, B. E. Kruschwitz, C. Dorrer, J. H. Kelly, K. U. Akli, P. K. Patel, A. J. Mackinnon, R. Betti, T. C. Sangster, and D. D. Meyerhofer, Phys. Rev. Lett. **105**, 235001 (2010).
8. A. Saemann *et al.*, Phys. Rev. Lett. **82**, 4843 (1999); P. Audebert *et al.*, Phys. Rev. Lett. **89**, 265001 (2002).
9. E. L. Clark *et al.*, Phys. Rev. Lett. **84**, 670 (2000); R. A. Snavely *et al.*, Phys. Rev. Lett. **85**, 2945 (2000).
10. P. K. Patel *et al.*, Phys. Rev. Lett. **91**, 125004 (2003).
11. P. A. Norreys *et al.*, Phys. Plasmas **6**, 2150 (1999).
12. M. H. Key, M. D. Cable, T. E. Cowan, K. G. Estabrook, B. A. Hammel, S. P. Hatchett, E. A. Henry, D. E. Hinkel, J. D. Kilkenny, J. A. Koch, W. L. Kruer, A. B. Langdon, B. F. Lasinski, R. W. Lee, B. J. MacGowan, A. MacKinnon, J. D. Moody, M. J. Moran, A. A. Offenberger, D. M. Pennington, M. D. Perry, T. J. Phillips, T. C. Sangster, M. S. Singh, M. A. Stoyer, M. Tabak, G. L. Tietbohl, M. Tsukamoto, K. Wharton, and S. C. Wilks, Phys. Plasmas **5**, 1966 (1998); M. Tabak *et al.*, Phys. Plasmas **1**, 1626 (1994).
13. H. Chen *et al.*, Phys. Rev. E **76**, 056402 (2007).
14. L. D. Landau, Phys. Z. Sowjetunion **10**, 154 (1936); L. Spitzer, *Physics of Fully Ionized Gases*, 2nd rev. ed., Interscience Tracts on Physics and Astronomy (Wiley Interscience, New York, 1962).
15. V. Bagnoud, I. A. Begishev, M. J. Guardalben, J. Puth, and J. D. Zuegel, Opt. Lett. **30**, 1843 (2005).
16. V. Bagnoud, J. D. Zuegel, N. Forget, and C. Le Blanc, Opt. Express **15**, 5504 (2007).
17. C. Stoeckl, W. Theobald, P. A. Jaanimagi, P. Nilson, M. Storm, J. A. Delettrez, R. Epstein, T. C. Sangster, D. Hey, A. J. MacKinnon, H.-S. Park, P. K. Patel, R. Shepherd, J. Green, K. L. Lancaster, and P. A. Norreys, Bull. Am. Phys. Soc. **52**, 67 (2007).
18. J. Myatt, W. Theobald, J. A. Delettrez, C. Stoeckl, M. Storm, T. C. Sangster, A. V. Maximov, and R. W. Short, Phys. Plasmas **14**, 056301 (2007).
19. A. J. Mackinnon *et al.*, Phys. Rev. Lett. **88**, 215006 (2002); Y. Sentoku *et al.*, Phys. Plasmas **10**, 2009 (2003); W. Theobald, K. Akli, R. Clarke, J. Delettrez, R. R. Freeman, S. Glenzer, J. Green, G. Gregori, R. Heathcote, N. Izumi, J. A. King, J. A. Koch, J. Kuba, K. Lancaster, A. J. MacKinnon, M. Key, C. Mileham, J. Myatt, D. Neely, P. A. Norreys, H.-S. Park, J. Pasley, P. Patel, S. P. Regan, H. Sawada, R. Shepherd, R. Snavely, R. B. Stephens, C. Stoeckl, M. Storm, B. Zhang, and T. C. Sangster, Phys. Plasmas **13**, 043102 (2006); S. D. Baton *et al.*, High Energy Density Phys. **3**, 358 (2007); P. M. Nilson, W. Theobald, J. Myatt, C. Stoeckl, M. Storm, O. V. Gotchev, J. D. Zuegel, R. Betti, D. D. Meyerhofer, and T. C. Sangster, Phys. Plasmas **15**, 056308 (2008); P. M. Nilson, W. Theobald, J. F. Myatt, C. Stoeckl, M. Storm, J. D. Zuegel, R. Betti, D. D. Meyerhofer, and T. C. Sangster, Phys. Rev. E **79**, 016406 (2009).
20. H. O. Wyckoff, *ICRU Report*, International Commission on Radiation Units and Measurements, Inc., Bethesda, MD (1984).
21. J. P. Santos, F. Parente, and Y.-K. Kim, J. Phys. B: At. Mol. Opt. Phys. **36**, 4211 (2003).

Experimental Studies of the Two-Plasmon-Decay Instability in Long-Scale-Length Plasmas

Introduction

Direct-drive inertial confinement fusion (ICF) is an encouraging path to high-gain inertial fusion energy.[1] In the direct-drive approach to ICF, high-power, moderate-intensity laser beams ($\sim 7 \times 10^{14}$ W/cm^2) produce and propagate through a high-temperature ($T_e \sim 3.5$ keV), long-scale-length ($L_n \sim 500$ μm) underdense plasma prior to depositing energy near the critical surface of a spherical capsule. A series of shocks are launched that adiabatically compress the nuclear fuel to fusion conditions.[2–4] For the most-efficient compression, the shocks are driven on a low adiabat[5] and ignition is susceptible to preheat; heating of the imploding shell by "hot" electrons increases the implosion adiabat, reducing the compression efficiency.

Electrons can be accelerated to high energies by two-plasmon-decay (TPD) instability[6] in which the incident electromagnetic wave decays into two electron-plasma waves.[7–9] The instability grows rapidly through the resonant coupling of the electric field of the incident laser beam and the longitudinal electrostatic field of the two electron-plasma waves. The dependence of TPD on the hydrodynamic conditions is evident in the convective (intensity) gain exponent for the instability of a single-plane electromagnetic wave [$G_{SB} \simeq 1.9 \times 10^{-2}\, I_s\, (\times 10^{14}\ \mathrm{W/cm^2})\, L_n\, (\mu\mathrm{m}) \big/ T_e(\mathrm{keV})$, where I_s is the single-beam intensity, L_n is the density scale length, T_e is the electron temperature, and all parameters are taken at $n_{cr}/4$, $n_{cr} \simeq 10^{22}$ cm^{-3}] (Ref. 10). Simulations based on a nonlinear Zakharov model[11] that includes test particles, indicate that electrons are stochastically accelerated to high energies (>50 keV) by enhanced electron-plasma waves. Once above threshold, the hot-electron temperature is shown to scale with $I_q L_n / T_e$ (Ref. 12), where I_q is the overlapped intensity at quarter critical.

Early experiments using CO_2 lasers measured the first hot electrons generated by TPD[13] and the associated electron-plasma waves using Thomson scattering.[14] More-recent experiments focusing on TPD in direct-drive–ignition conditions[15] demonstrated that the efficiency of hot-electron generation scaled with overlapped laser-beam intensity.[16] These studies showed a nearly constant electron temperature and saturation of the hot-electron generation at 0.1% of the incident laser energy when plotted as a function of the vacuum laser intensity.[17] This apparent saturation and low level of electron generation were results of the hydrodynamics; the small laser spots used to produce the highest intensities limited the scale length to less than $L_n < 200$ μm.

The work presented in this article uses the large laser spots and high ultraviolet intensities available on OMEGA EP[18] to produce a 400-μm-long-scale-length, 2.5-keV plasma, where $I_q L_n / T_e$ is increased by nearly a factor of 4 when the laser intensity is varied from 1.3 to 7×10^{14} W/cm^2. Over this range in intensities, a rapid increase in the hot-electron temperature (25 keV to 90 keV) is measured and for intensities above 3.5×10^{14} W/cm^2 the hot-electron efficiency generation is saturated at a nearly constant level of ~1% of the incident laser energy.[19] The rapid increase in hot-electron temperature is compared with simulations that use a Zakharov model designed to provide a physics-based predictive capability for TPD at ignition conditions.[20]

Experimental Setup

1. Target and Laser Configuration

The experimental configuration is shown in Fig. 129.23, where the long-scale-length CH plasma was produced by illuminating a 30-μm-thick CH layer deposited on 30 μm of Mo and backed with an additional 30 μm of CH. The CH thickness was chosen to avoid any burnthrough to the Mo layer. This was verified by the fact that no Mo spectral lines were observed except for the inner-shell K lines that were attributed to the TPD hot electrons. The Mo thickness was equal to a range of electrons with a typical energy of ~120 keV, which was confirmed by Monte Carlo simulations that showed that electrons with energies less than 120 keV were stopped within the Mo. This resulted in nearly all of the electrons accelerated by TPD being absorbed in the target.

The 17.5-keV Mo K_α line was sufficiently high in energy to ensure that photoexcitation from the $T_e \simeq 2.5$-keV coronal plasma region did not contribute to the K_α-emission measure-

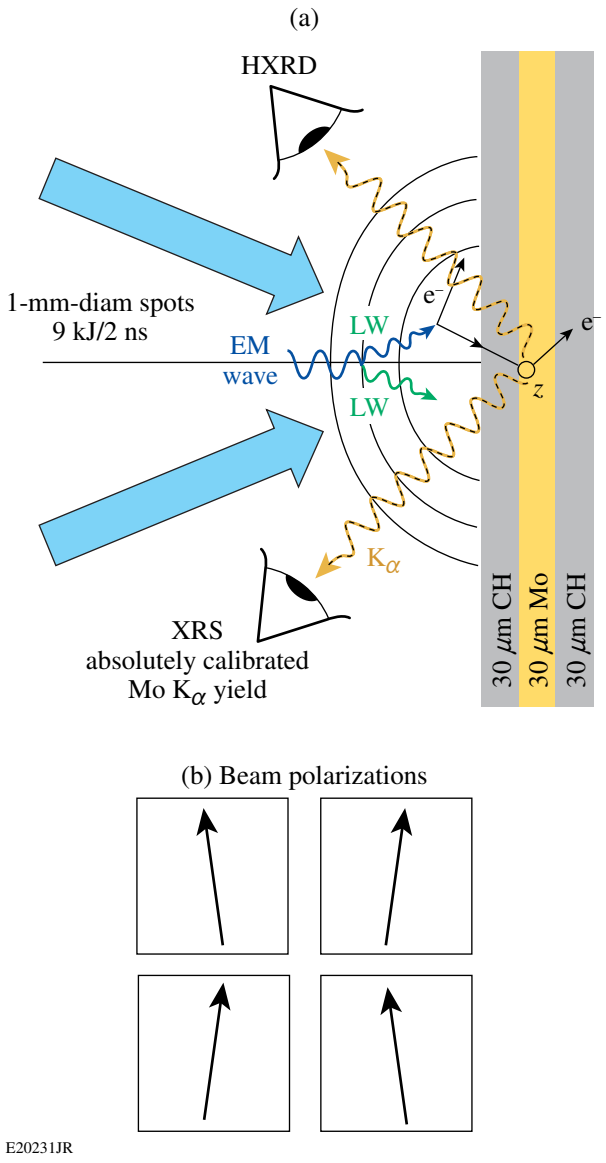

Figure 129.23
(a) The 2-mm × 2-mm target is illuminated by four UV laser beams. The 30-μm-thick Mo is used to capture the majority of the electrons produced by TPD. (b) The polarization of each laser beam is 8° from vertical as shown.

ments. This ensured that the measured K_α emission was a result of K-shell impact and hard x-ray photoionization caused by the hot electrons produced by TPD. This is confirmed by integrating the measured x-ray continuum above the K_α energy [$E(K_\alpha)$ = 17.5 keV] to obtain the total number of x rays (N). Assuming that all x rays are absorbed in the Mo, an upper bound for the contribution of the continuum to the K_α yield is $E_R \cong E(K_\alpha)\,\omega_k N$, where ω_k is the fluorescence yield. Even for the highest laser irradiance, the contribution of the x-ray continuum to the K_α yield is only a few percent of the measured K_α energy; therefore, the radiation contribution is negligible. There is an additional effect of K_α excitation by the bremsstrahlung emitted by the hot electrons; this secondary effect is included in the Monte Carlo–code calculations described in **Diagnostics** (p. 23), which were used to derive the total energy in hot electrons.

For this study, four ultraviolet ($\lambda_0 = 0.35\ \mu$m) beams available from the OMEGA EP Laser System[18] produced the required intensities over a large-diameter laser spot to create 400-μm plasma density scale lengths at $n_{cr}/4$ (Fig. 129.24). A maximum overlapped laser intensity of 7×10^{14} W/cm^2 was achieved using a total energy on target of 8.7 kJ in a 2-ns flattop laser pulse (Fig. 129.24). The four UV beams intersect the target at an angle of 23° with respect to the target normal and are linearly polarized

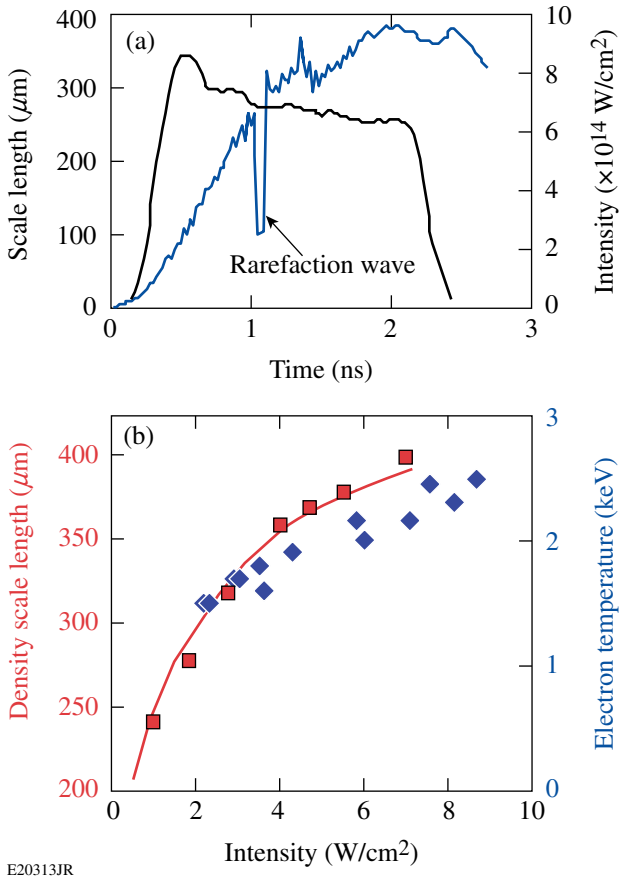

Figure 129.24
(a) The high UV laser power available (P_{max} = 4.5 TW) on OMEGA EP provides the necessary intensity (right axis) over a nearly 1-mm-diam laser spot to produce an electron-density scale length $L_n \simeq 400\ \mu$m. The simulated plasma scale length (left axis) increases to saturation after ~1.5 ns. (b) The maximum simulated density scale length (left axis) and electron temperature (right axis) at quarter critical are shown as a function of the overlapped intensity.

[Fig. 129.23(b)]. Two sets of distributed phase plates (DPP's)[21] were used (840-μm and 890-μm diameter measured at the 1/e intensity points) to produce a combined intensity distribution that has a super-Gaussian profile with a diameter of nearly 1 mm.

Figure 129.25 shows a time-integrated x-ray pinhole image of the focal spot. This radiation is emitted by the laser-heated CH layer and characterizes the interaction region. The x-ray profile in Fig. 129.25(b) has a width (at half-maximum) that is similar to that of the overlapped vacuum laser profile, but the flattop of the latter has been rounded in the x-ray image; this is mainly a result of the lateral heat conduction within the plasma.

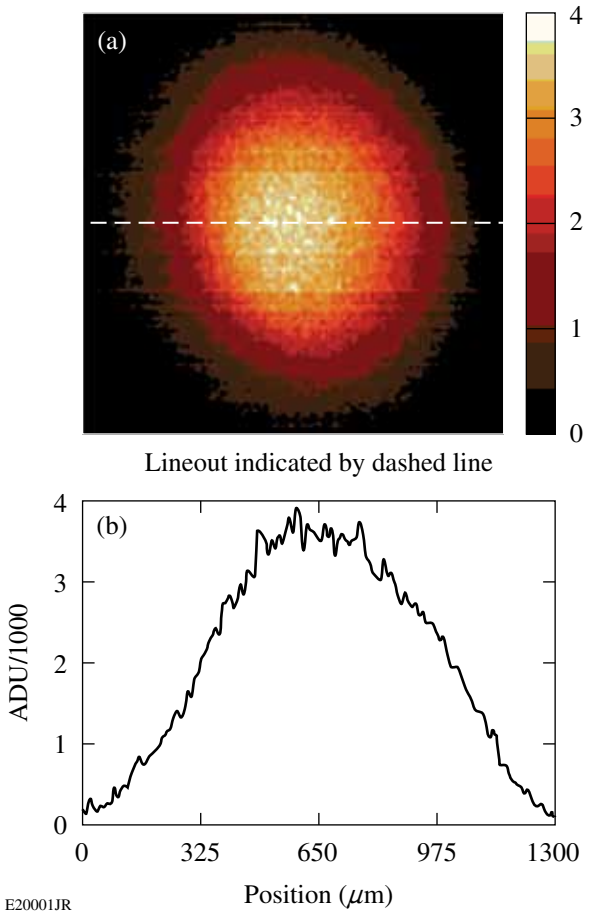

Figure 129.25
(a) X-ray image of the irradiated focal spot at 5×10^{14} W/cm^2 (in the photon-energy range of 2 to 7 keV). (b) This lineout is indicated by the horizontal dashed line in the image in (a).

2. Hydrodynamics

a. Simulations. Two-dimensional hydrodynamic simulations using the codes *SAGE*[22] and *DRACO*[23] show that the maximum-achievable scale length in planar geometry is obtained by maximizing the overlapped-laser-beam intensity while providing enough time for the plasma to reach steady state. Figure 129.24(a) shows that increasing the overlapped-laser-beam intensity increases both the scale length and the electron temperature at quarter critical $\left(L_n/T_e \approx 160\ \mu\text{m/keV}\right)$. Over this intensity range, the hydrodynamic simulations indicate that the intensity of the laser beams at $n_{cr}/4$, where TPD has the largest growth rate, is reduced from the vacuum intensity by ~55%. For the highest laser-beam energies available at 2 ns, the optimal laser spot size is ~1-mm diameter; a further increase in laser-spot size reduces the intensity on target, resulting in a shorter scale length. For the experimental conditions presented here, the scale length reaches a steady state after about 1.5 ns [Fig. 129.24(b)] and the asymptotic scale length is given by $L_n \simeq 250\ \mu\text{m}\ \langle I_{14} \rangle^{1/4}$.

b. X-ray continuum measurements. To check the reliability of the simulations, comparisons were made between calculated and measured plasma conditions at quarter critical and time- and space-integrated x-ray fluence in the energy range of ~5 to 8 keV. This radiation is emitted in the laser-heated CH layer. An example (using *SAGE*) from a shot at an irradiance of 2.7×10^{14} W/cm^2 is shown in Fig. 129.26. No intensity normalization was applied. Even though most of the radiation comes from layers deeper (and colder) than the quarter-critical surface, the ability of the codes to replicate the x-ray fluence in absolute magnitude makes the calculated plasma parameters (such as the TPD threshold below) credible.

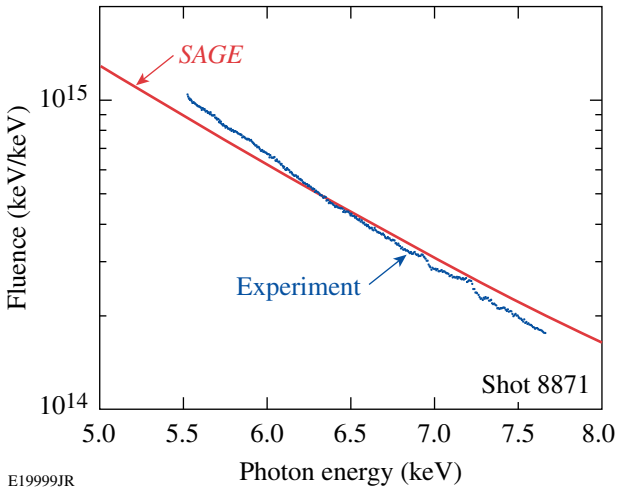

Figure 129.26
SAGE-calculated x-ray fluence from a shot at an irradiance of 2.7×10^{14} W/cm^2. No normalization of intensity was applied.

c. UV Thomson-scattering measurements. A more-rigorous test of the calculated plasma parameters was obtained using

Thomson scattering.[19] Figure 129.27 shows a Thomson-scattering spectrum where the ion-acoustic features are resolved and used to measure the electron and ion temperatures. The measured electron temperature is within a few percent of the simulations [Fig. 129.27(c)].

The rarefaction wave launched from the CH/Mo interface is observed in the Thomson-scattering spectrum 1.11 ns after the laser beams turns on, which is in excellent agreement with the hydrodynamic simulations [Fig. 129.24(a)]. Although the density scale length at quarter critical is not directly measured, the excellent agreement between the measured and simulated time of arrival of the rarefaction wave demonstrates the accuracy of the thermal conduction model and is a strong indication that the calculated density and temperature profiles are accurate.

The Thomson-scattering measurements were obtained on the OMEGA Laser System using the same target platform, pulse shape, and similar laser beam diameters (800-μm FWHM) as used on the OMEGA EP experiments. A 20-J, $\lambda_{4\omega} = 0.26$-μm, *f*/6.7 Thomson-scattering probe beam was focused to a diameter of 60 μm and the Thomson-scattered light was collected from a 60-μm × 75-μm × 75-μm volume located 200 μm from the initial target surface.[24] The Thomson-scattering diagnostic probes ion-acoustic waves propagating nearly parallel to the target [$k_a = 2\, k_{4\omega} \sin(\theta/2)$, where $k_{4\omega} = 2\pi/\lambda_{4\omega}$ and $\theta = 63°$ is the scattering angle].

3. Diagnostics

a. X-ray spectrometer. The determination of total hot-electron energy depends on an absolute calibration of the spectrometers measuring the Mo K_α line (at 17.5 keV). An x-ray spectrometer was used for all shots but checked for consistency on several shots by comparison with a Cauchois-type quartz crystal spectrometer (TCS)[26] and single-hit charge-coupled–device (CCD) array (SPC).[27] The energy in the Mo K_α-emission line (E_{K_α}) was measured using an absolutely calibrated planar LiF crystal spectrometer (XRS) that views the target from the incident laser side at an angle of 63° from the target normal [Fig. 129.23(a)].[28]

The LiF crystal was calibrated by LLE and the quartz crystal at NIST.[29] The CCD array (Spectral Instruments[30] model 800) was calibrated by Maddox *et al.*[31] for several photon energies, including correction for background. XRS and TCS used image plates to record the spectra; calibration data for the same plates and image scanner as used at LLE were published by Meadowcroft *et al.*[32] The results of the three instruments for a single shot at 6.4×10^{14} W/cm^2 are shown in Fig. 129.28. The energy in the Mo K_α line from the XRS and TCS spectra agrees to within 15%; that from TCS agrees with the first two to within 25%. The slightly different spectral resolution of the instruments does not impact the measurement of the total K_α energy. The agreement with the CCD instrument is particularly significant since, unlike the other two spectrometers, it does not use image plates. Figure 129.29 shows that the energy con-

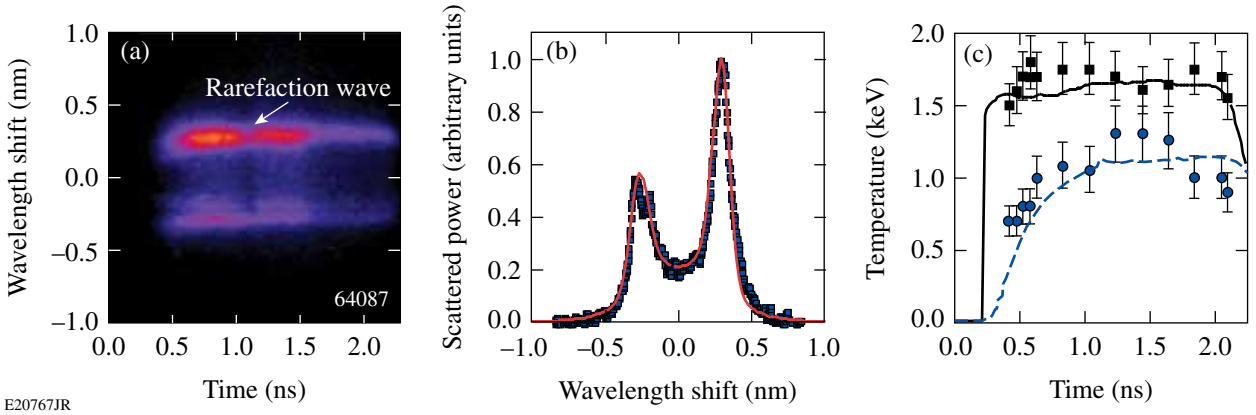

Figure 129.27

(a) Thomson-scattered light from near the quarter critical density for 3ω light is spectrally and temporally resolved to measure the ion-acoustic features. The electron and ion temperatures as a function of time are obtained by fitting the standard dynamic form factor[25] to the measured spectra that are averaged over 50 ps. (b) A best fit (red curve) to the measured spectrum at 0.8 ns (blue) is obtained for $T_e = 1.6$ keV, $T_i = 1.0$ keV. (c) The electron (solid) and ion (dashed) temperatures calculated by *DRACO* compare well to the measurements.

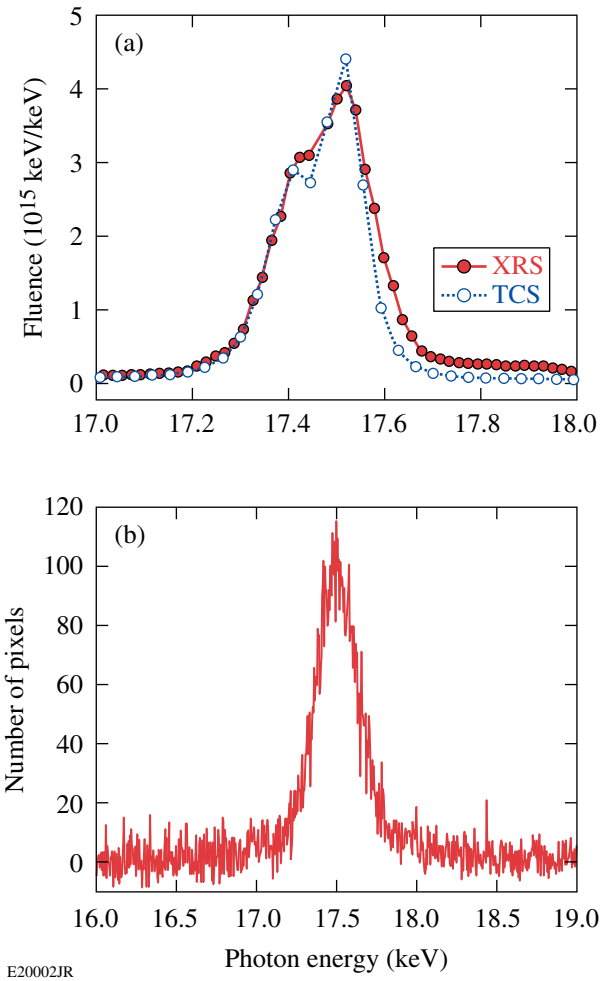

Figure 129.28
An example of the Mo K_α spectra measured on a single shot by three detectors: (a) a planar LiF crystal spectrometer and a Cauchois-type quartz crystal spectrometer and (b) a single-hit CCD array (SPC). The three measurements of K_α energy are consistent.

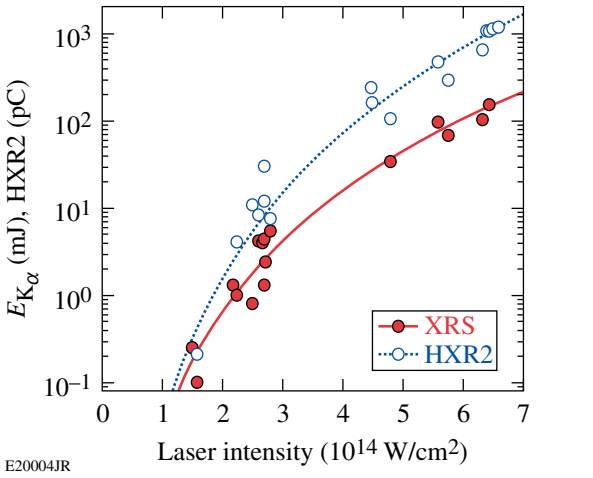

Figure 129.29
Mo K_α and hard x-ray (≳40-keV) yields. Both signals rise rapidly with laser intensity.

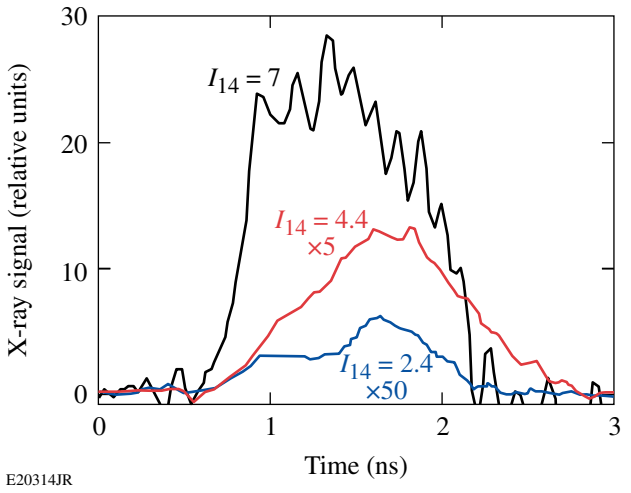

Figure 129.30
The measured hard x-ray emission (>40 keV) is shown for overlapped intensities of 7×10^{14} W/cm^2 (black), 4.4×10^{14} W/cm^2 (red), and 2.4×10^{14} W/cm^2 (blue).

tained within the Mo K_α line scales quasi-exponentially with laser intensity over nearly four orders of magnitude when the vacuum laser intensity is varied from 1.3 to 7×10^{14} W/cm^2.

b. Hard x-ray detector (HXRD). Figure 129.30 shows the hard x-ray emission as a function of time for one of the three x-ray channels used to measure the hot-electron temperature. The hot-electron temperature (T_{hot}) is assumed to be equal to the slope of the hard x-ray radiation that is determined by fitting an exponential decay [$\exp(-E/T_{hot})$] to the measured ratios of the x-ray radiation above ~40 keV, ~60 keV, and ~80 keV obtained using a three-channel scintillator detector (HXRD).[33]

The hard x-ray scaling provides an additional signature of hot-electron generation. Figure 129.29 compares the scaling with laser intensity of the K_α and bremsstrahlung yields. Both signals increase quasi-exponentially by several orders of magnitude, primarily because of the increase in the number of hot electrons. The hard x rays rise faster as a result of the corresponding increase in hot-electron temperature with intensity shown in **Results** (p. 26). This occurs because the bremsstrahlung emission increases with hot-electron temperature, whereas the cross section for Mo K_α excitation decreases with electron energy above ~50 keV.

c. Monte Carlo simulations. Monte Carlo simulations using the code *EGSnrc*[34] are used to relate the measured Mo K_α energy and the HXRD signal to the total energy in hot electrons. For the electron spectra discussed in this article (T_{hot} = 25 to 90 keV), the Monte Carlo simulations indicate that the total electron energy is directly related to the total K_α energy given the hot-electron temperature $E_{electrons}(J) \simeq 150\, E_{K_\alpha}(mJ/sr)/\sqrt{T_{hot}(keV)}$. This relationship is accurate to within 20% over the relevant hot-electron temperature range and is specific to the geometry of the experiment.

The Monte Carlo code calculates both the K_α and the associated bremsstrahlung spectrum (HXR) given an initial electron-beam spectrum. Both the K_α and HXR yields are calculated as functions of the observation angle. To obtain reliable results, 10^7 electrons are typically assumed to be normally incident on the target with a Maxwellian energy distribution at the experimentally determined temperature T_{hot}. The number of calculated K_α photons and HXR photons per energy bin is typically of the order of 10^3; therefore, a statistical precision of a few percent is obtained.

The calculated K_α energy was tested by comparison with experiment. Reference 35 shows extensive measurements of the Cu K_α line from an x-ray tube as a function of emission angle and tube voltage. The corresponding Monte Carlo simulations (assuming a monoenergetic electron beam) agree very closely with Ref. 35. The temperature of the input-electron distribution is taken to be the measured slope of the HXR. Figure 129.31 shows that the two temperatures are essentially the same; for an assumed electron temperature of 80 keV, the HXR slope is 79 keV.

Changing the assumed hot-electron divergence has a small effect on the calculated K_α signal because (a) the range of most electrons is smaller than the Mo thickness, (b) electron scattering changes the initially monodirectional distribution into a quasi-isotropic distribution, and (c) the target is large compared to the focal-spot size. This simplifies the determination of hot-electron generation but also precludes studying the electron divergence, which is important for determining preheat in spherical implosions. A similar situation exists with respect to the HXR radiation. For a low-Z target and unidirectional electrons, the HXR spectrum is peaked in the forward direction. The Monte Carlo–code calculations show that because of electron scattering in the Mo; however, the spectrum becomes quasi-isotropic in intensity and in shape (therefore T_{hot} is uniquely defined). Again, the spectrum is independent of initial electron divergence.

Before comparing the measured and simulated K_α energies, it is necessary to account for the angular dependence of K_α emission. The local emission of K_α is strictly isotropic, but its opacity through the molybdenum creates an angular distribution. Figure 129.32 shows the K_α emission per unit solid angle $\Delta\Omega$ for two hot-electron temperatures. As expected, the distri-

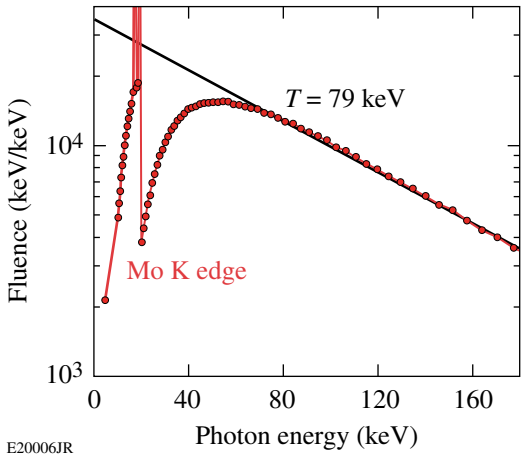

Figure 129.31
Monte Carlo–calculated HXR spectra for 10 million incident electrons. The slope of the HXR continuum (79 keV) is about equal to the hot-electron temperature assumed for the Monte Carlo–code run (80 keV). The smoothness of the curve is an indication of the good statistics obtained with 10 million electrons.

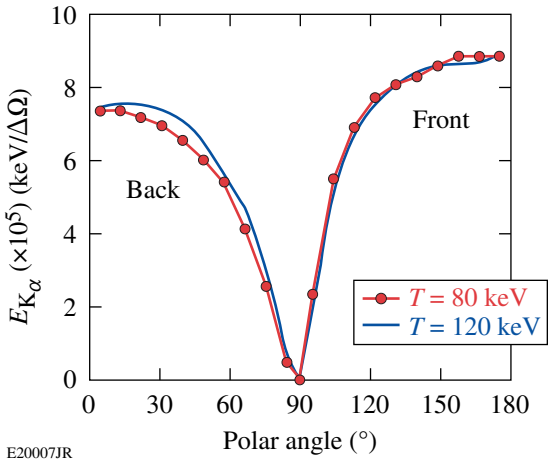

Figure 129.32
Monte Carlo–calculated angular distribution of Mo K_α as function of polar angle θ (relative to the target normal) per unit solid angle. "Back" stands for the back of the target (forward emission).

bution peaks in the forward and backward directions $\theta = 0°$ and $\theta = 180°$, where the K_α opacity is minimal. Figure 129.32 is used to relate the measured K_α emission per unit solid angle to the calculated emission in the direction of the spectrometer. The shape of the angular distribution across the detector is nearly the same for different hot-electron temperatures for the target thickness used in this study.

Based on the K_α yield calculated by the Monte Carlo code, Fig. 129.33 gives the total energy in hot electrons divided by the K_α energy per unit solid angle in the forward direction. Using Fig. 129.33, the measured energy in K_α (Fig. 129.29) can be converted into energy in hot electrons.

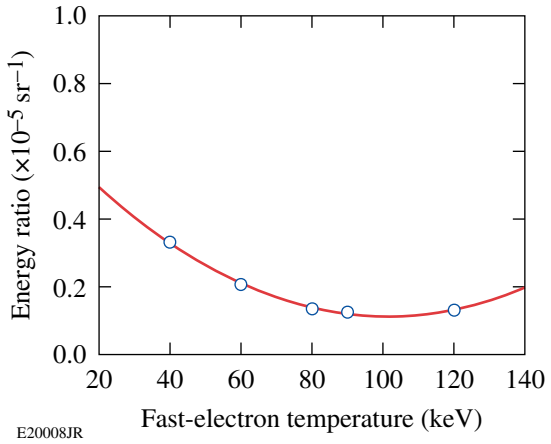

Figure 129.33
Monte Carlo–calculated ratio of the total incident electron energy and the K_α emission per unit solid angle in the target normal direction as a function of the hot-electron temperature. This curve is used to deduce the total energy in hot electrons from the measured Mo K_α energy.

Results

1. Hot-Electron Temperature

Figure 129.34(a) shows that the hot-electron temperature increases from 25 keV to 90 keV as the laser intensity is increased from 2 to 7×10^{14} W/cm^2. These experimental results are compared with calculations from two theoretical models of two-plasmon-decay instability for the exact parameters of the experiment. The open squares are results obtained from the code *ZAK*,[12] which solves the equations of the extended Zakharov model.[36] The saturating nonlinearities included in the model are density-profile modification,[37] Langmuir wave cavitation,[38] and the generation of ion-acoustic turbulence.[12,39] While this plasma fluid model is able to describe the growth and nonlinear saturation of the instability, it does not include kinetic effects responsible for hot-electron generation. An estimate for the hot-electron temperature is obtained from the nonlinearly

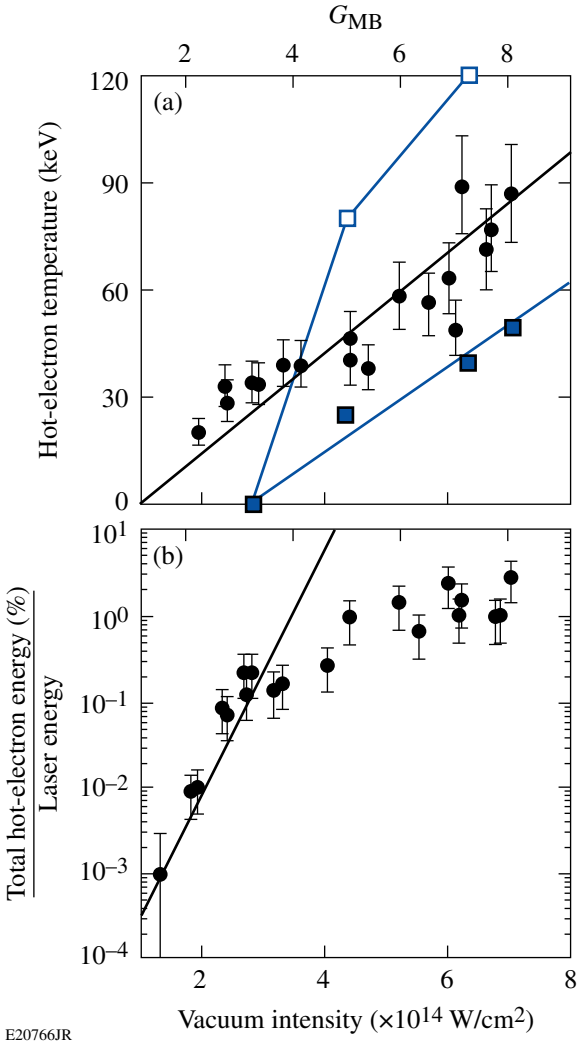

Figure 129.34
(a) The hot-electron temperature inferred from the HXRD measurements (circles) is shown as a function of the vacuum overlapped intensity and the multibeam convective gain. The hot-electron temperature is calculated by *ZAK* (open squares) and *QZAK* (solid squares) using the simulated $n_{cr}/4$ hydrodynamic parameters. (b) The fraction of total laser energy deposited into the hot electrons is plotted as a function of the vacuum overlapped intensity and the multibeam convective gain. An exponential scaling $\sim\exp\left(G_{MB}/0.3\right)$ is shown for comparison (line).

saturated state via the integration of test-electron trajectories in the electrostatic fields associated with the Langmuir turbulence (see Ref. 12 for more details).

The electron-plasma wave spectrum at saturation is found to be very broad, extending from small wave numbers up to the Landau cutoff ($k\lambda_D = 0.25$). When the effect of the turbulent electron-plasma wave spectrum on hot-electron production is investigated by integrating electron test particle trajectories,[12] the heating is found to be diffusive for electrons above a thresh-

old energy corresponding to the smallest phase velocity plasma waves (those at the Landau cutoff, $1/2 m_e v_\phi^2 \sim 20$ to 30 keV). The rate of diffusion (heating) was found to scale with $I_q L_n / T_e$ as a result of the interplay between the root-mean-square plasma-wave amplitudes and the available acceleration length.[12]

The solid squares show the results of a generalization of the *ZAK* model, called *QZAK*,[40] currently under development, where kinetic effects are taken into account self-consistently in the quasilinear approximation. The addition of kinetic effects reduces the amplitude of the electron-plasma waves, reducing the hot-electron temperature for a given $I_q L_n / T_e$. The difference between the two model predictions highlights the difficulty in making predictive calculations of a highly turbulent and complex physical system.

2. Fraction of Hot Electrons

Figure 129.34(b) shows the fraction of laser energy converted into hot electrons, which is estimated using the measured total K_α energy [Fig. 129.30(b)]. The large fraction of energy deposited into the hot electrons and the observed saturation of the TPD instability are direct consequences of the simultaneous high intensity and long scale lengths produced in these experiments.

It appears TPD is only convectively unstable in these experiments. The absolutely unstable electron-plasma waves, which depend only on the single-beam intensity, are well below the absolute intensity threshold (I_{th}) for the highest laser intensities tested;

$$\left\{\eta \equiv \frac{I_s}{I_{th}} = \frac{I_s\left(\times 10^{14}\ \mathrm{W/cm^2}\right) L_n(\mu\mathrm{m})}{230\ T_e(\mathrm{keV})} < 1\right\}$$

(Ref. 41), where I_s is the single-beam intensity at $n_{cr}/4$.

A convective gain for TPD that depends on the overlapped laser-beam intensity is presented in Ref. 42, where multiple laser beams are shown to drive common electron-plasma waves. For the experiments discussed here, the maximum convective gain is

$$G_{MB} \cong 1.5 \times 10^{-2} I_q \left(\times 10^{14}\ \mathrm{W/cm^2}\right) L_n(\mu\mathrm{m}) / T_e(\mathrm{keV}),$$

where I_q is the overlapped laser beam intensity at $n_{cr}/4$.

The multiple-beam gain is significantly larger than the single-beam gain $\left(G_{MB}/G_{SM} \simeq 3\right)$; note that the single-beam gain depends on the single-beam intensity $\left(I_s = I_q/4\right)$ and the intensity at $n_{cr}/4$ is ~55% less than the vacuum intensity. Figure 129.34 shows the experimental results plotted against the multiple-beam gain. A threshold for hot-electron generation is observed at a multiple-beam gain of ~2. It is likely that the actual gain for laser beams with DPP's (i.e., beams with speckles) is 2 to 5 times larger.[43]

At the highest overlapped-laser-beam intensity (7×10^{14} W/cm^2), the TPD gain increases approximately linearly in time over ~1.3 ns to a constant level of $G_{MB} \simeq 8$. When the gain reaches $G_{MB} \simeq 2.3$ ($t = 0.6$ ns), the hard x-ray signal begins to rapidly rise before reaching a nearly constant level [Fig. 129.30]. For the lowest intensities (1.3×10^{14} W/cm^2) where K_α radiation was detected (limited by signal to noise in the detector), the common-wave TPD gain is calculated to be $G_{MB} \simeq 2$, which is consistent with the gain threshold shown in Fig. 129.34.

Summary

This target platform was designed to account for all of the hot electrons generated by TPD. In general, the coupling of hot electrons to a fusion target will be reduced by the electron divergence, the distance between where the electrons are created and where they are absorbed, the electron energy distribution, and other loss mechanisms. The planar nature of these experiments, the fact that the laser beams are at near-normal incidence to the target, and the fact that they are linearly polarized in a common direction without polarization smoothing all tend to maximize the hot-electron generation. The multibeam linear gain depends on the geometry of the beams and their polarizations, which must be taken into account when applying these results to ignition designs.[42]

In summary, the high laser intensities generated over 1-mm-diam laser spots produced plasmas with a density scale length of 400 μm, causing two-plasmon decay to be driven to saturation. The hot-electron temperature is measured to increase rapidly (25 keV to 90 keV) with increasing laser-beam intensity (2×10^{14} W/cm^2 to 7×10^{14} W/cm^2). The total energy in hot electrons generated by TPD is measured to increase exponentially and saturate at a level of ~1% of the laser energy as the intensity is increased above 3×10^{14} W/cm^2. Uncertainties in the coupling of TPD electrons to the imploding shell and an accounting of the geometry and polarization of the laser beams prevent a quantitative assessment of the effect of TPD on direct-drive fusion, but these experiments suggest that maintaining the multibeam convective gain below 5 is a conservative approach to an acceptable level of hot-electron generation in direct-drive–ignition target designs.

ACKNOWLEDGMENT

We acknowledge the OMEGA EP operations team whose efforts provided the increased laser power necessary for these results. This work was supported by the U.S. Department of Energy Office of Inertial Confinement Fusion under Cooperative Agreement No. DE-FC52-08NA28302, the University of Rochester, and the New York State Energy Research and Development Authority. The support of DOE does not constitute an endorsement by DOE of the views expressed in this article.

REFERENCES

1. J. Nuckolls *et al.*, Nature **239**, 139 (1972).
2. R. L. McCrory, D. D. Meyerhofer, R. Betti, R. S. Craxton, J. A. Delettrez, D. H. Edgell, V. Yu Glebov, V. N. Goncharov, D. R. Harding, D. W. Jacobs-Perkins, J. P. Knauer, F. J. Marshall, P. W. McKenty, P. B. Radha, S. P. Regan, T. C. Sangster, W. Seka, R. W. Short, S. Skupsky, V. A. Smalyuk, J. M. Soures, C. Stoeckl, B. Yaakobi, D. Shvarts, J. A. Frenje, C. K. Li, R. D. Petrasso, and F. H. Séguin, Phys. Plasmas **15**, 055503 (2008).
3. T. R. Boehly, V. N. Goncharov, W. Seka, M. A. Barrios, P. M. Celliers, D. G. Hicks, G. W. Collins, S. X. Hu, J. A. Marozas, and D. D. Meyerhofer, Phys. Rev. Lett. **106**, 195005 (2011).
4. J. D. Lindl *et al.*, Phys. Plasmas **11**, 339 (2004).
5. V. N. Goncharov, T. C. Sangster, T. R. Boehly, S. X. Hu, I. V. Igumenshchev, F. J. Marshall, R. L. McCrory, D. D. Meyerhofer, P. B. Radha, W. Seka, S. Skupsky, C. Stoeckl, D. T. Casey, J. A. Frenje, and R. D. Petrasso, Phys. Rev. Lett. **104**, 165001 (2010).
6. H. Figueroa *et al.*, Phys. Fluids **27**, 1887 (1984).
7. M. V. Goldman, Ann. Phys. **38**, 95 (1966).
8. C. S. Liu, M. N. Rosenbluth, and R. B. White, Phys. Rev. Lett. **31**, 697 (1973).
9. B. B. Afeyan and E. A. Williams, Phys. Plasmas **4**, 3827 (1997).
10. M. N. Rosenbluth, R. B. White, and C. S. Liu, Phys. Rev. Lett. **31**, 1190 (1973).
11. D. F. DuBois, D. A. Russell, and H. A. Rose, Phys. Rev. Lett. **74**, 3983 (1995).
12. J. F. Myatt, J. Zhang, J. A. Delettrez, A. V. Maximov, R. W. Short, W. Seka, D. H. Edgell, D. F. DuBois, D. A. Russell, and H. X. Vu, Phys. Plasmas **19**, 022707 (2012).
13. N. A. Ebrahim *et al.*, Phys. Rev. Lett. **45**, 1179 (1980).
14. H. A. Baldis and C. J. Walsh, Phys. Rev. Lett. **47**, 1658 (1981).
15. W. Seka, D. H. Edgell, J. F. Myatt, A. V. Maximov, R. W. Short, V. N. Goncharov, and H. A. Baldis, Phys. Plasmas **16**, 052701 (2009).
16. C. Stoeckl, R. E. Bahr, B. Yaakobi, W. Seka, S. P. Regan, R. S. Craxton, J. A. Delettrez, R. W. Short, J. Myatt, A. V. Maximov, and H. Baldis, Phys. Rev. Lett. **90**, 235002 (2003).
17. An analytical error in the analysis of the HXRD used in Ref. 16 was identified and when corrected, the hot-electron temperature is reduced by ~40%.
18. J. H. Kelly, L. J. Waxer, V. Bagnoud, I. A. Begishev, J. Bromage, B. E. Kruschwitz, T. J. Kessler, S. J. Loucks, D. N. Maywar, R. L. McCrory, D. D. Meyerhofer, S. F. B. Morse, J. B. Oliver, A. L. Rigatti, A. W. Schmid, C. Stoeckl, S. Dalton, L. Folnsbee, M. J. Guardalben, R. Jungquist, J. Puth, M. J. Shoup III, D. Weiner, and J. D. Zuegel, J. Phys. IV France **133**, 75 (2006).
19. D. H. Froula, B. Yaakobi, S. X. Hu, P.-Y. Chang, R. S. Craxton, D. H. Edgell, R. Follett, D. T. Michel, J. F. Myatt, W. Seka, R. W. Short, A. Solodov, and "Saturation of the Two-Plasmon-Decay Instability in Long-Scale-Length Plasma Relevant to Direct-Drive Inertial Confinement Fusion," to be published in Physical Review Letters.
20. *LLE Review Quarterly Report* **127**, 109, Laboratory for Laser Energetics, University of Rochester, Rochester, NY, LLE Document No. DOE/NA/28302-1022 (2010).
21. T. J. Kessler, Y. Lin, J. J. Armstrong, and B. Velazquez, in *Laser Coherence Control: Technology and Applications*, edited by H. T. Powell and T. J. Kessler (SPIE, Bellingham, WA, 1993), Vol. 1870, pp. 95–104.
22. R. S. Craxton and R. L. McCrory, J. Appl. Phys. **56**, 108 (1984).
23. P. B. Radha, V. N. Goncharov, T. J. B. Collins, J. A. Delettrez, Y. Elbaz, V. Yu. Glebov, R. L. Keck, D. E. Keller, J. P. Knauer, J. A. Marozas, F. J. Marshall, P. W. McKenty, D. D. Meyerhofer, S. P. Regan, T. C. Sangster, D. Shvarts, S. Skupsky, Y. Srebro, R. P. J. Town, and C. Stoeckl, Phys. Plasmas **12**, 032702 (2005).
24. D. H. Froula, J. S. Ross, L. Divol. and S. H. Glenzer, Rev. Sci. Instrum. **77**, 10E522 (2006).
25. D. H. Froula, S. H. Glenzer, N. C. Luhmann, and J. Scheffield, *Plasma Scattering of Electromagnetic Radiation: Theory and Measurement Techniques*, 2nd ed. (Elsevier, Burlington, MA, 2011).
26. J. F. Seely *et al.*, Rev. Sci. Instrum. **81**, 10E301 (2010).
27. C. Stoeckl, W. Theobald, T. C. Sangster, M. H. Key, P. Patel, B. B. Zhang, R. Clarke, S. Karsch, and P. Norreys, Rev. Sci. Instrum. **75**, 3705 (2004).
28. B. Yaakobi, P.-Y. Chang, A. A. Solodov, C. Stoeckl, D. H. Edgell, R. S. Craxton, S. X. Hu, J. F. Myatt, F. J. Marshall, W. Seka, and D. H. Froula, Phys. Plasmas **19**, 012704 (2011).
29. U. Feldman *et al.*, Naval Research Laboratory and L. T. Hudson and S. Seltzer, National Institute of Standards and Technology, private communication (2011).
30. Spectral Instruments, Tucson, AZ 85745 (http://www.specinst.com/Products/800s_datasheet.pdf).
31. B. R. Maddox *et al.*, Rev. Sci. Instrum. **79**, 10E924 (2008).
32. A. L. Meadowcroft, C. D. Bentley, and E. N. Stott, Rev. Sci. Instrum. **79**, 113102 (2008).

33. C. Stoeckl, V. Yu. Glebov, D. D. Meyerhofer, W. Seka, B. Yaakobi, R. P. J. Town, and J. D. Zuegel, Rev. Sci. Instrum. **72**, 1197 (2001).

34. I. Kawrakow *et al*., NRC, Ottawa, Canada, NRCC Report PIRS-701 (May 2011); I. Kawrakow, Med. Phys. **27**, 485 (2000).

35. V. Metchnik and S. G. Tomlin, Proc. Phys. Soc. **81**, 956 (1963).

36. D. A. Russell and D. F. DuBois, Phys. Rev. Lett. **86**, 428 (1995).

37. A. B. Langdon, B. F. Lasinski, and W. L. Kruer, Phys. Rev. Lett. **43**, 133 (1979).

38. G. D. Doolen, D. F. DuBois, and H. A. Rose, Phys. Rev. Lett. **54**, 804 (1985).

39. R. Yan, A. V. Maximov, C. Ren, and F. S. Tsung, Phys. Rev. Lett. **103**, 175002 (2009).

40. D. A. Russell, presented at the Workshop on Laser Plasma Instabilities, sponsored by Lawrence Livermore National Laboratory and the University of Rochester's Laboratory for Laser Energetics, Livermore, CA, 3–5 April 2002.

41. A. Simon, R. W. Short, E. A. Williams, and T. Dewandre, Phys. Fluids **26**, 3107 (1983).

42. D. T. Michel, A. Maximov, B. Yaakobi, S. Hu, J. Myatt, A. Solodov, R. W. Short, and D. H. Froula, "Experimental Demonstration of the Two-Plasmon-Decay Common-Wave Process," submitted to Physical Review Letters.

43. H. A. Rose and D. F. DuBois, Phys. Rev. Lett. **72**, 2883 (1994).

A Front End for Ultra-Intense Optical Parametric Chirped-Pulse Amplification

Introduction

Ultra-intense laser systems are being developed that will use the full potential of deuterated potassium dihydrogen phosphate (DKDP) crystals for high-energy optical parametric chirped-pulse amplification (OPCPA).[1,2] Noncollinear pumping of DKDP produces broadband gain for supporting pulses as short as 10 fs. Large DKDP crystals (>400 × 400 mm) enable one to use Nd:glass lasers as kilojoule pump sources. The front ends for these systems must provide broadband pulses centered at ~910 nm to match the gain of DKDP noncollinear optical parametric amplifiers (NOPA's) when pumped at 527 nm. The amplified pulses must be compressible and focusable to maximize the on-target intensity, and the temporal prepulse contrast must be high enough to avoid perturbing the target. Previous front-end demonstrations used the idler from the first amplifier stage to seed subsequent amplifiers in either an angularly dispersed geometry[1] or a chirped collinear geometry.[2] An alternate approach, based on white-light–continuum (WLC) generation in a YAG plate,[3] is described in this article.

Development of a Mid-Scale, All-OPCPA System

Figure 129.35 shows the three phases of development of a 7.5-J, 15-fs optical parametric amplifier line (OPAL) that uses technologies scalable to kilojoule energies. Phase 1 has been completed, Phase 2 is in construction, and Phase 3 is being designed. In Phase 1, the first stages of a prototype front end

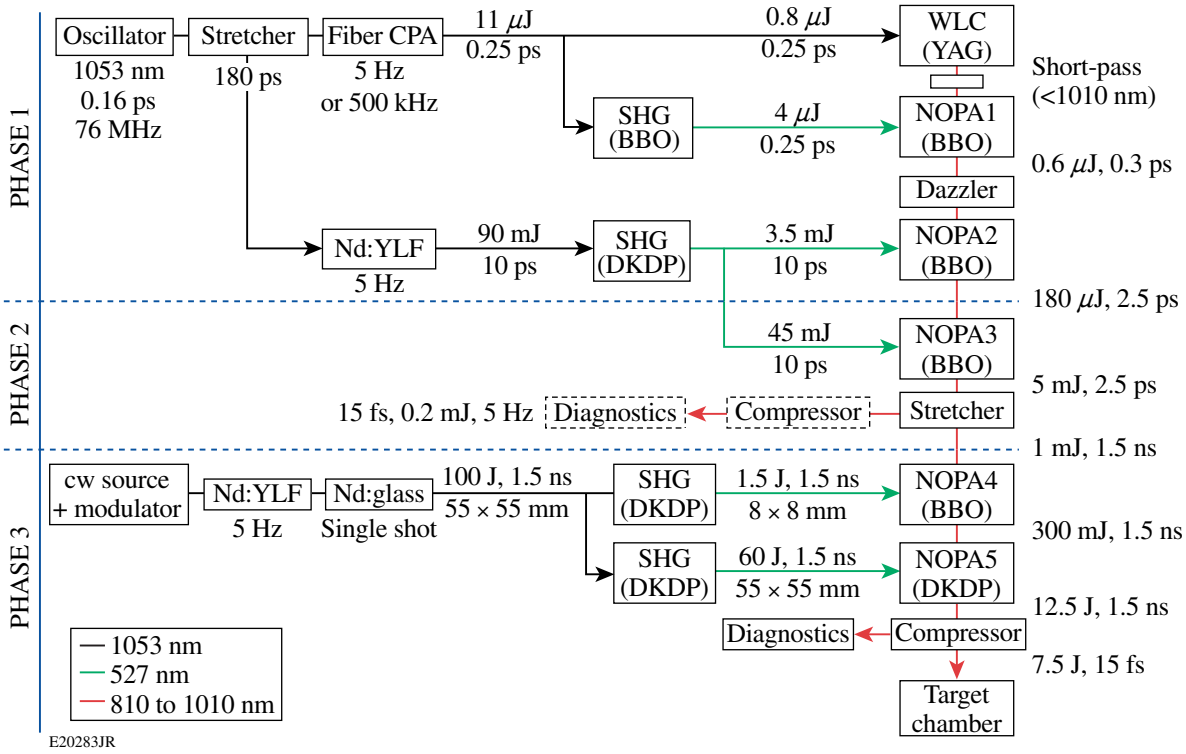

Figure 129.35
Schematic overview of a mid-scale optical parametric amplifier line (OPAL) that is in development. Phase 1 is completed, Phase 2 is in construction, and Phase 3 is being designed.

were developed to produce 180-μJ pulses with 200 nm of spectral support [160-nm full width at half maximum (FWHM)] centered at 910 nm (Fig. 129.36). Seeding the amplifiers with WLC simplifies the requirements for the seed oscillator and pump lasers and removes the need to eliminate the angular dispersion of the idler[1] or precisely set the spectral chirp of the pump.[2] Spectrum and spectral phase measurements made after recompression using a simple prism pair showed that the amplified white-light continuum was compressible to <13 fs, as expected [Fig. 129.36(b)].

Figure 129.37(a) shows a schematic of the nondegenerate NOPA-based cross-correlator[4] that was developed to measure the temporal contrast of the first NOPA stage. Measurements show a detection-limited prepulse contrast of greater than 120 dB up to −10 ps before the pulse [Fig. 129.37(b)].

Determining whether discrete peaks are real prepulses or artifacts caused by gate or pump postpulses is a problem common to all cross-correlators. For a NOPA-based device, however, the value of the peak can be determined from its scaling with the intensity of the pump.[4] By varying the pump-pulse energy before the cross-correlator and measuring the relative magnitudes of each peak, it was determined that all prepulses were caused by pump postpulses.

The second phase of OPAL is under construction. A pulse stretcher for the prototype front end has been developed based

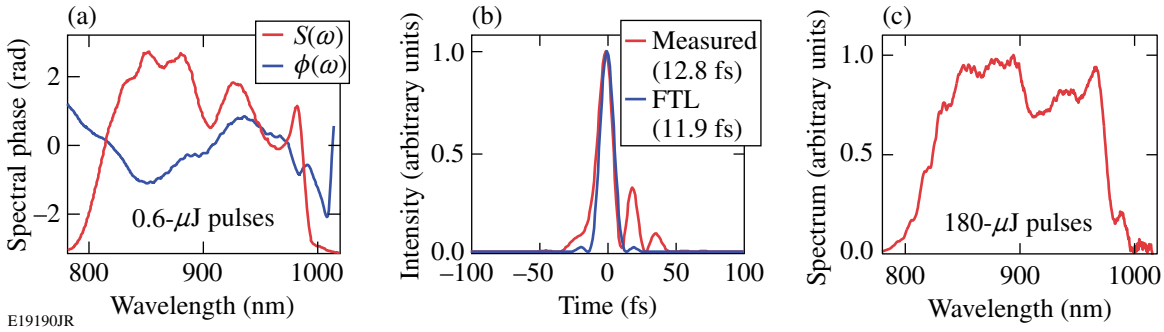

Figure 129.36
(a) Spectrum and spectral phase measurements after prism compression of NOPA1. (b) Calculations of the corresponding temporal intensity. (c) Spectrum after amplification to 180 μJ. FTL: Fourier transform limit.

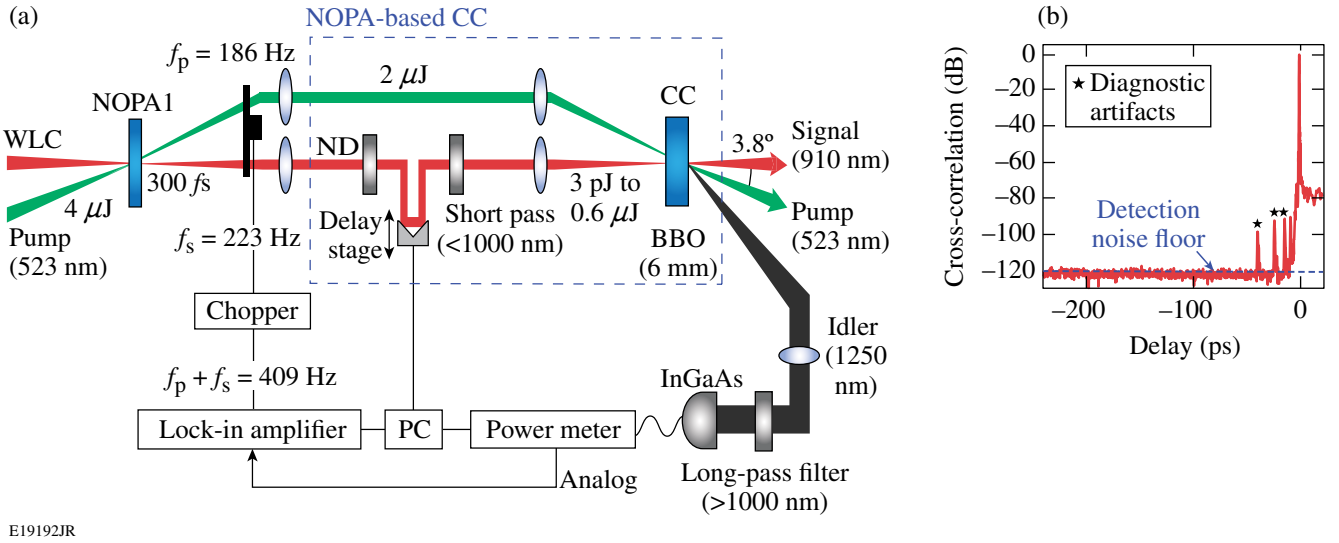

Figure 129.37
(a) Schematic of the NOPA-based cross-correlator for broadband (160-nm), high-sensitivity (39-dB gain), high-dynamic-range (120-dB) measurements of the prepulse contrast. (b) Temporal contrast measurements of the output of NOPA1 (before prism compression). BBO: beta-barium borate; CC: cross-correlator; InGaAs: indium gallium arsenide detector.

on a cylindrical Öffner design that has benefits beyond those originally proposed by Itatani *et al.*[5] Pulse stretchers with stretch ratios large enough for kilojoule systems (~10^5) must introduce minimal chromatic aberrations to ensure a high Strehl ratio at the laser focus.[6] They must permit preamplification using short-pulse–pumped parametric amplifiers to the millijoule level before stretching to improve temporal contrast.[7] Contrast degradation from their optical surface roughness imprinting on the spectral phase of the pulse must be minimized.[8] A cylindrical Öffner stretcher (COS) built to meet these requirements is being tested (Fig. 129.38). Modeling results in Fig. 129.38(b) show that a stretcher with cylindrical Öffner mirrors and two gratings (one at the center of curvature of the two Öffner mirrors) gives significantly better performance in these three areas than the standard spherical Öffner stretcher (SOS) with the same size optics and only one grating. Simulations predict that the mirror-limited temporal contrast is 30 dB better for the COS than a comparable-scale, single-grating SOS with similar surface quality because of the 50×-larger beam size on the secondary mirror.

In the third phase, the front end will seed a mid-scale optical parametric amplifier line (OPAL), which will be constructed next to LLE's Multi-Terawatt (MTW) laser.[9] Narrowband pulses from the MTW Nd:glass amplifier will be frequency doubled to provide up to 65 J for pumping the final beta-barium borate and DKDP amplifiers. OPAL will deliver 15-fs, 7.5-J pulses to an experimental target chamber at a rate of 1 shot/20 min. One stipulation for this system is that all technologies must be scalable to a full-kilojoule-scale OPAL, pumped by OMEGA EP's[10] four long-pulse beamlines, which could deliver 12 kJ of OPCPA pump energy at 527 nm.

Conclusion

OPAL provides a platform for addressing a number of technological challenges for ultra-intense lasers, many of which are shared with other ongoing projects. Areas that will be addressed include developing DKDP amplifiers and broadband and dichroic coatings with high damage thresholds; controlling spatial and spectral phases; relaying and up-collimating broadband, high-fluence beams; attaining high temporal contrast; and diagnosing the laser's single-shot performance.

ACKNOWLEDGMENT

This work was supported by the U.S. Department of Energy Office of Inertial Confinement Fusion under Cooperative Agreement No. DE-FC52-08NA28302, the University of Rochester, and the New York State Energy Research and Development Authority. The support of DOE does not constitute an endorsement by DOE of the views expressed in this article.

REFERENCES

1. V. V. Lozhkarev *et al.*, Laser Phys. **15**, 1319 (2005).
2. Y. Tang *et al.*, Opt. Lett. **33**, 2386 (2008).
3. M. Bradler, P. Baum, and E. Riedle, Appl. Phys. B **97**, 561 (2009).
4. J. Bromage, C. Dorrer, and J. D. Zuegel, in *Advanced Solid-State Photonics*, OSA Technical Digest (CD) (Optical Society of America, Washington, DC, 2011), Paper JWC2.
5. J. Itatani *et al.*, Opt. Commun. **134**, 134 (1997).
6. G. Chériaux *et al.*, Opt. Lett. **21**, 414 (1996).
7. C. Dorrer, I. A. Begishev, A. V. Okishev, and J. D. Zuegel, Opt. Lett. **32**, 2143 (2007).
8. J. Bromage, C. Dorrer, and R. K. Jungquist, "Temporal Contrast Degradation at the Focus of Ultrafast Pulses from High-Frequency

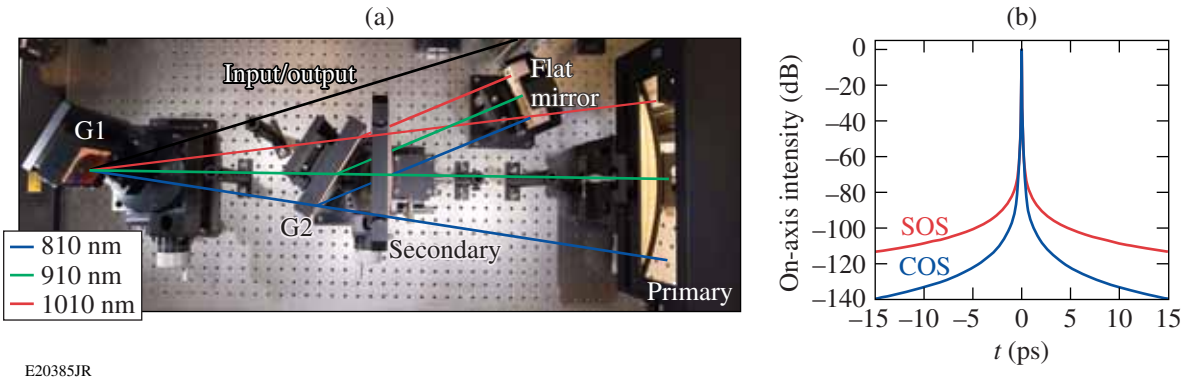

Figure 129.38
(a) Photograph of the cylindrical Öffner stretcher (COS) with an overlaid ray trace. (b) Calculated mirror-limited temporal contrast for the COS and a comparable-scale, single-grating spherical Öffner stretcher (SOS) with similar optical surface quality.

Spectral Phase Modulation," to be published in the Journal of the Optical Society of America B.

9. V. Bagnoud, J. Puth, I. Begishev, M. Guardalben, J. D. Zuegel, N. Forget, and C. Le Blanc, in *Conference on Lasers and Electro-Optics/Quantum Electronics and Laser Science and Photonic Applications, Systems and Technologies 2005* (Optical Society of America, Washington, DC, 2005).

10. J. H. Kelly, L. J. Waxer, V. Bagnoud, I. A. Begishev, J. Bromage, B. E. Kruschwitz, T. J. Kessler, S. J. Loucks, D. N. Maywar, R. L. McCrory, D. D. Meyerhofer, S. F. B. Morse, J. B. Oliver, A. L. Rigatti, A. W. Schmid, C. Stoeckl, S. Dalton, L. Folnsbee, M. J. Guardalben, R. Jungquist, J. Puth, M. J. Shoup III, D. Weiner, and J. D. Zuegel, J. Phys. IV France **133**, 75 (2006).

A Spherical Crystal Imager for OMEGA EP

Introduction

The unique capabilities of a crystal imaging system using spherically bent Bragg crystals are a narrow spectral width [$\lambda/\Delta\lambda$ >1000, (Ref. 1)], a high throughput (up to 100-fold improvement over pinhole imaging because of the larger solid angle), and a potentially high spatial resolution [<2 μm, (Ref. 2)]. Unlike a pinhole imager, a crystal imaging setup used in backlighting mode is insensitive to spatial nonuniformities in the backlighter intensity distribution because of its limited depth of field.[3] The major drawback of crystal imaging is the cost of the crystals and the complexity of the alignment. Crystal imaging has been frequently used on small- to medium-scale facilities, where the target chamber is vented between shots and direct operator access to the target chamber makes the alignment relatively easy.[1,2,4–7] On larger-scale facilities such as OMEGA EP,[8,9] where the target chamber stays at vacuum between shots, fully remote alignment of the crystal imager is required; consequently, only a very limited number of setups can be found in the literature.[3,10]

Experimental Setup

A crystal imaging system that can be remotely aligned and operated has been implemented on OMEGA EP (Fig. 129.39). In the first set of experiments this spherical crystal imaging (SCI) system used a quartz crystal, cut along the 2131 (211) planes for a $2d$ spacing of 0.3082 nm, to image the Cu K_α lines at ~8 keV. The Bragg angle of the quartz crystal for the Cu K_α is 88.7°, very close to normal incidence. The 25-mm-diam, ~150-μm-thick crystal was mounted by means of optical contact on a spherically shaped fused-silica substrate with a curvature radius of $R = 500$ mm. This curvature corresponds to a focal length of $f = R/2 = 250$ mm. The spherically bent crystal was fabricated by the Photonics Products Group, Inc. (PPGI).[11] The crystal is placed at a distance of 276 mm from the target, and the image is recorded on an image plate[12] located ~2.4 m from the target, resulting in a total magnification of ~10.

The SCI system uses two opposing ten-inch manipulators (TIM's) in its shot configuration, one housing the crystal and the other the image-plate detector. The TIM on OMEGA EP is a fully remote controllable three-axis diagnostic insertion system with an air lock, which allows the insertion of diagnostic modules of up to 25 cm in diameter and 50 kg of weight into the target chamber, without breaking vacuum.

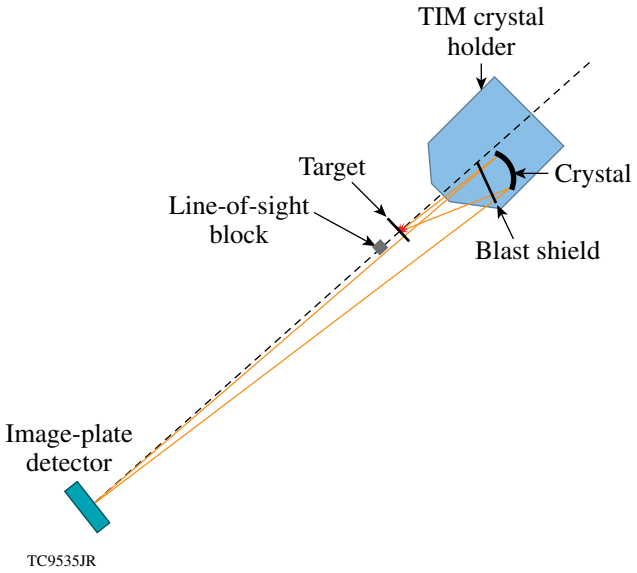

Figure 129.39
Schematic of the spherical crystal imager hardware in shot mode. One ten-inch manipulator (TIM) houses the crystal holder and another houses the image-plate detector. Both TIM's are on a common centerline indicated by the dashed line. A blast shield is placed in front of the spherically bent crystal, which images the target onto the detector. A direct line-of-sight tungsten block is placed opposite the crystal mount beyond the target to protect the detector from x-ray background emitted by the target.

The crystal is mounted on a motorized tip–tilt stage (New Focus 8817-V with PICO motor drive[13]) that sits on a TIM-mounted frame [Fig. 129.40(a)] and is inserted close to the target. A removable blast shield is placed in front of the crystal to protect it from debris. Because of the relatively high energy of the Cu K_α, the material and thickness of the blast shield are not critical even though the x rays must pass it twice. A blast shield of 10 to 20 μm of Al foil or 25 μm of Mylar coated with >100 nm of Al to prevent the scattered laser light from hitting

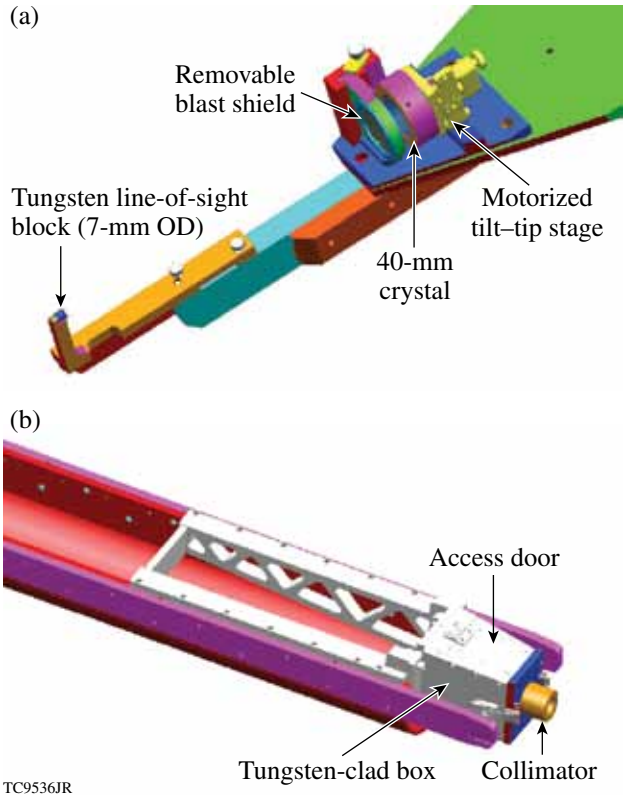

Figure 129.40
(a) CAD design of the crystal holder. The crystal is mounted on a motorized tip–tilt stage. A blast shield protects the crystal from target debris and can be removed for alignment. (b) CAD design of the image-plate holder. A tungsten-clad box houses the image plate, which records the image formed by the spherically bent crystal. An additional collimator is installed to further reduce the background from direct and Compton-scattered x rays. A filter foil is mounted in front of the collimator to optimize the signal level on the image-plate detector.

the crystal was sufficient for all experimental conditions. The blast-shield holder also accepts 1-mm-thick stainless-steel apertures to limit the active area of the crystal and to control the signal level on the detector. A 7.5-mm-thick, 7-mm-diam tungsten block protects the detector from x rays along the direct line of sight. The line-of-sight block is mounted on an arm attached to the crystal holder.

A CAD model of the image-plate detector's housing is shown in Fig. 129.40(b). A well-shielded, tungsten-clad box is mounted in the TIM opposing the crystal holder. An access door affords the operator easy access to insert the image-plate before the shot and remove it after the shot. A tungsten collimator reduces the field of view of the detector to suppress background from Compton scattering and fluorescence from structures in the target chamber. A Cu foil mounted in front of the collimator acts as a K-edge filter[14] to further improve the signal-to-background ratio. This filter is also used to optimize the signal level on the image-plate detector to prevent saturation. Typical filter thicknesses used in experiments range from 10 to 50 μm.

Alignment

The alignment procedure for the SCI system requires a number of steps. A pointer is first attached to the crystal holder hardware, and both the line-of-sight block and the blast shield are removed (Fig. 129.41). The tip of the pointer is optically aligned to target chamber center (TCC). The pointer is designed to set the distance from the crystal to the target to 276 mm, when the target is aligned to TCC. Mechanical alignment features in the pointer mount make a highly repeatable mounting of the pointer relative to the crystal mount possible. The pointer mount was designed not to block the two orthogonal lines of sight of the OMEGA EP Target Viewing and Alignment System. A precision of better than 100 μm can be achieved with this procedure.

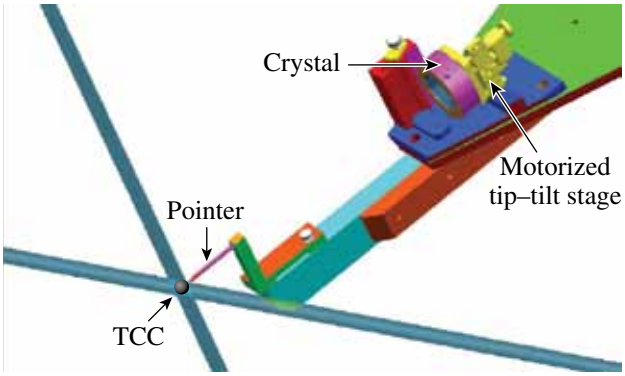

Figure 129.41
CAD design of the crystal holder in its pre-alignment configuration. A pointer is attached to the crystal holder hardware and optically aligned at target chamber center (TCC). The long, thin cylinders indicate the optical paths of the Target Viewing System.

In the next step the TIM coordinates are recorded, the TIM is retracted, and the pointer is removed from the crystal holder. The TIM is inserted again to its prerecorded position. Extensive tests have shown that this retract-and-insert cycle places the crystal back to the prerecorded position to within better than 100-μm accuracy. The tip of a single-mode fiber mounted in a third TIM is placed at TCC using the Target Viewing and Alignment System (Fig. 129.42). Light from an infrared (1053-nm) laser source is injected into the fiber. This light exits the fiber tip in an ~f/2 cone toward the spherically

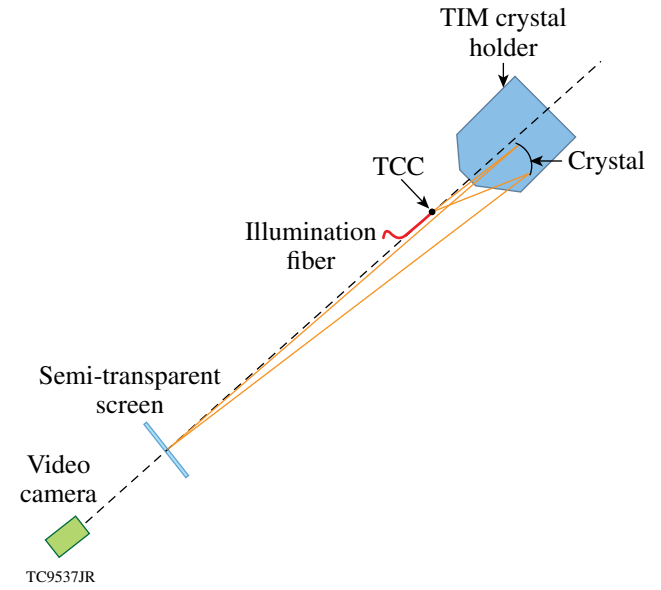

Figure 129.42
Schematic of the spherical crystal imager hardware in alignment mode. An illumination fiber is placed at TCC. Light from the fiber is reflected from the crystal to the semi-transparent screen. A video camera is used to optimize the focal spot on the screen.

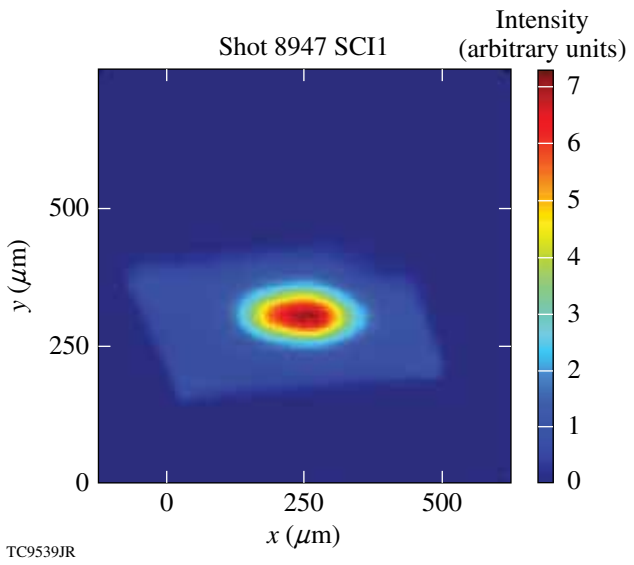

Figure 129.43
K_α image of a 500 × 500 × 20-μm^3 Cu foil, irradiated by an ~1-kJ, 10-ps, ~40-μm-diam OMEGA EP laser pulse. The spatial coordinates are scaled to the object plane.

bent crystal. A fraction of the infrared light is reflected off the crystal surface and sent toward the opposing TIM. The image-plate detector box in the opposing TIM is replaced by a semi-transparent screen, which is placed at the same distance from TCC as the image plate. This screen is viewed by an infrared-sensitive video camera. The motorized tip–tilt stages of the crystal mount are used to position the image formed by the spherical crystal at the center of the screen. Small corrections of the TIM insertion axis are used to optimize the focus of the crystal imager. The wavelength of the alignment source is not crucial. Off-line tests with a 680-nm-wavelength red laser have shown similar results. It is critical to use a single-mode fiber to generate a well-defined object, so that the crystal produces a clean image that can be used to optimize the focus.

Finally, the fiber is removed from its TIM, and the semi-transparent screen is replaced with the image-plate detector box. The crystal holder is retracted, and the blast shield and line-of-sight block are re-installed. The crystal holder is inserted again and the SCI system is ready for shots.

Experimental Data

Figure 129.43 shows one of the first images recorded with the SCI system. A 500 × 500 × 20-μm^3 Cu foil was irradiated by an ~1-kJ, 10-ps OMEGA EP laser pulse. The SCI views the target from an angle of 63° relative to the target normal, which leads to a foreshortening of the image in the vertical direction by a factor of ~2. Even though the laser focal spot is only ~40 μm in diameter, the image shows that the K_α radiation is emitted from the whole target area with an ~100-μm-diam bright spot located roughly where the laser hits the target. This image is consistent with other observations that show that most of the electrons generated in the laser–plasma interactions are confined to the target by strong electric fields set up when the first high-energy electrons leave the target and charge it to a multi-MeV potential.[15–17] The confined electrons flood the target and generate a quasi-uniform emission. The slightly darker area on the top-right corner of the target is due to the fact that the target is attached to a stalk at this corner, which allows the electrons to escape, thereby reducing the K_α emission.

The signal-to-background ratio is evaluated by measuring the average value of the signal on the image plate outside the object and comparing it to the signal measured at the edge of the image and the peak in the center of the image. With a typical background signal of 0.01 photostimulated luminescence (PSL) outside the image, ~1 PSL at the edge, and ~6 PSL at the peak, signal-to-background levels of 100 to 600 are observed.

To assess the spatial resolution of the SCI, lineouts are taken across the edge of the image at different locations (see Fig. 129.44). The rise of the signal from 10% to 90% of its

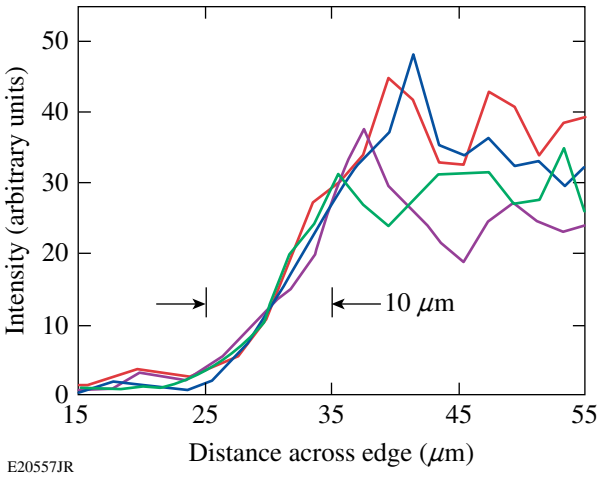

Figure 129.44
Edge lineouts of an image from the SCI at different locations. The signal rises from 10% to 90% of the peak in ~10 μm for the locations where the imager is in best focus.

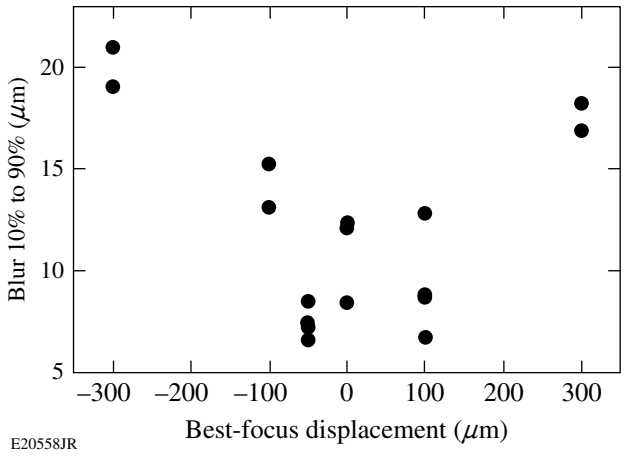

Figure 129.45
Edge rise from 10% to 90% of the peak as a function of defocus in the spherical crystal imager. Zero displacements are defined as the locations of the pre-shot optical alignment.

peak value is taken as a figure of merit for the resolution of the imaging system. This 10% to 90% criterion is a more-stringent measure of resolution, compared to a measurement of the modulation transfer function, where the resolution is usually defined at either a 50% or 10% contrast value. Since the imager has a limited depth of focus and views the object from a steep angle of 63° relative to the target normal, the resolution changes across the edge from ~10 μm, where the object is in best focus, to ~15 μm outside best focus.

A series of experiments were performed to measure the depth of focus of the imaging system by intentionally changing the crystal's distance from the target from the optimal position as determined by the pre-shot optical alignment (see Fig. 129.45). The best resolution of the SCI is observed in these experiments for displacements of <100 μm from the pre-shot alignment. At larger displacements the resolution deteriorates to values of the order of 20 μm at 300-μm displacement.

Summary and Conclusions

A crystal imaging system that can be fully remotely aligned has been implemented on OMEGA EP. A spherically bent quartz crystal is used to image the Cu K_α emission of targets irradiated with up to 1 kJ of laser energy at a 10-ps pulse duration. Experiments performed to map out the depth of focus of the crystal imager showed that the pre-shot optical alignment sets the SCI to its optimum focus condition. A best-focus resolution of ~10 μm, measured as the 10% to 90% rise on the edge of the image, has been achieved. The images show a very high signal-to-background ratio of >100, which indicates that the shielding concepts used in the setup of the SCI are effective and will provide adequate shielding even at the highest planned energies of 2.6 kJ at 10 ps on OMEGA EP. A similar crystal imaging system has been implemented on the OMEGA Laser System. Only minor adjustments to the mechanical layout of this system are required to adapt it to other spectral lines using different crystals and Bragg angles. Designs to modify the SCI to image the Si He_α spectral line are currently underway.

ACKNOWLEDGMENT

This work was supported by the U.S. Department of Energy Office of Inertial Confinement Fusion under Cooperative Agreement No. DE-FC52-08NA28302, the University of Rochester, and the New York State Energy Research and Development Authority. The support of DOE does not constitute an endorsement by DOE of the views expressed in this article.

REFERENCES

1. T. A. Pikuz *et al.*, in *EUV, X-Ray, and Neutron Optics and Sources*, edited by C. A. MacDonald *et al.* (SPIE, Bellingham, WA, 1999), Vol. 3767, pp. 67–78.
2. Y. Aglitskiy *et al.*, Appl. Opt. **37**, 5253 (1998).
3. J. A. Koch *et al.*, Rev. Sci. Instrum. **74**, 2130 (2003).
4. T. Missalla *et al.*, Rev. Sci. Instrum. **70**, 1288 (1999).
5. Ch. Reich *et al.*, Phys. Rev. E **68**, 056408 (2003).
6. S. Le Pape *et al.*, Rev. Sci. Instrum. **79**, 106104 (2008).
7. J. A. King, K. Akli, R. A. Snavely, B. Zhang, M. H. Key, C. D. Chen, M. Chen, S. P. Hatchett, J. A. Koch, A. J. MacKinnon, P. K. Patel,

T. Phillips, R. P. J. Town, R. R. Freeman, M. Borghesi, L. Romagnani, M. Zepf, T. Cowan, R. Stephens, K. L. Lancaster, C. D. Murphy, P. Norreys, and C. Stoeckl, Rev. Sci. Instrum. **76**, 076102 (2005).

8. L. J. Waxer, D. N. Maywar, J. H. Kelly, T. J. Kessler, B. E. Kruschwitz, S. J. Loucks, R. L. McCrory, D. D. Meyerhofer, S. F. B. Morse, C. Stoeckl, and J. D. Zuegel, Opt. Photonics News **16**, 30 (2005).

9. C. Stoeckl, J. A. Delettrez, J. H. Kelly, T. J. Kessler, B. E. Kruschwitz, S. J. Loucks, R. L. McCrory, D. D. Meyerhofer, D. N. Maywar, S. F. B. Morse, J. Myatt, A. L. Rigatti, L. J. Waxer, J. D. Zuegel, and R. B. Stephens, Fusion Sci. Technol. **49**, 367 (2006).

10. K. Fujita *et al.*, Rev. Sci. Instrum. **72**, 744 (2001).

11. Photonics Products Group, Inc., Northvale, NJ 07647.

12. A. L. Meadowcroft, C. D. Bentley, and E. N. Stott, Rev. Sci. Instrum. **79**, 113102 (2008).

13. New Focus, Inc., A Division of Newport Corporation, Irvine, CA 92606.

14. C. Stoeckl, W. Theobald, T. C. Sangster, M. H. Key, P. Patel, B. B. Zhang, R. Clarke, S. Karsch, and P. Norreys, Rev. Sci. Instrum. **75**, 3705 (2004).

15. J. Myatt, W. Theobald, J. A. Delettrez, C. Stoeckl, M. Storm, T. C. Sangster, A. V. Maximov, and R. W. Short, Phys. Plasmas **14**, 056301 (2007).

16. P. M. Nilson, W. Theobald, J. Myatt, C. Stoeckl, M. Storm, O. V. Gotchev, J. D. Zuegel, R. Betti, D. D. Meyerhofer, and T. C. Sangster, Phys. Plasmas **15**, 056308 (2008).

17. K. U. Akli, M. H. Key, H. K. Chung, S. B. Hansen, R. R. Freeman, M. H. Chen, G. Gregori, S. Hatchett, D. Hey, N. Izumi, J. King, J. Kuba, P. Norreys, A. J. Mackinnon, C. D. Murphy, R. Snavely, R. B. Stephens, C. Stoeckel, W. Theobald, and B. Zhang, Phys. Plasmas **14**, 023102 (2007).

Amplitude Distributions of Dark Counts and Photon Counts in NbN Superconducting Single-Photon Detectors Integrated with a High-Electron Mobility Transistor Readout

Introduction

Fast and reliable single-photon detectors (SPD's) have become a highly sought after technology in recent years.[1] Some of the most-interesting applications for SPD's, which include quantum communications and quantum key distribution[2] as well as satellite communications, require devices that can successfully operate at telecommunication wavelengths, namely 1310 nm and 1550 nm. Additional very desirable features for ideal SPD's are their photon-number resolution (PNR) capability,[3,4] e.g., for all-optical quantum computing, and their photon-energy sensitivity (PES),[5] e.g., for spectral observations of so-called photon-starved objects. InGaAs avalanche photodiodes work at telecommunication wavelengths and are commercially available; they do, however, suffer from severe after-pulsing and require time gating, which limits their maximum count rate. Presently, they also lack advanced PNR and PES capabilities.[6,7]

It has already been established that nanostructured, NbN superconducting SPD's (SSPD's) operate based on hot-spot formation and bias-current redistribution in ultrathin (4-nm), ultranarrow (100- to 120-nm), and long (~0.5-mm) meandering NbN superconductive nanostripes.[1,8] NbN SSPD's have been shown to have counting rates exceeding 250 MHz, with reported quantum efficiencies (QE's) up to 57% (Ref. 9) at 1550-nm wavelength and very low, <10-Hz to 10-kHz dark-count rates, depending on the operation bias point.[10]

Typically, the SSPD's are kept at temperatures between 1.7 and 4.2 K (far below the NbN critical temperature T_c) and biased at currents I_{bias} close to the meandering stripe critical current I_c. Once a photon is absorbed by the NbN nanostripe, it breaks a Cooper pair, and, subsequently, a large number of quasiparticles are generated through the electron–electron and electron–phonon interactions, creating a local hot spot, where superconductivity is suppressed or even destroyed. The hot spot expels the supercurrent from its volume and forces it to flow near the stripe edges, where it can exceed the I_c value, leading to the generation of phase-slip centers and the eventual formation of a resistive region (joule heating) across the width of the stripe.

When the SSPD device is directly connected to a transmission line with a characteristic impedance Z_0 equal to, e.g., 50 Ω, the above-mentioned resistive region, which is typically $\gg$50 Ω, forces the bias current to redistribute from the SSPD into the load, which means that the amplitude of the SSPD voltage response is always measured across the constant Z_0. The above conclusion would be true even if the SSPD were simultaneously illuminated by several photons and, consequently, several hot spots were simultaneously generated at various points along the meander. Therefore, in the above experimental arrangement, which is actually typical for the vast majority of published work, the SSPD photoresponse is insensitive to both the number and energy of incoming photons, and the device acts as a simple photon-event counter rather than an energy and/or spectrally sensitive detector.

We need to stress here that a biased SSPD can generate output electrical pulses even when the input light is completely blocked and there are no photons incident on the device. Those so-called dark-count pulses are transient voltage signals, spontaneously generated in a long, current-biased, superconducting nanostripe, and, when the device is connected to an output of a coaxial line, their amplitude is limited by Z_0 despite the fact that the physical origin of dark counts is different from that responsible for photon counts. In the case of dark counts, the transient resistive state across the SSPD nanostripe is actually caused by the current-induced generation and propagation of free vortex–antivortex pairs.[11,12] Therefore, in experimental studies of the SSPD performance, it would be very important to be able to distinguish the photon counts from the dark counts.

The goal of this work is to show that, with our recently developed new readout scheme that implements a low-noise, cryogenic, high-electron-mobility transistor (HEMT) and a high-load resistor next to the detector,[13] we are able, albeit not in real time, to resolve the difference between the SSPD dark- and photon-count events by collecting histograms of the output-pulse distributions and, subsequently, comparing their mean amplitudes and distribution widths. We also present our early findings that demonstrate that the same readout approach

can lead to some PNR functionality in SSPD's, as predicted in Ref. 14. We stress that although the research presented here is rather preliminary, it does represent an important step toward making SPD's true photon sensor-type devices with energy resolution.

This article begins with a brief description of the SSPD fabrication process and presents our experimental setup based on the high-input-impedance HEMT readout circuit. Next, we introduce a simple equivalent circuit of the SSPD, based on the fixed-equivalent-resistance hot-spot model and discuss its practical limitations, namely, the conditions that are needed to fulfill the requirement that the readout input impedance is always the dominant factor. Our experimental data are, subsequently, presented and consist of long, real-time SSPD traces collected either under photon illumination or in the dark. A statistical approach is used for the data analysis to calculate the corresponding distributions functions. The comparison between the distributions' mean amplitudes and widths enables one to quantitatively distinguish photon absorption events from dark counts. The presented analysis demonstrates how experimental data collected by an SSPD directly connected to the high-impedance readout can either shed light on the average photon number of the incident ultraweak flux of monochromatic light or provide some spectral characterization of multicolor pulses. Finally, a summary and concluding remarks are presented.

Device Description and Experimental Setup

SSPD's were patterned from epitaxial-quality NbN films, deposited by dc reactive magnetron sputtering onto sapphire substrates.[15] The films were characterized by a sheet resistance between 400 and 500 Ω/sq at room temperature, with T_c between 10 and 11 K, and the critical current density $J_c \approx 10^6$ A/cm^2. The meander patterning was done by e-beam lithography and reactive-ion etching. It is important to note here that while the films were deposited at the Moscow State Pedagogical University, they were patterned at Delft University of Technology. Apparently, slight differences in geometry or in the patterning method were responsible for the fact that the SSPD's in this work had 3×- to 4×-lower I_c's (~5 to 10 μA) than the typical Moscow devices.[15] The QE's, however, were on a par with the standard 10×10-μm^2 SSPD's, with the devices measured in this work having QE ≈ 3% to 5% at λ = 800 nm.

The standard SSPD operation setup is shown in Fig. 129.46(a). The device was wire bonded to a 50-Ω microstrip transmission line, coupled to a multimode optical fiber, and immersed in liquid helium.[16] The microstrip was then connected to a semi-rigid coaxial cable and, at room temperature, connected to a custom-made, wideband bias-tee (0.08- to 26-GHz bandwidth). The bias-tee enabled us to simultaneously amplify the transient photoresponse signal using a tandem of two broadband amplifiers (0.08- to 8.5-GHz bandwidth, 22-dB gain) and to dc bias both the SSPD and HEMT. The amplified output signals, corresponding to photon counts and/or dark counts, were recorded by using either a Tektronix digital single-shot oscilloscope (6-GHz bandwidth) or a pulse counter. As a photon source, we used a train of 100-fs-wide, 800-nm-wavelength pulses, generated by a mode-locked Ti:sapphire laser at a rate of 82 MHz. The pulses were heavily attenuated to precisely control the average number of photons per pulse. For dark-count measurements, the detector was blocked from all incoming radiation, i.e., shielded inside the Dewar by a metallic enclosure.

An equivalent electrical model of the SSPD photoresponse is shown in Fig. 129.46(b). Kinetic inductance L_k is in series with a parallel arrangement of a hot-spot resistance R_{hs}, and a switch S represents the photodetection (switching) event in the SSPD.[17] The detector is then connected to a dc bias source and a readout circuit, which, in this case, consists of a transmission line with input impedance Z_0 = 50 Ω. In the simulations presented on p. 41, we also took into account [not shown in Fig. 129.46(b)] a small, parasitic on-board capacitance and a bandpass filter representing the bandwidth of an outside (room-temperature) amplifier. Finally, V_{out} is the experimentally observed transient voltage pulse during photodetection.

Initially, the switch is closed and there is no voltage drop. Once a photon is absorbed by our nanostripe, the switch opens, and as R_{hs} grows to a value much larger than Z_0, most of the

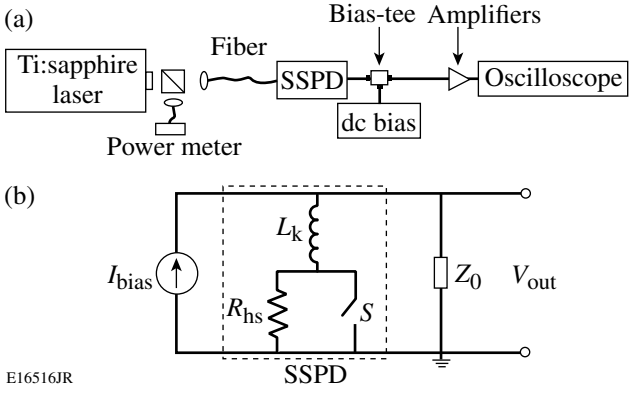

Figure 129.46
(a) Experimental setup and (b) standard electrical photoresponse model of SSPD (superconducting single-photon detector).

current redistributes into Z_0, and the resultant voltage pulse amplitude is simply $V_{out} \approx Z_0(I_{bias} - I_{ret})$, where I_{ret} is the value of current flowing through the device at the highest value of R_{hs} (Ref. 17). Therefore, independent of the number or energy of the absorbed incident photons, V_{out} always has the same value for a given I_{bias} for the circuit shown in Fig. 129.46(b).

Our high-impedance readout scheme, presented in Fig. 129.47, was first described in Ref. 13 and, as already outlined there, it implements a commercial HEMT, operated cryogenically, and mounted next to (on the same board) the SSPD. The HEMT acts as an infinite-impedance element to separate the 50-Ω output transmission line from the SSPD. Because the HEMT input impedance is very high, a 500-Ω load (or shunt) resistor R_L is also used in parallel with the detector and the HEMT, as shown in Fig. 129.47. As mentioned previously, both the SSPD and HEMT were biased through the same custom-made, wideband bias-tee. Such an integrated arrangement enables one to bias the devices using R_{bias} = 150 kΩ, mounted on the board together with the rest of the components and, simultaneously, to read out the ac photoresponse voltage signal.

By applying the detector transient response to the gate of the HEMT, one can read out the drain voltage, which should, ideally (for $R_L \gg R_{hs}$), be proportional to the hot-spot resistance and equal to V_{out}. If the number of photons simultaneously absorbed in the SSPD meander happens to be larger than 1, the photons are likely to form separate hot spots and their resistances will add up in series. The HEMT output voltage in this simplest case should be $V_{out} \approx (I_{bias} - I_{ret})nR_{hs}$, where n is the number of absorbed photons per pulse (actually, the number of created hot spots). Therefore, for relatively small n's, and in the case of $nR_{hs} < R_L$, the output-pulse height of our setup is proportional to n, effectively leading to PNR, as was theoretically discussed and modeled in Ref. 14.

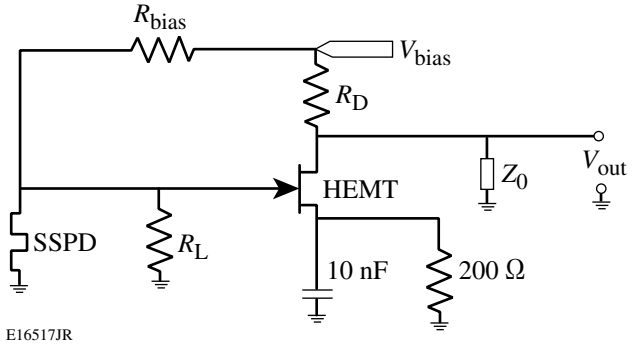

Figure 129.47
Circuit schematics implementing a HEMT (high-electron-mobility transistor) amplifier and 500-Ω load resistor R_L. The 10-nF capacitor sets the maximum ac gain and the 200-Ω resistor sets the dc current for the HEMT; R_{bias} and R_D are the biasing and pull-up resistors, respectively.

Based on an intrinsic difference in the physics mechanisms of the generation of photon and dark-count transients in SSPD's discussed above, the HEMT setup should also enable one to distinguish pulses generated in response to either a single-photon absorption event (photon count) or a spontaneous voltage transient (dark count). In the case of dark counts, one can expect only a single localized resistive region, created by the vortex–antivortex pair's (VAP's) motion across the stripe,[12] with the effective resistance different than R_{hs}, resulting in a somewhat different value of V_{out}. In the full analogy, it is expected that photons of different energies should produce hot spots with different R_{hs} values, so our SSPD with the HEMT readout should possess PES functionality.

Readout Circuit Simulations and Model Limitations

Our HEMT approach takes advantage of the simple fact that the greater the R_L, the more sensitive the readout in terms of either PNR or PES. Unfortunately, this cannot be easily accomplished since the large R_L values lead to an underdamped circuit behavior (see Fig. 129.48) because of a very large value of the indicator ($L_k \sim 400$ nH) of our SSPD[17] in parallel with R_L. Figure 129.48(a) shows the PSpice[a]-simulated pulses for different values of R_L. Critical damping yields R_L = 270 Ω (red curve) in Fig. 129.48(a), and it can be seen that for R_L = 500 Ω (green curve), the circuit is already slightly underdamped since a small, damped oscillation follows the main pulse. Figure 129.48(b) shows an experimental voltage pulse (black line) obtained using our HEMT readout approach, as well as a simulated one (red dashed line). The slow, damped oscillations behind the measured main pulse are caused by some second-order, capacitive effects from the HEMT circuit and/or stainless-steel coaxial line. An associated small parasitic capacitance (not shown in Fig. 129.47) has been estimated to be 2 to 3 pF, by looking at the oscillation frequency of the underdamped pulse.

Our tested SSPD's typically exhibited $I_c \approx 5\ \mu$A, leading to the roughly estimated R_{hs} value to be between 600 and 1000 Ω. Therefore, based on the behavior observed in Fig. 129.48, we selected R_L = 500 Ω for all our experiments as a compromise between the optimal value (minimal oscillations) from the

[a]PSpice (currently available from OrCAD Corp. of Cadence Design Systems) is a PC version of SPICE, originally developed at the Electronics Research Laboratory of the University of California, Berkeley (1975).

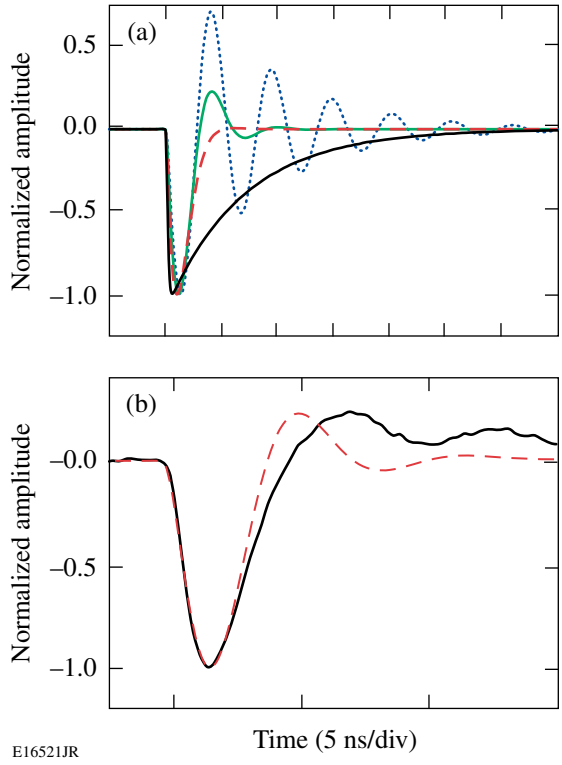

Figure 129.48
(a) PSpice simulations of voltage transients at different values of R_L: 50 Ω (black curve), 270 Ω (red dashed curve), 500 Ω (green curve), and 2 kΩ (blue dotted curve); (b) measured photoresponse (black curve) and simulated photoresponse (red dashed curve) for R_L = 500 Ω.

circuit point of view and the need to have R_L as large as possible to achieve PNR functionality. Since R_L = 500 Ω is at best comparable to R_{hs}, the experimentally measured V_{out} readout signal amplitude is proportional to a parallel connection of R_L and R_{hs}, limiting the ability to fully quantitatively distinguish between the different types of SSPD counting events. Therefore, the experimental observations presented here are mainly qualitative. In addition, since real-time analysis has been inconclusive, it was decided to use a statistical approach to analyze our experimental data.

Our approach of an SSPD integrated with an HEMT readout with a fixed R_L = 500 Ω value can work satisfactorily, as will be shown later, but only for devices with rather small I_c and, consequently, typically, low QE. In large-QE SSPD's biased close to I_c, as shown in Ref. 18, the R_{hs} can be as large as 5.5 kΩ, mainly because of joule heating. Joule heating of the nanostripe turns it completely resistive and occurs in parallel with the hot-spot cooling process and current redistribution.[18] The latter can be well illustrated looking at the time-domain evolution of the photoresponse transient. Based on the electrical model shown in Fig. 129.47, the difference in amplitude for different hot-spot resistances stem from variations in the time interval it takes for the current initially biasing the device to redistribute into the readout circuit. In other words, for a given R_L, current redistribution time decreases with increasing R_{hs}. For the hot spot to stop growing and the cooling mechanism to take over, the current through the device must drop to a value below approximately 20% of I_c (Ref. 19). When the SSPD photoresponse is modeled such that R_{hs} is a simple resistor, the fall and rise time constants of the transient V_{out} are simply $\tau_{fall} = L_k/(R_{hs} + R_L)$ and $\tau_{rise} = L_k/R_L$ (Ref. 17), respectively. On the other hand, if R_{hs} progressively increases during the current redistribution, the entire process becomes nonlinear and the transient decay cannot be modeled by a simple exponential function. From the readout circuit point of view, this is a very challenging problem since even if it were possible to find a cryogenic amplifier with large enough R_L, the readout scheme would not work because the current would not be able to redistribute into the load fast enough to prevent a runaway heating effect that would cause the device to simply latch.

We believe the best approach to restrict the uncontrolled growth of R_{hs} and, consequently, suppress the heat runaway effect is to significantly improve the heat transport between the superconductor and the substrate (single-crystal sapphire for "standard" SSPD's), either by using substrates, which are a better acoustic-phonon match to NbN, or by changing the nanostripe material. In the latter case, the ferromagnet/superconductor nanostructured bilayers are very promising because, as has recently been shown, they exhibit much-faster electron–phonon dynamics, as compared to plain Nb or NbN.[20,21]

Results and Discussion

During the course of our experiments, we have collected very long (millions of pulses) real-time traces by continuously recording either photon-count events or dark counts. In the latter case, the voltage response was measured when an SSPD was completely isolated from the outside world. Figures 129.49(a) and 129.49(b) present randomly selected, short sections of photon-count traces of output pulses (after amplification) recorded in time-domain when an SSPD was connected either according to the conventional 50-Ω scheme [Fig. 129.46(b)] or a scheme with an HEMT readout (Fig. 129.47), respectively. The incident laser intensity was adjusted in such a way that nearly every photon pulse was registered by the detector (for an SSPD with QE ≈ 5% that corresponds to ~500 photons per pulse). These plots are intended to illustrate a qualitative difference in the recorded photoresponse signals, since even from such short "snapshots," it can clearly be seen that while in the

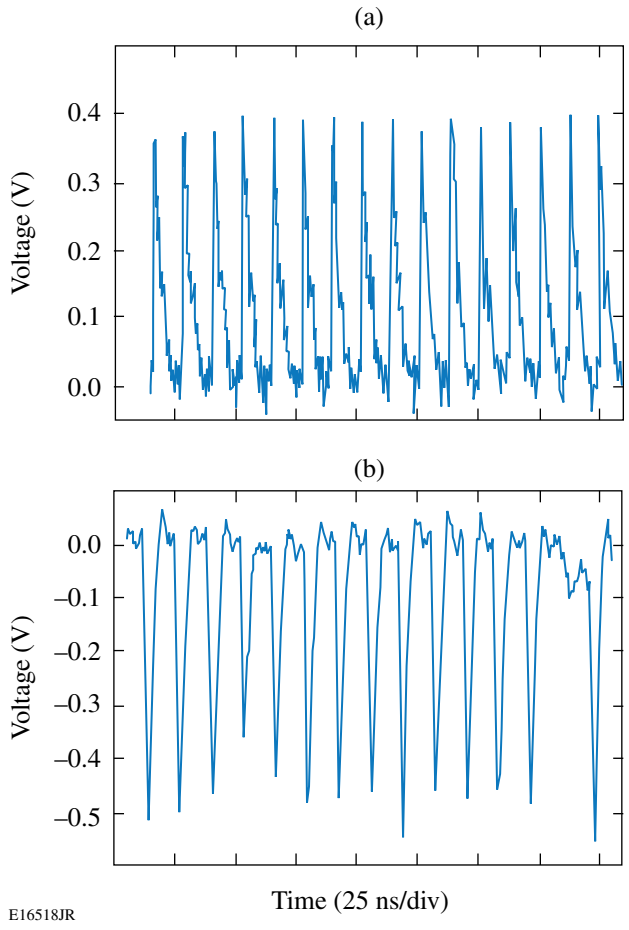

Figure 129.49
Comparison of live oscilloscope time-domain traces for (a) a traditional scheme and (b) an HEMT readout scheme, taken at similar laser intensities, such that $n \leq 1$ (HEMT is an inverting amplifier; therefore the pulses are negative). Here, n is the number of absorbed photons per pulse. The laser repetition rate is 82 MHz.

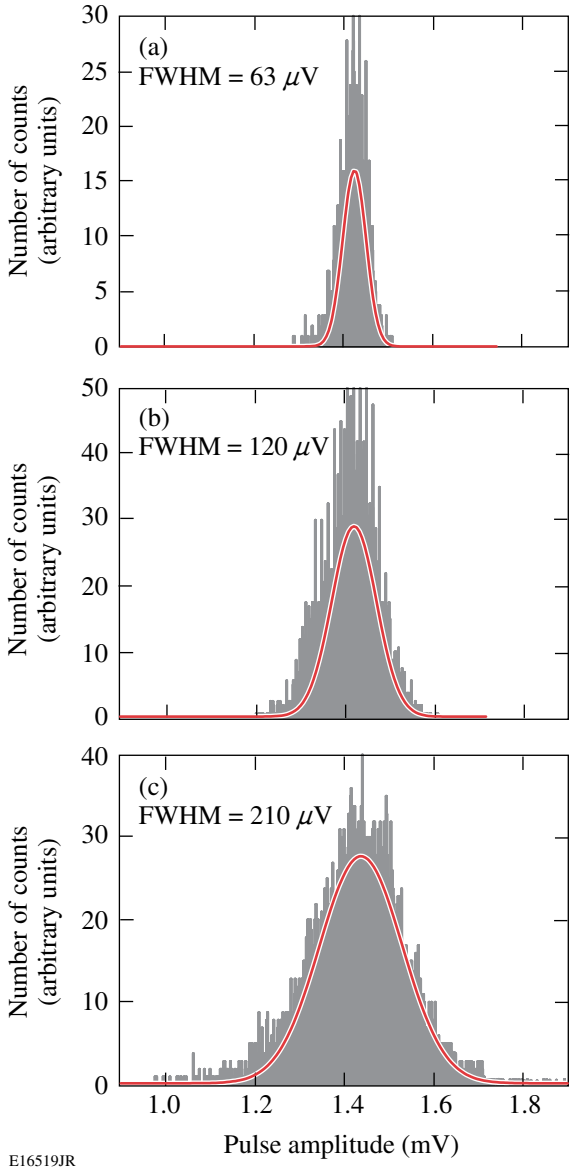

Figure 129.50
(a) Pulse-amplitude histograms of dark counts, (b) photon counts in the single-photon regime $n \sim 1$, and (c) multiphoton regime $n \geq 1$. All measurements performed the HEMT readout at 4.2 K and at $I_{bias} = 0.9\ I_c$. The SSPD output-voltage amplitudes are divided by the amplifier gain.

case of the conventional biasing technique, pulse amplitudes remain essentially constant, the HEMT readout allows one to record at least some quantitative differences between the different SSPD counting events.

For a more-quantitative analysis, a statistical approach was used to compute the distribution functions of amplitudes of pulses recorded under different experimental conditions. Figure 129.50 shows histograms that compare pulse-amplitude distributions of dark counts [Fig. 129.50(a)], as well as the photon counts collected at two different laser intensities [Figs. 129.50(b) and 129.50(c)]. All data were taken using the HEMT readout and in each case the SSPD was biased using $I_{bias} = 0.9\ I_c$. All histograms were fitted with a simple Gaussian function and it is clear that the dark counts [Fig. 129.50(a)] exhibit the narrowest full-width-at-half-maximum (FWHM) distribution. For the photon counts, we observe a widening of the Gaussian distribution as we move from the single-photon regime [$n \sim 1$; Fig. 129.50(b)] to the multiphoton case [$n \geq 1$; Fig. 129.50(c)]. In principle, the observed increase in the width of the Gaussian distribution for the photon counts could have resulted from excess shot noise. To verify this hypothesis, we have additionally recorded a histogram (Fig. 129.51) of output pulses collected when the SSPD was operated under the same

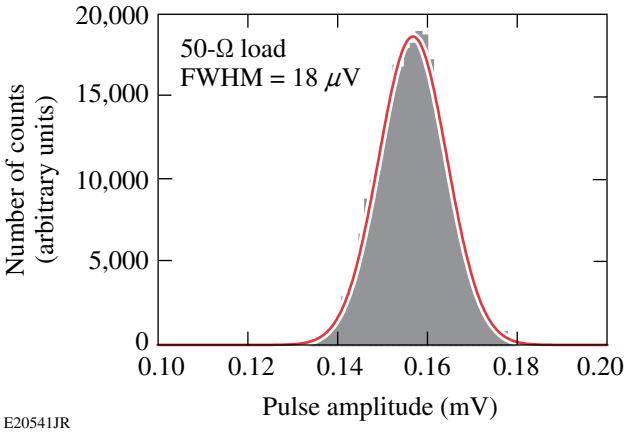

Figure 129.51
Pulse-amplitude histogram of photon counts in the single-photon regime ($n \sim 1$), when the SSPD was directly connected to the 50-Ω output coaxial line (no HEMT readout). All measurements were performed at 4.2 K and $I_{bias} = 0.9\, I_c$. The SSPD output-voltage amplitudes are divided by the amplifier gain.

conditions as in Fig. 129.50(b), namely, in the single-photon regime; however, in that case, our detector was directly connected to the 50-Ω output line. We note that the histogram shown in Fig. 129.51 exhibits almost a perfect Gaussian distribution with a very narrow, noise-delimitated width. Therefore, the impact of the shot noise is negligible and we can conclude that, indeed, the HEMT readout allows one to get at least a quantitative insight on the amplitude variations of the SSPD voltage output pulses, when the device is operated under different experimental conditions, e.g., the different incident photon flux levels.

A large number of histograms of the type presented in Fig. 129.50 have been collected under different SSPD biasing and optical illumination conditions. The correlation between the photon flux (average number of photons per pulse) incident upon the detector and the FWHM of the resulting distribution of the response pulse amplitudes was very reproducible and is summarized in Fig. 129.52, where the FWHM of the signal amplitude histograms versus the SSPD normalized current bias I_{bias}/I_c is presented, for both the dark counts (open squares) and the photon counts corresponding to the multiphoton ($n \geq 1$, closed triangles), single-photon ($n \sim 1$; open triangles), and heavily attenuated ($n \ll 1$; closed circles) illumination. We see that the dark-count signals exhibit the narrowest FWHM, which, in addition, is independent of the bias. Substantial differences also exist between the FWHM values corresponding to different incident photon fluxes. The general trend is that the distribution width increases with increasing I_{bias}/I_c, which is caused by the increased SSPD sensitivity in the $I_{bias} \approx I_c$

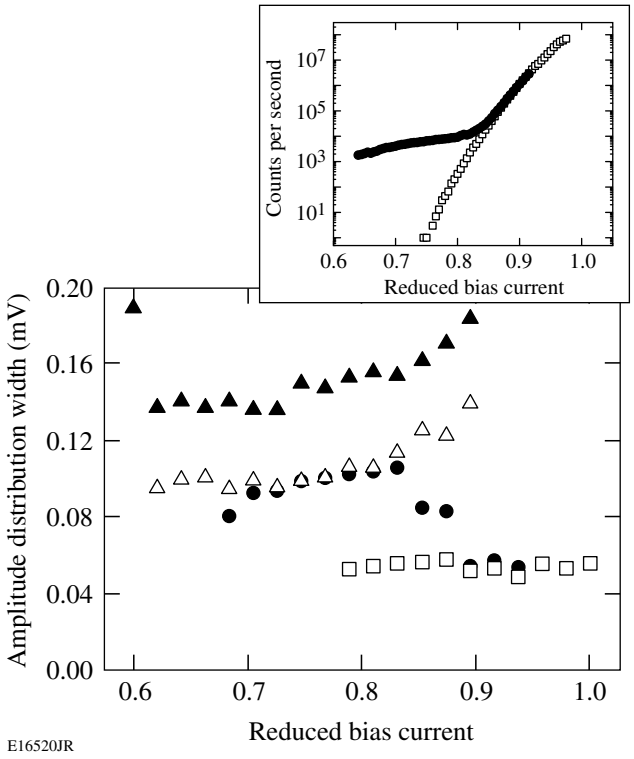

Figure 129.52
Amplitude distribution width (FWHM of Gaussian fits) for dark counts (open squares), $n \ll 1$ (closed circles), $n \sim 1$ (open triangles), and $n \geq 1$ (closed triangles). The inset shows the counting rate as a function of bias current for dark counts (open squares) and $n \ll 1$ (closed circles).

biasing regime, where even photons hitting the edges of the nanostripe are likely to be counted.[22] On the other hand, for a very low photon flux ($n \ll 1$; closed circles in Fig. 129.52), the amplitude distribution FWHM starts to drop around $I_{bias} = 0.83\, I_c$, eventually overlapping (open squares) at $I_{bias} > 0.9\, I_c$, as the dark counts dominate over the photon counts. The latter behavior agrees very well with our earlier observation[11] of the near-exponential dependence of the rate of dark counts in SSPDs on the I_{bias}/I_c ratio and their dominance in the $I_{bias} \approx I_c$ limit, as shown in the inset in Fig. 129.52.

The significant difference (a factor of several) in the FWHM values of the histograms for the dark- and photon-count events collected for the SSPD with the HEMT readout must have come from the intrinsic difference in the physics of triggering those counts. As demonstrated in Ref. 12, when a current-biased SSPD is blocked from all incoming radiation (shielded by a metallic enclosure) and placed in liquid helium, the spontaneous transient voltage pulses, or dark counts, are primarily caused by topological excitations. The thickness of the NbN stripe is 4 nm and the width is ~100 nm, which puts

the SSPD nanostripe in a two-dimensional (2-D) superconductor regime because its thickness is smaller, but the width is much larger than the NbN Ginsburg–Landau coherence length (~6 nm at $T = 0$ K). In 2-D systems in general, true long-range superconducting order is not possible, and in an ultrathin film, topological excitations come in the form of VAP's.[23] At typical SSPD operating temperatures far below T_c and in the absence of I_{bias}, all VAP's are bound and there is no dissipation in the NbN stripe. Once I_{bias} is applied, it exerts a Lorentz force on the VAP's, and at I_{bias} close to I_c, this force is strong enough to exceed the VAP binding energy and to break them. The latter effect creates free vortices and antivortices—analogue to excited electrons and holes in semiconductors—and allows them to move in opposite directions toward the edges of the NbN stripe, causing dissipation and resulting in the resistive state.[24] Since the VAP breaking events originate exclusively at the "weakest" (narrowest and/or localized) constriction spots of the SSPD meander, the normal region produced from these events is going to have only minimal variations in the resistance and, consequently, the histogram of the corresponding voltage pulses is expected to exhibit a very narrow distribution.

The fact that the photon-count amplitude distributions have FWHM's consistently wider than those corresponding to the dark counts (even in the single-photon regime) can be well understood based on the hot-spot–driven photon-detection events. Photon absorption and resulting hot-spot formation can happen at any point along the meander, leading to natural variations in the size of the resistive state.[22] Since the device I_c is determined by the narrowest and thinnest section(s) of the stripe, fabrication-related fluctuations in the stripe's cross section (variations in the width and/or thickness of the NbN stripe very likely to occur in our relatively low-QE SSPD's) must lead to the R_{hs} variations, which, in the case of our HEMT readout scheme, will be detected as the amplitude spread of photon-count responses. Finally, when the light intensity is relatively high ($n \geq 1$), multiphoton-absorption events are likely to happen, especially for I_{bias} approaching I_c, as more sections of the SSPD meander are activated. As a result, we should observe enhanced fluctuations in the response pulse amplitudes and, correspondingly, to the widest distribution FWHM, as, indeed, is presented in Figs. 129.50(c) and 129.52.

Toward Photon-Number Resolution

As mentioned before and predicted in Ref. 14, the integrated, cryogenic HEMT readout should not only allow one to distinguish dark counts from photon counts but also enable one to achieve PES and PNR in SSPD's. According to Ref. 14, a clear, real-time resolution between, e.g., the single- and two- or three-photon events, requires $R_L \gg R_{hs}$. Since in our HEMT readout R_L is fixed and equal to 500 Ω, the latter condition is not fulfilled in our experiments, as already discussed in **Device Description and Experimental Setup**, p. 40, and we have to restrict ourselves to the statistical, post-processing analysis. Such an approach is obviously not practical for, e.g., optical quantum computing but can find extended applications in spectral characterization of unknown ultraweak light sources in astronomical observations.

We have already successfully implemented the statistical approach to demonstrating the SSPD PES capability in conventionally biased devices, where, by measuring the SSPD system's detection efficiency at different bias currents, we were able to resolve the wavelength of the incident photons with a resolution of 50 nm (Ref. 5). Using the statistical method, we have also demonstrated earlier that SSPD's operating in the HEMT readout configuration are able to distinguish photons of different energies.[13] Therefore, here we focus on the PNR capability of an SSPD connected directly to HEMT.

As stressed before, in the case of devices with $I_c \approx 5\ \mu$A and the HEMT $R_L = 500\ \Omega$, one should still be able to distinguish, at least qualitatively, between the single- and multiphoton events. Indeed, when the laser intensity and I_{bias} were increased so that the detector started to register nearly every incident light pulse while the dark counts were still low, one could observe that, in time-domain traces of the photoresponse counts, some pulses exhibited visibly higher amplitudes than the rest. Figure 129.53 shows an example of such a real-time trace, which although convincing, is absolutely insufficient to conclude that these large pulses were indeed caused by double-photon events, instead of, e.g., a single-photon event arriving close in time to a dark-count event, or even resulting from a large inhomogeneity of the meandering stripe. It was, therefore, again necessary to look at the statistics of the pulse-amplitude distributions. This time, both the intensity of laser pulses and I_{bias} were varied for each case, and amplitudes of several million pulses were collected. Ultraviolet photons (frequency-tripled Ti:sapphire beams) were used to increase the photon-detection efficiency of the SSPD.

The results are presented in Fig. 129.54. When $I_{bias} \approx 0.7\ I_c$, the amplitude distribution can be fit with a simple Gaussian function, as shown in Figs. 129.54(a) and 129.54(b). Once I_{bias} reached $0.9\ I_c$, however [as shown in Figs. 129.54(c) and 129.54(d)], one could see a spreading of the distribution, which now had to be fit with two Gaussians. Although the two-Gaussian distribution can be explained as a result of

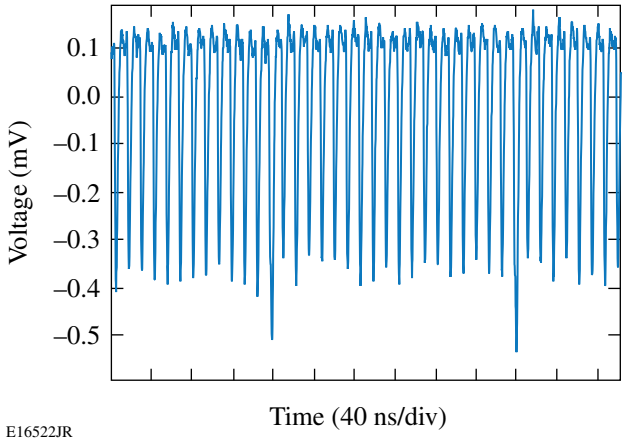

Figure 129.53
Live oscilloscope time-domain trace, showing higher amplitudes of some pulses.

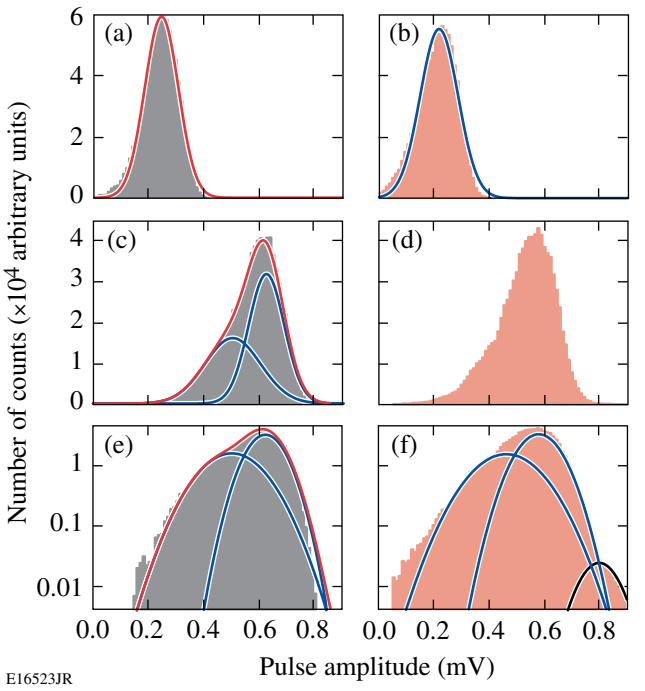

Figure 129.54
Pulse-amplitude histograms for (a) $n \ll 1$, $I_{bias} = 0.7\ I_c$; (b) $n \leq 1$, $I_{bias} = 0.7\ I_c$; (c) $n \ll 1$, $I_{bias} = 0.9\ I_c$; (d) $n \leq 1$, $I_{bias} = 0.9\ I_c$; (e) semi-log plot of (c); and (f) semi-log plot of (d). Gray histograms indicate the same incident photon flux for the $n \ll 1$ regime; red histograms indicate the same incident photon flux for the $n \leq 1$ regime.

significant nonuniformity variations of the NbN stripe rather than the PNR phenomenon, a more-detailed analysis of the presented plots favors the PNR interpretation. Figures 129.54(e) and 129.54(f) show the same data as Figs. 129.54(c) and 129.54(d), respectively; however, they are replotted on a semi-log scale. In Fig. 129.54(f) one can notice that, in the single-photon $n \leq 1$ regime, there is actually a third small Gaussian peak. This peak, however, is completely absent in the $n \ll 1$ regime [Fig. 129.54(e)], as well as when I_{bias} is far below I_c [Figs. 129.54(a) and 129.54(b)]. This third peak also cannot be a result of dark counts since the dark counts are most pronounced in the case of $n \ll 1$ illumination, as demonstrated in Fig. 129.52. Taking into account that the mean amplitude of this third Gaussian peak is the largest, the most-reasonable, although tentative, explanation is that it is indeed a result of the SSPD detection of multiphoton events. Further analysis is needed, however, to either support or disprove this conclusion.

Conclusion

In conclusion, we were able to observe the difference between dark counts and photon counts generated in our meander-type NbN SSPD's by utilizing an HEMT readout technique and, subsequently, examining distribution widths of the histograms of amplitudes of the collected in real-time dark- and photon-count signals. The distribution width for the dark count events was very narrow and independent of the bias current, while the FWHM of the distribution in the case of photon counts was up to 4× wider and was directly related to the photon flux (the average number of photons per pulse) incident on the SSPD. The differences in the measured FWHM values of the output-pulse distributions could be satisfactorily explained by the different physical origin of the dark-count events (VAP breaking and Lorentz-force dissipation) and the photon-count events (photon-induced hot-spot formation). It has also been demonstrated that the HEMT readout offers a promise of PNR functionality in SSPD measurements. The next step in this direction is likely to come from implementing ferromagnet/superconductor bilayer nanostripes (e.g., NiCu/NbN heterostructures), which are not only characterized by picosecond quasiparticle-phonon relaxation dynamics but also exhibit almost an order-of-magnitude larger superconductor critical-current densities.[25]

ACKNOWLEDGMENT

The authors thank Prof. G. Gol'tsman and his group at the Moscow State Pedagogical University for their assistance in the sample preparation and Prof. H. Mooij for very helpful discussions. Research in Warsaw was supported by the Polish Ministry of Science under Project No.4426/B/TO2/2007/33. R. S. thanks the Spanish Ministry of Education and the University of Salamanca for their financial support and hospitality during his one-semester-long research visit in Salamanca, Spain.

REFERENCES

1. W. Słysz, M. Węgrzecki, J. Bar, P. Grabiec, M. Górska, V. Zwiller, C. Latta, P. Böhi, A. J. Pearlman, A. S. Cross, D. Pan, J. Kitaygorsky, I. Komissarov, A. Verevkin, I. Milostnaya, A. Korneev, O. Minayeva, G. Chulkova, K. Smirnov, B. Voronov, G. N. Gol'tsman, and R. Sobolewski, J. Mod. Opt. **54**, 315 (2007).

2. C. Bennett and G. Brassard, in *International Conference on Computers, Systems, and Signal Processing* (IEEE Computer Society, IEEE Circuits and Systems Society, and Indian Institute of Science, Bangalore, India, 1984), pp. 175–179.

3. E. Waks, A. Zeevi, and Y. Yamamoto, Phys. Rev. A **65**, 052310 (2002).

4. E. Knill, R. Laflamme, and G. J. Milburn, Nature **409**, 46 (2001).

5. E. Reiger, S. Dorenbos, V. Zwiller, A. Korneev, G. Chulkova, I. Milostnaya, O. Minaeva, G. Gol'tsman, J. Kitaygorsky, D. Pan, W. Słysz, A. Jukna, and R. Sobolewski, IEEE J. Sel. Top. Quantum Electron. **13**, 934 (2007).

6. Y. Kang *et al.*, Appl. Phys. Lett. **85**, 1668 (2004).

7. G. Ribordy *et al.*, J. Mod. Opt. **51**, 1381 (2004).

8. G. N. Gol'tsman, O. Okunev, G. Chulkova, A. Lipatov, A. Semenov, K. Smirnov, B. Voronov, A. Dzardanov, C. Williams, and R. Sobolewski, Appl. Phys. Lett. **79**, 705 (2001).

9. K. M. Rosfjord *et al.*, Opt. Express **14**, 527 (2006).

10. J. Kitaygorsky, J. Zhang, A. Verevkin, A. Sergeev, A. Korneev, V. Matvienko, P. Kouminov, K. Smirnov, B. Voronov, G. Gol'tsman, and R. Sobolewski, IEEE Trans. Appl. Supercond. **15**, 545 (2005).

11. A. Engel *et al.*, Phys. Stat. Sol. C **2**, 1668 (2005).

12. J. Kitaygorsky, I. Komissarov, A. Jukna, D. Pan, O. Minaeva, N. Kaurova, A. Divochiy, A. Korneev, M. Tarkhov, B. Voronov, I. Milostnaya, G. Gol'tsman, and R. Sobolewski, IEEE Trans. Appl. Supercond. **17**, 275 (2007).

13. J. Kitaygorsky, S. Dorenbos, E. Reiger, R. Schouten, V. Zwiller, and R. Sobolewski, IEEE Trans. Appl. Supercond. **19**, 346 (2009).

14. M. G. Bell *et al.*, IEEE Trans. Appl. Supercond. **17**, 289 (2007).

15. G. N. Gol'tsman, K. Smirnov, P. Kouminov, B. Voronov, N. Kaurova, V. Drakinsky, J. Zhang, A. Verevkin, and R. Sobolewski, IEEE Trans. Appl. Supercond. **13**, 192 (2003).

16. W. Słysz, M. Węgrzecki, J. Bar, P. Grabiec, M. Górska, V. Zwiller, C. Latta, P. Bohi, I. Milostnaya, O. Minaeva, A. Antipov, O. Okunev, A. Korneev, K. Smirnov, B. Voronov, N. Kaurova, G. Gol'tsman, A. Pearlman, A. Cross, I. Komissarov, A. Verevkin, and R. Sobolewski, Appl. Phys. Lett. **88**, 261113 (2006).

17. A. J. Kerman *et al.*, Appl. Phys. Lett. **88**, 111116 (2006).

18. J. K. W. Yang *et al.*, IEEE Trans. Appl. Supercond. **17**, 581 (2007).

19. A. VI. Gurevich and R. G. Mints, Rev. Mod. Phys. **59**, 941 (1987).

20. T. Taneda, G. P. Pepe, L. Parlato, A. A. Golubov, and R. Sobolewski, Phys. Rev. B **75**, 174507 (2007).

21. D. Pan, G. P. Pepe, V. Pagliarulo, C. De Lisio, L. Parlato, M. Khafizov, I. Komissarov, and R. Sobolewski, Phys. Rev. B **78**, 174503 (2008).

22. A. Pearlman, A. Cross, W. Słysz, J. Zhang, A. Verevkin, M. Currie, A. Korneev, P. Kouminov, K. Smirnov, B. Voronov, G. Gol'tsman, and R. Sobolewski, IEEE Trans. Appl. Supercond. **15**, 579 (2005).

23. J. E. Mooij, in *Percolation, Localization, and Superconductivity*, edited by A. M. Goldman and S. A. Wolf, NATO ASI, Series B, Vol. 109 (Plenum Press, New York, 1984), pp. 325−370.

24. A. M. Kadin, J. Appl. Phys. **68**, 5741 (1990).

25. N. Marrocco, G. P. Pepe, A. Capretti, L. Parlato, V. Pagliarulo, G. Peluso, A. Barone, R. Cristiano, M. Ejrnaes, A. Casaburi, N. Kashiwazaki, T. Taino, H. Myoren, and R. Sobolewski, Appl. Phys. Lett. **97**, 092504 (2010).

Thermal Conductivity of Solid Deuterium by the 3ω Method

Introduction

Targets for inertial confinement fusion (ICF) require layers of solid D_2 or DT that have been formed and smoothed by sublimation and recondensation.[1] This "layering" process,[2,3] which typically takes hours, can result in a variety of internal structures in the layer that constitute departures from the desired uniformity of the layer. Knowing the thermal conductivity of the layer and how changes in structure may alter the conductivity are important to modeling the layering process.[4] Although the layering process is most easily accomplished at a temperature just below the triple point, optimizing the internal gas density of the target for ICF requires a temperature ~1.5 K below the triple point.[5] Lowering the temperature after obtaining a uniform layer can result in significant thermal contraction of the layer. This contraction can produce stresses and cracks because the solid D_2 is not free-standing but is attached to a plastic spherical surface.

A critical requirement for ICF experiments is achieving a uniformly thick shell of ice inside a spherical capsule. Analysis of the crystalline structure shows this ice layer to be hexagonally close-packed.[6] In this ice configuration heat is conducted radially out of the sphere along the *a* plane of the crystal over most of the sphere, and along the *c* axis over the remainder of the sphere. Should the thermal conduction along the *c* axis and the *a* plane be significantly different, the ice layer would have an intrinsic limit as to how uniform it could be.

In the 3ω method of measuring thermal conductivity, a wire or strip line whose resistivity is a strong function of temperature is employed as both the heater and the temperature sensor.[7–11] A sinusoidal current with angular frequency $\omega = 2\pi f$ passes through a wire or strip line that is embedded in or thermally anchored to the medium whose thermal conductivity is to be measured. Heat generated in the wire is proportional to the square of the current and therefore has a frequency component at 2ω in addition to a steady-state component, resulting in a temperature with an oscillating component at 2ω. If the wire is a high-purity metal such as Pt, its resistance varies strongly with temperature (for the wire used here, the resistance variation is 5% to 7% per K). Accordingly, the resistance also has an oscillating component at frequency 2ω. The resulting voltage between two points on the wire (the product of current at frequency ω and resistance) therefore has a component of amplitude V_ω at frequency ω and a small component of amplitude $\tilde{V}_{3\omega}$ at frequency 3ω. [See Eqs. (6)−(9) of Ref. 8.] The component $\tilde{V}_{3\omega}$ is expressed as a complex amplitude to take into account the phase shift (with respect to the fundamental, after tripling its frequency) resulting from thermal inertia in the wire and in the medium. It is straightforward to show that the amplitude $\tilde{T}$ of temperature variation in the wire is proportional to $\tilde{V}_{3\omega}$,

$$\tilde{T} = 2\frac{\tilde{V}_{3\omega}}{V_\omega}\frac{R}{\mathrm{d}R/\mathrm{d}T}, \tag{1}$$

where R is the resistance of the wire (between the voltage leads) at the ambient temperature T. Equation (1) is equivalent to Eq. (12) of Cahill (as corrected in the erratum)[7] and is implicitly given in Eq. (9) of Birge *et al.*[8] This equation is valid even if there is a small temperature variation along the wire and, in that case, gives the average temperature amplitude. Since the temperature amplitude $\tilde{T}$ depends strongly on the amount of heat conducted away by the medium, it can be used as a measure of the thermal conductivity of the medium. By making the wire one arm of a bridge circuit, sensitivity to V_ω is minimized and $\tilde{V}_{3\omega}$ can be amplified and measured with a lock-in amplifier. In this work, the principal source of error is noise in the first stage of amplification, which is partially overcome by using the lock-in amplifier to achieve a narrow bandwidth and a long averaging time.

Cahill introduced the useful concept of "thermal penetration depth," which gives an estimate of the distance that a temperature oscillation penetrates into the medium. This quantity is given by $\left[\kappa/(2\rho\omega C)\right]^{1/2}$, where κ is the thermal conductivity in the medium, ρ is the density, and C is the specific heat.[7] This indicator of how far the wire must be from other parts of the apparatus is in agreement with temperature distributions in the medium calculated by the numerical model described in **Numerical Model**, p. 51.

A more-conventional method for measuring thermal conductivity is imposing a thermal gradient on a bulk sample and measuring the resulting heat flow. A drawback to this method for D_2 is the shrinkage (a 14% increase in density upon solidification and an additional 3% upon cooling from the triple point to 10 K) pulling the medium out of contact with one of the heating or sensing elements. This problem was discussed by Collins *et al.*[12] and Souers.[13] Daney[14] overcame this problem by observing the rate of ice growth on a cooled rod immersed in liquid and inferring the thermal conductivity from that rate. In the method used here, the solid forms around a wire of very small diameter (15 μm). Shrinkage upon further cooling may produce stresses in the solid D_2, but it is not expected to pull the D_2 away from the wire. This expectation is confirmed by observation [see later in Fig. 129.60(c)]. Conventional measurements of the thermal conductivity of liquid are subject to errors caused by convection. The high-frequency method used here should be virtually immune to convection issues.

Some proposed targets for ICF use solid D_2 or DT inside low-density polymer foam. Liquid D_2 soaks readily into such foams,[15] and it was found (using silica aerogel foam) by Daney and Mapoles[16] that the thermal conductivity of liquid in foam is very close to that of liquid by itself. When the liquid solidifies, voids may develop that affect both the thermal conductivity and the performance of ICF foam targets. The presence of a sizeable void content could be confirmed by embedding a wire in the foam and measuring its thermal conductivity by the 3ω method.

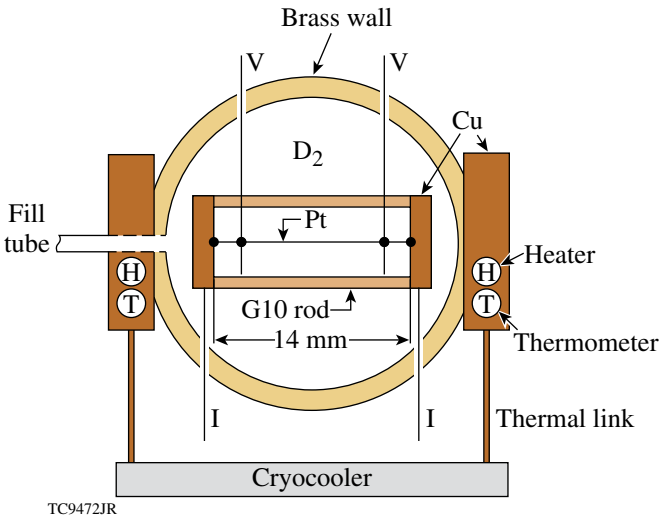

Figure 129.55
Apparatus employed to measure the thermal conductivity of D_2. Glass windows parallel to the plane of this figure allow one to observe the condensation and solidification process. The Pt wire is 1.0 mm from one window, 1.8 mm from the other window, and 2.8 mm from the G10 rods. Copper blocks on either side of the brass chamber have heaters (H) and thermometers (T) that allow one to impose a thermal gradient during the solidification process. Thermal links to the cryocooler are sized to provide adequate cooling, while allowing for a sufficient thermal gradient during the solidification process. The voltage leads (V) and current leads (I) exit the chamber through vacuum feedthroughs.

Experimental Setup

The active element used in this work is a 15.0±0.2-μm-diam Pt wire (measured by a scanning electron microscope). The wire is annealed and is of 99.99% purity.[17] As shown in Fig. 129.55, the Pt wire is soldered to Cu blocks 14 mm apart and attached to voltage leads (25-μm-diam stainless steel). The Cu blocks are held apart by G10 rods (insulating polymer-glass composite) that also provide support for the voltage leads. The voltage leads are attached to points on the Pt wire ~10 mm apart, either with solder or electrically conductive epoxy. Care is taken to avoid flexing or stretching of the Pt wire and to minimize the mass of the connection to the voltage leads. To minimize stresses on the Pt wire, a three-axis positioner is used to mount the Pt wire and to solder the voltage leads to it. After assembly, the distances between the attachment points are precisely measured using a micrometer stage under a microscope. Although the stainless steel of the voltage leads is more thermally conductive than the D_2 (by a factor of ~6 for solid D_2 at the triple point), its heat capacity is small and its thermal conductivity is a factor of ~30 smaller than that of the Pt. The voltage leads are assumed not to be a significant thermal perturbation to the experiment.

The resistance R of the Pt wire was measured as a function of temperature (T), since an accurate knowledge of $R/(\mathrm{d}R/\mathrm{d}T)$ is required to determine the temperature amplitude. A third-order polynomial provides a good fit to the resistance as a function of temperature, as seen in Fig. 129.56. Of five Pt wires used at different times, three agreed in resistance per unit length over the experimental temperature range (11 K to 26 K), while two wires showed slightly greater resistance. It is likely that mechanical flexing and stretching in the course of mounting these delicate wires sometimes resulted in increased resistance. In one instance, the wire was noticeably deformed by the rapid melting of solid D_2 and thereafter exhibited increased resistance. The thermal conductivity of the Pt wire as a function of temperature is obtained from the Metalpak program of Arp,[18] based on the residual resistance ratio (RRR) of the Pt wire (i.e., the ratio of resistance at 273 K to the resistance at a temperature ≤4 K). The value of RRR was determined by measuring the ratios of resistance at 294 K to the resistance values in the range 14 K to 18 K and comparing these ratios to the corresponding ratios given by Ref. 18. This procedure

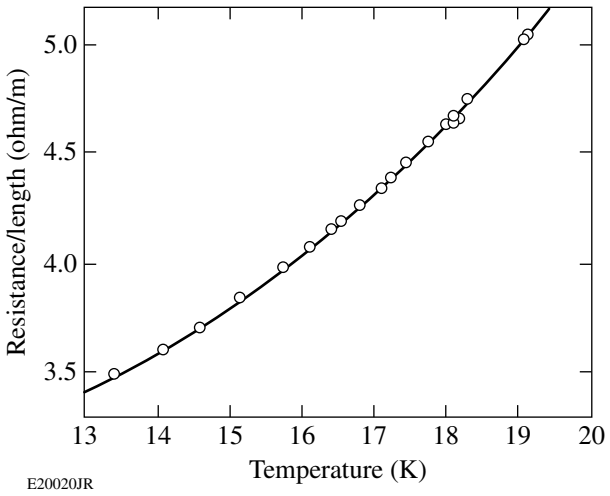

Figure 129.56
Resistance per unit length of a Pt wire as a function of temperature. The measured data are fit with a third-order polynomial.

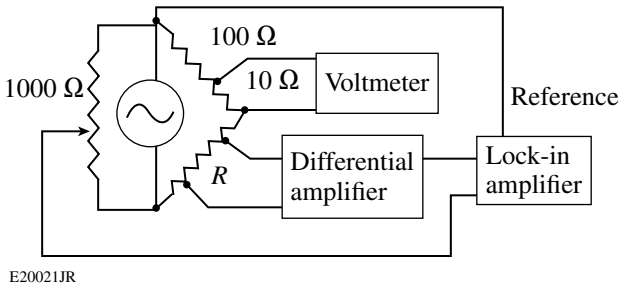

Figure 129.57
Circuit for measuring thermal conductivity. The voltmeter monitors current through the Pt-wire sample resistance *R*. The bridge is balanced with the lock-in amplifier set to detect the fundamental frequency, and the output of the oscillator (which is internal to the lock-in amplifier) is attenuated. After balancing the bridge at a single frequency, the lock-in amplifier is reset to detect the third harmonic. A LabVIEW program collects and averages data at a series of frequencies. No bandwidth limitations are imposed in amplification since these would produce phase shifts. The differential amplifier is Stanford Research Systems model SR560, and the lock-in amplifier (which also uses a differential input) is model SR830.

yields RRR = 186 to 196 and Pt conductivity values ranging from 350 W/(m K) at 18 K to 410 W/(m K) at 14 K. The range of values for RRR produces ≤2% uncertainty in the Pt thermal conductivity values and does not add any uncertainty to the thermal conductivity values obtained for solid D_2.

The chamber in Fig. 129.55 consists of a vacuum-tight brass cylinder with electrical feedthroughs soldered in and glass windows sealed to the chamber by compression of indium gaskets. The windows allow one to backlight and image the D_2 liquid or solid. Materials were chosen that would provide the thermal gradients necessary to fill the chamber with solid deuterium. Copper blocks of high purity on each side of the brass cylinder have very high thermal conductivity compared with the brass and glass (by a factor of >10) and facilitate establishing and measuring the thermal gradient. The experimental chamber is thermally linked to the cold finger of the cryostat. The thermal links are somewhat weak to allow one to impose a thermal gradient, using heaters. After the heaters are turned off and temperatures stabilize, a small thermal gradient of ~0.2 K/cm remains in the region of the apparatus containing the Pt wire. This gradient is a consequence of the necessary weakness of the thermal links to the cold finger and not a significant source of experimental error. The experimental chamber is surrounded by a copper radiation shield at 40 K. Windows in the radiation shield are coated with ~10 nm of Au to reduce thermal radiation coming into the chamber.

The electrical configuration is shown in Fig. 129.57. After stabilizing the temperature in the D_2, the resistance of the Pt wire between the voltage leads is determined. The bridge circuit is then balanced by manually adjusting the variable resistor, while the lock-in amplifier is set to detect the fundamental frequency of the sine-wave oscillator. A single frequency is used to determine resistance and balance the bridge; these functions are found to be insensitive to the choice of this frequency. The oscillator, internal to the lock-in amplifier, is of high spectral purity, with harmonic distortion of −80 dB (Ref. 19). It is assumed that any component of distortion at frequency 3ω is partially removed by balancing the bridge. Replacing the Pt wire by a Cu wire at room temperature with a similar resistance demonstrates that the influence of oscillator distortion is insignificant. Some measured values of $\tilde{V}_{3\omega}$ for solid D_2 at <17 K are as small as 17 nV (rms), which is 96 dB below the value of V_ω, i.e., 1.1 mV (rms).

To obtain a value of thermal conductivity, the third-harmonic voltage $\tilde{V}_{3\omega}$ is measured as a function of frequency. Each value of voltage is recorded as a complex number, the values in phase or out of phase with the driving current. Holding the ambient temperature constant, data are taken at a series of frequencies increasing at logarithmic intervals from ~1 Hz to >1000 Hz. This scan typically takes 2 to 20 min and is repeated to ensure that the state of the solid D_2 has not changed. The data at each frequency are averaged, after an initial settling time that is governed by the time constant selected on the lock-in amplifier. Some scans are rejected after finding that the state of the solid D_2 has apparently changed between the first and second scans. Non-repeatable scans are found to be especially likely if there is a visible crack or cavity somewhere in the solid D_2.

In such a case, heat generated in the Pt wire hollows out a new cavity around the wire itself, and the gas that is generated is able to find a path to the original cavity and recondense there. When large enough, a cavity around the wire becomes visible through a microscope with an attached video camera. When a cavity develops around the wire, there is a sudden rise in the in-phase temperature amplitude, and the data are rejected.

Data are fitted with the two-dimensional (2-D) numerical model described in **Numerical Model**, which includes, as input parameters, the dimensions of the wire and the medium, the density, specific heat and thermal conductivity of Pt,[18] and the density,[20] specific heat,[21,22] and thermal conductivity of D_2. The latter five parameters are highly temperature dependent. The only fitting parameter is the thermal conductivity of the D_2 since the other parameters are presumed to be known to sufficient accuracy. At the temperatures employed here, the heat capacity per unit volume of the liquid or solid D_2 is a factor of 4 to 7 greater than that of the wire. These ratios, much greater than those often found with other materials at higher temperatures, facilitate the measurement by overcoming the loss of sensitivity resulting from the very small wire resistance. If the voltage leads are located sufficiently far from the ends of the wire, the numerical model yields results very close to the analytical solution [Eq. (21)] of Chen *et al.*[9] for a one-dimensional (1-D) problem where it is assumed that the wire is infinitely long (i.e., no heat flow in the direction of the axis of the wire) and that the wire has a much greater thermal conductivity than the surrounding medium.

To maintain purity of the D_2 against possible contamination by air or other gases, impurities are removed with each cryogenic cycle. Between uses, the D_2 is stored as a room-temperature gas at ~1 atm. After condensing the D_2 in the experimental chamber and taking data, the chamber is warmed to ~30 K, evaporating the D_2, but leaving residual air (if any) frozen. After isolating the D_2 and warming the apparatus, the contaminants are pumped away.

For some of the data, the D_2 was converted from normal D_2 to ortho D_2 using a catalyst. To achieve this conversion, the D_2 was first condensed into a separate chamber of volume 5 cm^3 containing 2 g of hydrated iron oxide[23] (catalyst grade, 30/50 mesh). Prior to cooling, the catalyst was baked in vacuum (150°C for ~2 h, until the outgassing rate became small). The D_2 was kept in this chamber for several days as liquid just above the triple point, while the adjacent experimental chamber was kept several K higher to prevent any condensation there. After several days, it was presumed that all the D_2 had been converted[24] to ortho D_2. Some of the D_2 was then distilled into the experimental chamber (volume 0.9 cm^3) by reversing the relative temperatures of the two chambers.

Numerical Model

A computer program modeled this experiment to relate the measured temperature amplitude to the thermal conductivity in the medium. The model takes into account the 2-D geometry of the experiment and includes thermal conduction along the wire, as well as conduction in the medium both perpendicular and parallel to the wire. This model has been used to determine the significance of 2-D effects and to provide improved accuracy over 1-D numerical solutions, which ignore heat flow in the direction of the wire axis.

The 2-D domain used by the model is shown in Fig. 129.58. The model assumes a cylindrically symmetric (r,z) geometry consisting of the wire, the medium, and surrounding heat baths. While the distance from the wire to the boundary varies from 1 to 3 mm in the experiment (see Fig. 129.55), the cylindrical geometry is valid for all but the lowest frequencies because the oscillating temperature T falls to zero within distances significantly less than 1 mm. The radius of the wire (7.5 μm) is small when compared with the radial width of the outer boundary (1 mm); therefore, a variable-size grid was implemented in the medium, wherein the radial widths of the cells increase geometrically with their distance from the wire. The cell widths in z are kept uniform for all media. The model is similar to that presented in Jacquot *et al.*,[25] who performed

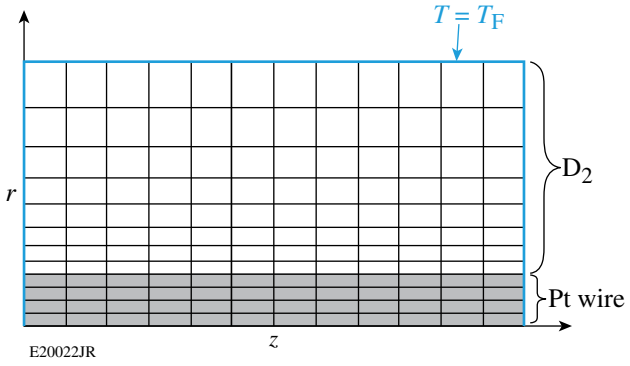

Figure 129.58
Schematic of the 2-D domain used by the numerical code. The Pt wire (shaded region) is fine zoned in the radial direction, matched to variable zoning in the D_2. Azimuthal symmetry is assumed with a fixed temperature $T = T_F$ specified on each of the three boundaries. An oscillatory current is applied uniformly through the wire. The code solves a 2-D diffusion equation for the complex 2ω temperature component.

initial-value heat-flow calculations in a different geometry for a 3ω experiment using a rectangular metal strip as the heater placed on top of the sample.

To achieve accurate solutions, 50 uniformly spaced cells were used in the axial direction, with >400 uniformly spaced radial cells in the wire and 1300 geometrically spaced cells in the medium. The large number of radial cells in the wire was required to ensure continuity of cell size across the wire–medium boundary. Small cells in the medium close to the wire are required to resolve the spatial variations at high frequencies. The average of the Pt and D_2 conductivities is used at the Pt–D_2 boundary. There is no heat flux across the lower boundary of the Pt wire (the z axis). The temperature T is fixed on the three sides of the domain that are heat baths. The heat source is nonzero only for in Pt cells.

For each cell

$$\rho C \frac{\partial T}{\partial t} + \nabla \cdot Q = W \tag{2}$$

is solved, where the heat flux Q is given by $Q = -\kappa \nabla \mathrm{T}$ and W is the heat deposited in the wire per unit volume. The code can solve Eq. (2) as an initial-value problem using a conventional finite-difference technique. Energy conservation is ensured by expressing the heat flux between two cells as a quantity proportional to the difference in temperature between the cells. Implicit differencing of Eq. (2) leads to a matrix equation for the new temperature T of the form $MT = S$, where M is a five-diagonal matrix and S is a vector evaluated at the previous time step. The matrix equation is solved using Kershaw's incomplete Cholesky conjugate gradient (ICCG) method.[26] Details of the numerical implementation are given in Ref. 27. Since it would be excessively time consuming to solve the initial value problem for the present experiment, where the asymptotic second-harmonic response to the oscillating current is required, an alternative approach is used that yields the oscillating temperature amplitude $\tilde{T}(r,z)$ directly. Assuming that the current varies as $\cos(\omega t)$, the heat deposition W may be written as

$$W(t) = W_0 + \frac{1}{2}\left(\tilde{W} e^{i2\omega t} + \tilde{W} e^{-i2\omega t}\right), \tag{3}$$

where W_0 is the time-averaged deposition and $\tilde{W} = W_0$. The asymptotic temperature is then given by

$$T(r,z,t) = T_0(r,z) + \frac{1}{2}\left[\tilde{T}(r,z) e^{2i\omega t} + \tilde{T}^{*}(r,z) e^{-2i\omega t}\right], \tag{4}$$

where $T_0(r,z)$ is the steady-state solution satisfying $-\nabla \bullet (\kappa \nabla T_0) = W_0$. Inserting Eqs. (3) and (4) into Eq. (2), one finds

$$i\omega\rho C\tilde{T} - \frac{1}{2}\nabla \cdot \kappa \nabla \tilde{T} = \tilde{W}. \tag{5}$$

This equation is differenced as for the initial value solution, and $\tilde{T}(r,z) = 0$ is imposed on the physical boundaries. A similar five-diagonal matrix equation is obtained, but the central diagonal of the matrix contains complex numbers and the solution $\tilde{T}(r,z)$ is complex. It has been found[27] that Kershaw's ICCG method generalized to operate with complex numbers converges to provide the complex solution $\tilde{T}(r,z)$. Noting that the resistivity of the wire (which is linear in temperature over small-enough temperature excursions) has a second-harmonic component proportional to $\tilde{T}(r,z)$ and the resistance along the wire combines in series, it is easy to see that the third-harmonic voltage $\tilde{V}_{3\omega}$ is that given in Eq. (1), where $\tilde{T}$ is the average value of $\tilde{T}(r,z)$ between the two voltage leads. In practice, because of the high thermal conductivity and small radius of the Pt wire, the r dependence of $\tilde{T}(r,z)$ in the wire is very small and it is the z variations of $\tilde{T}(r,z)$ that determine the average.

By solving the initial value problem, it is found that the time taken for the wire to reach a constant ambient temperature in vacuum is <40 ms. Longer times are required for solid D_2, but over the several-minute averaging time of the measurement, transient effects are negligible. Figure 129.59 illustrates the use of the numerical model to obtain the spatial distribution of the temperature amplitude in the wire and in the medium. In Figs. 129.59(a) and 129.59(b), it is seen that thermal conduction along the wire reduces the temperature amplitude near the end of the wire, but that locating the voltage leads ~2 mm from the ends places them in a region of constant temperature amplitude. This constant amplitude is found to be the same (within 0.5%) as that calculated by the 1-D model [Eq. (21)] of Ref. 9. In Figs. 129.59(c) and 129.59(d), the radial temperature distribution in the wire and in the solid D_2 is shown [(c) in phase and (d) out of phase], starting from the mid-point of the wire. In Fig. 129.59(e) the in-phase temperature amplitude in the wire is magnified at a single frequency to show a 1-μK temperature drop between the center and the edge at 7.5 μm.

To understand departures of the experimental data from the numerical model, particularly at frequencies >1 KHz, two modifications were introduced. Neither of these yielded an improved fit to the observed data, but they are mentioned here as strategies available to users of the 3ω method. A thin layer of frozen air on the wire was added to the model but failed to

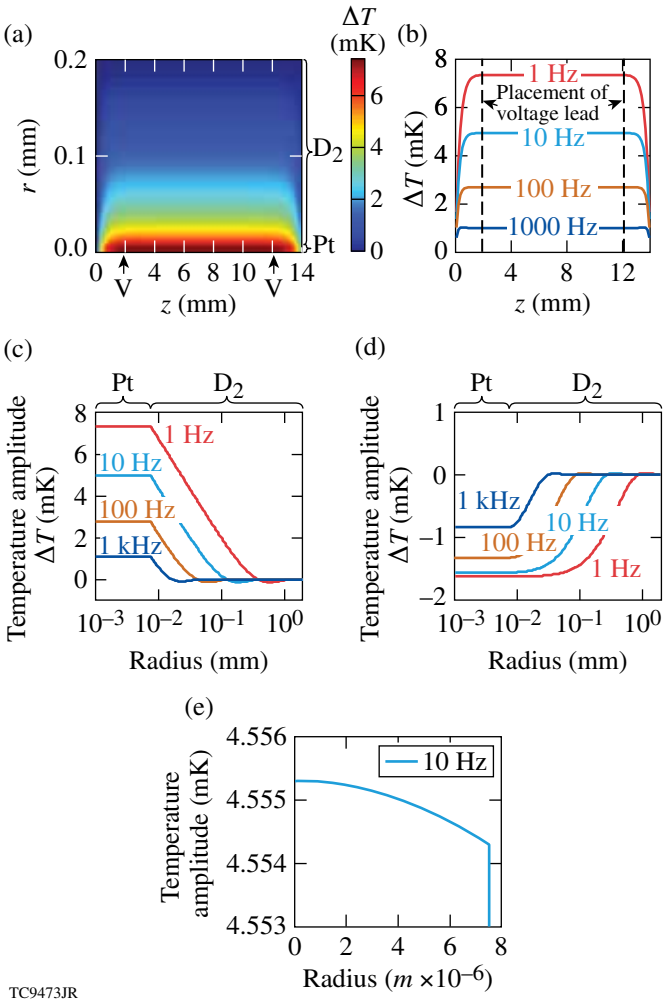

Figure 129.59
Illustrative results of the 2-D model. (a) Calculated contour plot of temperature amplitude (the in-phase component) in and around the Pt wire embedded in solid D_2 at 18 K. A sinusoidal current at 1 Hz results in dissipation of 45 μW between the voltage leads, labeled V. (b) In-phase temperature amplitude as a function of distance along the wire. (c) In-phase and (d) out-of-phase temperature amplitudes as a function of radial distance from the center of the wire starting at the mid-point of the wire. (e) Magnification of (c) showing a 1.0-μK drop in the temperature amplitude between the center and edge of the wire at 10 Hz.

improve the fit. Surface irregularities on the 1-μm level were added to the Pt wire but also failed to improve the fit.

Results

Before measurements on solid D_2 are undertaken, significant effort is required to obtain solid D_2 free of obvious cavities and cracks. The chamber is observed visually while liquid is condensing and then while solidification proceeds in the presence of an imposed thermal gradient. The solid grows slowly (over several hours) from the cold side to the warm side, with the liquid in the fill tube being the last to solidify. Because of the 14% increase in density upon solidification of the liquid D_2, gas cavities can easily be trapped in the solid. If this happens, the warm side is reheated until the cavities are filled with liquid, and the solidification process is then resumed. If cavities are allowed to remain, they can cause the thermal conductivity measurement to fail because they gradually move (by sublimation on the warm side of the cavity and recondensation on the cold side) in response to residual thermal gradients and often find their way to the Pt wire.

Before a measurement, the D_2 solid is evaluated visually as shown in Fig. 129.60. Figure 129.60(a) shows the interface between liquid and solid as the solid grows, and the resulting solid is shown in Fig. 129.60(b). Upon lowering the temperature of clear solid D_2 as seen in Fig. 129.60(b), many visual features appear, such as cracks and regions where the solid has apparently pulled slightly away from a window or the wire supports, as seen in Fig. 129.60(c). After remaining at a constant temperature for a period of several hours to a day, cracks and other features appear to heal, the solid again becomes visually clear, and a repeatable measurement of thermal conductivity can be made. The crystallinity of the solid is examined by viewing it in polarized light as shown in Figs. 129.60(d) and

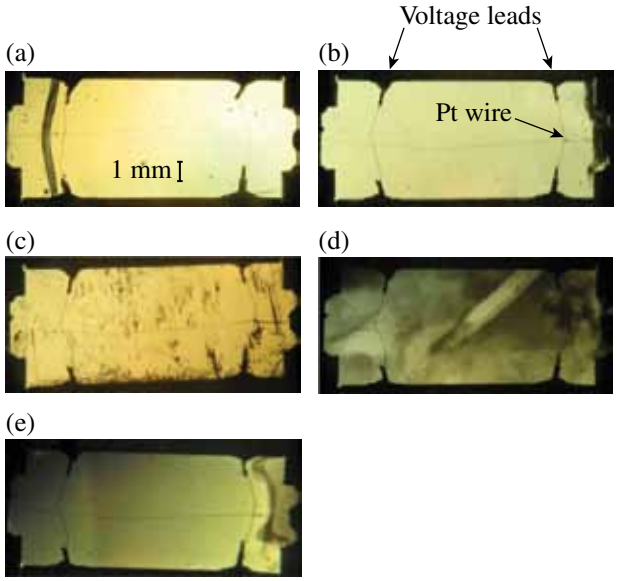

Figure 129.60
Various views of solid D_2 formed around the Pt wire and the voltage leads. (a) Solid forming on the left side with liquid on the right, in the presence of a thermal gradient. The dark line is caused by refraction at the interface between solid and liquid. (b) Solid successfully formed, free of apparent flaws. (c) Solid with cracks after suddenly lowering the temperature by 2 K. [(d) and (e)] Two examples of solid in polarized light revealing features of the crystallinity.

129.60(e). In both cases the solid was visually clear when viewed without polarizers and provided repeatable thermal conductivity data. Typically, several domains are seen, random in shape, with dimensions in the range of 1 to 8 mm. These domains are revealed by variations in color and shading as the polarizers are slowly rotated. It appears that the Pt wire passes through several large crystallites. If a single crystal could be grown around the Pt wire, conductivity might be measured as a function of crystal orientation.

To obtain a value of thermal conductivity at a particular temperature, temperatures are allowed to stabilize for 20 min or more. Using a constant current, $\tilde{V}_{3\omega}$ is measured at a series of frequencies and converted to temperature amplitude $\tilde{T}$ using Eq. (1). Typical results are shown in Fig. 129.61(a) for solid D_2, in Fig. 129.61(b) for liquid D_2, and in Fig. 129.61(c) for D_2 gas. Each pair of data points requires 20 to 60 s of averaging, which is performed by a LabVIEW[28] program. The variance in a typical averaged data point is usually consistent with the noise figure (4 nV/Hz$^{1/2}$) of the first stage of amplification.[19] The data in Fig. 129.61 are fitted, using the numerical model, varying only the thermal conductivity of the D_2. It is verified experimentally that the temperature amplitude is proportional to the power dissipated in the Pt wire, so the drive current is maximized (but without noticeably raising the ambient temperature measured on the chamber) to reduce the relative importance of amplifier noise.

For Figs. 129.61(a) and 129.61(b), the numerical model fits the in-phase data very closely from 1 Hz to >1000 Hz, while fitting the out-of-phase data over a smaller frequency range, ~8 Hz to ≥300 Hz. This is typical of many data sets. The reasons for the departures from the fit outside these frequency ranges are not known. Several authors[8,9] use the fitting process to also obtain the specific heat of the medium. This does not work for solid D_2 since varying the specific heat from the literature value simply requires a different value of thermal conductivity to fit the data. This is confirmed by the discussion in Ref. 9 that gives the range of parameters required for sensitivity to specific heat. The data obtained in this study are at frequencies too low to obtain specific heat values.

Data for D_2 gas around the Pt wire show acceptable qualitative fits, as seen in Fig. 129.61(c). As expected, the smaller thermal conductivity of the gas yields much greater thermal amplitudes and the curves differ in shape from those of liquid and solid. In this case, much of the heat dissipated in the Pt wire is conducted along the wire to the ends. To use this method to measure the thermal conductivity of a gas would require extra care in establishing the temperature of the Cu blocks at the ends of the Pt wire, and a greater distance from the wire to other parts of the apparatus would be helpful. Additional discussion of the data for D_2 gas and similar data for vacuum, including temperature profiles along the wire and in the gas, is presented in Ref. 27.

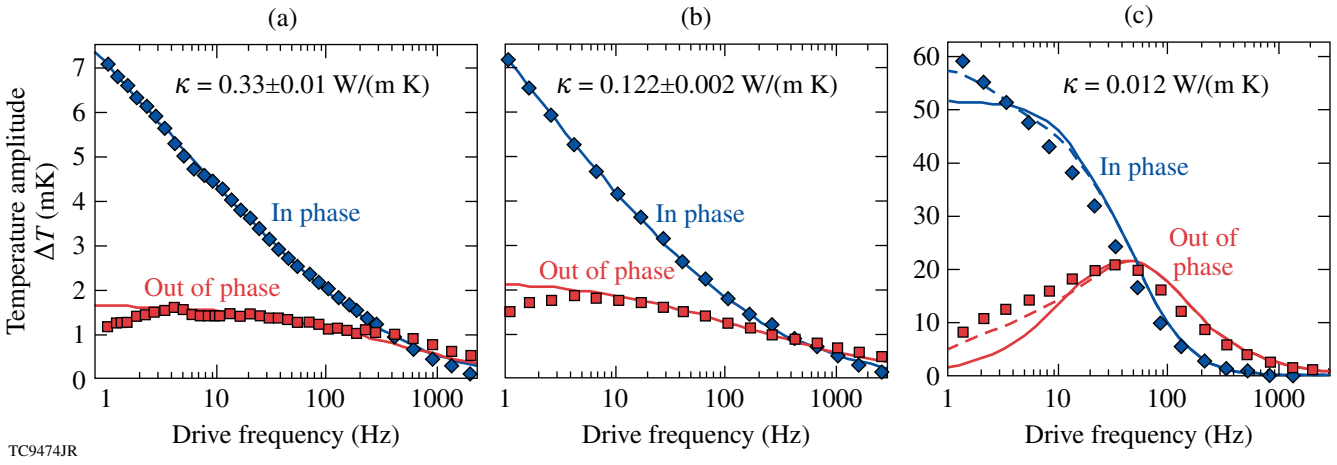

Figure 129.61
Measured (points) and calculated (lines) in-phase and out-of-phase temperature amplitudes of the wire as a function of drive frequency for (a) solid D_2 at 18.2 K with a power dissipation of 45 μW, (b) liquid D_2 at 26 K with a power dissipation of 10 μW, and (c) D_2 gas at 21 K with a pressure of 21 Torr and a power dissipation of 10 μW. (The negative of out-of-phase values is shown.) Fits were obtained by treating only the thermal conductivity κ as a variable. In (c) the fit is qualitative. The effect of choosing the distance to the simulation boundary to be 1 mm (solid lines) or 3 mm (dashed lines) is seen to be significant at low frequencies.

A summary of results for solid D_2 is shown in Fig. 129.62 (solid points). These include data taken for ortho D_2 and instances in which the growth direction of the solid was aligned either with the Pt wire or perpendicular to it. These data are fitted with a second-order polynomial $\kappa = (6.168 - 0.0635\,T + 0.0173\,T^2)$ W/(m K), where T is in units of K. No difference is seen among these data sets. This partially addresses a concern that directionality of crystal growth in the ICF fuel layer could affect the thermal conductivity across the layer and, therefore, the final profile of the layer. The data indicate that ortho-conversion would be an ineffective method, at temperatures between 14 K and the triple point, for altering the conductivity of a fuel layer. The data obtained here are consistent with the published data from Daney[14] and Gorodilov[29] (open symbols), but with the conductivities on average 5% larger than those of Daney. Some data are obtained at lower temperatures than is possible using Daney's method. At the lower temperatures shown in Fig. 129.62, increased thermal conductivity along with reduced resistance of the Pt wire results in lower voltages and the increasing importance of amplifier noise. At these lower temperatures, a longer time is required for the solid D_2 to recover from the stresses that result from shrinkage caused by temperature change. As a result, data are increasingly more difficult to obtain as the temperature is lowered.

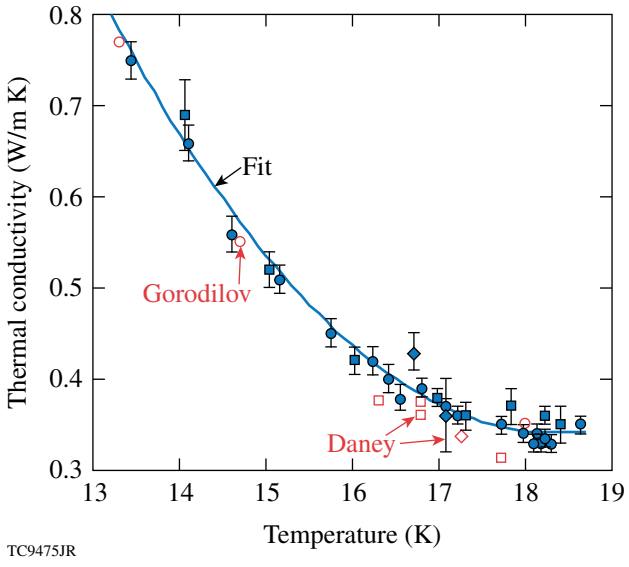

Figure 129.62
Measured values of thermal conductivity of solid D_2 as a function of temperature (solid blue data points). Solid circles are for normal D_2 with the wire parallel to the direction of ice growth. Solid squares (diamonds) are for ortho D_2 with the wire parallel (perpendicular) to the direction of ice growth. The curve is a second-order polynomial fit to the data. Shown for comparison are the data of Daney (open squares for normal D_2 and open diamonds for ortho D_2) and the data of Gorodilov (open circles).

Conclusions

The 3ω method has obtained accurate values of thermal conductivity for solid D_2 in a temperature range lower than any for which it has previously been used. The method operates on a small distance scale appropriate for ICF fuel layers and is somewhat less susceptible to concerns about thermal contraction and formation of cavities than conventional methods of measuring thermal conductivity. Values of thermal conductivity are slightly higher (5%) than those obtained by Daney. The results are all from "good" ice that is free of visible features like cracks and that shows large single crystals when viewed in polarized light. Normal D_2 and ortho D_2 show the same values of thermal conductivity over the temperature range examined. This confirms that ortho-conversion cannot be used at these temperatures as a tool for altering fuel-layer formation. No dependence of thermal conductivity on the direction of solid growth was detected.

ACKNOWLEDGMENT

This work was supported by the U.S. Department of Energy Office of Inertial Confinement Fusion under Cooperative Agreement No. DE-FC52-08NA28302, the University of Rochester, and the New York State Energy Research and Development Authority. The support of DOE does not constitute an endorsement by DOE of the views expressed in this article.

REFERENCES

1. D. R. Harding, D. D. Meyerhofer, S. J. Loucks, L. D. Lund, R. Janezic, L. M. Elasky, T. H. Hinterman, D. H. Edgell, W. Seka, M. D. Wittman, R. Q. Gram, D. Jacobs-Perkins, R. Early, T. Duffy, and M. J. Bonino, Phys. Plasmas **13**, 056316 (2006).
2. J. K. Hoffer and L. R. Foreman, Phys. Rev. Lett. **60**, 1310 (1988).
3. P. S. Ebey, J. M. Dole, D. A. Geller, J. K. Hoffer, J. Morris, A. Nobile, J. R. Schoonover, D. Wilson, M. Bonino, D. Harding, C. Sangster, W. Shmayda, A. Nikroo, J. D. Sheliak, J. Burmann, B. Cook, S. Letts, and J. Sanchez, Fusion Sci. Technol. **54**, 375 (2008); A. S. Bozek *et al.*, Fusion Eng. Des. **82**, 2171 (2007).
4. E. L. Alfonso, I. Anteby, and D. R. Harding, Fusion Technol. **38**, 149 (2000).
5. B. J. Kozioziemski *et al.*, Fusion Sci. Technol. **59**, 14 (2011).
6. B. J. Kozioziemski *et al.*, J. Appl. Phys. **105**, 093512 (2009).
7. D. G. Cahill, Rev. Sci. Instrum. **61**, 802 (1990); erratum **73**, 3701 (2002).
8. N. O. Birge and S. R. Nagel, Rev. Sci. Instrum. **58**, 1464 (1987).
9. F. Chen *et al.*, Rev. Sci. Instrum. **75**, 4578 (2004).
10. L. Lu, W. Yi, and D. L. Zhang, Rev. Sci. Instrum. **72**, 2996 (2001).
11. C. Dames and G. Chen, Rev. Sci. Instrum. **76**, 124902 (2005).

12. G. W. Collins *et al.*, Phys. Rev. B **41**, 1816 (1990).

13. P. C. Souers, *Hydrogen Properties for Fusion Energy* (University of California Press, Berkeley, CA, 1986), pp. 78–80.

14. D. E. Daney, Cryogenics **11**, 290 (1971); D. E. Daney, W. G. Steward, and R. O. Voth, National Bureau of Standards, Washington, DC, NBSIR 73-339 (October 1973).

15. T. Norimatsu *et al.*, J. Vac. Sci. Technol. A **6**, 3144 (1988).

16. D. E. Daney and E. Mapoles, Cryogenics **27**, 427 (1987).

17. Goodfellow Corporation, Berwyn, PA 19312-1780.

18. V. Arp, METALPAK™ software version 1.10, Horizon Technologies, Littleton, CO, 80128; using data from R. J. Corruccini and J. J. Gniewek, *Specific Heats and Enthalpies of Technical Solids at Low Temperatures*, National Bureau of Standards, Monograph 21 (U.S. Government Printing Office, Washington, DC, 1960).

19. Stanford Research Systems, Inc., Sunnyvale, CA 94089.

20. P. C. Souers, *Hydrogen Properties for Fusion Energy* (University of California Press, Berkeley, CA, 1986), p. 79.

21. *ibid.*, 68 and 96.

22. K. Clusius and E. Bartholomé, Z. Phys. Chem. Abt. B **30**, 237 (1935).

23. Sigma-Aldrich, St. Louis, MO 63178.

24. P. C. Souers, *Hydrogen Properties for Fusion Energy* (University of California Press, Berkeley, CA, 1986), pp. 315–316.

25. A. Jacquot *et al.*, J. Appl. Phys. **91**, 4733 (2002).

26. D. S. Kershaw, J. Comput. Phys. **26**, 43 (1978).

27. A. She, *2007 Summer Research Program for High School Juniors at the University of Rochester's Laboratory for Laser Energetics*, University of Rochester, Rochester, NY, LLE Report No. 353, LLE Document No. DOE/SF/19460-809 (2008).

28. National Instruments Corporation, Austin, TX 78759-3504.

29. B. Ya. Gorodilov *et al.*, Sov. J. Low Temp. Phys. **7**, 208 (1981).

OMEGA Polar-Drive Target Designs

Introduction

With the use of polar drive (PD),[1] direct-drive experiments can be conducted at laser facilities such as the National Ignition Facility (NIF),[2] while they are configured for x-ray drive. In this approach to inertial confinement fusion, laser beams directly irradiate a capsule, causing the outer material to ablate and drive the rest of the shell like a rocket. Since the x-ray drive configuration has no beams at the equator, several modifications of traditional symmetric direct drive[3] are employed to achieve adequate symmetry. An important modification repoints beams from higher latitudes toward the equator, resulting in oblique irradiation on target. Laser-energy absorption of the expanding corona is dominated by collisional absorption, where maximum laser energy is deposited at the turning point of the laser rays. The electron density at the turning point of a laser ray scales as $\cos^2\theta$, where θ is the angle subtended by the laser rays. As a result, laser absorption occurs at lower coronal densities for larger values of θ, which correspond to the oblique beams.[1] This results in reduced shell velocity (or the hydrodynamic efficiency, defined as the ratio of the maximum shell kinetic energy to the incident laser energy), relative to when the beams are at normal incidence. Pulse-shape variations among the beams and tailored individual spatial-beam profiles are necessary to recover the shell velocity while achieving adequate shell symmetry. These variations are critical to the polar-drive–ignition design.[4] In the symmetric-drive configuration, the laser irradiation is incident from a range of latitudes including the equator. This results in more-normal incident laser irradiation and for a given ablator material, the maximum-possible energy deposited leading to maximum shell velocity.

Similar to symmetric drive, ignition in PD geometry relies on the formation of a hot spot with a minimum areal density of 300 mg/cm^2 and an electron temperature of ~5 keV. Assuming spherical symmetry, the adiabat and shell implosion velocity are the critical parameters that determine target performance. The minimum laser energy required for ignition, $E_{\min}$, has been shown to depend on α_{inn}, the adiabat on the inside of the compressing shell, defined as the ratio of the pressure to the Fermi-degenerate pressure, the velocity of the shell at maximum kinetic energy or the implosion velocity V_{imp}, and the pressure P on the outside of the fuel when it reaches the implosion velocity:[5]

$$E_{\min}(\text{kJ}) = 50.8\,\alpha_{\text{inn}}^{1.88} \times \left(\frac{V_{\text{imp}}}{3\times 10^7\ \text{cm/s}}\right)^{-5.89}\left(\frac{P}{100\ \text{Mbar}}\right)^{-0.77}. \quad (1)$$

Equation (1) indicates that a lower adiabat on the inside of the shell, a high implosion velocity, and retaining the driving pressure on the outside of the shell until the onset of deceleration are extremely important to lowering the minimum energy required for ignition. The implosion velocity can be written as

$$V_{\text{imp}} \sim \sqrt{\langle\alpha\rangle^{0.6} \times \text{IFAR} \times 1^{0.27}}, \quad \text{(Ref. 6)} \quad (2)$$

where $\langle\alpha\rangle$ is the density-averaged adiabat in the shell, IFAR = R/Δ_{if} is defined as the ratio of the shell radius R to the shell thickness (Δ_{if} is defined as the distance between the 1/e radii of peak density) when the shell has traveled a distance that is 2/3 that of the average of the initial inner and outer target radii, and I is the on-target intensity. A higher implosion velocity can be obtained by increasing $\langle\alpha\rangle$, IFAR, or intensity.

The leverage in $\langle\alpha\rangle$ to increase V_{imp} is limited since it is challenging to increase $\langle\alpha\rangle$ and retain a low value of α_{inn}. Based on multidimensional considerations, IFAR has an upper limit because of nonuniformities seeded by the laser beams and target imperfections that can compromise implosion performance. Short-wavelength nonuniformities ($\ell \geq 10$, where ℓ is the Legendre mode number describing the nonuniformity) grow primarily by the Rayleigh–Taylor (RT) instability[7] and can significantly distort the in-flight shell, thereby increasing α_{inn} (Ref. 8). The number of linear growth factors for $\ell \geq 10$ for RT growth (defined as $N_e = \gamma t$, where γ is the RT growth rate and t is the time over which the shell accelerates) of the most dangerous mode (defined as the mode with wave number k, such that $k\Delta_{\text{if}} \sim 1$) scales approximately as $\sqrt{\text{IFAR}}$ (Ref. 9).

Too high an intensity can compromise target performance by seeding laser–plasma instabilities (LPI's) that reduce the energy coupled to the target (for example, through cross-beam transfer)[10] and/or preheating the shell and raising α_{inn} [via energetic electrons produced by two-plasmon-decay (TPD) instability].[11] As a result, the peak intensity, defined at the initial target radius, is typically restricted to $8 \times 10^{14} \lesssim I \lesssim 1 \times 10^{15}$ W/cm^2. At these intensities the effects of LPI are not completely understood.[12] Nonlocal heat transport by coronal electrons from the tail of the distribution function[13] also plays an important role in establishing the ablation pressure. It is necessary for OMEGA PD implosions to span this range of on-target intensities to permit studies relating to the heat conduction and LPI.

A second aspect of PD designs is the symmetry of the hot spot. Hot-spot symmetry is determined by longer wavelength perturbations ($\ell \leq 10$) that reduce the clean volume and decrease the hot-spot temperature, lowering the neutron yield.[14] In symmetric direct drive, hot-spot distortions are seeded by ice roughness, energy imbalance, beam-pointing variations, and beam-timing variations between the various beams incident on the target. The beam port configuration or beam geometry can cause additional hot-spot distortions to occur in PD.

Target performance, including the extension to multidimensional effects, has been quantified in a recent work by Haan *et al*. in terms of the ignition threshold factor (ITF).[15] A higher value of ITF indicates a greater probability of ignition; a value of 1 for this quantity indicates a 50% probability of ignition. ITF scales as

$$\text{ITF} \sim V_{\text{imp}}^{8} \alpha^{-4} (1 - 1.2\,\sigma) \left(\frac{M_{\text{clean}}}{M_{\text{DT}}} \right), \tag{3}$$

where σ is a measure of the hot-spot distortion given by the root-mean-square distortion of the hot spot, where longer wavelengths are weighted less than the shorter wavelengths, and $M_{\text{clean}} / M_{\text{DT}}$ is the ratio of the clean mass of the hot spot, i.e., the deuterium–tritium (DT) mass that is not contaminated by high-mode mixing of the ablator material, to the total target mass. High-mode mix caused by short-wavelength RT growth and the presence of isolated defects on the target surface is not considered in this article. The effect of this mix on target performance can be studied empirically through implosions by varying the IFAR, similar to what has been done in symmetric drive.[8] Engineering efforts to decrease the number of defects on the capsule surface are ongoing and have already resulted in improved implosion performance.[16] Modifications to the target design through techniques such as radiation preheat[17] and the use of lower-density ablators such as foam[1] can be considered to limit the effect of short-wavelength RT growth. The emphasis in this article is on minimizing hot-spot distortion related to beam geometry on the OMEGA Laser System[18] and to establish the basis for ignition-relevant platforms that can be used to study LPI and heat conduction in PD geometry. In particular, this implies the identification of beam profiles that minimize hot-spot distortion in OMEGA PD designs with ignition-relevant parameters.

In symmetric drive, implosions are primarily designed in one dimension (assuming spherical symmetry) and then simulated in multiple dimensions to verify target performance. Since beam-port geometry has a very small effect on target performance in symmetric drive,[19] it can be ignored in the primary design. Beam profiles for OMEGA beams have been designed for symmetric drive by minimizing the nonuniformity related to the beam geometry when projected on a sphere.[20] This assumes that the laser deposition and hydrodynamic efficiency are uniform in polar angle around the target, valid for symmetric drive where the beams are nearly normally incident on the target. For polar drive, it is critical to account for the nonuniformities imposed by the beam-port geometry and to correct for them using techniques such as an optimal choice of beam profiles, beam pulse shapes, and beam repointing. The PD approach therefore requires iterative multidimensional simulations to design implosions.

Beam profiles are implemented on OMEGA using distributed phase plates (DPP's).[21] The intensity profile across the OMEGA beam, $I_{\text{b}}(x,y)$, is described by a super-Gaussian,

$$I_{\text{b}}(x,y) = I_0 e^{-\left(\frac{\sqrt{x^2+y^2}}{\delta} \right)^n}, \tag{4}$$

where n is the desired super-Gaussian order (approximately 3.7 for the existing phase plates on OMEGA[22]). The $1/e$ radius of the phase plates, δ, is determined by the relationship between the laser energy and target radius and the required scaling between NIF (1.5 MJ) and OMEGA (30 kJ) to conduct ignition-relevant symmetric drive studies on OMEGA ($\delta = 380\ \mu$m for the existing OMEGA Laser System[21]). For PD implosions, a smaller value of n is required to achieve greater irradiation control over localized regions of the target. This can effectively compensate for the reduced equatorial irradiation.

In OMEGA PD experiments, 40 of the 60 beams emulate the NIF x-ray–drive beam-port configuration. A subset of the

20 omitted drive beams at the equator irradiate a Ti/Fe foil to backlight the compressing shell to obtain information about its symmetry. The primary goal of OMEGA experiments is to validate models used to predict ignition. This implies that for low-adiabat implosions with relevant implosion velocities and on-target intensities, necessary models must be developed and simulations validated to reproduce experimental observables. Adiabat-related observables are primarily shock velocity,[23] areal density,[24] and bremsstrahlung radiation from energetic electrons produced from TPD that can potentially preheat the shell.[25] The implosion velocity is related to observations of neutron-production time[26] and scattered light[27] and is primarily determined by laser-energy coupling and heat conduction. Symmetry is inferred experimentally from backlit x-ray images of the converging shell[28] and is determined by adiabat, implosion velocity, and nonuniformity growth. An additional useful metric of PD target performance is the comparison of PD and symmetric-drive implosions at the same laser energy and adiabat.

Current OMEGA warm PD implosions[29] are irradiated with approximately 13 kJ on target at a relatively low intensity at the initial target radius ($\sim 3.5 \times 10^{14}$ W/cm^2). The low-intensity values are driven primarily by the available energy for PD. Since 40 of the 60 beams are used, only 2/3 of the available energy is used to drive the capsule, resulting in low on-target intensity. In this article, we first present cryogenic designs for the existing system that predict implosion velocities of 3.6×10^7 cm/s at low on-target laser intensity. We then present higher-intensity PD designs that use smaller targets ($R_{\text{target}} = 300$ μm) driven with smaller custom laser-beam profiles (with a 1/e radius of ~183 μm or a radius at 5% of peak intensity of 300 μm), with lower values of the super-Gaussian order ($n = 2.2$) and elliptical beam profiles for the equatorial beams. This results in a higher on-target intensity, at the initial target radius, of $\sim 9 \times 10^{14}$ W/cm^2, allowing for LPI and heat-conduction studies.

In the next section, cryogenic-DT polar-drive–implosion designs are presented for the current OMEGA system. It is predicted that the PD implosions will result in reduced implosion velocity relative to symmetric drive implosions at the same energy by ~10%. Observations from warm (CH) implosion related to a similar loss of implosion velocity in PD relative to symmetric drive are also presented in the next section. In the following sections, a PD cryogenic deuterium–tritium (DT) design is presented at ignition-relevant intensities with smaller targets. The sensitivity of these designs to beam profiles is also studied. In addition, a warm plastic (CH) design with ignition-relevant intensities is presented. Observations related to an additional loss of ~10% in PD implosion velocity relative to simulations that include only collisional absorption are discussed and the conclusions are presented.

Low-Intensity Designs for the Current OMEGA Laser System

OMEGA cryogenic-DT implosion designs using laser beams with a super-Gaussian profile of $n = 3.7$ are presented here. The NIF beam configuration [Fig. 130.1(a)] is emulated by using 40 of the 60 OMEGA beams arranged in three rings [Fig. 130.1(b)]. Beams from the higher latitudes are repointed toward the equator in the PD configuration to achieve adequate symmetry [Fig. 130.1(c)]. This is equivalent to each beam in an

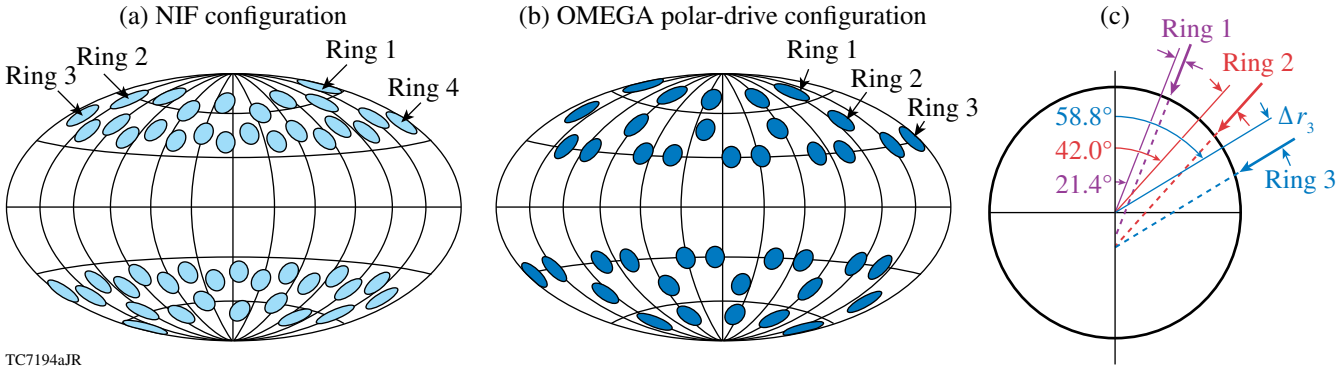

Figure 130.1
(a) NIF beam configuration. (b) Forty of the 60 OMEGA beams, arranged in three rings, emulate the NIF beam configuration. (c) Each ring is repointed by a distance (Δr_3 is shown as an example for Ring 3) toward the equator to improve symmetry. Solid lines—original beam pointing; dashed lines—repointed beams.

OMEGA ring being displaced by a distance Δr perpendicular to the beam axis. Each PD configuration is described by three distances (Δr_1, Δr_2, Δr_3) or equivalently by three angles:

$$\left[\sin^{-1}\left(\Delta r_1 / R_{\text{target}}\right), \sin^{-1}\left(\Delta r_2 / R_{\text{target}}\right), \sin^{-1}\left(\Delta r_3 / R_{\text{target}}\right)\right].$$

The latter description is advantageous because it is independent of the target radius and allows for comparison of OMEGA- and NIF-scale designs. To allow one to make a comparison with previous OMEGA PD work,[28,29] both descriptions are retained here. Implosions are simulated with the two-dimensional (2-D) axisymmetric radiation hydrodynamic code *DRACO* using multigroup diffusive radiation transport and flux-limited heat conduction.[19] A full three-dimensional (3-D) ray trace that uses collisional absorption to deposit the laser energy[30] is employed to accurately model laser ray trajectories of the oblique beams.

The design of a PD implosion begins with a symmetric design that is then iteratively optimized using *DRACO*. Parameters of the 60-beam symmetric design (design A), simulated with collisional absorption and a flux-limited ($f = 0.06$) heat-conduction model, using the spherically symmetric code *LILAC*,[31] are shown in Table 130.I. The laser pulse shape has three pickets followed by a main pulse. This pulse shape has been used to demonstrate a high areal density of nearly 300 mg/cm^2 in previous cryogenic implosions.[32] The PD ignition design[4] also uses a pulse shape of this type. The maximum-possible OMEGA laser energy in the PD configuration is used in this design. This design has an ignition-relevant adiabat implosion velocity and an IFAR comparable to an ignition design value of 36 (Ref. 4). The convergence ratio at bang time is 20, comparable to the ignition design value of 23. The overlapped-beam intensity at the initial target radius is 4.2×10^{14} W/cm^2. While the intensity defined at the initial target radius provides a useful rule of thumb in defining the relevant range for target designs, the physically more-relevant quantity is the intensity at the quarter-critical surface. The quarter-critical intensity $I_{n/4}$ is somewhat less than the intensity at the initial target radius because of absorption in the lower-density corona. For this design, this value is 3×10^{14} W/cm^2, which is significantly lower than the values in the ignition design ($\sim 8 \times 10^{14}$ W/cm^2). Consequently, the TPD threshold parameter, defined as

$$\eta = I_{n/4}\left(10^{14}\ \text{W/cm}^2\right) L_{n/4}(\mu\text{m}) \Big/ 233\, T^{\text{e}}_{n/4}\,(\text{keV}) \text{ (Ref. 11)},$$

where $L_{n/4}$ and $T^{\text{e}}_{n/4}$ are the density scale length and the electron temperature at the quarter-critical surface, respectively, is less than 1, indicating a marginal effect of TPD on electron generation and capsule preheat.[33]

A 40-beam PD implosion with the same energy, based on this design, is optimized using *DRACO* (Fig. 130.2). In the PD case, the single-beam energies are increased by 3/2 to ensure

Table 130.I: Parameters of 60-beam, symmetric-drive OMEGA cryogenic-DT designs simulated with collisional absorption and flux-limited heat conduction. Polar-drive optimization using the 2-D axisymmetric hydrodynamics code *DRACO*[19] is based on these designs (see text).

	Design A	Design B	Design C
R_{outer} (μm)	430	300	300
Ice thickness (μm)	35	35	65
CH ablator (μm)	9	9	9
Peak power (TW)	10	10	10
E (kJ)	15.5	11.5	12.8
V_{imp} (cm/s)	3.6×10^7	3.4×10^7	2.5×10^7
IFAR	32	22	12
DT yield	1.2×10^{14}	2.7×10^{13}	5.0×10^{12}
ρR_{max} (mg/cm^2)	243	240	236
R_{hs} (μm)	20	15	15
CR	20	17	15
$L_{n/4}$ (μm)	150	110	110
$I_{n/4}$ (W/cm^2)	3×10^{14}	7×10^{14}	7×10^{14}
$T^{\text{e}}_{n/4}$ (keV)	2.1	2.8	2.8
$\eta_{\text{TPD}} = I_{n/4}\left(10^{14}\ \text{W/cm}^2\right) L_{n/4}(\mu\text{m}) \Big/ 233\, T^{\text{e}}_{n/4}\,(\text{keV})$	0.9	1.3	1.3

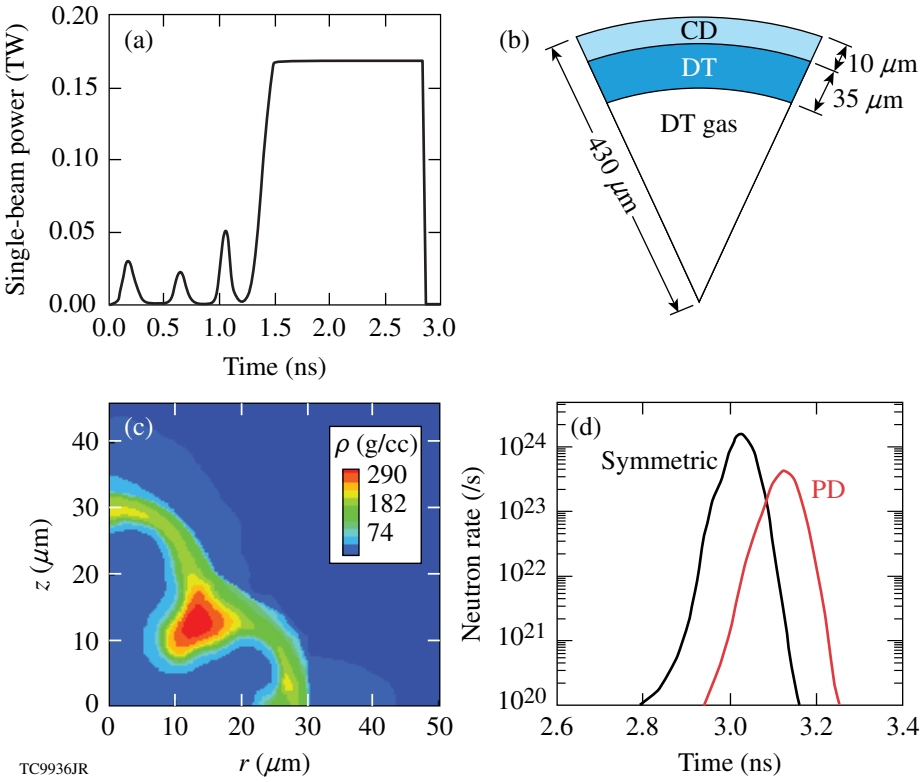

Figure 130.2
(a) Pulse shape and (b) target for cryogenic DT polar-drive (PD) design on the existing OMEGA Laser System with n = 3.7 phase plates. (c) Mass-density profiles at peak neutron production. (d) Neutron-rate histories—symmetric drive (black) and PD (red).

that the target is irradiated with the same total picket energies and total energy [Fig. 130.2(a)]. This PD configuration corresponds to beam ring displacements of 90 μm, 150 μm, and 150 μm. As the density contours at peak neutron production [Fig. 130.2(b)] indicate, the core has a small $\ell = 2$ and a large $\ell = 4$. The implosion velocity for the PD design is approximately 10% less than that of the symmetric design. Bang time, defined as the time of the onset of the neutron yield above the experimental noise threshold, is an important observable to quantify the implosion velocity. For the typical temperatures in these implosions, neutron rate Y_{1n} scales with mass density ρ and the fusion reaction rate as ion temperature T_i of the fuel as $Y_{1n} \sim \rho^2 \langle \sigma v \rangle d^3 r$, where $\langle \sigma v \rangle \sim T_i^4$. Using $T_i \sim \alpha^{-0.15} V_{imp}^{1.3}$ (Ref. 9), the neutron rate can be written in terms of implosion velocity as $Y_{1n} \sim \rho^2 \alpha^{-0.6} V_{imp}^{5.2}$. The measured rate can deviate from this one-dimensional (1-D) formulation because the growth of nonuniformity can reduce both T_i and the neutron-producing volume (or "clean volume"). Simulations indicate that nonuniformity does not significantly influence the rate in these implosions early during the deceleration phase. Therefore comparing the bang time provides a measure of the implosion velocity. This reduced velocity is shown as the delay in neutron-production history in Fig. 130.2(c).

Additional variables, including beam energies and shimming, can be employed to optimize the design. The best symmetry for the PD equivalent of design A is obtained with only beam displacements. Beam profiles are predetermined and no combination of beam energies and displacement can improve upon the symmetry of the design shown in Figs. 130.2(a) and 130.2(b). Since it is challenging to achieve adequate equatorial drive in the PD configuration, thinning the DT ice or ablator near the equator or shimming may improve the density uniformity locally near the equator. This is not studied in this work.

The final optimized PD design typically differs somewhat from the original symmetric design because of the retuning of the shocks to achieve adequate uniformity and timing with oblique beams. Since the difference in peak areal density between the original symmetric design (design A) and the PD-optimized design is less than 5%, the original design A is retained as the symmetric equivalent of the optimized PD

design. The predicted PD yield is 27% of the symmetric-drive yield. This reduction is due to the $\ell = 4$ nonuniformity and the reduced implosion velocity in PD relative to symmetric drive. These predictions are similar to observations from warm CH PD implosion experiments.

In warm PD OMEGA implosion experiments, triple-picket laser pulse shapes (Fig. 130.3) irradiate a 9-atm-deuterium-filled, 27-μm-thick CH shell with approximately 13 kJ of laser energy. Full beam smoothing [smoothing by spectral dispersion (SSD)][34] and polarization smoothing (PS)[35] are used in all of the implosions. These implosions are designed to achieve a convergence ratio (CR) of 19, where CR is defined as the ratio of the initial inner shell radius to the hot-spot radius (defined as a radius that is 1/e of peak density) at peak neutron production. It has been shown previously[29] that very good agreement in picket shock velocities and catch-up at the equator is obtained in PD geometry as measured through VISAR (a velocity interferometer system for any reflector)[23] and simulated with *DRACO*.[19] Approximately 100% of the predicted value of areal density (ρR), measured through the energy loss of charged particles,[24] is obtained in these implosions. Since $\rho R \sim \alpha^{-0.6}$ (Ref. 36), this indicates that the predicted adiabat is achieved in the implosion. By comparing the simulated and measured neutron-production time ("bang time" is defined as the time when the neutron rate rises above the experimental noise level), it is estimated that simulations overpredict implosion velocity by ~10%. This will be discussed in the context of CBET (cross-beam energy transfer). The predicted shell asymmetry was well reproduced in these implosions,[29] until the shell converged by a factor of only 7, the latest time at which shell nonuniformity can be reliably inferred from experimental images.

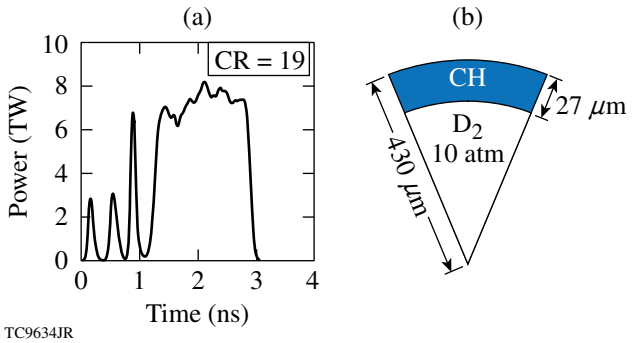

Figure 130.3
(a) Laser pulse shape used to irradiate the target shown in (b) in current OMEGA polar-drive experiments.

The ratio of PD yields to the equivalent energy symmetric-drive yields versus the on-target laser energy is shown in Fig. 130.4(a) for different PD configurations. The average experimental symmetric drive yield is $(1.2\pm0.2) \times 10^{10}$ (averaged over four shots) compared to an average simulated value of $(1.12\pm0.3) \times 10^{11}$. The experimental reduction in the symmetric drive yield is due to nonuniformities such as beam imbalances, including primarily beam mistiming and target-surface rough-

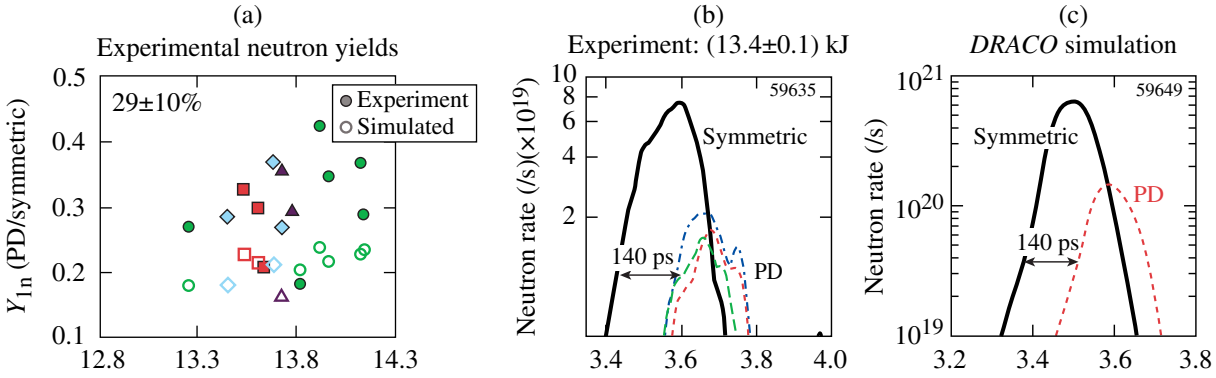

Figure 130.4
(a) Ratio of D_2 neutron yield from PD implosions to symmetric-drive implosions versus laser energy. Each symbol represents a shot. Solid circles represent experimental ratios for PD and symmetric-drive implosions; open circles represent simulated ratios for PD and symmetric-drive implosions. PD configurations are 90 μm, 120 μm, and 120 μm (circles); 90 μm, 150 μm, and 150 μm (squares); 90 μm, 133 μm, and 133 μm (triangles); and 30 μm, 150 μm, and 150 μm (diamonds). The average experimental ratio is 29±10% compared to the average simulated ratio of 20±10%. (b) Measured symmetric drive (solid) neutron rate compared to measured PD (dashed) neutron rates. Different curves correspond to different shots. (c) Simulated neutron rate for symmetric drive (solid) compared to simulated PD (dashed) neutron rate.

ness. Polar-drive yields are further reduced from the symmetric drive yields. The average reduction in the experimental ratio [Fig. 130.4(a)] is (29±10)% compared to the simulated reduction of (20±11)%, which is in good agreement.

The delay in the PD bang time relative to symmetric drive is evident from Fig. 130.4(b). Experimentally the (140±50)-ps delay in the PD bang time relative to the symmetric drive bang time requires a reduction of about 10% in the implosion velocity relative to symmetric drive. Simulations reproduced this delay in bang time [Fig. 130.4(c)]. Using the scaling of the neutron rate with the implosion velocity presented earlier, nearly 80% improvement in the absolute PD neutron yield can be achieved by increasing the implosion velocity by 10%.

The four experimental PD configurations correspond to beam distance displacements of 90 μm, 120 μm, and 120 μm; 30 μm, 150 μm, and 150 μm; 90 μm, 150 μm, and 150 μm; and 90 μm, 133 μm, and 133 μm. The extent of beam repointing in all these configurations is quite significant and results in reduced energy deposited (these repointed configurations also have a significant amount of energy that misses the target, contributing to the reduced energy deposition) and, therefore, reduced hydrodynamic efficiency. To compare these values with those in the NIF ignition design, these numbers are converted to scale invariant angles corresponding to 12°, 16°, and 16°; 4°, 20°, and 20°; 12°, 20°, and 20°; and 12°, 18°, and 18°.

The NIF ignition design also significantly repoints the beams—corresponding to 1.5°, 14.5°, 0°, 38.5°, and 33° for each ring on the NIF,[4] respectively. However, individual laser-spot profiles are optimally designed to prevent energy from going over the horizon of the target; beams are truncated asymmetrically, so that only insignificant beam energy misses the target. Moreover, sufficient energy is available on the NIF to compensate for the reduced hydrodynamic efficiency. Asymmetrically truncated beam profiles are not currently available on OMEGA and, as will be pointed out later, are also not practical for future OMEGA designs. For OMEGA-scale implosions, where the energy is limited, recovering this implosion velocity is important for studying the relative performance of PD and symmetric drive. Better control over the energy deposition in polar angle over the target, by choosing a different spatial beam profile, can make it possible to recover the implosion velocity in OMEGA-scale implosions, as discussed in the next section.

High-Intensity OMEGA Designs

Beam profiles with a relatively high super-Gaussian (SG) order result in a broad deposition region over the target. The spatial beam profiles from individual beams are compared for two different SG orders with δ = 383 μm in Fig. 130.5. The higher SG order (n = 3.7) is characterized by a flat-top in intensity distribution, whereas the lower SG order (n = 2.2) is more center peaked. This center-peaked distribution allows for more-localized on-target intensity when the overlap of all beams within a ring is considered. As a result, the laser irradiation can be more effectively pointed toward the equator with the lower SG order (Fig. 130.6). For the n = 3.7 beam profiles currently on OMEGA, the overlapped-intensity distribution from each ring is broadly incident over a large range of polar angles [Fig. 130.6(a)]. The normalized overlapped intensity (normalized to the maximum value among the three rings, which corresponds to the Ring 1 intensity at the pole) is shown in Fig. 130.6(a) for the un-repointed beam configuration. With the lower SG order, again, for the un-repointed configuration, particularly for Rings 2 and 3, the intensity distribution on target is more peaked toward the equator [Fig. 130.6(b)]. The overlapped intensities from each ring are compared when the beams are repointed [Figs. 130.6(c) and 130.6(d)]. The beam displacements correspond to (16 μm, 21 μm, 68 μm) or (3°, 4°, 13°) values that result in optimized designs, as will be shown below. The equator is under driven by nearly 20% relative to the pole for n = 3.7 [Fig. 130.6(c), dashed lines], whereas the n = 2.2 beam profiles permit nearly the same intensities at the equator and pole [Fig. 130.6(d), dashed lines]. A purely elliptical beam profile described by

$$I_b(x,y) = I_0 e^{-\left[\frac{\sqrt{\eta_3 x^2 + y^2}}{\delta}\right]^n} \quad (5)$$

with ellipticity η_3 = 1.2 for Ring 3 permits greater intensity at the equator relative to a purely circular beam profile in both

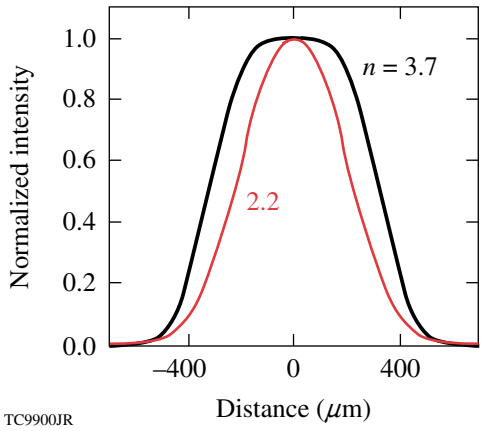

Figure 130.5
Beam profiles for two different super-Gaussian orders: n = 3.7 (black) and n = 2.2 (red).

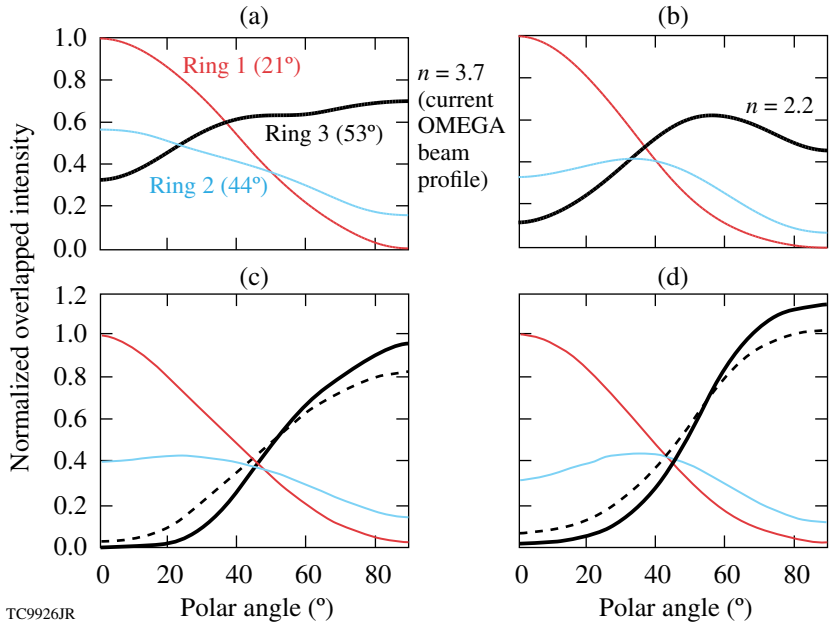

Figure 130.6
On-target normalized overlapped beam intensity attributed to each OMEGA ring versus polar angle: (a) $n = 3.7$ and (b) $n = 2.2$. A lower super-Gaussian order provides a more-localized intensity pattern toward the equator (polar angle = 90°). (c) Overlapped on-target normalized beam intensity attributed to each OMEGA ring versus polar angle for the repointed configuration (16 μm, 21 μm, 28 μm) when only circular $n = 3.7$ beam profiles are used for all rings (solid), when an elliptical profile is used only for Ring 3 with ellipticity $\eta_3 = 1.2$ (dashed), and (d) only circular $n = 2.2$ beam profiles are used for all rings (solid), elliptical profile only for Ring 3 with ellipticity $\eta_3 = 1.2$ (dashed).

cases (solid line). With the same beam displacement, the lower SG order with elliptical beam profiles for Ring 3 is the more-favorable option to compensate for the reduced equatorial drive. This combination irradiates the equator with higher intensity than the pole by nearly 20% compared to the higher SG order.

To increase on-target laser intensity closer to ignition-relevant values, an appropriate value of δ and target radius (R_{target}) is required. The goal is to irradiate the target with NIF-relevant laser quarter-critical intensity. There is no simple scaling argument for the quarter-critical intensity when two different target sizes and laser energies are compared. The NIF target radius is 3 to 4 times that of an OMEGA-scale target, resulting in a proportionately longer coronal density scale length. More absorption occurs in the lower-density corona in the NIF designs because of the longer scale length, leading to a different dependence for the quarter-critical intensity on the incident laser intensity in the NIF designs versus the OMEGA designs. Dimensional scaling relating the required laser energy for a given plasma energy is used as a starting point for a target radius. This is then iteratively adjusted to achieve similar simulated quarter-critical intensity in both designs. Using the scaling for the laser energy E contributing to a given plasma energy, $E \sim R^3$, and typical NIF and OMEGA parameters $R_{\text{NIF}} = 1700$ μm, $E_{\text{NIF}} = 1.5$ MJ, and $E_{\Omega}^{\text{PD}} = 12$ kJ, one gets $R_{\Omega}^{\text{PD}} = 350$ μm. If one instead uses a 15% smaller target radius, the intensity at the quarter-critical surface will increase from 4.5×10^{14} W/cm^2 to 6.5×10^{14} W/cm^2 [Fig. 130.7(a)], a value closer to the PD ignition design value, which varies between 7 and 9×10^{14} W/cm^2 in the polar angle on target [Fig. 130.7(b)]. Higher intensities in the OMEGA designs can be obtained by increasing laser energy (an additional 20% is available for the design as described below) or by further reducing the target radius. The latter approach typically results in lower convergence and is therefore not preferred.

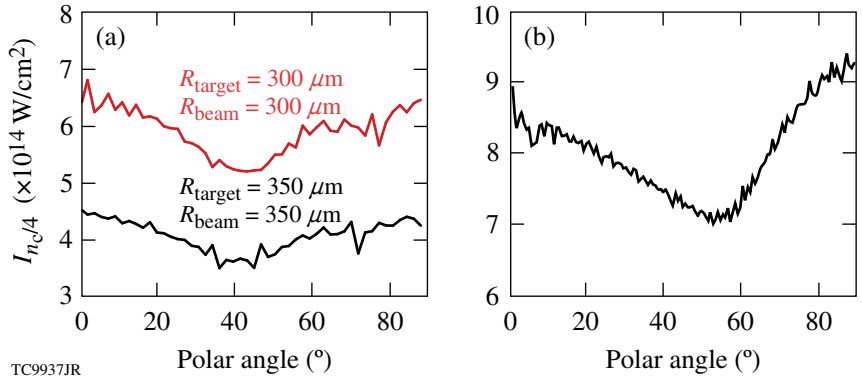

Figure 130.7
(a) Overlapped on-target intensity at the quarter-critical surface at the end of the laser pulse for two different target radii. The beam radius equals the target radius in each case. (b) Overlapped on-target intensity at the quarter-critical surface for the NIF design.[4]

Parameters for the 60-beam OMEGA cryogenic-DT symmetric target designs are shown in Table 130.I. The target has a radius of 300 μm with a 35-μm-thick (design B) or 65-μm-thick (design C) DT layer inside a 9-μm-thick CH shell. This CH thickness is chosen so that only CH is present throughout the laser pulse at the quarter-critical surface in the corona. The presence of DT at the quarter-critical surface is associated with a greater production of energetic electrons from TPD, which can potentially preheat the target.[37] The 65-μm layer thickness corresponds to ongoing symmetric-drive OMEGA cryogenic-DT experiments.[16] With the smaller target radius, initial experiments will be performed using this thicker, more-stable shell. This design deliberately uses only about 80% of the laser energy available on OMEGA; this can be increased by increasing either the intensity, the length of the pulse, or the relative energies of the rings. It is important to note that OMEGA experiments with ignition-relevant intensities are possible at this target radius. The smaller target radius results in a smaller convergence ratio for designs B and C. This can be increased by decreasing the shell adiabat by selecting a main pulse with a step as in Ref. 32. At the values of $I_{n/4}$ accessible in these designs, the TPD threshold parameter η_{TPD} exceeds 1 and has values similar to those in current symmetric-drive OMEGA experiments.[38]

Parameters of the PD design corresponding to the symmetric design C are summarized in Table 130.II. In PD, Ring 3 has 25% more energy than Rings 1 and 2 (parameterized by the variable E_{mod}). An elliptical beam profile [Eq. (5)] is chosen for Ring 3, increasing the equatorial drive (Fig. 130.8). The mass-density profile in Fig. 130.9(a) shows the shock as it breaks out of the DT layer for the 65-μm-thick DT design. The shock front is nonuniform, with the equator being somewhat underdriven compared to the rest of the target. The density contours at peak neutron production indicate a fairly uniform shell [Fig. 130.9(b)]. Little evidence of the underdriven equator is observed at peak neutron production because of shock dynamics. The return shock at the equator is weaker than the shock elsewhere. As a result, the shell at the equator travels a greater distance before it decelerates. Ideally, PD target design should optimize different phases of the implosion. In the NIF design, this is achieved by varying the pulse shapes of each ring independently in time. Picket energies vary between rings relative to the energy in the main pulse to ensure uniformity throughout the implosion. Only overall beam energies can be varied on OMEGA; therefore, only an overall optimization of the implosion is possible.

When beam energies are varied, the equivalency of symmetric drive and PD implosions is less apparent. Here, since Ring 1 is nearly normally incident and the variations in pointing and beam energies relative to symmetric drive for the other rings are used to correct for beam obliquity, Ring 1's picket energies correspond to the equivalent symmetric-drive pulse shape for the optimized PD design. These are the same energies as the original symmetric design C. The peak power in the PD-equivalent symmetric design is appropriately chosen to keep the overall laser energy constant. Nearly 1-D areal density is achieved with a peak-to-valley variation of less than 10% [Fig. 130.10(a)]. The PD design obtains the same bang time as

Table 130.II: Parameters for the nominal high-intensity PD cryogenic OMEGA implosion based on design C in Table 130.I. E_{mod} is the overall energy multiplier to the pulse shape for Design C in Table 130.I; n is the super-Gaussian order for the rings; δ is the $1/e$ radius of the beam profile [Eq. (5)], η is the ellipticity of the beam profiles defined as the ratio of the major to minor axis of the beams (Eq. 5); and Δr is the extent to which the beams are repointed.

	Ring 1	Ring 2	Ring 3
E_{mod}	1.00	1.00	1.25
n	2.2	2.2	2.2
δ	183 μm	183 μm	183 μm
η	1.0	1.0	1.2
Δr	16 μm	21 μm	68 μm

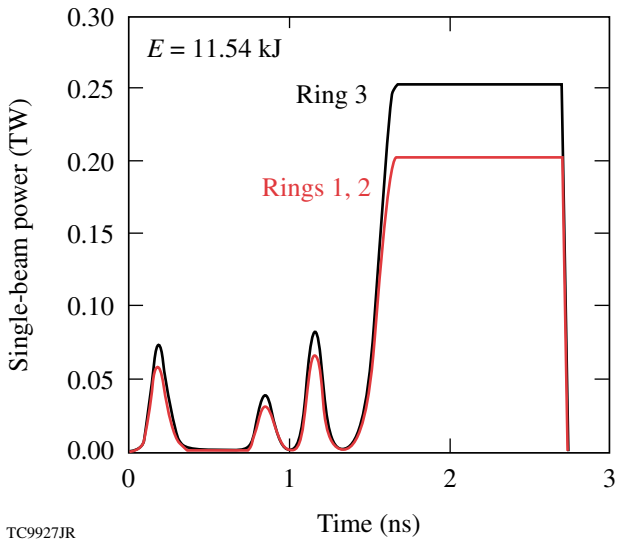

Figure 130.8
Cryogenic target design used with the beam repointing in Fig. 130.6. Laser pulse shapes used for each of the rings irradiating the target in design C.

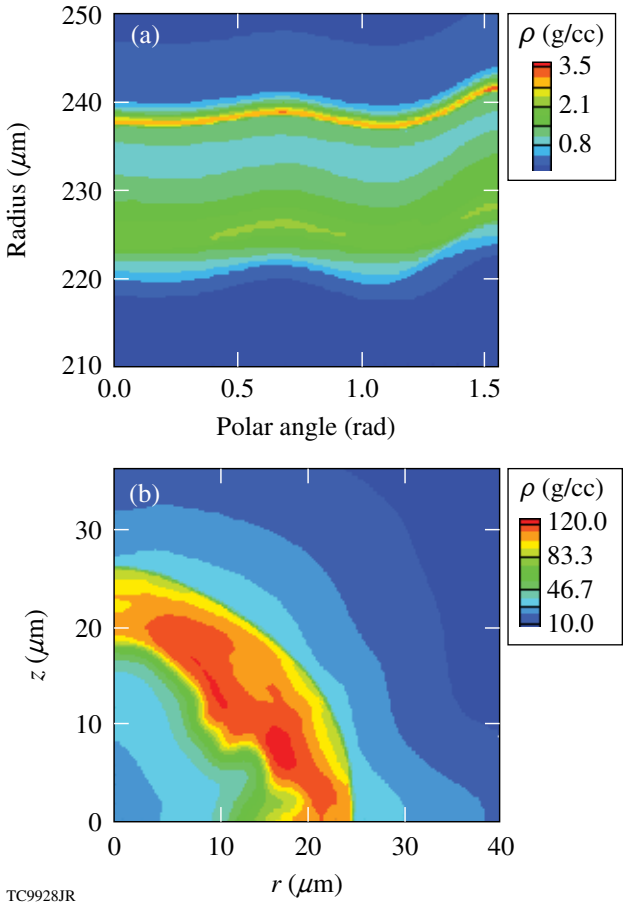

Figure 130.9
(a) Mass-density contours shortly after shock breakout (1.7 ns) for the design in Fig. 130.8 with parameters in Table 130.II. (b) Mass-density contours at peak neutron production (2.8 ns) for the target design shown in Fig. 130.7.

the symmetric design, indicating that the symmetric drive's hydroefficiency is achieved in the PD design [Fig. 130.10(b)]. Nearly 55% of the symmetric drive's yield is obtained in the PD design. This reduction in PD yield is due to the residual nonuniformity, primarily $\ell = 4$.

The OMEGA beam profiles differ from the NIF beam profiles in two respects: The NIF design uses a circular spot modulated by an offset ellipse to provide greater uniformity locally near the equator. In the OMEGA design a similar spot for Ring 3 eliminates the weaker shock near the equator [Fig. 130.9(a)]. This spot is impractical on OMEGA, however, given the dispersion required by SSD. The extent of SSD dispersion (~180 μm) is comparable to the minor radius of the required ellipse, which then necessitates an extremely small (~10 μm) sized pre-SSD ellipse. Such a variation in intensity is impractical to manufacture through a phase plate. The second source of difference is in the beam truncation scheme employed in the NIF design. NIF beam profiles are asymmetrically truncated such that the laser energy spilling over the target horizon is minimized. This allows more energy to couple to the target. On OMEGA, however, this truncation is unnecessary. OMEGA designs require less repointing to achieve optimal symmetry because the beam-port arrangement on OMEGA is more optimal and the smaller-scale targets provide better hydrodynamic efficiency. Beam truncation is required when the repointing is significant since it permits adequate irradiation of the equator without loss of laser energy over the horizon. The optimal beam repointing on OMEGA is small enough that the effect of beam truncation is a simulated unobservable increase of ~2% in the implosion velocity.

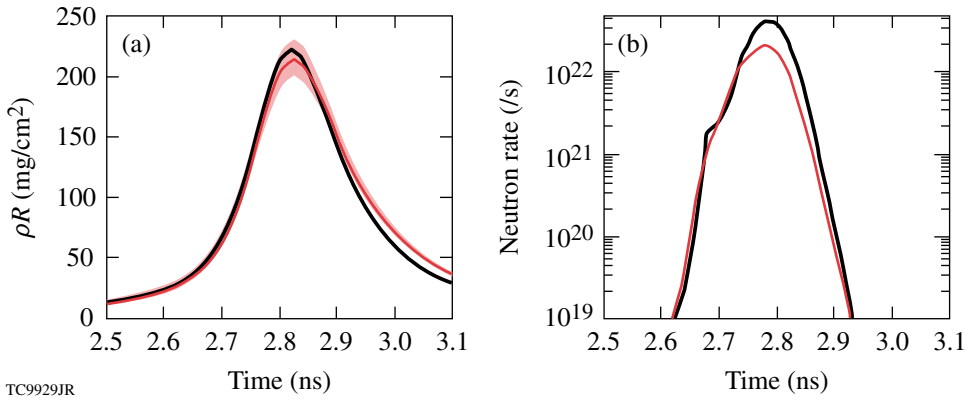

Figure 130.10
(a) Areal-density history for symmetric drive (black) compared to the PD implosion (red). The shaded region indicates the range in areal densities in polar angle. (b) Neutron rate for symmetric drive (black) compared to PD (red). No significant difference in neutron-production timing is calculated indicating that the symmetric-drive implosion velocity is achieved in the PD simulation.

Sensitivities to the OMEGA beam profiles are investigated by systematically varying their parameters (Fig. 130.11). Hot-spot distortion, defined here as the ratio of the standard root-mean-square deviation of the hot-spot radius (defined as the inner 1/*e* location of peak density) to the mean hot-spot radius is used as a measure of implosion quality. This quantity is further broken down into the contribution from the various modes; the ratio of the amplitude of an individual mode to the hot-spot radius is also shown in Fig. 130.11. Super-Gaussian orders of each of the rings and the ring ellipticity are varied individually. As Fig. 130.11 indicates, Legendre modes with $\ell = 2$ and $\ell = 4$ dominate hot-spot distortion. For 10% variations in the SG order, no significant variation in target performance is observed, indicating the robustness of the design. Neutron yields do not change significantly when the beam profile parameters are varied. The parameter that is most sensitive to implosion quality is the ellipticity of the Ring 3 beams' profiles. For Ring 3 ellipticity, the most-sensitive determinant of implosion quality, the neutron yield relative to symmetric drive varies between 58% (for $\eta_3 = 1.0$) and 54% (for $\eta_3 = 1.25$) (see Fig. 130.12).

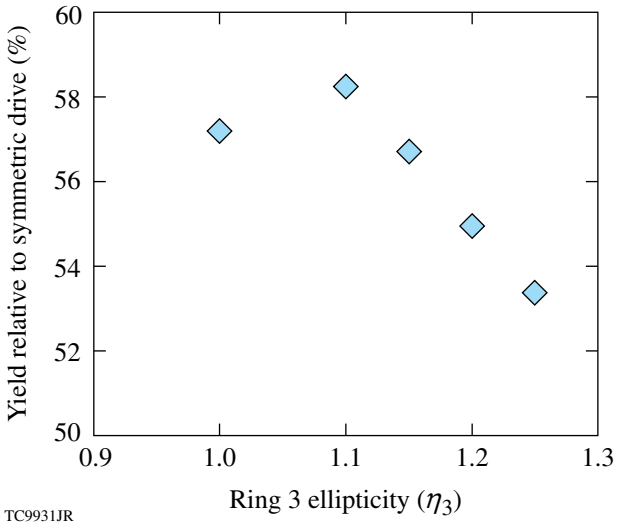

Figure 130.12
Yield relative to symmetric drive versus Ring 3 ellipticity. The PD yield for $\eta_3 = 1.15$ coresponds to 2.3×10^{12}, whereas the symmetric drive yield is 4×10^{12}.

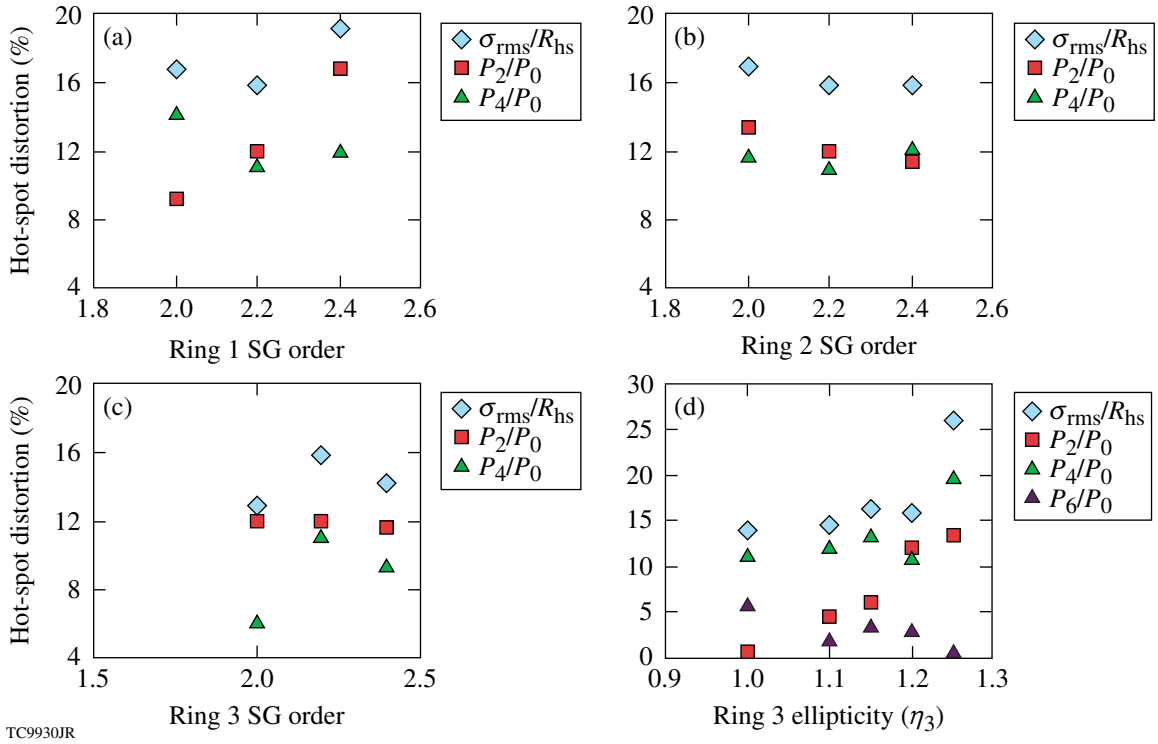

Figure 130.11
(a) Sensitivity of hot-spot distortion to super-Gaussian (SG) order of Ring 1 beams; (b) sensitivity of hot-spot distortion to super-Gaussian order of Ring 2 beams; (c) sensitivity of hot-spot distortion to super-Gaussian order of Ring 3 beams; (d) sensitivity of hot-spot distortion to ellipticity of Ring 3 beams, η_3. Diamonds: ratio of σ_{rms} of hot spot to radius of hot spot (R_{hs} is defined as the 1/*e* of peak density); squares: ratio of amplitude of Legendre-mode P_2 to R_{hs}; green triangles: ratio of amplitude of Legendre-mode P_4 to R_{hs}; dark purple triangles: ratio of amplitude of Legendre-mode P_2 to R_{hs}.

Manufacturing uncertainties introduce variability among phase plates. Such variations can cause the on-target intensity profile to deviate from the pure Legendre mode assumptions used in the design. To constrain the range of acceptable beam profiles, simulations are performed with varying ellipticity for Ring 3 beams. A randomly selected ellipticity for each beam in Ring 3, with η_3 varying uniformly between 1.1 and 1.2, is used in the simulations. The effect of varying ellipticities is bracketed by two different models of the nonuniformity (Fig. 130.13): (1) Only the $m = 0$ modes in the Legendre decomposition of the asymmetry in the 2-D axisymmetric simulation are used as the initial perturbation ampltiudes. (2) The amplitude of the $m \neq 0$ modes is added in quadrature to reach the amplitude of the Legendre mode used in the simulation, where the effect of the 3-D perturbation introduced by beam profile variations can be approximated. The middle point, $\eta_3 = 1.15$, corresponds to a single ellipticity chosen for all the beams in Ring 3. Marginal variations in hot-spot symmetry and neutron yield relative to symmetric drive are modeled in Figs. 130.13(a) and 130.13(b), respectively.

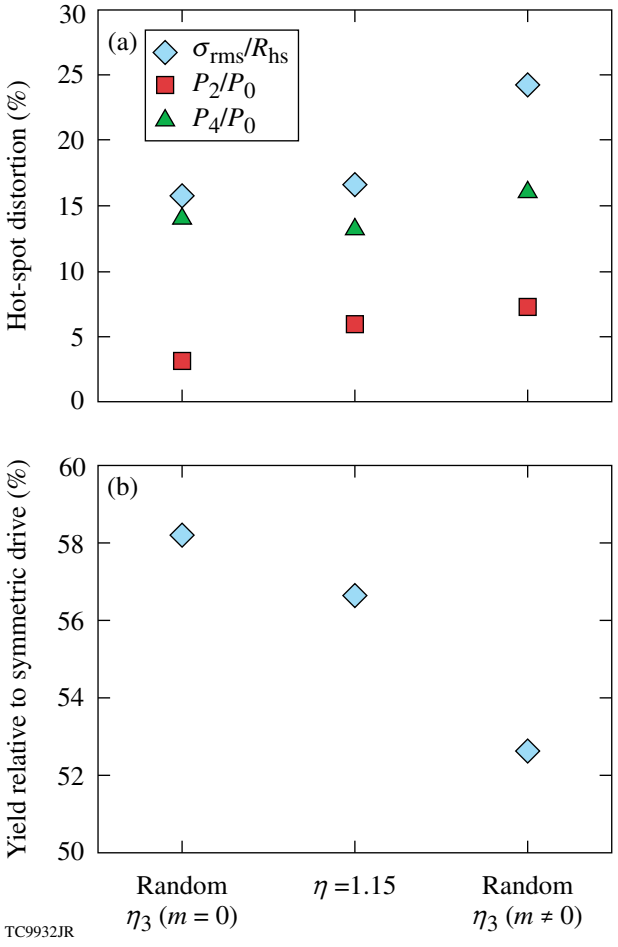

Figure 130.13
(a) Hot-spot distortion for varying ellipticities for each beam in Ring 3. Random ellipticities correspond to a randomly selected ellipticity for each beam in Ring 3 with η_3 varying uniformly between 1.1 and 1.2. Such a variation of ellipticities results in a breakdown of azimuthal symmetry. This is modeled by including only the $m = 0$ modes in the Legendre decomposition of the asymmetry in the 2-D axisymmetric simulation. The middle point, $\eta = 1.15$, corresponds to a single ellipticity chosen for all the beams in Ring 3. The third set of points corresponds to the inclusion of the amplitude of the $m \neq 0$ modes in quadrature in the amplitude of the Legendre mode used in the simulation. (b) Yield relative to symmetric drive for each of the cases in (a).

Warm implosions offer the advantage that frequent, highly repeatable experiments can be conducted to study the relevant coronal physics. A warm CH, PD implosion design also predicts good performance relative to symmetric drive with the same set of beam profiles (Fig. 130.14). As in the cryogenic design, ring energies are varied [Fig. 130.14(a)] to minimize hot-spot distortion [Fig 130.14(b)]. Polar-drive–implosion velocity is very close to the symmetric-drive velocity as shown by the similar bang times between the two simulations [Fig. 130.14(c)].

Effect of Cross-Beam Transfer and Nonlocal Heat Transport in Symmetric and Polar Drives

As mentioned earlier, CBET has been invoked to explain the observed delay in bang time between experiment and simulation for symmetric-drive implosions.[10] The role of CBET in PD implosions is unclear. Experiments to measure scattered light in PD geometry and efforts to model CBET in *DRACO* are ongoing. Similar to symmetric drive, a delay in bang time is observed in warm OMEGA implosion experiments in PD geometry (Fig. 130.15). Bang time is delayed by ~180 ps in PD experiments relative to PD simulations [Fig. 130.15(a)]. This delay is similar for the various PD configurations and also similar to the delay observed for symmetric drive [Fig. 130.15(b)]. CBET's dependence on beam obliquity is also unclear. Apart from an overall delay in the absolute time, observations of shell asymmetry agree with simulations.[29] The latest time at which these measurements can be made is still relatively early, when the shell has converged by a factor of ~7. It is therefore unclear if CBET preferentially compromises laser-energy absorption at some latitudes relative to others. All the 60-beam symmetric designs presented in this article are sensitive to the model of cross-beam transfer[10] and nonlocal transport[13] implemented in *LILAC*. The implosion velocity is reduced by approximately 10% and neutron yield by approximately a factor of 3 when effects of cross-beam transfer are included in *LILAC* simulations. Areal density is also reduced by nearly 10% primarily due to the introduction of a coasting phase in the implosion caused by the driving pressure not being retained until the onset

of deceleration. One possible CBET mitigation strategy is to reduce the beam size relative to the target size; for example, the ratio of ~0.85 improves implosion velocity while imposing optimal levels of nonuniformity on target.[39] With the target radius selected in the previous section, the flexibility can perform such studies in PD. The high-intensity design deliberately uses only about 80% of the maximum energy available on OMEGA; the additional 20% in laser energy is available to drive larger targets, if necessary.

Conclusions

Cryogenic-DT and warm CH polar-drive designs for the OMEGA laser have been presented. Given the available energy on OMEGA, it is challenging to get both ignition-relevant

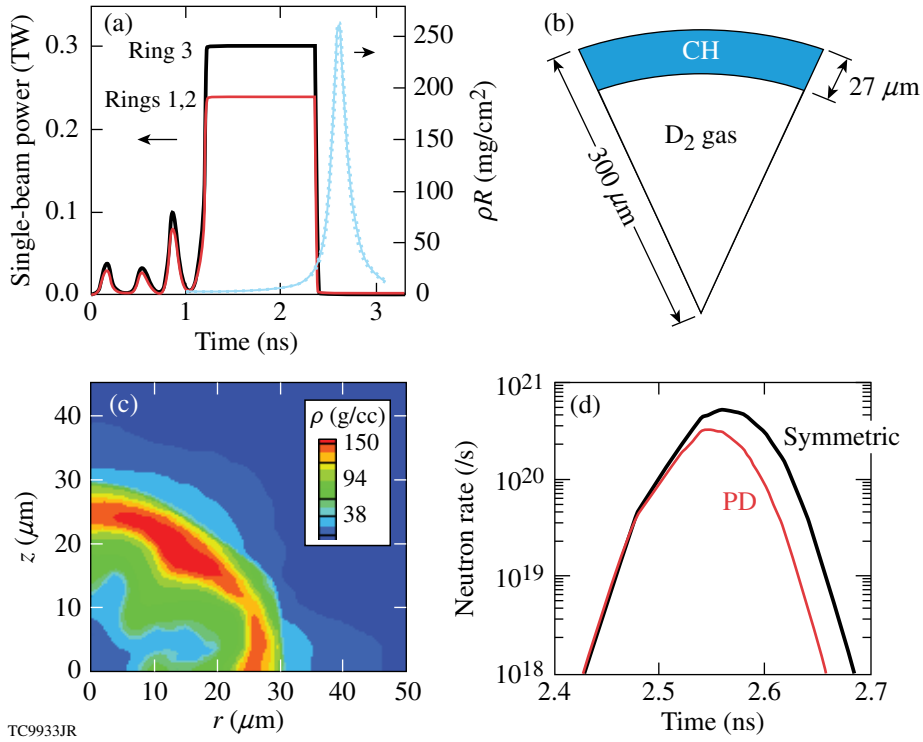

Figure 130.14
(a) Ring pulse shapes (left axis) and areal-density history (right axis) for (b) a warm, plastic-shell target. (c) Mass-density contours at peak neutron production (2.56 ns). (d) Neutron-rate histories for symmetric drive (black) compared to the PD simulation (red). No delay in bang time is observed, indicating that the symmetric-drive–implosion velocity is achieved in the PD simulation.

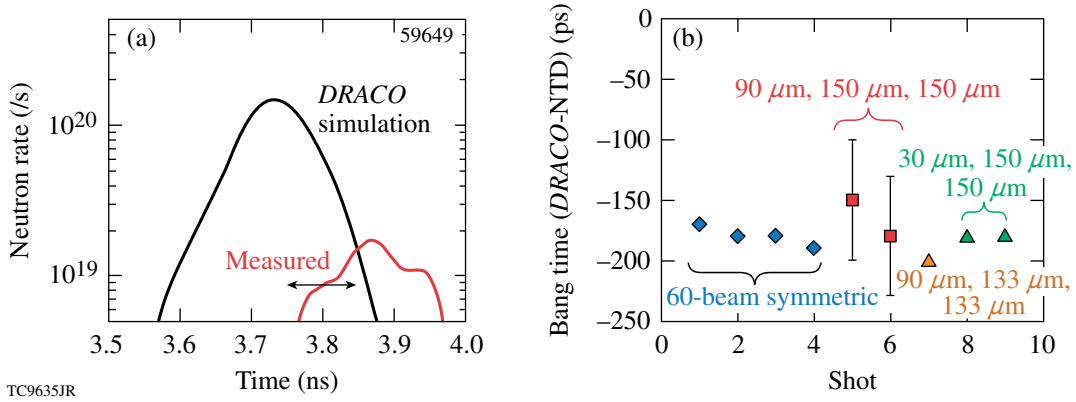

Figure 130.15
(a) Comparison of neutron rates between the measured (red) and the simulated (black) with only collisional absorption and flux-limited heat conduction values in PD configuration. (b) Difference in the simulated and measured bang times for symmetric drive and three different PD configurations. Bang time occurs earlier in the simulations when only collisional absorption of the laser pulse is assumed.

intensity (to study LPI effects and heat conduction) and high in-flight aspect ratio (to study effects of instability growth) in one design. Instead, two designs have been presented, each of which addressed one issue. A low-intensity optimized PD cryogenic DT design using the existing OMEGA phase plates predicts ~27% of the symmetric-drive yield. This yield reduction is due to reduced implosion velocity in PD relative to symmetric drive and the dominant $\ell = 4$ nonuniformity. These predictions are similar to observations from warm CH implosions on OMEGA, where a similar modal nonuniformity is observed and simulated. The observed warm implosion PD yield is reduced relative to spherically symmetric implosion experiments and is due to an inferred loss of ~10% in implosion velocity. High-intensity cryogenic and warm CH designs with smaller targets for future PD experiments on OMEGA have been presented. These designs repoint beams less by making a judicious choice of beam profiles and beam energies, permitting adequate symmetry while reducing the extent of repointed beams. Simulations indicate the recovery of symmetric-drive–implosion velocity in these designs. Weak sensitivity of target performance such as neutron yield and hot-spot distortion on beam profile parameters indicate that the designs are robust. Measurements from current OMEGA PD experiments also indicate an additional loss of ~10% in implosion velocity relative to PD simulations that include only collisional absorption as the mechanism of laser-energy deposition and flux-limited heat conduction. This reduction in implosion velocity is similar to that observed in symmetric drive, where it has been attributed to cross-beam transfer. Mitigation options include reducing the beam size relative to target radius. The beam profile radii chosen for the high-intensity design presented in this article will permit such mitigation studies by varying the target radii. Detailed experimental studies and code development to model the effect of cross-beam transfer in PD geometry are ongoing. Implosion results from the combined set of implosions should yield valuable data to develop and validate models of laser-energy deposition, heat conduction, nonuniformity growth, and fuel assembly in PD geometry.

ACKNOWLEDGEMENT

This work was supported by the U.S. Department of Energy Office of Inertial Confinement Fusion under Cooperative Agreement No. DE-FC52-08NA28302, the University of Rochester, and the New York State Energy Research and Development Authority. The support of DOE does not constitute an endorsement by DOE of the views expressed in this article.

REFERENCES

1. S. Skupsky, J. A. Marozas, R. S. Craxton, R. Betti, T. J. B. Collins, J. A. Delettrez, V. N. Goncharov, P. W. McKenty, P. B. Radha, T. R. Boehly, J. P. Knauer, F. J. Marshall, D. R. Harding, J. D. Kilkenny, D. D. Meyerhofer, T. C. Sangster, and R. L. McCrory, Phys. Plasmas **11**, 2763 (2004).

2. E. Moses, presented at The Seventh International Conference on Inertial Fusion Sciences and Applications, Bourdeaux-Lac, France, 12–16 September 2011.

3. J. Nuckolls *et al*., Nature **239**, 139 (1972).

4. T. J. B. Collins, J. A. Marozas, K. S. Anderson, R. Betti, R. S. Craxton, J. A. Delettrez, V. N. Goncharov, D. R. Harding, F. J. Marshall, R. L. McCrory, D. D. Meyerhofer, P. W. McKenty, P. B. Radha, A. Shvydky, S. Skupsky, and J. D. Zuegel, Phys. Plasmas **19**, 056308 (2012).

5. M. C. Herrmann, M. Tabak, and J. D. Lindl, Nucl. Fusion **41**, 99 (2001).

6. J. D. Lindl, *Inertial Confinement Fusion: The Quest for Ignition and Energy Gain Using Indirect Drive* (Springer-Verlag, New York, 1998).

7. S. E. Bodner, Phys. Rev. Lett. **33**, 761 (1974); H. Takabe *et al*., Phys. Fluids **28**, 3676 (1985); R. Betti, V. N. Goncharov, R. L. McCrory, and C. P. Verdon, Phys. Plasmas **5**, 1446 (1998).

8. P. B. Radha, C. Stoeckl, V. N. Goncharov, J. A. Delettrez, D. H. Edgell, J. A. Frenje, I. V. Igumenshchev, J. P. Knauer, J. A. Marozas, R. L. McCrory, D. D. Meyerhofer, R. D. Petrasso, S. P. Regan, T. C. Sangster, W. Seka, and S. Skupsky, Phys. Plasmas **18**, 012705 (2011).

9. C. D. Zhou and R. Betti, Phys. Plasmas **14**, 072703 (2007).

10. I. V. Igumenshchev, D. H. Edgell, V. N. Goncharov, J. A. Delettrez, A. V. Maximov, J. F. Myatt, W. Seka, A. Shvydky, S. Skupsky, and C. Stoeckl, Phys. Plasmas **17**, 122708 (2010).

11. A. Simon, R. W. Short, E. A. Williams, and T. Dewandre, Phys. Fluids **26**, 3107 (1983).

12. W. Seka, D. H. Froula, D. H. Edgell, J. F. Myatt, R. W. Short, I. V. Igumenshchev, V. N. Goncharov, and A. V. Maximov, Bull. Am. Phys. Soc. **56**, 327 (2011); V. N. Goncharov, T. C. Sangster, R. Epstein, S. X. Hu, I. V. Igumenshchev, D. H. Froula, R. L. McCrory, D. D. Meyerhofer, P. B. Radha, W. Seka, S. Skupsky, C. Stoeckl, D. T. Casey, J. A. Frenje, and R. D. Petrasso, Bull. Am. Phys. Soc. **56**, 240 (2011).

13. V. N. Goncharov, T. C. Sangster, P. B. Radha, R. Betti, T. R. Boehly, T. J. B. Collins, R. S. Craxton, J. A. Delettrez, R. Epstein, V. Yu. Glebov, S. X. Hu, I. V. Igumenshchev, J. P. Knauer, S. J. Loucks, J. A. Marozas, F. J. Marshall, R. L. McCrory, P. W. McKenty, D. D. Meyerhofer, S. P. Regan, W. Seka, S. Skupsky, V. A. Smalyuk, J. M. Soures, C. Stoeckl, D. Shvarts, J. A. Frenje, R. D. Petrasso, C. K. Li, F. Séguin, W. Manheimer, and D. G. Colombant, Phys. Plasmas **15**, 056310 (2008).

14. R. Kishony and D. Shvarts, Phys. Plasmas **8**, 4925 (2001).

15. S. W. Haan, J. D. Lindl, D. A. Callahan, D. S. Clark, J. D. Salmonson, B. A. Hammel, L. J. Atherton, R. C. Cook, M. J. Edwards, S. Glenzer, A. V. Hamza, S. P. Hatchett, M. C. Herrmann, D. E. Hinkel, D. D. Ho, H. Huang, O. S. Jones, J. Kline, G. Kyrala, O. L. Landen, B. J. MacGowan, M. M. Marinak, D. D. Meyerhofer, J. L. Milovich, K. A. Moreno, E. I. Moses, D. H. Munro, A. Nikroo, R. E. Olson, K. Peterson, S. M. Pollaine, J. E. Ralph, H. F. Robey, B. K. Spears, P. T. Springer, L. J. Suter, C. A. Thomas, R. P. Town, R. Vesey, S. V. Weber, H. L. Wilkens, and D. C Wilson, Phys. Plasmas **18**, 051001 (2011).

16. T. C. Sangster, V. N. Goncharov, D. H. Edgell, D. H. Froula, V. Yu. Glebov, D. R. Harding, S. X. Hu, F. J. Marshall, R. L. McCrory, P. W. McKenty, D. D. Meyerhofer, J. F. Myatt, P. B. Radha, W. Seka, C. Stoeckl, B. Yaakobi, J. A. Frenje, M. G. Johnson, and R. D. Petrasso, Bull. Am. Phys. Soc. **56**, 241 (2011).

17. S. P. Obenschain *et al*., Phys. Plasmas **9**, 2234 (2002).

18. T. R. Boehly, D. L. Brown, R. S. Craxton, R. L. Keck, J. P. Knauer, J. H. Kelly, T. J. Kessler, S. A. Kumpan, S. J. Loucks, S. A. Letzring, F. J. Marshall, R. L. McCrory, S. F. B. Morse, W. Seka, J. M. Soures, and C. P. Verdon, Opt. Commun. **133**, 495 (1997).

19. P. B. Radha, V. N. Goncharov, T. J. B. Collins, J. A. Delettrez, Y. Elbaz, V. Yu. Glebov, R. L. Keck, D. E. Keller, J. P. Knauer, J. A. Marozas, F. J. Marshall, P. W. McKenty, D. D. Meyerhofer, S. P. Regan, T. C. Sangster, D. Shvarts, S. Skupsky, Y. Srebro, R. P. J. Town, and C. Stoeckl, Phys. Plasmas **12**, 032702 (2005).

20. F. J. Marshall, J. A. Delettrez, R. Epstein, R. Forties, V. Yu. Glebov, J. H. Kelly, T. J. Kessler, J. P. Knauer, P. W. McKenty, S. P. Regan, V. A. Smalyuk, C. Stoeckl, J. A. Frenje, C. K. Li, R. D. Petrasso, and F. H. Séguin, Bull. Am. Phys. Soc. **48**, 56 (2003).

21. *LLE Review Quarterly Report* **65**, 1, Laboratory for Laser Energetics, University of Rochester, Rochester, NY, LLE Document No. DOE/SF/19460-117, NTIS Order No. DE96011927 (1995).

22. R. A. Forties and F. J. Marshall, Rev. Sci. Instrum. **76**, 073505 (2005).

23. T. R. Boehly, D. H. Munro, P. M. Celliers, R. E. Olson, D. G. Hicks, V. N. Goncharov, G. W. Collins, H. F. Robey, S. X. Hu, J. A. Marozas, T. C. Sangster, O. L. Landen, and D. D. Meyerhofer, Phys. Plasmas **16**, 056302 (2009).

24. F. H. Séguin, C. K. Li, J. A. Frenje, D. G. Hicks, K. M. Green, S. Kurebayashi, R. D. Petrasso, J. M. Soures, D. D. Meyerhofer, V. Yu. Glebov, P. B. Radha, C. Stoeckl, S. Roberts, C. Sorce, T. C. Sangster, M. D. Cable, K. Fletcher, and S. Padalino, Phys. Plasmas **9**, 2725 (2002).

25. C. Stoeckl, R. E. Bahr, B. Yaakobi, W. Seka, S. P. Regan, R. S. Craxton, J. A. Delettrez, R. W. Short, J. Myatt, A. V. Maximov, and H. Baldis, Phys. Rev. Lett. **90**, 235002 (2003).

26. R. A. Lerche, D. W. Phillion, and G. L. Tietbohl, Rev. Sci. Instrum. **66**, 933 (1995).

27. W. Seka, D. H. Edgell, J. P. Knauer, J. F. Myatt, A. V. Maximov, R. W. Short, T. C. Sangster, C. Stoeckl, R. E. Bahr, R. S. Craxton, J. A. Delettrez, V. N. Goncharov, I. V. Igumenshchev, and D. Shvarts, Phys. Plasmas **15**, 056312 (2008).

28. F. J. Marshall, P. W. McKenty, J. A. Delettrez, R. Epstein, J. P. Knauer, V. A. Smalyuk, J. A. Frenje, C. K. Li, R. D. Petrasso, F. H. Séguin, and R. C. Mancini, Phys. Rev. Lett. **102**, 185004 (2009).

29. P. B. Radha, F. J. Marshall, T. R. Boehly, T. J. B. Collins, R. S. Craxton, R. Epstein, V. N. Goncharov, J. A. Marozas, R. L. McCrory, P. W. McKenty, D. D. Meyerhofer, T. C. Sangster, A. Shvydky, S. Skupsky, J. A. Frenje, and R. D. Petrasso, presented at the 7th International Conference on Inertial Fusion Sciences and Applications, Bordeaux, France, 12–16 September 2011.

30. J. A. Marozas, F. J. Marshall, R. S. Craxton, I. V. Igumenshchev, S. Skupsky, M. J. Bonino, T. J. B. Collins, R. Epstein, V. Yu. Glebov, D. Jacobs-Perkins, J. P. Knauer, R. L. McCrory, P. W. McKenty, D. D. Meyerhofer, S. G. Noyes, P. B. Radha, T. C. Sangster, W. Seka, and V. A. Smalyuk, Phys. Plasmas **13**, 056311 (2006).

31. J. Delettrez, R. Epstein, M. C. Richardson, P. A. Jaanimagi, and B. L. Henke, Phys. Rev. A **36**, 3926 (1987).

32. V. N. Goncharov, T. C. Sangster, T. R. Boehly, S. X. Hu, I. V. Igumenshchev, F. J. Marshall, R. L. McCrory, D. D. Meyerhofer, P. B. Radha, W. Seka, S. Skupsky, C. Stoeckl, D. T. Casey, J. A. Frenje, and R. D. Petrasso, Phys. Rev. Lett. **104**, 165001 (2010).

33. C. Stoeckl, P. B. Radha, R. E. Bahr, J. A. Delettrez, D. H. Edgell, V. Yu. Glebov, V. N. Goncharov, I. V. Igumenshchev, T. C. Sangster, W. Seka, J. A. Frenje, and R. D. Petrasso, Bull. Am. Phys. Soc. **56**, 241 (2011).

34. S. Skupsky, R. W. Short, T. Kessler, R. S. Craxton, S. Letzring, and J. M. Soures, J. Appl. Phys. **66**, 3456 (1989).

35. T. R. Boehly, V. A. Smalyuk, D. D. Meyerhofer, J. P. Knauer, D. K. Bradley, R. S. Craxton, M. J. Guardalben, S. Skupsky, and T. J. Kessler, J. Appl. Phys. **85**, 3444 (1999).

36. R. Betti and C. Zhou, Phys. Plasmas **12**, 110702 (2005).

37. T. C. Sangster, V. N. Goncharov, P. B. Radha, V. A. Smalyuk, R. Betti, R. S. Craxton, J. A. Delettrez, D. H. Edgell, V. Yu. Glebov, D. R. Harding, D. Jacobs-Perkins, J. P. Knauer, F. J. Marshall, R. L. McCrory, P. W. McKenty, D. D. Meyerhofer, S. P. Regan, W. Seka, R. W. Short, S. Skupsky, J. M. Soures, C. Stoeckl, B. Yaakobi, D. Shvarts, J. A. Frenje, C. K. Li, R. D. Petrasso, and F. H. Séguin, Phys. Rev. Lett. **100**, 185006 (2008).

38. P. B. Radha, J. P. Knauer, T. C. Sangster, V. N. Goncharov, I. V. Igumenshchev, R. Betti, R. Epstein, D. D. Meyerhofer, and S. Skupsky, Bull. Am. Phys. Soc. **52**, 143 (2007).

39. D. H. Froula, B. Yaakobi, S. X. Hu, P.-Y. Chang, R. S. Craxton, D. H. Edgell, R. Follett, D. T. Michel, J. F. Myatt, W. Seka, R. W. Short, A. Solodov, and C. Stoeckl, Phys. Rev. Lett. **108**, 165003 (2012).

Cryogenic Deuterium and Deuterium–Tritium Direct-Drive Implosions on OMEGA

Introduction

To ignite the deuterium–tritium (DT) fuel in a conventional, hot-spot ignition scheme in inertial confinement fusion (ICF), ion temperature and areal density of the central, lower-density region (hot spot) of the final fuel assembly must be sufficient to create fuel self-heating by alpha particles produced as a result of fusing D and T (Refs. 1 and 2). In addition, the areal density (ρR) of the main fuel must be large enough to provide confinement time sufficient to burn a significant portion of that fuel. A typical target consists of a higher-density shell filled with a lower-density fuel vapor. The shell has an outer layer of ablator material and an inner layer of frozen fuel. To compress the main fuel layer and initiate a burn wave propagating from the vapor through the main fuel, the shell is accelerated inward by a temporally shaped pressure drive created by laser energy that is delivered either directly to the target (direct drive) or indirectly by converting its energy to x rays inside the hohlraum (indirect drive).[1,2] As convergence causes pressure to build up in the vapor, the shell begins to decelerate when the vapor pressure exceeds shell pressure and an outgoing shock wave is launched into the incoming shell. During deceleration, hot-spot areal density and temperature increase as the shell's kinetic energy is converted into internal energy of the hot spot and main fuel. Achieving ignition conditions requires the areal density of the hot spot to exceed the stopping range of the alpha particles produced by fusing D and T. This leads to $(\rho R)_{\rm hs} \geq 0.3$ g/cm^2 (Refs. 1 and 2). In addition, the hot-spot ion temperature $T_{\rm hs}$ must be larger than ~5 keV so that the alpha heating exceeds bremsstrahlung losses.[1,2] Since both hot-spot areal density and temperature depend on in-flight shell kinetic energy, there is a threshold value of this energy below which a target fails to ignite.

A target design starts by calculating how much energy the drive pressure must provide to the shell so ignition requirements are met at stagnation. Numerical simulations give the following expression for the minimum shell kinetic energy required for ignition:[3,4]

$$E_{\rm k,min}({\rm kJ}) = 51\,\alpha^{1.9}\left(\frac{V_{\rm imp}}{3\times 10^7}\right)^{-5.9}\left(\frac{p_{\rm a}}{100\ {\rm Mbar}}\right)^{-0.8}. \quad (1)$$

This expression depends on the following in-flight hydrodynamic parameters, crucial for achieving ignition: (1) the peak in mass-averaged main fuel velocity (implosion velocity) $V_{\rm imp}$; (2) the in-flight fuel adiabat α [defined as the ratio of the shell pressure p to the Fermi-degenerate pressure at shell density ρ; for DT fuel, $p \simeq \mu\alpha\rho^{5/3}$ and $\mu = 2.2\ {\rm Mbar}\big/({\rm g/cm}^{3/5})$]; and (3) the drive (ablation) pressure $p_{\rm a}$. Even though Eq. (1) provides a very useful scaling law, it gives very little insight into the physical processes that determine this scaling. To provide such an insight, a simplified model of hot-spot formation is developed and presented next.

1. A Simple Ignition Model

To calculate minimum shell kinetic energy of an igniting target, nearly all this energy is assumed to be converted into the internal hot-spot and fuel energy at stagnation,

$$E_{\rm k} \sim p_{\rm max}R^3 \sim \left(\rho_{\rm hs}T_{\rm hs}R\right)^3\Big/ p_{\rm max}^2, \quad (2)$$

where $p_{\rm max} \sim \rho_{\rm hs}T_{\rm hs}\big/m_{\rm i}$ is the peak hot-spot pressure and $m_{\rm i}$ is ion mass. Since the minimum value of product $(\rho R)_{\rm hs}T_{\rm hs}$ is 0.3 g/cm$^2 \times$ 5 keV, as described earlier, then[2]

$$E_{\rm k,min} \sim 1\Big/ p_{\rm max}^2 \quad (3)$$

and calculation of $E_{\rm k,min}$ is reduced to determine the peak hot-spot pressure.

The maximum pressure is calculated by assuming that the hot-spot radius at peak convergence is R, and a fraction $f_{\rm shl}$ of shell kinetic energy $E_{\rm k} = MV_{\rm imp}^2\big/2$ has been transferred at that time to the hot-spot internal energy $2\pi p_{\rm max}R^3$, where M is the unablated shell mass. Then, the maximum hot-spot pressure is

$$p_{\rm max} \sim f_{\rm shl}E_{\rm k}\Big/R^3. \quad (4)$$

With the goal of expressing $E_{\rm k,min}$ and $p_{\rm max}$ in terms of in-flight shell parameters, stagnation variables must be related to these at the beginning of shell deceleration. Since the hot spot is adiabatic during deceleration,[4,5] $p_{\rm max}$ can be written in

terms of vapor pressure p_d and radius of vapor region R_d at the beginning of shell deceleration:

$$p_{\max} = p_d\left(R_d/R\right)^5. \tag{5}$$

Equating the right-hand sides of Eqs. (4) and (5) gives a hot-spot convergence ratio during deceleration,

$$\frac{R_d}{R} \sim \sqrt{\frac{f_{\rm shl}E_{\rm k}}{p_d R_d^3}}. \tag{6}$$

Then, using Eqs. (5) and (6) defines the maximum hot-spot pressure as a ratio of the shell's kinetic energy to the internal energy of the vapor at the beginning of deceleration:[5]

$$p_{\max} \sim p_d\left(\frac{f_{\rm shl}E_{\rm k}}{p_d R_d^3}\right)^{5/3} \sim p_d\left(\frac{f_{\rm shl}M}{p_d R_d^3}\right)^{5/2} V_{\rm imp}^5. \tag{7}$$

For $f_{\rm shl} = 1$, Eqs. (3) and (7) give $p_{\max} \sim V_{\rm imp}^5$ and $E_{\rm k,min} \sim V_{\rm imp}^{-10}$, similar to the result of the isobaric model.[6] The fraction $f_{\rm shl}$, however, is smaller than unity and depends on in-flight shell parameters. Keeping in mind that the shell is decelerated by the outgoing shock wave, $f_{\rm shl}$ can be defined as a fraction of the shell mass (an effective mass $M_{\rm eff}$) overtaken by this shock while the hot spot converges inward. In the strong shock limit, the Hugoniot conditions across the shock give

$$M_{\rm eff} \equiv f_{\rm shl}M \sim \sqrt{\rho_{\rm shl}p_{\max}}\,R^2\Delta t, \tag{8}$$

where $\rho_{\rm shl}$ is the shell density ahead of the shock front. The hot-spot time of confinement by the shell inertia is determined by Newton's law, $M_{\rm eff}R/(\Delta t)^2 \sim p_{\max}R^2$, which yields[7]

$$\Delta t \sim \sqrt{M_{\rm eff}/p_{\max}R}. \tag{9}$$

Then, Eqs. (8) and (9) lead to

$$M_{\rm eff} \sim \rho_{\rm shl}R^3. \tag{10}$$

With the help of the latter equation, Eq. (4) yields intuitively simple scaling

$$p_{\max} \sim \rho_{\rm shl}V_{\rm imp}^2. \tag{11}$$

The maximum pressure, however, does not scale as $V_{\rm imp}^2$, as Eq. (11) would suggest, since $\rho_{\rm shl}$ is different from the in-flight shell density. As the unshocked part of the incoming shell keeps converging during deceleration, its density $\rho_{\rm shl}$ increases inversely proportional to the surface area:

$$\rho_{\rm shl} \simeq \rho_d\left(\frac{R_d}{R}\right)^2. \tag{12}$$

Combining Eqs. (5), (11), and (12) defines the hot-spot convergence ratio in terms of in-flight shell quantities

$$\frac{R_d}{R} \sim \left(\frac{V_{\rm imp}^2\rho_d}{p_d}\right)^{1/3}. \tag{13}$$

Substituting Eq. (13) into Eqs. (10) and (12) gives the effective shell mass and $\rho_{\rm shl}$:

$$M_{\rm eff} \sim \rho_d R_d^3\frac{R_d}{R} \sim \rho_d R_d^3\left(\frac{p_d}{\rho_d V_{\rm imp}^2}\right)^{1/3} \tag{14}$$

and

$$\rho_{\rm shl} \sim \rho_d\left(\frac{V_{\rm imp}^2\rho_d}{p_d}\right)^{2/3}. \tag{15}$$

Finally, the scaling for the maximum pressure is obtained by combining Eqs. (7) and (14):

$$p_{\max} \sim \rho_d V_{\rm imp}^2\left(\frac{V_{\rm imp}^2\rho_d}{p_d}\right)^{2/3} = p_d\left(\frac{V_{\rm imp}^2\rho_d}{p_d}\right)^{5/3}. \tag{16}$$

Pressure at the beginning of the deceleration phase is proportional to the drive ablation pressure, $p_d \sim p_{\rm a}$, and shell density is related to the drive pressure through the in-flight shell adiabat α, $p_d({\rm Mbar}) \sim 2.2\,\alpha\rho_d^{5/3}$. This gives

$$p_{\max} \sim \frac{p_{\rm a}^{1/3}V_{\rm imp}^{10/3}}{\alpha}. \tag{17}$$

This scaling of $p_{\max}$ with $V_{\rm imp}$ is similar to that derived using self-similar analysis,[8] which leads to $p_{\max}^{\text{self-similar}} \sim V_{\rm imp}^3$. Substituting Eq. (17) back into Eq. (3) gives a scaling law similar to that obtained using simulation results [see Eq. (1)]:

$$E_{\rm k,min} \sim 1/p_{\max}^2 \sim V_{\rm imp}^{-20/3}p_{\rm a}^{-2/3}\alpha^2. \tag{18}$$

Equation (17) shows that the maximum pressure has a weaker implosion velocity dependence than $V_{\rm imp}^5$ obtained assuming that all kinetic energy of the shell is transferred to the internal energy of the fuel at stagnation. The weaker dependence is due to the fact that the kinetic energy fraction contributing to the fuel's internal energy is proportional to the fraction of the shell mass overtaken by the outgoing shock wave during the hot-spot confinement time. Several competing effects define this fraction: First, the mass flux per unit area across the shock increases with hot-spot convergence since both shell density $\rho_{\rm shl}$ and maximum pressure $p_{\rm max}$ increase with R_d/R [see Eqs. (5) and (12)], so $\sqrt{\rho_{\rm shl}p_{\rm max}} \sim \sqrt{\rho_d p_d}\left(R_d/R\right)^{7/2}$. Multiplied by the surface area of the shock front, the mass flux across the shock is $\sqrt{\rho_{\rm shl}p_{\rm max}}\,R^2 \sim \sqrt{\rho_d p_d}\,R_d^2\left(R_d/R\right)^{3/2}$. The convergence ratio increases with the implosion velocity, as shown in Eq. (13), giving

$$\text{mass flux} \sim \sqrt{\rho_{\rm shl}p_{\rm max}}\,R^2 \sim V_{\rm imp}. \tag{19}$$

The confinement time, on the other hand, decreases with convergence ratio and implosion velocity. Indeed, writing $\Delta t \sim R/V_{\rm imp}$ [this can be obtained by substituting Eqs. (10) and (11) into Eq. (9)] and using Eq. (13) gives

$$\text{confinement time} \sim \frac{R}{V_{\rm imp}} \sim \left(\frac{R_d}{R}\right)^{-5/2} \sim V_{\rm imp}^{-5/3}. \tag{20}$$

Then, the product of mass flux and confinement time gives the effective mass and fraction of kinetic energy that contributes to the stagnation pressure $M_{\rm eff} \sim f_{\rm shl} \sim V_{\rm imp}^{-2/3}$, in agreement with Eq. (14). Negative power in velocity dependence of the effective mass changes pressure scaling from $V_{\rm imp}^5$ to $V_{\rm imp}^{10/3}$.

The maximum pressure, on the other hand, has a stronger dependence on $V_{\rm imp}$ than that given by the dynamic pressure argument $p_{\rm max} \sim \rho_{\rm shl} V_{\rm imp}^{10/2}$. This is due to convergence effects and an increase in the unshocked shell density during deceleration. Since $\rho_{\rm shl}$ rises with convergence ratio, as shown in Eq. (12), the maximum pressure scales as

$$p_{\rm max} \sim \left(\rho_{\text{in flight}} V_{\rm imp}^{2\times 2/3}\right) V_{\rm imp}^2 \sim V_{\rm imp}^{10/3},$$

in agreement with Eq. (17).

Since $E_{\rm k,min}$ is strongly dependent on the implosion velocity, as shown in Eqs. (1) and (18), it is crucial that a shell reaches the designed value of $V_{\rm imp}$ to achieve ignition in an experiment. The minimum $V_{\rm imp}$ can be estimated by the following argument: Balancing a fraction of the kinetic energy of the shell and the internal energy of the fuel yields

$$MV_{\rm imp}^2/2 > 2\pi p_{\rm max} R^3. \tag{21}$$

For fully ionized gas with ion charge Z and ion mass $m_{\rm i}$,

$$p_{\rm max} = (1+Z)\rho_{\rm hs}T_{\rm hs}/m_{\rm i}.$$

For DT fuel this gives $p_{\rm max} \simeq 4\rho_{\rm hs}T_{\rm hs}/m_{\rm p}$, where $m_{\rm p}$ is proton mass. Finally, writing shell mass at stagnation as $M \sim 4\pi R^2 \rho_{\rm fuel}\Delta$ leads to

$$V_{\rm imp} > \sqrt{\frac{4}{5}\frac{(\rho R)_{\rm hs}}{(\rho\Delta)_{\rm fuel}}\frac{T_{\rm hs}}{m_{\rm p}}}, \tag{22}$$

where $\rho_{\rm fuel}$ and Δ are the density and thickness of compressed fuel, respectively. To create a hot spot and trigger burn propagation into the cold fuel, the hot-spot areal density and temperature must exceed, as discussed earlier, $(\rho R)_{\rm hs}T_{\rm hs} > 0.3$ g/cm$^2 \times$ 5 keV. To burn enough cold fuel and achieve gain = fusion energy/laser energy > 1 requires, on the other hand, $(\rho\Delta)$fuel > 1 g/cm^2 (Refs. 1 and 2). Substituting these three conditions back into Eq. (22) gives

$$V_{\rm imp} > 3\times 10^7 \text{ cm/s}. \tag{23}$$

This leads to a requirement on stagnation pressure $p_{\rm max}$. Indeed, the ablation pressure in an ICF implosion is $p_{\rm a} \sim$ 100 Mbar, and the effective dynamic pressure of the accelerated shell at $V_{\rm imp} = 3\times 10^7$ cm/s and $\alpha = 1$ is $\rho V^2 \simeq (100/2.2)^{3/5}$ $[3\times 10^7]^2 \simeq 9$ Gbar. In general, $\rho \simeq \left[p(\text{Mbar})/2.2\,\alpha\right]^{3/5}$ and the dynamic pressure is

$$\text{dynamic pressure}_{\text{in flight}} \simeq$$

$$9\left(\frac{p_{\rm a}}{100\text{ Mbar}}\right)^{3/5}\alpha^{-3/5}\left(\frac{V_{\rm imp}}{3\times 10^7}\right)^2 \text{Gbar}. \tag{24}$$

An additional amplification in dynamic pressure is due to shell convergence during deceleration. As described earlier, unshocked-shell density amplification is proportional to the hot-spot convergence ratio to the second power [see Eq. (12)]. According to Eq. (13), the hot spot converges by a factor of 4.4 during deceleration for $\alpha \sim 1$ and $V_{\rm imp} \sim 3\times 10^7$ cm/s. This

gives an additional increase by a factor of $4.4^2 = 20$ in the dynamic pressure, leading to a maximum hot-spot pressure in an igniting target of $p_{\max} > 200$ Gbar, or for a given implosion velocity and drive pressure,

$$p_{\max} \simeq 180\left(\frac{p_a}{100\ \text{Mbar}}\right)^{1/3}\alpha^{-1}\left(\frac{V_{\text{imp}}}{3\times 10^7}\right)^{10/3}\ \text{Gbar}. \quad (25)$$

Using the numerical factor obtained in Eq. (25), one can recover a numerical factor in Eq. (18) as well:

$$E_{k,\min} \simeq 30\,\alpha^2\left(\frac{V_{\text{imp}}}{3\times 10^7}\right)^{-20/3}\left(\frac{p_a}{100\ \text{Mbar}}\right)^{-2/3}\text{kJ}. \quad (26)$$

The numerical coefficient in Eq. (26) is 40% smaller than that in the fitting formula shown in Eq. (1). This is a consequence of the fact that only a fraction f_{shl} of the total shell kinetic energy is transferred to the fuel at stagnation. Typically, $f_{\text{shl}} \sim 0.5$ to 0.6, which brings the numerical coefficient in Eq. (26) in closer agreement with the numerical result.

2. Sensitivity of Ignition Condition on Implosion Parameters

The minimum shell kinetic energy required for ignition depends strongly on the shell's velocity and adiabat [see Eq. (1)]. When a particular target design is considered for an ignition experiment, one of the important design parameters is margin [this is also referred to as an ignition threshold factor (ITF)][9] defined as the ratio of the shell kinetic energy E_k to its minimum value required for ignition $E_{k,\min}$,

$$\text{ITF} = \frac{E_k}{E_{k,\min}}. \quad (27)$$

In using Eq. (1) to determine $E_{k,\min}$, one must keep in mind that Eq. (1) does not account for asymmetry effects (such as shell and hot-spot nonuniformity growth, mix of ablator material and fuel, etc.). A more-complete analysis using 2-D and 3-D hydrodynamic simulations results in correction factors related to these effects (for details, see Ref. 9). Since the main purpose of this article is to address accuracy in the modeling of average 1-D hydrodynamic parameters, the terms proportional to multidimensional effects will be neglected.

Robustness of a particular design is determined by how much uncertainty in velocity, adiabat, and the drive pressure it can tolerate before the probability of achieving ignition becomes very small. Such maximum uncertainty values depend on ITF.

The target fails to ignite if the shell's kinetic energy E_k in an experiment is lower than the ignition energy threshold $E_{k,\min}$ or the actual energy threshold $E_{k,\min}$ is higher than calculated $E_{k,\min}$ as a result of inaccuracies in modeling of hydro-dynamic quantities. If E_k^{design} and $E_{k,\min}^{\text{design}}$ are design values of the shell's kinetic energy and energy threshold, respectively, and $\text{ITF} = E_k^{\text{design}}\big/E_{k,\min}^{\text{design}}$, then the maximum deviations in V_{imp}, α, and p_a (denoted as δV_{imp}, $\delta\alpha$, and δp_a, respectively) from predictions are determined from the condition $E_k^{\text{limit}}\big/E_{k,\min}^{\text{limit}} = 1$, where $E_k^{\text{limit}} = M\left(V_{\text{imp}} - \delta V_{\text{imp}}\right)^2\big/2$,

$$E_{k,\min}^{\text{limit}} = E_{k,\min}\left(\alpha + \delta\alpha, V_{\text{imp}} - \delta V_{\text{imp}}, p_a - \delta p_a\right),$$

$$E_k^{\text{design}} = MV_{\text{imp}}^2\big/2, \text{ and } E_{k,\min}^{\text{design}} = E_{k,\min}\left(\alpha, V_{\text{imp}}, p_a\right).$$

This reads as

$$1 = \text{ITF}\left(1 - \frac{\delta V_{\text{imp}}}{V_{\text{imp}}}\right)^{7.9}\left(1 + \frac{\delta\alpha}{\alpha}\right)^{-1.9}\left(1 - \frac{\delta p_a}{p_a}\right)^{0.8}. \quad (28)$$

Since it is very difficult to assess the fuel adiabat by a direct measurement, the adiabat increase $\delta\alpha$ is replaced in this analysis with energy deposited in the fuel ΔE that leads to an adiabat increase $\delta\alpha$. This energy is expressed in terms of a fraction ε_E of the shell kinetic energy $\Delta E = \varepsilon_E E_{k,0}$. To relate $\delta\alpha$ and ΔE, we write internal energy as a product of pressure and volume $E = 3/2\ pV$. Replacing pressure by the drive ablation pressure p_a and the fuel volume by fuel mass over shell density, $V = M/\rho$, gives $E = 3p_aM/2\rho$. Shell density is related to the ablation pressure as $\rho \sim \left(p_a\big/\alpha\right)^{3/5}$. Then, collecting all appropriate numerical coefficients leads to

$$E(\text{kJ}) = 1.5\left(\frac{p_a}{100\ \text{Mbar}}\right)^{2/5}\alpha^{3/5}M\left(\text{mg}\right). \quad (29)$$

Fixing shell mass and drive pressure gives $1 + \delta\alpha/\alpha = (1 + \Delta E/E_0)^{5/3}$. Then, Eq. (28) takes the form

$$\left(1 - \frac{\delta V_{\text{imp}}}{V_{\text{imp}}}\right)^{-7.9}\left[1 + \frac{30\,\varepsilon_E\left(V_{\text{imp}}\big/3\times 10^7\right)^2}{\left(p_a\big/100\ \text{Mbar}\right)^{2/5}\alpha^{3/5}}\right]^{3.1}$$

$$\times\left(1 - \frac{\delta p_a}{p_a}\right)^{-0.8} = \text{ITF}. \quad (30)$$

Figure 130.16 plots (a) the reduction in shell velocity, (b) shell preheat as a percentage fraction of the shell's kinetic energy, and (c) reduction in drive pressure that lead to ignition failure in a design with a given value of ITF. Figure 130.16 shows that for NIF-scale ignition designs with ITF ~ 3.5 to 5, ignition fails if velocity reduction is greater than ~15% and the shell is preheated by more than ~1% of the shell's kinetic energy. The drive pressure, according to Fig. 130.16(c), can be reduced as much as 80% before ignition will fail. This number, however, does not account for a reduction in the implosion velocity associated with reduced drive. Therefore, Fig. 130.16(c) must be used in combination with Fig. 130.16(a). In addition to ignition failure caused by a significant deviation from predicted 1-D hydrodynamic parameters (velocity, adiabat, drive pressure), other failure mechanisms are due to asymmetries in an implosion. Nonuniformity sources caused by both target imperfections (such as ice roughness and ablator roughness) and asymmetry in laser illumination are amplified by the Rayleigh–Taylor (RT) and Richtmyer–Meshkov (RM) instabilities[1,2] during an implosion. Nonuniformity growth could either disrupt the shell or lead to significant hot-spot distortions. The distortion region width inside the hot spot exceeding 20% to 40% of the 1-D hot-spot radius is typically sufficient to reduce alpha-particle production and ion temperature and quench the burn.[7]

Even though control of the multidimensional effect is one of the main challenges for any ignition design, validation of code ability to adequately model target-drive efficiency and the amount of the fuel preheat is a primary goal of the ICF experiments. This article will describe how these global hydrodynamic parameters predicted by hydrosimulations were experimentally validated using direct-drive implosions on OMEGA.

Early Direct-Drive Target Designs and Target Stability Properties

1. All-DT, Direct-Drive, NIF-Scale Ignition Target Design

The original direct-drive target design[10,11] for the National Ignition Facility (NIF) Laser System[12] is a 350-μm-thick, solid-DT layer inside a very thin (~3-μm) plastic shell (shown in Fig. 130.17). Because the plastic shell ablates early in the pulse and the DT layer acts as both the main fuel and ablator, this design is referred to as an "all-DT" design. The fact that the ablator and the main fuel are the same material (DT) has several advantages: (1) It eliminates the interface between the fuel and ablator. Any mismatch in density or opacity between two neighboring materials in the shell usually leads to an enhancement in the early-time perturbation growth or the RT instability growth factor.[13] (2) Because of its initial low density, DT gives both the lowest in-flight aspect ratio (IFAR)

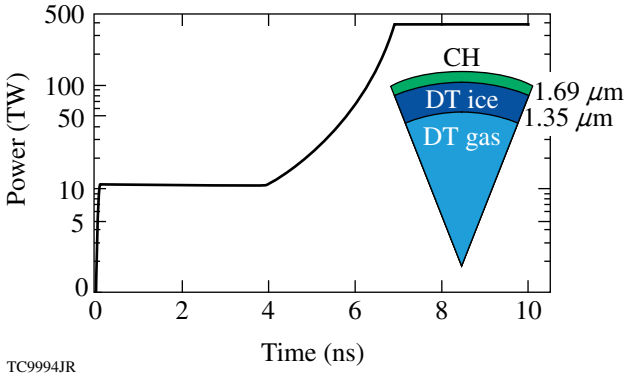

Figure 130.17
An α = 3, "all-DT," 1.5-MJ, direct-drive–ignition target design with a 1-D gain of 45.

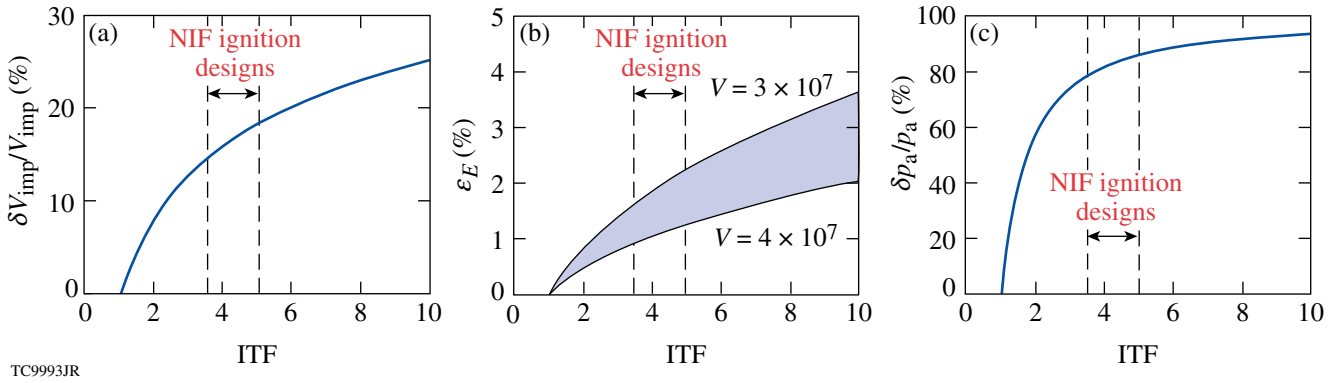

Figure 130.16
(a) Maximum velocity reduction, (b) maximum preheat energy as fractions of the shell's kinetic energy, and (c) maximum pressure reduction versus ITF.

for the same shell mass and the largest ablative stabilization factor in the RT instability growth rate formula compared to other ablator materials [see **Rayleigh–Taylor Instability** below for more details on design stability properties]. The biggest downside of using DT as an ablator, as demonstrated in OMEGA experiments, is the low absorption fraction caused by inverse bremsstrahlung and low threshold for the two-plasmon-decay (TPD) instability,[14] which generates suprathermal electrons that preheat the fuel. Currently, there is no experimental demonstration of low-adiabat, high fuel compression in direct-drive designs with DT or D_2 ablators driven at ignition-relevant intensities above 5×10^{14} W/cm^2 (this will be discussed further in **Cryogenic D_2 Implosions on the OMEGA Upgrade Laser System from 2001 Until Mid-2008**, p. 85). In the design presented in Fig. 130.17, the fuel is accelerated by 1.5 MJ of laser energy to a peak velocity of $V_{\rm imp} = 4.3 \times 10^7$ cm/s at adiabat $\alpha = 3$. The target ignites and gives a 1-D gain of 45 with an ITF of 5. This design uses a continuous pulse shape (as opposed to the picket pulse described in the next section), launching the initial shock that sets the in-flight shell adiabat. Later, at $t = 4$ ns, the intensity gradually rises, launching a compression wave. The head of this wave catches up with the first shock in the vapor region, soon after it breaks out of the shell. Timing the first shock and compression wave breaking out of the fuel and preventing the compression wave from turning into a shock inside the fuel are crucial to achieving ignition in this design.

2. Target Stability Properties: Rayleigh–Taylor Instability Growth and Target IFAR

A shell kinetic energy required to ignite DT fuel in an ICF implosion is strongly dependent on the maximum shell velocity. According to Eq. (1), increasing the shell's velocity to well above the minimum value of $V_{\rm imp} \sim 3 \times 10^7$ cm/s is beneficial for reducing the laser-energy requirement. Increasing implosion velocity, however, must be achieved without compromising the the shell's integrity due to hydrodynamic instability growth.

To understand how $V_{\rm imp}$ scales with target parameters, we start by writing

$$V_{\rm imp} \sim g t_{\rm accel}, \tag{31}$$

where g is shell acceleration and $t_{\rm accel}$ is the acceleration time. The acceleration is determined from Newton's law,

$$M_{\rm shell}\, g \sim 4\pi R^2 p_{\rm a} \longrightarrow g \sim 4\pi \frac{p_{\rm a} R^2}{M_{\rm shell}}, \tag{32}$$

where $M_{\rm shell}$ is the initial shell mass, R is shell radius, and $p_{\rm a}$ is ablation pressure. The acceleration time for a given laser energy $E_{\rm laser}$ and drive intensity I is

$$t_{\rm accel} \sim \frac{E_{\rm laser}}{4\pi R^2 I}. \tag{33}$$

Substituting Eqs. (32) and (33) into Eq. (31) gives

$$V_{\rm imp} \sim p_{\rm a} E_{\rm laser} \big/ M_{\rm shell} I.$$

Results of simulations lead to a numerical factor of 0.8 in the latter equation. Therefore,

$$V_{\rm imp} \simeq 0.8 \frac{p_{\rm a} E_{\rm laser}}{M_{\rm shell} I}. \tag{34}$$

Since $p_{\rm a} \sim I^{0.8}$ to $I^{0.7}$ (Refs. 1 and 2), implosion velocity increases, for a given shell mass and laser energy, by reducing drive intensity. This intuitively contradictory result can be explained by noting that a lower laser drive is overcompensated by the duration of the shell's acceleration, as shown in Eq. (33). The acceleration distance is longer for lower-intensity drives: $R \sim V_{\rm imp} t_{\rm accel} \sim p_{\rm a} E_{\rm laser}^2 \big/ M_{\rm shell} I^2 R^2$, so $R^3 \sim p_{\rm a} E_{\rm laser}^2 \big/ M_{\rm shell} I^2 \sim I^{-1.2}$. The implosion velocity can also be increased, according to Eq. (34), by reducing shell mass. An increase in $V_{\rm imp}$, however, is beneficial for reducing $E_{\rm k,min}$ only up to the point where multidimensional effects (asymmetry growth) start to affect target performance. Hydrodynamic instabilities put severe constraints on target designs, limiting the values of the shell mass and adiabat used in a robust target design. To determine such constraints, we next identify target parameters that affect the target stability.

a. Rayleigh–Taylor instability. The dominant hydrodynamic instability in an ICF implosion is the Rayleigh–Taylor (RT) instability.[1,2] The RT instability develops in systems where the heavier fluid is accelerated by the lighter fluid.[15] In an ICF implosion, the heavier shell material is accelerated by the lighter blowoff plasma, creating the condition for RT instability. This instability amplifies shell distortions, seeded by both the ablator and ice roughness, and laser illumination nonuniformities (laser "imprint"[13]). Excessive growth of these perturbations leads to shell breakup during acceleration, limiting the final compression and hot-spot temperature. An example of a direct-drive implosion simulation is shown in Fig. 130.18. Shell distortions developed due to the RT instability during

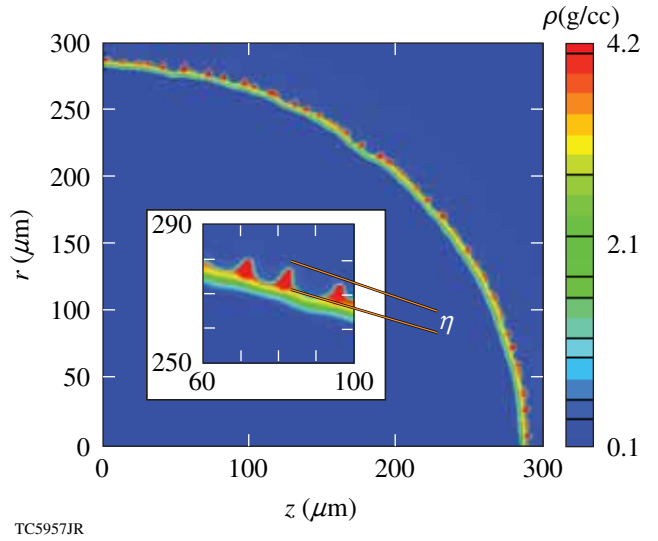

Figure 130.18
Two-dimensional simulation of a direct-drive implosion using the hydrocode *DRACO*. Rayleigh–Taylor instability causes shell distortions with amplitude η to grow in time.

acceleration are clearly visible in this simulation. The small initial perturbation amplitude η_0 grows in time as

$$\eta \sim \eta_0 e^{\gamma_{\mathrm{RT}} t}, \tag{35}$$

where γ_{RT} is the growth rate. In the classical RT configuration where a heavier fluid with density ρ_2 is supported by a lighter fluid of density ρ_1 in a gravitational field g directed from heavier to lighter fluids, the RT growth rate is[15]

$$\gamma_{\mathrm{RT,classical}} = \sqrt{A_T k g}, \quad A_T = \frac{\rho_2 - \rho_1}{\rho_2 + \rho_1}, \tag{36}$$

where A_T is Atwood number, $k = 2\pi/\lambda$ is the perturbation wave number, and λ is the perturbation wavelength. In an ICF implosion, the thermal conduction (electron dominant in direct-drive implosions and x-ray radiation dominant in indirect-drive implosions) that drives the ablation process significantly reduces the growth rate from its classical value.[16] The full expression for the growth rate in this case is rather complicated and can be found in Ref. 17. Here, we show the growth rate in the limit $kL_0 < 1$, where L_0 is the effective thickness of the ablation front,

$$\begin{aligned} \gamma_{\mathrm{RT,ICF}} &\simeq \sqrt{kg - \Omega_{\mathrm{bl}}^2 + \Omega_{\mathrm{a}}^2} - \Omega_{\mathrm{a}}, \\ \Omega_{\mathrm{bl}} &= k\sqrt{V_{\mathrm{a}} V_{\mathrm{bl}}}, \\ \Omega_{\mathrm{a}} &= 2kV_{\mathrm{a}}, \end{aligned} \tag{37}$$

where V_{a} and V_{bl} are the ablation and blowoff velocities, respectively (for the definition of V_{bl}, see Ref. 17). Because mass density in the plasma blowoff region is much smaller than shell density, $A_T \simeq 1$ for modes with $kL_0 < 1$. There are two stabilizing terms in $\gamma_{\mathrm{RT,ICF}}$: the first is proportional to Ω_{bl} and the other to Ω_{a}. Both of them are due to the mass ablation driven by thermal conduction; physical mechanisms of the two, however, are different.

The ablation process is characterized by the ablation velocity V_{a}, defined as the ratio of the mass ablation rate per unit area of target surface, $\left(\mathrm{d}M/\mathrm{d}t\right)\Big/\left(4\pi R^2\right)$, and the shell density at the ablation front $\rho_{\mathrm{shell,abl}}$ (see Fig. 130.19),

$$V_{\mathrm{a}} = \frac{\mathrm{d}M}{\mathrm{d}t}\Big/\left(4\pi R^2 \rho_{\mathrm{shell,abl}}\right), \tag{38}$$

where R is the ablation-front radius. When mass ablation is included, several physical mechanisms reduce the ablation-front perturbation growth and, in some cases, totally suppress it. These are illustrated in Fig. 130.20. First, different plasma blowoff velocities at different parts of the corrugated ablation region create modulation in the dynamic pressure or "rocket effect" that leads to a stabilizing restoring force.[13,18,19] Indeed,

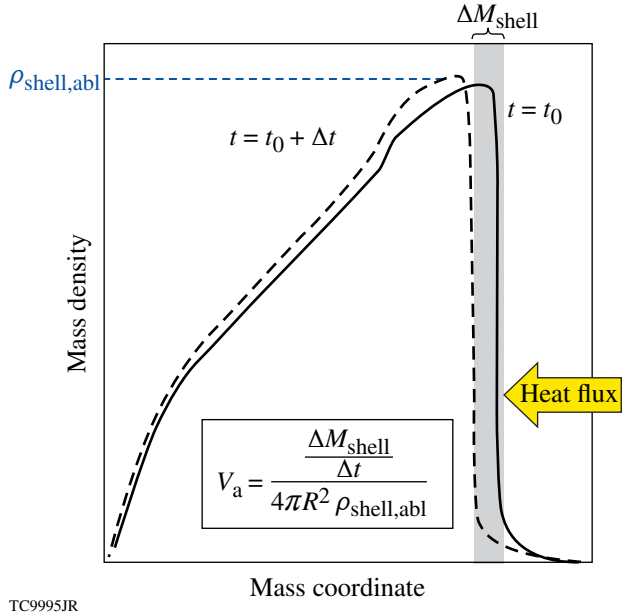

Figure 130.19
Ablation velocity is defined as mass ablation rate, $\Delta M/\Delta t \simeq \mathrm{d}M/\mathrm{d}t$, divided by the ablation region surface area $4\pi R^2$ and the shell density at the ablation front $\rho_{\mathrm{shell,abl}}$.

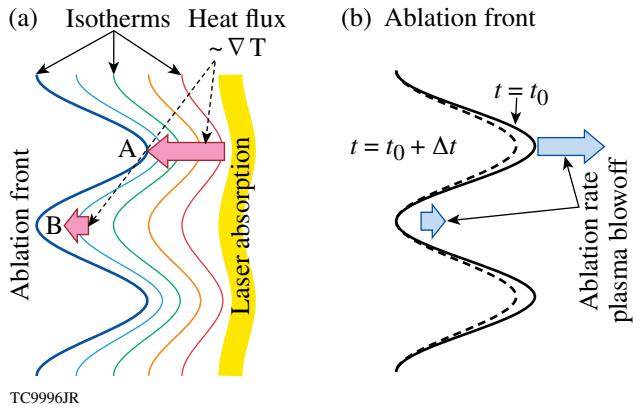

Figure 130.20
(a) Ablation-front modulation creates stronger temperature gradients at perturbation peaks (A) and weaker gradients at valleys (B). Since heat flux is proportional to such gradients, this leads to a slightly enhanced heat flux at A and a reduced heat flux at B. (b) Modulation in heat flux results in modulation in the mass ablation rate. The mass removed by ablation at point A is larger than that at point B, leading to both a fire-polishing effect and a restoring force caused by dynamic overpressure.

as a result of the perturbation growth, the peaks [point A in Fig. 130.20(a)] of the ablation-front ripple protrude into the hotter plasma corona, and the valleys [point B in Fig. 130.20(a)] recede toward the colder shell material. Since the temperature is uniform along the ablation front,[16] the temperature gradients and the heat fluxes are slightly enhanced at the peaks and reduced at the valleys, as shown in Fig. 130.20(a). An excess/deficiency in the heat flux speeds up/slows down the ablation front. This is illustrated in Fig. 130.20(b), where the solid and dashed lines indicate the positions of the ablation front at two instances in time separated by Δt. The ablation front at the peaks (point A) propagates further into the shell than at the valleys (point B). This increases velocity of the blowoff material ("exhaust" velocity, if an analogy of the ablatively driven shell with a rocket is used) at point A and reduces it at point B. A modulation in the blowoff velocity leads to a modulation in the dynamic pressure, creating a restoring force and reducing perturbation growth [see terms with Ω_{bl}^2 in Eq. (37)]. The second stabilizing mechanism caused by ablation is an increased mass ablation rate at the perturbation peaks in comparison with the valley. This leads to faster mass removal at point A and slower removal at point B (so-called "fire-polishing" effect). The latter effect gives the stabilizing terms proportional to Ω_a in Eq. (37).

Since the ablation and blowoff velocities are inversely proportional to the shell density at the ablation front, and density and ablation pressure are related as $\rho_{\text{shell,abl}} \sim \left(p_a/\alpha_{\text{abl}}\right)^{3/5}$, the velocities scale with the adiabat near the ablation front α_{abl} as

$$V_a \sim V_{bl} \sim \alpha_{\text{abl}}^{3/5}. \tag{39}$$

Equation (39) shows that reducing shell density or increasing shell adiabat at the ablation front enhances shell stability.

b. Target in-flight aspect ratio (IFAR). The other important parameter characterizing shell stability is the shell's in-flight aspect ratio (IFAR) defined as the ratio of the shell's radius R to the in-flight shell thickness $\Delta_{\text{in flight}}$ (see Fig. 130.21). Designs with thicker shells are less sensitive to the instability growth because they break up at a larger distortion amplitude and have smaller seeding of the deceleration RT instability. Such an instability develops as lower-density vapor pushes against the higher-density shell. During the shell acceleration, perturbations feed through from the unstable ablation front to the inner shell $\eta_{\text{inner}} \sim \eta_{\text{ablation}} e^{-k\Delta_{\text{in flight}}}$. As the shell decelerates, the inner surface distortions start to grow from η_{inner}, leading to hot-spot deformation at peak compression. Therefore, the thicker the shell, the smaller the feedthrough factor, and the smaller the finite hot-spot deformation.

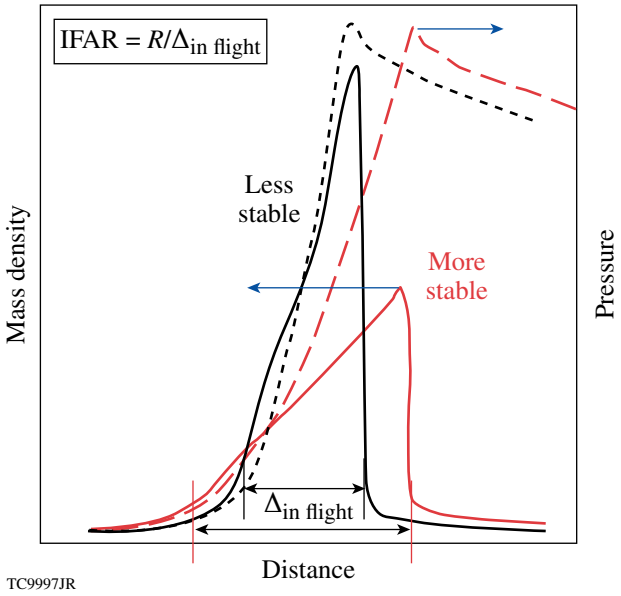

Figure 130.21
In-flight aspect ratio is defined as the ratio of the shell's radius to the in-flight shell thickness. Designs with smaller IFAR are less sensitive to the shell's distortion growth since they break up at larger distortion amplitudes.

Next, we find a scaling of IFAR with implosion parameters. As defined, IFAR = $R/\Delta_{\text{in flight}}$. The in-flight shell thickness is the initial shell thickness Δ_0 reduced by shell compression during acceleration (effect of mass ablation is neglected in this analysis),

$$\Delta_{\text{in flight}} \simeq \Delta_0 \frac{\rho_0}{\langle\rho\rangle_{\text{in flight}}} \frac{R_0^2}{R^2}, \tag{40}$$

where ρ_0 and $\langle\rho\rangle$ are initial and average in-flight shell densities, respectively, and R_0 is the initial shell radius. For the all-DT design where the shell consists mainly of DT, $\langle\rho\rangle_{\text{in flight}} = \left[p_a(\text{Mbar})/2.2\langle\alpha\rangle\right]^{3/5}$, where $\langle\alpha\rangle$ is the mass-averaged shell adiabat. This gives

$$\text{IFAR} = \frac{R}{\Delta_{\text{in flight}}}$$

$$\simeq 10\frac{R_0}{\rho_0\Delta_0}\left(\frac{R}{R_0}\right)^3\left(\frac{p_a}{100\ \text{Mbar}}\right)^{3/5}\langle\alpha\rangle^{-3/5}. \tag{41}$$

Multiplying the numerator and denominator of Eq. (41) by $4\pi R_0^2$ and replacing $4\pi R_0^2\Delta_0\rho_0$ with the shell mass M_{shell} yields

$$\text{IFAR} = 10\left(\frac{4\pi R_0^3}{M_{\text{shell}}}\right)\left(\frac{R}{R_0}\right)^3\left(\frac{p_a}{100\ \text{Mbar}}\right)^{3/5}\langle\alpha\rangle^{-3.5}. \tag{41a}$$

Initial shell radius in an optimized design is proportional to shell's velocity times acceleration time, $R_0 \sim V_{\text{imp}} t_{\text{accel}}$ and the required shell mass is given by Newton's law $MR_0/t_{\text{accel}}^2 \sim 4\pi p_a R_0^2$. Eliminating t_{accel} from the latter two equations gives

$$\frac{4\pi R_0^3}{M} = \frac{V^2}{p_a}. \tag{42}$$

Combining Eqs. (41a) and (42) leads to

$$\text{IFAR} = 90\frac{R^3}{R_0^3}\left(\frac{V_{\text{imp}}}{3\times 10^7}\right)^2\left(\frac{p_a}{100\ \text{Mbar}}\right)^{-2/5}\langle\alpha\rangle^{-3/5}. \tag{43}$$

Equation (43) shows that IFAR's value decreases as the shell implodes (the ratio R/R_0 gets smaller), reaching its peak value at the beginning of the shell's acceleration, when drive intensity reaches its peak value. Then, the stability property of a design is characterized by this peak IFAR value. Fit to the results of numerical simulations gives[20]

$$\max(\text{IFAR}) \simeq 60\left(\frac{V_{\text{imp}}}{3\times 10^7}\right)^2\left(\frac{p_a}{100\ \text{Mbar}}\right)^{-2/5}\langle\alpha\rangle^{-3/5}, \tag{44}$$

which can be recovered from Eq. (43) by using $R \simeq 0.9R_0$. Numerical simulations of directly driven cryogenic implosions (both on OMEGA and the NIF) show that to keep the shell from breaking up because of the short-scale perturbation growth during the acceleration, IFAR should not exceed

$$\text{IFAR}_{\max} \simeq 40. \tag{45}$$

Using Eq. (44), we conclude that increasing implosion velocity by reducing the drive intensity alone, as Eq. (34) suggests, is not the best strategy from a stability point of view since two factors cause IFAR in this case to increase: (1) an increase in V_{imp} and (2) a reduction in p_a. The fact that reduction in drive pressure increases IFAR is a consequence of the larger traveled distances required to accelerate a shell to a given V_{imp} if the drive pressure is lower. Larger acceleration distances mean larger initial shell radius and higher IFAR. This is illustrated in Fig. 130.22, where initial shell dimensions are schematically shown for different drive intensities. The smallest drive intensity requires the largest initial and in-flight aspect ratios.

Increasing the implosion velocity by reducing shell mass has a lesser effect on IFAR since the latter increases only as a

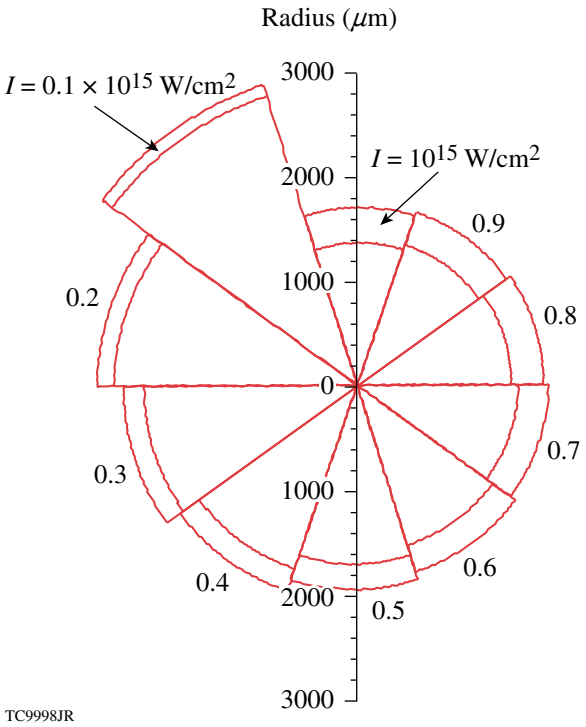

Figure 130.22
Initial shell dimensions for all-DT designs driven at indicated intensities using $E_{\text{laser}} = 1.5$ MJ.

result of larger V_{imp} [see Eq. (43)]. This approach, however, has limited beneficial effects: As the IFAR exceeds the maximum value set by the stability considerations, the target performance begins to degrade. Improving shell stability while reducing shell mass can be accomplished, according to Eq. (44), by increasing the average shell adiabat $\langle\alpha\rangle$. This must be done, however, without raising the adiabat of the unablated fuel since that is set by the condition on maximum fuel pressure at stagnation, as shown in Eq. (25). An adiabat-shaping technique[21] was proposed and implemented in the direct-drive designs to raise the adiabat only at the outer part of the shell, without degrading the adiabat at the inner part of the fuel. The designs with adiabat shaping will be discussed in **Cryogenic D_2 Implosions on the OMEGA Upgrade Laser System from 2001 Until Mid-2008**, p. 85).

Experimental Cryogenic Program on OMEGA

The experimental cryogenic program on OMEGA is designed to study fundamental physics of direct-drive ICF implosions. In particular, the following key questions are addressed:

(1) Is a low-adiabat compression of cryogenic fuel possible in a spherical implosion driven by direct laser illumination?

(2) Can cryogenic fuel be accelerated to velocities in excess of 3×10^7 cm/s in such implosions?

(3) At what drive intensities does the laser drive become inefficient in accelerating low-adiabat fuel, creating an excessive amount of fuel preheat because of suprathermal electrons, and scattering a significant fraction of the incident laser light as a result of laser–plasma interaction?

(4) Can asymmetry growth be controlled during an implosion, so

   (a) the short-scale perturbations with wavelength $\lambda \sim \Delta_{\text{in flight}}$ do not compromise shell integrity, and

   (b) hot-spot deformation is not severe enough to significantly reduce hot-spot ion temperature and quench the yield?

To answer these questions, various experimental techniques were developed and used to diagnose OMEGA implosions. Selecting a specific technique is based on measurement accuracy, which must be high enough to be able to tune the physics models and to meet the predictive accuracy goals discussed in **Sensitivity of Ignition Condition on Implosion Parameters** (p. 75). Next, we list the experimental techniques that are used to address these key questions.

1. Adiabat

The shell adiabat during an implosion can be inferred from shell density and temperature measurements. Two techniques have been developed and used on OMEGA implosions to measure these quantities: spectrally resolved x-ray scattering[22,23] and time-resolved x-ray absorption spectroscopy.[24] X-ray scattering requires large scattering volumes to keep signal-to-noise ratio at acceptable levels. This significantly limits the accuracy of measuring the adiabat at inner parts of the shells in designs with spatial adiabat gradients. The x-ray absorption technique, on the other hand, is designed to be much more local since the temperature and density are inferred by analyzing the spectral shapes of a backlighter source attenuated by a buried mid-Z tracer layer inside the shell. Hydrodynamic instabilities developed during shell implosion, however, redistribute the signature layer material throughout the shell, making temperature and density measurements dependent on the accuracy of mix models.

A significant progress in understanding how to infer the fuel adiabat in a spherical implosion was made after Ref. 21 demonstrated that the peak in areal density in an optimized implosion depends mainly on laser energy and the average adiabat of the unablated mass,

$$\max\left(\rho R\right)_{\text{optimized}} \simeq 2.6\frac{\left[E_{\text{laser}}(\text{MJ})\right]^{1/3}}{\alpha^{0.54}}. \tag{46}$$

This scaling can be understood based on the following consideration: The unablated mass at the beginning of shell deceleration can be written as

$$M \sim \rho_d \Delta_d R_d^2, \tag{47}$$

where $\Delta_d = R_d/A_d$ is the shell thickness and A_d is the shell aspect ratio at the start of shell deceleration, respectively. The mass is related to drive pressure (or shell pressure at the beginning of deceleration, p_d) using Newton's law,

$$M\frac{R_d}{t_{\text{accel}}^2} \sim p_d R_d^2 \longrightarrow M \sim p_d R_d t_{\text{accel}}^2, \tag{48}$$

where t_{accel} is defined in Eq. (33). Equating the right-hand sides of Eqs. (47) and (48) yields

$$R_d \sim t_{\text{accel}} \sqrt{\frac{p_d}{\rho_d} A_d} \sim \left(\frac{E_{\text{laser}}}{V_{\text{imp}}^2 I}\right)^{1/3} \sqrt{\frac{p_d}{\rho_d} A_d}. \tag{49}$$

At peak compression, the main contribution to areal density is given by the shock-compressed region. Therefore, rewriting Eq. (14) as

$$M_{\text{eff}} \sim (\rho\Delta)_{\text{shocked}} R^2 \sim \rho_d R_d^2 \frac{R}{R_d} \tag{50}$$

leads to

$$\max(\rho R) \sim (\rho\Delta)_{\text{shocked}} \sim \rho_d R_d \left(\frac{R_d}{R}\right). \tag{51}$$

Substituting Eqs. (49) and (13) into Eq. (51) results in

$$\max(\rho R) \sim p_d \left(\frac{\rho_d}{p_d}\right)^{5/6} \frac{E_{\text{laser}}^{1/3}}{I^{1/3}} \sqrt{A_d}. \tag{52}$$

Finally, replacing ρ_d with $\sim \left(p_{\text{a}}/\alpha\right)^{3/5}$

$$\max(\rho R) \sim \frac{p_d^{2/3}}{I^{1/3}} \sqrt{A_d} \frac{E_{\text{laser}}^{1/3}}{\sqrt{\alpha}}. \tag{53}$$

Shell aspect ratio at the start of the deceleration phase has a weak dependence on implosion parameters: For an implosion with a higher shell adiabat, the shell is thicker but the deceleration phase starts while the shell is at larger radius, so the ratio R_d/Δ_d is approximately a constant $A_d \simeq 2$ for all implosion conditions. For a well-tuned implosion when the drive pressure keeps pushing the shell up to the beginning of shell deceleration (shell coasting is minimized), $p_d \sim p_{\text{a}}$. Since $p_{\text{a}} \sim I^{2/3}$, Eq. (53) becomes

$$\max(\rho R)_{\text{optimized}} \sim I^{1/9} \sqrt{A_d} \frac{E_{\text{laser}}^{1/3}}{\sqrt{\alpha}}, \tag{54}$$

which agrees with the numerical fit shown in Eq. (46), taking into account the weak dependence of $\sqrt{A_d} I^{1/9}$ on implosion parameters. When ablation drive is terminated early and the shell starts to decompress during the coasting phase, p_d drops, reducing the maximum areal density [see Eq. (53)].

Equation (53) shows that the adiabat of an unablated mass in an implosion without a significant coasting phase can be inferred by measuring the areal density close to the shell's peak convergence. The areal density in an ICF implosion is measured using either x-ray backlighting,[25] Compton radiography,[26] or charged-particle spectrometry.[27,28] While the first two techniques are still under development, the areal density in current cryogenic experiments is inferred by measuring the spectral shapes of fusion-reaction products. Areal density in D_2 fuel is determined from energy downshift in secondary protons[27] created in D–^{3}He reactions [primary reaction creates a neutron and ^{3}He ion, D + D ⟶ n(2.45 MeV) + ^{3}He (0.82 MeV), and a secondary reaction creates an α particle and a proton, ^{3}He + D ⟶ α (6.6–1.7 MeV) + p (12.6–17.5 MeV)]. This is shown in Fig. 130.23.

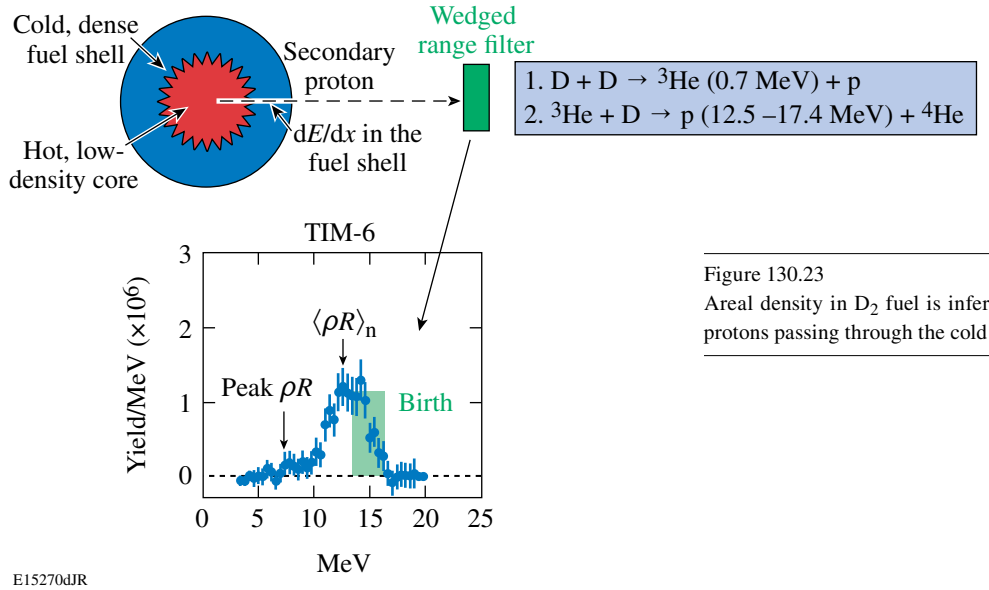

Figure 130.23
Areal density in D_2 fuel is inferred from energy attenuation of secondary protons passing through the cold shell material.

For DT fuel, the areal density is inferred by using a magnetic recoil spectrometer (see Fig. 130.24) that measures the fraction of neutrons down-scattered from fuel deuterons and tritons[28] (this fraction is directly proportional to the fuel ρR).

The main advantage to using charged-particle spectrometry to measure areal densities is that the peak in the reaction rate and peak fuel compression are not far apart (for OMEGA implosions they are separated by 20 to 30 ps with the peak in neutron production being earlier), so the reaction products sample areal density close to its peak value. The fusion rates are affected, on the other hand, by the nonuniformity growth that reduces both the fuel ion temperature and fuel "clean" volume where reactions take place. This changes timing and sampling of areal density by fusion-reaction products. The sensitivity of areal density measurement to neutron-production timing can be shown by noting that areal density evolves on a time scale $\Delta t_{\rho R} \sim 2\Delta t$, where Δt is the confinement time defined in Eq. (9). For OMEGA-scale targets this gives

$$\Delta t_{\rho R} \sim 2\frac{R}{V_{\rm imp}} \sim 2\frac{2\times 10^{-3}\ {\rm cm}}{3\times 10^{7}\ {\rm cm/s}} \simeq 130\ {\rm ps}, \qquad (55)$$

while the temporal width of neutron production in a spherically symmetric implosion is twice less,

$$\Delta t_{\rm n} \simeq \Delta t \simeq 70\ {\rm ps}. \qquad (56)$$

The areal density and neutron production histories for a typical cryogenic-DT target are shown in Fig. 130.25. Since the temporal scale of ρR evolution is short, the effect of perturbation growth on neutron-production timing and duration must be taken into account when comparing the experimentally inferred ρR values with the predictions.

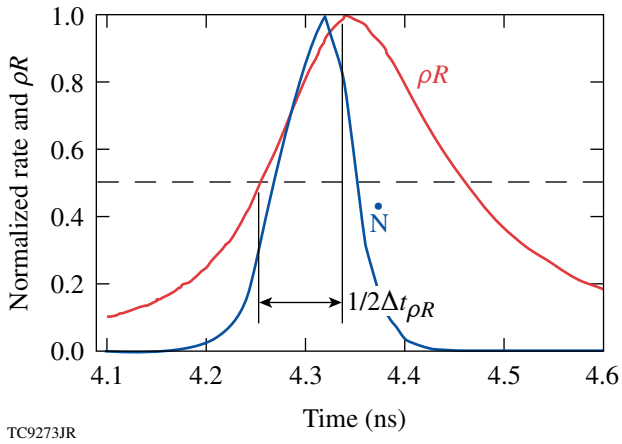

Figure 130.25
Areal density and neutron-production–rate evolution for a typical cryogenic implosion on OMEGA.

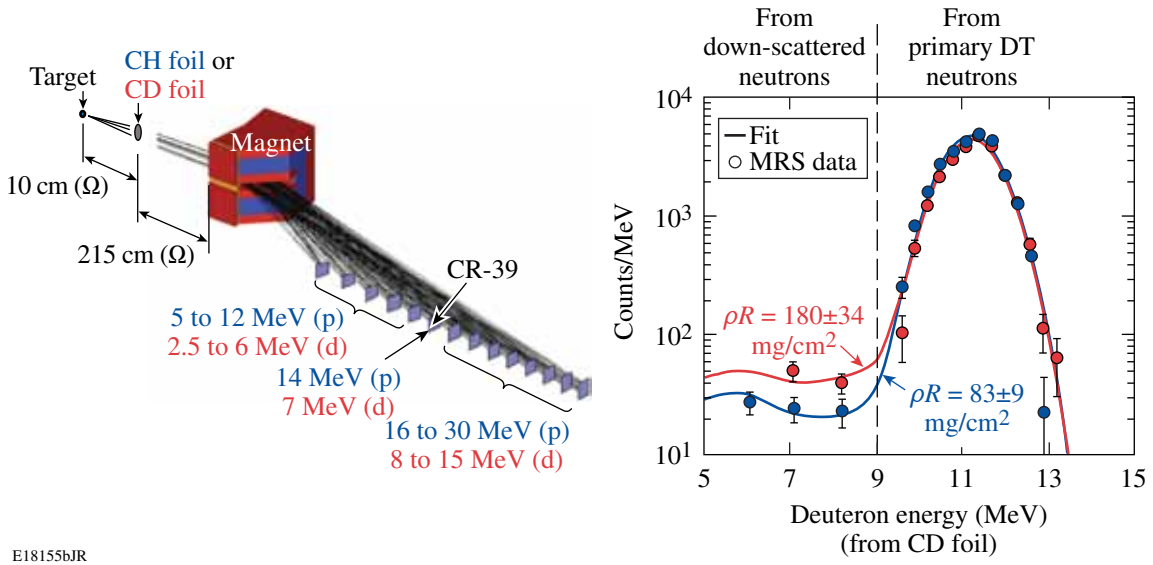

Figure 130.24
Areal density in DT fuel is inferred from measurements of the down-scattered fraction of primary neutrons produced in a D + T reaction.

2. Implosion Velocity

Implosion velocity is the key parameter that determines how much kinetic energy the fuel must acquire to ignite [see Eq. (1)]. Shell velocity can be inferred from trajectory measurements using either time-resolved x-ray–backlit images[29] of an imploding shell or time-resolved self-emission images.[25,30] The most-accurate measurement (although indirect) of hydrocoupling efficiency in implosions on OMEGA is done by measuring the onset of neutron production. Temporal history of the neutron rate is measured on OMEGA using neutron temporal diagnostics (NTD).[31] The absolute timing of NTD is calibrated to better than ±50 ps, which is equivalent to a spread in the implosion velocity of ±3.5% for OMEGA-scale targets. Figure 130.26 illustrates the sensitivity of neutron-production timing to the variation in shell velocity. Here, the shell velocity (dashed lines) and neutron rate (solid lines) histories are calculated using two different laser-deposition models. The implosion velocity predicted with the less-efficient drive (red lines) is 5% lower than that predicted for higher-efficiency drive (blue lines), resulting in a 200-ps delay in neutron production. Such a delay is easily observed in an experiment since this time difference is well outside the measurement error bar.

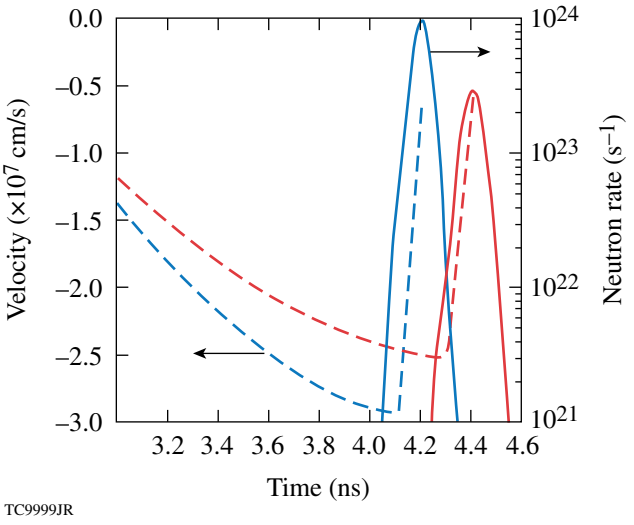

Figure 130.26
Shell velocity (left axis, dashed lines) and neutron production rates (right axis, solid lines) calculated for an OMEGA cryogenic design using two different laser-deposition models. The less-efficient laser absorption (red lines) predicts smaller shell velocity and later neutron-production timing.

3. Ion Temperature at Time of Peak Neutron Production

The fuel ion temperature at peak neutron production depends on the shell's kinetic energy during the acceleration phase of implosion and on the growth of the hot-spot distortions while the shell decelerates. The ion temperature in an implosion is inferred by measuring the temporal width of the primary-neutron signal.[32] The thermal broadening of the neutron energy distribution ΔE_{FWHM} is related to the local ion temperature T_{i} as[33]

$$\Delta E_{\mathrm{FWHM}} = 177\sqrt{T_{\mathrm{i}}}, \tag{57}$$

where both ΔE_{FWHM} and T_{i} are measured in keV. Then, measuring the neutrons' time of flight (TOF) from the target to a detector, TOF = $72.3\, L/\sqrt{E_{\mathrm{n}}}$, the neutron-averaged ion temperature is inferred relating TOF broadening Δ_{TOF} with ΔE and using Eq. (57),

$$\left\langle T_{\mathrm{i}}\right\rangle_{\mathrm{n,exp}} = 68\frac{\Delta^2_{\mathrm{TOF}}}{L^2}, \tag{58}$$

where L is the distance from detector to target in meters, E_{n} = 14.1 is the energy (in MeV) of primary neutrons in the D + T reaction, and TOF is measured in nanoseconds. Strictly speaking, the neutron spectral width is determined not only by thermal broadening, but also by gradients in the bulk fluid velocity of the reacting fuel. The latter contribution is not very important in a spherically symmetric implosion since the peak in neutron production occurs while the fuel is close to stagnation. When drive and target nonuniformities are taken into account, however, fuel flow caused by asymmetry growth can make a significant contribution to neutron spectral width. Therefore, comparing $\langle T_{\mathrm{i}}\rangle_{\mathrm{n,exp}}$ with calculations, the bulk fluid motion must be taken into account in this case. To generalize Eq. (57), including the effect of bulk motion, we start with Eq. (29) of Ref. 33 and write the neutron kinetic energy as

$$E_{\mathrm{n}} \simeq \frac{m_\alpha}{m_{\mathrm{n}}+m_\alpha}Q + \left(\mathbf{V}\cdot\mathbf{e}_{\mathrm{n}}\right)\sqrt{\frac{2m_{\mathrm{n}}m_\alpha Q}{m_{\mathrm{n}}+m_\alpha}}, \tag{59}$$

where Q is nuclear energy released in a fusion reaction (Q = 17.6 MeV for D + T reaction), m_{n} and m are masses of reaction products (neutron and alpha-particle mass, respectively, for DT), $\mathbf{V}$ is the velocity of the center of mass of reaction products, and $\mathbf{e}_{\mathrm{n}}$ is a unit vector in the direction of neutron velocity (and direction to a neutron detector). If $\mathbf{V_f}$ is the fluid velocity, then averaging over thermal motion gives

$$\left\langle E_{\mathrm{n}}\right\rangle \simeq E_0 + V_f\cos\theta_{\mathrm{n}}\sqrt{2m_{\mathrm{n}}E_0}, \tag{60}$$

where $E_0 = m_\alpha/\left(m_{\mathrm{n}}+m_\alpha\right)Q$ (E_0 = 14.1 MeV for DT), and θ_{n} is the angle between fluid flow and neutron velocity. Next, using Eq. (36) of Ref. 33, the neutron distribution at a particular location in a plasma with ion temperature T_{i} becomes

$$f_{\rm n}(E) = e^{-\left(\frac{E-E_0}{\Delta E} - M_a \cos\theta_{\rm n}\right)^2}, \quad \Delta E = 2\sqrt{\frac{m_{\rm n} T_{\rm i} E_0}{m_{\rm n} + m_\alpha}}, \qquad (61)$$

where $M_a = V_f / c_s$ is the flow Mach number $c_s = \sqrt{T_{\rm i}/m_{\rm i}}$ is the ion sound speed, and $m_{\rm i} = \left(m_{\rm n} + m_\alpha\right)/2$ is the average fuel ion mass. According to Eq. (61), a fluid velocity, uniform in the direction of the neutron detector, affects only the position in the peak of the distribution function, but not its width. Averaging the distribution function over the fuel volume gives

$$\left\langle f_{\rm n}(E)\right\rangle_V = \frac{\int {\rm d}V n^2 \left\langle\sigma v\right\rangle e^{-\left[\alpha(E) - M_a \mu\right]^2}}{\int {\rm d}V n^2 \left\langle\sigma v\right\rangle}, \qquad (62)$$

where $\mu = \cos\theta$, $\left\langle\sigma v\right\rangle$ is reaction cross section, n is ion density, $\alpha(E) = \left(E - E_0\right)/\Delta E$. Taking the integral over the angles assuming spherical symmetry in Eq. (62) yields

$$\left\langle f_{\rm n}(E)\right\rangle_V =$$

$$\sqrt{\pi}\,\frac{\int_0^R {\rm d}r r^2 n^2 \left\langle\sigma v\right\rangle \left\{{\rm erf}\left[\alpha(E) + M_a\right] - {\rm erf}\left[\alpha(E) - M_a\right]\right\}}{4 M_a \int_0^R {\rm d}r r^2 n^2 \left\langle\sigma v\right\rangle}, \qquad (63)$$

where erf is the error function. Integrating Eq. (63) over the neutron-production time and fitting the result with a Gaussian with FWHM = $\Delta E_{\rm fit}$,

$$\int {\rm d}t \left\langle f_{\rm n}(E)\right\rangle_V \xrightarrow{\rm fit} \exp\left[-4\ln 2\left(\frac{E-E_0}{\Delta E_{\rm fit}}\right)^2\right],$$

defines an effective temperature $\left\langle T_{\rm i}\right\rangle_{\rm n,fit} = \left(\Delta E_{\rm fit}/177\right)^2$ to be compared with the measurements [see Eq. (58)]. A bulk flow with velocity distribution not pointing in the same direction broadens the neutron spectrum, leading to a higher effective ion temperature. This is illustrated by evaluating the angular integral in Eq. (62), assuming $M_a \ll 1$ and spherical symmetry,

$$\frac{1}{2}\int_{-1}^{1} {\rm d}\mu e^{-\alpha^2 + 2\alpha M_a \mu} \simeq \frac{e^{-\alpha^2}}{2}\int_{-1}^{1} d\mu \left[1 + 2\left(\alpha M_a\right)^2 \mu^2\right]$$

$$\simeq e^{-\alpha^2}\Big/\left(1 + 2M_a^2/3\right). \qquad (64)$$

Equation (64) gives

$$\left\langle T_{\rm i}\right\rangle_{\rm fit} = T_{\rm i}\left(1 + \frac{2}{3}M_a^2\right) = T_{\rm i} + \frac{2}{3} m_{\rm i} V_f^2.$$

For a spherically symmetric flow, $\left\langle T_{\rm i}\right\rangle_{\rm fit}$ tracks $T_{\rm i}$ within a few percent since the fuel is close to stagnation at the neutron-production time. When significant asymmetries are present, bulk flow can lead to a significant contribution to $\left\langle T_{\rm i}\right\rangle_{\rm fit}$, making an inferred ion temperature larger than the actual thermodynamic value.

Early Experiments on the OMEGA-24 Laser

The first experiments with layered DT targets were performed on the OMEGA-24 Laser System[34] in the late 1980s (Refs. 35 and 36). The targets were spherical 3- to 5-μm-thick glass shells with outer radii of 100 to 150 μm. The cryogenic, 5- to 10-μm-thick solid DT layers were produced using a fast-freeze technique.[37] These targets were driven with 1 to 1.2 kJ of UV energy delivered with 650-ps Gaussian pulses (with a peak in drive intensity of up to 6×10^{14} W/cm^2). The target and drive pulse are shown in Fig. 130.27(a). The predicted convergence ratios in these implosions were relatively high, $C_r \sim 20$ (C_r is defined as the ratio of the initial to the minimum radius of the fuel–glass interface) with a peak DT density of ~300 g/cm^3 and a peak fuel areal density of 150 mg/cm^2. For comparison, the all-DT ignition design described in **All-DT, Direct-Drive, NIF-Scale Ignition Target Design** (p. 76) has $C_r = 27$. Targets were held inside the U-shaped cradle using three to five spider silks. These early designs were highly susceptible to the RT instability since the peak of the in-flight aspect ratio (IFAR) approached 70, a much higher value than currently considered to be acceptable for a robust design, IFAR < 40 (see **Target In-Flight Aspect Ratio**, p. 79). The areal densities in these experiments were directly measured (the first such measurement performed in an ICF implosion at that time) by counting the down-scattered fraction of deuterium and tritium atoms.[38] Even though the inferred fuel areal density and mass density were the highest measured to date, they were lower than predictions by 40% to 60%. Figure 130.27(b) plots the predicted value of fuel areal density using the 1-D hydrocode *LILAC*[39] and inferred areal densities using knock-on statistics. A significant deviation in the predicted value has occurred for an effective fuel adiabat $\alpha < 4$. This is not surprising considering the high IFAR of these shells. If perturbation growth causes a shell to break up during acceleration, it creates a low-density precursor ahead of the imploding shell, which causes the shell to stagnate at a larger radius with a smaller peak areal density.

Cryogenic D_2 Implosions on the OMEGA Upgrade Laser System from 2001 Until Mid-2008

The fast-freezing technique employed to make cryogenic targets on OMEGA-24 could not be used to produce thicker fuel layers required for ignition-relevant OMEGA-scaled designs.

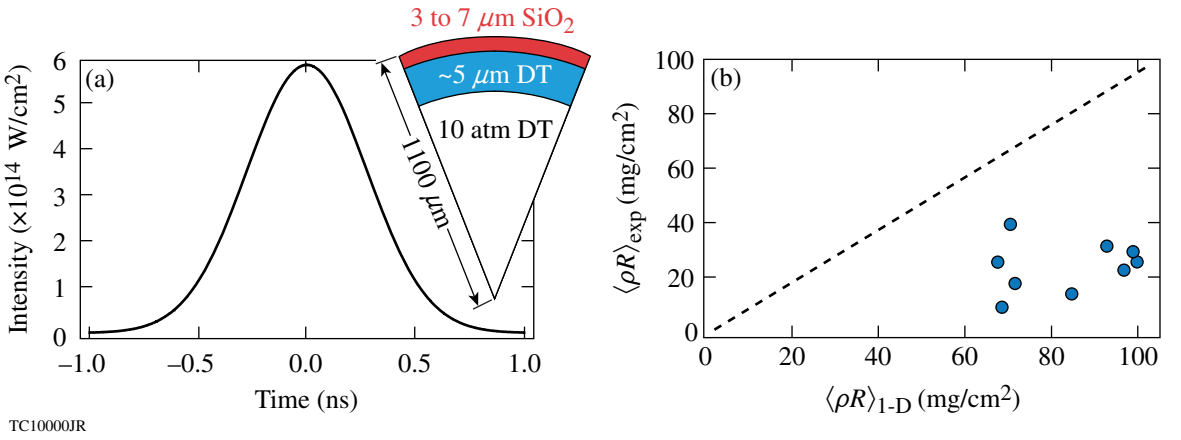

Figure 130.27
(a) Pulse shape and target and (b) predicted and inferred fuel areal densities for cryogenic implosions on the OMEGA-24 Laser System.

Novel techniques for producing smooth DT and D_2 layers were introduced in the 1980s and 1990s. A "β-layering" was demonstrated to make uniform solid DT layers,[40] and IR radiation was shown to produce layer smoothing in cryogenic D_2 fuel by exciting the vibration–rotation band.[41] The newly developed cryogenic system[42] on the OMEGA Upgrade (30 kJ of UV energy, 60-beam system)[43] employed both these techniques for cryogenic target production. Cryogenic experiments on the new system started in 2000 by imploding D_2 targets.[44] DT was introduced in February 2006, after completion of an extensive system readiness review associated with the radiological impact of using tritium.[45] Since target production was on a learning path to improving D_2-layer quality, the first implosions used a square laser drive pulse with laser energy ~23 kJ to set the cryogenic fuel on a high adiabat $\alpha \sim 25$ (see green dashed line in Fig. 130.28). The acceleration phase in this design was very short so the impact of the RT growth on target performance was minimal. The yields, areal densities (30 to 60 mg/cm^2), and timing of neutron production were consistent with 1-D and 2-D hydrocode simulations.[44,46]

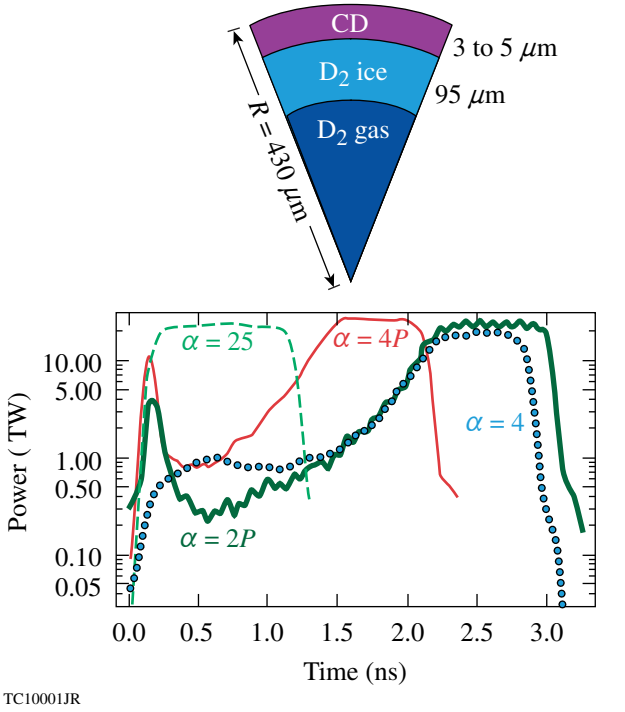

Figure 130.28
Pulse shapes and target for $\alpha = 25$ (dashed), $\alpha = 4$ (red solid and blue dotted lines), and $\alpha = 2$ (thick green line) designs on OMEGA. The designs with the decaying-shock adiabat shaping are shown with solid lines.

As the uniformity of ice layers dramatically improved from σ_{rms} = 9 to 15 μm down to 1 to 3 μm in 2002, experiments began using designs that approached the OMEGA-scaled version of the all-DT ignition designs.[47] These were 3- to 5-μm-thick CD shells overcoated over 95- to 100-μm-thick D_2 ice layers driven at $I \sim 10^{15}$ W/cm^2 on $\alpha = 4$ adiabat (see dotted line in Fig. 130.28). These shells were somewhat thicker than required for hydrodynamic scaling (<1 μm) since fill time was shorter and overall long-wavelength shell nonuniformities were smaller. By the middle of 2005, a large data set of these implosions was built sufficient to conclude that the measured areal densities were significantly lower than predicted, as shown with solid circles in Fig. 130.29. For the lowest adiabat (highest ρR) in this series, degradation in areal density was up to 50%, which is equivalent to adiabat degradation [according to Eq. (46)], by up to 70%! The 2-D calculations using the hydrocode *DRACO*[48] and results of the stability postproces-

sor[49] indicated that the shells in the low-adiabat implosions were sufficiently stable (the ratio of the mix width to the shell thickness did not exceed 50%, where the short-scale mix at the ablation front, seeded mainly by laser imprint, was amplified by the RT instability). Measurements of the imprint efficiencies made earlier on planar targets,[50] however, suggested that calculations could be underestimating imprint amplitude as much as by a factor of 2, and the shell in low-adiabat implosions could be broken by the imprint growth. Since shell stability was a main concern at that time, LLE was working on perturbation growth mitigation strategies. A novel technique for reducing the RT growth was proposed in 2002. The idea was to shape the adiabat through the shell (adiabat-shaping designs[20]). This can be accomplished either by launching a shock wave of decaying strength [decaying-shock (DS) design] through the shell[20] or by relaxing the shell material with a short-duration picket and recompressing it later with the shaped main pulse [adiabat shaping by relaxation (RX) design].[51] This sets the outer part of the ablator on a higher adiabat, keeping the inner part of the shell on a lower adiabat. The higher adiabat at the ablation front increases the ablation velocity, mitigating the impact of the RT instability on target performance, as described in **Rayleigh–Taylor Instability**, p. 77.

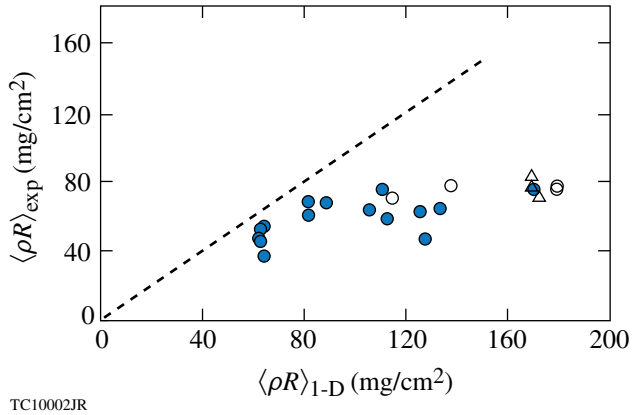

Figure 130.29
Measured and predicted areal densities for cryogenic-D_2 implosions using the $\alpha = 4$ pulses shown in Fig. 130.28 (solid circles) and $\alpha = 4P$ (open circles).

Pulse shapes, similar to ones shown in Fig. 130.28 with thin and thick solid lines, were used to implement adiabat-shaping designs on OMEGA. Calculations predicted a significant improvement in shell stability in designs with adiabat shaping in comparison with the original flat-foot designs (see Fig. 130.30). The experiments, however, did not show any significant improvement in measured areal densities, which continued to saturate at ~80 mg/cm^2. These are shown as open circles in Fig. 130.29. To further support the conclusion that the short-scale mix caused by the RT growth at the ablation front was not the main contributor to the observed ρR degradation, a series of implosions were performed with an enhanced laser-imprint level by turning off the smoothing by spectral dispersion (SSD).[52] The target yield dropped by a factor of 2 in these implosions, but the areal density remained unchanged (see open triangles in Fig. 130.29).

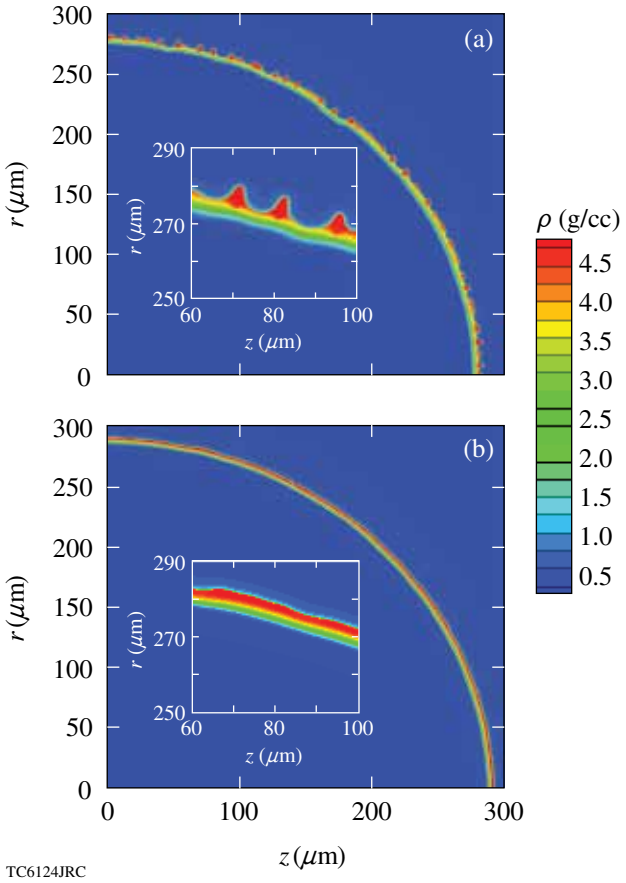

Figure 130.30
In-flight shell density contours in designs (a) without and (b) with adiabat shaping.

Since the source of excessive shell heating, not accounted for in a hydrosimulation, was unknown at the time, several scenarios explaining the areal-density deficiency were considered: Excessive shell heating could have been due to (1) suprathermal electrons with $T_{hot} > 40$ keV, (2) radiation, or (3) shock waves. Next, we describe how each of these possibilities were addressed in OMEGA experiments.

1. Suprathermal Electrons

Suprathermal electrons are always present in a plasma because of high-energy tails in the electron distribution function. In addition, laser–plasma interaction processes, such as

two-plasmon-decay (TPD) instability and stimulated Raman scattering (SRS),[53] can generate electrons with energies above 20 keV. These electrons can penetrate the ablator and fuel in OMEGA designs and deposit their energy close to the inner part of the fuel, degrading peak ρR. The electrons in the energetic tails of the distribution function will be addressed first.

a. Electron distribution tails and nonlocal thermal transport. To model electron thermal transport in ICF experiments, a flux-limited model[54] is conventionally used in hydrocode simulations. Thermal conduction in such a model is calculated using the Spitzer expression[55] q_{sp}, which is derived assuming that the electron mean free path is much shorter than the gradient scale-length of hydrodynamic variables.[56] In a narrow region, near the peak of the laser deposition, the temperature profile is steep enough to break the validity condition of the Spitzer formula. The heat flux in this case is calculated as a fraction $f < 1$ of the free-stream conduction $q_{fs} = nTv_T$, where n and T are electron density and temperature, respectively, $v_T = \sqrt{T/m}$ is the electron thermal velocity, and m is electron mass. The limiting factor f is referred to as "flux limiter." The flux-limiter value of $f = 0.06$ is typically used to simulate direct-drive experiments.

Although it was successfully applied to simulate many experimental observables,[57] the flux-limited thermal transport model neglects the effect of finite electron-stopping ranges and cannot be used to access the amount of shell preheat from the energetic electrons in plasma. To account for this effect, a simplified thermal transport model was developed and implemented in the 1-D hydrocode *LILAC*. The model used the Krook-type approximation[58] to the collisional operator to solve the Boltzmann equation without making the high collisionality approximation used in the "classical" Chapman–Enskog method.[56] The modified energy-dependent Krook-type operator[57] conserves particles and energy by renormalizing local electron density and electron temperature (which depend on gradients in hydrodynamic profiles) in the symmetric part of the distribution function (Maxwellian modified to include effects of the laser electric field[59]). When applied to the OMEGA experimental data, the nonlocal model showed no significant inner fuel preheat caused by the energetic electrons in the distribution tail (see Fig. 130.31). These electrons, instead, preheated the ablation front region [see how electron temperature in the calculation using the nonlocal model (thick dashed line in Fig. 130.31) increases toward the ablation front], leading to a greater ablative stabilization of the RT growth. This preheat of the outer region of the shell can explain very little sensitivity of the measured ρR to variation in the source of short-scale perturbations described earlier in this section. Ablation-front preheating from the nonlocal electrons is also consistent with the short-wavelength stabilization of the RT growth observed in experiments with accelerated planar foils.[60]

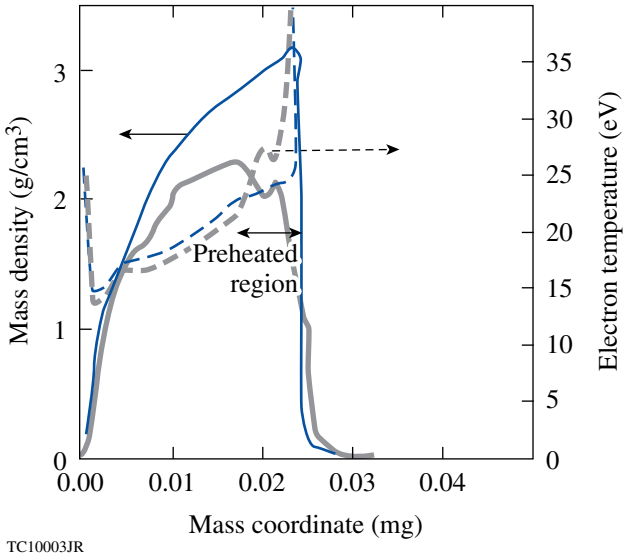

Figure 130.31
In-flight shell density (solid lines) and electron temperature (dashed) with (thin lines) and without (thick lines) nonlocal effects in electron thermal conduction.

In addition to the ablation region preheating, the strength of the first shock and a compression wave were significantly modified in calculations using the nonlocal electron-transport model.[57] At the beginning of the laser drive, where the hydrodynamic scale lengths are short, the shock strength predicted using the nonlocal model was larger compared to the results of the flux-limited model. This effectively led to shock mistiming and an adiabat degradation prior to the shell acceleration. Experimental validation of the nonlocal model predictions by direct shock-velocity measurement in spherical geometry was not available at that time (the experimental platform was developed in 2008). The existing shock-velocity data in planar geometry, on the other hand, were not very sensitive to differences in predictions using the nonlocal and flux-limited models.[57] Measurements of early-time perturbation evolution (ablative Richtmyer–Meshkov instability[61]), however, clearly indicated that the higher heat fluxes, predicted by the nonlocal model at the beginning of the pulse, are consistent with the observations.[62] In addition, the absorption measurements of Gaussian pulses with FWHM of 200 ps and peak laser intensity varied from 5×10^{13} to 1.2×10^{15} W/cm^2 (Ref. 63) were in much closer agreement with the results of the nonlocal heat-transfer model. These are shown in Fig. 130.32. In addition to the inverse bremsstrahlung, the resonance absorption[53] resulting from tunneling of the laser electric field from the

turning point to the critical surface and exciting plasma waves was included in these simulations.[57,64] The resonant absorption effects were important only early in the pulse when the density scale length is short.

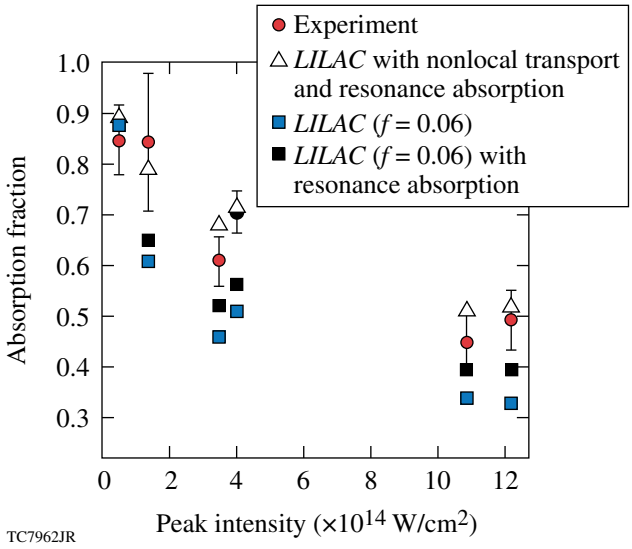

Figure 130.32
Absorption fraction of the incident laser energy for a 20-μm-thick CH shell driven by a 200-ps Gaussian pulse at different peak intensities.

When the nonlocal model was used, the calculated areal densities were in closer agreement with the data compared to the results of the flux-limited model (see Fig. 130.33). Nevertheless, some discrepancies in ρR, especially for implosions with the lowest adiabat, still remained.

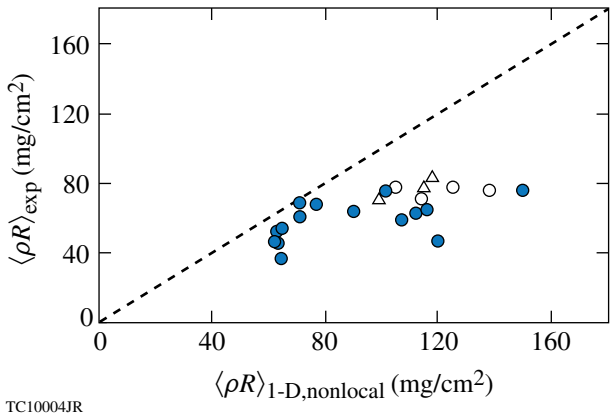

Figure 130.33
Same as in Fig. 130.29, except these calculations were performed using the nonlocal thermal transport model.

The next step in the cryogenic campaign was to redesign the drive pulse design, taking into account modified coupling efficiency early in the pulse, as predicted by the new thermal transport model. Both the RX and DS designs driven at peak intensities of ~6×10^{14} W/cm^2 were used in this "retuning" campaign. The experimental ρR values have marginally improved from 80 up to 100 mg/cm^2 (looking at this result with the knowledge that we have now, this 20% increase in areal density was mainly due to a reduction in peak intensity from 9 to 6×10^{14} W/cm^2, which also reduced the strength of secondary hydrodynamic waves launched by the pulse) but fell short of predicted values that were in the range of 150 to 170 mg/cm^2. Even though this campaign did not succeed in significantly increasing areal densities, it revealed a very interesting trend: the measured areal densities showed very strong dependence on CD shell thickness. These results are plotted in Fig. 130.34. Such a dependence was not predicted in hydrocode simulations. Among the hypotheses explaining

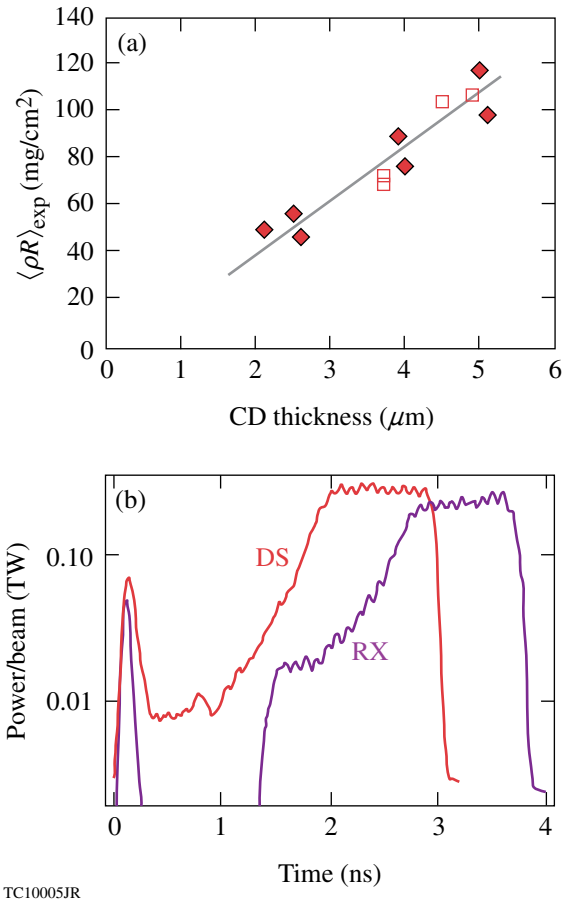

Figure 130.34
(a) Measured areal densities as a function of CD shell thickness and (b) pulse shapes used in this series. DS: decaying shock; RX: relaxation.

this trend are radiation preheat caused by mix at the CD–D_2 interface (as discussed in **Radiation Preheat**, p. 91), increased preheat as a result of suprathermal electron generation by the TPD instability, or short-scale magnetic-field generation at the CH–D_2 interface as the latter travels through the ablation front and conduction zone. None of these hypotheses, however, could account for a factor-of-2.5 reduction in areal density when the CD thickness decreased from 5 to 2.5 μm. The true explanation of this observation is still not found.

b. Suprathermal electrons generated by two-plasmon-decay (TPD) instability. In parallel to the study of the effect of nonlocal thermal transport on implosion performance, a different cryogenic design was proposed and used on OMEGA experiments to address a possible preheat issue caused by the suprathermal electrons created by the TPD instability. The threshold factor for the absolute TPD instability[65] is

$$\eta = \frac{I_{14} L_n(\mu\text{m})}{230\, T_{\text{keV}}}. \tag{65}$$

It exceeds unity in direct-drive implosions on OMEGA when drive intensities are above $\sim 3 \times 10^{14}$ W/cm^2. Here, I_{14} is the laser intensity at quarter-critical surface in units of 10^{14} W/cm^2, L_n is the electron-density scale length in microns, and T is the electron temperature in keV. At these intensities, hard x-ray bremsstrahlung radiation, emitted by suprathermal electrons as they slow down in the plasma, is observed in OMEGA implosions[66] (see dotted line in Fig. 130.35). To prove that the preheat signal has its origin in the TPD instability, the measured hard x-ray signal must correlate with 3/2ω and ω/2 emission.[63] An example of such a correlation in a cryogenic implosion with a 5-μm CD shell is shown in Fig. 130.35. Here, an ω/2 signal is shown with a thick green solid line. Both signals are observed when the calculated threshold parameter (shown by the dashed line marked "Threshold η") exceeds unity. The scale length for OMEGA spherical implosions, $L_n \simeq 150$ μm, is set by the target size. Therefore, the main parameter that controls the TPD instability in an experiment is the laser intensity. Since the hard x-ray emission increases with laser intensity,[66] as plotted in Fig. 130.36, a "low-intensity" series of cryogenic implosions were designed with peak laser intensity reduced to below 3×10^{14} W/cm^2. Lowering drive intensity eliminates a possibility of fuel preheating caused by the suprathermal electrons.[67] The first results of this campaign, shown in Fig. 130.37(a) by three solid circles, were very encouraging: for the first time the areal density measured in a low-adiabat ($\alpha \sim 3$) cryogenic implosion agreed with the simulation result! This initial success in the ability to accurately predict fuel compression in a cryogenic implosion, however, was short lived. With the goal of increasing areal density in a low-drive design, the first picket energy was reduced and the intensity foot was reduced and extended in time [see dashed line in Fig. 130.37(b)]. The measurements, however, showed no areal density increase predicted in simulations [see open circles in Fig. 130.37(a)]. Instead, the data followed the same trend observed in higher-intensity

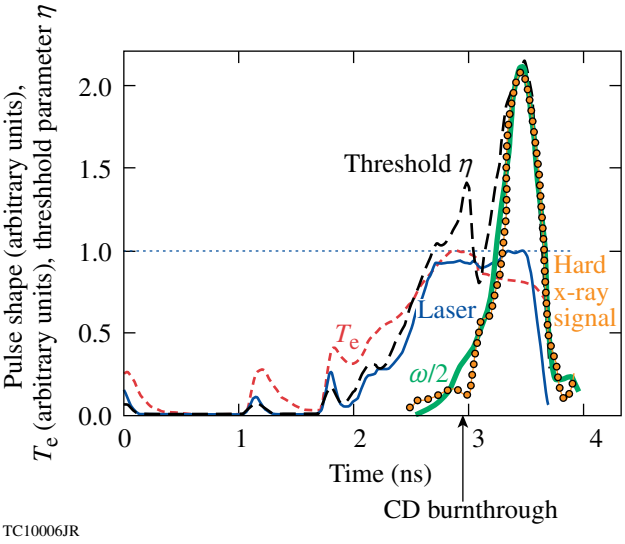

Figure 130.35
Laser pulse shape (thin solid line), electron temperature at quarter-critical surface (short-dashed line), TPD instability threshold factor (long-dashed line), measured hard x-ray signal (dotted line), and measured ω/2 signal (green solid line) for a cryogenic implosion with a 5-μm-thick CD shell.

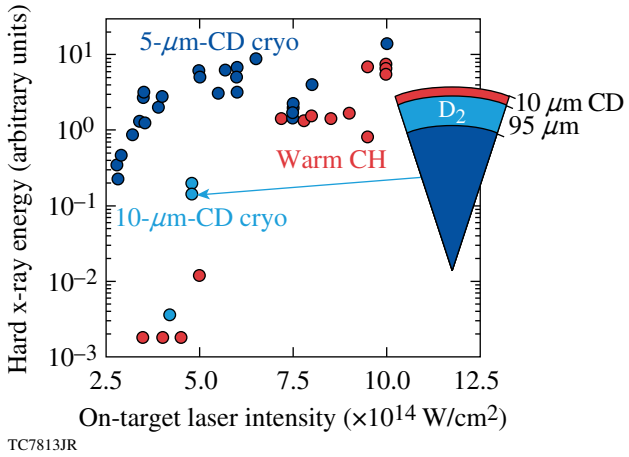

Figure 130.36
Measured energy of hard x rays (above 40 keV) as a function of incident laser intensity for a variety of OMEGA implosions.

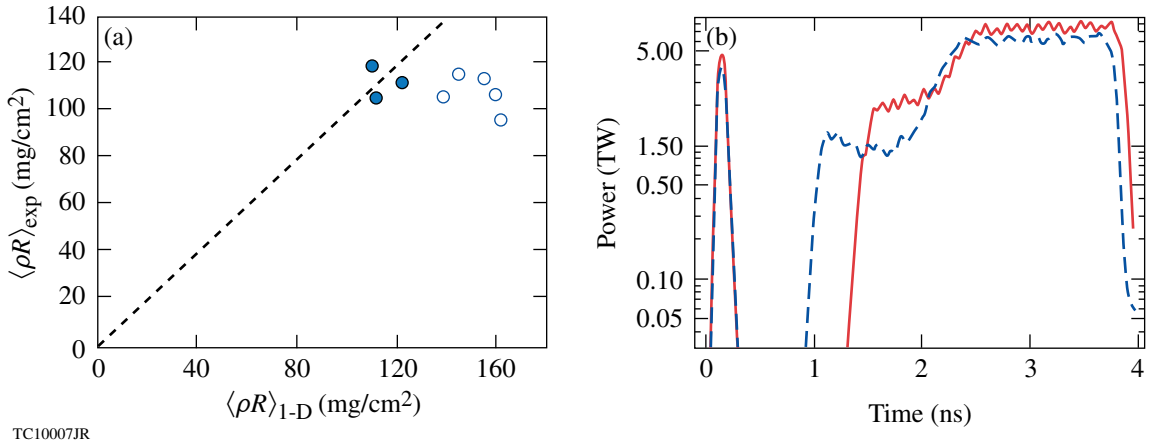

Figure 130.37
(a) Measured and (b) predicted areal densities for low-intensity RX drive pulses. Solid symbols correspond to the design shown with the solid red line in (b). The open symbols correspond to the lower-adiabat design shown with the dashed line in (b).

implosions: areal density saturated at a value independent of the predicted adiabat.

Additional evidence supporting the conclusion that the suprathermal electrons alone cannot explain the areal density degradation (as shown in Fig. 130.33) was obtained using a "dropping-intensity" design, where the drive intensity was reduced from its peak value of 5×10^{14} down to 3×10^{14} W/cm^2 starting from the time of onset of the suprathermal electron generation. This design and its comparison with the original flat-top design are shown in Fig. 130.38. While the suprathermal electron preheat signal was substantially reduced, the dropping-intensity design has also failed to achieve areal densities above the saturation value of 80 to 100 mg/cm^2.

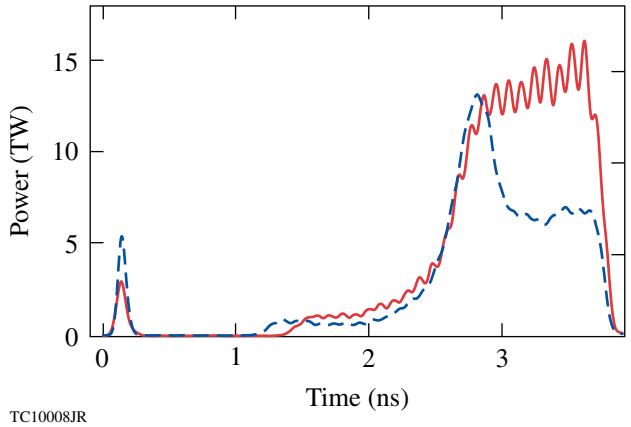

Figure 130.38
The original (solid red line) and modified (dashed line) design to reduce suprathermal electron production.

c. Radiation preheat. In addressing the second scenario for ρR degradation, excessive radiation preheating of the main fuel, the radiation x-ray power from plasma corona was measured using Dante.[68] Figure 130.39(a) shows the total radiated x-ray power as a function of time for cryogenic implosion with a 5-μm-thick CD shell. The result of a *LILAC* simulation is also plotted. The measured radiation power starts to deviate from the predictions at 3 ns. An x-ray radiation spectrum, plotted in Figs. 130.39(b) and 130.39(c), also shows agreement with calculations early in the pulse. The spectrum deviates from calculations at t = 3.48 ns in the energy range from 100 eV to 1 keV. The plastic shell is totally ablated by that time, and the CD–D_2 interface starts to move into the plasma corona. Radiation in the hydrocode calculation diminishes at this time because a higher-Z carbon is replaced by a lower-Z hydrogen in the x-ray–emitting region. Experimental data, on the other hand, showed a persistent signal after the burnthrough time. One plausible explanation of this effect is the mix of carbon and hydrogen at the CD–D_2 interface. This would cause carbon to stay longer at the higher-density region and significantly enhance the radiated x-ray power. An estimated 200 J was irradiated from the plasma corona in this experiment in excess of hydrocode predictions. Based on these observations, a new target design was proposed for cryogenic implosions on OMEGA.

d. Thick plastic cryogenic designs. Observations of an enhanced x-ray emission showed that increasing the CD shell thickness from 5 to 10 μm is beneficial. The thicker shell is predicted to ablate just at the end of the pulse, protecting the fuel layer from any excessive radiation in the corona. Thicker plastic ablators also increase the threshold factor of the TPD instabil-

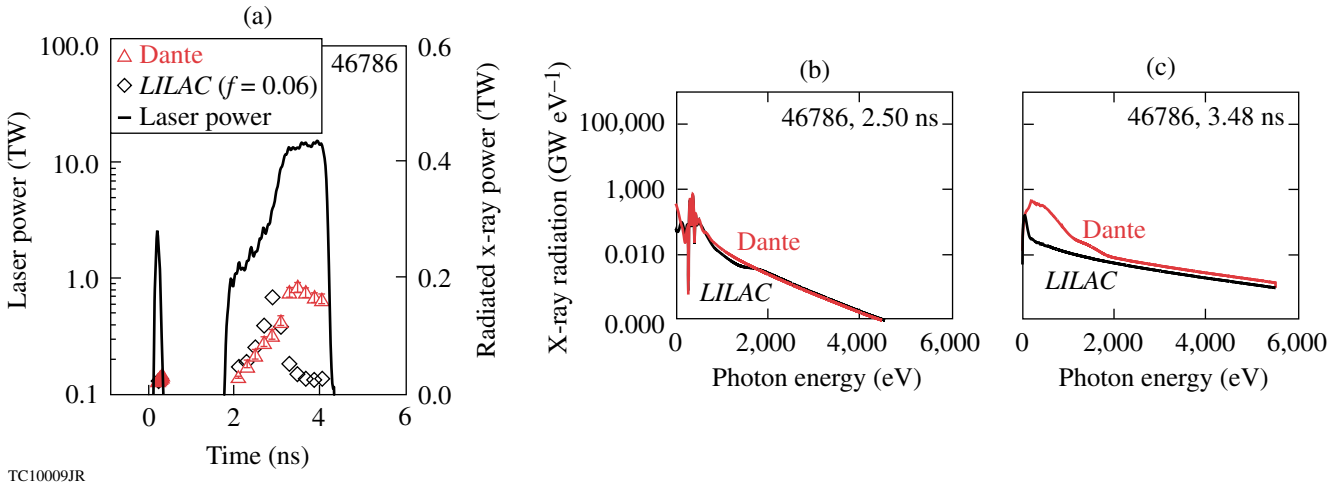

Figure 130.39
(a) Total radiated x-ray power and pulse shape and (b) x-ray radiation spectrum as measured using Dante at t = 2.5 ns and (c) t = 3.48 ns.

ity later in the pulse by raising the temperature in the plasma corona. Such a temperature increase is caused by a larger laser absorption fraction caused by the presence of higher-Z carbon in the absorption region. A higher absorption fraction farther away in the corona also reduces irradiation intensity that reaches a quarter-critical surface. Both these effects lead to a reduction in η [see Eq. (65)]. The cryogenic design with a 10-μm-thick CD ablator driven at $\sim 5 \times 10^{14}$ W/cm^2 is shown in Fig. 130.40. Four shots with this design produced areal densities 200 mg/cm^2, matching code predictions.[57,69] Figure 130.41 shows predicted and measured spectra of down-scattered secondary protons, confirming prediction accuracy. The areal densities and fuel compression in these implosions were the highest ever achieved in an ICF implosion. As expected, both the hard x-ray signal (see points marked "10-μm-CD cryo" in Fig. 130.36) and x-ray energy below 1 keV, emitted in excess to the predicted value, were significantly reduced in these experiments.

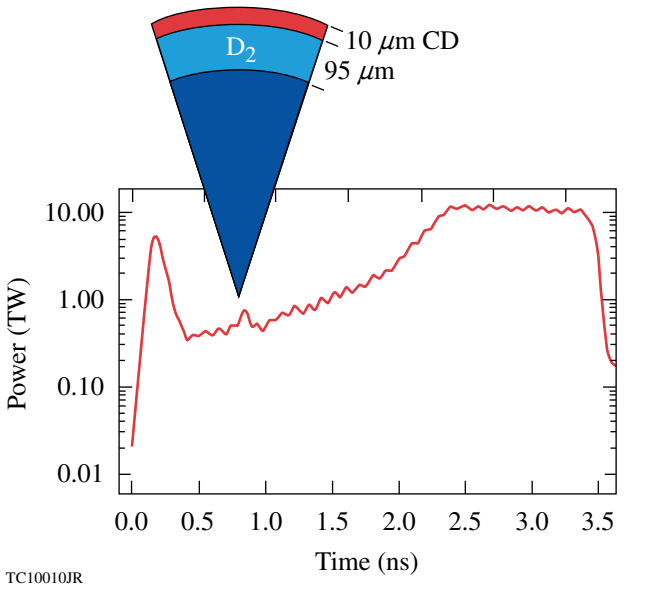

Figure 130.40
Pulse shape and target dimensions for the thick plastic cryogenic design.

Even though the designs with a thicker ablator demonstrated high compression, the drive intensity and implosion velocity $V_{imp} \sim 2.2 \times 10^7$ cm/s were smaller than required for a robust direct-drive–ignition design, $I \sim 8 \times 10^{14}$ W/cm^2 and $V_{imp} > 3.5 \times 10^7$ cm/s, respectively (see **A Simple Ignition Model**, p. 72). The next step was to increase both the drive intensity and the implosion velocity (by reducing the shell mass). This turned out to be a very challenging task. Figure 130.42(a) shows modifications made to the pulse shape in an attempt to increase the drive intensity. Raising the intensity also increases the electron preheat signal. Figure 130.42(b) shows measured areal densities as a function of the preheat signal (solid symbols). The measured areal density decreased dramatically even for minor variations in the laser pulse with very little or no sensitivity to the preheat signal. Reducing the thickness of the frozen D_2 layer from 95 to 80 μm also resulted in a decreased measured areal density (the predictions were ~200 mg/cm^2 for all cases). This is shown with open symbols in Fig. 130.42(b) . These results demonstrated that the continuous-pulse designs cannot be easily extended to the ignition-relevant drive intensities and implosion velocities.

e. Shock heating. The breakthrough in understanding cryogenic target performance came in 2008 when the shock-velocity

measurement technique matured enough to give information on the formation of shock and compression waves in spherical geometry.[70] These measurements addressed the third scenario for explaining areal-density degradation—excessive shock heating. Accuracy of shock timing was verified by measuring the velocity of the leading shock wave using the velocity interferometry system for any reflector (VISAR).[71] The targets in these experiments were spherical, 5- or 10-μm-thick CD shells fitted with a diagnostic cone. The shell and cone were filled with liquid deuterium. An example of VISAR measurement performed using the continuous pulse design is shown in Fig. 130.43. The measured shock velocity, as a function of

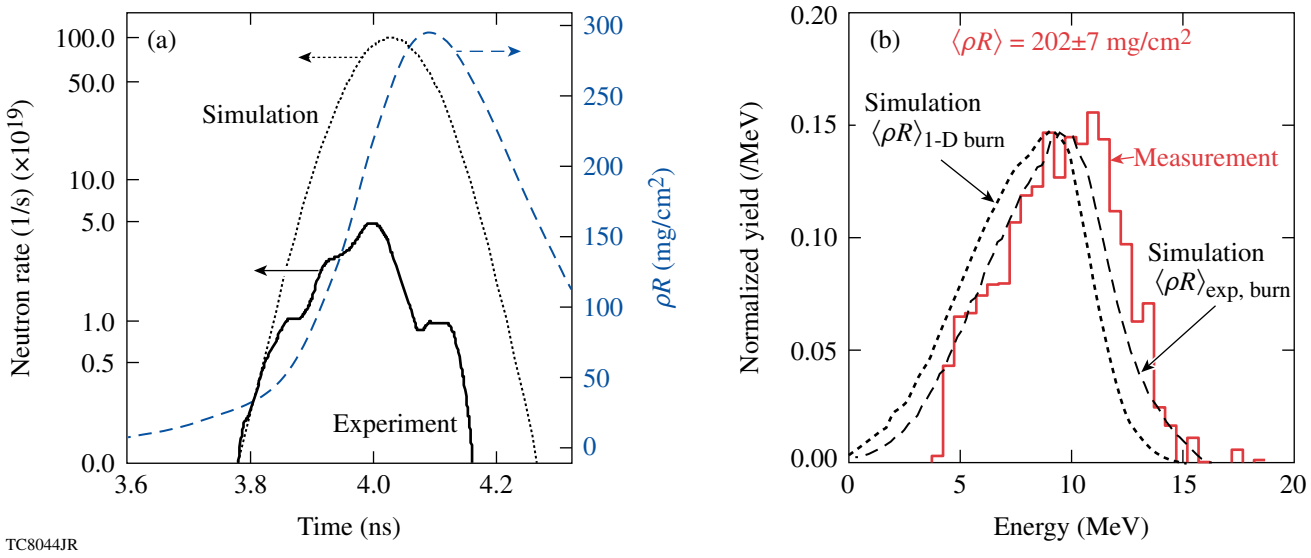

Figure 130.41
(a) The neutron-production history measured (solid line) and predicted (dotted line) for the design shown in Fig. 130.40. The ρR evolution calculated using the 1-D code *LILAC* (dashed line, right axis) is also shown. (b) Measured secondary-proton spectrum (solid line). The dotted line shows the calculated spectrum averaged over the predicted 1-D neutron production, and the dashed line represents the calculated spectrum averaged over the experimental neutron-production history.

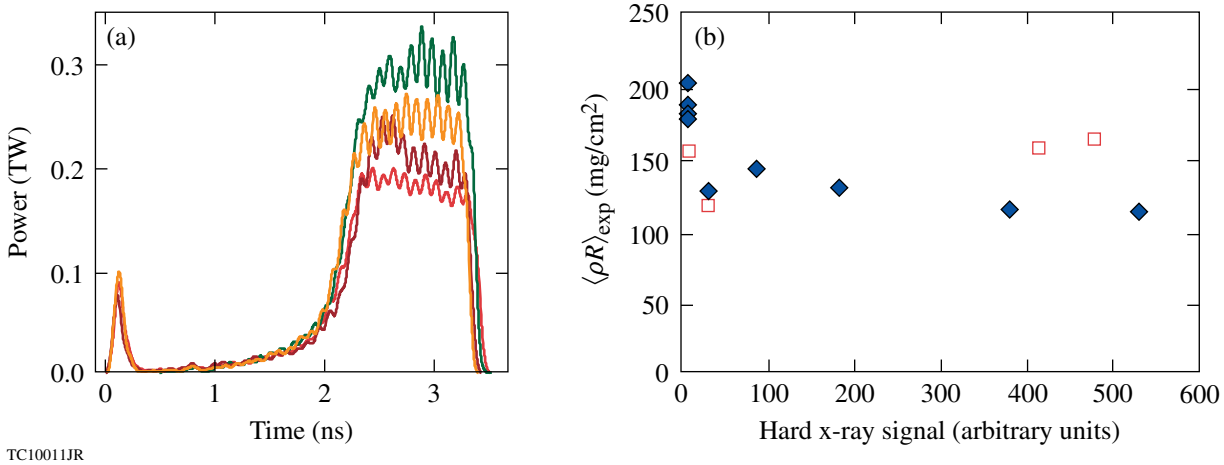

Figure 130.42
(a) Variation to the target design shown in Fig. 130.40 and (b) resulting measured areal densities for designs with 95-μm (solid symbols) and 80-μm (open symbols) D_2 ice thickness.

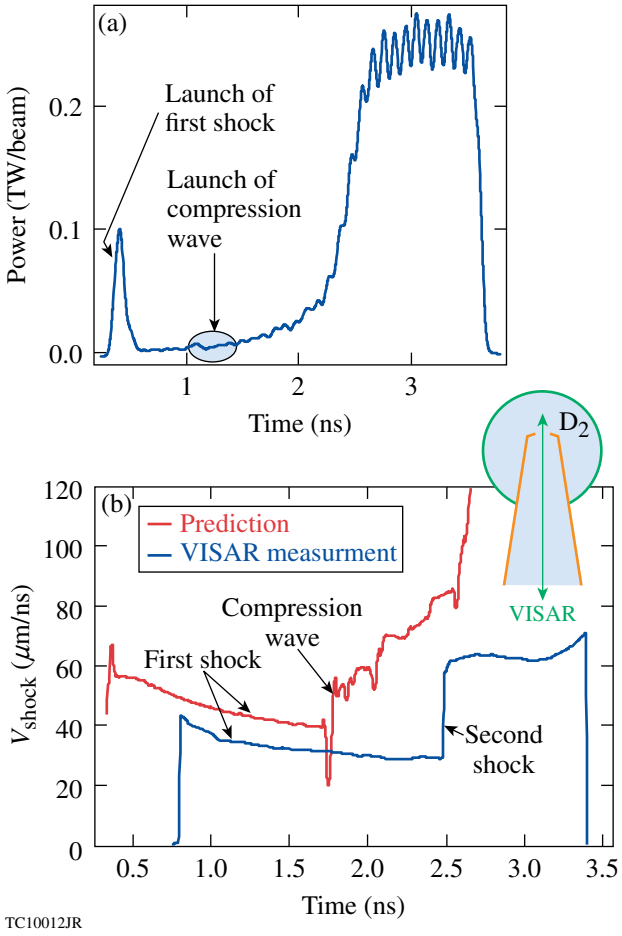

Figure 130.43
(a) Pulse shape and (b) leading shock velocity measured (lower curve) and predicted (upper curve).

time, is compared with 1-D predictions obtained using a *LILAC* simulation. An intensity picket at the beginning of the drive pulse sends a shock wave of decaying strength. As the drive intensity starts to rise from its minimum value, a compression wave is launched into the ablator at $t \simeq 1$ ns. After the head of the compression catches up with the first shock, strength and velocity of the leading shock increase gradually in time. The measured velocity history, however, shows a much steeper velocity increase that takes place later in the pulse, indicating that the compression wave turns into a shock prior to its coalescence with the first shock. Such a transition from adiabatic to shock compression raises the fuel adiabat at the inner part of the shell, limiting the final target convergence and peak fuel ρR. Since the effect of the compression wave steepening into a shock, not predicted by a simulation, is exacerbated by an increasing peak drive pulse or changing the shell thickness, difficulty in tuning continuous-pulse designs can be explained by excessive shock heating.

After obtaining the VISAR results, the cryogenic program at LLE quickly moved to multiple-picket designs[72] by introducing double-picket and, later, triple-picket pulses (see Fig. 130.44). To set the fuel on a low adiabat $\alpha \sim 1$ to 3, the double-picket design still requires a moderate-intensity foot (1/4 to 1/3 of peak intensity) and a gradual intensity increase to compress the fuel adiabatically (dashed line in Fig. 130.44). The triple-picket design (solid line in Fig. 130.44), on the other hand, does not rely on an adiabatic compression and requires a short step at the beginning of the main pulse to control the strength of the main shock.

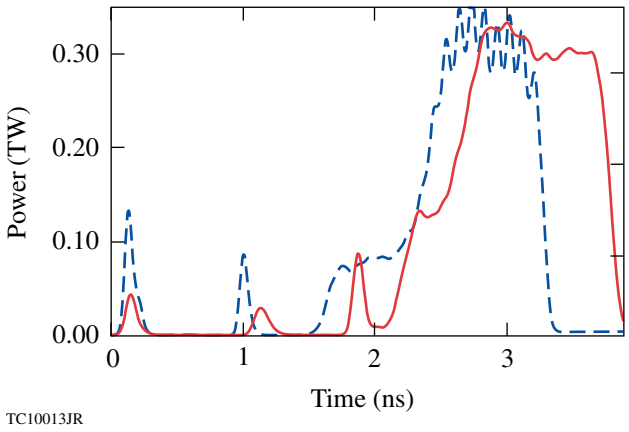

Figure 130.44
Two- (dashed line) and three-picket (solid line) cryogenic OMEGA target designs.

Current Triple-Picket Cryogenic-DT Implosions

The main advantage in using multiple-picket designs is the ability to control all hydrodynamic waves launched by the drive pulse.[72] As described in **All-DT, Direct-Drive, NIF-Scale Ignition Target Design** (p. 76), designs with continuous pulses rely on adiabatic fuel compression while the drive pressure increases by a factor of 50 or more. The observed premature steepening of the adiabatic compression wave into a shock inside the shell makes it impractical to experimentally tune the shell adiabat in these designs. In the multiple-picket designs shown in Fig. 130.44, the required increase in drive pressure from a few Mbar to ~100 Mbar is accomplished by launching a sequence of shocks that can be well controlled by adjusting the timing and energy of each individual intensity picket. Two types of the triple-picket pulse shapes are used in current cryogenic implosions on OMEGA. The laser power in the first design, shown in Fig. 130.45(a), consists of three pickets and the main drive in the form of a square pulse. To control the strength of the main shock, a short intensity step is introduced at the beginning of the main drive in the second design [shown

in Fig. 130.45(b)]. The stronger main shock launched in the first design sets the fuel on α = 2.5 to 3. A weaker shock in the second design reduces the adiabat to α = 2 to 2.5. Next, we describe how shock tuning was accomplished in these designs using OMEGA experiments.

1. Shock Tuning

Accuracy in predicting shock timing is verified by measuring the velocity of the leading shock wave using VISAR. The targets in these experiments were spherical, 5- or 10-μm-thick CD shells fitted with a diagnostic cone.[73] The shell and cone were filled with liquid deuterium. For an optimized design,[72] all shocks should coalesce within 100 ps, soon after they break out of the shell. For the purpose of code validation, the time separation between shock coalescence events was increased in these experiments to accurately infer leading shock velocity after each coalescence. An example of such a measurement is shown in Fig. 130.46. Because of radiation precursor, the shock is not visible to VISAR early in time while it travels through the plastic layer. Then, at $t \sim 300$ ps, the shock breaks out of CD into D_2 with a velocity of ~60 μm/ns. The shock is not supported by the laser at this time (picket duration is ~80 ps). Therefore, the shock strength and its velocity decrease with time. Then, the second shock is launched at t = 1.1 ns. It travels through

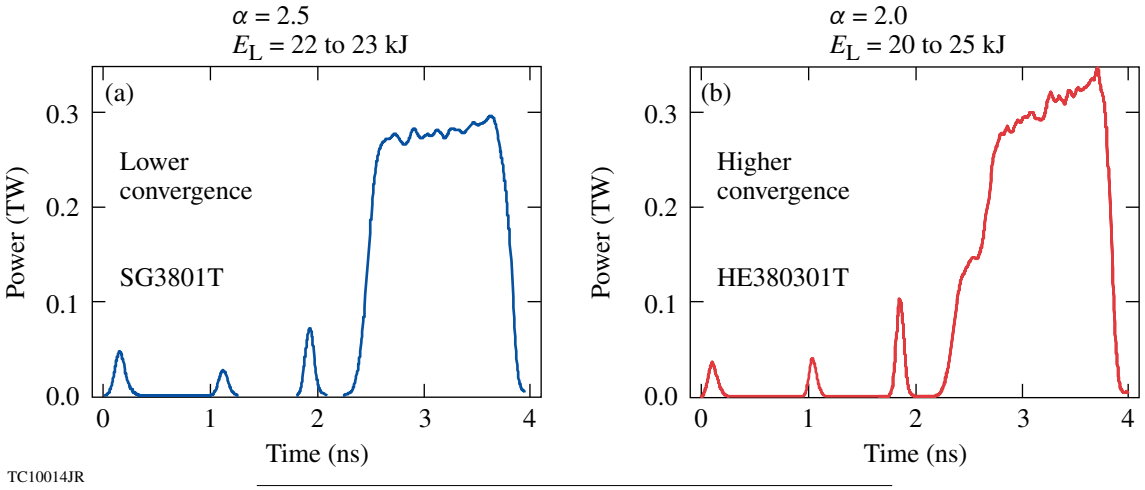

Figure 130.45
Two triple-picket target designs used in cryogenic implosions on OMEGA.

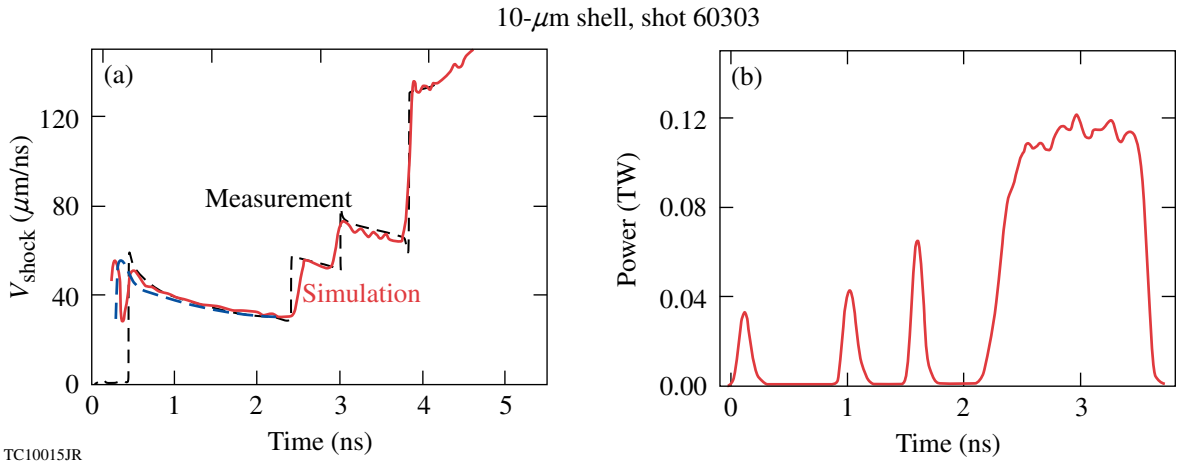

Figure 130.46
(a) Measured (dashed line) and predicted (solid line) leading shock velocity in (b) a triple-picket design.

the relaxed density and pressure profiles established by the first shock. At $t = 2.5$ ns the second shock catches up with the first, resulting in a jump in leading shock velocity from 35 up to 60 μm/ns. The third picket and the main pulse launch two additional shocks that coalesce with the leading shock at $t =$ 3.0 and 3.9 ns, respectively.

Matching both shock velocities and coalescence times is a good test of a thermal-conduction model used in a hydrocode simulation. The thermal conduction affects hydrodynamic profiles that determine energy coupling. The flux-limited model with $f = 0.06$ predicts a lower laser-absorption fraction than that calculated using the nonlocal thermal transport model, leading to a slower shock. The difference between two transport models increases with the energy in the first picket. The comparison between model predictions and experimental data is shown in Fig. 130.47. As seen in this figure, agreement between prediction and measurement improves when the nonlocal thermal-transport model is used in the simulations.

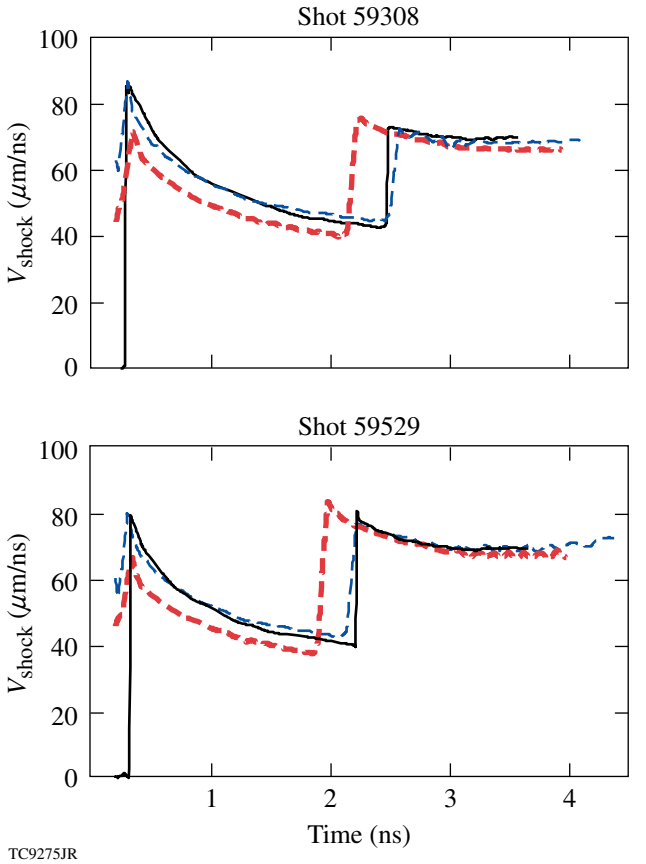

Figure 130.47
Measured (solid lines) and predicted leading shock velocity using the flux-limited (thick red dashed lines) and nonlocal (thin dashed lines) electron thermal-transport models for two shots.

Matching the predicted and measured shock velocities and coalescence times ensures that the shock heating is properly modeled. The in-flight shell adiabat, set by the shocks, can be degraded during the implosion by electron or radiation preheat as well as by secondary shock waves. As described in **Adiabat** (p. 81), the in-flight adiabat can be inferred from areal-density measurements if no significant shell decompression is induced by the prolonged coasting phase [see discussion after Eq. (53)]. The extended coasting phase could result from a loss in hydro-efficiency during shell acceleration. The latter would reduce shell implosion velocity and delay the time of neutron production. Therefore, to connect any observable degradation in areal density with fuel preheat or any other effects that enhance in-flight adiabat, one must verify that hydrodynamic efficiency is accurately modeled and no extended coasting phase is present in the implosion. This will be addressed in the next subsection.

2. Laser Coupling and Hydrodynamic Efficiency

Accurate modeling of hydrodynamic efficiency of an imploding shell (defined as the ratio of the peak in shell kinetic energy to the total laser energy) is crucial for optimizing high-convergence target designs, since a loss in the shell's implosion velocity and kinetic energy leads to shell coasting after the laser drive turns off. During such coasting, both shell density and pressure drop. This reduces ρR [see Eq. (53)] and gives a lower fuel ion temperature at the time of neutron production. One of the diagnostics that is most sensitive to deviations in the shell's implosion velocity is a measurement of timing and temporal shape of primary neutrons produced as a result of fusion reactions. This is accomplished by using NTD (see discussion in **Implosion Velocity**, p. 84). Currently, NTD is calibrated on OMEGA to ~50-ps absolute timing accuracy with ~10-ps shot-to-shot timing variation. In addition to the neutron-production timing, the laser-absorption measurement is performed using two full-aperture backscattering stations (FABS).[63] Time-resolved scattered-light spectroscopy and time-integrated calorimetry in these stations are used to infer the absorption of laser light. Laser absorption, however, is not a direct measurement of hydrodynamic efficiency since only a small fraction of the incident laser energy (~5%) is converted (through the mass ablation) into the shell's kinetic energy and the majority of the absorbed energy goes into heating the underdense plasma corona. Also, some fraction of laser energy can be deposited into plasma waves that accelerate suprathermal electrons and do not directly contribute to the drive.

Figures 130.48(a) and 130.48(b) compare the measured scattered laser light and Fig. 130.48(c) compares neutron production history with the predictions (blue solid lines represent

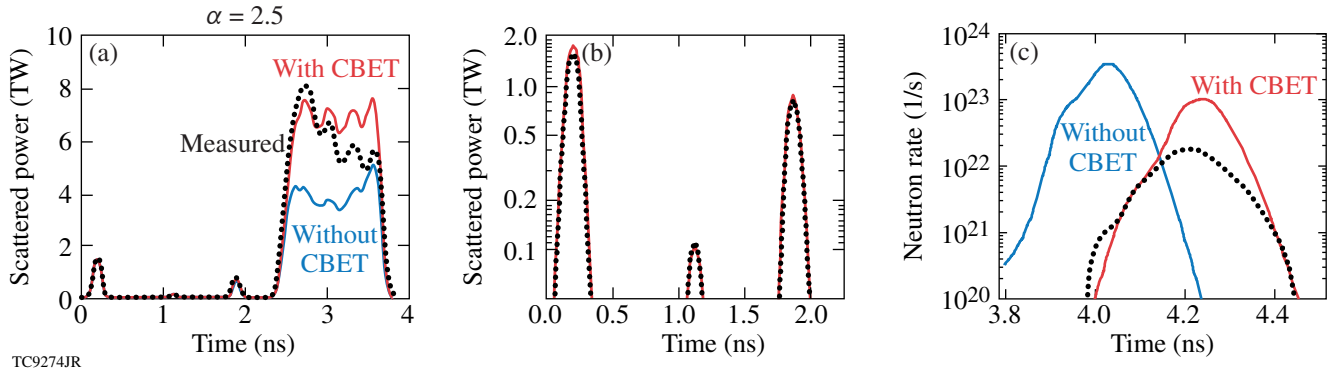

Figure 130.48
[(a) and (b)] Measured (dotted lines) and predicted (solid lines) scattered-light data. (c) Neutron-production history for the $\alpha = 2.5$ design shown in Fig. 130.45(a).

without CBET) for an $\alpha = 2.5$ design. As seen in Fig. 130.48(b), calculations are in very good agreement with the measured scattered-light data (dotted line) for the picket portion of the pulse. At the main drive, however, the predicted laser absorption overestimates the data, especially at the beginning of the drive. Higher predicted laser coupling results in an earlier bang time, as shown in Fig. 130.48(c). On average, the rise of the neutron rate is earlier in simulations by 200 ps. Since calculations fail to accurately reproduce the laser-absorption fraction and neutron-production timing, an additional mechanism explaining a reduced laser coupling must be present in the experiments.

Such a mechanism, as discussed in a recent publication,[74] is due to the cross-beam energy transfer (CBET).[75] In the geometric optics approximation where each laser beam is subdivided into rays, the incoming ray in the central part of the beam interacts (through the ion-acoustic waves) with the outgoing ray on the outer edge of the beam, transferring its energy to that ray. This is illustrated in Fig. 130.49. Since the central part of the beam propagates closest to the target, CBET reduces the fraction of the beam energy that reaches the higher-density plasma corona, decreasing overall laser absorption. Because CBET reduces the total laser absorption, and, furthermore, the absorbed energy is deposited in corona farther away from the target surface, the hydroefficiency of laser drive in directly driven implosions is degraded by 15% to 20% in OMEGA implosions. When implemented into the hydrocode *LILAC*, a CBET model predicts a 10% to 15% reduction in the absorbed energy, in agreement with experimental data. Shown in Fig. 130.48 solid lines marked "with CBET" are (a) the scattered light and (c) neutron-production rate calculated using a combination of the nonlocal thermal transport and CBET models. The neutron-production timing matches data very well. The scattered-light power, however, deviates from the measurements at later times. This late-time discrepancy is likely due

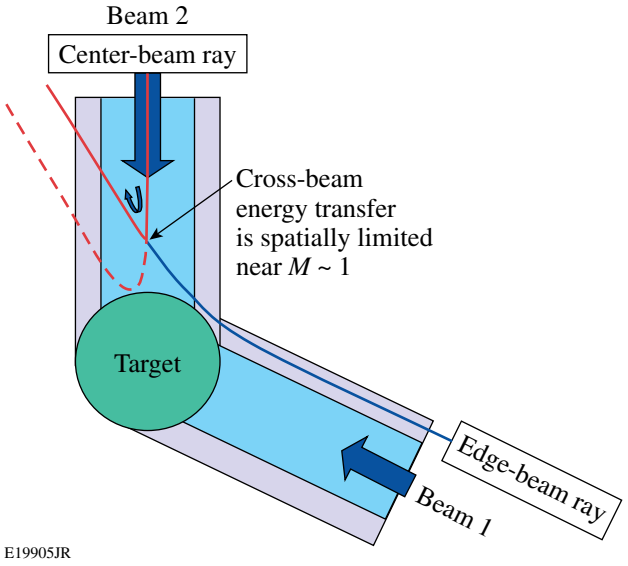

Figure 130.49
The incoming ray in the central part of Beam 2 interacts with the outgoing ray on the outer edge of Beam 1, transferring its energy to that ray.

to extra absorption of laser energy by plasma waves excited by the TPD instability.[14] Figure 130.50 shows the drive pulses and threshold parameters for $\alpha = 2.5$ designs. The threshold parameter first oscillates around $\eta = 1$ and then rises above unity at $t \sim 3.2$ to 3.3 ns. This matches the time when the experimental scattered light starts deviating from the predictions. To further support the assertion that the observable fraction of laser energy is being deposited into plasma waves, the scattered-light measurement and prediction are plotted in Fig. 130.51 for an implosion at a slightly higher drive intensity where the TPD instability threshold is exceeded at the beginning of the main drive [see Fig. 130.51(b)]. The calculated scattered-light power starts deviating from measurements earlier in this case, which is consistent with the timing of η exceeding unity.

Incorporating the CBET model into hydrocode simulations shows only a marginal reduction (on average by ~5%) in neutron-averaged areal densities. This confirms that the areal densities in cryogenic implosions on OMEGA are affected mainly by the in-flight shell adiabat and the effect of shell decompression during the coasting phase is small.

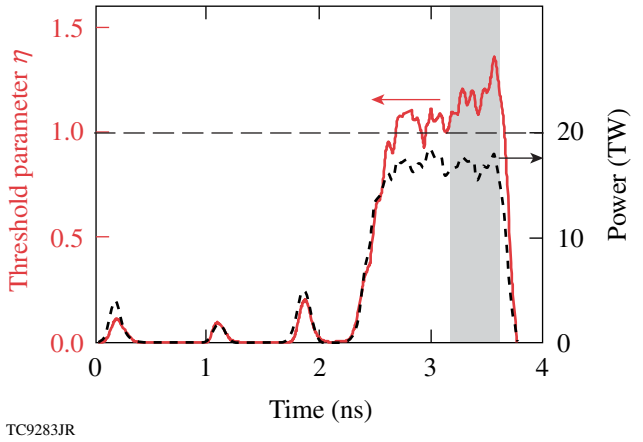

Figure 130.50
Pulse shape (dashed line) and threshold parameter η of TPD instability.

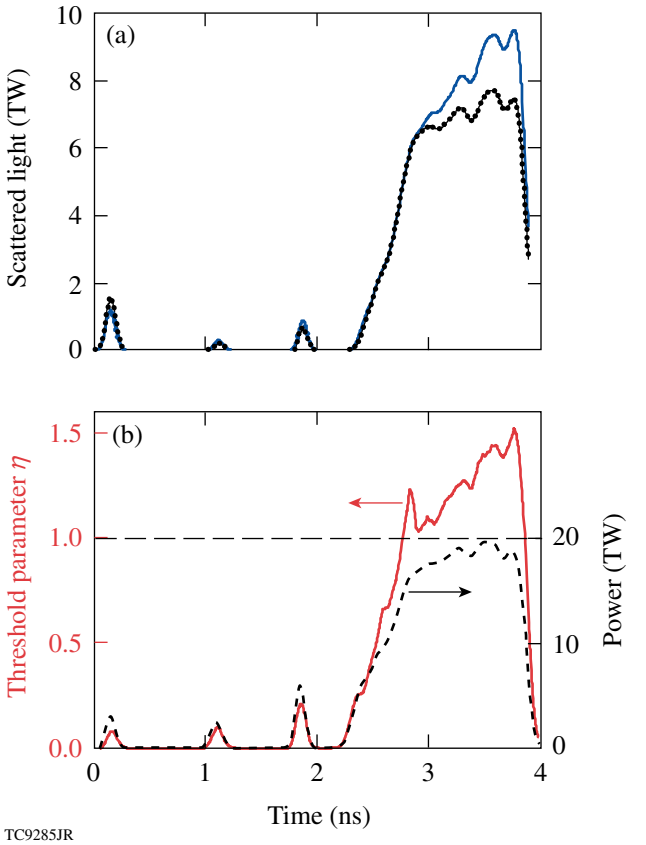

Figure 130.51
(a) Measured (dotted line) and predicted scattered power. (b) Pulse shape (dashed line) and threshold parameter η of TPD instability (solid line).

3. Areal Densities in a Triple-Picket Cryogenic Implosions

In this section we compare the calculated neutron-averaged areal density $\langle \rho R \rangle_n$ with the measurements. Since the predicted $\langle \rho R \rangle_n \sim 150$ to 200 mg/cm^2 for $\alpha = 2.5$ and $\langle \rho R \rangle_n \sim 220$ to 300 mg/cm^2 for $\alpha = 2$, the areal density is currently inferred using a single-view measurement with a magnetic recoil spectrometer (MRS).[28] The MRS measures the number of primary neutrons and the number of neutrons scattered in the dense DT fuel. The ratio of these two is proportional to the fuel areal density during the neutron production. Two charged-particle spectrometers (CPS's) were also used to measure the spectrum of knock-on deuterons, elastically scattered by primary DT neutrons. These measurements, however, are insensitive to $\langle \rho R \rangle_n >$ 180 mg/cm^2 and were used to assess low-ℓ-mode ρR asymmetries for implosions where areal density along the CPS's line of sight is below 180 mg/cm^2. Such asymmetries arise from errors in target positioning (offset) and ice roughness amplified during shell implosion. Since only a single-view MRS measurement is used for ρR analysis, it is important to take long-wavelength asymmetries into account when comparing the simulated and measured areal densities for high-convergence implosions. Strictly speaking, even a single MRS measurement averages fuel ρR over a solid angle of ~1.5π since the down-scattered neutrons have a finite spectral width and neutrons with different energies sample different parts of the shell (see Fig. 130.52). The scattering angle θ of a primary neutron (marked with "n" in Fig. 130.52) depends on down-scattered neutron ("n′") energy. MRS is sensitive to 8- to 13-MeV neutrons. The minimum scattering angle $\theta_{min} = 29°$ and 23° correspond to 13-MeV neutrons scattered by tritons and deuterons, respectively. The maximum angle $\theta_{max} = 80°$ and 62° corresponds to 8-MeV neutrons. The dark shell region in Fig. 130.52 corresponds to a region sampled by the down-scattered neutrons in a single-view MRS measurement on OMEGA. Taking into account such averaging, Fig. 130.53 plots a calculated variation in areal density as would be observed by the MRS in a single-view measurement taken along a different direction with respect to the target offset. The results are shown for the offset values of $\Delta_{offset} = 10$ μm (black line) and 30 μm (green line). The calculations were performed by post-processing results of 2-D *DRACO* simulations[76] using the Monte Carlo–based particle transport code *IRIS*. The error bars in Fig. 130.53 represent counting statistics errors in a typical cryogenic implosion on OMEGA. These calculations show that the $\langle \rho R \rangle_n$ variation across the target can be approximated by a linear function of the offset,

$$\frac{\max\langle\rho R\rangle_{\rm n} - \min\langle\rho R\rangle_{\rm n}}{\langle\rho R\rangle_{\rm n}}\% \simeq \Delta_{\rm offset}(\mu{\rm m}). \qquad (66)$$

In addition to the target offset, the low-ℓ modes ($\ell \le 2$) seeded by the ice roughness also lead to an azimuthal variation in the measured areal density. In plotting the predicted $\langle\rho R\rangle_{\rm n}$, we assign the error bar for each point taking into account the ρR variation caused by target offset and low-mode ice roughness measured for each target. The result is shown in Fig. 130.54 (see also Ref. 72), where squares and circles correspond to $\alpha = 2$ and $\alpha = 2.5$ designs, respectively. In general, there is good agreement between the experimental data and calculations. This confirms that the adiabat is modeled accurately in low-adiabat cryogenic implosions on OMEGA using the triple-picket designs.

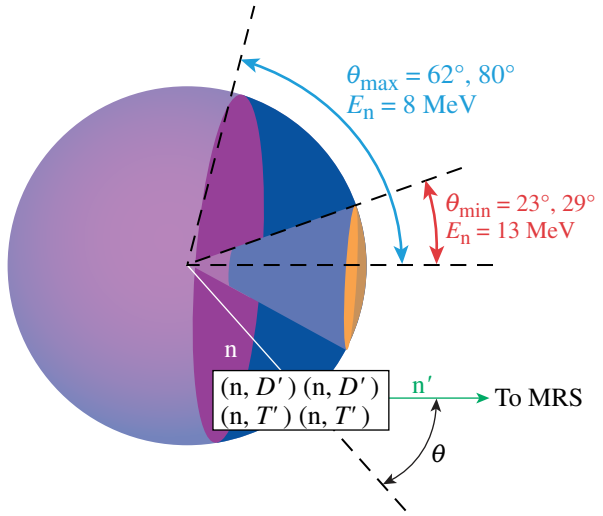

Figure 130.52
The scattering angle θ of a primary neutron (marked with "n") depends on down-scattered neutron ("n′") energy. MRS is sensitive to neutrons with energies between 8 and 13 MeV. The minimum scattering angles $\theta_{\rm min} = 29°$ and 23° correspond to 13-MeV neutrons scattered by tritons and deuterons, respectively. The maximum angles $\theta_{\rm max} = 80°$ and 62° correspond to 8-MeV neutrons. The dark shell region corresponds to a region sampled by the down-scattered neutrons in a single-view MRS measurement on OMEGA.

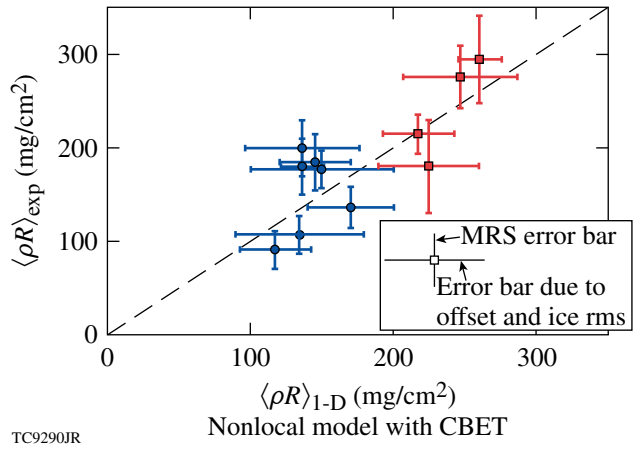

Figure 130.54
Measured versus predicted areal densities for triple-picket cryogenic implosions on OMEGA.

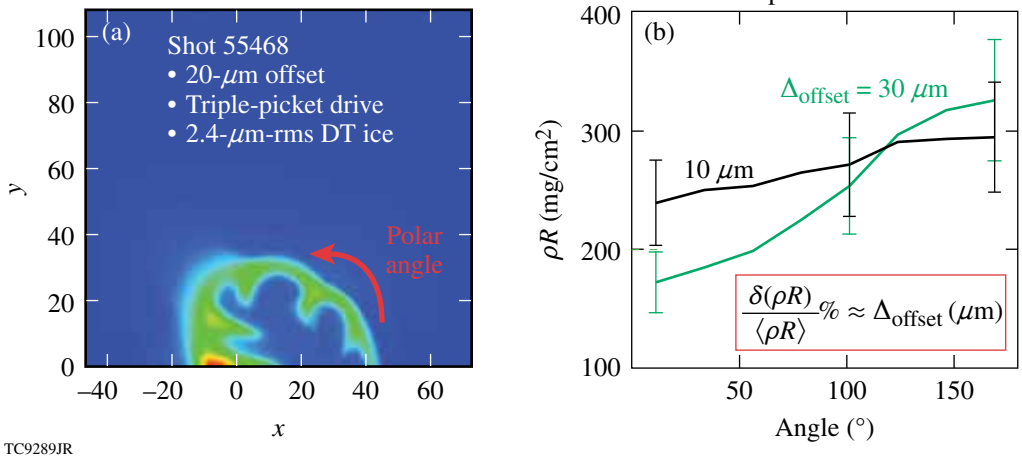

Figure 130.53
(a) Density contour of 2-D *DRACO* simulation of a cryogenic implosion on OMEGA (shot 55468) with a target offset of 20 μm. (b) Predicted variation in areal density as would be observed by the MRS in a single-view measurement taken along a different direction with respect to the target offset.

Based on the good performance of the triple-picket design on OMEGA, this design was extended to a 1.5-MJ direct-drive–ignition design[72] for the National Ignition Facility (see Fig. 130.55). Driven at a peak intensity of 8×10^{14} W/cm^2, the shell reaches $V_{imp} = 3.5$ to 4×10^7 cm/s, depending on the thickness of the fuel layer. This design is predicted to ignite with a gain $G = 48$.

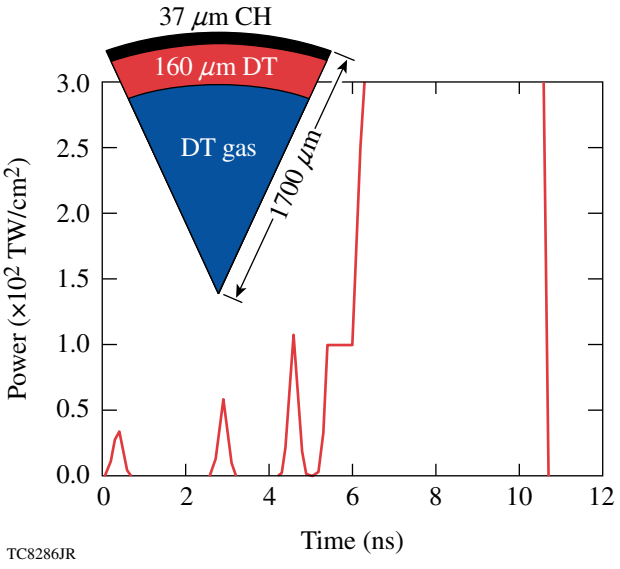

Figure 130.55
Triple-picket, symmetric direct-drive design for the NIF.

ACKNOWLEDGEMENT

This work was supported by the U.S. Department of Energy Office of Inertial Confinement Fusion under Cooperative Agreement No. DE-FC52-08NA28302, the University of Rochester, and the New York State Energy Research and Development Authority. The support of DOE does not constitute an endorsement by DOE of the views expressed in this article.

REFERENCES

1. J. D. Lindl, *Inertial Confinement Fusion: The Quest for Ignition and Energy Gain Using Indirect Drive* (Springer-Verlag, New York, 1998).
2. S. Atzeni and J. Meyer-ter-Vehn, *The Physics of Inertial Fusion: Beam Plasma Interaction, Hydrodynamics, Hot Dense Matter*, International Series of Monographs on Physics (Clarendon Press, Oxford, 2004).
3. M. C. Herrmann, M. Tabak, and J. D. Lindl, Phys. Plasmas **8**, 2296 (2001).
4. R. Betti, K. Anderson, V. N. Goncharov, R. L. McCrory, D. D. Meyerhofer, S. Skupsky, and R. P. J. Town, Phys. Plasmas **9**, 2277 (2002).
5. V. N. Goncharov, in *Laser-Plasma Interactions*, edited by D. A. Jaroszynski, R. Bingham, and R. A. Cairns, Scottish Graduate Series (CRC Press, Boca Raton, FL, 2009), pp. 409–418.
6. J. Meyer-ter-Vehn, Nucl. Fusion **22**, 561 (1982).
7. R. Betti, P. Y. Chang, B. K. Spears, K. S. Anderson, J. Edwards, M. Fatenejad, J. D. Lindl, R. L. McCrory, R. Nora, and D. Shvarts, Phys. Plasmas **17**, 058102 (2010).
8. A. Kemp, J. Meyer-ter-Vehn, and S. Atzeni, Phys. Rev. Lett. **86**, 3336 (2001).
9. S. W. Haan, J. D. Lindl, D. A. Callahan, D. S. Clark, J. D. Salmonson, B. A. Hammel, L. J. Atherton, R. C. Cook, M. J. Edwards, S. Glenzer, A. V. Hamza, S. P. Hatchett, M. C. Herrmann, D. E. Hinkel, D. D. Ho, H. Huang, O. S. Jones, J. Kline, G. Kyrala, O. L. Landen, B. J. MacGowan, M. M. Marinak, D. D. Meyerhofer, J. L. Milovich, K. A. Moreno, E. I. Moses, D. H. Munro, A. Nikroo, R. E. Olson, K. Peterson, S. M. Pollaine, J. E. Ralph, H. F. Robey, B. K. Spears, P. T. Springer, L. J. Suter, C. A. Thomas, R. P. Town, R. Vesey, S. V. Weber, H. L. Wilkens, and D. C Wilson, Phys. Plasmas **18**, 051001 (2011).
10. C. P. Verdon, Bull. Am. Phys. Soc. **38**, 2010 (1993).
11. P. W. McKenty, V. N. Goncharov, R. P. J. Town, S. Skupsky, R. Betti, and R. L. McCrory, Phys. Plasmas **8**, 2315 (2001).
12. J. Paisner *et al.*, Laser Focus World **30**, 75 (1994).
13. V. N. Goncharov, S. Skupsky, T. R. Boehly, J. P. Knauer, P. McKenty, V. A. Smalyuk, R. P. J. Town, O. V. Gotchev, R. Betti, and D. D. Meyerhofer, Phys. Plasmas **7**, 2062 (2000).
14. W. L. Kruer, *The Physics of Laser–Plasma Interactions*, Frontiers in Physics, Vol. 73, edited by D. Pines (Addison-Wesley, Redwood City, CA, 1988), Chap. 4, p. 81.
15. S. Chandrasekhar, in *Hydrodynamic and Hydromagnetic Stability*, International Series of Monographs on Physics (Clarendon Press, Oxford, 1961), p. 428.
16. J. Sanz, Phys. Rev. Lett. **73**, 2700 (1994); V. N. Goncharov, R. Betti, R. L. McCrory, P. Sorotokin, and C. P. Verdon, Phys. Plasmas **3**, 1402 (1996).
17. R. Betti, V. N. Goncharov, R. L. McCrory, and C. P. Verdon, Phys. Plasmas **5**, 1446 (1998).
18. J. Sanz, Phys. Rev. E **53**, 4026 (1996).
19. V. N. Goncharov, O. V. Gotchev, E. Vianello, T. R. Boehly, J. P. Knauer, P. W. McKenty, P. B. Radha, S. P. Regan, T. C. Sangster, S. Skupsky, V. A. Smalyuk, R. Betti, R. L. McCrory, D. D. Meyerhofer, and C. Cherfils-Clérouin, Phys. Plasmas **13**, 012702 (2006).
20. V. N. Goncharov, J. P. Knauer, P. W. McKenty, P. B. Radha, T. C. Sangster, S. Skupsky, R. Betti, R. L. McCrory, and D. D. Meyerhofer, Phys. Plasmas **10**, 1906 (2003).
21. H. Sawada, S. P. Regan, D. D. Meyerhofer, I. V. Igumenshchev, V. N. Goncharov, T. R. Boehly, R. Epstein, T. C. Sangster, V. A. Smalyuk, B. Yaakobi, G. Gregori, S. H. Glenzer, and O. L. Landen, Phys. Plasmas **14**, 122703 (2007).
22. D. Zhou and R. Betti, Phys. Plasmas **14**, 072703 (2007).
23. A. L. Kritcher *et al.*, Phys. Rev. Lett. **107**, 015002 (2011).

24. H. Sawada, S. P. Regan, P. B. Radha, R. Epstein, D. Li, V. N. Goncharov, S. X. Hu, D. D. Meyerhofer, J. A. Delettrez, P. A. Jaanimagi, V. A. Smalyuk, T. R. Boehly, T. C. Sangster, B. Yaakobi, and R. C. Mancini, Phys. Plasmas **16**, 052702 (2009).

25. F. J. Marshall, P. W. McKenty, J. A. Delettrez, R. Epstein, J. P. Knauer, V. A. Smalyuk, J. A. Frenje, C. K. Li, R. D. Petrasso, F. H. Séguin, and R. C. Mancini, Phys. Rev. Lett. **102**, 185004 (2009).

26. R. Tommasini, S. P. Hatchett, D. S. Hey, C. Iglesias, N. Izumi, J. A. Koch, O. L. Landen, A. J. MacKinnon, C. Sorce, J. A. Delettrez, V. Yu. Glebov, T. C. Sangster, and C. Stoeckl, Phys. Plasmas **18**, 056309 (2011).

27. F. H. Séguin, C. K. Li, J. A. Frenje, D. G. Hicks, K. M. Green, S. Kurebayashi, R. D. Petrasso, J. M. Soures, D. D. Meyerhofer, V. Yu. Glebov, P. B. Radha, C. Stoeckl, S. Roberts, C. Sorce, T. C. Sangster, M. D. Cable, K. Fletcher, and S. Padalino, Phys. Plasmas **9**, 2725 (2002).

28. J. A. Frenje, C. K. Li, F. H. Séguin, D. T. Casey, R. D. Petrasso, T. C. Sangster, R. Betti, V. Yu. Glebov, and D. D. Meyerhofer, Phys. Plasmas **16**, 042704 (2009); J. A. Frenje, D. T. Casey, C. K. Li, F. H. Séguin, R. D. Petrasso, V. Yu. Glebov, P. B. Radha, T. C. Sangster, D. D. Meyerhofer, S. P. Hatchett, S. W. Haan, C. J. Cerjan, O. L. Landen, K. A. Fletcher, and R. J. Leeper, Phys. Plasmas **17**, 056311 (2010).

29. D. G. Hicks, B. K. Spears, D. G. Braun, R. E. Olson, C. M. Sorce, P. M. Celliers, G. W. Collins, and O. L. Landen, Phys. Plasmas **17**, 102703 (2010).

30. J. P. Knauer, K. Anderson, R. Betti, T. J. B. Collins, V. Yu. Glebov, V. N. Goncharov, F. J. Marshall, D. D. Meyerhofer, P. B. Radha, S. P. Regan, C. Stoeckl, J. A. Frenje, C. K. Li, R. D. Petrasso, and F. H. Séguin, Bull. Am. Phys. Soc. **50**, 113 (2005).

31. C. Stoeckl, V. Yu. Glebov, S. Roberts, T. C. Sangster, R. A. Lerche, R. L. Griffith, and C. Sorce, Rev. Sci. Instrum. **74**, 1713 (2003).

32. T. J. Murphy *et al*., Rev. Sci. Instrum. **66**, 930 (1995).

33. H. Brysk, Plasma Phys. **15**, 611 (1973).

34. J. M. Soures, R. J. Hutchison, S. D. Jacobs, L. D. Lund, R. L. McCrory, and M. C. Richardson, in *Proceedings of the 10th Symposium on Fusion Engineering* (IEEE, New York, 1983), p. 1392.

35. F. J. Marshall, S. A. Letzring, C. P. Verdon, S. Skupsky, R. L. Keck, J. P. Knauer, R. L. Kremens, D. K. Bradley, T. Kessler, J. Delettrez, H. Kim, J. M. Soures, and R. L. McCrory, Phys. Rev. A **40**, 2547 (1989).

36. R. L. McCrory, J. M. Soures, C. P. Verdon, F. J. Marshall, S. A. Letzring, S. Skupsky, T. J. Kessler, R. L. Kremens, J. P. Knauer, H. Kim, J. Delettrez, R. L. Keck, and D. K. Bradley, Nature **335**, 225 (1988).

37. D. L. Musinski *et al*., J. Appl. Phys. **51**, 1394 (1980).

38. S. Kacenjar, L. M. Goldman, A. Entenberg, and S. Skupsky, J. Appl. Phys. **56**, 2027 (1984); S. Skupsky and S. Kacenjar, J. Appl. Phys. **52**, 2608 (1981).

39. J. Delettrez, R. Epstein, M. C. Richardson, P. A. Jaanimagi, and B. L. Henke, Phys. Rev. A **36**, 3926 (1987).

40. J. K. Hoffer and L. R. Foreman, Phys. Rev. Lett. **60**, 1310 (1988); A. J. Martin, R. J. Simms, and R. B. Jacobs, J. Vac. Sci. Technol. A **6**, 1885 (1988).

41. G. W. Collins *et al*., J. Vac. Sci. Technol. A **14**, 2897 (1996).

42. *LLE Review Quarterly Report* **81**, 6, Laboratory for Laser Energetics, University of Rochester, Rochester, NY, LLE Document No. DOE/SF/19460-335 (1999).

43. T. R. Boehly, D. L. Brown, R. S. Craxton, R. L. Keck, J. P. Knauer, J. H. Kelly, T. J. Kessler, S. A. Kumpan, S. J. Loucks, S. A. Letzring, F. J. Marshall, R. L. McCrory, S. F. B. Morse, W. Seka, J. M. Soures, and C. P. Verdon, Opt. Commun. **133**, 495 (1997).

44. C. Stoeckl, C. Chiritescu, J. A. Delettrez, R. Epstein, V. Yu. Glebov, D. R. Harding, R. L. Keck, S. J. Loucks, L. D. Lund, R. L. McCrory, P. W. McKenty, F. J. Marshall, D. D. Meyerhofer, S. F. B. Morse, S. P. Regan, P. B. Radha, S. Roberts, T. C. Sangster, W. Seka, S. Skupsky, V. A. Smalyuk, C. Sorce, J. M. Soures, R. P. J. Town, J. A. Frenje, C. K. Li, R. D. Petrasso, F. H. Séguin, K. Fletcher, S. Padalino, C. Freeman, N. Izumi, R. Lerche, and T. W. Phillips, Phys. Plasmas **9**, 2195 (2002).

45. T. C. Sangster, R. Betti, R. S. Craxton, J. A. Delettrez, D. H. Edgell, L. M. Elasky, V. Yu. Glebov, V. N. Goncharov, D. R. Harding, D. Jacobs-Perkins, R. Janezic, R. L. Keck, J. P. Knauer, S. J. Loucks, L. D. Lund, F. J. Marshall, R. L. McCrory, P. W. McKenty, D. D. Meyerhofer, P. B. Radha, S. P. Regan, W. Seka, W. T. Shmayda, S. Skupsky, V. A. Smalyuk, J. M. Soures, C. Stoeckl, B. Yaakobi, J. A. Frenje, C. K. Li, R. D. Petrasso, F. H. Séguin, J. D. Moody, J. A. Atherton, B. D. MacGowan, J. D. Kilkenny, T. P. Bernat, and D. S. Montgomery, Phys. Plasmas **14**, 058101 (2007).

46. P. W. McKenty, T. C. Sangster, M. Alexander, R. Betti, R. S. Craxton, J. A. Delettrez, L. Elasky, R. Epstein, A. Frank, V. Yu. Glebov, V. N. Goncharov, D. R. Harding, S. Jin, J. P. Knauer, R. L. Keck, S. J. Loucks, L. D. Lund, R. L. McCrory, F. J. Marshall, D. D. Meyerhofer, S. P. Regan, P. B. Radha, S. Roberts, W. Seka, S. Skupsky, V. A. Smalyuk, J. M. Soures, K. A. Thorp, M. Wozniak, J. A. Frenje, C. K. Li, R. D. Petrasso, F. H. Séguin, K. A. Fletcher, S. Padalino, C. Freeman, N. Izumi, J. A. Koch, R. A. Lerche, M. J. Moran, T. W. Phillips, G. J. Schmid, and C. Sorce, Phys. Plasmas **11**, 2790 (2004).

47. F. J. Marshall, R. S. Craxton, J. A. Delettrez, D. H. Edgell, L. M. Elasky, R. Epstein, V. Yu. Glebov, V. N. Goncharov, D. R. Harding, R. Janezic, R. L. Keck, J. D. Kilkenny, J. P. Knauer, S. J. Loucks, L. D. Lund, R. L. McCrory, P. W. McKenty, D. D. Meyerhofer, P. B. Radha, S. P. Regan, T. C. Sangster, W. Seka, V. A. Smalyuk, J. M. Soures, C. Stoeckl, S. Skupsky, J. A. Frenje, C. K. Li, R. D. Petrasso, and F. H. Séguin, Phys. Plasmas **12**, 056302 (2005).

48. P. B. Radha, V. N. Goncharov, T. J. B. Collins, J. A. Delettrez, Y. Elbaz, V. Yu. Glebov, R. L. Keck, D. E. Keller, J. P. Knauer, J. A. Marozas, F. J. Marshall, P. W. McKenty, D. D. Meyerhofer, S. P. Regan, T. C. Sangster, D. Shvarts, S. Skupsky, Y. Srebro, R. P. J. Town, and C. Stoeckl, Phys. Plasmas **12**, 032702 (2005).

49. V. N. Goncharov, P. McKenty, S. Skupsky, R. Betti, R. L. McCrory, and C. Cherfils-Clérouin, Phys. Plasmas **7**, 5118 (2000).

50. T. R. Boehly, V. N. Goncharov, O. Gotchev, J. P. Knauer, D. D. Meyerhofer, D. Oron, S. P. Regan, Y. Srebro, W. Seka, D. Shvarts, S. Skupsky, and V. A. Smalyuk, Phys. Plasmas **8**, 2331 (2001).

51. K. Anderson and R. Betti, Phys. Plasmas **11**, 5 (2004).

52. S. Skupsky, R. W. Short, T. Kessler, R. S. Craxton, S. Letzring, and J. M. Soures, J. Appl. Phys. **66**, 3456 (1989).

53. W. L. Kruer, *The Physics of Laser-Plasma Interactions*, Frontiers in Physics, Vol. 73, edited by D. Pines (Addison-Wesley, Redwood City, CA, 1988).

54. R. C. Malone, R. L. McCrory, and R. L. Morse, Phys. Rev. Lett. **34**, 721 (1975).

55. L. Spitzer, Jr. and R. Härm, Phys. Rev. **89**, 977 (1953).

56. S. Chapman and T. G. Cowling, *The Mathematical Theory of Non-Uniform Gases; An Account of the Kinetic Theory of Viscosity, Thermal Conduction and Diffusion in Gases*, 3rd. ed. (Cambridge University Press, Cambridge, England, 1970).

57. V. N. Goncharov, T. C. Sangster, P. B. Radha, R. Betti, T. R. Boehly, T. J. B. Collins, R. S. Craxton, J. A. Delettrez, R. Epstein, V. Yu. Glebov, S. X. Hu, I. V. Igumenshchev, J. P. Knauer, S. J. Loucks, J. A. Marozas, F. J. Marshall, R. L. McCrory, P. W. McKenty, D. D. Meyerhofer, S. P. Regan, W. Seka, S. Skupsky, V. A. Smalyuk, J. M. Soures, C. Stoeckl, D. Shvarts, J. A. Frenje, R. D. Petrasso, C. K. Li, F. Séguin, W. Manheimer, and D. G. Colombant, Phys. Plasmas **15**, 056310 (2008).

58. N. A. Krall and A. W. Trivelpiece, *Principles of Plasma Physics* (San Francisco Press, Inc., San Francisco, 1986).

59. V. N. Goncharov and G. Li, Phys. Plasmas **11**, 5680 (2004).

60. V. A. Smalyuk, S. X. Hu, V. N. Goncharov, D. D. Meyerhofer, T. C. Sangster, D. Shvarts, C. Stoeckl, B. Yaakobi, J. A. Frenje, and R. D. Petrasso, Phys. Rev. Lett. **101**, 025002 (2008).

61. V. N. Goncharov, Phys. Rev. Lett. **82**, 2091 (1999).

62. O. Gotchev, V. N. Goncharov, J. P. Knauer, T. R. Boehly, T. J. B. Collins, R. Epstein, P. A. Jaanimagi, and D. D. Meyerhofer, Phys. Rev. Lett. **96**, 115005 (2006).

63. W. Seka, D. H. Edgell, J. P. Knauer, J. F. Myatt, A. V. Maximov, R. W. Short, T. C. Sangster, C. Stoeckl, R. E. Bahr, R. S. Craxton, J. A. Delettrez, V. N. Goncharov, I. V. Igumenshchev, and D. Shvarts, Phys. Plasmas **15**, 056312 (2008).

64. I. V. Igumenshchev, V. N. Goncharov, W. Seka, D. Edgell, and T. R. Boehly, Phys. Plasmas **14**, 092701 (2007).

65. A. Simon, R. W. Short, E. A. Williams, and T. Dewandre, Phys. Fluids **26**, 3107 (1983).

66. C. Stoeckl, V. Yu. Glebov, D. D. Meyerhofer, W. Seka, B. Yaakobi, R. P. J. Town, and J. D. Zuegel, Rev. Sci. Instrum. **72**, 1197 (2001).

67. V. A. Smalyuk, D. Shvarts, R. Betti, J. A. Delettrez, D. H. Edgell, V. Yu. Glebov, V. N. Goncharov, R. L. McCrory, D. D. Meyerhofer, P. B. Radha, S. P. Regan, T. C. Sangster, W. Seka, S. Skupsky, C. Stoeckl, B. Yaakobi, J. A. Frenje, C. K. Li, R. D. Petrasso, and F. H. Séguin, Phys. Rev. Lett. **100**, 185005 (2008).

68. H. N. Kornblum, R. L. Kauffman, and J. A. Smith, Rev. Sci. Instrum. **57**, 2179 (1986); K. M. Campbell *et al*., Rev. Sci. Instrum. **75**, 3768 (2004).

69. T. C. Sangster, V. N. Goncharov, P. B. Radha, V. A. Smalyuk, R. Betti, R. S. Craxton, J. A. Delettrez, D. H. Edgell, V. Yu. Glebov, D. R. Harding, D. Jacobs-Perkins, J. P. Knauer, F. J. Marshall, R. L. McCrory, P. W. McKenty, D. D. Meyerhofer, S. P. Regan, W. Seka, R. W. Short, S. Skupsky, J. M. Soures, C. Stoeckl, B. Yaakobi, D. Shvarts, J. A. Frenje, C. K. Li, R. D. Petrasso, and F. H. Séguin, Phys. Rev. Lett. **100**, 185006 (2008).

70. T. R. Boehly, D. H. Munro, P. M. Celliers, R. E. Olson, D. G. Hicks, V. N. Goncharov, G. W. Collins, H. F. Robey, S. X. Hu, J. A. Marozas, T. C. Sangster, O. L. Landen, and D. D. Meyerhofer, Phys. Plasmas **16**, 056302 (2009).

71. L. M. Barker and R. E. Hollenbach, J. Appl. Phys. **43**, 4669 (1972); P. M. Celliers *et al*., Appl. Phys. Lett. **73**, 1320 (1998).

72. V. N. Goncharov, T. C. Sangster, T. R. Boehly, S. X. Hu, I. V. Igumenshchev, F. J. Marshall, R. L. McCrory, D. D. Meyerhofer, P. B. Radha, W. Seka, S. Skupsky, C. Stoeckl, D. T. Casey, J. A. Frenje, and R. D. Petrasso, Phys. Rev. Lett. **104**, 165001 (2010).

73. T. R. Boehly, V. N. Goncharov, W. Seka, M. A. Barrios, P. M. Celliers, D. G. Hicks, G. W. Collins, S. X. Hu, J. A. Marozas, and D. D. Meyerhofer, Phys. Rev. Lett. **106**, 195005 (2011).

74. I. V. Igumenshchev, D. H. Edgell, V. N. Goncharov, J. A. Delettrez, A. V. Maximov, J. F. Myatt, W. Seka, A. Shvydky, S. Skupsky, and C. Stoeckl, Phys. Plasmas **17**, 122708 (2010).

75. C. J. Randall, J. R. Albritton, and J. J. Thomson, Phys. Fluids **24**, 1474 (1981).

76. S. X. Hu, V. N. Goncharov, P. B. Radha, J. A. Marozas, S. Skupsky, T. R. Boehly, T. C. Sangster, D. D. Meyerhofer, and R. L. McCrory, Phys. Plasmas **17**, 102706 (2010).

Experimental Reduction of Laser Imprinting and Rayleigh–Taylor Growth in Spherically Compressed, Medium-*Z*–Doped Plastic Targets

Introduction

The performance of inertial confinement fusion (ICF) ignition targets[1,2] can be compromised by implosion asymmetries caused by hydrodynamic instabilities. If the target deformation is large enough, it causes mixing of the inner hot area of the target ("hot spot") with the outer colder shell, quenching the fusion reactions. The Rayleigh–Taylor (RT) instability[3] is the primary hydrodynamic instability that develops during the compression of an ICF capsule. Small nonuniformities, seeded at the outer ablation interface by imperfections in the laser irradiation and/or by target surface roughness, are amplified during the acceleration phase, feed through the shell, and seed the RT growth at the inner surface of the shell, which becomes unstable during the stagnation phase.

Because of the paramount importance of this instability to the success of ICF, a great amount of theoretical and experimental research has been devoted to reducing the seed nonuniformities and mitigating the instability growth. To reduce the initial beam imprint and improve the laser radiation uniformity, LLE's OMEGA Laser System[4] employs 60 beams on the surface of a spherical capsule augmented by advanced nonuniformity reduction techniques such as laser-beam two-dimensional (2-D) smoothing by spectral dispersion (SSD),[5] distributed phase plates (DPP's),[6] polarization smoothing (DPR),[7] and temporal shaping of the laser pulse.[8,9]

Techniques for RT mitigation such as coating the target with a high-*Z* material and the shell's volumetric doping with impurities have been studied elsewhere.[10–13] Radiation preheat, enhanced by impurities, reduces the peak density, increases the ablation velocity, and increases the density-gradient scale length; all of which decrease the RT growth rate.[14] Expansion of the ablated doped plasma reduces the laser imprint by increasing the separation between the absorption region and the ablator surface. Experiments with planar targets in the Nike facility demonstrated reduction of the instability for targets coated with thin Pd or Au layers.[11] On OMEGA, coating deuterium-filled plastic spherical capsules with a thin layer of palladium resulted in a twofold increase in the neutron yield.[12] Capsules volumetrically doped with Si and Ge were imploded and their neutron yield doubled as well.[13]

This article presents time-resolved measurements of the RT growth of target areal-density modulations during the spherical implosion of thin plastic shells volume doped with Si and Ge. The targets were imploded with 48 laser beams with a low-adiabat, triple-picket laser pulse shape[8] with an intensity of 4×10^{14} W/cm^2 and a duration of 2.5 ns. To seed the initial nonuniformities, SSD[5] was turned off. The targets were backlit with x rays generated by irradiating a Ta backlighter target with six overlapping beams with the same pulse shape. The x rays passing through the shell were recorded by a fast framing camera,[15] and the density (areal density) perturbation of the shell was inferred from the x-ray absorption.[16] The results indicate that the initial perturbation amplitude at the beginning of the compression phase was reduced by a factor of 2.5±0.5 for CH [4.3% Si] targets and by a factor of 3±0.5 for CH [7.4% Si] and CH [3.9% Ge] targets. At the end of compression the reduction factor in the density modulation became 3±0.5 and 5±0.5, respectively. The instability growth rate was reduced by a factor of 1.5 in doped targets in comparison to undoped ones. These results agree with simulations using the 2-D, radiation–hydrodynamics code *DRACO*.[17]

This article is organized as follows: The experimental configuration is described; the main results are presented; and the discussion is summarized.

Experimental Configuration

The experimental configuration, diagnostics, and data analysis are similar to those described in Refs. 16, 18, and 19. The experimental setup is illustrated in Fig. 130.56. The targets were smooth spherical plastic (CH) shells with an outer diameter of 860 μm and a shell thickness of 22 μm. Pure plastic shells and plastic shells volumetrically doped with Si (4.3% and 7.4%) and Ge (3.9%) were used. The targets were irradiated with 48 OMEGA beams (out of the remaining 12 beams, six beams were used for backlighter irradiation and six beams incident on the diagnostic hole in the target were not used) with

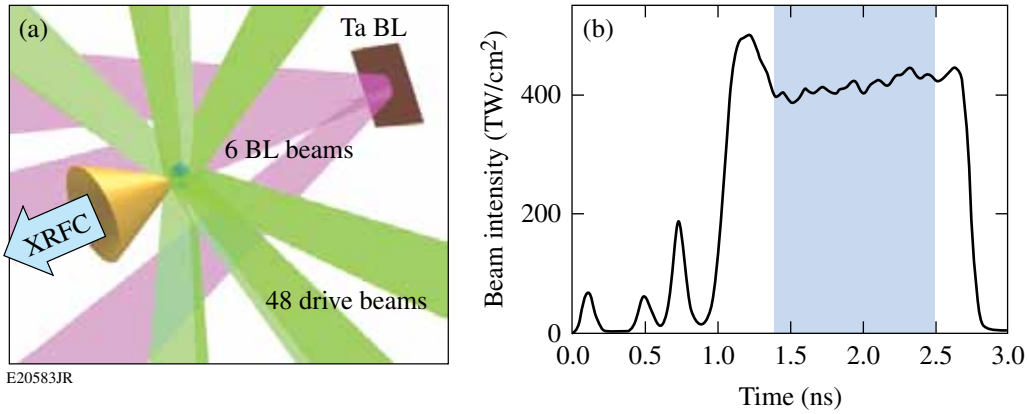

Figure 130.56
(a) Experimental setup. A spherical plastic shell was imploded by 48 beams (green) and the Ta backlighter (BL) was irradiated by 6 beams (violet). The shells had an outer diameter of 860 μm and a thickness of 22 μm. Each shell had a round opening with a diameter of 400 μm into which was inserted a gold cone shield with a tip opening of 400 μm, a height of 3 mm, and an opening angle of 53°. A Ta foil backlighter ($500 \times 500 \times 20$ μm^3) was placed 9 mm from the target. The target was x-ray radiographed by an x-ray framing camera (XRFC) during a time interval of 1.4 ns to 2.5 ns. (b) Laser power shape. The measurement interval from 1.4 ns to 2.5 ns is highlighted.

the triple-picket pulse laser shape at a total energy of 14.4 kJ (300 J per beam) and a main drive time duration of 2.5 ns. To seed the initial nonuniformities, SSD was turned off. The shells were backlit by x rays from a Ta foil backlighter ($500 \times 500 \times 20$ μm^3) placed 9 mm from the target and irradiated with six beams with the same pulse shape.

Similar to Ref. 19, the shells had a round opening with a diameter of 400 μm through which one could monitor the transmission of the x rays through the shell. To shield the opening and the line of sight against direct x-ray exposure from the coronal plasma, a gold cone with a tip opening of 400 μm, a height of 3 mm, and an opening angle of 53° was inserted into the shell's opening.

The x rays, with a peak energy of about 2.8 keV, were recorded with a fast x-ray framing camera (XRFC),[15] and the shell's areal-density variation was inferred from spatial modulation of the x-ray transmission. The camera's 16-pinhole array was situated at 3 cm from the target and the images were recorded with a charge-coupled device (CCD) situated at a distance of 36 cm from the pinhole array. The pinholes had a diameter of 10 μm, and the CCD had 2048×2048 pixels with a size of 18 μm $\times$ 18 μm each. This viewing geometry resulted in a magnification of 12 and provided a field of view at the shell's surface of approximately 400 μm in diameter. The modulation transfer function (MTF) of the imaging system was 50% at a wavelength of approximately 20 μm and 10% at a wavelength of approximately 10 μm, the latter representing the limit of spatial resolution. The framing camera was triggered at 1.4 ns, and 16 images were recorded during a time interval of 1.4 ns to 2.5 ns [highlighted in Fig. 130.56(b)] with a frame-to-frame time interval of ~60 ps.

Experimental Results

1. X-Ray Absorption

Attenuation of x rays with a reasonably narrow spectrum (the measured spectrum had a relative width $\Delta E/E \approx 20\%$) can be described as $I = I_{\mathrm{BL}} \exp\left(-\bar{\mu}\rho\delta\right)$, where ρ and δ are correspondingly the shell's mass density and thickness, $\bar{\mu}$ is the spectrum-averaged mass attenuation coefficient, and I_{BL} is the backlighter intensity. To measure the x-ray absorption in the shell, a series of shots were conducted using undriven shells that had laser-drilled, round, 200-μm-diam openings facing the backlighter. In a single shot, within the 400-μm field of view set by the framing camera, the intensities of x rays passing unattenuated through the 200-μm opening and attenuated through the shell were compared. The mass attenuation coefficient was calculated as $\bar{\mu} = (\rho\delta)^{-1} \ln\left(I_{\mathrm{open}}/I_{\mathrm{shell}}\right)$, where I_{open} and I_{shell} are, respectively, the x-ray intensities passing through the opening and the shell and δ is the shell thickness. The values for the mass attenuation coefficients obtained are given in Table 130.III. To simplify further notations, the bar sign over $\bar{\mu}$ will be omitted.

2. Areal-Density Modulation

For the shell-density modulation measurement, SSD beam smoothing was turned off so the laser beams' speckle created a broadband spectrum of seed-density perturbation at the time of the first picket. The areal-density modulation was determined

Table 130.III: Measured mass attenuation coefficient for undoped (CH) and doped shells. The amount and type of doping were 4.3% Si, 7.4% Si, and 3.9% Ge.

	CH	CH [4.3% Si]	CH [7.4% Si]	CH [3.9% Ge]
(g/cm^3)	1.02	1.07	1.29	1.34
$\bar{\mu}\left(\mathrm{cm}^2/\mathrm{g}\right)$	110±26	317±50	420±67	517±62

by taking a natural logarithm of the modulation of the image intensity I:

$$\ln I = \ln I_{\mathrm{BL}} - \mu\rho r, \tag{1}$$

where I_{BL} is the backlighter intensity. The product $\mu\rho r$ is commonly called optical density (OD). A typical image of the natural ln of XRFC intensity taken at $t = 2.12$ ns is shown in Fig. 130.57. A CH target doped with 3.4% of Si was used.

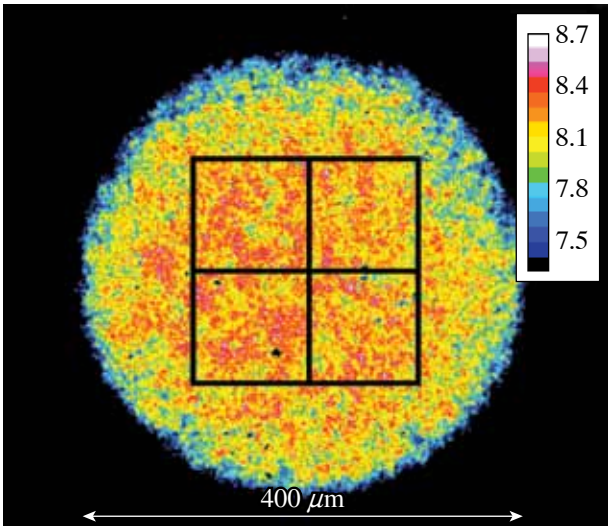

E20584JR

Figure 130.57
An XRFC image of ln(I) for a CH target doped with 4.3% Si taken in t = 2.12 ns. The size of the image is approximately 400 μm. The large 192 × 192-μm^2 square (128 × 128 pixels) was used to calculate modulation rms. The four 96 × 96-μm^2 subregions were used to calculate error.

As the first step of data analysis, high-frequency digital noise in the XRFC signal was reduced by smoothing over two CCD pixels, equivalent to filtering out spatial frequencies higher than 300 mm^{-1}. Large-scale variations of the backlighter intensity were removed using 2-D, fourth-order polynomial fitting to ln$I$ (Ref. 18). Equation (1) describes the remaining fine-scale spatial modulation of the areal density ρr and the optical density (OD) $\mu\rho r$.

One way to characterize the density modulation is to calculate its rms (root-mean-square) value averaged over a certain area. A region of interest (ROI) of 128 × 128 pixels selected in each image corresponds to a 192 × 192-μm^2 area at the shell's surface (Fig. 130.57). Each ROI was subdivided into four smaller ROI's, 64 × 64 pixels each, and the rms calculation (described below) was repeated for each subregion. The standard deviation of results obtained for each subregion is considered as the measurement error represented by the "error bars" in the figures that follow.

The modulation of the backlighter intensity and the shell density are assumed to be uncorrelated. Therefore, the rms of the signal intensity fluctuations is comprised of the rms of the shell's optical-density modulation added in quadrature to the rms of the backlighter modulation:

$$\sigma^2_{\ln I} = \sigma^2_{\mathrm{OD}} + \sigma^2_{\ln I_{\mathrm{BL}}}. \tag{2}$$

The second term in the right-hand side of Eq. (2) can be treated as the background or the noise floor of the measurement and is subtracted from the signal rms to obtain the true rms of the areal-density modulation. Because the backlighter intensity varies with time for each shot and changes from shot to shot, the background subtraction must be done carefully. To scale the background noise with the mean intensity of the transmitted x rays, a series of shots with undriven shells was performed, so the density fluctuation was absent and any fluctuation of the signal resulted from modulation of the backlighter intensity (and statistical noise). This dependence (shown in Fig. 130.58) is fitted by a power fit $\sigma^2_{\ln I_{\mathrm{BL}}} = 0.46\,\bar{I}^{-0.59}$, where $\bar{I}$ is the mean value of the transmitted intensity. Using Eq. (2) the rms of the areal-density modulation is

$$\sigma_{\rho r} = \mu^{-1}\sigma_{\mathrm{OD}} = \mu^{-1}\sqrt{\sigma^2_{\ln I} - 0.46\,\bar{I}^{-0.59}}. \tag{3}$$

The time evolution of the areal-density perturbation for undoped and doped targets is shown in Fig. 130.59 and compared with simulations using the 2-D, radiation–hydrodynamics code *DRACO*[17] (shown as solid lines). Cross-beam energy

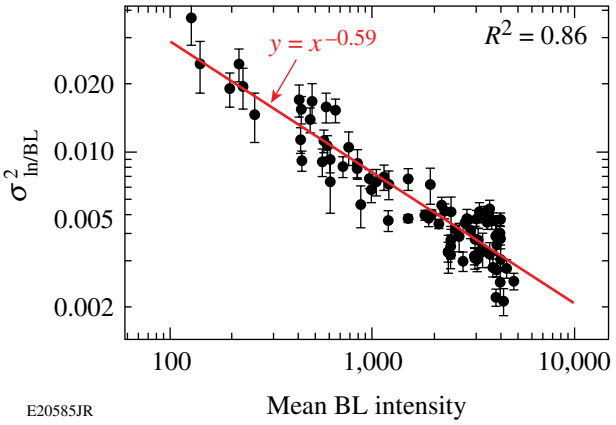

Figure 130.58
Measured rms of backlighter intensity as a function of mean backlighter intensity. A power fit is shown as the red line.

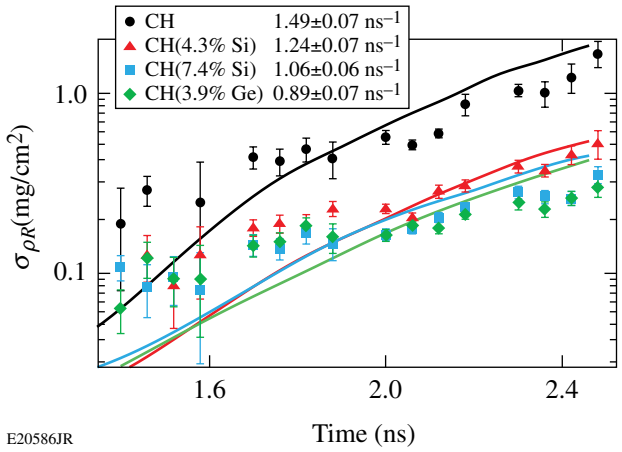

Figure 130.59
The time evolution of the areal-density perturbation amplitude for undoped and doped targets. The symbols are the measured data and the solid lines of the same color are the *DRACO* calculations. The corresponding measured growth rates, calculated as the slopes of the respective exponential fits, are shown in the legend box.

transfer (CBET)[20] was taken into account, providing a slightly reduced drive.

The initial perturbation amplitude at the beginning of the acceleration phase was reduced by a factor of 2.5±0.5 for CH [4.3% Si] targets and by a factor of 3±0.5 for CH [7.4% Si] and CH [3.9% Ge] targets. At the end of compression the reduction factor in the density modulation becomes 3±0.5 and 5±0.5, correspondingly. All targets exhibit exponential perturbation growth, and their growth rates are calculated as the slopes of the respective exponential fits. The doped targets demonstrate a reduction in the growth rate from ≈1.5 ns^{-1} for pure-CH targets to ≈0.9 ns^{-1} for targets doped with 3.9% Ge. The reduction in the growth rate also agrees well with the growth rates for the dominant wavelengths calculated by *DRACO*: 1.46 ns^{-1} for pure-CH targets and 0.92 ns^{-1} for targets doped with 3.9% Ge. A more-detailed comparison can be found in Ref. 21.

The 2-D simulations reproduce the experimental trend of reduction in modulation and the growth rate reasonably well except at the beginning of acceleration when the measured perturbations are somewhat larger than predicted by *DRACO*. The discrepancy could be caused by a small signal amplitude and a large noise contribution at the beginning of acceleration. A similar deviation was observed in earlier spherical compression experiments.[19] At the end of the acceleration phase, the signal is much larger and agreement with numerical simulations is much better.

3. Spectral Composition

To gain insight into the structure of the shell's density modulation, its spatial power spectrum is calculated by performing 2-D, MTF-corrected Fourier decomposition. Typical power spectra for driven and undriven CH spherical targets are shown in Fig. 130.60 as functions of the spatial frequency. As expected, the driven and undriven spectra merge at a frequency corresponding to the MTF-limited resolution. The difference between the two power spectra is the spectrum of the areal-density fluctuation. The power spectra of the optical-density modulation for CH [3.9% Ge] targets at different times are shown in Fig. 130.61. The power spectra calculated by *DRACO* are shown in the same plots and are in reasonable agreement

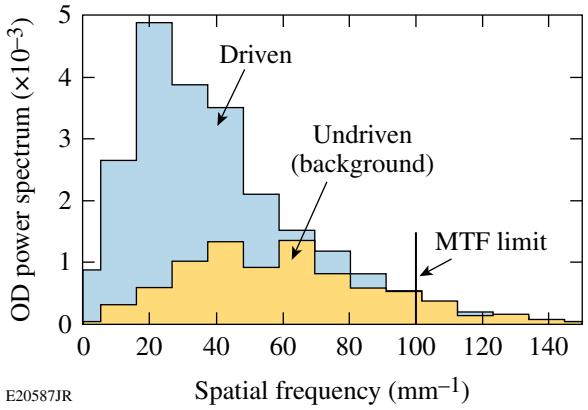

Figure 130.60
Spatial power spectra of optical-density modulation for undriven and driven spherical CH targets at t = 2.4 ns. The undriven target's modulation is caused by the nonuniformities in the backlighter radiation and is subtracted from the driven target's modulation to obtain the modulation in the shell's areal density.

with the measured spectra. The results indicate that during the acceleration phase, the spectral power is shifting from high spatial frequencies (short wavelengths) at the beginning to shorter spatial frequencies (long wavelengths) later in time, similar to what was observed for planar targets.[22,23]

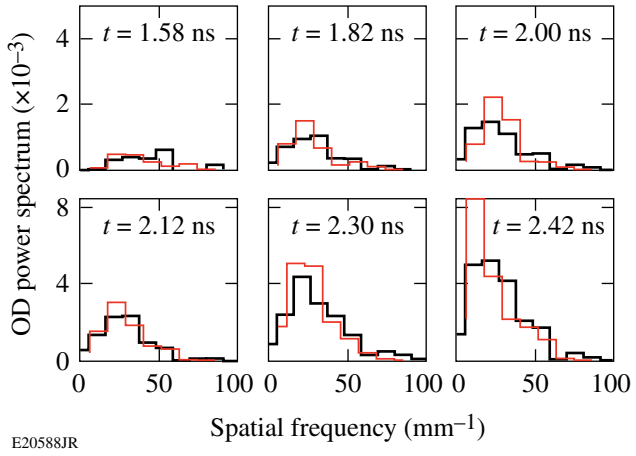

Figure 130.61
Plots of OD power spectra for CH [3.9% Ge] spherical targets at different times. The measured spectra are shown as thick (black) lines and the calculated spectra are shown as thin (red) lines.

Discussion and Conclusions

The experiments have demonstrated that doping plastic shells with a several-percent concentration of medium-Z impurity such as Si or Ge substantially decreases the initial imprint and the growth rate, leading to a significant reduction of the shell's areal-density perturbation. The initial perturbation amplitude at the beginning of the compression phase was reduced by a factor of 2.5±0.5 for CH [4.3% Si] targets and by a factor of 3±0.5 for CH [7.4% Si] and CH [3.9% Ge] targets. At the end of compression the reduction factor in the density modulation becomes 3±0.5 and 5±0.5, correspondingly. The doped targets demonstrate a reduction in the growth rate from ≈1.5 ns^{-1} for pure-CH targets to ≈0.89 ns^{-1} for targets doped with 3.9% Ge. The results agree well with numerical simulations using *DRACO*. From the analysis of the simulation results described in Ref. 21, the main mechanisms of the growth suppression are (a) an increase in the stand-off distance between the laser-absorption region to the ablation front and (b) enhanced coronal radiation preheating in doped shells. The simulations show that the ablation velocity increases from V_a = 5.95 μm/s for CH targets to V_a = 13.5 μm/s for CH [3.9% Ge] targets, which reduces the RT linear growth rate according to the fitting formula[14] $\gamma_k = 0.94\sqrt{kg/(1+kL_n)} - 1.5\,kV_a$, where k is the modulation wave vector, g is the acceleration, and L_n is the gradient length. Ignition-scale direct-drive target designs would require doping only the outer half of the ablator material to prevent excessive radiation preheating of the main fuel. Future experiments will address the imprint reduction effects in shells with the dopant introduced only into the outer layer of the ablator.

ACKNOWLEDGMENT

This work was supported by the U.S. Department of Energy Office of Inertial Confinement Fusion under Cooperative Agreement No. DE-FC52-08NA28302, the University of Rochester, and the New York State Energy Research and Development Authority. The support of DOE does not constitute an endorsement by DOE of the views expressed in this article.

REFERENCES

1. J. D. Lindl, *Inertial Confinement Fusion: The Quest for Ignition and Energy Gain Using Indirect Drive* (Springer-Verlag, New York, 1998).
2. J. D. Lindl, R. L. McCrory, and E. M. Campbell, Phys. Today **45**, 32 (1992).
3. S. Chandrasekhar, in *Hydrodynamic and Hydromagnetic Stability*, International Series of Monographs on Physics (Clarendon Press, Oxford, 1961).
4. T. R. Boehly, D. L. Brown, R. S. Craxton, R. L. Keck, J. P. Knauer, J. H. Kelly, T. J. Kessler, S. A. Kumpan, S. J. Loucks, S. A. Letzring, F. J. Marshall, R. L. McCrory, S. F. B. Morse, W. Seka, J. M. Soures, and C. P. Verdon, Opt. Commun. **133**, 495 (1997).
5. S. Skupsky, R. W. Short, T. Kessler, R. S. Craxton, S. Letzring, and J. M. Soures, J. Appl. Phys. **66**, 3456 (1989).
6. Y. Lin, T. J. Kessler, and G. N. Lawrence, Opt. Lett. **20**, 764 (1995).
7. T. R. Boehly, V. A. Smalyuk, D. D. Meyerhofer, J. P. Knauer, D. K. Bradley, R. S. Craxton, M. J. Guardalben, S. Skupsky, and T. J. Kessler, J. Appl. Phys. **85**, 3444 (1999).
8. V. N. Goncharov, J. P. Knauer, P. W. McKenty, P. B. Radha, T. C. Sangster, S. Skupsky, R. Betti, R. L. McCrory, and D. D. Meyerhofer, Phys. Plasmas **10**, 1906 (2003).
9. J. P. Knauer, K. Anderson, R. Betti, T. J. B. Collins, V. N. Goncharov, P. W. McKenty, D. D. Meyerhofer, P. B. Radha, S. P. Regan, T. C. Sangster, V. A. Smalyuk, J. A. Frenje, C. K. Li, R. D. Petrasso, and F. H. Séguin, Phys. Plasmas **12**, 056306 (2005).
10. N. Ohnishi *et al.*, J. Quant. Spectrosc. Radiat. Transf. **71**, 551 (2001).
11. S. P. Obenschain *et al.*, Phys. Plasmas **9**, 2234 (2002).
12. A. N. Mostovych, D. G. Colombant, M. Karasik, J. P. Knauer, A. J. Schmitt, and J. L. Weaver, Phys. Rev. Lett. **100**, 075002 (2008).
13. V. N. Goncharov, T. C. Sangster, P. B. Radha, R. Betti, T. R. Boehly, T. J. B. Collins, R. S. Craxton, J. A. Delettrez, R. Epstein, V. Yu. Glebov, S. X. Hu, I. V. Igumenshchev, J. P. Knauer, S. J. Loucks, J. A. Marozas, F. J. Marshall, R. L. McCrory, P. W. McKenty, D. D. Meyerhofer, S. P. Regan, W. Seka, S. Skupsky, V. A. Smalyuk, J. M.

Soures, C. Stoeckl, D. Shvarts, J. A. Frenje, R. D. Petrasso, C. K. Li, F. Séguin, W. Manheimer, and D. G. Colombant, Phys. Plasmas **15**, 056310 (2008).

14. R. Betti, V. N. Goncharov, R. L. McCrory, and C. P. Verdon, Phys. Plasmas **5**, 1446 (1998).

15. D. K. Bradley, P. M. Bell, O. L. Landen, J. D. Kilkenny, and J. Oertel, Rev. Sci. Instrum. **66**, 716 (1995).

16. V. A. Smalyuk, T. R. Boehly, L. S. Iwan, T. J. Kessler, J. P. Knauer, F. J. Marshall, D. D. Meyerhofer, C. Stoeckl, B. Yaakobi, and D. K. Bradley, Rev. Sci. Instrum. **72**, 635 (2001).

17. P. B. Radha, V. N. Goncharov, T. J. B. Collins, J. A. Delettrez, Y. Elbaz, V. Yu. Glebov, R. L. Keck, D. E. Keller, J. P. Knauer, J. A. Marozas, F. J. Marshall, P. W. McKenty, D. D. Meyerhofer, S. P. Regan, T. C. Sangster, D. Shvarts, S. Skupsky, Y. Srebro, R. P. J. Town, and C. Stoeckl, Phys. Plasmas **12**, 032702 (2005).

18. J. P. Knauer, R. Betti, D. K. Bradley, T. R. Boehly, T. J. B. Collins, V. N. Goncharov, P. W. McKenty, D. D. Meyerhofer, V. A. Smalyuk, C. P. Verdon, S. G. Glendinning, D. H. Kalantar, and R. G. Watt, Phys. Plasmas **7**, 338 (2000).

19. V. A. Smalyuk, S. X. Hu, J. D. Hager, J. A. Delettrez, D. D. Meyerhofer, T. C. Sangster, and D. Shvarts, Phys. Rev. Lett. **103**, 105001 (2009).

20. I. V. Igumenshchev, D. H. Edgell, V. N. Goncharov, J. A. Delettrez, A. V. Maximov, J. F. Myatt, W. Seka, A. Shvydky, S. Skupsky, and C. Stoeckl, Phys. Plasmas **17**, 122708 (2010).

21. S. X. Hu, G. Fiksel, V. N. Goncharov, S. Skupsky, D. D. Meyerhofer, and V. A. Smalyuk, "Mitigating Laser Imprints in Direct-Drive ICF Implosions with High-*Z* Dopants," submitted to Physical Review Letters.

22. V. A. Smalyuk, T. R. Boehly, D. K. Bradley, V. N. Goncharov, J. A. Delettrez, J. P. Knauer, D. D. Meyerhofer, D. Oron, and D. Shvarts, Phys. Rev. Lett. **81**, 5342 (1998).

23. V. A. Smalyuk, O. Sadot, J. A. Delettrez, D. D. Meyerhofer, S. P. Regan, and T. C. Sangster, Phys. Rev. Lett. **95**, 215001 (2005).

Shell-Trajectory Measurements from Direct-Drive–Implosion Experiments

In direct-drive inertial confinement fusion (ICF), laser beams are focused directly onto a fusion capsule that is imploded to reach thermonuclear ignition. The laser beams ablate the target surface and, through the rocket effect, drive the shell to high velocities. Accurate velocity measurements are critical since the minimum total laser energy for ignition is proportional to V_{imp}^{-6}, where V_{imp} is the implosion velocity.[1] Hydrodynamic models show 10% differences in the velocity (~200 km/s) for typical direct-drive implosions on OMEGA.[2,3] To distinguish among models, the velocity must be measured to within an accuracy of 2%. To achieve this accuracy over 200 ps, the radius and time must be measured to within accuracies of ~1 μm and ~5 ps, respectively.

X-ray radiography has long been applied to ICF experiments[4,5] to measure the shell's velocity, but this technique requires backlighter beams that are taken from the 60 OMEGA drive beams, which reduces the available drive beams, thereby reducing the drive symmetry and efficiency. The accuracy of the radial measurements is often dominated by errors in Abel inversion. X-ray radiography is typically possible only when the laser is turned off because the self-emission adds significant noise to the measurements.

In this article, we present a technique[2,3] where the soft x-ray self-emission of a directly driven target is measured with an x-ray framing camera (XRFC)[6,7] and used to determine the trajectory of the imploding shell. A coronal plasma extending from the ablation surface of the imploding shell to the underdense plasma produces a ring of soft x rays that are imaged to the diagnostic plane. With the proper choice of filtration, a combination of the limb effect and an optically thick shell produces an instrument-limited (~5-μm) emission gradient. This steep gradient and the ability to average over many angles enables one to measure the radius of the imploding shell to an accuracy of better than 1 μm. Combined with the well-characterized XRFC timing (an accuracy of ~5 ps over 200 ps), a 2% velocity measurement is obtained.

The diagnostic obtains 16 radial measurements of the shell during the implosion by imaging the x-ray self-emission of the target integrated along the direction of the diagnostic [Fig. 130.62(a)]. A high contrast is observed between the intensity of the surrounding part and the inner part of the images [Fig. 130.62(a)]. The maximum intensity corresponds to the limb effect produced by the x rays emitted by the coronal plasma. When the cold shell reaches significant convergence, it becomes optically thick, absorbing radiation coming from the back of the sphere, which further enhances the contrast. The radius measurement (corresponding to the position of the sharp intensity gradient at the inner circle) is obtained without knowledge of the path-integrated x-ray emission through plasma and absorption through the shell (i.e., no Abel inversion is required and the measurement is insensitive to the x-ray emission profile).

An array of 16 6-μm-diam pinholes are used to produce 16 x-ray images of the target on a four-strip XRFC.[6,7] For optimum resolution, 12× magnification was used with a distance between the target and the detector plane of 38.1 cm. The resolution of the system was calculated by convolving the pinhole with a multichannel plate (MCP)[8] using the ray-tracing program FRED,[9] resulting in an edge spread function that increases from 10% to 90% over 5 μm. The MCP integration time was 40 ps (Ref. 7). The interstrip timing was 200 ps and determined within 5 ps using the Multi-Terawatt laser.[10]

To determine the optimum filtering, Spect3D[11] was used to post-process hydrodynamic simulations of a 20-μm plastic shell implosion and obtain the x-ray emission at the diagnostic plane. Figure 130.62(b) shows the calculated spectrum, at the detector plane, along a line extending from the center of the target (R = 0) to beyond the coronal plasma ($R \approx 400$ μm). Three distinct x-ray emission regions are observed with varying contrast: (1) for low photon energies (<250 eV), a narrow, ~50-μm emission region with a medium contrast is observed; (2) for medium photon energies (250 to 500 eV), three distinct

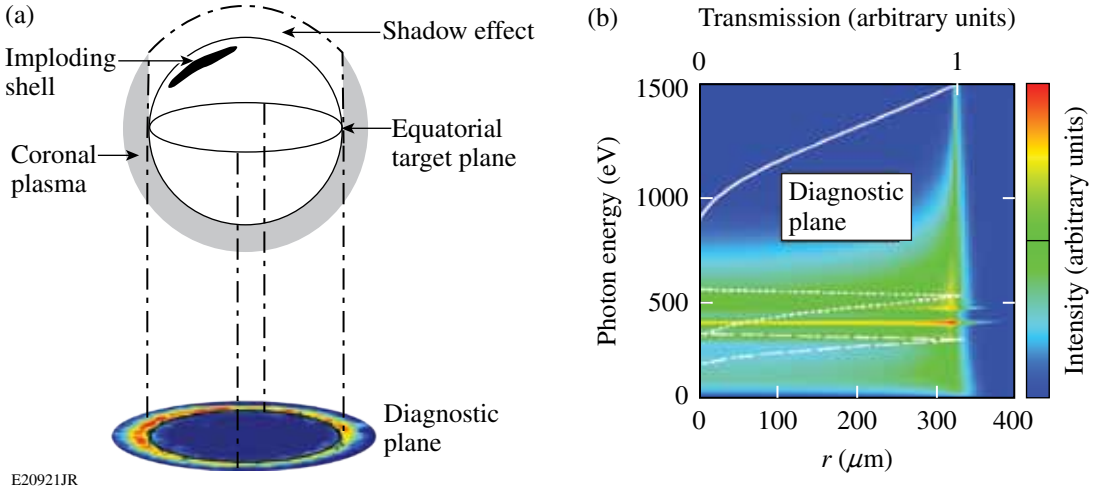

Figure 130.62
(a) Schematic of the limb and shadow effects; (b) simulated spectrally resolved emission at the diagnostic plane integrated along the diagnostic line of sight. The normalized spectral transmission of the low-photon-energy filter (dashed curve), the medium-photon-energy filter (dotted curve), and the high-photon-energy filter (solid curve).

spectral features corresponding to the line emission of the carbon and a low contrast are observed; and (3) for high photon energies (>800 eV), a very thin emission region with a high contrast is observed.

Figure 130.63 shows the results of an experiment performed to investigate the three x-ray-emission regions. The normalized filter transmissions are plotted in Fig. 130.62(b). The low-photon-energy filter used a 3° reflection from Al and transmission through 5-μm-thick parylene N to create a passband filter at ~200 eV. The medium-photon-energy filter used a 3° reflection from Al and transmission through 1-μm-thick vanadium to create a passband filter at ~400 eV. The high-photon-energy filter used 25.4-μm-thick beryllium to create a high-pass filter at ~100 eV. Figure 130.63(c) shows the optimal filtering (with high photon energy) with high contrast, leading to a sharp inner edge to the x-ray emission.

Figure 130.64(a) compares the simulated x-ray emission, spectrally integrated after passing through the high-photon-energy filter, with the corresponding measurements. The location of the middle intensity point in the sharp inner gradient [black curve in Fig. 130.64(c)] is used to determine the shell's radius. After moderate compression, the shell becomes

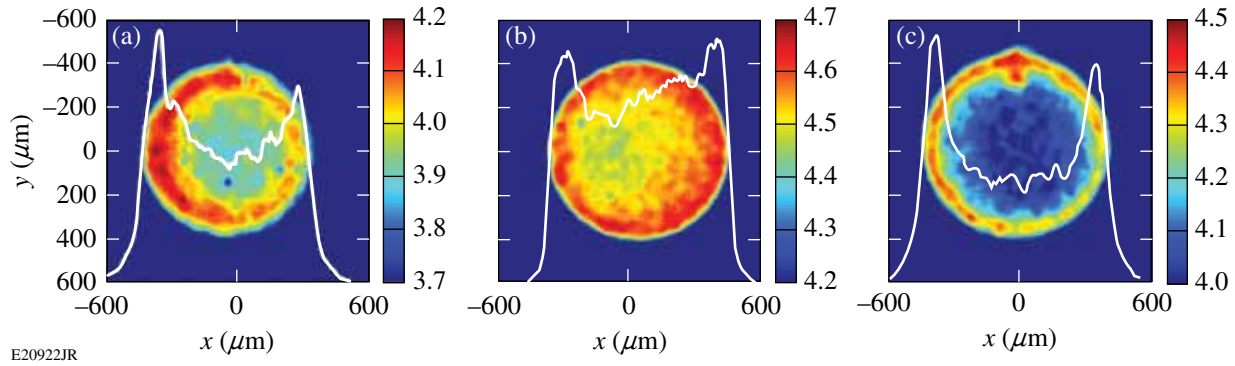

Figure 130.63
Self-emission images and lineouts (white) obtained with the XRFC with a 4× magnification using three different filters: (a) low photon energy; (b) medium photon energy; and (c) high photon energy.

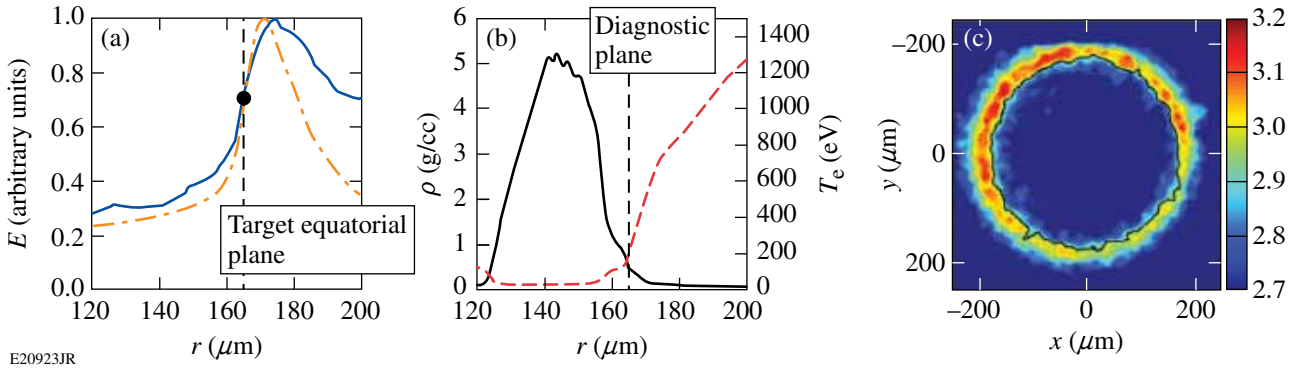

Figure 130.64
(a) Emission at the diagnostic plane obtained by post-processing hydrodynamic simulations and passing through a high-energy filter (orange dashed/dotted line) and experimental emission measured with the XRFC (blue line). The curves are normalized to their maximum values. (b) The calculated electron density (solid black line) and temperature (red dashed line) in the target equatorial plane. (c) Example of an experimental image measured with the XRFC; the black curve corresponds to the curve of the inner gradient, middle intensity point for different angles.

optically thick to x rays above 500 eV, removing the emission from the back of the shell, reducing the signal in the center of the image by a factor of 2, and enhancing the inner gradient [shadow effect represented in Fig. 130.62(a)]. When the laser is on, the middle intensity point corresponds to the ablation surface [Fig. 130.64(b)]. The ablation front follows the mass average point [Fig. 130.65].

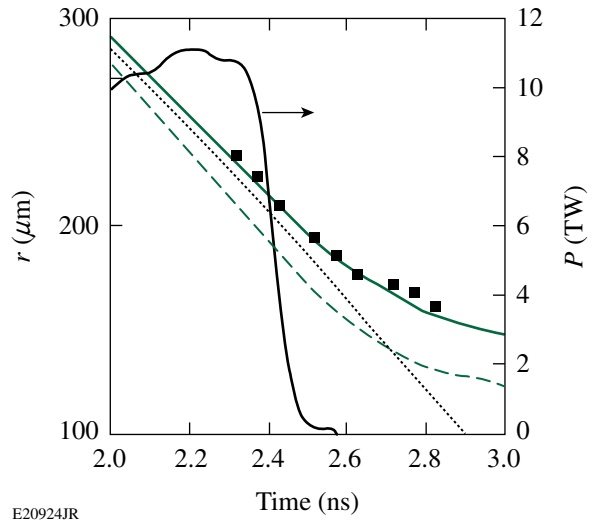

Figure 130.65
Temporal evolution of the laser beams (black solid curve, right axis), shell radius post-processed with Spect3D for simulations with (green solid curve) and without (green dashed curve) cross-beam energy transfer (CBET) and experimental shell trajectories (black squares). For reference, the shell mass averaged point is plotted for the simulations that include CBET (dotted curve). At the end of the laser pulse, the plasma is no longer heated, which results in a decoupling of the x-ray absorption and the shell position.

The accuracy in determining the radius of the middle intensity point is ~3 μm given by σ_n/ρ, where σ_n is the standard deviation of the photon intensity noise and ρ is the slope of the gradient. A standard deviation from the average radius obtained from different angular measurements is 3.5 μm. An accuracy of <1 μm is obtained when averaging the measurements over different angles; this increases the accuracy by a factor of $1/\sqrt{N}$, where N is the number of independent measurements of the radius along different chords passing through the center of the shell (for a shell radius of 150 μm, $\sqrt{N} \sim 10$).

As an example of a use of the diagnostic technique described above, Fig. 130.65 compares the measured and simulated shell trajectories with and without cross-beam energy transfer (CBET) (the experiment is described in detail in Ref. 3). The diagnostic measurements validate the CBET model in *LILAC* simulations.[3] The averaged shell velocity is measured between 2.3 and 2.5 ns to be 200±2 km/s.

ACKNOWLEDGMENT

This work was supported by the U.S. Department of Energy Office of Inertial Confinement Fusion under Cooperative Agreement No. DE-FC52-08NA28302, the University of Rochester, and the New York State Energy Research and Development Authority. The support of DOE does not constitute an endorsement by DOE of the views expressed in this article.

REFERENCES

1. M. C. Herrmann, M. Tabak, and J. D. Lindl, Nucl. Fusion **41**, 99 (2001).

2. D. H. Froula, I. V. Igumenshchev, D. T. Michel, D. H. Edgell, R. Follett, V. Yu. Glebov, V. N. Goncharov, J. Kwiatkowski, F. J. Marshall, P. B. Radha, W. Seka, C. Sorce, S. Stagnitto, C. Stoeckl, and T. C. Sangster, Phys. Rev. Lett. **108**, 125003 (2012).

3. I. V. Igumenshchev, W. Seka, D. H. Edgell, D. T. Michel, D. H. Froula, V. N. Goncharov, R. S. Craxton, L. Divol, R. Follett, J. H. Kelly, T. Z. Kosc, P. Michel, R. L. McCrory, A. V. Maximov, D. D. Meyerhofer, J. F. Myatt, T. C. Sangster, A. Shvydky, S. Skupsky, and C. Stoeckl, "Crossed-Beam Energy Transfer in Direct-Drive Implosions," to be published in Physics of Plasmas.

4. D. G. Hicks, B. K. Spears, D. G. Braun, R. E. Olson, C. M. Sorce, P. M. Celliers, G. W. Collins, and O. L. Landen, Phys. Plasmas **17**, 102703 (2010).

5. F. J. Marshall, P. W. McKenty, J. A. Delettrez, R. Epstein, J. P. Knauer, V. A. Smalyuk, J. A. Frenje, C. K. Li, R. D. Petrasso, F. H. Séguin, and R. C. Mancini, Phys. Rev. Lett. **102**, 185004 (2009).

6. D. K. Bradley, P. M. Bell, J. D. Kilkenny, R. Hanks, O. Landen, P. A. Jaanimagi, P. W. McKenty, and C. P. Verdon, Rev. Sci. Instrum. **63**, 4813 (1992).

7. D. K. Bradley *et al*., Rev. Sci. Instrum. **66**, 716 (1995).

8. V. A. Smalyuk, T. R. Boehly, D. K. Bradley, J. P. Knauer, and D. D. Meyerhofer, Rev. Sci. Instrum. **70**, 647 (1999).

9. Photon Engineering, accessed 9 April 2012, http://www.photonengr.com.

10. V. Bagnoud, I. A. Begishev, M. J. Guardalben, J. Puth, and J. D. Zuegel, Opt. Lett. **30**, 1843 (2005).

11. J. J. MacFarlane *et al*., High Energy Density Phys. **3**, 181 (2007).

Spherical Shock-Ignition Experiments with the 40 + 20-Beam Configuration on OMEGA

Introduction

Shock ignition (SI)[1] is a promising new concept in direct-drive inertial confinement fusion (ICF) that achieves thermonuclear ignition and burn by a strong focusing shock wave in a precompressed DT shell.[2] Shock ignition, as described in Ref. 1, is a two-step scheme designed to enhance the hot-spot compression with respect to the single-step conventional hot-spot ignition.[3] SI uses a moderate-intensity assembly laser pulse followed by a subnanosecond high-intensity spike that launches a strong shock wave (the ignitor shock) into the imploding shell. It is important to emphasize that SI does not use a shock wave to directly ignite the dense fuel;[4] instead, it relies on the collision of the ignitor and the rebound shock waves at the inner shell surface to raise the hot-spot pressure.[1] A non-isobaric fuel assembly with a centrally peaked pressure profile makes SI more energy efficient by lowering the ignition threshold compared to isobaric assemblies.[1] Thick-shell targets containing more fuel can be compressed on a low adiabat with a low implosion velocity, which promises high fusion gains[1,2,5–7] at moderate laser energies. One-dimensional (1-D) simulations[7,8] have described igniting SI designs with as low as ~300 kJ of total laser energy. The SI requirements for laser pulse shaping are more demanding than in conventional hot-spot–ignition designs but are still within the pulse-shaping capabilities of currently operating laser systems like the National Ignition Facility (NIF).[9] Proof-of-principle experiments on the NIF were recently proposed;[10] also, SI is considered to be a viable option[8] for the European direct-drive HiPER project.[11]

The intensity of the spike pulse is expected to be a few times of 10^{15} W/cm^2. At these high intensities, parametric plasma instabilities[12] such as stimulated Brillouin scattering (SBS), stimulated Raman scattering (SRS), and the two-plasmon-decay (TPD) instability are of concern in an ignition target design for two reasons: The instabilities generate energetic electrons that might preheat the shell with the consequence of reducing the final core compression and they increase the back-reflection of the laser light from the target, degrading the laser-energy coupling to the capsule. SI designs typically apply lower laser intensity during the main part of the drive than in hot-spot designs, so these issues might be less important during the early compression phase. Strong growth of laser–plasma instabilities and significant transfer of laser energy to hot electrons are expected during the high-intensity ignitor spike. The areal density increases during the implosion, and if the range of the hot electrons is less than the shell thickness, the electrons are stopped in the outer regions of the shell and do not considerably increase the adiabat of the inner part of the shell.[13] The hot electrons might then be advantageous for SI because they improve the shock strength. The effect of hot electrons on a NIF-scale SI target[13] was modeled in 1-D for a marginal igniting target using a multigroup diffusion model[14] for the hot electrons. The ignition (time) window for shock launching is considerably wider when the effects of moderate-energy hot electrons are included. The simulations[13] show that a NIF-scale target can efficiently stop up to 150-keV electrons that are generated during the spike pulse. Hot electrons can be beneficial for SI as long as their range is shorter than the shell's thickness. Important parameters are therefore the hot-electron temperature, the amount of laser energy that is transferred into electrons, and the time of generation.

This article presents SI experiments on the OMEGA laser[15] that use a novel beam configuration called the 40 + 20-beam configuration. Preliminary results with this configuration are discussed in Ref. 16. It uses 40 of the 60 OMEGA beams to implode the target with a low-intensity laser pulse, and the remaining 20 beams are tightly focused to launch a late shock into the imploding shell. Compared to the highly symmetric 60-beam implosions, irradiation nonuniformity with normal-incidence beams is higher in the 40 + 20 configuration. The implosion performance was also studied with a beam configuration with repointed beams. The experiments demonstrated significant improvement in implosion performance (higher neutron yield, higher areal density, and rounder core in x-ray images) with repointed beams. Two-dimensional (2-D) hydrodynamic simulations were performed for the repointed beam configuration. A similar concept, using a dedicated group of beams with a low-intensity pulse to implode the capsule and a second group of beams with a short high-intensity pulse for the

ignitor shock wave, might be implemented on the NIF.[17] The 40 + 20 configuration makes it possible to study high-intensity coupling on OMEGA and to measure hot-electron production and laser backscattering for intensities that are SI relevant. Previous spherical target SI experiments[18] on OMEGA studied the fuel assembly with 60-beam symmetric implosions. In those experiments, the shock wave was launched by a spike at the end of the pulse on all 60 beams with a maximum intensity of $\sim 7 \times 10^{14}$ W/cm^2. OMEGA cannot produce the requisite SI intensity with a compression pulse using the symmetric 60-beam configuration on a standard target because it leads to intensities that are too low to study laser–plasma instabilities. Switching to the 40 + 20-beam configuration allows one to use two separate pulse shapes with high-intensity beams tightly focused to reach intensities up to $\sim 8 \times 10^{15}$ W/cm^2. While the surface-averaged intensity is still rather low ($\sim 9 \times 10^{14}$ W/cm^2), the single-beam intensities are sufficiently high to study laser–plasma interactions at shock-ignition–relevant intensities. The objectives of this work are to study the implosion performance in the 40 + 20-beam configuration, the coupling of laser energy from high-intensity beams into a spherically imploding capsule, and the laser–plasma instabilities at SI-relevant laser intensities.

This article is organized as follows: the beam configurations are presented; the targets, laser pulse shapes, and diagnostics are described; the areal-density measurements and neutron measurements, including 2-D hydrodynamic simulations, are discussed; and the time-resolved hard x-ray and laser backscatter measurements are presented.

Beam Configurations

OMEGA is a 60-beam laser that was built for direct-drive experiments operating at the third harmonic (λ = 351 nm) of the Nd:glass laser wavelength. The 60 beams are symmetrically distributed around the target chamber in a soccer-ball geometry with the beams located at the vertices of hexagons and pentagons. OMEGA consists of three laser legs, each feeding two clusters with ten beams per cluster; leg 1 feeds clusters 1 and 4, leg 2 feeds clusters 2 and 5, and leg 3 feeds clusters 3 and 6. It is possible to use two independent pulse shapes: one pulse shape in one of the legs and the other pulse shape in the other two legs. For SI studies with a spherical target, this opens up the opportunity to use two separate pulse shapes with independent control over the two beam groups. One pulse shape in two legs implodes the capsule and a short high-intensity spike pulse in the third leg drives a late shock. Two different beam-pointing configurations were used; they are designated A and B in the following configurations. Configuration A used clusters 1, 3, 4, and 6 for the drive and clusters 2 and 5 for the spike with all beams pointed to target center. The configuration with this particular choice of clusters resulted in significant target illumination nonuniformity because of the spatial and temporal separation between both beam groups. The pattern of the 40 drive beams is not as regular as in a standard 60-beam implosion, and, assuming perfect power balance, the irradiation nonuniformity was calculated to be ~11% root-mean-square (rms) variation compared to less than ~1% in a standard 60-beam spherically symmetric case.[19] A beam profile with a super-Gaussian shape given by $I(r_\mu) = I_0 \exp\left[-(r_\mu/352)^{4.1}\right]$ (where r_μ is the radius in microns) was assumed in the 40 drive beams. The focal spot for the 40 drive beams is obtained with distributed phase plates[20] with a super-Gaussian intensity distribution of fourth order, and the laser light was smoothed with polarization smoothing.[21] In configuration B, clusters 1, 2, 4, and 5 were used for the drive and clusters 3 and 6 for the spike. The irradiation nonuniformity in the 40 drive beams was ~7% rms in this configuration, which was lower than in the previous configuration. It was further improved to ~3% rms by repointing the beams. Most of the 40 drive beams were moved individually, as shown in Fig. 130.66, with the arrows representing direction and amount of shift for each beam.

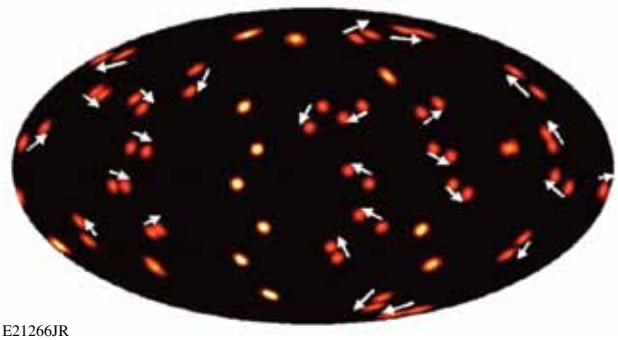

Figure 130.66
Aitoff representation of the original beam positions and repointed positions of the 40 drive beams. Arrows indicate the direction and amount of displacement. Some beams were not moved. The configuration with repointed beams is referred to as configuration B, while in configuration A all beams are pointed to target center.

Figure 130.67 shows the intensity variation of the 40 repointed drive beams in (a) an Aitoff presentation and (b) a 3-D rendering. The illumination pattern in Fig. 130.67(b) was averaged over the azimuthal angle, which resulted in the axisymmetric illumination pattern shown in Fig. 130.67(c) that was used as input in 2-D cylindrical symmetric simulations with the radiation–hydrodynamic code CHIC.[22] Figure 130.68 shows the laser-intensity variation of the axisymmetric irradia-

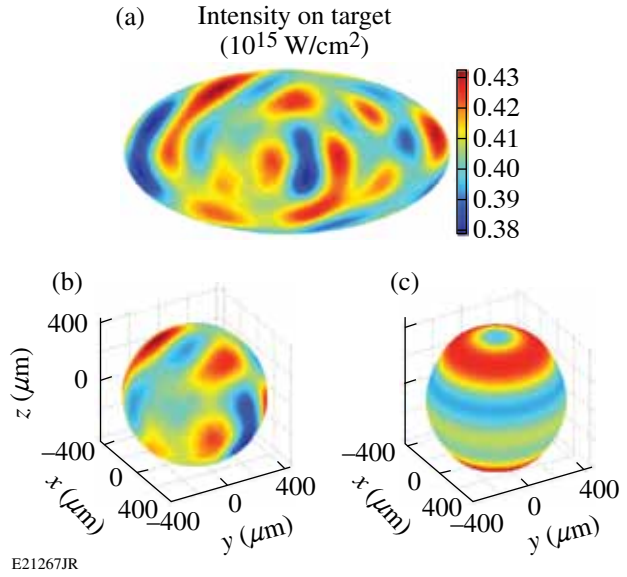

Figure 130.67
Intensity variation of 40 repointed drive beams (configuration B) in (a) an Aitoff representation and (b) a 3-D rendering. (c) The azimuthally averaged intensity distribution was used as input in 2-D cylindrical symmetric hydrodynamic simulations with the code CHIC.[22]

tion pattern versus polar angle and a Legendre-mode analysis, indicating that the modes $\ell = 2$, 4, 6, and 7 are dominant. In addition, a robustness study with respect to power imbalance was performed. A power imbalance of about ±8% on the illumination was assumed. From six random power configurations, the results show that the nonuniformity increases by ~25% to ~3.5% rms. Besides the Legendre mode $\ell = 2$, the odd modes 1 and 3 are considerably increased in the presence of power imbalance. Moreover, the maximum of the $\ell = 1$ amplitude is equivalent to a target offset of 5 μm, which further indicates that the 40-beam configuration is sensitive to power imbalance.

To achieve best symmetry in configuration B, a beam repointing from target center was also performed for the 20 spike beams, as shown in Fig. 130.69. The 20 beams were moved to the vertices of a dodecahedron pattern. This means that the beams were repointed on four rings at the following polar angles: 37.4°, 79.2°, 100.8°, and 142.6°. Figure 130.69 shows that each of the 20 spike beams was moved individually, where the arrows represent the direction and the amount of shift of each beam. Significantly larger shifts were used in the 20 spike beams.

The single-beam laser intensity of the 20 spike beams on target was controlled by changing the radial beam's focal position. It is important to make a clear distinction between the average intensity $\langle I_{\text{spike}} \rangle$ and the single-beam intensity (SBI) of the spike beams on the capsule surface. The SBI ranges from $I_{\text{spike}} \sim 0.5 \times 10^{15}$ to $\sim 8 \times 10^{15}$ W/cm^2, while the average intensity on target is not affected as much by the focusing and is $\langle I_{\text{spike}} \rangle \sim 0.5 \times 10^{15}$ W/cm^2. The average intensity is the relevant quantity to determine the shock strength and the

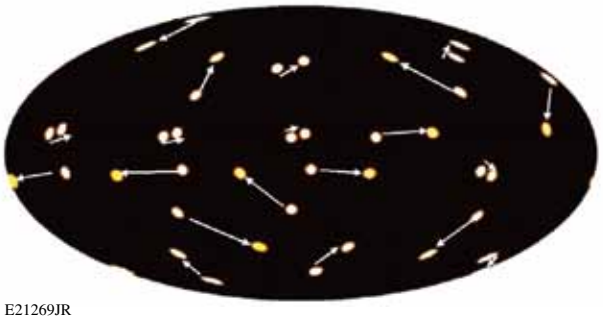

Figure 130.69
Aitoff representation of the original beam positions and repointed positions of the 20 spike beams. Arrows indicate the direction and amount of displacement.

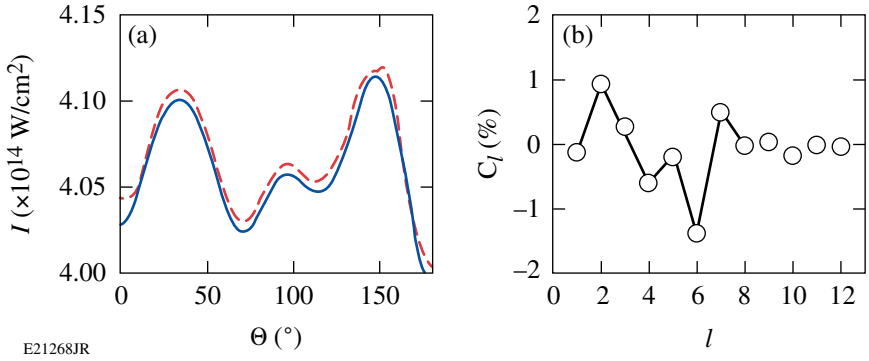

Figure 130.68
Laser-intensity variation on target of the axisymmetric irradiation pattern from Fig. 130.67(c) as a function of (a) polar angle (solid curve—initial irradiation; dashed curve—Legendre polynomial representation) and (b) Legendre-mode analysis of the pattern for ℓ below 12. Dominant modes are $\ell = 2$, 4, 6, and 7.

equivalent pressure from the spike beams. The nominal single-beam laser intensity is quoted for vacuum at the location of the critical-density plasma surface at the time when the spike pulse was launched during the implosion as calculated by simulations with the radiation–hydrodynamic codes *LILAC*[14] and CHIC. The distance from the critical-density surface to the capsule center was ~0.3 mm at 2.7 ns. At best focus, the diameter of the spike beams was estimated with ~80 μm, which gave an SBI of ~8×10^{15} W/cm^2 in vacuum. The actual intensity might be different as a result of plasma effects. Figure 130.70 shows the intensity pattern of the 20 spike beams for the following spot sizes: ~140 μm (SBI ~ 2.5×10^{15} W/cm^2), ~220 μm (SBI ~ 1×10^{15} W/cm^2), and ~580 μm (SBI ~ 0.5×10^{15} W/cm^2) without the drive beams. The foci of the 20 spike beams did not overlap at the critical-density surface for most lens positions. Only at the lowest intensity for an ~580-μm spot size did the beams partially overlapped. This created local peak intensities of ~0.7×10^{15} W/cm^2 in some regions where several beams overlapped. Except for some shots with small-spot phase plates,[23] phase plates were not used in the spike beams for most of the shots.

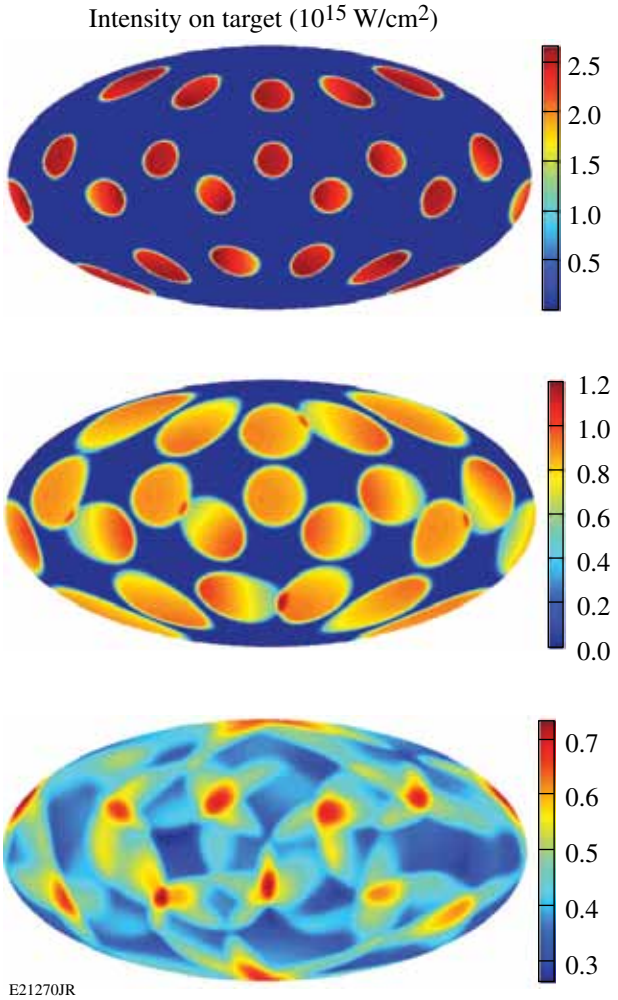

Figure 130.70
Intensity variations of the 20 repointed spike beams (configuration B), on the dodecahedron vertices in an Aitoff representation. Different lens defocus positions resulted in single-beam spike intensities of ~2.5×10^{15} W/cm^2, ~1×10^{15} W/cm^2, and ~0.5×10^{15} W/cm^2, respectively (from top to bottom).

Targets, Pulse Shapes, and Diagnostics

The targets were ~34- to 36-μm-thick, ~430-μm-outer-radius, deuterated plastic shells coated outside with a 0.1-μm layer of aluminum. They were filled with D_2 gas at a pressure of ~25 atm. The capsules were imploded on a low adiabat ($\alpha \sim$ 2.4) with a drive pulse shape that is shown for a single beam by the solid curve in Fig. 130.71. The adiabat α is defined as the ratio of the plasma pressure to the Fermi pressure of a degenerate electron gas. The pulse shape contained ~14 kJ of laser energy in 40 beams. Standard 60-beam implosions with the same pulse shape and similar targets, but higher drive energy, are discussed in Refs. 18 and 24. The drive pulse consists of an ~100-ps full-width-at-half-maximum (FWHM) picket pulse preceding a shaped main drive portion with a total duration of 2.7 ns. The 20 spike beams delivered a total energy of ~5 kJ on target and used an ~600-ps FWHM square pulse (dashed curve in Fig. 130.71).

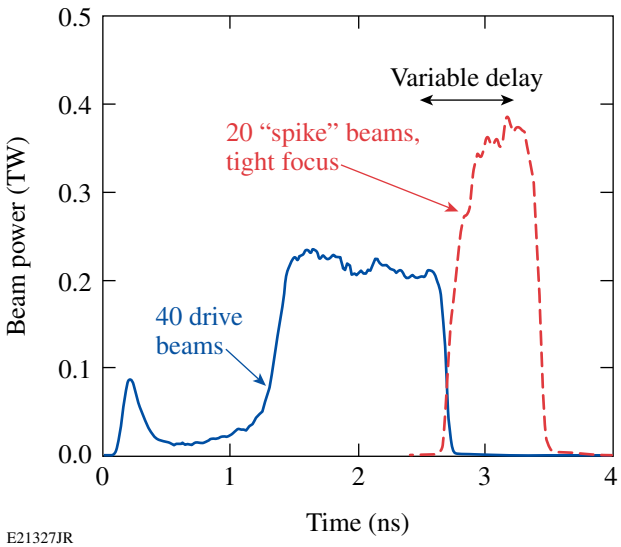

Figure 130.71
Single-beam power versus time of the drive-pulse shape (solid) for the 40 beams and the high-intensity pulse (dashed) for the 20 spike beams. Beam delay and spike intensity were varied.

The experimental observables were the spatially resolved x-ray emission from pinhole cameras,[25] the neutron yield,[26] the neutron-rate,[27] the backscattered laser energy,[28] the hard x-ray signal,[29] and the neutron-rate–averaged areal density (ρR).[30] The laser light reflected back from the imploded capsule was measured from two adjacent beam ports (a spike-beam and a drive-beam port), which were equipped with a full-aperture backscatter station (FABS).[28] Time-resolved spectra were recorded by two streaked spectrometers covering the wavelength ranges of 351±3 nm for SBS and 450 to 700 nm for SRS. The total backscattered energy in either of these spectral ranges was measured by calorimeters with an uncertainty of ±10%. The hard x-ray (HXR) signals were measured with ~100-ps temporal resolution by the HXR detector with four channels measuring x rays >20, >40, >60, and >80 keV, respectively.[29] The HXR measurements were used to infer the hot-electron temperature.[29]

Areal-Density Measurements and CHIC Simulations

Close to stagnation of the imploded shell, secondary deuterium fusion reactions in the central hot-spot region produce protons that pass through the dense, cold shell, where they lose energy. Measurement of the downshifted kinetic-energy spectrum provides information about the shell's areal density. This technique makes it possible to accurately reconstruct the proton spectrum and to infer ρR, as discussed in detail in Ref. 30. Figure 130.72(a) shows two spectra taken at an SBI of $\sim 3 \times 10^{15}$ W/cm^2. Each spectrum represents the average over several spectra from various lines of sight. The solid histogram is from an implosion with configuration A and the dashed histogram is from configuration B. Lower proton energy indicates a higher ρR. The corresponding ρR from the different lines of sight versus the target chamber polar angle is plotted in Fig. 130.72(b) with cross and circle symbols. The corresponding lines represent the average value. The ρR is almost a factor of 2 higher with configuration B, showing that repointing the beams significantly improved the implosion performance. The ρR varies with the observation direction, indicating considerable modulation in ρR, which is primarily due to illumination nonuniformities.

Two-dimensional simulations with the code CHIC studied the density and temperature modulations of the imploded capsule at stagnation for configuration B [see Fig. 130.73(a)]. Figure 130.73(b) shows simulated (curves) and measured (circles) areal density as a function of the polar angle. The black solid curve is from the 2-D simulation while the dashed line is from a 1-D simulation. The squares mark the 2-D–simulated values at those polar angles used in the measurement. The

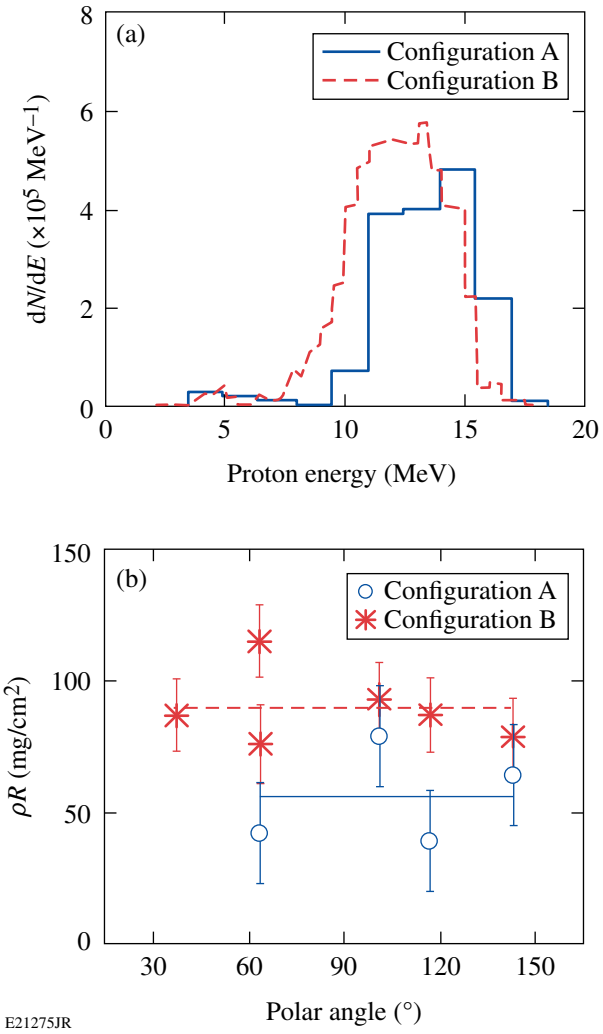

Figure 130.72
(a) Secondary proton spectra from an implosion with beam configuration A (solid) and for configuration B (dashed) under similar conditions with SBI ~ 3×10^{15} W/cm^2 and spike onset at ~2.3 ns. A lower proton energy spectrum indicates higher areal density. (b) Corresponding neutron-rate–averaged areal densities from different lines of sight are plotted versus the target chamber polar angle.

dotted line is the averaged experimental value. Note that the simulation values are higher because they represent ρR at peak neutron production, while the experimental values are temporally averaged over the neutron-production rate.

The ρR was measured for various onsets of the spike beams with respect to the start of the drive pulse and various SBI. The spike onset was varied from 2.1 to 2.8 ns (see Fig. 130.71). Figure 130.74 shows the measured angular-averaged ρR. The symbols represent 40 + 20 implosions, and the line in Fig. 130.74(b) represents a 40-beam implosion with no spike and ~14 kJ of

energy. In configuration A [Fig. 130.74(a)], the proton yield from implosions with only 40 beams was too low to provide a ρR measurement. The ρR values are consistently higher in configuration B [see Fig. 130.74(b)], showing improved implosion performance. For SBI > 1.5×10^{15} W/cm^2 there is a tendency of lower ρR for early spike onset. The lower ρR is correlated with a higher hard x-ray signal [see Fig. 130.74(c)], which could indicate preheating by hot electrons.

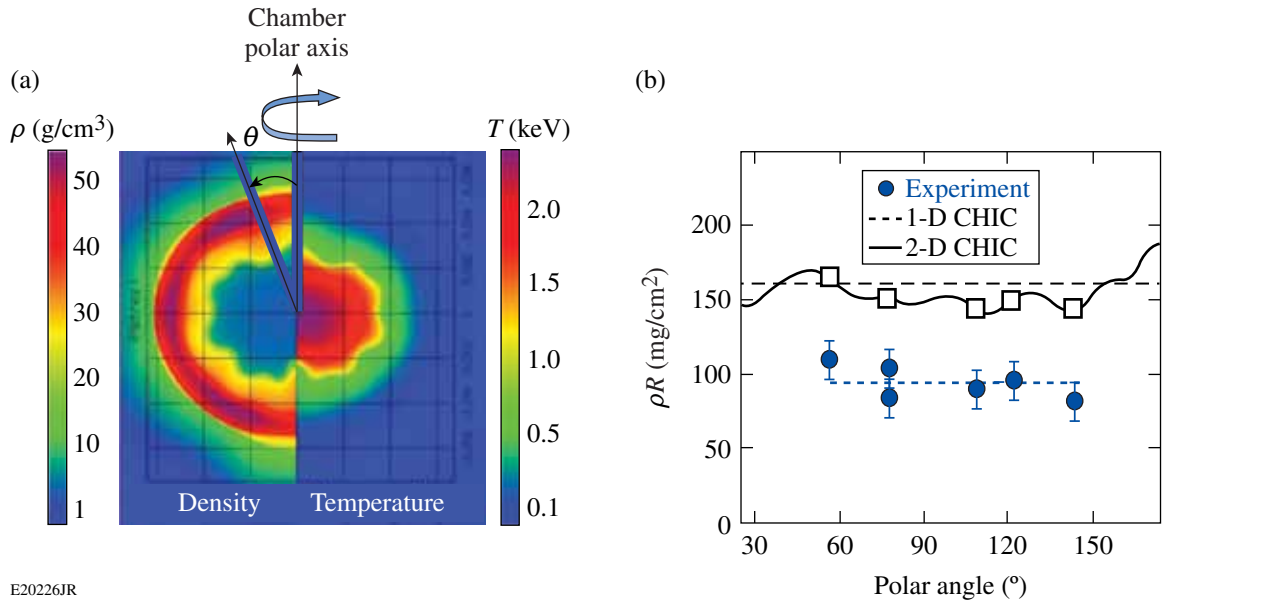

Figure 130.73
Two-dimensional (2-D) CHIC[22] simulations show significant modulations in the compressed shell. (a) Simulated density and temperature map of a 40 + 20-beam implosion close to stagnation. (b) Simulated (solid and dashed curves, squares) and measured areal density (circles) as functions of the polar angle. The SBI was ~3×10^{15} W/cm^2 and spike onset was at ~2.6 ns.

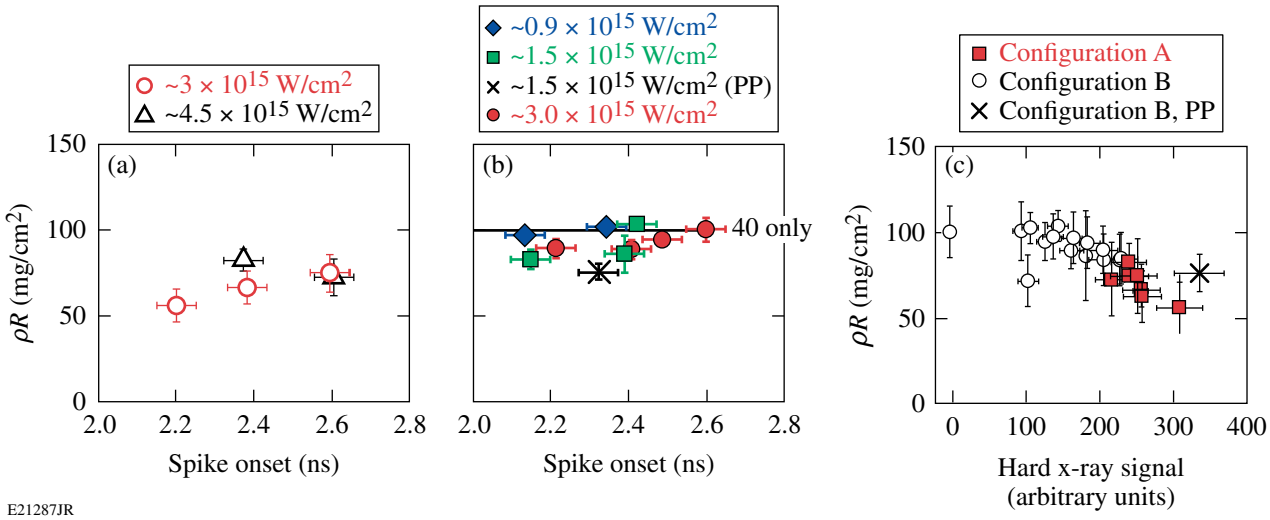

Figure 130.74
Measured areal densities from 40 + 20 implosions for (a) configuration A, (b) configuration B, and (c) both configurations versus the measured hard x-ray signal. The solid line in (b) represents the measured areal density of a 40-beam implosion. The spike onset and SBI were varied. The solid squares and open circles in (c) represent the measurements in configurations A and B, respectively, and × represents the measurement with phase plates in the spike beams in configuration B.

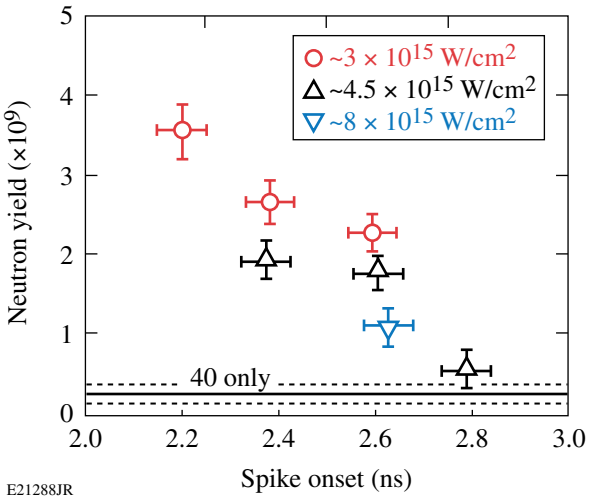

Figure 130.75
Measured neutron yield in 40 + 20-beam implosions for various spike-onset times and single-beam intensities for configuration A.

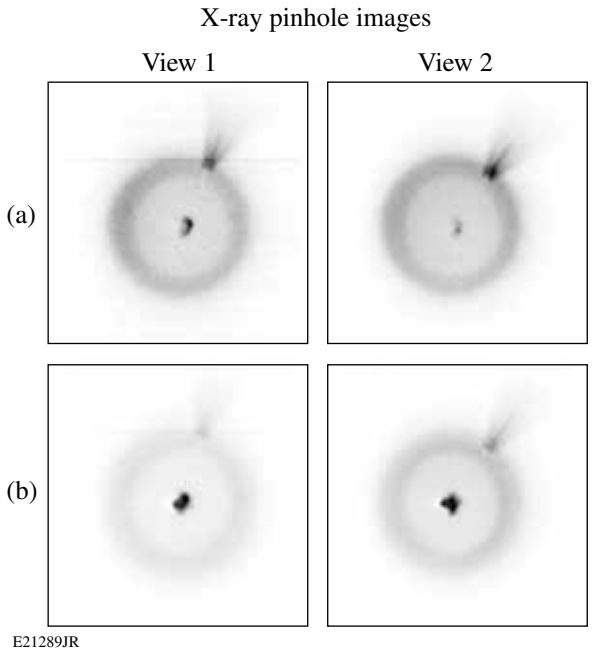

Figure 130.76
Measured time-integrated x-ray pinhole images for configuration A. Two views from different directions are shown in each row. (a) The top row represents a 40-beam implosion and (b) the lower row a 40 + 20 implosion. The V-shaped feature in the top right is the emission from the target stalk.

Neutron Measurements and CHIC Simulations

Figure 130.75 shows the measured neutron yield for beam configuration A for various spike-onset times and single-beam intensities. A maximum yield of ~3.5×10^9 was measured for the shortest time delay. Two reference implosions with only the 40 drive beams produced neutron yields of 1.4×10^8 and 3.7×10^8; the solid line in Fig. 130.75 represents the average of those yields. The low yield of the 40-beam implosion is caused by the large illumination nonuniformity in configuration A, which was also seen in a strongly perturbed core in x-ray pinhole camera images. The x-ray images[25] from two different views are shown in Fig. 130.76(a). The recorded x-ray emission is from the 2- to 7-keV range and comes from the outer-shell region, the target stalk, and the core region. Adding the spike beams mitigated the nonuniformities, leading to less core distortions [Fig. 130.76(b)] and an ~14× increase in neutron yield for the shortest spike onset. This shows that a significant amount of the energy from the high-intensity beams was coupled into the capsule. The large illumination nonuniformity in configuration A was partially mitigated by the spike beams, which led to the recovery of the neutron yield. At high intensities, the experimental yield may be affected by a high plasma reflectivity (see **Backscatter Measurements**, p. 124), which lowers the coupling efficiency. With later spike onset, there was less temporal overlap between the drive and the spike pulse and a lower neutron signal was measured. The drive and spike pulses were completely separated at 2.8 ns, which is when the lowest neutron yield was measured in the 40 + 20 implosions. For configuration A, neutron yields were strongly affected by 3-D effects in a highly perturbed core.

Similar implosions were performed with configuration B, where the illumination uniformity was significantly improved. This was demonstrated by a much rounder core in the x-ray pinhole camera images [compare Fig. 130.77(a) to Fig. 130.76(a)]. Adding the 20 spike beams did not further improve the roundness of the core emission. Figures 130.77(b) and 130.77(c) show corresponding images using (b) no phase plates and (c) small spot phase plates in the 20 spike beams, respectively. Core distortions are even slightly worse than in Fig. 130.77(a). A stronger x-ray emission is observed in Fig. 130.77(c) with phase plates. Figure 130.78 shows the (a) measured and (b) simulated neutron yields for these implosions. Implosions with repointed 40 drive beams produced neutron yields of ~1.5×10^9 [solid line in Fig. 130.78(a)], which is a factor of ~6 higher than in the implosions where beams were pointed to target center. Adding the 20 spike beams, and therefore more energy on target, enhances the yield further by a factor of up to 2.3, with a trend of slightly lower yields at longer times. With 20 spike beams, the overall neutron yield is very similar to configuration A. The neutron yield shows no significant dependence on the spike intensity. A similar trend is observed in the predicted neutron yield from 1-D CHIC simulations [Fig. 130.78(b)]. There the enhancement is up to a factor of ~3.5 when the spike beams are added, slightly more than what was measured. Configuration B

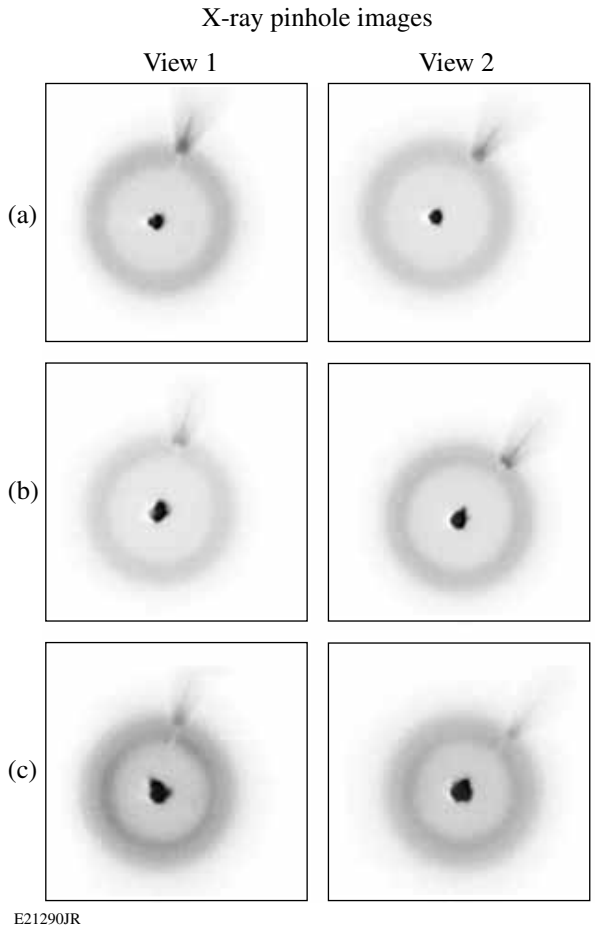

Figure 130.77
Measured time-integrated x-ray pinhole images for configuration B. Two views from different directions are shown in each row. (a) The top row represents a 40-beam implosion, (b) the middle row a 40 + 20 implosion (no phase plates in the spike beams), and (c) the lower row a 40 + 20 implosion with phase plates in the spike beams.

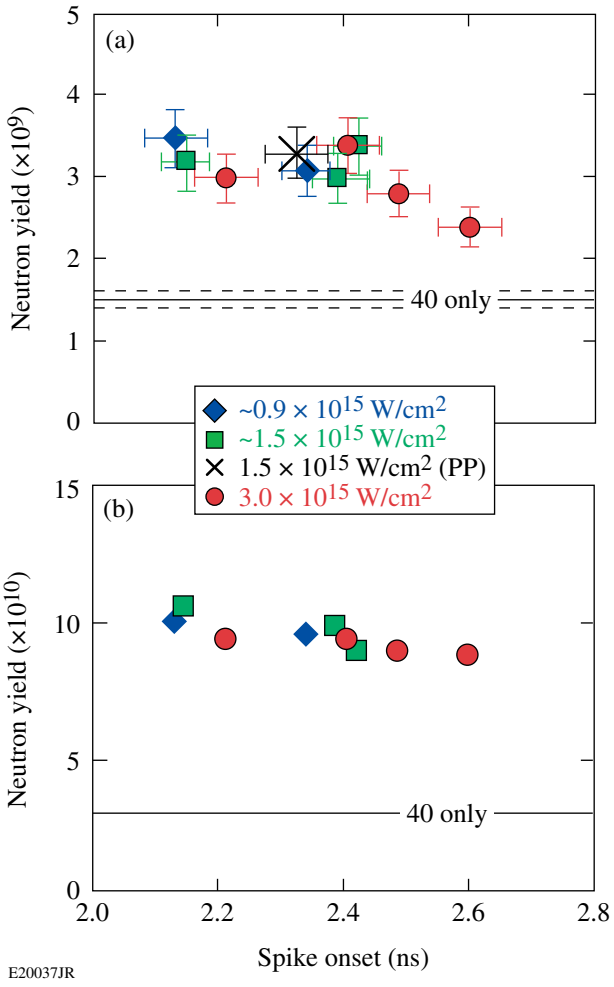

Figure 130.78
(a) Measured and (b) 1-D–simulated neutron yields for configuration B.

starts with a good illumination pattern in the 40 drive beams, but the 20 spike beams probably increased nonuniformities, which is seen in the x-ray pinhole images in Figs. 130.77(b) and 130.77(c). This might explain why the yield increase is less than predicted. The yield-over-clean (YOC) ratio, defined as the measured-to-predicted neutron number, is 3% to 5% for these experiments. The low YOC can be explained by a strong Rayleigh–Taylor instability growth during the acceleration phase in these low-velocity plastic-shell implosions and a substantial shell–fuel mixing that quenches fusion reactions.[18]

The neutron temporal diagnostic[27] recorded the fusion reaction-rate history in most of the implosions, provided that the neutron yield was above ~1×10^9. The signals were noisy and the peak of the measured neutron rate or "bang time" was obtained by fitting a Gaussian curve to the signals. The error in determining the bang time is estimated with ~50 ps. The bang time versus spike onset is plotted in Fig. 130.79(a). Bang times are earlier in configuration A for a given spike onset. The general trend for both data sets is that the bang time is later with a later onset of the spike pulse. The gray band marks the range of measured bang times from 40 drive beam implosions in configuration B. The solid line is a linear fit through the squares. The slope of this line is ~1.6× larger than the slope of the dashed line, which is a linear fit through the circles. This indicates a stronger effect of the spike pulse in configuration A. However, the earliest bang time (~3.59 ns) was measured in one 40 + 20 shot with phase plates in the spike beams and in configuration B. This is ~200 ps earlier than in the 40-drive-beam implosions. Figure 130.79(b) shows that it is not so much the particular beam configuration that is important for the bang time; the amount of hot electrons that are generated (see **Hard**

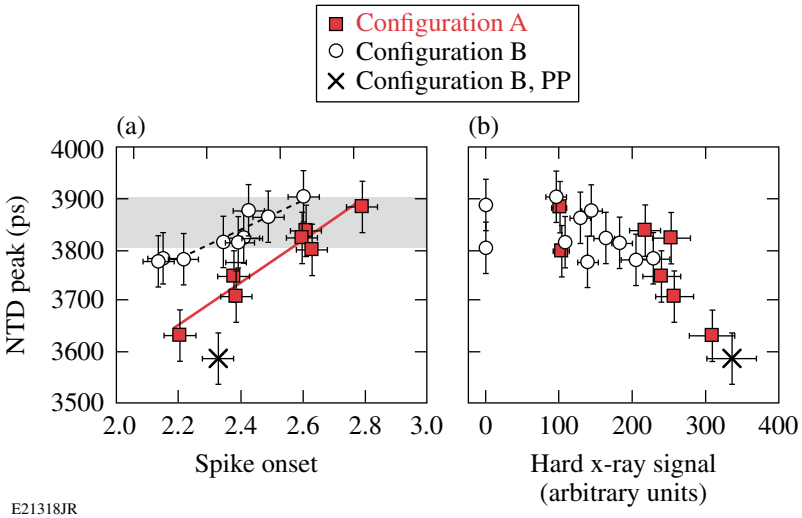

Figure 130.79
Measured neutron bang time versus (a) the spike onset time and (b) the hard x-ray signal. The solid squares and open circles represent the measurements in configurations A and B, respectively, and × represents the measurement with phase plates in the spike beams in configuration B. The gray band in (a) denotes the range of measured bang times in 40-beam implosions.

X-Ray Measurements, p. 122) is more important. A clear correlation of the bang time with the measured hard x-ray signal is observed. An earlier bang time correlates with a higher x-ray signal, indicating that the hot electrons responsible for the hard x-ray emission affect the hydrodynamic implosion.

Figure 130.80 shows electron-temperature and pressure maps obtained from various 2-D CHIC simulations for configuration B. Hot electrons were not included in the simulations. This is probably justified for most of the shots in configuration B without phase plates since those shots are less affected by hot electrons (see Fig. 130.79). Figure 130.80(a) shows the case without a spike pulse. The 40-beam illumination corresponds to that rendered in Fig. 130.67(c). In this case the corona temperature and pressure are isotropic during the shell implosion, and the shock pressure is about 50 Mbar at the end of the drive pulse ($t = 2.6$ ns). Figures 130.80(b)–130.80(d) show 2-D simulations 300 ps after the spike onset for different focusing conditions of the spike beams (see Fig. 130.70), i.e., with different SBI. The temperature in Fig. 130.80(d) shows weak laser imprint in the corona from the spike illumination pattern, while with lower intensity the temperature becomes more symmetric because of a better spatial overlap of the 20 spike beams. Independent of the spike intensity on target, however, the pressure remains fairly symmetric with the same value of ~75 Mbar. Some slight pressure modulations are observed at the highest intensity. The simulations show that the temperature in the conduction layer is always symmetric, which explains why the spike pressure keeps the same values in all the cases. For all focus conditions, the equivalent pressure can be estimated from the average spike intensity, which is $\langle I_{\text{spike}} \rangle \sim 0.5 \times 10^{15}$ W/cm^2. The total intensity on target is the sum of the spike intensity and the compression intensity ($I_{\text{comp}} = \sim 0.4 \times 10^{15}$ W/cm^2). For a laser absorption of about 70%, the absorbed intensity is

$$I_{\text{abs}} = \sim 0.7\left(I_{\text{comp}} + \langle I_{\text{spike}} \rangle\right) = \sim 0.6 \times 10^{15} \text{ W/cm}^2,$$

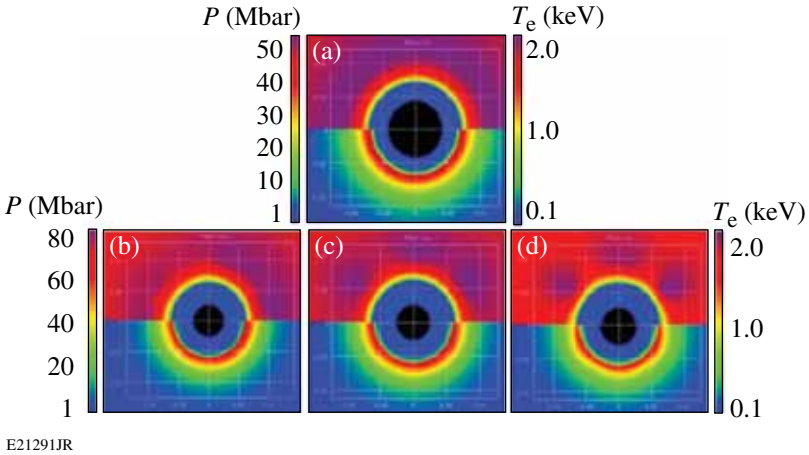

Figure 130.80
Two-dimensional CHIC simulations. Electron temperature (top half) and pressure (bottom half): (a) without a spike at the end of the drive pulse (2.6 ns) and with a spike, 300 ps after the spike onset (2.9 ns) with (b) SBI = 0.5×10^{15} W/cm^2, (c) SBI = 1×10^{15} W/cm^2, and (d) SBI = 2.5×10^{15} W/cm^2. The temperature and pressure scales are the same for (b)–(d).

and the expected pressure is ~80 Mbar for this intensity from a simple scaling law model,[31] in agreement with the simulated value. The 2-D simulations explain why for all SBI's, the spike pressure remains constant, as does, consequently, the neutron yield. This argument applies only for the experiments with configuration B, while for configuration A, the neutron yields are dominated by the illumination nonuniformities and their mitigation by the spike beams.

Hard X-Ray Measurements

The hard x-ray (HXR) detector provides information on the temperature of the electron distribution. The measured time-resolved hard x-ray pulse from the >40-keV channel is shown in Fig. 130.81 for various spike-onset times. The hard x-ray pulse correlates with the spike laser pulse, with respect to both the onset and its duration. The hard x rays and, therefore, the hot electrons are predominantly produced by the high-intensity laser spike and are negligible when only the 40 low-intensity drive beams are used.

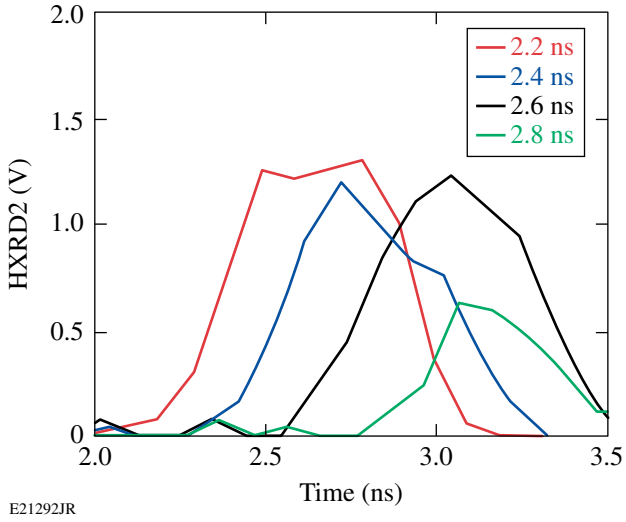

Figure 130.81
Measured time-resolved hard x-ray pulses for energies >40 keV. The times in the legend indicate the onset of the spike pulse. The hard x-ray pulse is clearly correlated with the spike pulse, in both onset and duration.

The hot-electron temperature for configuration A [Fig. 130.82(a)] was determined by fitting estimated values from the convolution of an exponentially decaying hard x-ray spectrum with the sensitivity of the different channels of the HXR detector to the three measured higher-energy channels.[29] The lowest-energy channel was excluded from the fit. A hot-electron–energy distribution with a temperature of ~30 keV was measured, independent of laser intensity and timing. Large-scale, collisional, 1-D particle-in-cell (PIC) simulations[32] for

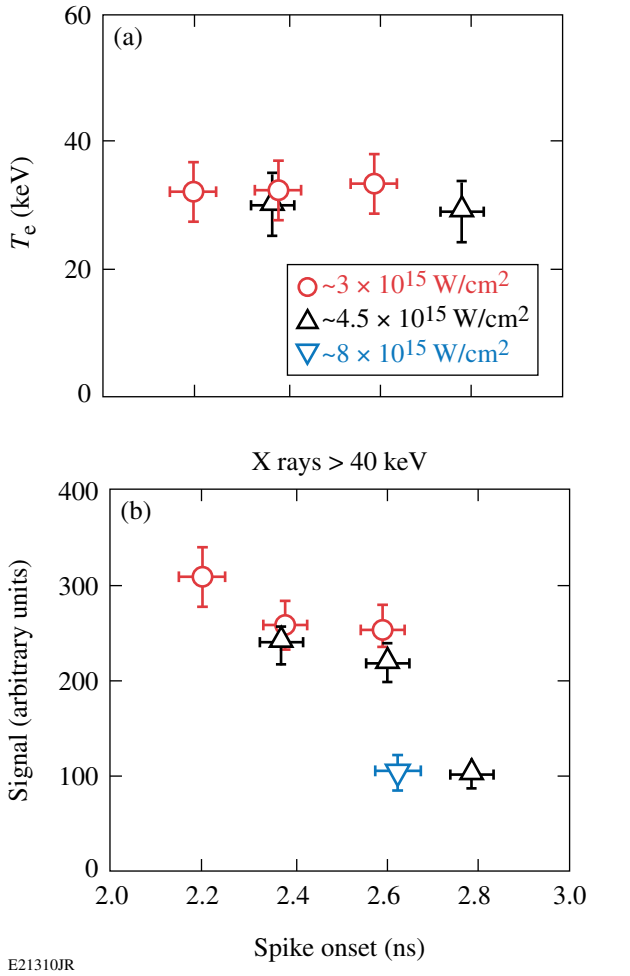

Figure 130.82
(a) Inferred hot-electron temperature and (b) measured, time-integrated hard x ray signal >40 keV for configuration A.

laser intensities of 10^{15} to 10^{16} W/cm^2 using very similar plasma parameters, as in these experiments, reported hot-electron temperatures of ~25 keV, with the primary source for hot electrons being SRS. Remarkably, the simulations[32] predict a relatively low, constant hot-electron temperature that will not change with laser intensity, in agreement with the experimental observation.

Figure 130.82(b) shows the time-integrated hard x-ray yield of the >40-keV channel. It is interesting to note that for implosions in configuration A, there is a clear correlation between the measured neutron signal (Fig. 130.75) and the hard x-ray signal [Fig. 130.82(b)], which suggests that the yield increase from adding the spike beams was partially due to hot electrons coupled into the outer regions of the compressing target. It can be excluded that hard x ray interfered with the neutron-yield measurements because of proper shielding of the diagnostics and time-resolved measurements. Hard x rays are measured

during the time of the spike pulse, while the neutron time-of-flight signal is measured much later in time. As mentioned before, the neutron signal is very sensitive to the condition of the target illumination. Adding the 20 spike beams in configuration A probably mitigated the nonuniformities, resulting in a much-higher (×14) neutron yield when the 20 spike beams were added. This indicates that the spike beam's energy is partially coupled by hot electrons that slowed down in the dense shell.

Higher hard x-ray signals were measured for early spike onset, probably caused by a longer temporal overlap between drive and spike pulse, which suggests that electron plasma waves seeded by the drive pulse are amplified by the high-intensity spike. More overlap provides a longer time period when the electron-plasma waves are driven; therefore, more hot electrons and higher hard x-ray signals are generated. Hot-electron generation is caused by the SRS and TPD instabilities.[33] The foci of the 20 spike beams did not overlap at the critical density for those measurements, so effects from overlapping beams[33] are not expected and the hot-electron production is dominated by single-beam interactions with the target. At 2.6 ns, there are three shots with different intensities. The hard x-ray signal decreases with higher intensity. Two causes might explain this effect: First, the backscatter losses increase from ~10% to ~35% (see below) with higher intensity, reducing the coupling efficiency of the spike beams. Second, since the SBI was varied through the focus size w-hile holding the energy constant, a higher intensity corresponds to a smaller spot size. This affects the total number of generated hot electrons and the hard x-ray signal. The number of hot electrons is proportional to the plasma volume intercepted by the high-intensity beams. When normalizing the measured hard x-ray signal by the estimated laser beam area at quarter-critical density, the yield actually increases with laser intensity (see Fig. 130.83). This shows that the hot-electron production per area increases with laser intensity, presumably because of a larger growth of laser–plasma instabilities. As in previous experiments performed under similar conditions,[33] the hard x-ray signal saturates at intensities above ~2×10^{15} W/cm^2.

Similar measurements were performed for beam configuration B (see Fig. 130.84). Here, the SBI was varied between 0.9×10^{15} and ~3×10^{15} W/cm^2. In contrast to the previous experiment, the foci of the spike beams were large enough at the lowest intensity so that they partially overlapped [see Fig. 130.70(c)]. Not surprising, the lowest hard x-ray signal was measured for the lowest intensity. The inferred temperature was

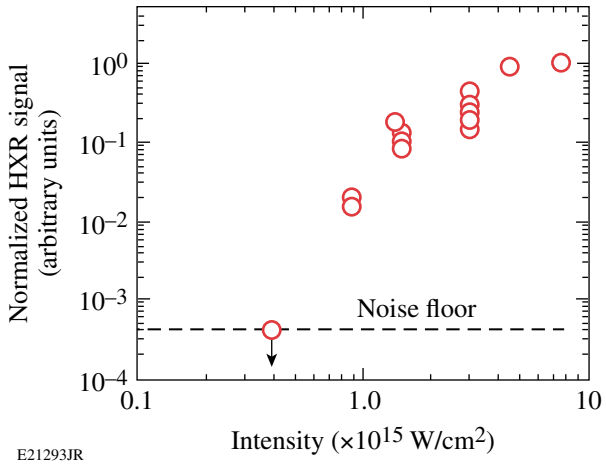

Figure 130.83
Hard x-ray signal divided by the estimated laser-beam area at quarter-critical density as a function of SBI. The maximum signal was normalized to unity. Data from both configurations are plotted.

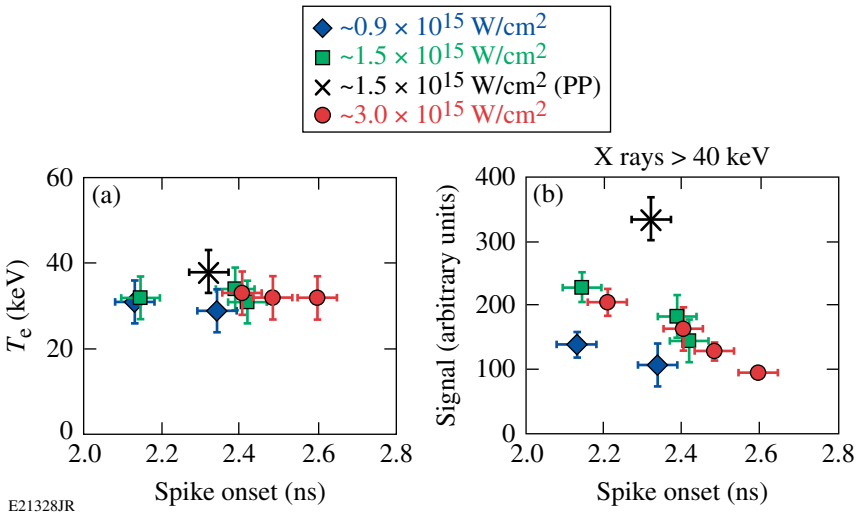

Figure 130.84
(a) Inferred hot-electron temperature and (b) measured hard x-ray signal for configuration B.

~30 keV for all the shots without phase plates, independent of laser intensity and timing, which is very similar to the temperature in configuration A. A slightly higher temperature of ~40 keV was measured with phase plates, which also produced the highest hard x-ray signal for this beam configuration. Less backscattering (see **Backscatter Measurements** below) and less beam filamentation are expected with phase plates,[34] which should lead to higher laser intensity at quarter-critical density. It is expected that the laser–plasma instabilities are driven harder, which could then lead to a hotter electron population and more electrons. Only for this shot with phase plates, a measureable 3/2-harmonic signal[33] was present; the 3/2 signal was absent in all other shots without phase plates. The hotter electron distribution might therefore be caused by some contribution from TPD, while the shots without phase plates were dominated by SRS instability (see **Backscatter Measurements** below).

For beam configuration B, there is no clear correlation between the neutron signal [Fig. 130.78(a)] and hard x-ray signal [Fig. 130.84(b)]. This can be explained by the fact that in configuration B a relatively uniform 40-beam implosion is distorted when the 20 spike beams are added. The 20 spike beams impose a dodecahedron imprint pattern and seed modulations [see Fig. 130.80(d)] that increase the core deformation at peak compression (Fig. 130.73). Larger core distortions were also observed in x-ray pinhole images when the spike beams were added [Figs. 130.77(b) and 130.77(c)]. This led to more Rayleigh–Taylor instability growth and reduced the neutron yields despite the additional energy that was coupled into the imploding shell. In general, adding laser energy from the spike beams should help to compress the shell more and boost the neutron yield, but there is a trade-off between more energy coupled into the target and more seeds for instabilities.

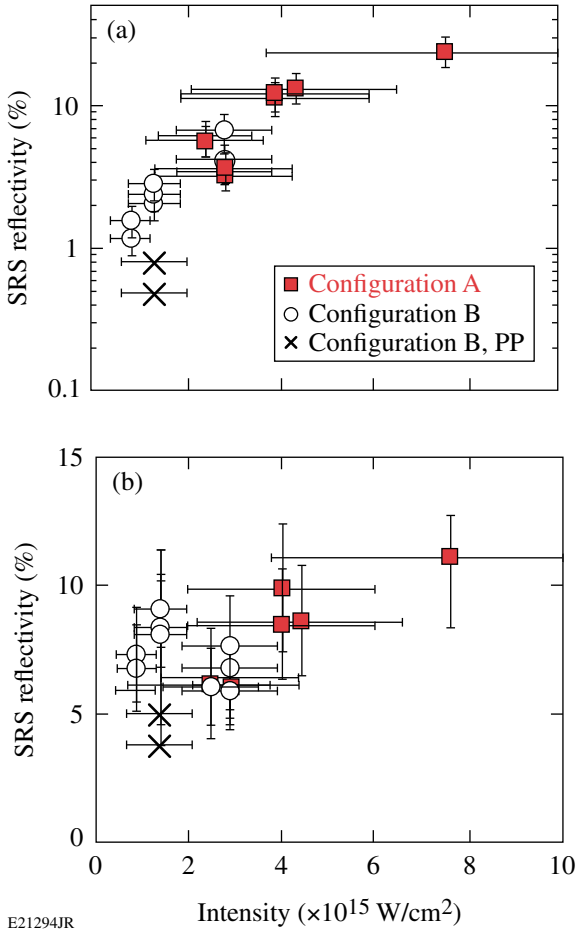

Figure 130.85
Percentage of back-reflected laser light in a spike beam port by (a) SRS and (b) SBS as a function of SBI. Most of the high-intensity shots were done with configuration A denoted by the full symbols. The open symbols represent repointed beams (configuration B). The lowest reflectivity was measured with configuration B and phase plates (cross).

Backscatter Measurements

The plasma reflectivity was measured for various laser intensities. Figure 130.85 shows the percentage of back-reflected light in the (a) SRS and (b) SBS channels of one of the spike beams. The SRS signal increased in intensity by more than a factor of ~10 to up to 24% and dominated the backscattering at the highest intensity, while SBS increased moderately from ~5% to 12%. A very low level of SRS backscattering (~0.5%) was measured at $\sim 1.5 \times 10^{15}$ W/cm^2 with phase plates in the spike beams. The simultaneously measured back-reflection through the neighboring drive-beam port, i.e., one of the 40 beam ports delivering the assembly pulse, was low and remained constant at the same level as in implosions without the 20 spike beams for all timings and intensities (see Fig. 130.86). In the drive beam, SRS stayed below 1% and SBS stayed in the 2% to 4% range. This shows that the light from the spike beams was scattered back in a narrow cone and did not spill over into adjacent ports.

It has been shown[35,36] that smoothing the intensity distribution in the focal spot with spatial, temporal, and polarization smoothing schemes can substantially reduce the backscattering. This is attributed to a reduction of filamentation.[34] In most of the shots, no phase plates were used in the spike beams, which could explain the high levels of backscattering. The sum of SBS and SRS backscatter was lowest (~6%) with phase plates, while without phase plates, the reflectivity increased from ~8% at $\sim 0.9 \times 10^{15}$ W/cm^2 to ~36% at $\sim 8 \times 10^{15}$ W/cm^2. Most of the high-intensity shots were done with configuration A, but some shots were taken at 3×10^{15} W/cm^2 with both beam configurations. The backscatter was the same within the measurement

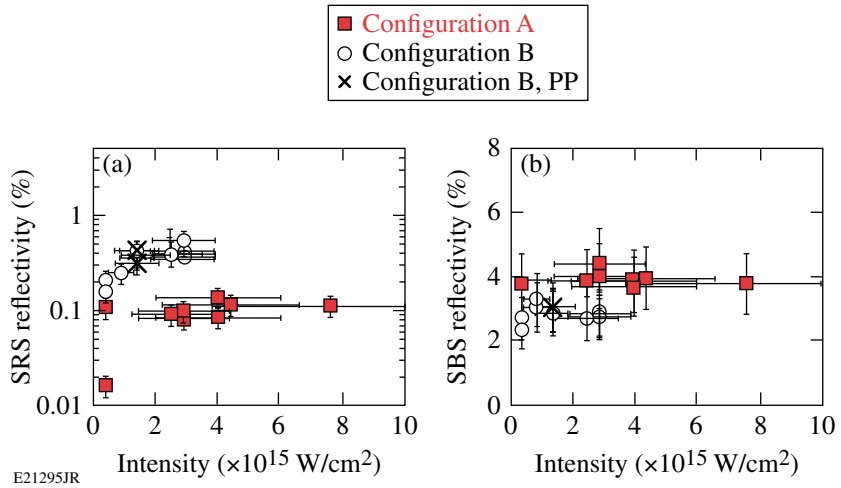

Figure 130.86
Percentage of reflected laser light in a drive beam port by (a) SRS and (b) SBS as a function of SBI. See Fig. 130.85 for an explanation of the different symbols.

uncertainty. In contrast to the experiment, collisional PIC simulations[32] for similar plasma conditions predict that the calculated reflected laser energy should remain constant at ~35% when the laser intensity increases from 1×10^{15} W/cm^2 to 8×10^{15} W/cm^2. The simulations show that the fraction of energy absorbed by the collisionless processes significantly increased with intensity, while the collisional absorption decreased proportionally.

A 2-D radiation–hydrodynamics code *DRACO*[37] simulation was performed to study the heating and profile modification of the plasma under the interaction of a single high-intensity (~5×10^{15} W/cm^2) spike beam with the imploding shell on the pole. The simulation shows the formation of a density depression in the underdense plasma and the steepening of the density profile at the critical density. Figure 130.87(a) shows axial density profiles for various times during the spike interaction. Figure 130.87(b) shows the density scale length at the critical density n_c (circles) and at $n_c/4$ (squares) along with the spike pulse's profile (dashed). Profile steepening at n_c occurs during the spike interaction, and the density scale length is reduced from ~20 μm to ~2 μm. In contrast, the scale length at $n_c/4$ does not change significantly and remains ~170 μm until the end of the spike pulse. As a result of this density profile modification, the spike pulse creates a channel through the underdense plasma. Scattered light is guided by this channel and is dominantly reflected back into the incident beam with very little sidescattering. This is supported by the small amount of scatter in the drive beam (Fig. 130.86) and the negligible amount of sidescattering shown by the near-backscatter diagnostic around the spike beam.

Time-resolved spectra of the SBS back-reflected light were recorded. Figure 130.88 shows two examples of the SBS sig-

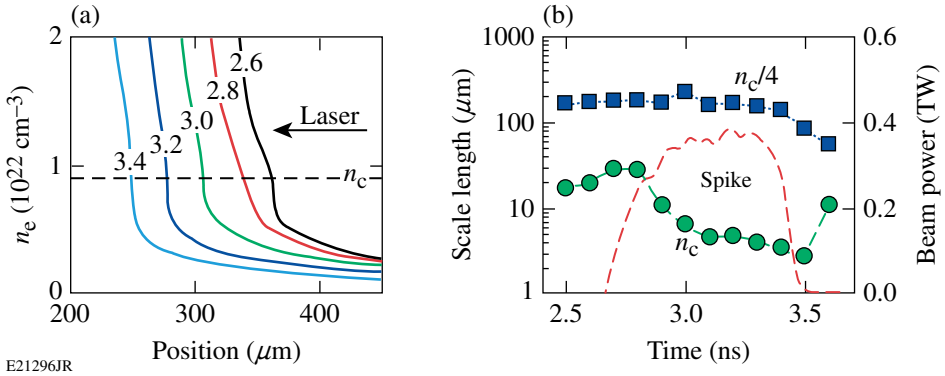

Figure 130.87
(a) Density profiles from a 2-D hydrodynamics code *DRACO*[37] simulation along the channel axis of a high-intensity spike beam interacting with the imploding shell. The numbers indicate the time in nanoseconds. The critical density is marked by the dashed line. (b) Density scale length at critical (circles) and quarter-critical (squares) density. Profile steepening occurs when the spike pulse (dashed) interacts.

nal for a medium- and high-intensity shot. The white curve represents the composite pulse shape of the drive and spike pulses. The SBS signal is produced only during the spike curve. The frequency spectrum of the SBS light is affected by the plasmas temperature and the Doppler shift with respect to the incident laser light. The amount of blue shift is given by $\omega - \omega_0 = 2k_0 c_s (M-1)\sqrt{1 - n_e/n_c}$ (Ref. 38), where ω and ω_0 are the angular frequencies of the scattered and incident light, respectively, k_0 is the wave number of the incident light, c_s is the ion sound velocity, and M is the Mach number. Supersonic movement of the plasma region where SBS occurs will cause a blue shift of the SBS spectrum. The experiment shows that the blue shift is reduced with increasing laser intensity, indicating that SBS originates from plasma regions with lower flow velocities. A comparison with 2-D hydro simulations shows that lower flow velocities occur at higher plasma densities. The corresponding plasma density is indicated in Fig. 130.88 by the ratio of electron density to n_c. For an intensity of ~2.5×10^{15} W/cm^2, the SBS active region is located at a plasma density of ~$0.03\, n_c$.

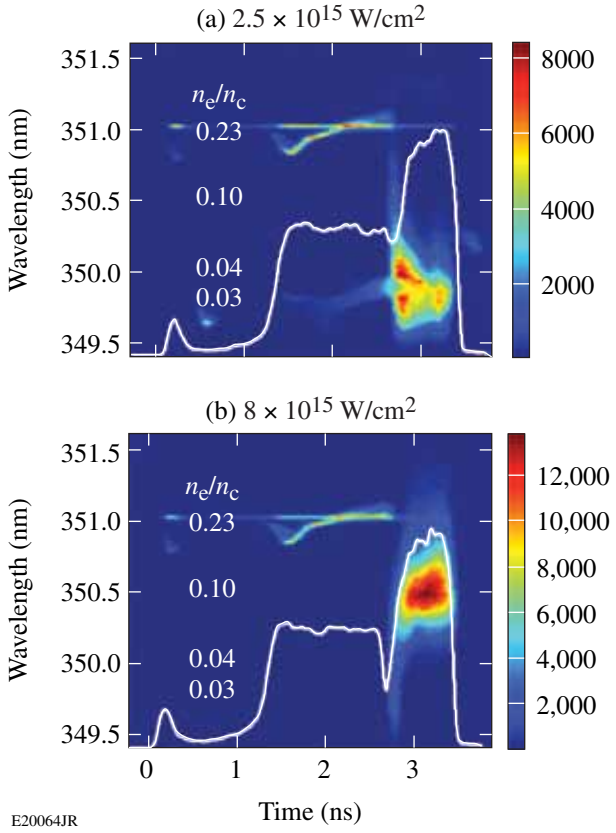

Figure 130.88
Streaked SBS spectra for (a) medium (SBI = 2.5×10^{15} W/cm^2) and (b) high (SBI = 8×10^{15} W/cm^2) spike intensity. The numbers in the figures indicate the plasma density normalized to the critical density. The white curve is the composite pulse shape of the drive and spike pulses.

For ~4.5×10^{15} W/cm^2 (not shown), the peak emission shifted to ~$0.05\, n_c$ with a weak SBS signal coming from up to ~$n_c/4$ later in time. At the highest intensity [Fig. 130.88(b)], the SBS active region shifts up to ~0.1 to $0.2\, n_c$ with a clear indication of a signal coming from above $n_c/4$. The laser-intensity threshold for SBS can be estimated with

$$I_{SBS} \approx \left(T_{keV}/L_v \lambda_\mu\right) \times \left(n_c/n_e\right) \times 7 \times 10^{15} \text{ W/cm}^2 \text{ (Ref. 39)},$$

where T_{keV}, L_v, and λ_μ are the electron temperature in keV, scale length of the Mach number profile in microns, and the laser wavelength in microns, respectively. The resulting threshold is $I_{SBS} \approx 5 \times 10^{14}$ W/cm^2 for the current plasma conditions and $n_e/n_c = 0.04$. The drive-pulse intensity is below the threshold, while the spike intensity is above the threshold.

The laser-intensity threshold for the TPD instability can be estimated from $I_{TPD} \approx \left(82 \times T_{keV}/L_\mu \lambda_\mu\right) \times 10^{14}$ W/cm^2 (Ref. 40), where L_μ is the density scale length in microns and λ_μ is the laser wavelength in microns. For SRS, the threshold at around $\sim n_c/4$ is given by

$$I_{SRS} \approx \left(T_{keV}/L_\mu^{4/3} \lambda_\mu^{2/3}\right) \times 5 \times 10^{16} \text{ W/cm}^2 \text{ (Ref. 39)}.$$

DRACO simulations predict $T_{keV} \approx 1.8$, which results in $I_{TPD} \approx 2.5 \times 10^{14}$ W/cm^2 and $I_{SRS} \approx 2 \times 10^{14}$ W/cm^2 for the current plasma conditions. The thresholds are lower than the peak intensity in the drive beams, but no SRS or TPD signatures were measured with only the 40 drive beams. With increasing intensity, a strong reduction in the TPD instability is observed, which is evident by the reduction in optical emission at the half-harmonic ($\omega/2$) of the laser wavelength. The $\omega/2$ signal decreased by more than two orders of magnitude in the applied intensity range. At the maximum intensity, the $\omega/2$ signal was below the detection threshold, indicating no significant contribution of TPD to the hot-electron production. This and the relatively low hot-electron temperature of ~30 keV support the conjecture that SRS plays the dominant role in hot-electron production in these experiments. The strong reduction of TPD with intensity, together with the observed shift of the SBS active region to $\sim n_c/4$, might indicate that driven ion-acoustic waves at $\sim n_c/4$ play a role in the reduction of TPD.

Conclusions

Spherical shock-ignition experiments were performed on OMEGA by using a beam configuration that separates low-intensity compression beams and high-intensity spike beams. D_2-filled plastic shells were compressed on a low adiabat by 40 of the 60 OMEGA beams, and the remaining 20 spike beams

were delayed and tightly focused onto the imploding shell to deliver a late shock. This article studied the implosion performance with the new beam configuration and used the platform to measure hot-electron production and laser backscattering for laser intensities that are relevant for shock ignition. Two different beam-pointing configurations were used: one that used the standard pointing to target center and another in which the beams were repointed to improve target illumination uniformity. Significant improvement in areal density and neutron yield and a rounder core in x-ray images were observed for the repointed beam configuration. The coupling of high-intensity spike beam energy into the imploding capsule was studied in experiments and simulations. Implosions in the standard configuration show a correlation between the measured neutron yield and the hard x-ray signal, which suggests that the yield increase was partially due to hot electrons coupled into the compressing target. The spike beams mitigated the large beam illumination nonuniformities in this configuration, which led to the recovery of the neutron yield by a factor of ~14. Several indications suggest that when spike beams are equipped with phase plates, a stronger coupling of the spike beam energy into the imploding shell is achieved. With phase plates the following observations were made: lower backscatter losses, stronger x-ray emission in the 2- to 7-keV and >20-keV ranges, lower ρR, and an earlier bang time. This indicates that higher coupling is achieved through increased thermal and hot-electron components. Two-dimensional hydrodynamic simulations were performed and show significant modulation in areal density. Similar modulations were observed in the experiments. Laser–plasma instabilities were studied for single-beam peak laser intensities of up to $\sim 8 \times 10^{15}$ W/cm^2, measuring backscattering of laser energy of up to 36% at the highest intensity. Hard x-ray measurements reveal a relatively low hot-electron temperature of ~30 keV, which is independent of intensity and spike onset time. With increasing laser intensity, the region where stimulated Brillouin scattering occurs shifts to higher densities. At the highest intensity it occurs near and above the quarter-critical density. With higher intensity the two-plasmon-decay instability is suppressed and hot-electron production is dominated by stimulated Raman scattering.

These experiments measured a low hot-electron temperature, not too high backscatter losses, and a good coupling of spike beam energy into an imploding capsule at laser intensities of up to $\sim 8 \times 10^{15}$ W/cm^2, which is encouraging for the shock-ignition concept. A low hot-electron temperature is beneficial since these electrons are stopped in the outer layer of the imploding target, augmenting the strong hydrodynamic shock. Further shock-ignition experiments are required, however, to study laser–plasma instabilities and hot-electron production at plasma conditions with longer density scale lengths and higher electron temperatures that are closer to those of an ignition design.

ACKNOWLEDGMENT

This work was supported by the U.S. Department of Energy Office of Fusion Energy Sciences under contract DE-FC02-04ER54789 and by the Office of Inertial Confinement Fusion under Cooperative Agreement No. DE-FC52-08NA28302, the University of Rochester, and the New York State Energy Research and Development Authority. The support of DOE does not constitute an endorsement by DOE of the views expressed in this article. This work was partially supported by the Aquitaine Region Council and the European Union's Seventh Framework Program: the HiPER project #211737.

REFERENCES

1. R. Betti, C. D. Zhou, K. S. Anderson, L. J. Perkins, W. Theobald, and A. A. Solodov, Phys. Rev. Lett. **98**, 155001 (2007).
2. R. L. McCrory, D. D. Meyerhofer, R. Betti, R. S. Craxton, J. A. Delettrez, D. H. Edgell, V. Yu Glebov, V. N. Goncharov, D. R. Harding, D. W. Jacobs-Perkins, J. P. Knauer, F. J. Marshall, P. W. McKenty, P. B. Radha, S. P. Regan, T. C. Sangster, W. Seka, R. W. Short, S. Skupsky, V. A. Smalyuk, J. M. Soures, C. Stoeckl, B. Yaakobi, D. Shvarts, J. A. Frenje, C. K. Li, R. D. Petrasso, and F. H. Séguin, Phys. Plasmas **15**, 055503 (2008).
3. J. D. Lindl, *Inertial Confinement Fusion: The Quest for Ignition and Energy Gain Using Indirect Drive* (Springer-Verlag, New York, 1998).
4. V. A. Shcherbakov, Sov. J. Plasma Phys. **9**, 240 (1983).
5. R. Betti and C. Zhou, Phys. Plasmas **12**, 110702 (2005).
6. X. Ribeyre *et al*., Plasma Phys. Control. Fusion **50**, 025007 (2008).
7. A. J. Schmitt, J. W. Bates, S. P. Obenschain, S. T. Zalesak, D. E. Fyfe, and R. Betti, Fusion Sci. Technol. **56**, 377 (2009).
8. X. Ribeyre *et al*., Plasma Phys. Control. Fusion **51**, 015013 (2009).
9. E. I. Moses *et al*., Phys. Plasmas **16**, 041006 (2009).
10. L. J. Perkins, R. Betti, K. N. LaFortune, and W. H. Williams, Phys. Rev. Lett. **103**, 045004 (2009).
11. M. Dunne, Nat. Phys. **2**, 2 (2006); HiPER, accessed 7 May 2012, http://www.hiper-laser.org/index.asp.
12. W. L. Kruer, *The Physics of Laser-Plasma Interactions*, Frontiers in Physics, Vol. 73, edited by D. Pines (Addison-Wesley, Redwood City, CA, 1988).
13. R. Betti, W. Theobald, C. D. Zhou, K. S. Anderson, P. W. McKenty, S. Skupsky, D. Shvarts, V. N. Goncharov, J. A. Delettrez, P. B. Radha, T. C. Sangster, C. Stoeckl, and D. D. Meyerhofer, J. Phys., Conf. Ser. **112**, 022024 (2008).
14. J. Delettrez, R. Epstein, M. C. Richardson, P. A. Jaanimagi, and B. L. Henke, Phys. Rev. A **36**, 3926 (1987); M. C. Richardson, P. W. McKenty, F. J. Marshall, C. P. Verdon, J. M. Soures, R. L. McCrory, O. Barnouin,

R. S. Craxton, J. Delettrez, R. L. Hutchison, P. A. Jaanimagi, R. Keck, T. Kessler, H. Kim, S. A. Letzring, D. M. Roback, W. Seka, S. Skupsky, B. Yaakobi, S. M. Lane, and S. Prussin, in *Laser Interaction and Related Plasma Phenomena*, edited by H. Hora and G. H. Miley (Plenum Publishing, New York, 1986), Vol. 7, pp. 421–448.

15. T. R. Boehly, D. L. Brown, R. S. Craxton, R. L. Keck, J. P. Knauer, J. H. Kelly, T. J. Kessler, S. A. Kumpan, S. J. Loucks, S. A. Letzring, F. J. Marshall, R. L. McCrory, S. F. B. Morse, W. Seka, J. M. Soures, and C. P. Verdon, Opt. Commun. **133**, 495 (1997).

16. W. Theobald, K. S. Anderson, R. Betti, R. S. Craxton, J. A. Delettrez, J. A. Frenje, V. Yu. Glebov, O. V. Gotchev, J. H. Kelly, C. K. Li, A. J. Mackinnon, F. J. Marshall, R. L. McCrory, D. D. Meyerhofer, J. F. Myatt, P. A. Norreys, P. M. Nilson, P. K. Patel, R. D. Petrasso, P. B. Radha, C. Ren, T. C. Sangster, W. Seka, V. A. Smalyuk, A. A. Solodov, R. B. Stephens, C. Stoeckl, and B. Yaakobi, Plasma Phys. Control. Fusion **51**, 124052 (2009).

17. R. S. Craxton, L. Tucker, T. Mo, K. S. Anderson, R. Betti, L. J. Perkins, G. P. Schurtz, X. Ribeyre, and C. A. Casner, Bull. Am. Phys. Soc. **55**, 26 (2010).

18. W. Theobald, R. Betti, C. Stoeckl, K. S. Anderson, J. A. Delettrez, V. Yu. Glebov, V. N. Goncharov, F. J. Marshall, D. N. Maywar, R. L. McCrory, D. D. Meyerhofer, P. B. Radha, T. C. Sangster, W. Seka, D. Shvarts, V. A. Smalyuk, A. A. Solodov, B. Yaakobi, C. D. Zhou, J. A. Frenje, C. K. Li, F. H. Séguin, R. D. Petrasso, and L. J. Perkins, Phys. Plasmas **15**, 056306 (2008).

19. F. J. Marshall, J. A. Delettrez, R. Epstein, R. Forties, R. L. Keck, J. H. Kelly, P. W. McKenty, S. P. Regan, and L. J. Waxer, Phys. Plasmas **11**, 251 (2004).

20. Y. Lin, T. J. Kessler, and G. N. Lawrence, Opt. Lett. **21**, 1703 (1996).

21. T. R. Boehly, V. A. Smalyuk, D. D. Meyerhofer, J. P. Knauer, D. K. Bradley, R. S. Craxton, M. J. Guardalben, S. Skupsky, and T. J. Kessler, J. Appl. Phys. **85**, 3444 (1999).

22. P.-H. Maire *et al*., SIAM J. Sci. Comput. **29**, 1781 (2007).

23. S. P. Regan, T. C. Sangster, D. D. Meyerhofer, W. Seka, R. Epstein, S. J. Loucks, R. L. McCrory, C. Stoeckl, V. Yu. Glebov, O. S. Jones, D. A. Callahan, P. A. Amendt, N. B. Meezan, L. J. Suter, M. D. Rosen, O. L. Landen, E. L. DeWald, S. H. Glenzer, C. Sorce, S. Dixit, R. E. Turner, and B. MacGowan, J. Phys., Conf. Ser. **112**, 022077 (2008).

24. C. D. Zhou, W. Theobald, R. Betti, P. B. Radha, V. A. Smalyuk, D. Shvarts, V. Yu. Glebov, C. Stoeckl, K. S. Anderson, D. D. Meyerhofer, T. C. Sangster, C. K. Li, R. D. Petrasso, J. A. Frenje, and F. H. Séguin, Phys. Rev. Lett. **98**, 025004 (2007).

25. F. J. Marshall, T. Ohki, D. McInnis, Z. Ninkov, and J. Carbone, Rev. Sci. Instrum. **72**, 713 (2001).

26. V. Yu. Glebov, D. D. Meyerhofer, C. Stoeckl, and J. D. Zuegel, Rev. Sci. Instrum. **72**, 824 (2001).

27. R. A. Lerche, D. W. Phillion, and G. L. Tietbohl, Rev. Sci. Instrum. **66**, 933 (1995).

28. W. Seka, D. H. Edgell, J. P. Knauer, J. F. Myatt, A. V. Maximov, R. W. Short, T. C. Sangster, C. Stoeckl, R. E. Bahr, R. S. Craxton, J. A. Delettrez, V. N. Goncharov, I. V. Igumenshchev, and D. Shvarts, Phys. Plasmas **15**, 056312 (2008).

29. C. Stoeckl, V. Yu. Glebov, D. D. Meyerhofer, W. Seka, B. Yaakobi, R. P. J. Town, and J. D. Zuegel, Rev. Sci. Instrum. **72**, 1197 (2001).

30. F. H. Séguin, J. A. Frenje, C. K. Li, D. G. Hicks, S. Kurebayashi, J. R. Rygg, B.-E. Schwartz, R. D. Petrasso, S. Roberts, J. M. Soures, D. D. Meyerhofer, T. C. Sangster, J. P. Knauer, C. Sorce, V. Yu. Glebov, C. Stoeckl, T. W. Phillips, R. J. Leeper, K. Fletcher, and S. Padalino, Rev. Sci. Instrum. **74**, 975 (2003).

31. S. Atzeni and J. Meyer-ter-Vehn, *The Physics of Inertial Fusion: Beam Plasma Interaction, Hydrodynamics, Hot Dense Matter*, International Series of Monographs on Physics (Clarendon Press, Oxford, 2004), p. 225.

32. O. Klimo *et al*., Phys. Plasmas **18**, 082709 (2011).

33. C. Stoeckl, R. E. Bahr, B. Yaakobi, W. Seka, S. P. Regan, R. S. Craxton, J. A. Delettrez, R. W. Short, J. Myatt, A. V. Maximov, and H. Baldis, Phys. Rev. Lett. **90**, 235002 (2003).

34. C. Labaune *et al*., Phys. Fluids B **4**, 2224 (1992).

35. B. J. MacGowan *et al*., Phys. Plasmas **3**, 2029 (1996).

36. J. D. Moody *et al*., Phys. Rev. Lett. **86**, 2810 (2001).

37. P. B. Radha, T. J. B. Collins, J. A. Delettrez, Y. Elbaz, R. Epstein, V. Yu. Glebov, V. N. Goncharov, R. L. Keck, J. P. Knauer, J. A. Marozas, F. J. Marshall, R. L. McCrory, P. W. McKenty, D. D. Meyerhofer, S. P. Regan, T. C. Sangster, W. Seka, D. Shvarts, S. Skupsky, Y. Srebro, and C. Stoeckl, Phys. Plasmas **12**, 056307 (2005).

38. T. P. Hughes, in *Laser-Plasma Interactions*, edited by R. A. Cairns and J. J. Sanderson (SUSSP Publications, Edinburgh, 1980), p. 44.

39. H. A. Baldis, E. M. Campbell, and W. L. Kruer, in *Handbook of Plasma Physics*, edited by A. Rubenchik and S. Witkowski, Physics of Laser Plasma, edited by M. N. Rosenbluth and R. Z. Sagdeev (North-Holland, Amsterdam, 1991), Vol. 3, p. 377.

40. A. Simon, R. W. Short, E. A. Williams, and T. Dewandre, Phys. Fluids **26**, 3107 (1983).

A Single-Shot, Multiwavelength Electro-Optic Data-Acquisition System for Inertial Confinement Fusion Applications

Introduction

On large inertial confinement fusion (ICF) laser systems like the National Ignition Facility (NIF),[1] the signals from diagnostic instruments originate in an environment where the ionizing radiation and electromagnetic interference (EMI) can significantly degrade the signal-to-noise ratio (SNR) of the measurement or even damage the recording equipment. In addition, there are many recording channels to which these considerations must apply. The cost of the recording system can be reduced if the signals from several detectors can be multiplexed together onto a single, protected oscilloscope channel. Modern high-bandwidth oscilloscopes have nearly infinite record lengths that make this serial multiplexing possible. The prototype system described here is focused on the set of 36 vacuum x-ray photodiodes (XRD's) of the NIF Dante instruments[2] that produce temporally resolved x-ray spectra.

In high-EMI environments, an electro-optic (EO) data-acquisition system is desirable. Fiber optics provide a means of isolating the recording equipment from the harsh detector environment. The signals from the XRD's are converted into the optical domain with fiber-optic Mach–Zehnder modulators (MZM's).[3] The MZM's are typically built to telecom specifications that make it possible for them to survive not only voltage transients of 250 V for 1 μs (Ref. 4), but also the EMI in an ICF environment and the maximum output of an XRD. Once the signals are in the optical domain, they can propagate on single-mode optical fiber that provides high-bandwidth (BW) transmission over long distances. The BW of the fibers is much larger than the signals being recorded, so arbitrarily long fiber delays can be added to the signal paths. These long delays, coupled with wavelength-selective fiber-coupling techniques, allow one to serially combine multiple signals onto a single photodetector.

The system described here was designed as a prototype for the NIF Dante instruments. These instruments use XRD's to measure the x-ray spectra of ICF implosions. There are 36 channels spread over two instruments. The specifications require that signals be acquired in a temporal window at least 200 ns long. The response time of the XRD's is 120 ps, so the system requires a minimum BW of 2.75 GHz. The system was actually designed to a 6-GHz BW to accommodate multifringe events, which will be discussed later. The XRD's can deliver a maximum unsaturated signal of 200 V. The minimum meaningful signal is 50 mV and the desired SNR at this level is 5, which implies a dynamic range (DR) of greater than 4000:1. This DR exceeds the capabilities of the current electronics. With this newly adopted requirement the instrument will be able to record signals without changing any radio-frequency (rf) attenuators.

Experimental

This data-acquisition system is designed to operate in the near-IR optical C band with wavelengths from 1530 nm to 1560 nm, which are used by the telecommunications industry. A layout of the system is shown in Fig. 130.89. The optical carriers are provided by continuous-wave (cw), fiber-coupled laser diodes (LD's) that use distributed-feedback Bragg gratings to maintain narrow-bandwidth operation. The International Telcommunication Union (ITU) has specified a standard set of wavelengths separated by approximately 1.6 nm (200 GHz) around which telecom components are fabricated.[5] The output power of these types of devices ranges from 20 to 100 mW (13 to 20 dBm) with a typical noise figure of –140 dB/Hz. The prototype system used a 20-mW LD at 1552 nm and a 60-mW LD at 1557 nm. The 20-mW version is less expensive and more readily available at all wavelengths on the ITU 200 grid. The 60-mW laser is better suited to compensate for losses in the system. However, cw illumination is inappropriate for this application because of the requirement to multiplex signals. The cw wings of the serially combined signals would overlap, thereby overwhelming the photodetector or forcing a reduction of the signal amplitude by *N*, the number of serially overlapped signals.

The cw lasers are converted into pulsed lasers via acousto-optic modulators (AOM's). These optical modulators have very high contrast ratios (50 dB) with a rise time of 10 ns. They also allow for both digital and analog modulation. In the prototype described here, the AOM's produced pulses that were 40 ns

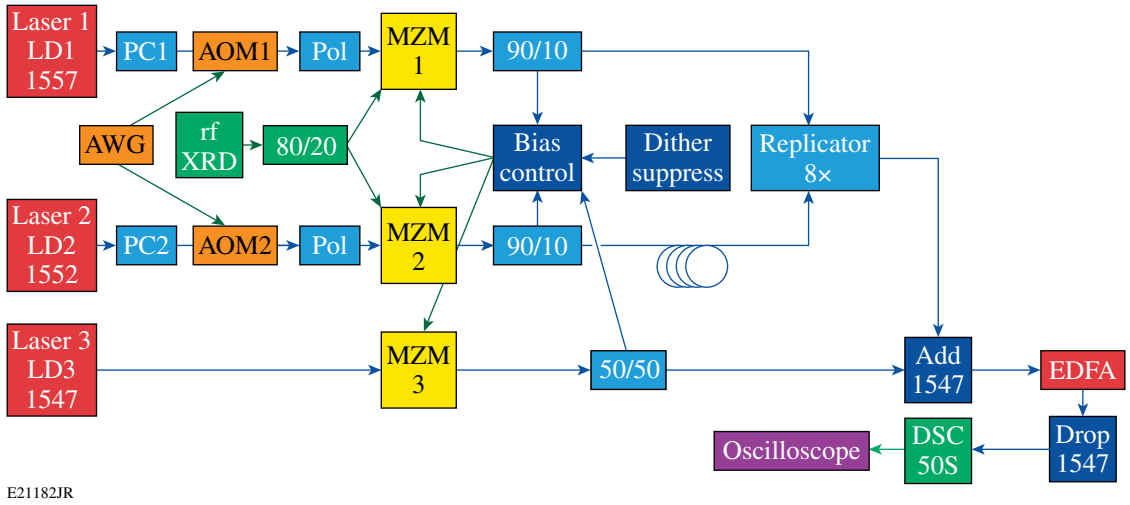

Figure 130.89
In the EO data-acquisition system, the cw outputs of LD1 and LD2 are pulse shaped with an AOM with the shaping pulse provided by the arbitrary waveform generator (AWG). The light is polarized (pol) before being modulated by the MZM. The MZM's are driven by a single XRD through an 80/20 splitter. The 90/10 splitters provide an optical feedback signal to the bias control loop. The signals from the two MZM's are combined at the input of the 8× replicator. After the replicator, another cw source (LD3) is added to provide a cw input to the EDFA. The LD3 signal is removed before detection by the photodiode (DSC50s) and oscilloscope.

wide (10% width) with a 20-ns flattop acquisition window. This window is sufficient for tests performed on the OMEGA Dante system.

For this prototype we chose to multiplex the signal from two MZM's, which was sufficient to demonstrate all concepts that will be incorporated into the final system. To further enhance the DR, the same rf signal was used to drive both MZM's. The single signal is fed to an rf splitter with a BW of 18 GHz and a 4:1 power split ratio. The asymmetric split means that the optical signal from one modulator will be 4× more sensitive to low-voltage signals, thereby extending the lower edge of the dynamic range. On the other hand, the attenuated channel can be subjected to a 4×-higher signal without exceeding $V_\pi/2$ of the modulator. Exceeding this voltage would generate a fringe jump in the sinusoidal response of the MZM. When combined, these two signals will have an enhanced DR.

The MZM's are from EOSpace and have a –3-dB EO response of between 12 GHz and 14 GHz. The modulators were chosen because they have a low V_π of 3.6 V at 1 GHz. A dc bias was applied to the MZM such that it operated quadrature point (50% transmission) with a negative slope, $Q-$. This gives a linear response at low voltage. Conversely, the sensitivity is low at the extrema, $V = \pm MV_\pi/2$, where M is an odd integer. In the low-signal regime, the modular sensitivity is approximately inversely proportional to V_π, so the low V_π values enhance the DR at the lower end of the range. However, the bias points of MZM's are prone to drift with time. To maintain the operating point, a commercial monitoring circuit was employed. This circuit applied a 20-mV, 1-kHz dither to the dc bias. This dither voltage introduces harmonics of the dither frequency on the transmitted optical signal.[6] Ten percent of the light, after the MZM, is split off with a fiber-optic splitter. This signal was used to monitor the harmonics, therefore enabling the controller to maintain the $Q-$ operating point. However, this scheme works only if the light through the MZM is cw, which it is not. Using the analog modulation capabilities of the AOM, an optical pulse shape was constructed that was at a quasi-cw level of 5% of the peak intensity. To accommodate the optical replicator, which will be described later, the cw level was turned off 2 μs before the 40-ns pulse described above was formed at the 100% transmission level. After the pulse, the AOM output was again blanked for 2 μs before returning to the 5% level. The quasi-cw light was used for the dither control. Any dither voltage that occurred during the 40-ns pulse would look like a baseline drift in the signal; therefore, the commercial controller was modified to suppress the dither voltage during the 4-μs cw blanking window.

There are two options for multiplexing the signals from the two MZM's onto a single optical fiber for additional processing and detection. A dense wavelength-division multiplexer (DWDM) with eight channels on the ITU 200 grid was used

to combine the two wavelengths. This means that in the final system, up to eight MZM's could be multiplexed onto a photodiode attached to a single oscilloscope channel. However, the DWDM has a loss of –2.5 dB or a transmission of 56% plus two additional fiber connections with their associated losses (85% transmission). Since the prototype has only two wavelengths, a lower-loss option was to use the two inputs of the next component in the system—the optical replicator.

The optical replicator is a set of 2×2, 3-dB fused-fiber splitters, as shown in Fig. 130.90 (Ref. 7). Optical interference at the output of the fused-fiber splitters causes half of the light from each of the two input fibers to be distributed equally between the two output fibers. The splitting is independent of the wavelength over the operational band of the device. The outputs of the first 2×2 are connected to inputs of the second with an extra 12 m of fiber (60 ns) inserted into one of the connections. The output of the second 2×2 is then two identical optical pulses separated by 60 ns. The output of the second 2×2 is fed into the third 2×2 with the additional delay increased by a factor of 2 to 120 ns. This process was repeated until eight copies of the original pulse were spread over 480 ns. The input pulse cannot extend beyond 60 ns; otherwise, the tails of the pulses will overlap in time in the 2×2 splitters and produce interference with 100% modulation. This is why the AOM was configured to produce 40-ns pulses. The future version to be deployed on the NIF will require longer delays.

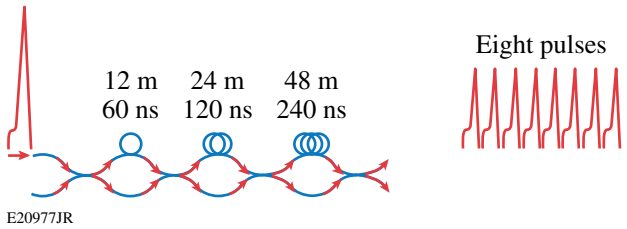

Figure 130.90
The replicator is constructed with 2×2 optical splitters. The outputs of the three stages are connected to the inputs of the subsequent stage with one of the connections having an additional length of fiber. Therefore, the eight replicated pulses arrive at the output at different times.

When detected by the photodiode, each of the optical replicas constitutes an independent measurement of the optical pulse from the MZM. These measurements can be averaged together to produce a measurement with the SNR improved by $\sqrt{N}$, where N is the number of replicas. For this prototype we expect an improvement in the SNR of 2.8. However, if there is any noise imprinted on the optical pulse before the replicator, e.g., noise from the LD, that noise will not average out. Since each XRD is optically encoded with two MZM's and two LD's, any noise arising before the replicator is reduced by $\sqrt{2}$.

The replicator is a passive device, so creating eight replicas reduces the amplitude of each pulse by a factor of 8, without taking into account the coupling losses between each splitter. Therefore, increasing the number of replicas improves the SNR, but it may also decrease the signal below the detection threshold of the photodiode.

The sensitivity of the InGaAs photodiodes is approximately 0.8 A/W. When coupled into the 50-Ω input of the oscilloscope, the sensitivity can be rewritten as 40 mV/mW. At the input of the system, either 20 mW or 60 mW of optical power is available at 1552 nm or 1557 nm, respectively. In an ideal system, this power is simply gated in time and passed through to the output with analog modulation imposed. Distributing the power over eight pulses, the maximum signals that could be expected at the oscilloscope would be 100 mV and 300 mV. The system is not ideal and each component has intrinsic losses associated with it. In addition many of the components were joined together with fiber connectors rather than fusion splicing to maintain the flexibility to reconfigure the system. Table 130.IV lists the major components in the system and the associated losses in decibels (dB).

Table 130.IV: Losses in the system.

Component	Loss (dB)
Acousto-optic modulator (AOM)	–6
Polarizer	–0.6
Mach–Zehnder modulator (MZM)	–2
10/90 splitter	–1
Wavelength-division multiplexer (WDM)	–1
Miscellaneous coupling losses	–2.6
Total	–13.2

The total losses are approximately 13.2 dB or a factor of 21, which reduces the maximum-possible signals to 5 and 14 mV, respectively. Signals that are this small seriously compromise the DR of the oscilloscope measurements because they represent only a small fraction of the full-scale range, even on the most-sensitive settings. To achieve a DR of 4000:1, the optical signal must be amplified. The signal was amplified by a commercial Er-doped fiber amplifier (EDFA). This device can provide 20 db of linear gain over a wide spectral range center at 1547 nm.

The detector was a highly linear DSC50S from Discovery Semiconductor. This 50-μm detector is large with respect to the core of the optical fiber (7 μm) so it will collect all of the light from the single-mode fiber. The photodiodes have a linear response down to the dark-current limit of 10 nA. Because the system operates at the negative quadrature point of the MZM, the dark current does not affect the low-voltage sensitivity. The photodiode has a 3-dB cutoff frequency of 12 GHz.

The oscilloscope that was used to record the data was a Tektronix TDS6604 with a 6-GHz analog BW and a sampling rate of 20 GS/s, providing a temporal resolution of 50 ps. The oscilloscope has an 8-bit digitizer, nominally providing a DR of 256, which is typical for modern digitizing oscilloscopes. Unfortunately, at full BW, digitizing noise reduces this to approximately 6 bits for a DR of about 64 in single-shot mode. This is insufficient for the NIF Dante requirements and is the primary reason the optical replicas were introduced into the system.

Data-Reduction Method

Several calibration steps are necessary to convert the complicated data record at the photodetector. Figure 130.91 shows the full pulse train at the photodetector. First, the replicator output without an rf signal applied to the MZM is recorded to determine relative positions of the 16 optical pulses. The individual elements of the two sets of eight pulses are nominally identical. Their relative timing can be determined by extracting a window around each pulse and aligning the windows via a cross-correlation. These relative timings are fixed so they may be recorded for future analysis. The eight pulses, aligned in time, are then averaged together to generate an average pulse shape: $I_{J,0}(t)$. The subscript J indicates the number of the MZM. Next a small rf signal $V_{\rm rf}(t)$ is applied to the MZM and $I_{J,{\rm rf}}(t)$ is recorded along with $V_{\rm rf}(t)$. The eight modulated pulses are then averaged together to produce a low-noise version of the MZM output. At each point in time, eight independent measurements are averaged. The standard deviation is given by the root-mean-square (rms) variation about the mean of the eight light pulses, $\Delta I_{J,{\rm opt}}(t)$. The SNR at each point is easily determined as $I_{J,{\rm opt}}(t)/\Delta I_{J,{\rm opt}}(t)$. The MZM transmission is given by

$$I_J(t) = I_{J,0}\sin\left\{\frac{\pi\left[V_{\rm rf}(t)+V_{J,0}\right]}{V_{J,\pi}}\right\} + I_{J,d}, \qquad (1)$$

where the parameter $V_{J,\pi}$ is the half-wave voltage, $V_{J,0}$ is the phase-equivalent, bias-point voltage, and $I_{J,d}$ is the combined optical leakage and bias. These values are approximately known. The manufacturer specifies $V_{J,\pi}$. The Q– operating point implies $V_{J,0}$ is $1.5 \times V_\pi$ and $I_{J,d} \sim I_{J,0}$. For $V_{\rm rf}(t) \ll V_{J,\pi}$, the response is essentially linear and Eq. (1) can be easily inverted over a time window that encompasses the flattop portion of the optical pulse without having to account for multifringe effects. The clean, optically measured $V_{\rm rf}(t)$ can then be compared with the applied, electronically measured $V_{\rm rf}(t)$ and cross-correlated to determine the relative phase. Using the averaged pulse shape makes it less likely that the cross-correlation will be biased by noisy data. Once the temporal alignment is established, the magnitude of $V_{\rm rf}(t)$ can be increased to values greater than $V_\pi/2$ to map out the entire transmission function. The algorithm specified in IEEE standard 1240 (Ref. 8) is used to determine the best-fit values for the constants for the system calibration. Each MZM is now calibrated with a baseline optical transmission curve and three scalar constants. The system is now ready to measure arbitrary rf signals.

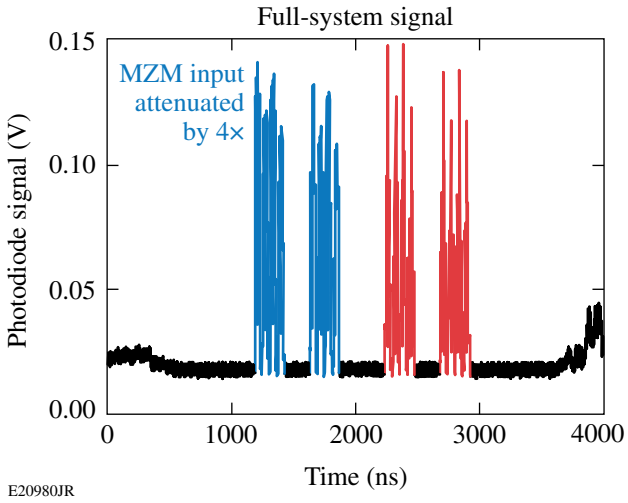

Figure 130.91
The optical signal detected at the oscilloscope at the output of the instrument has 16 serially combined pulses, eight from each Mach–Zehnder modulator (MZM).

The baseline optical transmission with $V_{\rm rf}(t) = 0$ should be reacquired shortly before the actual data are taken to account for drifts in the performance of the many EO components in the system. The arbitrary rf signal is then measured. The eight pulses from the MZM with highest attenuation (J = 1, λ_1 = 1557 nm) are averaged and then converted using calibrated sinusoidal transmittance of the modulator. Ideally, the attenuation is set such that the voltage applied to $\rm MZM_1$ never exceeds $V_{1,\pi}$. The unfolded $V_{1,{\rm rf}}(t)$ from the first MZM is used in conjunction with the calibrated $V_{2,\pi}$ of the lowest-attenu-

ation MZM to determine when the voltage applied to MZM_2 exceeded $V_{2,\pi}/2$. Normally, the arcsine function is calculated on the interval from $(M + 1/2)\pi$ to $(M + 1.5)\pi$, where M is an integer. Note that the sign flips between adjacent intervals. By noting whether M is even or odd, the multivalued unfolding can be made unambiguously single valued.

The averaged and unfolded signals from the two MZM's can be cross-correlated to determine the temporal alignment. The next step is to combine the two EO measured signals. As described above, the SNR can be calculated at each temporal point of the two waveforms. These SNR's can be quite different between the two curves, particularly when MZM_2 reaches the vicinity of $V_{2,\pi}/2$. The slope of the transmission function is zero at this point. The unfolding function has the form

$$V_{\mathrm{rf}}(t) = \frac{V_{J,\pi}}{\pi} \sin^{-1}\left[\frac{I_J(t) - I_{J,d}}{I_{J,0}}\right] - V_{J,0}. \tag{2}$$

Taking the derivative with respect to I_{opt} and multiplying by $\Delta I_{\mathrm{opt}}(t)$, the standard deviation of the optical measurements at each point, the variation in $V_{\mathrm{rf}}(t)$ as a function of $I_{\mathrm{opt}}(t)$ and $\Delta I_{\mathrm{opt}}(t)$ can be determined.

$$\Delta V_{J,\mathrm{rf}}(t) = \Delta I_J(t)\frac{\mathrm{d}V_{J,\mathrm{rf}}}{\mathrm{d}I_J} = \frac{V_{J,\pi}\Delta I_J(t)}{I_{J,0}\pi\sqrt{1 - \left[\dfrac{I_J(t) - I_{J,d}}{I_{J,0}}\right]^2}}, \tag{3}$$

when $V_{\mathrm{rf}}(t)$ equals $V_{J,\pi}/2$, $I_{J,\mathrm{opt}}(t)$ is approximately zero, and the derivative diverges. Small errors in the measurement $\Delta I_{J,\mathrm{opt}}(t)$ lead to large changes in the variation of the EO measured rf voltage $\Delta V_{J,\mathrm{rf}}(t)$. A weighted average based on standard deviations of the two signals was used to combine the two MZM's. To calculate the standard deviation, the rms deviation of the light pulses $\Delta I_{J,\mathrm{opt}}(t)$, was fed into Eq. (2) as

$$I_{J,\mathrm{opt}^+}(t) = I_{J,\mathrm{opt}}(t) + \Delta I_{J,\mathrm{opt}}(t) \tag{4a}$$

and

$$I_{J,\mathrm{opt}^-}(t) = I_{J,\mathrm{opt}}(t) - \Delta I_{J,\mathrm{opt}}(t). \tag{4b}$$

These substitutions generated $\Delta V_{J,\mathrm{rf}^+}(t)$ and $\Delta V_{J,\mathrm{rf}^-}(t)$, respectively. The rms variation in $V_{J,\mathrm{rf}}(t)$ was then defined as

$$\Delta V_{J,\mathrm{rf}}(t) = \left[\Delta V_{J,\mathrm{rf}^+}(t) + \Delta V_{J,\mathrm{rf}^-}(t)\right]/2. \tag{5}$$

The weighting function for the averaging was taken as the inverse of the standard deviation of the raw data $1/\Delta I_{J,\mathrm{opt}}(t)$ normalized by the sum of all the weights:

$$W_J(t) = \left[1/\Delta I_{J,\mathrm{opt}}(t)\right]/\sum\left[1/\Delta I_{J,\mathrm{opt}}(t)\right]; \tag{6}$$

$$\left\langle V_{\mathrm{rf}}(t)\right\rangle = \sum\left[V_{J,\mathrm{rf}} W_J(t)\right]. \tag{7}$$

Likewise, the final rms variation at each point is the weighted rms sum or the variations from each modulator:

$$\Delta\left\langle V_{\mathrm{rf}}(t)\right\rangle = \sqrt{\sum \Delta V_{J,\mathrm{rf}}(t)\Delta V_{J,\mathrm{rf}}(t) W_J(t)} \tag{8}$$

and the SNR is $\left\langle V_{\mathrm{rf}}(t)\right\rangle / \Delta\left\langle V_{\mathrm{rf}}(t)\right\rangle$.

With the hardware and signal-processing algorithms in place, the system was incorporated into the Dante instrument on LLE's OMEGA laser. An rf splitter was used to tap off half of the signal feeding one of the Dante SCD5000 transient digitizers. In this way we could directly compare the current system and the prototype. Figure 130.92 shows the averaged optical output of the two MZM's. Each averaged output is bracketed by curves representing +1 and –1 standard deviation. The data from the highly attenuated modulator vaguely resemble an inverted copy of the output of the XRD. The low-attenuation MZM output is highly distorted because the voltage exceeded $V_{\pi}/2$. This signal required the unfolded signal from the highly attenuated MZM to remove the multivalue ambiguities. This procedure is fully automated. Figure 130.93 shows the combined average of the two MZM's and the purely electrical measurement from the SCD5000. The average rms difference between the two waveforms is 2.6%. Another way to compare the measurements from the different instruments is to look at the spectral content. Figure 130.94 shows the fast Fourier transform (FFT) of both waveforms. The spectra match out to a frequency of about 3.5 GHz. The rise time of the XRD's is approximately 120 ps, giving a maximum frequency of 2.75 GHz. Therefore, we expect the EO acquisition system to capture all of the frequency delivered by the XRD.

Using an offline electronic pulse generator to simulate the NIF Dante XRD's, signals as large as 18 V were measured with the prototype system. Using the analysis described above, the SNR was calculated and is plotted against unfolded and averaged signals in Fig. 130.95. The peak SNR was approximately 500:1. The horizontal line is at an SNR of 1 and represents the minimum signal detectable by the instrument. The measured

points cross this line at 30 mV, so the demonstrated DR is 600:1. The relevance of Fig. 130.95 is illustrated in Fig. 130.96, where the system output for a 30-mV input pulse is plotted. The output is very noisy and just barely discernible.

Conclusions

A prototype EO acquisition system, the NIF Dante, has been built and tested. The system has a DR of 600:1 and a peak SNR of 500:1. The prototype has demonstrated that the concept works, but not all of the specifications of the NIF Dante upgrade have been met. In particular, the DR demonstrated so far is too small. On the high end, the maximum signal is limited to the voltage that drives both MZM's beyond $V_{\pi}/2$. At that point the automated reduction routines cannot define a unique unfolding. The solution to this problem is to add an additional MZM with still-higher attenuation on its rf input. Other strategies must be employed to reach an SNR of 5 at a signal of 50 mV over a 200-ps interval. We now have an SNR of 1 at 30 mV over

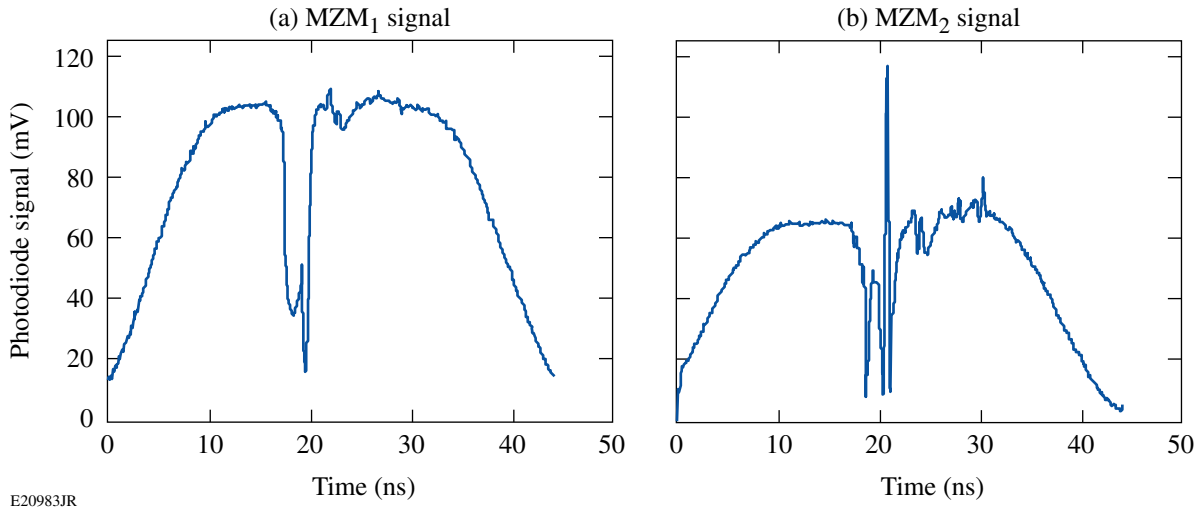

Figure 130.92
The averaged output of the two MZM's. (a) The signal from MZM_1 is approximately an inverted replica of the radio frequency (rf) input. (b) The signal from MZM_2 is highly distorted as a result of fringe shifts.

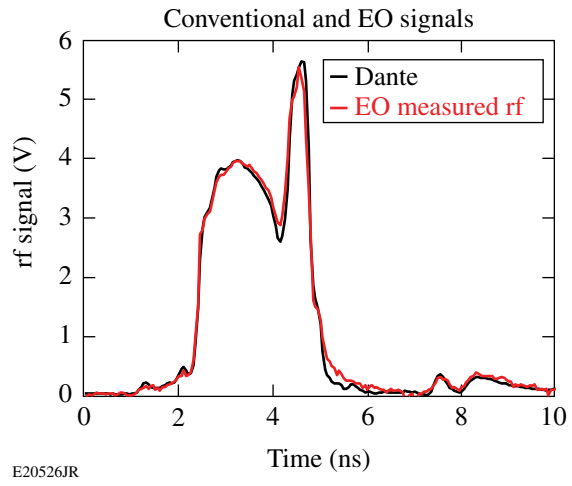

Figure 130.93
The electro-optic (EO) measurement agrees with that of a high-dynamic-range digitizer.

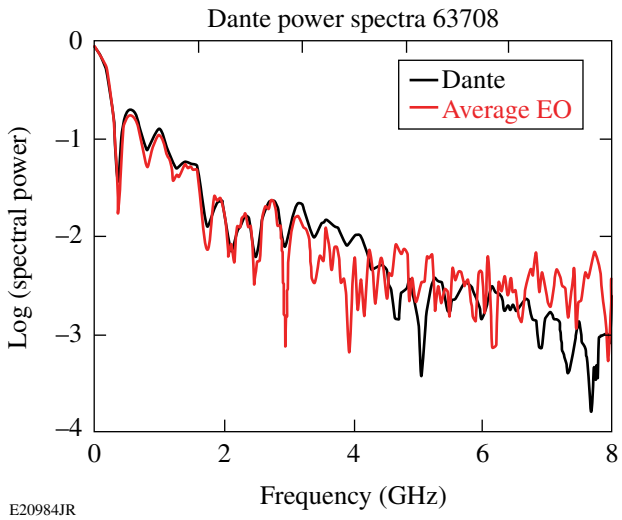

Figure 130.94
The frequency content of the SCD5000 and the EO measurements match out to 3.75 GHZ, which is greater than the bandwidth of the x-ray photodiode.

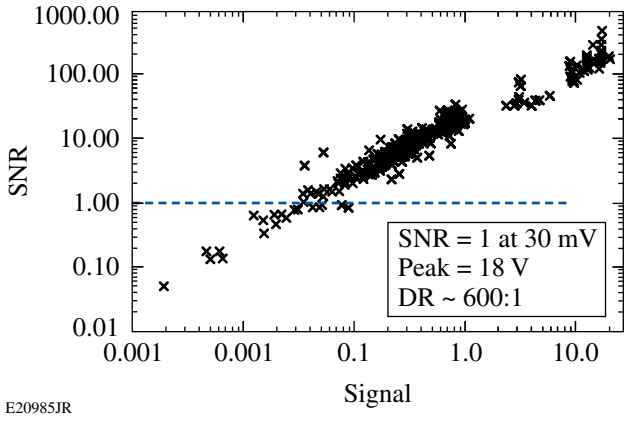

Figure 130.95
The signal-to-noise ratio (SNR) plotted against the EO measured signal clearly shows that the minimum-detectable signal occurs at 30 mV, where the SNR crosses the horizontal line. The DR is ~600:1.

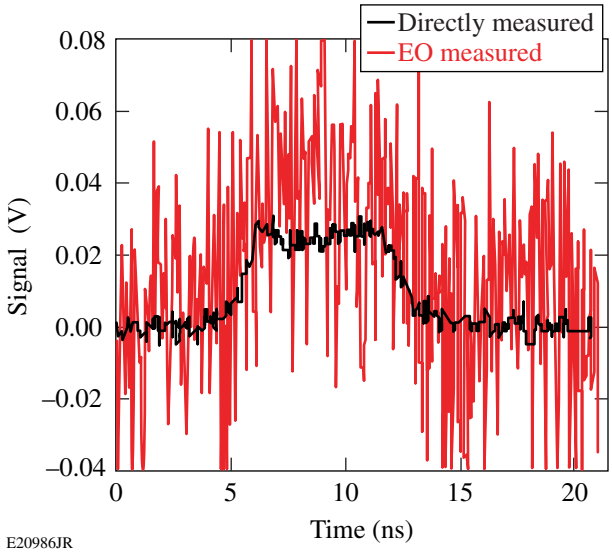

Figure 130.96
At 30 mV, the EO measured output (red curve) is noisy with respect to the directly measured radio frequency (black curve).

a 50-ps time interval. Figure 130.95 implies an SNR of 1.7 at 50 mV. Averaging four points to get to the 200-ps interval will improve the SNR by a factor of 2, giving an SNR of 3.4, which almost meets the specification. The number of replicas can probably be increased to 32 without adding an undue burden of optical fiber management on the system. This will increase the SNR by a factor of 2, and, therefore, will meet the specification. Using a 12-GHz, 40-GS/s oscilloscope will accomodate an eight-point temporal smoothing that could increase the SNR by $\sqrt{8}$. Beyond that, it will be necessary to explore using quieter lasers and an EDFA with lower noise figures.

ACKNOWLEDGMENT

This work was supported by the U.S. Department of Energy Office of Inertial Confinement Fusion under Cooperative Agreement No. DE-FC52-08NA28302, the University of Rochester, and the New York State Energy Research and Development Authority. The support of DOE does not constitute an endorsement by DOE of the views expressed in this article.

REFERENCES

1. E. I. Moses, Fusion Sci. Technol. **54**, 361 (2008).
2. E. L. Dewald *et al.*, Rev. Sci. Instrum. **75**, 3759 (2004).
3. E. L. Wooten *et al.*, IEEE J. Sel. Top. Quantum Electron. **6**, 69 (2000).
4. *Generic Reliability Assurance Requirements for Optoelectronic Devices Used in Telecommunications Equipment*, Telcordia Technologies, Inc., Piscataway, NJ, Document No. GR-468-CORE, Issue 2 (September 2004).
5. Fiberdyne Labs, Inc., accessed 26 April 2012, http://www.fiberdyne.com/products/itu-grid.html.
6. E. I. Ackerman and C. H. Cox III, in *International Topical Meeting on Microwave Photonics, 2000* (IEEE, New York, 2000), pp. 121–124.
7. W. R. Donaldson, J. R. Marciante, and R. G. Roides, IEEE J. Quantum Electron. **46**, 191 (2010).
8. *IEEE Std. 1241-2000, IEEE Standard for Terminology and Test Methods for Analog-to-Digital Converters* (IEEE, New York, 2001).

Shock-Ignition Experiments with Planar Targets on OMEGA

In inertial confinement fusion (ICF), a capsule containing cryogenic deuterium–tritium fusion fuel is rapidly compressed to high temperatures and areal densities sufficient for thermonuclear fusion. If the α particles generated via D–T fusion reactions in the central hot spot of an imploded capsule deposit their energy in the compressed core, the capsule ignites. Provided the confinement time determined by the fuel-mass inertia is sufficiently long, the energy released via the fusion burn can exceed the incident driver energy and the fusion gain exceeds unity. The demonstration of this concept is the main goal of ICF research.[1] In laser-driven ICF the compression drive is provided by coupling laser energy into an ablator surrounding a spherical fuel capsule, either directly through symmetric irradiation of the fusion target or indirectly via a thermal x-ray bath generated from laser illumination of the inner walls of a cavity (hohlraum). In the shock-ignition (SI) concept,[2] the fuel-assembly and ignition stages are separated by using shaped, nanosecond laser pulses. During the compression stage of the laser, the fuel is assembled to a high areal density (ρR) at sub-ignition velocity, resulting in a central hot-spot temperature insufficient for ignition. A high-intensity laser spike at the end of the assembly pulse then launches a strong shock wave, the timing of which is such that the return shock, caused by the rising hot-spot pressure, collides with the strong shock inside the fuel.[3] This results in two new shocks, one of which propagates inward, heating and compressing the hot spot to ignition conditions and causing a *non-isobaric* pressure profile peaked at the center. This is energetically favorable compared to the *isobaric* distribution in conventional hot-spot ignition, where both hot spot and fuel are compressed to the same pressure $p_{\rm iso}$, and is a key advantage of shock ignition. It can be shown that the energy required to achieve shock ignition decreases as $\sim(p/p_{\rm iso})^3$, where the non-isobaric hot-spot pressure p directly depends on the initial laser-driven shock strength at the ablator and its amplification through spherical convergence in the fuel.[4]

Taking full advantage of the SI scheme requires laser-generated shocks at the ablator of ~300-Mbar, launched in the presence of a long-scale-length pre-plasma generated by the assembly laser pulse. For such strong shocks, on-target intensities exceeding 10^{15} W/cm^2 are necessary and laser–plasma instabilities (LPI's) play an important role in the coupling of laser energy to the target. These lead to energy losses through stimulated Raman and Brillouin scattering (SRS and SBS, respectively) and hot-electron generation and potential fuel preheat by fast electrons produced through SRS and two-plasmon decay. Hot electrons are predominantly generated by the laser spike late in the target evolution when the areal density grows rapidly. Provided the electron stopping distance is within the shell thickness, they can even augment the ignitor shock strength and enhance the target performance.[5]

The idea of separating fuel assembly and ignition is conceptually similar to fast ignition.[6] For SI, however, complicated cone-in-shell targets are not necessary, and SI can use the pulse-shaping capabilities of existing facilities designed for hot-spot ignition rather than requiring an additional short-pulse, multipetawatt ignitor laser. This significantly relaxes the technical and financial constraints on fielding this concept experimentally or in a fusion-energy context.

SI has received considerable attention as an alternative path to ignition, e.g., for the National Ignition Facility,[7] HiPER,[8] and the LMJ project.[9] Theoretical studies have investigated target design and robustness,[10] but only a few experimental studies have been performed. Preliminary work on the OMEGA Laser System[11] using warm, spherical plastic targets driven by a SI-type laser pulse showed ~30% higher ρR, larger neutron yields, and better implosion stability than hydrodynamic- and energy-equivalent implosions without a high-intensity shock spike.[4]

This article presents experimental results on LPI and laser-driven shock propagation in planar geometry and at SI-relevant intensities performed using OMEGA. To infer initial shock properties, the data are compared to two-dimensional (2-D) radiative–hydro-dynamic simulations that show very good agreement with the experiment. Based on the numerical results, the experiment discussed here represents the first demonstration of a laser-driven, 70-Mbar shock in the presence of a long-scale-length pre-plasma.

Figure 131.1(a) shows a schematic of the experimental setup. The planar targets consisted of three layers: a 40-μm plastic ablator onto which the laser was focused, followed by 30 μm of Mo and 140 μm of SiO_2. The Mo was used to shield hot electrons from propagating into the final layer and to infer the hot-electron population through time-integrated recording of the Mo-K_α emission with an absolutely calibrated x-ray spectrometer. The final SiO_2 layer was used to observe the shock temperature through streaked optical pyrometry (SOP)[12] and the shock propagation via two VISAR (velocity interferometer system for any reflector) diagnostics with different velocity responses (10.4 and 6.4 μm/ns/fringe) (Ref. 13). Since the Mo is opaque to optical wavelengths, the laser-driven shock could be observed only after entering the SiO_2 layer. The quartz also acted as a "get-lost" layer that prevented refluxing of hot electrons in the Mo. In addition, a CH washer was attached to the front of the target to stop diffracted laser light from hitting the target's sides and to stop electrons from streaming around the target. Further diagnostics included a four-channel, time-resolved, hard x-ray detector that measured the hot-electron temperature[14] and backscattering diagnostics that determined SRS and SBS levels within the focal cone of two beams in the strong-shock drive as well as one location between two strong-shock beams.[15]

Figure 131.1(b) shows an example for the temporal on-target intensity profile of the 351-nm-wavelength laser light at the position of the unperturbed target surface. With an on-target energy between ~5 kJ and 7.2 kJ, the total irradiation profile [dashed line in Fig. 131.1(b)] was achieved by stacking three laser cones in time with individual focusing parameters. Beam smoothing was achieved with polarization smoothing[16] and distributed phase plates (DPP's).[17] Beams in Cones 2 and 3 (blue and green, respectively) were focused to a 1/*e* intensity radii of 412 μm and 310 μm, respectively, using "SG8" and defocused "SG4" DPP's. These two cones formed a pre-plasma for ~1.6 ns, while the overlap between Cones 1 (red) and 2 provided the high-intensity spike driving a strong shock into the target. Beams in Cone 1 were focused to a 302-μm radius using defocused "IDI300" DPP's. Cone 3 consisted of eight beams at an incidence angle of 62.3°; Cones 1 and 2 comprised six spatially overlapping beams at 23.4° and 47.8°, respectively. While Cones 2 and 3, and therefore the pre-plasma conditions, were kept the same throughout the experiment, the energy contained in Cone 1 was varied to give an overlapped "spike intensity" ranging from ~0.6 to 1.4 × 10^{15} W/cm^2.

Results for the hot-electron temperature and population as a function of the nominal spike intensity are displayed in Fig. 131.2. The electron temperature [Fig. 131.2(a)] rises with intensity, indicating an increase in LPI, and reaches a peak of ~70 keV at the highest-intensity case considered here. The total energy in the hot-electron component [Fig. 131.2(b)] was inferred from comparing the time-integrated Mo-K_α yield to Monte Carlo simulations.[18] The emission of hard x rays was strongly correlated to the high-intensity spike of the drive laser. Therefore, the hot-electron conversion efficiency, plotted on the right *y* axis of Fig. 131.2(b), is given by comparing the energy contained in the hot-electron component to that in the laser spike, i.e., the energy incident on target during the overlap between Cones 1 and 2. As expected, it increased with

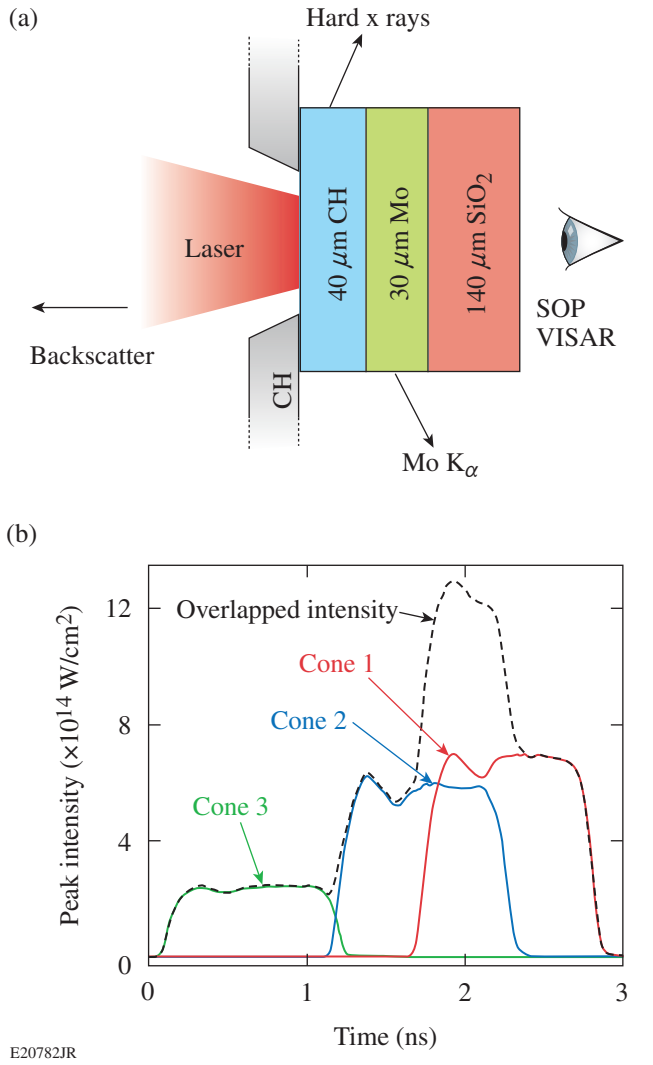

Figure 131.1
(a) Schematic of the planar target driven by a laser pulse as shown in (b). The pulse was generated by stacking three laser cones in time and space, each with its own energy and focusing parameters. SOP: streaked optical pyrometry; VISAR: velocity interferometer system for any reflector.

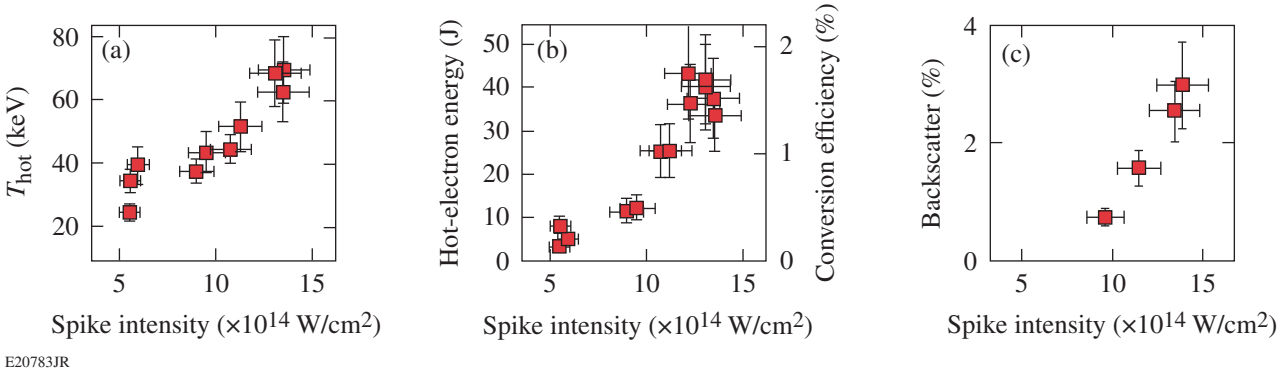

Figure 131.2
(a) Hot-electron temperature as a function of peak laser intensity; (b) laser conversion efficiency and total energy contained in the hot-electron component; (c) fraction of backscattered laser energy (SRS + SBS) within the strong-shock beam cones as a function of peak intensity.

rising intensity, and at the highest intensity, 1.8% of the spike energy was converted to hot electrons. The error bars in these data are dominated by the precision of the measured K_α yield (~25%) (Ref. 18).

Results for the backscattered laser light (SRS and SBS) within the shock-beam focal cones are plotted as a function of peak intensity in Fig. 131.2(c). This also increased with incident intensity, reaching ~3% for the highest-intensity case. Sidescatter was also observed but was not fully quantified and is not included in Fig. 131.2(c). Since the light reflection is nonuniform, and there are too few diagnostics to infer a full scattering profile, so the interpretation of the data with respect to a total backscattered energy in these planar experiments is difficult. The sidescatter is not expected to exceed the in-beam scattering, giving an upper limit for the total amount of scattered light of ~10% at 1.4×10^{15} W/cm^2.

Examples for shock-evolution data obtained with VISAR and SOP diagnostics are shown in Figs. 131.3(a) and 131.3(c),

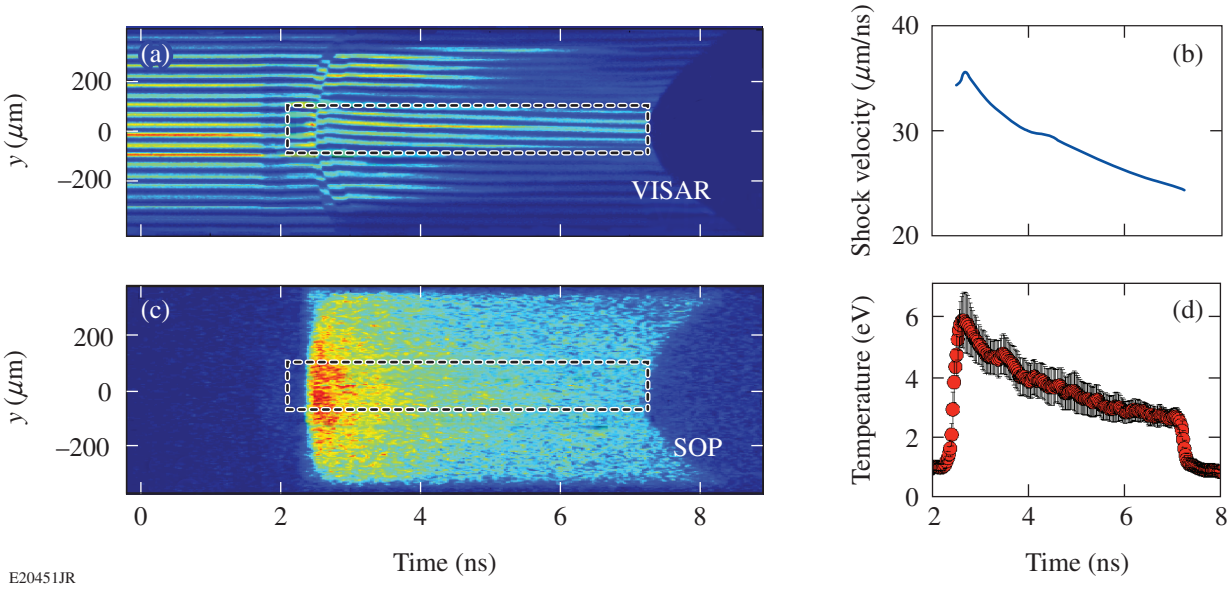

Figure 131.3
Experimental shock-propagation data obtained with (a) VISAR and (c) SOP at a peak intensity of 9×10^{14} W/cm^2; (b) and (d) show extracted shock velocity and temperature, respectively.

respectively. These data were taken with a spike intensity of ~9×10^{14} W/cm^2, and all figures are plotted as a function of time with $t = 0$ corresponding to the onset of the laser pulse [see Fig. 131.1(b)]. The slight drop in signal strength of the VISAR data at ~1.7 ns is caused by the laser spike hitting the target. This results in the generation of hot electrons, some of which reach the SiO_2 layer and alter the refractive index of the material through ionization, causing partial absorption of the probe laser. Since the Mo layer is opaque, no shock front can be observed until its breakout from the Mo into the SiO_2 at ~2.5 ns. This causes a strong fringe shift in the VISAR and a signal onset in the SOP. The subsequent slowly varying fringe shift in Fig. 131.3(a) is indicative of a decelerating shock. At ~7.2 ns the shock breaks out into vacuum through the rear of the target, as evidenced by the pronounced signal drop in both data sets. The shock is strongest and fastest in the center, where the drive laser's intensity is at its peak, and edge rarefactions cause a strong curvature of the shock front and the breakout feature. These data can be used to extract a shock velocity in the range of 30 μm/ns [Fig. 131.3(b)] and an emission temperature of a few eV [Fig. 131.3(d)] inside the SiO_2 layer.

The incident laser pulse launched multiple shocks into a target, but the primary goal was to characterize the strong shock driven by the high-intensity spike. The conditions inside the ablator cannot be observed directly. Instead, the strong shock's initial conditions were inferred by matching numerical simulation results to the experimental data. For this purpose the 2-D radiative hydrocode *DRACO* was used[19] Note that a 2-D treatment is strictly necessary as evidenced by the curvature of the rear shock-breakout feature in Figs. 131.3(a) and 131.3(c). Figure 131.4 shows snapshots of the pressure distribution from a simulation using the experimental conditions for the data in Fig. 131.3. The x axis denotes the target's thickness; the y axis is the lateral extent of the target. The simulations assumed azimuthal symmetry and $y = 0$ corresponds to the point of peak laser intensity. The laser drives the target from the left and the shocks propagate to the right. A schematic of the initial target layout is shown at the top of Fig. 131.4(a), and the dashed lines indicate unperturbed interface positions.

At 2.5 ns [Fig. 131.4(a)] the foremost shock reaches the Mo/SiO_2 interface, which agrees well with the data in Fig. 131.3. At this time, ~200 ps after the end of the high-intensity drive, the strong shock is already starting to decrease in strength and has almost caught up with the weaker shock generated by the pre-plasma laser pulse. This is also in good agreement with the VISAR data, which exhibit two subsequent fringe jumps within ~100 ps: the first upon the breakout of the pre-plasma shock into the SiO_2 layer, quickly followed by the coalescence with the trailing strong shock. At 7.1 ns of the simulated target evolution [Fig. 131.4(b)], the shock front reaches the target/vacuum interface at the rear, also agreeing very well with the experimental data, which exhibit this event at 7.2 ns.

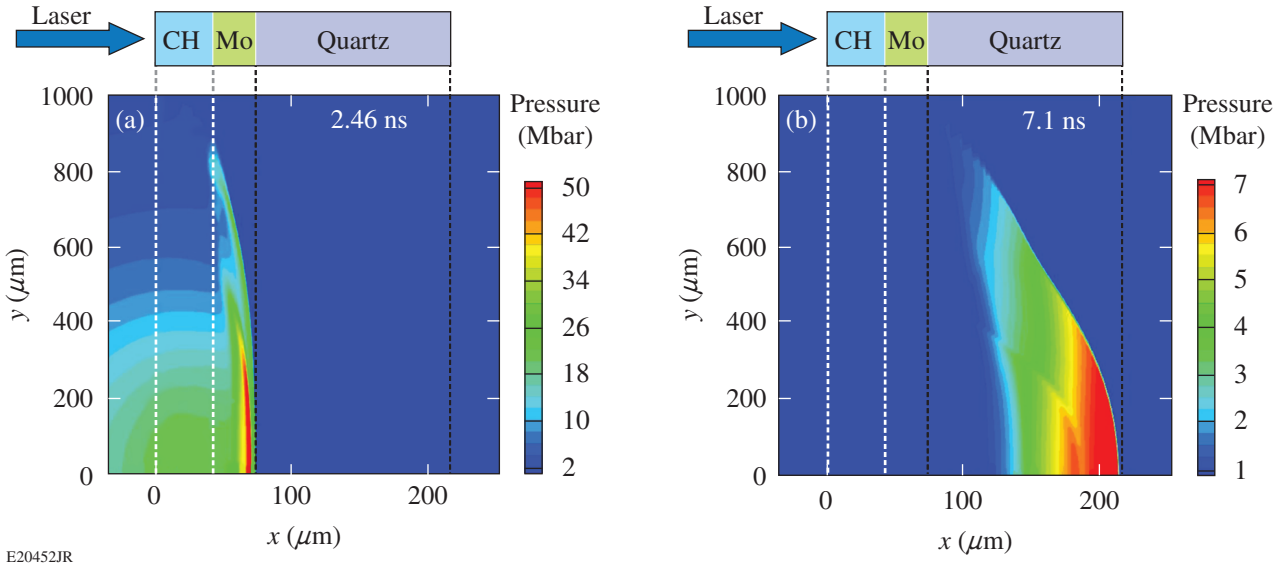

Figure 131.4
Snapshots of the pressure distribution at (a) 2.46 ns and (b) 7.1 ns from *DRACO* simulations using the experimental conditions for the data in Fig. 131.3. A schematic of the initial target layout is shown above (a) and (b). The dashed lines indicate initial interface positions.

The simulated target evolution is reproduced well over the range of intensities used in the experiment. Figure 131.5(a) shows the rear shock-breakout time as a function of spike intensity, with the squares denoting experimental data and the circles numerical results. The lowest-intensity case corresponds to no energy in Cone 1, i.e., no laser spike is incident on the target. The agreement between the simulated shock-propagation time to the experimentally measured one is better than 5% over the full intensity range, indicating a good numerical treatment of the laser–target interaction and ablator physics.

To extract the ablatively driven shock strength in the plastic layer from these simulations, the impedance mismatch between the plastic and Mo needs to be taken into account. The heavier Mo causes a partial shock reflection that overlaps with the laser-driven one, leading to an increase of the observed strong-shock strength in the ablator at the time of peak intensity. The purely ablatively driven shock strength was inferred through simulations using the same laser conditions, but an all-CH target. This results in a reduction of ~25% in the peak pressure, when compared to the CH/Mo/SiO_2 targets. The simulated ablation pressures corrected for the impedance mismatch are plotted as the blue circles in Fig. 131.5(b). The simulation results provide a scale relating shock propagation and ablation pressure, which was then used to infer ablation pressures via the experimentally observed shock-propagation time [red squares in Fig. 131.2(b)]. The error bars for the numerical results reflect temporal variations of the simulated pressure. This, in addition to the experimental uncertainty in the shock-propagation time, determines the error for the inferred pressures. Based on these results, a peak ablation pressure of ~70 Mbar was achieved with a drive intensity of ~1.2×10^{15} W/cm^2 in the presence of a long-scale-length pre-plasma. The simulated plasma density scale length at quarter-critical in these experiments is ~350 μm at the time of the high-intensity spike, with coronal temperatures between 2.0 keV and 2.9 keV, depending on the spike intensity. This compares well to previous experimental and numerical results for laser intensities of mid-10^{14} W/cm^2 (Refs. 18 and 20) but is lower than expected for a NIF-scale shock-ignition target (~450 μm, ~8 keV). The scale length in these experiments is limited by the focal-spot size, and the temperature by the spike intensity.

In Ref. 21 the stationary ablation pressure in a pure plastic target was derived to be $p_a = 40\left(I_{15}/\lambda_{\mu m}\right)^{2/3}$, where I_{15} denotes the absorbed laser intensity in units of 10^{15} W/cm^2 and $\lambda_{\mu m}$ is the laser wavelength in microns. The absorption fraction of the high-intensity spike observed in the simulations is typically ~90%. The simulations do not include hot electrons,

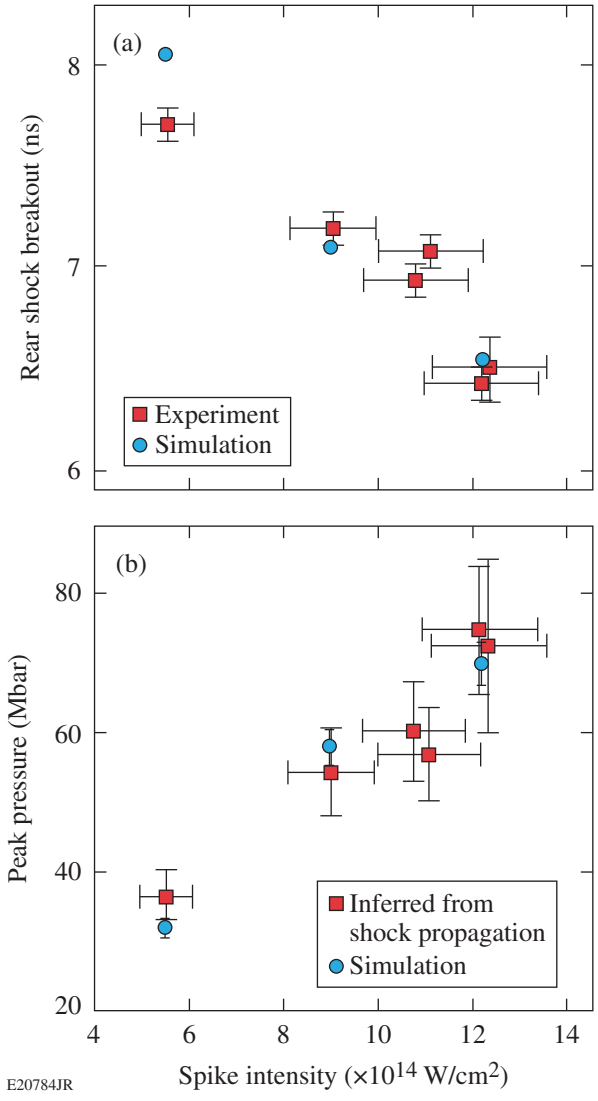

Figure 131.5
(a) Simulated (circles) and experimental (squares) shock-propagation time as a function of peak intensity; (b) laser-driven ablation pressure inferred from all-CH target simulations as a function of peak intensity.

but this contributes, at most, a few percent [Fig. 131.2(b)], and the agreement between simulated and observed target evolution gives confidence in the numerical treatment of the laser–target interaction. Applying the numerical absorption fraction to the pressure scaling overestimates the ablation pressure by 20% to 50%. This mismatch is not surprising since the pressure scaling makes the simplified assumption that laser absorption is limited to the critical surface, and therefore cannot be expected to capture the absorption physics correctly.

The simulations may be used to calculate the expected target conditions at full shock-ignition intensities. With a spike

intensity of ~10^{16} W/cm^2, pressures of ~300 Mbar should be achieved for a simulated 70% absorption of the high-intensity spike—sufficient to drive a shock-ignition experiment. As before, the simulations do not include a treatment of hot electrons, and whether this extrapolation is valid needs to be investigated. The impact of the hot-electron component on the strong-shock strength is still under investigation and will depend on the temperature of the electron distribution.[5] Clearly, more experiments are required to characterize the plasma and shock conditions at such high intensities.

In conclusion, experiments investigating shock strength and the impact of LPI at SI-relevant laser conditions have been performed. Planar targets were irradiated with laser pulses comprising a pre-plasma–generating foot and a high-intensity spike to launch a strong shock. At a peak intensity of 1.4×10^{15} W/cm^2, an electron temperature of 70 keV was measured with ~1.8% of the spike energy being converted to hot electrons, and $\lesssim$10% of the laser energy was scattered. Simulations using the radiative 2-D hydrocode *DRACO* show very good agreement with the observed shock propagation. Based on these results, at an intensity of 1.2×10^{15} W/cm^2, a 70-Mbar shock was generated in the presence of a 350-μm pre-plasma. This is the highest pressure reported at SI-relevant conditions, and these experiments constitute an important step toward validating the shock-ignition concept experimentally.

ACKNOWLEDGMENT

This work has been supported by the U.S. Department of Energy under Cooperative Agreement Nos. DE-FC02-04ER54789 and DE-FC52-08N28302, the University of Rochester, and the New York State Energy Research and Development Authority. The support of DOE does not constitute an endorsement by DOE of the views expressed in this article. We acknowledge useful discussions with P. M. Celliers.

REFERENCES

1. S. Atzeni and J. Meyer-ter-Vehn, *The Physics of Inertial Fusion: Beam Plasma Interaction, Hydrodynamics, Hot Dense Matter*, International Series of Monographs on Physics (Clarendon Press, Oxford, 2004).
2. R. Betti, C. D. Zhou, K. S. Anderson, L. J. Perkins, W. Theobald, and A. A. Solodov, Phys. Rev. Lett. **98**, 155001 (2007).
3. R. Nora and R. Betti, Phys. Plasmas **18**, 082710 (2011).
4. W. Theobald, R. Betti, C. Stoeckl, K. S. Anderson, J. A. Delettrez, V. Yu. Glebov, V. N. Goncharov, F. J. Marshall, D. N. Maywar, R. L. McCrory, D. D. Meyerhofer, P. B. Radha, T. C. Sangster, W. Seka, D. Shvarts, V. A. Smalyuk, A. A. Solodov, B. Yaakobi, C. D. Zhou, J. A. Frenje, C. K. Li, F. H. Séguin, R. D. Petrasso, and L. J. Perkins, Phys. Plasmas **15**, 056306 (2008).
5. R. Betti, W. Theobald, C. D. Zhou, K. S. Anderson, P. W. McKenty, S. Skupsky, D. Shvarts, V. N. Goncharov, J. A. Delettrez, P. B. Radha, T. C. Sangster, C. Stoeckl, and D. D. Meyerhofer, J. Phys., Conf. Ser. **112**, 022024 (2008).
6. M. Tabak *et al*., Phys. Plasmas **1**, 1626 (1994).
7. L. J. Perkins, R. Betti, K. N. LaFortune, and W. H. Williams, Phys. Rev. Lett. **103**, 045004 (2009).
8. X. Ribeyre *et al*., Plasma Phys. Control. Fusion **51**, 015013 (2009).
9. B. Canaud and M. Temporal, New J. Phys. **12**, 043037 (2010).
10. S. Atzeni, A. Schiavi, and A. Marocchino, Plasma Phys. Control. Fusion **53**, 035010 (2011); O. Klimo *et al*., Phys. Plasmas **18**, 082709 (2011); M. Lafon, X. Ribeyre, and G. Schurtz, Phys. Plasmas **17**, 052704 (2010); X. Ribeyre *et al*., *ibid*. **18**, 102702 (2011); C. Riconda *et al*., *ibid*. **18**, 092701 (2011); A. J. Schmitt *et al*., *ibid*. **17**, 042701 (2010).
11. T. R. Boehly, D. L. Brown, R. S. Craxton, R. L. Keck, J. P. Knauer, J. H. Kelly, T. J. Kessler, S. A. Kumpan, S. J. Loucks, S. A. Letzring, F. J. Marshall, R. L. McCrory, S. F. B. Morse, W. Seka, J. M. Soures, and C. P. Verdon, Opt. Commun. **133**, 495 (1997).
12. J. E. Miller, T. R. Boehly, A. Melchior, D. D. Meyerhofer, P. M. Celliers, J. H. Eggert, D. G. Hicks, C. M. Sorce, J. A. Oertel, and P. M. Emmel, Rev. Sci. Instrum. **78**, 034903 (2007).
13. P. M. Celliers, D. K. Bradley, G. W. Collins, D. G. Hicks, T. R. Boehly, and W. J. Armstrong, Rev. Sci. Instrum. **75**, 4916 (2004).
14. C. Stoeckl, V. Yu. Glebov, D. D. Meyerhofer, W. Seka, B. Yaakobi, R. P. J. Town, and J. D. Zuegel, Rev. Sci. Instrum. **72**, 1197 (2001).
15. W. Seka, D. H. Edgell, J. P. Knauer, J. F. Myatt, A. V. Maximov, R. W. Short, T. C. Sangster, C. Stoeckl, R. E. Bahr, R. S. Craxton, J. A. Delettrez, V. N. Goncharov, I. V. Igumenshchev, and D. Shvarts, Phys. Plasmas **15**, 056312 (2008).
16. T. R. Boehly, V. A. Smalyuk, D. D. Meyerhofer, J. P. Knauer, D. K. Bradley, R. S. Craxton, M. J. Guardalben, S. Skupsky, and T. J. Kessler, J. Appl. Phys. **85**, 3444 (1999).
17. Y. Lin, T. J. Kessler, and G. N. Lawrence, Opt. Lett. **20**, 764 (1995).
18. B. Yaakobi, P.-Y. Chang, A. A. Solodov, C. Stoeckl, D. H. Edgell, R. S. Craxton, S. X. Hu, J. F. Myatt, F. J. Marshall, W. Seka, and D. H. Froula, Phys. Plasmas **19**, 012704 (2012).
19. P. B. Radha, V. N. Goncharov, T. J. B. Collins, J. A. Delettrez, Y. Elbaz, V. Yu. Glebov, R. L. Keck, D. E. Keller, J. P. Knauer, J. A. Marozas, F. J. Marshall, P. W. McKenty, D. D. Meyerhofer, S. P. Regan, T. C. Sangster, D. Shvarts, S. Skupsky, Y. Srebro, R. P. J. Town, and C. Stoeckl, Phys. Plasmas **12**, 032702 (2005).
20. D. H. Froula, B. Yaakobi, S. X. Hu, P.-Y. Chang, R. S. Craxton, D. H. Edgell, R. Follett, D. T. Michel, J. F. Myatt, W. Seka, R. W. Short, A. Solodov, and C. Stoeckl, Phys. Rev. Lett. **108**, 165003 (2012).
21. J. D. Lindl, Phys. Plasmas **2**, 3933 (1995).

Inelastic X-Ray Scattering from Shocked Liquid Deuterium

Extreme states of matter existing in astrophysical objects (e.g., stars and planetary interiors) can be created in the laboratory with high-intensity laser beams, particle beams, and *Z*-pinch generators.[1] High-energy-density physics (HEDP) encompasses the research of matter having energy densities of ~10^{11} J/m^3 or more or, equivalently, pressures greater than 1 Mbar (Refs. 1 and 2). A subset of this field involves the study of warm, dense matter (WDM)[1,2] with electron temperatures around the Fermi temperature and the ratio of the potential energy to the kinetic energy of the ions greater than unity. The latter can be quantified by an ion–ion coupling parameter[2] $\Gamma_{ii} = (Ze)^2 \big/ d_i k_B T > 1$, where Ze is the electric charge of the ion, d_i is the mean ion spacing, k_B is the Boltzmann constant, and T is the temperature. In shock-compressed matter at these extreme conditions, the determination of the system properties, in particular the equation of state (EOS), is complicated by the highly correlated nature of the medium, consisting of a system of strongly coupled ions immersed in a fluid of partially degenerate electrons. Understanding the physical properties (e.g., opacity,[3] conductivity,[4] EOS,[5] and compressibility[6]) of WDM is, however, very important for inertial confinement fusion (ICF) research[7,8] and the study of planetary interiors[9] because theoretical models differ by factors of several when predicting these quantities. In the past decade, developments in laser-produced plasma sources and detector efficiencies have made inelastic x-ray scattering a powerful diagnostic providing electron temperature (T_e), electron density (n_e), and ionization (Z) for critical EOS measurements in ICF and planetary science research.[10–14]

This article describes the first experimental observation of noncollective, inelastic x-ray Thomson scattering from liquid deuterium driven by a laser-produced ~10-Mbar shock wave. The average electron temperature, electron density, and ionization are inferred from spectral intensity of the elastic (Rayleigh) and inelastic (Compton) components of the scattered Cl Ly$_\alpha$ emission at 2.96 keV. Two-dimensional (2-D) hydrodynamic simulations using EOS models designed for the extreme conditions found in ICF research and planetary interiors predict an average state of the plasma that is consistent with the x-ray scattering measurements.

The EOS of hydrogen for pressures <10 Mbar along the Hugoniot remains uncertain,[15–17] where detailed validation of experimental techniques and numerical modeling is of utmost importance. While the present work has not obtained density measurements with accuracy below a few percent, it provides a needed alternative experimental platform where such validation could take place. The reason is twofold: X-ray scattering experiments at near solid densities or above ($n_e > 10^{22}$ cm^{-3}) have been successfully performed at laser facilities[10] because of the high initial density. In the case of deuterium, as described here, a significant technological advance was necessary to observe the x-ray Thomson scattering with the development of dedicated cryogenic target hardware for the x-ray scattering experimental platform. This allowed liquid deuterium to be shock heated to reach densities comparable to previous x-ray scattering experiments. Since an elastic scattering cross section goes as Z^2, cryogenic liquid deuterium scatters significantly less x rays than previous experiments using room-temperature solids. To overcome the reduction in scattering fraction and achieve a reasonable signal-to-noise ratio, a target geometry with a large collection volume inside the cryogenic cell was adopted for this proof-of-principle experiment at a cost of spatial resolution and accuracy in the density measurements.

This research provides an experimental platform for the detailed study of compressed deuterium and is an important step toward measuring all the thermodynamic variables needed for EOS research, i.e., pressure (p), mass density (ρ), electron density (n_e), electron temperature (T_e), and ionization (Z), by combining inelastic x-ray scattering with shock-velocity and optical pyrometry measurements.[5,15–17]

The platform to measure the spectrally resolved inelastic x-ray scattering from shocked deuterium was developed on the 60-beam, 30-kJ, 351-nm OMEGA Laser System.[18] Inelastic x-ray scattering is predominantly collective or noncollective, depending on the scattering parameter $\alpha_s = 1/k\lambda_s$, where the wave number of the scattered x ray is given by $k = 4\pi/\lambda_0 \sin(\theta/2)$ with the incident wavelength $\lambda_0 = 4.188$ Å, λ_s is electron screening length of the plasmas, and θ is the scattering angle. For the

partially ionized conditions in WDM, the screening length may be calculated from the Fermi distribution via a single integral.[19] An easier fourth-order interpolation between the classical Debye length and the Thomas–Fermi screening length valid for $T = 0$ yields the correct results within 2% (Ref. 19). If $\alpha_s < 1$, the scattering is dominated by independent electrons and is referred to as noncollective.[12] In this case, the free-electron contribution experiences a significant Compton shift $\Delta E_C = \hbar^2 k^2 / 2m_e$ and is Doppler broadened. The width of this scattering feature is sensitive to the electron temperature for nondegenerate plasmas. If $\alpha_s \gg 1$, the scattering by the collective modes, which are known as plasma waves or plasmons, is dominant and the scattering is referred to as collective.[2,10] To lowest order, the position of the energy-downshifted plasmon feature is related to the electron plasma frequency $\omega_{pe} = \sqrt{n_e e^2 / \varepsilon_0 m_e}$, providing an electron-density diagnostic. The Compton downshift for this experiment is 16.5 eV, and the plasma conditions and scattering geometry result in a scattering parameter of $\alpha_s \sim 1$. Since the electrons are partially degenerate, this implies that this inelastic scattering geometry is sensitive to both electron density and temperature, which is a novel regime for inelastic x-ray scattering.[10] Additional information on the plasma temperature is given by the height of the elastic scattering feature.[20]

The experimental setup is shown in Fig. 131.6(a). The 8-μm-thick plastic ablator containing a planar layer of liquid

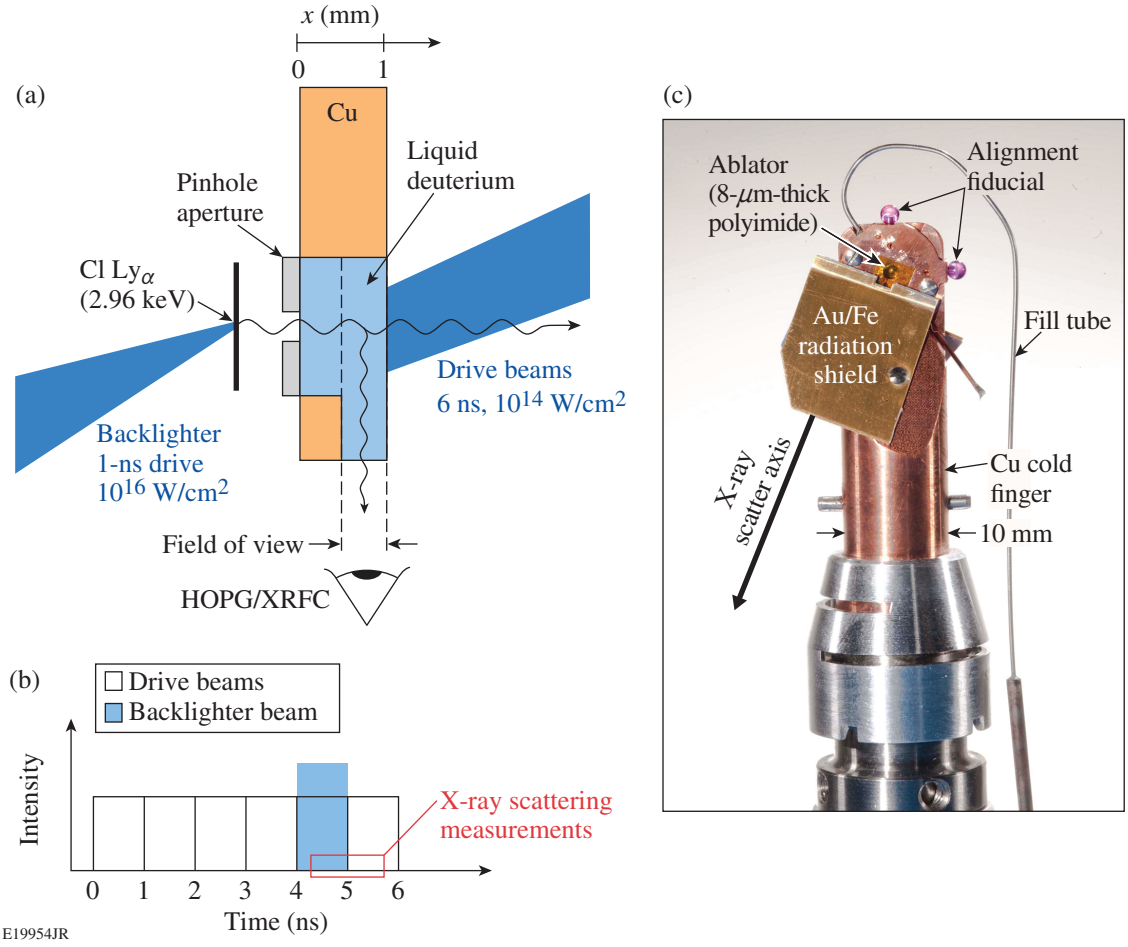

Figure 131.6

(a) Schematic of the x-ray Thomson-scattering (XRTS) experiment. An 8-μm CH ablator was irradiated with a constant-intensity, 6-ns UV laser drive, launching a shock wave through a cryogenic cell filled with liquid deuterium and creating warm, dense matter. Sixteen tightly focused beams irradiated a parylene D backlighter at 10^{16} W/cm^2, producing Cl Ly$_\alpha$ emission; this was scattered at ~90° and detected with an x-ray framing camera outfitted with a HOPG (highly oriented pyrolytic graphite) crystal spectrometer. (b) Timing of the drive and backlighter beams and the x-ray scattering measurements. (c) Photograph of the cryogenic XRTS target. The fill tube directs deuterium gas into the cryogenic cell, where it condenses into liquid. The ruby tooling balls on the top and right side of the Cu cold finger are target-alignment fiducials. The Au/Fe shield blocks a direct line of sight between the laser-produced plasmas and the detector, which is positioned ~90° to the laser drive axis.

deuterium was irradiated with a constant-intensity UV laser drive with 10^{14} W/cm^2. The laser drive, formed with six pairs of beams staggered in time as shown in Fig. 131.6(b), was uniform over a 0.5-mm diameter. Each laser beam was smoothed with a phase plate, producing a super-Gaussian spatial-intensity profile $I(r) = I_0 \exp\left[-(r/\delta)^n\right]$, with a 1/$e$ half-width $\delta = 438$ μm and super-Gaussian power $n = 4.5$. A laser-ablation–driven shock wave was launched through the liquid deuterium, creating warm, dense compressed matter. Sixteen tightly focused beams irradiated a parylene D backlighter with 10^{16} W/cm^2, generating a source of Cl Ly$_\alpha$ emission ($\lambda_0 = 4.188$ Å, $h\nu = 2960$ eV) (Ref. 21). These x rays were then scattered at $\theta = 87.8°$ from the shocked liquid deuterium and detected with an x-ray framing camera (XRFC) outfitted with a highly oriented pyrolytic graphic (HOPG) crystal spectrometer.[22] The backlighter x rays were collimated with a 200-μm-diam pinhole. The timing of the backlighter beams is shown in Fig. 131.6(b). The integration time of the x-ray scattering measurements is ~0.25 ns. A photograph of the cryogenic target with x-ray Thomson scattering (XRTS) capabilities mounted on the OMEGA planar cryogenic system is shown in Fig. 131.6(c), with the main components highlighted. The fill tube directs deuterium gas into the cryogenic cell, where it condenses into liquid. The ruby tooling balls on the top and right side of the Cu cold finger structure are target alignment fiducials. The Au/Fe shield blocks a direct line of sight between the laser-produced plasmas and the detector, which is positioned ~90° to the laser drive axis.

Two-dimensional hydrodynamic simulations of the experiment were performed with the *DRACO* code, which uses the *SESAME* EOS, a three-dimensional (3-D) laser ray trace model that calculates the laser absorption via inverse bremsstrahlung, a flux-limited thermal-transport approximation with a flux limiter of 0.06, and a multigroup diffusion radiation transport approximation using opacity tables created for astrophysics.[23] The simulation results shown in Fig.131.7, with the laser irradiation side and the location of the Cu wall indicated, predict at peak compression a mass density of $\rho \sim 0.8$ g/cm^3, a temperature of $T_e \sim 5$ to 15 eV, and an ionization stage of $Z \sim 0.5$ to 0.8 for the shocked liquid deuterium 5 ns after the drive beams were incident on the target ($t = 5$ ns). The shock front was predicted to have advanced ~375 μm at $t = 5$ ns and the shocked liquid deuterium had a compressed thickness of ~90 μm. As seen in Fig. 131.7, the spatial-intensity profile of the laser drive creates a curved shock front. The uniformly shocked liquid deuterium region occurs within $r < 0.25$ mm (see Fig. 131.7), and the underdriven shocked liquid deuterium is located at $r >$ 0.25 mm. The predicted plasma conditions in the underdriven shocked portion of the target are lower than the uniform drive portion. The measured spectrum of the scattered x rays is spatially integrated and weighted to the shocked liquid deuterium region, which has the highest density. The field of view of the x-ray scattering channel either extends from $z = 0.5$ mm to $z =$ 1.0 mm (see horizontal scale in Fig. 131.7) or is reduced to $z =$ 0.5 mm to $z = 0.75$ mm by positioning a 250-μm-wide slit in

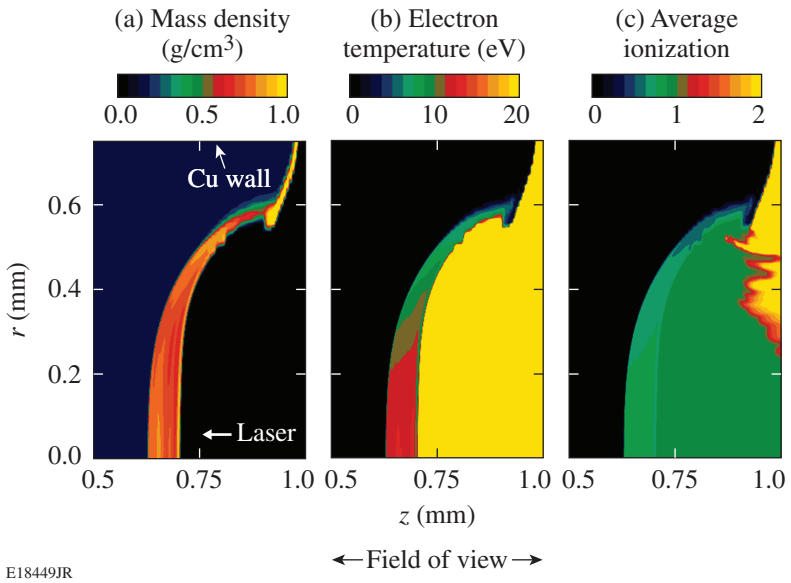

Figure 131.7
Contour plots of (a) mass density, (b) electron temperature, and (c) average ionization of shocked liquid deuterium at 5 ns, predicted using *DRACO*.

the scattering channel. The slit reduces the field of view of the scattering diagnostic to primarily the portion of the shocked liquid deuterium with uniform plasma conditions and blocks the scattering signal from the underdriven portion of the target.

The estimated number N of detected scattered photons[24] is calculated using

$$N = \left(\frac{E_T \eta_T}{h\nu}\right)\left(\frac{\Omega_T}{4\pi}\right)\left(\frac{n_e \sigma_T x}{\alpha_s^2 + 1}\right)\left(\frac{\Omega_x R}{4\pi}\right)\eta_d,$$

where, $E_T = 8$ kJ is the total UV laser energy incident on the parylene D backlighter foil, $\eta_T = 0.003$ is the UV to Cl Ly$_\alpha$ emission conversion efficiency, $h\nu = 2.96$ keV is the backlighter photon energy, $\Omega_T = 0.06$ steradian is the solid angle of the backlighter plasma sampled by the pinhole, $n_e = 2.2 \times 10^{23}$ cm^{-3} is the electron density of the shocked liquid deuterium, $\sigma_T = 6.6525 \times 10^{-25}$ cm^2 is the Thomson-scattering cross section, $x = 90$ μm is the thickness of the shocked liquid deuterium, $\alpha_s = 1.3$ is the scattering parameter, $\Omega_x = 0.02$ rad is the angle subtended by the detector in the direction perpendicular to the plane of dispersion, $R = 3$ mrad is the integrated reflectivity of the HOPG Bragg crystal, and $\eta_d = 0.01$ is the detector efficiency including filter transmissions. For a sampling time of ~0.25 ns, the total number of detected photons is $N \sim 700$. The thickness of the shocked liquid deuterium is an order of magnitude smaller than the radiatively heated Be targets studied in earlier XRTS experiments;[11,14] consequently, the number of scattered photons in the shocked liquid deuterium experiment is at least an order of magnitude less than the Be experiment.

The scattered spectrum of the Cl Ly$_\alpha$ emission taken at $t = 5$ ns with a 250-μm slit in the scattering channel is shown in Fig. 131.8(a). The measurement taken without the slit is shown in Fig. 131.8(b), and the incident spectrum is shown in Fig. 131.8(c). The observed noise in the measured scattered x-ray spectrum is consistent with the estimated signal level. The incident spectrum is measured by irradiating a parylene D foil target on a separate laser shot. The scattered spectrum has a strong Rayleigh peak around 2960 eV and a Compton-downshifted feature. Scattered x-ray spectra were calculated using the x-ray scattering (XRS) code, which uses the finite-temperature random-phase approximation with static local field corrections to obtain the spectral shape of the inelastic (Compton) feature caused by scattering from free electrons.[25] The elastic scattering intensity strongly depends on the degree of ion–ion correlations in the plasma via the structure factor S_{ii} (Ref. 20). To constrain the value for S_{ii}, density functional theory molecular dynamics (DFT-MD) simulations were performed using the VASP package.[26,27] The simulations indicate weak ionic correlations for the conditions similar to the average of the plasma probed. This means the ion–ion structure factor S_{ii} at the relevant scattering wave number is close to unity for

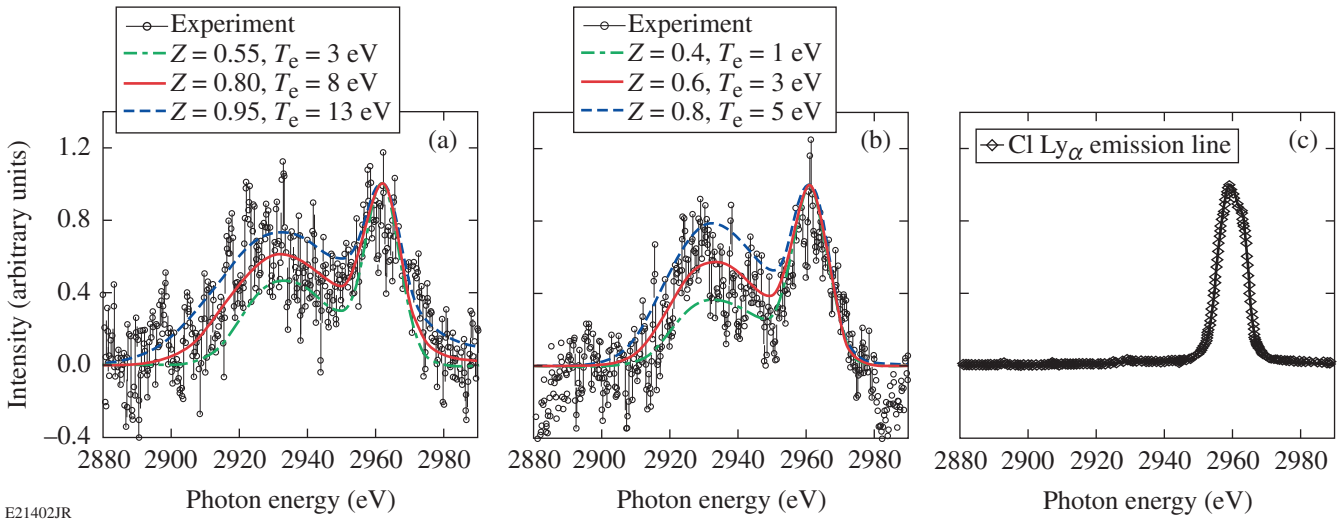

Figure 131.8
Measurement of (a) Cl Ly$_\alpha$ emission scattered from shocked liquid deuterium with a 250-μm slit in the scattering channel and simulated scattering spectra; (b) Cl Ly$_\alpha$ emission scattered from shocked liquid deuterium without a 250-μm slit in the scattering channel and simulated scattering spectra; and (c) Cl Ly$_\alpha$ emission incident on the shocked liquid deuterium. The inferred plasma conditions in (a) are $T_e = 8 \pm 5$ eV, $Z \sim 0.8$ (–0.25, +0.15), and $n_e = 2.2(\pm 0.5) \times 10^{23}$ cm^{-3} and in (b) are $T_e = 3 \pm 2$ eV, $Z \sim 0.6 \pm 0.2$, and $n_e = 2.0(\pm 0.5) \times 10^{23}$ cm^{-3}.

most of the conditions probed. With this information, the elastic scattering feature can be used to constrain the temperature and the ionization degree of the system. Structure factors close to unity are also found for the unshocked deuterium liquid. In addition to Doppler broadening, the width and position of the inelastic feature depend on the density for $\alpha_s \sim 1$. This fact allows us to bracket the electron density and estimate the ionization charge based on the initial mass density of the sample. The simulated scattering spectra computed using XRS provided the best fit to the spectrum measured with the slit for the following plasma conditions: $T_e = 8\pm5$ eV, $Z \sim 0.8$ (–0.25, +0.15), and $n_e = 2.2(\pm0.5) \times 10^{23}$ cm^{-3}. The *DRACO* simulations are in close agreement with the experimental results. These plasma conditions were repeatable on a subsequent laser shot. The plasma conditions inferred from the spectrally resolved x-ray spectrum recorded without the slit in the x-ray scattering channel are lower with $T_e = 3\pm2$ eV, $Z \sim 0.6\pm0.2$, and $n_e = 2.0(\pm0.5) \times 10^{23}$ cm^{-3}. The lower plasma pressure created by the lower-intensity portion of the laser drive causes the bowing of the shock front, as observed in Fig. 131.7. When the slit is placed in the scattering channel, the x rays scattered from this underdriven portion of the target are blocked from the detector. This leads to higher inferred values of T_e, Z, and n_e more representative of the uniformly shocked region.

In conclusion, this article reports the first experimental observation of noncollective, inelastic x-ray scattering from shocked liquid deuterium. An electron temperature of $T_e = 8\pm5$ eV, ionization $Z \sim 0.8$ (–0.25, +0.15), and electron density $n_e = 2.2(\pm0.5) \times 10^{23}$ cm^{-3} are inferred from the shapes and intensities of the elastic (Rayleigh) and inelastic (Compton) components in the scattering spectra. These plasma conditions are Fermi degenerate with similar electron and Fermi temperatures $\left(T_e / T_F \sim 1\right)$. Two-dimensional hydrodynamic simulations using EOS models suited for the extreme conditions indicate that the predicted average state of the probed plasma are consistent with the x-ray scattering measurements. Differently from previous VISAR measurements, the x-ray scattering experimental platform offers the considerable advantage of probing off-Hugoniot states. This experimental result is a significant step toward achieving accurate measurements of all thermodynamic variables needed to provide stringent tests of EOS models, which would require at least three thermodynamic variables like pressure, mass density, and temperature.

ACKNOWLEDGMENT

The authors acknowledge the excellent support of the OMEGA Laser System team, especially M. J. Bonino, R. Earley, S. G. Noyes, D. Turner, K. Lintz, and D. R. Harding. The work of K. F., C. D. M., and G. G. was funded by EPSRC grant no. EP/G007187/1 and by the HiPER fund. The work of J. V. and D. O. G. was partially funded by EPSRC grant no. EP/D062837. This work was supported by the U.S. Department of Energy Office of Inertial Confinement Fusion under Cooperative Agreement No. DE-FC52-08NA28302, the University of Rochester, and the New York State Energy Research and Development Authority. This work was performed under the auspices of the U.S. Department of Energy by Lawrence Livermore National Laboratory under Contract DE-AC52-07NA27344. The support of DOE does not constitute and endorsement by DOE of the views expressed in this article.

REFERENCES

1. National Research Council (U.S.) Committee on High Energy Density Plasma Physics, *Frontiers in High Energy Density Physics: The X-Games of Contemporary Science* (National Academies Press, Washington, DC, 2003).
2. S. Ichimaru, Rev. Mod. Phys. **54**, 1017 (1982).
3. J. E. Bailey *et al*., Phys. Rev. Lett. **99**, 265002 (2007).
4. K. Widmann *et al*., Phys. Rev. Lett. **92**, 125002 (2004).
5. J. Eggert, S. Brygoo, P. Loubeyre, R. S. McWilliams, P. M. Celliers, D. G. Hicks, T. R. Boehly, R. Jeanloz, and G. W. Collins, Phys. Rev. Lett. **100**, 124503 (2008).
6. S. X. Hu, V. A. Smalyuk, V. N. Goncharov, J. P. Knauer, P. B. Radha, I. V. Igumenshchev, J. A. Marozas, C. Stoeckl, B. Yaakobi, D. Shvarts, T. C. Sangster, P. W. McKenty, D. D. Meyerhofer, S. Skupsky, and R. L. McCrory, Phys. Rev. Lett. **100**, 185003 (2008).
7. R. L. McCrory, D. D. Meyerhofer, R. Betti, R. S. Craxton, J. A. Delettrez, D. H. Edgell, V. Yu Glebov, V. N. Goncharov, D. R. Harding, D. W. Jacobs-Perkins, J. P. Knauer, F. J. Marshall, P. W. McKenty, P. B. Radha, S. P. Regan, T. C. Sangster, W. Seka, R. W. Short, S. Skupsky, V. A. Smalyuk, J. M. Soures, C. Stoeckl, B. Yaakobi, D. Shvarts, J. A. Frenje, C. K. Li, R. D. Petrasso, and F. H. Séguin, Phys. Plasmas **15**, 055503 (2008).
8. J. D. Lindl *et al*., Phys. Plasmas **11**, 339 (2004).
9. D. Saumon and G. Chabrier, Phys. Rev. A **44**, 5122 (1991).
10. S. H. Glenzer and R. Redmer, Rev. Mod. Phys. **81**, 1625 (2009).
11. S. H. Glenzer *et al*., Phys. Rev. Lett. **90**, 175002 (2003).
12. G. Gregori *et al*., Phys. Rev. E **67**, 026412 (2003).
13. H. Sawada, S. P. Regan, D. D. Meyerhofer, I. V. Igumenshchev, V. N. Goncharov, T. R. Boehly, R. Epstein, T. C. Sangster, V. A. Smalyuk, B. Yaakobi, G. Gregori, S. H. Glenzer, and O. L. Landen, Phys. Plasmas **14**, 122703 (2007).
14. S. H. Glenzer *et al*., Phys. Rev. Lett. **98**, 065002 (2007).
15. G. W. Collins *et al*., Science **281**, 1178 (1998).
16. P. M. Celliers *et al*., J. Appl. Phys. **98**, 113529 (2005).
17. K. Falk, S. P. Regan, J. Vorberger, M. A. Barrios, T. R. Boehly, D. E. Fratanduono, S. H. Glenzer, D. G. Hicks, S. X. Hu, C. D. Murphy, P. B.

Radha, S. Rothman, A. P. Jephcoat, J. S. Wark, D. O. Gericke, and G. Gregori, High Energy Density Phys. **8**, 76 (2012).

18. T. R. Boehly, D. L. Brown, R. S. Craxton, R. L. Keck, J. P. Knauer, J. H. Kelly, T. J. Kessler, S. A. Kumpan, S. J. Loucks, S. A. Letzring, F. J. Marshall, R. L. McCrory, S. F. B. Morse, W. Seka, J. M. Soures, and C. P. Verdon, Opt. Commun. **133**, 495 (1997).
19. D. O. Gericke *et al*., Phys. Rev. E **81**, 065401(R) (2010).
20. E. García Saiz *et al*., Nat. Phys. **4**, 940 (2008).
21. M. K. Urry *et al*., J. Quant. Spectrosc. Radiat. Transf. **99**, 636 (2006).
22. A. Pak *et al*., Rev. Sci. Instrum. **75**, 3747 (2004).
23. P. B. Radha, V. N. Goncharov, T. J. B. Collins, J. A. Delettrez, Y. Elbaz, V. Yu. Glebov, R. L. Keck, D. E. Keller, J. P. Knauer, J. A. Marozas, F. J. Marshall, P. W. McKenty, D. D. Meyerhofer, S. P. Regan, T. C. Sangster, D. Shvarts, S. Skupsky, Y. Srebro, R. P. J. Town, and C. Stoeckl, Phys. Plasmas **12**, 032702 (2005).
24. O. L. Landen *et al*., J. Quant. Spectrosc. Radiat. Transf. **71**, 465 (2001).
25. G. Gregori *et al*., High Energy Density Phys. **3**, 99 (2007).
26. G. Kresse and J. Furthmüller, Phys. Rev. B **54**, 11169 (1996).
27. J. Vorberger *et al*., Phys. Rev. B **75**, 024206 (2007).

Enhancement of the Laser-Induced–Damage Threshold in Multilayer Dielectric Diffraction Gratings Through Targeted Chemical Cleaning

Introduction

Chirped-pulse amplification (CPA) has been an enabling technology in the development of ultrashort-pulse, high-power laser systems.[1–5] In a CPA setup, a pair of diffraction gratings is used to "chirp" the signal by stretching it in time, reducing the laser pulse to a much lower intensity before the beam travels through the amplifier. The amplified pulse passes through another set of gratings to recompress it to its original pulse duration. At LLE, eight sets of tiled multilayer dielectric (MLD) gratings are used in pulse compressor chambers for OMEGA EP's two short-pulse beamlines. Each grating segment is 10 cm thick, 47 cm wide, and 43 cm tall; a complete tiled-grating assembly (TGA) is 1.4 m wide and includes three grating segments. The requirements on these critical, large-aperture optics are rigorous: laser-induced damage thresholds greater than 2.7 J/cm^2 (beam normal) for a 10-ps pulse at 1054 nm incident at 61° and a minimum diffraction efficiency of 97%. Because these demands have not yet been met, OMEGA EP's short-pulse beamlines are currently operated at ~60% of their design energy.

Surface contamination can dramatically reduce a grating's resistance to laser-induced damage.[5–13] OMEGA EP pulse compressor gratings are fabricated by etching a periodic groove structure (1740 lines/mm) into the top layer of a hafnia/silica multilayer mirror using interference lithography. Optionally, a bottom antireflective coating (BARC) is applied to the multilayer mirror to mitigate standing-wave effects during lithography and to improve fidelity. The grating fabrication process leaves large quantities of manufacturing residues and debris on the grating's surface that must be removed before the optic can go into service. Residues of hardened organic polymer BARC, in particular, are especially difficult to remove during final grating cleaning. Any photoresist or BARC residues, metal contaminants, surface debris, or light organic matter ultimately left on the grating can absorb energy during laser irradiation, initiating intense local heating and catastrophic laser-induced damage. Therefore, a final grating cleaning process that removes a broad spectrum of contaminant materials is essential. Mechanical contact with the delicate, microtextured grating surface must be absolutely avoided during cleaning, and cleaning techniques must not be so aggressive that they cause damage or defects. Additionally, short processing times and low temperatures are desirable for practical implementation on large parts and to mitigate thermal stress concerns.

MLD Grating Cleaning

Although surface contamination is a well-known cause of poor optical performance and laser-damage resistance, relatively few papers on cleaning methods for MLD gratings are available in the literature. Ashe *et al.*[9,10] were among the first to publish on this topic. They compared a number of chemical wet-cleaning methods commonly used in the semiconductor industry. Acid piranha, a mixture of sulfuric acid (H_2SO_4) and hydrogen peroxide (H_2O_2), was identified as the most-promising chemistry for MLD grating cleaning based on post-cleaning diffraction efficiency (DE) and laser-induced–damage threshold (LIDT) results. Other groups[11–14] have reported on the successful use of acid piranha to clean MLD gratings. Britten and Nguyen[13] developed a cleaning method for diffraction gratings that involved stripping bulk photoresist with an aqueous base and employing an oxidizing acid solution to remove residues; oxygen plasma was used as an intermediate step to remove fluorinated hydrocarbon residues. Plasma cleaning with oxygen and other gases has been suggested as a method for removing bulk organic layers of BARC[9,14] and photoresist[15,16] from gratings.

Britten *et al.*[17,18] demonstrated that briefly exposing an MLD grating to dilute buffered hydrofluoric acid (HF) solution after cleaning could increase resistance to laser-induced damage. HF lightly etches the silica pillars, simultaneously enhancing grating performance by removing surface residues and reducing the duty cycle (linewidth/period). Low duty cycles (tall, thin pillars) can enhance a grating's LIDT by minimizing electric-field enhancement.[19] Because low-duty-cycle gratings are considerably more difficult to fabricate than those having a traditional surface profile, the discovery of HF linewidth tailoring was a major advancement. The authors reported an average LIDT increase of 18.5% after etchback for 10-ps, 1053-nm damage

testing at 76.5° incidence. Britten *et al*. indicated that the HF linewidth-tailoring treatment "requires densified coating layers,"[18] but did not elaborate.

A few grating cleaning methods[10,17,19] have been shown to meet the OMEGA EP grating LIDT requirement of 2.7 J/cm^2 for a 1054-nm, 10-ps pulse using small grating samples.[(a)] Attempts to achieve similarly high damage thresholds on full-size OMEGA EP pulse compressor gratings and witness optics have so far been unsuccessful. One problem is that most damage-testing data have been reported for an air environment, while OMEGA EP gratings are operated in high vacuum. The testing environment can have a significant effect on results, especially for nondensified, porous MLD coatings (such as those used by LLE) because humidity and the volatility of contaminant materials in the vacuum chamber can play important roles. A second consideration is that the next generation of OMEGA EP gratings will, preferably, be fabricated with a BARC layer over the multilayer stack to minimize interference effects and distortion of the grating line structures at low duty cycles. Since many grating manufacturers do not use BARC, little information is available on stripping it from MLD gratings during final cleaning. Finally, wet-cleaning of MLD gratings has typically been performed at high temperatures (60°C to 110°C), especially when acid piranha is used to strip photoresist.[9–12] Such elevated processing temperatures have recently raised concerns about thermal-stress–induced defects, such as blistering and localized coating delamination, that can occur during cleaning. Two examples of coating failure observed in our lab on hafnia/silica MLD's and MLD gratings following elevated-temperature cleaning are given in Fig. 131.9. Figure 131.9(a) shows a group of ~40-μm-diam "blister" defects that nucleated near scratches on an MLD during piranha cleaning at 90°C. Figure 131.9(b) is a tiled micrograph showing localized delamination of an MLD grating after piranha cleaning at 70°C. To compound concerns about thermal stresses, the behavior of small witness gratings may not be representative of full-scale pulse compressor gratings. Large optics may be susceptible to modes of thermal-stress–induced failure not predicted by small witness parts.[20]

To resolve the above issues, we sought a grating cleaning process that (1) meets OMEGA EP's specifications for DE and in-vacuum LIDT; (2) is compatible with standard, nondensified reactive-evaporation MLD coatings; (3) effectively strips both photoresist and BARC; and (4) requires no chemical processing at temperatures above 40°C, to reduce thermal-stress concerns.

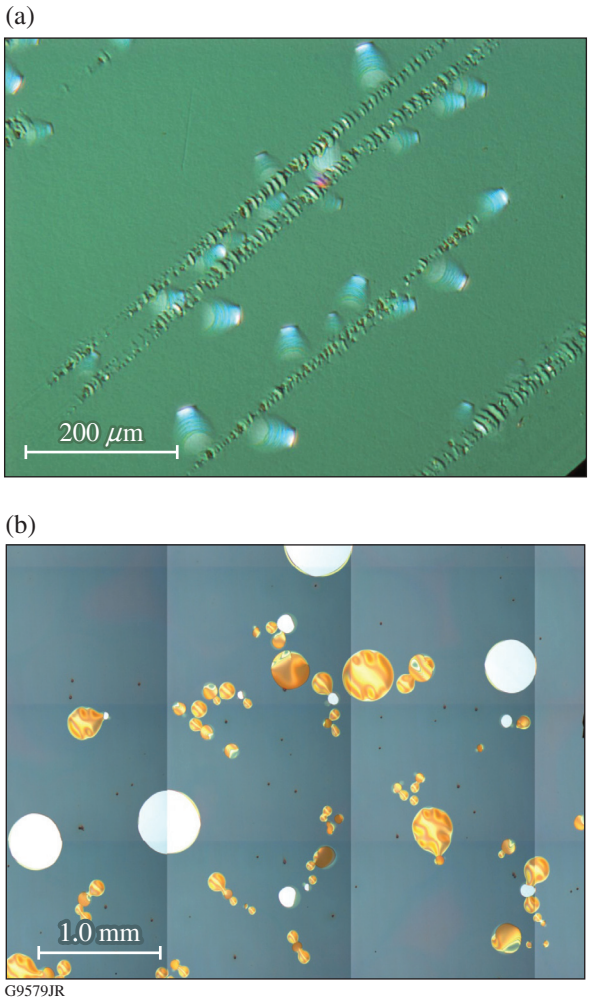

Figure 131.9
Coating failure observed after elevated-temperature acid piranha cleaning: (a) formation of "blister" defects observed on a multilayer dielectric (MLD) coating (no grating) after acid piranha cleaning at 90°C; (b) localized delamination observed on an MLD grating after acid piranha cleaning at 70°C.

Experimental

1. MLD Grating Samples

Cleaning experiments were performed on small-scale MLD grating coupons. Ten 100-mm-diam, 3-mm-thick, round hafnia/silica MLD gratings were broken into eight equally sized, wedge-shaped coupons (80 samples total). Figure 131.10 shows the sample geometry. The multilayer coating was a modified quarter-wave thin-film stack[21] with hafnia (HfO_2) and silica (SiO_2) used as the high- and low-index materials, respectively. The total coating thickness was 4.8 μm. The MLD was deposited by reactive evaporation at 150°C using oxygen backfill

[(a)]Only Ashe[10] reported LIDT data for 61° beam incidence (OMEGA EP specification). Neauport's[19] and Nguyen's[17] data were reported for 77.2° and 76.5° incidences, respectively.

pressures of 2.0×10^{-4} Torr for hafnia deposition and zero for silica layer deposition. A BARC layer was applied over the multilayer to mitigate interference effects during photolithography. Grooves (1740 lines/mm) were etched into the top silica layer of the MLD. The samples were "identical" in that they were produced in the same coating run and processed together up until the final cleaning stage. Except as noted, all cleaning experiments described in this article were performed on *uncleaned* gratings with BARC and photoresist still intact (that is, they were not subjected to any photoresist stripping or other cleaning operations other than those described here).

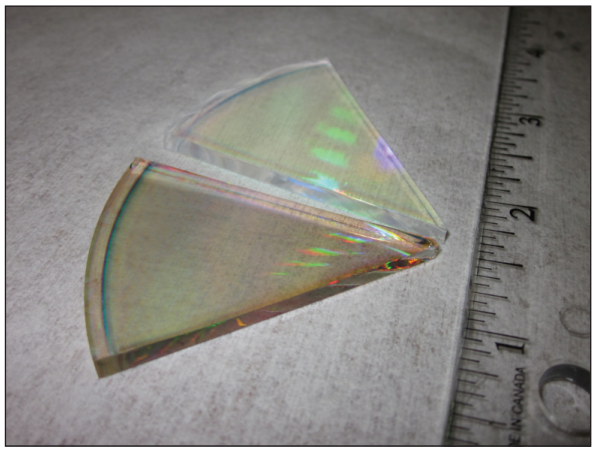

G9650JR

Figure 131.10
Grating wedge samples used in cleaning experiments, shown before (bottom) and after cleaning (top).

2. Laser-Induced–Damage Testing

Damage testing was performed at LLE's Damage Testing Facility on the short-pulse (10-ps) system, which can be operated in both air and high-vacuum (4×10^{-7} Torr) environments. MLD grating samples were tested using *s*-polarized light at 1054 nm, with an incident beam angle of 61° and an irradiation spot size of 370 μm (e^{-1} in intensity) in the far field. Laser-damage assessment was performed *in situ* using a white-light imaging system (~100× magnification). Damage was defined as a feature on the sample's surface that was not observed before laser irradiation. When switching between testing environments, samples were allowed to reach equilibrium with the environment (air or vacuum) for 24 h before testing continued. Damage thresholds are reported as beam normal fluences.

Each sample was tested in both 1-on-1 and *N*-on-1 testing regimes. The 1-on-1 damage threshold is determined by irradiating a sample site with one pulse and observing the sample for damage. This is then repeated with increasing fluences on nonirradiated sample sites until damage is observed. The 1-on-1 threshold is the average of the fluence for the last site that did *not* damage the sample and the fluence for the first site that *did* damage, and the measurement error recorded is half the difference between these two numbers. *N*-on-1 damage testing is conducted by irradiating the sample site at a fluence significantly below the 1-on-1 threshold for ten shots. If no damage is detected, the fluence is increased and the same site is irradiated with five more shots. If no damage is observed after these shots, the fluence is increased again and another five shots are taken. This is continued until damage is observed in white light, at which point the damage onset fluence is recorded as the *N*-on-1 threshold for that site. The *N*-on-1 test is repeated for five sites on each MLD grating sample to generate an average and a standard deviation, which are reported as the *N*-on-1 threshold and measurement error, respectively.

3. Acid Piranha Cleaning at Low Temperatures

Many of the techniques used to clean MLD gratings have been developed from methods used for wafer cleaning in the semiconductor industry. Acid piranha, for example, has been known as a photoresist stripper since at least 1975 (Ref. 22), and its use is prevalent in the semiconductor industry. Standard operating procedure for acid piranha varies, but typical acid/peroxide ratios are in the range 2:1 to 7:1 (2 to 7 parts 99% sulfuric acid to 1 part 30% hydrogen peroxide) and typical processing temperatures are in the range 90°C to 140°C (Refs. 23 and 24). Optimized piranha-cleaning processes for MLD gratings documented in the open literature have been consistent with these ranges.[10–12] Ashe *et al.*[10] found that laser-damage resistance was maximized when high cleaning temperatures were used and when the proportion of H_2O_2 in the piranha solution was high. Piranha 2:1 (two parts sulfuric acid, one part hydrogen peroxide) at 100°C gave the best LIDT results. The authors recorded *N*-on-1 damage thresholds as high as 3.27 J/cm^2 in air after piranha cleaning—exceeding the OMEGA EP pulse compressor grating performance specification of 2.7 J/cm^2. Thresholds above 2.7 J/cm^2, however, were observed only for grating samples cleaned at temperatures of 80°C or higher, and these were in-air values only.

Because of thermal stress concerns, we chose to work at temperatures of 40°C or below. Table 131.I shows cleaning parameters and post-cleaning DE and LIDT results for a group of grating samples cleaned for 30 min at 40°C in an acid piranha bath. Some experiments involved two piranha treatments. This methodology was motivated by Beck *et al.*,[22] who suggested a two-step photoresist strip that employed first

Table 131.I: Treatments and results for 30-min acid piranha soak cleaning experiments, illustrating that acid piranha alone does not clean MLD gratings effectively at 40°C.

Part ID	Ratio H_2SO_4:H_2O_2 / duration		Cleaning temperature	Post-cleaning DE	Post-cleaning LIDT (J/cm^2) *in vacuum*	
	Treatment 1	Treatment 2			1-on-1	*N*-on-1
555-2	10:1/15 min	5:1/15 min	40°C	84.6±0.8%	0.66±0.01	0.97±0.03
555-1	5:1/15 min	2:1/15 min	40°C	91.7±1.5%	0.84±0.06	1.08±0.11
555-6	10:1/30 min		40°C	90.8±1.2%	0.76±0.02	1.00±0.05
555-5	5:1/30 min		40°C	81.3±1.0%	0.94±0.05	1.04±0.04
556-3	2:1/30 min		40°C	91.0±1.6%	0.95±0.04	1.08±0.06

an acid-rich dehydrating bath, followed by a peroxide-rich oxidizing bath, to exploit the complementary material-removal mechanisms of acid piranha (dehydration and oxidation).

The experiments clearly demonstrated that at these low temperatures, acid piranha cleaning was inadequate. During damage testing, the unamplified laser beam used for alignment "wrote a track" onto the grating as it scanned across the samples, indicating that photoresist was not completely removed. A scanning electron microscope (SEM) observation of sample #555-5 (5:1 piranha, 30 min, 40°C) revealed intact photoresist over the entire grating surface. In areas irradiated during damage testing, the photoresist was deformed and/or stripped away, as shown in Fig. 131.11. The laser treatment provided a "cleaning" effect in the center of the damage site, where the photoresist was entirely removed by the incident laser beam. Near the edges of the region there was significant scatter from partially removed, deformed, and peeling strands of photoresist.

4. Targeted Chemical Cleaning

While acid piranha may be an effective solitary cleaning chemistry for MLD gratings at high temperatures, such was not our experience at 40°C. The intentionally low processing temperature necessitated a new approach. Because gratings are sensitive to surface pollutants of many different types, we developed a multistep technique to ensure broadband removal of performance-limiting contaminants. Cleaning techniques were adapted and combined from various sources to develop the optimized method detailed in Table 131.II. Drawn from semiconductor wafer processing and grating cleaning literature, the references describe other applications for each cleaning technique.

The cleaning process includes six major steps: First, acid piranha is used to strip photoresist and BARC. The piranha strip is followed by plasma cleaning in room air to clear away partially removed BARC and photoresist. Microscopic

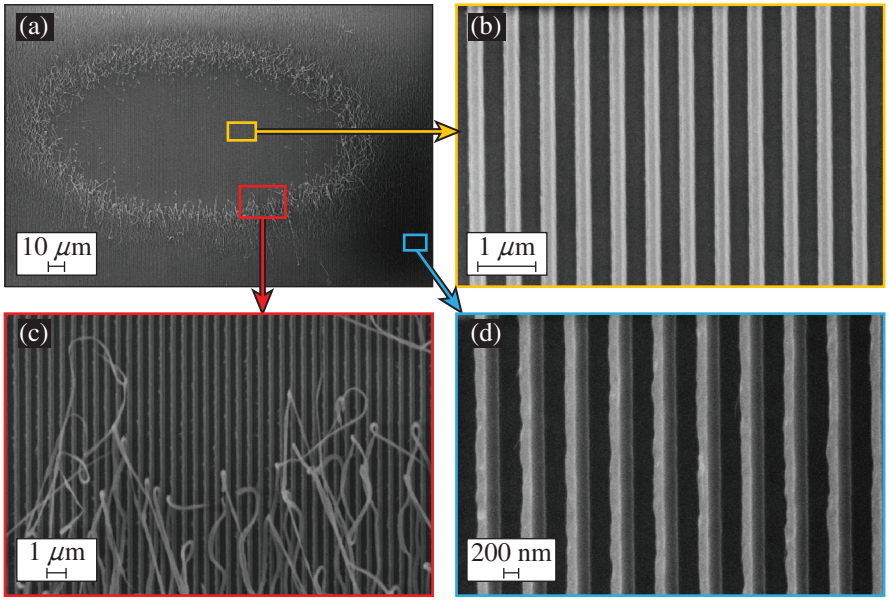

G9651JR

Figure 131.11
Scanning electron microscope (SEM) images of damage site on sample #555-5 irradiated at 1.40 J/cm^2 (1-on-1, 1054 nm, 10 ps, in vacuum, 61° incidence): (a) entire damage site; (b) intact pillars at center of site where all photoresist has been removed via laser irradiation ("cleaning" effect); (c) photoresist peeling away from pillars near the edge of the central region; (d) grating pillars near the edge of the damage site, where the photoresist layer is tilted over and partially detached from the grating pillars due to the 61° incident angle of the laser beam.

Table 131.II: Optimized cleaning method.

Process	Purpose	Method	Chemistry	Duration	Temperature
1. Piranha strip (Refs. 9–12, 22–24)	Strips/softens photoresist and BARC.	Spray onto optic; DI water rinse	H_2SO_4:H_2O_2 (5:1, 2:1)	5:1/15 min, 2:1/15 min	40° to 70°C
2. Plasma clean (Refs. 13,15, 16,23,24)	Removes light organics and partially removed material.	Room air used as process gas	n/a	10 min	Room temperature
3. Ionic clean (SC-2) (Refs. 23,24)	Eliminates remaining ionic/ metallic contamination.	Beaker soak; DI water rinse	HCl:H_2O_2:H_2O (1:1:6)	10 min	40° to 70°C
4. Plasma clean (Refs. 13,15, 16,23,24)	Removes light organics and partially removed material.	Room air used as process gas	n/a	10 min	Room temperature
5. Oxide etch (Refs. 18, 23,24)	Removes a thin layer of SiO_2 along with any stubbornly adhered contaminants; thins pillars slightly, reducing duty cycle.	Beaker soak; DI water rinse	HF:buffers (1:2500 to 1:3000)	5 min	Room temperature
6. Plasma clean (Refs. 13,15, 16,23,24)	Removes light organics and partially removed material.	Room air used as process gas	n/a	10 min	Room temperature

examination of samples suggested that BARC flakes off rather than gradually dissolving in piranha solution, and the plasma treatment ensures that material has been completely removed before proceeding to the next cleaning step. The third step in the cleaning process is an ionic clean with a Standard Clean 2 (SC-2) solution, a mixture of hydrochloric acid and hydrogen peroxide commonly used in the microelectronics industry to remove metallic contamination from silicon wafers. The inclusion of an ionic clean was motivated by the detection of molybdenum, a metal, on grating samples (see the next section). The ionic clean is followed by a second plasma treatment to clear away light organic matter collected on the sample. The next step is the oxide etch, which reduces the grating duty cycle and eliminates any remaining contaminants on the grating by removing a thin layer of silica.[17] Grating performance was quite sensitive to the concentration of the buffered oxide etch used. We found that dilutions in the range of 2500 to 3000 parts water/buffers to one part hydrofluoric acid were optimal for a 5-min etch (results discussed later in this section). The final step is a third air plasma treatment, which cleans the surface by removing light organics.

A total of 14 grating samples were cleaned according to the process steps shown in Table 131.II. The samples were then evaluated for damage threshold and diffraction efficiency; results are listed in Table 131.III. Average in-air damage thresholds were 4.01 J/cm^2 and 3.40 J/cm^2 in the 1-on-1 and *N*-on-1 regimes, respectively. For the five samples tested in a vacuum environment, average damage thresholds were 3.36 J/cm^2 (1-on-1) and 2.76 J/cm^2 (*N*-on-1) for 10-ps pulses at 1054 nm in vacuum. The data show good repeatability. For all samples except for the one having the lowest LIDT (562-7), the 1-on-1 threshold exceeded the *N*-on-1 threshold. This is not a typical result. *N*-on-1 thresholds are generally higher because contamination and debris on the grating surface are cleared away by low-fluence laser shots as beam fluence is ramped up, an effect known as "laser conditioning."[5] The absence of a laser-conditioning effect for the samples cleaned using the optimized method indicates that these gratings were already quite clean when damage testing began.

To our knowledge, this is the first time laser-induced–damage thresholds exceeding the OMEGA EP requirement of 2.7 J/cm^2 *in vacuum* have been reported for MLD gratings. These may also be the highest-reported 10-ps, 1054-nm damage thresholds for gratings fabricated using BARC. The average DE was 97.6%, meeting the OMEGA EP requirement on grating diffraction efficiency. Figure 131.12 compares SEM cross sections of a grating sample before and after cleaning, showing that BARC and photoresist were completely removed and that pillars were slightly narrowed.

The steps shown in Table 131.II were optimized using the set of 80 grating samples described in **MLD Grating Samples** (p. 150). Damage thresholds were found to be especially sensitive to the dilution of HF used in the oxide etch step. As shown in Fig. 131.13, LIDT results were best for grating samples prepared using buffer:HF ratios in the range 2500:1 to 3000:1. An 1800:1 ratio (not shown) led to total delamination of the grating MLD during the 5-min etch.

A major advantage of the targeted cleaning approach is its effectiveness at low temperatures. Lower temperatures lessen concerns about thermal stresses and reduce susceptibility to blistering and delamination defects. Initial piranha-cleaning experiments at low temperatures (see **Acid Piranha Cleaning at Low Temperatures**, p. 151) suggested that at temperatures

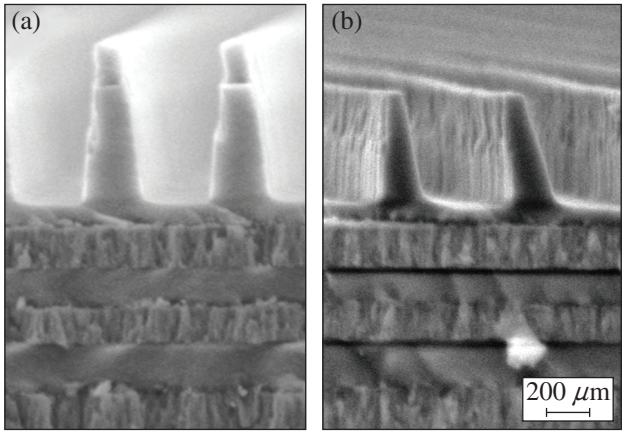

Figure 131.12
SEM images showing MLD grating cross section (a) before chemical cleaning, with BARC and photoresist layers intact and (b) after cleaning, with BARC and photoresist stripped and grating pillars narrowed.

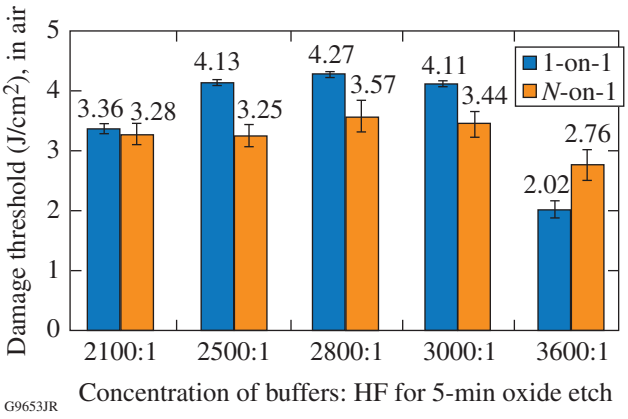

Figure 131.13
Effect of oxide etch concentration on laser-induced–damage threshold of MLD gratings.

Table 131.III: LIDT and DE results for grating samples cleaned using the optimized method.

Part ID	HF dilution (HF:buffers)	Cleaning temperature (piranha strip, ionic clean)	Post-cleaning DE	Post-cleaning LIDT (J/cm^2) *in air*		Post-cleaning LIDT (J/cm^2) *in vacuum*	
				1-on-1	*N*-on-1	1-on-1	*N*-on-1
562-6	2500:1	40°C	98.1±0.4%	4.40±0.17	3.49±0.17	3.30±0.19	2.74±0.14
566-1	2800:1	40°C	97.3±0.4%	3.87±0.13	3.32±0.18		
566-2*	2800:1	40°C	97.4±0.5%	3.32±0.13	3.20±0.12		
564-8**	2800:1	40°C	97.4±0.2%	4.24±0.18	3.44±0.21		
562-7	2500:1	50°C	97.4±0.4%	3.11±0.10	3.19±0.19	3.32±0.02	2.69±0.07
566-6	2800:1	50°C	97.4±0.5%	3.90±0.12	3.51±0.07		
557-2***	2800:1	50°C	96.4±0.7%	4.50±0.08	3.55±0.26	3.29±0.10	2.66±0.07
566-7	2800:1	60°C	97.5±0.3%	3.91±0.15	3.33±0.18		
555-5***	3000:1	60°C	97.0±0.3%	4.11±0.05	3.44±0.21		
564-7*	2500:1	70°C	98.7±0.3%	4.25±0.16	3.54±0.12		
564-6**	2500:1	70°C	97.6±0.3%	4.28±0.20	3.06±0.25		
562-3	2500:1	70°C	97.0±0.3%	4.07±0.01	3.39±0.10	3.19±0.16	2.90±0.04
566-8	2800:1	70°C	98.3±0.5%	3.89±0.20	3.56±0.31	3.70±0.16	2.82±0.20
555-2***	2800:1	70°C	97.8±0.4%	4.27±0.05	3.57±0.26		
Average (14 samples)			97.6%	4.01	3.40	3.36	2.76
Standard deviation (14 samples)			0.55%	0.40	0.16	0.20	0.10

*Piranha 2:1 only (30 min)
**Piranha 5:1 only (30 min)
***A re-used grating sample was used for this experiment. The earlier cleaning experiment did not remove photoresist/BARC.

of 40°C and below, acid piranha could not remove BARC and photoresist from an MLD grating. The cleaning approach shown in Table 131.II is much less temperature sensitive. Figure 131.14 shows in-air damage testing results for six samples cleaned using the optimized method at cleaning temperatures ranging from room temperature to 70°C. Differences in damage threshold results for the four samples cleaned in the range of 40°C to 70°C were not statistically significant, suggesting that cleaning temperatures can be safely reduced to the goal temperature of 40°C without negatively impacting grating performance.

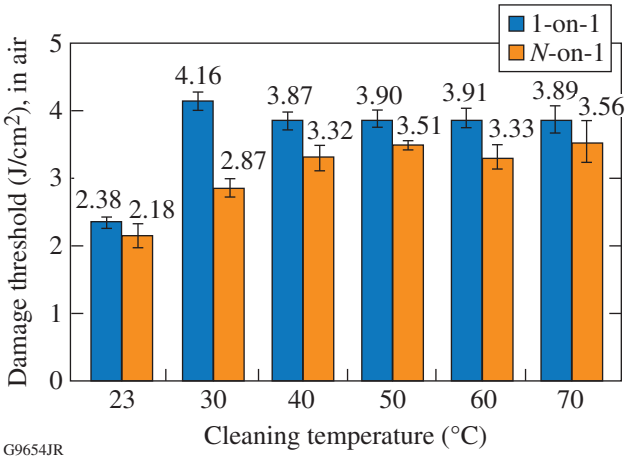

Figure 131.14
Relationship between in-air LIDT and cleaning temperature.

A unique aspect of the grating cleaning process shown in Table 131.II is the use of room air as the process gas in our plasma-cleaning setup. Plasmas generated from oxygen gas (O_2) are more commonly used.[13–16] We found oxygen plasma to be over aggressive, however, and using room air provides a gentler alternative. Figure 131.15 compares plasma-cleaning results for the two process gases. Grating samples were initially cleaned according to the method of Table 131.II and then plasma cleaned for 1, 3, 5, or 10 min using either oxygen or room air as the process gas in a Harrick PDC-32G plasma cleaner. All samples treated with room-air plasma saw an increase in diffraction efficiency (average, +0.43%) and met the OMEGA EP specification of 97% after cleaning, while all samples treated with oxygen plasma saw a drop in DE (average, –0.63%) and only two of four met the OMEGA EP specification. Shorter treatment times (15 and 30 s) were considered for oxygen plasma. The 15-s treatment improved diffraction efficiency modestly (+0.45%), but precise timing was a challenge for such short process durations because initial adjustments to generate a stable plasma require several seconds. The 30-s

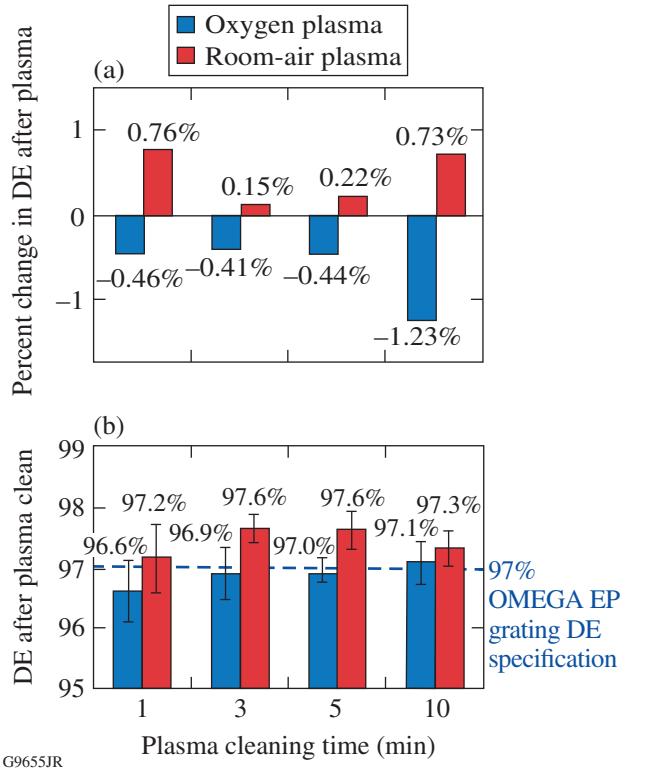

Figure 131.15
Comparison of oxygen and room-air plasma cleaning at room temperature. (a) Oxygen plasma cleaning for 1 to 10 min had a negative effect on diffraction efficiency, whereas room-air plasma cleaning enhanced DE. (b) All four samples treated with room-air plasma exceeded the 97% OMEGA EP grating DE specification, while only two of the four samples treated with oxygen plasma met this specification.

treatment had a negative effect on DE (–0.39%). Because room-air plasma was gentler, process control was superior because cleaning times could be longer.

Room-air plasma was found to be useful in "cleaning up" grating surfaces that failed to meet DE specifications after initial cleaning. Figure 131.16 shows the effect of a 15-min plasma treatment on three piranha-cleaned samples having initially poor diffraction efficiencies. Each of the three samples was improved from 86% to 87% to greater than 95% efficiency. We hypothesize that the air plasma treatment cleared away BARC and photoresist material that may have been softened or been partially removed in previous cleaning steps. Air plasma cleaning is effective at removing organic materials accumulated on the surface during storage and handling. In the optimized clean (Table 131.II), a plasma treatment is included after each wet-processing step to ensure that contaminants introduced (or partially removed) during previous cleaning steps are stripped away before moving on to the next cleaning phase.

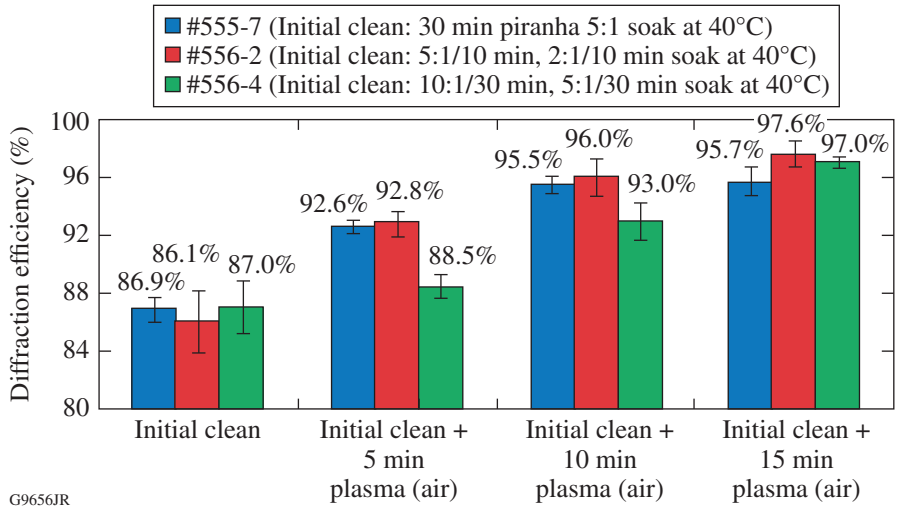

Figure 131.16
Diffraction efficiency enhancement of MLD gratings after room-air plasma cleaning.

5. X-Ray Photoelectron Spectroscopy Results

X-ray photoelectron spectroscopy (XPS) was used to evaluate the composition of materials on the grating surface at different phases in the cleaning process. Grating samples were prepared according to Table 131.II, with acid piranha and ionic cleaning steps performed at 70°C and an HF ratio of 3000:1. A piece of grating was reserved for XPS analysis after each process. XPS testing was performed by the Penn State Materials Characterization Lab (sample #555-4), the University of Dayton Research Institute (samples #562-4A, #562-4B, #562-4C, and #562-4D), and the Cornell Center for Materials Research (sample #555-5). Identically prepared samples were also submitted for laser-induced–damage testing. Results are shown in Table 131.IV.

Since the top layer of the grating is SiO_2, the "ideal" XPS result for a well-cleaned grating would be 33% Si, 67% O, and nothing else. However, because samples are quickly contaminated with organic materials from the environment, some carbon is also expected. The detection of other elements (or large amounts of carbon) is undesirable and indicates insufficient removal of BARC, photoresist, and/or contaminants. In addition to silicon and oxygen (from the SiO_2 top layer), 42% carbon, 8% fluorine, and 3% molybdenum were detected on the uncleaned grating sample (#555-4). Much of the carbon is attributed to the organic photoresist/BARC layers still intact on the part. Fluorine contamination most likely occurred during reactive-ion beam etching of the grating's groove structure, as has been reported by others.[9,11,12] The detection of molybdenum was surprising and motivated the inclusion of a hydrochloric-acid–based ionic cleaning step to specifically target metallic contamination (see Table 131.II). The ionic clean may also remove trace contaminants such as potassium, sodium, chromium, iron, and aluminum. While not identified in XPS scans of our grating

Table 131.IV: Elements detected on MLD gratings at various stages of cleaning and corresponding damage-testing results.

Processing	Sample ID (XPS)	Elements detected by XPS (at. %)							Sample ID (damage testing)	LIDT *in air* (J/cm^2)	
		O	Si	C	F	Mb	Hf	N		1-on-1	*N*-on-1
Uncleaned	555-4	35.2	12.0	41.8	8.00	2.60	–	–	555-4	<0.13	
Piranha	562-4A	45.6	16.4	32.4	1.63	–	–	4.0	560-3	1.41±0.06	1.87±0.11
Piranha + plasma	562-4B	60.3	26.7	13.1	–	–	–	–	560-3	2.13±0.11	2.27±0.09
Piranha + plasma + ionic clean	562-4C	61.0	26.6	12.4	–	–	–	–	560-3	2.28±0.05	2.45±0.12
Piranha + plasma + ionic clean + plasma	562-4D	61.3	26.8	11.9	–	–	–	–	560-3	2.13±0.04	2.34±0.13
Piranha + plasma + ionic clean + plasma + oxide etch + plasma	555-5	60.1	23.8	14.2	–	–	1.0	1.0	555-5	4.11±0.05	3.44±0.21

samples, Ashe *et al.*[9,10] detected these ions on similarly prepared MLD grating samples using the much more sensitive ToF-SIMS (time-of-flight secondary ion-mass spectrometry) technique. Metals absorb strongly at 1054 nm, so damage resistance is quite sensitive to this type of contaminant.

After the piranha and plasma treatments, fluorine and molybdenum levels were below the XPS detection limit and carbon levels had dropped to 13.1%. The biggest drop in carbon level occurred after the plasma treatment (rather than the piranha step), supporting our hypothesis that room-air plasma strips partially removed BARC and photoresist. The remaining cleaning steps (ionic clean, plasma, oxide etch, and plasma) did not have significant effects on the XPS spectra. Figure 131.17 shows contaminants detected side-by-side with LIDT results. After bulk removal of photoresist and BARC, XPS may not be sensitive enough to identify trace contaminants that limit resistance to laser-induced damage.

Conclusions

A low-temperature cleaning method was developed to remove manufacturing residues from MLD pulse-compressor gratings manufactured with polymer BARC. The process, which is effective at processing temperatures as low as 40°C, targets specific families of contaminants in a sequence of cleaning operations. Samples cleaned using the optimized method had outstanding performance: laser-induced–damage thresholds averaged 4.01 J/cm^2 in air and 3.36 J/cm^2 in vacuum (1-on-1 testing regime, 10 ps, 1054 nm, 61°), and average diffraction efficiency was 97.6%.

ACKNOWLEDGMENT

This work was supported by the U.S. Department of Energy Office of Inertial Confinement Fusion under Cooperative Agreement No. DE-FC52-08NA28302, the University of Rochester, and the New York State Energy Research and Development Authority. The support of DOE does not constitute an endorsement by DOE of the views expressed in this article.

REFERENCES

1. L. J. Waxer, D. N. Maywar, J. H. Kelly, T. J. Kessler, B. E. Kruschwitz, S. J. Loucks, R. L. McCrory, D. D. Meyerhofer, S. F. B. Morse, C. Stoeckl, and J. D. Zuegel, Opt. Photonics News **16**, 30 (2005).
2. D. Strickland and G. Mourou, Opt. Commun. **56**, 219 (1985).
3. G. A. Mourou, in *Encyclopedia of Modern Optics*, edited by R. D. Guenther, D. G. Steel, and L. P. Bayvel (Elsevier Academic Press, Amsterdam, 2005), pp. 83–84.

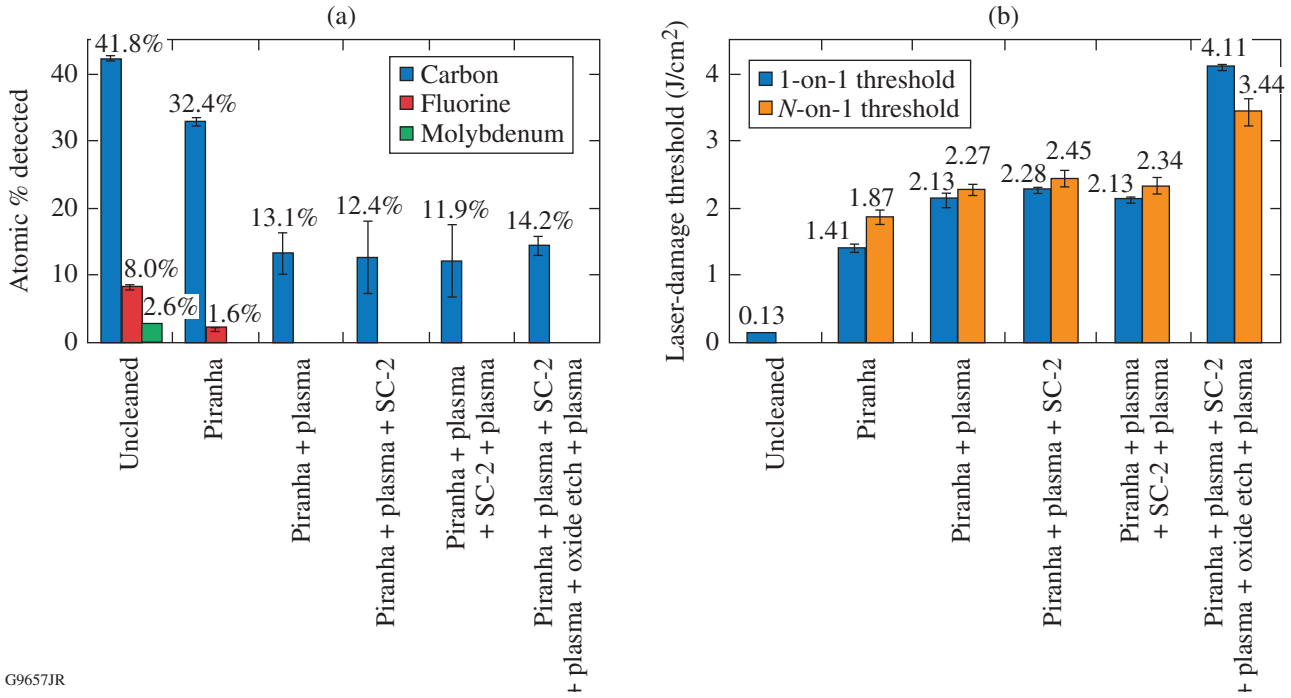

Figure 131.17
(a) Levels of carbon, fluorine, and molybdenum detected after each cleaning step; (b) corresponding laser-induced–damage thresholds.

4. J. A. Britten *et al*., in *Laser-Induced Damage in Optical Materials: 1995*, edited by H. E. Bennett *et al*. (SPIE, Bellingham, WA, 1996), Vol. 2714, pp. 511–520.

5. I. Jovanovic *et al*., in *Laser-Induced Damage in Optical Materials: 2004*, edited by G. J. Exarhos *et al*. (SPIE, Bellingham, WA, 2005), Vol. 5647, pp. 34–42.

6. B. Ashe, K. L. Marshall, D. Mastrosimone, and C. McAtee, in *Optical System Contamination: Effects, Measurements, and Control 2008*, edited by S. A. Straka (SPIE, Bellingham, WA, 2008), Vol. 7069, p. 706902.

7. W.-J. Kong *et al*., Chin. Phys. Lett. **22**, 1757 (2005).

8. W. Kong *et al*., Microelectron. Eng. **83**, 1426 (2006).

9. B. Ashe, K. L. Marshall, C. Giacofei, A. L. Rigatti, T. J. Kessler, A. W. Schmid, J. B. Oliver, J. Keck, and A. Kozlov, in *Laser-Induced Damage in Optical Materials: 2006*, edited by G. J. Exarhos *et al*. (SPIE, Bellingham, WA, 2007), Vol. 6403, p. 64030O.

10. B. Ashe, C. Giacofei, G. Myhre, A. W. Schmid, in *Laser-Induced Damage in Optical Materials: 2007*, edited by G. J. Exarhos *et al*. (SPIE, Bellingham, WA, 2007), Vol. 6720, p. 67200N.

11. S. Chen *et al*., High Power Laser Part. Beams **23**, 2106 (2011).

12. S. Chen *et al*., in *5th International Symposium on Advanced Optical Manufacturing and Testing Technologies: Advanced Optical Manufacturing Technologies*, edited by L. Yang *et al*. (SPIE, Bellingham, WA, 2010), Vol. 7655, p. 765522.

13. J. A. Britten *et al*., U.S. Patent Application No. US 2008/0062522 A1 (13 March 2008).

14. B. Xu *et al*., in *Proceedings of the 50th Annual Technical Conference of the Society of Vacuum Coaters* (Society of Vacuum Coaters, Louisville, KY, 2007), pp. 369–376.

15. Y. Hong *et al*., Vacuum **45**, 25 (2008).

16. A. Bodere *et al*., Mater. Sci. Eng. B **28**, 293 (1994).

17. H. T. Nguyen, C. C. Larson, and J. A. Britten, in *Laser-Induced Damage in Optical Materials: 2010*, edited by G. J. Exarhos *et al*. (SPIE, Bellingham, WA, 2010), Vol. 7842, p. 78421H.

18. J. Britten, C. Larson, M. Feit, and H. Nguyen, presented at the ICUIL 2010 Conference, Watkins, Glen, NY, 26 September–1 October 2010.

19. J. Neauport *et al*., Opt. Express **15**, 12508 (2007).

20. H. Howard, J. C. Lambropoulos, and S. Jacobs, in *Optical Fabrication and Testing*, OSA Technical Digest (online) (Optical Society of America, Washington, DC, 2012), Paper OW3D.3.

21. J. B. Oliver, T. J. Kessler, H. Huang, J. Keck, A. L. Rigatti, A. W. Schmid, A. Kozlov, and T. Z. Kosc, in *Laser-Induced Damage in Optical Materials: 2005*, edited by G. J. Exarhos *et al*. (SPIE, Bellingham, WA, 2005), Vol. 5991, pp. 402–408.

22. W. Beck *et al*., U.S. Patent No. 3,900,337 (19 August 1975).

23. G. W. Gale, R. J. Small, and K. A. Reinhardt, in *Handbook of Silicon Wafer Cleaning Technology*, 2nd ed., edited by K. A. Reinhardt and W. Kern, Materials Science & Process Technology Series (William Andrew, Norwich, NY, 2008), pp. 201–265.

24. D. W. Burns, in *MEMS Materials and Processes Handbook*, edited by R. Ghodssi and P. Lin (Springer, New York, 2011), Chap. 8, pp. 457–665.

Magnetic-Field Generation by Rayleigh–Taylor Instability in Laser-Driven Planar Plastic Targets

Target designs predicted to achieve ignition by inertial confinement fusion (ICF) rely on understanding Rayleigh–Taylor (RT) instability.[1–3] When an ICF capsule is imploded, the ablation front during the acceleration phase and the pusher–fuel interface during the deceleration and stagnation phases are RT unstable.[4,5] At the unstable interface, spikes of higher-density plasma penetrate into lower-density plasma and bubbles of lower-density plasma rise through the higher-density plasma. Understanding RT instability is important because it can amplify capsule perturbations and destroy implosion uniformity.

Previous theoretical work showed that a plasma subject to RT instability should generate spontaneous magnetic fields.[6,7] These fields may exist in inertial fusion plasmas and modify electron thermal transport.[8,9] If present and unaccounted for, these fields may degrade implosion performance compared to theoretical predictions.[10–12] Magnetic fields can be generated in high-energy-density plasmas by many different mechanisms,[13] including the thermoelectric effect,[14,15] anisotropic hot-electron velocity distributions,[16] and thermoelectric instability.[17] Recently the first measurement of RT-induced magnetic fields was reported,[18] which showed RT-induced magnetic fields in laser-accelerated targets with preimposed target-surface modulations from experiments on the OMEGA Laser System.[19] Magnetic fields with strengths of up to 0.1 MG were inferred in the linear growth phase of RT instability using face-on monoenergetic proton radiography.[20] The monoenergetic protons were generated from D–^{3}He fusion inside an imploding capsule.

This article reports on magnetic-field generation during the nonlinear growth phase of RT instability in an ablatively driven plasma using ultrafast laser-driven proton radiography.[21] Thin plastic foils were irradiated with ~4-kJ, 2.5-ns laser pulses focused to ~10^{14} W/cm^2 on LLE's OMEGA EP Laser System.[22] The driven foils were probed with an ultrafast proton beam that revealed the magnetohydrodynamic (MHD) evolution of the target. The target modulations were seeded by laser nonuniformities and amplified during the target-acceleration phase. These experiments show, for the first time, MG-level magnetic fields inside a laser-driven foil broken apart by RT instability. The experimental results are consistent with two-dimensional (2-D) MHD calculations using the code *DRACO*.[23,24]

Figure 131.18 shows a schematic of the experimental setup. Two long-pulse beams irradiated a 15- or 25-μm-thick CH foil.

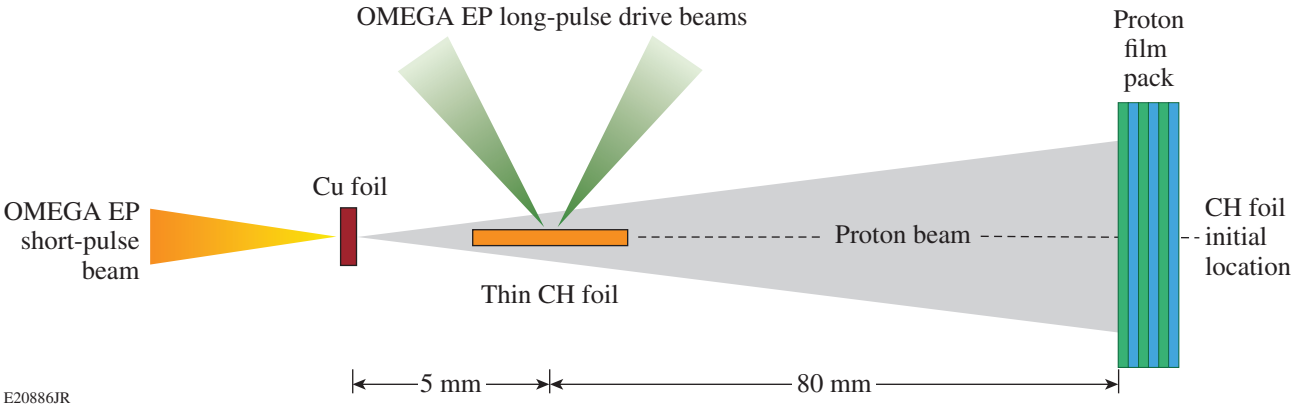

Figure 131.18
Experimental setup.

The foil area was 5×5 mm^2. Only a central ~1-mm-diam part of the foil was driven. Each laser beam delivered an ~2-kJ pulse with a wavelength of 351 nm and a 2.5-ns square temporal profile at 23° to the target normal. The laser beams were focused to ~850-μm-diam focal spots using distributed phase plates.[25] The average overlapped intensity was ~4×10^{14} W/cm^2.

The CH foil was probed in a direction orthogonal to the main interaction with an ultrafast proton beam.[26,27] The proton source was generated by irradiating a planar, 20-μm-thick Cu foil with an ~1-kJ, 10-ps pulse at a wavelength of 1.053 μm. The laser pulse was focused with a 1-m-focal-length, *f*/2 off-axis parabolic mirror onto the Cu foil at normal incidence, providing an intensity of ~5×10^{18} W/cm^2. The relative timing between the long-pulse and short-pulse beams was measured with an x-ray streak camera. Protons were accelerated from the surface of the Cu foil to tens of MeV by target normal sheath acceleration (TNSA).[28] The TNSA mechanism generated a highly laminar proton beam with a micron-scale virtual source size,[29] providing high spatial resolution for probing the main interaction with point-projection radiography.[21]

Combining a filtered stack detector with time-of-flight dispersion provided a multiframe imaging capability.[30] The high-energy protons that passed through the driven CH target were detected with a stack of radiochromic film interleaved with aluminum filters. Soft x rays were filtered with an additional aluminum foil on the front surface of the stack. Each film layer recorded a different probe time because the transit time for protons to the CH foil varied with energy. Protons with different energies deposited energy inside various film layers corresponding to their energy-dependent Bragg peak. The temporal coverage obtained in these experiments on a single shot was ~120 ps, with spatial and temporal resolutions of ~5 to 10 μm and ~10 ps, respectively. The image magnification $M = (L + l)/l$, where l is the distance from the proton-source foil to the CH target and L is the distance from the CH target to the radiochromic film detector. For these experiments, M was ~17 to 20, depending on the radiochromic film layer.

Figure 131.19 shows a typical proton radiograph of a 25-μm-thick CH foil unbroken by instability formation. This radiograph was obtained with 13-MeV protons at time $t = t_0 +$ 2.56 ns, where t_0 is the arrival time of the long-pulse beams at the target surface. The undriven foil horizon is indicated. The long-pulse beams irradiated the target from the left and the blowoff plasma accelerated the central part of the foil toward the right. The driven foil had a transverse size comparable with the laser focal spot. At this time, the foil had a velocity

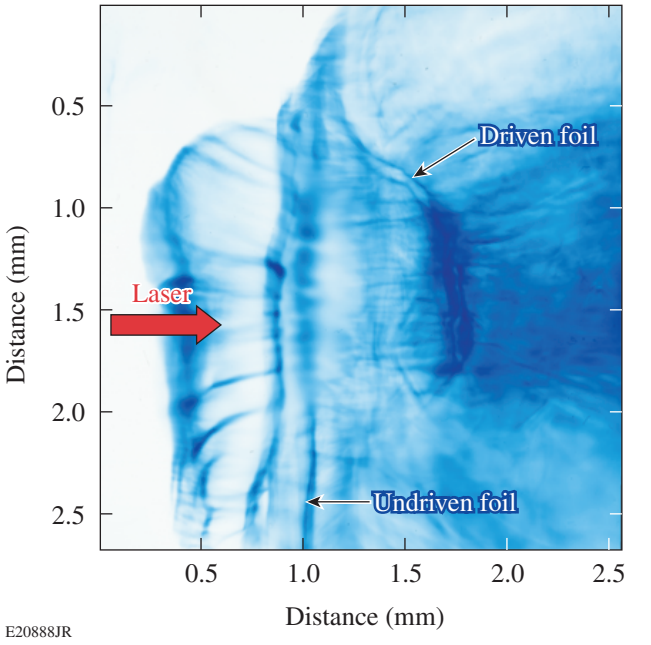

Figure 131.19
Proton radiograph of a 25-μm-thick CH foil taken with 13-MeV protons at $t = t_0 + 2.56$ ns. The laser drive, the undriven foil horizon, and the bow-shaped driven foil are indicated.

of $(3 \pm 1) \times 10^7$ cm/s, calculated from the measured driven-foil trajectory history.

Thinner-foil targets were broken by instability formation during the acceleration phase. Figure 131.20 shows proton radiographs for a 15-μm-thick CH foil driven with the same laser conditions as the 25-μm-thick foil case. These data were obtained with 13-MeV protons. The relative timing with respect to t_0 was varied from 2.11 ns to 2.56 ns. At $t = t_0 + 2.56$ ns, the foil has traveled a greater distance than the 25-μm-thick foil because less mass was accelerated. In this case, bubble-like structures are observed in the proton radiographs. These perturbations grow in time and show that the target has broken apart during the acceleration phase. Larger-scale structures at $t = t_0 + 2.56$ ns indicate this growth.

Further evidence for the broken foil is provided by the appearance of plasma beyond the driven target. Figure 131.20 shows a plasma sheath ahead of the RT-unstable region. Hot plasma in the laser-ablation region has fed through the compromised foil and formed a halo around the unstable expanding matter. A sheath electric field forms at the plasma/vacuum interface and is detected in the proton radiographs. This effect is not observed in the radiographs of the stable, 25-μm-thick foil, uncompromised by instability growth (see Fig. 131.19).

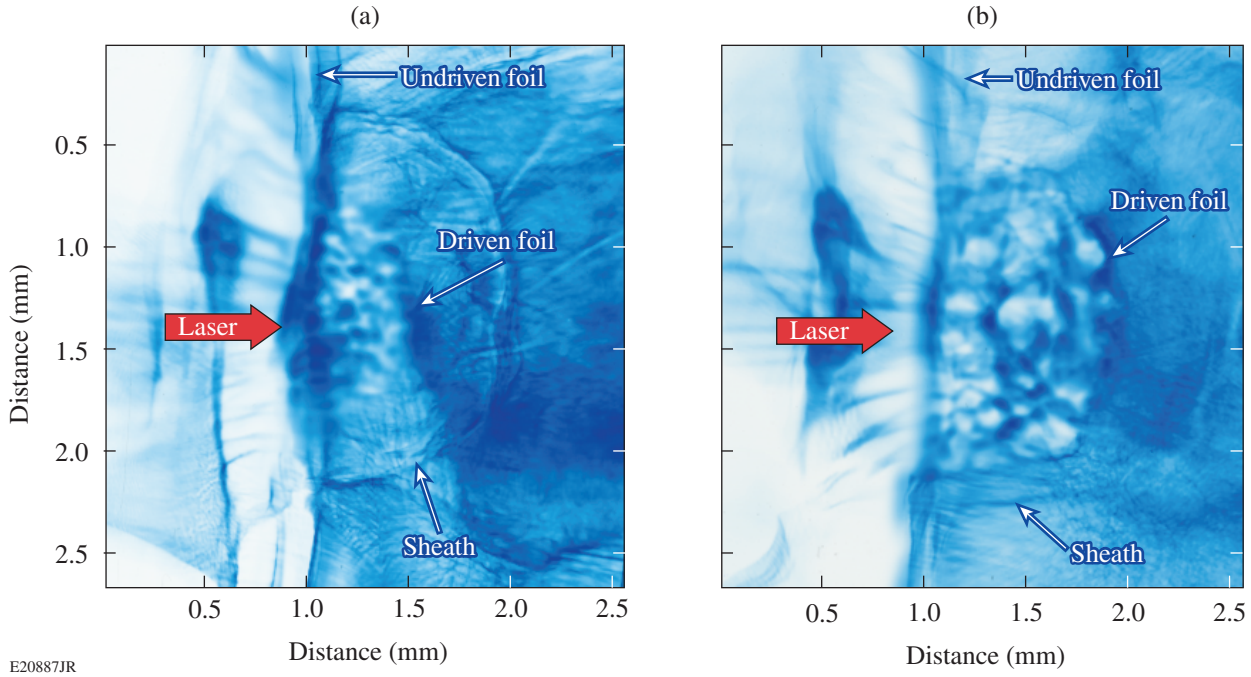

Figure 131.20
Proton radiographs of a 15-μm-thick CH foil taken with 13-MeV protons at (a) $t = t_0 + 2.11$ ns and (b) $t = t_0 + 2.56$ ns. The laser drive, the undriven foil horizon, the RT-unstable plasma, and the sheath field formed by hot-plasma feedthrough are indicated.

The main observation from these data is the electromagnetic fields that are generated during the RT-instability growth. In proton radiography, proton beam density modulations are caused by deflections from electromagnetic fields and by collisional scattering and stopping inside the probed target. For these experiments, collisional scattering and proton stopping are small. For example, collisional energy losses for 13-MeV protons passing through ~30-μm-thick solid CH are $\Delta E/E <$ 1%. Electromagnetic fields must play a dominant role in generating the bubble-like structures observed in the radiography data. The broken foil is revealed in the data by electromagnetic fields that are generated at the RT-unstable interface.

This interpretation is supported by numerical modeling with the 2-D resistive MHD code *DRACO*.[23,24] *DRACO* has a 2-D cylindrical geometry. The equation governing the magnetic field is

$$\frac{\partial \vec{B}}{\partial t} = \nabla \times \left(\vec{V} \times \vec{B}\right) + \frac{c}{e}\left[\nabla \times \left(\frac{\nabla p_e}{n_e}\right) - \nabla \frac{\left(\nabla \times \vec{B}\right) \times \vec{B}}{4\pi n_e} - \nabla \times \frac{\vec{R_T} + \vec{R_u}}{n_e}\right], \quad (1)$$

where $\vec{B}$ is the magnetic induction, p_e is the electron pressure, n_e is the electron number density, e is the fundamental unit of charge, $\vec{V}$ is the flow velocity, and $\vec{R_T}$ and $\vec{R_u}$ are the thermal and frictional forces,[8] respectively. The second term on the right-hand side of Eq. (1) is the thermoelectric source term that is driven by nonparallel density and temperature gradients. The nonuniform ∇p_e force induces poloidal current loops that wrap around the magnetic toroids. The full Braginskii transport coefficients,[8] including the Nernst term[31] and cross-gradient thermal fluxes, were used to calculate $\vec{R_T}$ and $\vec{R_u}$. The temporal evolution of the laser power was provided by experimental measurements. The seeds for the growth of RT instability in the calculations were pre-imposed surface perturbations with a 50-μm wavelength and a 1-μm peak-to-valley amplitude.

The *DRACO* calculations show a 15-μm-thick foil broken apart by RT instability, generating MG-level magnetic fields at the RT-unstable interface. Figure 131.21(a) shows the calculated target-density profile at $t = t_0 + 2.1$ ns. Density perturbations that have grown by RT instability are greater in extent than the target thickness, breaking the foil apart. Large density and temperature gradients form in this unstable plasma and spontaneously generate MG-level magnetic fields. Figure 131.21(b) shows the predicted magnetic-field distribution at $t = t_0 + 2.1$ ns.

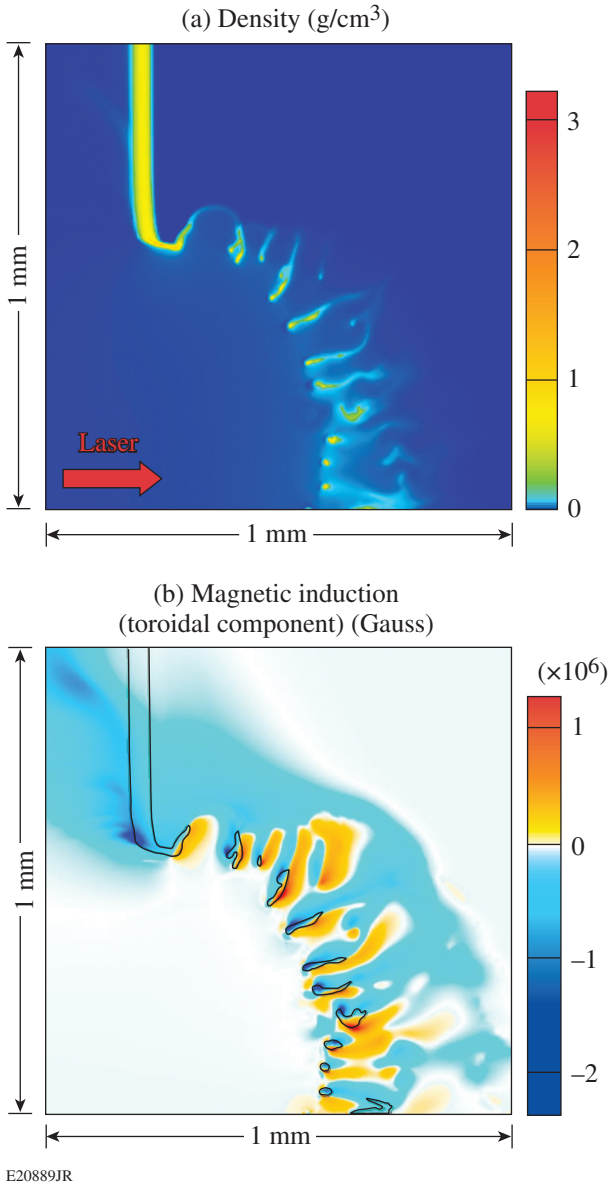

Figure 131.21
(a) Simulated density profile at $t = t_0 + 2.1$ ns. The modeled target is axisymmetric about the horizontal axis. (b) Self-generated magnetic-field distribution at $t = t_0 + 2.1$ ns. The density contour for $\rho = 0.05$ g/cm^3 is overlaid.

Overlaid on this field distribution is the calculated density contour for $\rho = 0.05$ g/cm^3, indicating the position of the target. Magnetic fields generated at the ablation surface are convected toward the lower-density corona by the ablated plasma and to higher-density regions by hot electrons that carry the heat flux (the Nernst effect).[31] In our case, the Nernst convection significantly overperforms the convection by the ablation flow. Magnetic fields of up to 2 MG are observed in these conditions beyond the coronal plasma and inside the driven foil.

DRACO simulations show that the dynamic effect of the generated magnetic fields on the RT instability is negligible in the linear and the moderately nonlinear stages of its evolution. The fields begin to enhance the RT growth in the highly nonlinear stages when the spike sizes are comparable to and larger than the perturbation wavelengths. The *DRACO* calculations reproduce the measured foil velocity to within experimental error, indicating that the gross hydrodynamics of the driven foil are as predicted. For a 25-μm-thick target, *DRACO* calculations show that the RT instability does not break the foil apart and no significant small-scale magnetic fields are generated.

The magnitude of the generated magnetic fields is estimated by measuring the angular deflection θ of protons from their original trajectory while passing through the field region. When the apparent displacement of protons is δ in the target plane, the angular deflection θ is calculated by $\tan\theta = M\delta/D$, where M is the geometric magnification and D is the distance between the main target and the radiochromic film detector. The proton-path–integrated B field caused by the Lorentz force acting upon the proton probe beam is $\int \vec{B} \times \mathrm{d}\vec{l} = m_\mathrm{p} v \sin\theta / e$, where m_p is the proton mass and v is the proton speed. In our experiments, the protons are deflected by azimuthal magnetic fields generated around the RT spikes. At $t = t_0 + 2.11$ ns, a δ of 25 μm results in a deflection angle θ of 0.31°. Assuming an integration path length slightly larger than the target thickness ($L \sim 25$ μm) gives a magnetic-field strength of ~1.4 MG, which is in good agreement with the *DRACO* simulations.

At the RT-unstable interface, narrow spikes are formed where the dense matter falls through the light matter, and bubbles are generated when the light material rises into the dense material.[3] This process generates magnetic fields that wrap around the troughs of the spikes. The growth of the spatial scale length of the perturbed features is caused by magnetic-field evolution as the RT instability develops. The magnetic-field topology in *DRACO* is different from the real three-dimensional (3-D) situation. In 3-D RT instability, azimuthal magnetic fields are formed around single spikes and bubbles. The magnitude and the predominant wavelength of the magnetic fields, however, are expected to be accurate.

A proton ray-tracing code using electromagnetic field distributions from the 2-D *DRACO* calculations supports

the dominant role of magnetic fields in deflecting protons in these experiments. The initial proton-source details and the radiography geometry were taken from the experiments. The accumulated proton numbers were monitored in the ray-tracing code at a simulated detector plane. Figure 131.22 shows the effect of electric and magnetic fields in this process. The predicted proton distribution is unchanged when electric fields are turned off in the calculations, while few proton deflections are observed when magnetic fields are turned off. Self-generated magnetic fields at the RT-unstable interface are the dominant cause for proton-beam deflections in these experiments. Two-dimensional Fourier analysis of the measured proton radiographs shows that the characteristic spatial scale length of the bubble-like features at $t = t_0 + 2.11$ ns is ~82 μm, growing to ~115 to 230 μm at $t = t_0 + 2.56$ ns. Broadly consistent with this experimental trend, Fourier analysis of the proton distribution in Fig. 131.22 gives a characteristic spatial scale length of ~93 μm, growing to ~220 μm at the latest time.

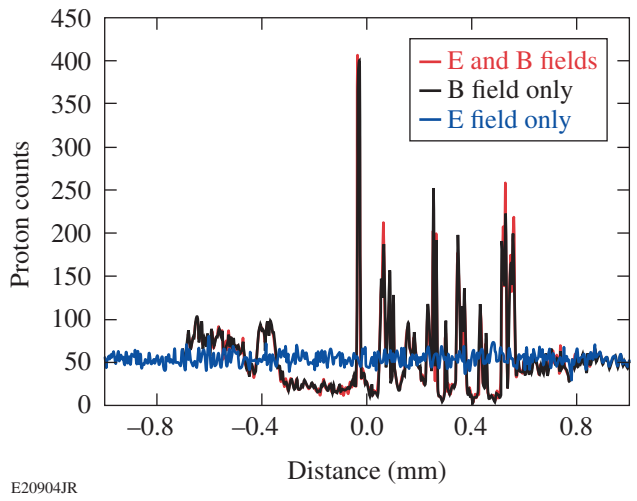

Figure 131.22
Proton tracking code results. Proton deflections are modeled based on electromagnetic field distributions predicted by 2-D *DRACO* calculations.

In summary, magnetic-field generation during the nonlinear growth of target perturbations by RT instability in ablatively driven foils was studied. Measurements of MG-level magnetic fields were supported by recovering characteristic spatial scale lengths of the proton deflections using a particle ray-tracing code that incorporates electromagnetic-field distributions from a 2-D MHD model. Electric fields were found to be negligible compared to the generated magnetic fields in producing the modulated patterns in the proton radiography beam profile. Simulations suggest that the dynamic effect of these magnetic fields on RT growth is not significant.

ACKNOWLEDGMENT

This work was supported by the U.S. Department of Energy Office of Inertial Confinement Fusion under Cooperative Agreement No. DE-FC52-08NA28302, the University of Rochester, and the New York State Energy Research and Development Authority. The support of DOE does not constitute an endorsement by DOE of the views expressed in this article.

REFERENCES

1. Lord Rayleigh, Proc. London Math Soc. **XIV**, 170 (1883).
2. G. Taylor, Proc. R. Soc. London Ser. A **201**, 192 (1950).
3. R. Betti and J. Sanz, Phys. Rev. Lett. **97**, 205002 (2006).
4. J. D. Lindl, Phys. Plasmas **2**, 3933 (1995).
5. R. L. McCrory, D. D. Meyerhofer, S. J. Loucks, S. Skupsky, R. Betti, T. R. Boehly, T. J. B. Collins, R. S. Craxton, J. A. Delettrez, D. H. Edgell, R. Epstein, K. A. Fletcher, C. Freeman, J. A. Frenje, V. Yu. Glebov, V. N. Goncharov, D. R. Harding, I. V. Igumenshchev, R. L. Keck, J. D. Kilkenny, J. P. Knauer, C. K. Li, J. Marciante, J. A. Marozas, F. J. Marshall, A. V. Maximov, P. W. McKenty, S. F. B. Morse, J. Myatt, S. Padalino, R. D. Petrasso, P. B. Radha, S. P. Regan, T. C. Sangster, F. H. Séguin, W. Seka, V. A. Smalyuk, J. M. Soures, C. Stoeckl, B. Yaakobi, and J. D. Zuegel, J. Phys. IV France **133**, 59 (2006).
6. J. A. Stamper *et al*., Phys. Rev. Lett. **26**, 1012 (1971).
7. K. Mima, T. Tajima, and J. N. Leboeuf, Phys. Rev. Lett. **41**, 1715 (1978).
8. S. I. Braginskii, in *Reviews of Plasma Physics*, edited by Acad. M. A. Leontovich (Consultants Bureau, New York, 1965), Vol. 1, p. 205.
9. M. G. Haines, Phys. Rev. Lett. **78**, 254 (1997).
10. J. A. Stamper, Laser Part. Beams **9**, 841 (1991).
11. R. G. Evans, Plasma Phys. Control. Fusion **28**, 1021 (1986).
12. B. Srinivasan, G. Dimonte, and X.-Z. Tang, Phys. Rev. Lett. **108**, 165002 (2012).
13. M. G. Haines, Can. J. Phys. **64**, 912 (1986).
14. J. A. Stamper and B. H. Ripin, Phys. Rev. Lett. **34**, 138 (1975).
15. D. G. Colombant and N. K. Winsor, Phys. Rev. Lett. **38**, 697 (1977).
16. K. Estabrook, Phys. Rev. Lett. **41**, 1808 (1978).
17. M. G. Haines, Phys. Rev. Lett. **47**, 917 (1981).
18. M. J. E. Manuel, C. K. Li, F. H. Séguin, J. Frenje, D. T. Casey, R. D. Petrasso, S. X. Hu, R. Betti, J. D. Hager, D. D. Meyerhofer, and V. A. Smalyuk, Phys. Rev. Lett. **108**, 255006 (2012).

19. T. R. Boehly, D. L. Brown, R. S. Craxton, R. L. Keck, J. P. Knauer, J. H. Kelly, T. J. Kessler, S. A. Kumpan, S. J. Loucks, S. A. Letzring, F. J. Marshall, R. L. McCrory, S. F. B. Morse, W. Seka, J. M. Soures, and C. P. Verdon, Opt. Commun. **133**, 495 (1997).

20. C. K. Li, F. H. Séguin, J. A. Frenje, J. R. Rygg, R. D. Petrasso, R. P. J. Town, P. A. Amendt, S. P. Hatchett, O. L. Landen, A. J. Mackinnon, P. K. Patel, V. A. Smalyuk, T. C. Sangster, and J. P. Knauer, Phys. Rev. Lett. **97**, 135003 (2006).

21. M. Borghesi *et al*., Phys. Rev. Lett. **92**, 055003 (2004).

22. L. J. Waxer, D. N. Maywar, J. H. Kelly, T. J. Kessler, B. E. Kruschwitz, S. J. Loucks, R. L. McCrory, D. D. Meyerhofer, S. F. B. Morse, C. Stoeckl, and J. D. Zuegel, Opt. Photonics News **16**, 30 (2005).

23. D. Keller, T. J. B. Collins, J. A. Delettrez, P. W. McKenty, P. B. Radha, B. Whitney, and G. A. Moses, Bull. Am. Phys. Soc. **44**, 37 (1999).

24. I. V. Igumenshchev, F. J. Marshall, J. A. Marozas, V. A. Smalyuk, R. Epstein, V. N. Goncharov, T. J. B. Collins, T. C. Sangster, and S. Skupsky, Phys. Plasmas **16**, 082701 (2009).

25. *LLE Review Quarterly Report* **33**, 1, Laboratory for Laser Energetics, University of Rochester, Rochester, NY, LLE Document No. DOE/DP/40200-65, NTIS Order No. DE88008065 (1987).

26. E. L. Clark *et al*., Phys. Rev. Lett. **85**, 1654 (2000).

27. R. A. Snavely, M. H. Key, S. P. Hatchett, T. E. Cowan, M. Roth, T. W. Phillips, M. A. Stoyer, E. A. Henry, T. C. Sangster, M. S. Singh, S. C. Wilks, A. MacKinnon, A. Offenberger, D. M. Pennington, K. Yasuike, A. B. Langdon, B. F. Lasinski, J. Johnson, M. D. Perry, and E. M. Campbell, Phys. Rev. Lett. **85**, 2945 (2000).

28. S. C. Wilks, A. B. Langdon, T. E. Cowan, M. Roth, M. Singh, S. Hatchett, M. H. Key, D. Pennington, A. MacKinnon, and R. A. Snavely, Phys. Plasmas **8**, 542 (2001).

29. T. E. Cowan *et al*., Phys. Rev. Lett. **92**, 204801 (2004).

30. A. J. Mackinnon, P. K. Patel, M. Borghesi, R. C. Clarke, R. R. Freeman, H. Habara, S. P. Hatchett, D. Hey, D. G. Hicks, S. Kar, M. H. Key, J. A. King, K. Lancaster, D. Neely, A. Nikkro, P. A. Norreys, M. M. Notley, T. W. Phillips, L. Romagnani, R. A. Snavely, R. B. Stephens, and R. P. J. Town, Phys. Rev. Lett. **97**, 045001 (2006).

31. A. Nishiguchi, T. Yabe, and M. G. Haines, Phys. Fluids **28**, 3683 (1985).

High-Resolution Spectroscopy Used to Measure Inertial Confinement Fusion Neutron Spectra on OMEGA

Introduction

Nuclear diagnostics are essential to interpreting the condition of the DT fuel during compression in inertial confinement fusion (ICF) experiments.[1] Measurable parameters that determine the performance of ICF implosions include the ion temperature (T_i), areal density (ρR), and the primary DT neutron yield (Y_n) (Ref. 2). To achieve thermonuclear ignition, the alpha-particle heating must exceed the energy losses from the hot spot.[3] The DT fuel in the hot spot must have an areal density high enough to stop the alpha particles leaving the hot spot (typically >300 mg/cm^2), which boosts the core temperature into the ignition regime.[4]

A number of scaling laws have been developed where measurable parameters represent the progress toward fuel conditions necessary for ignition. The simplest of these laws depends on the T_i and ρR described by the 1-D parameter

$$\chi_{1\text{-D}} \approx \rho R^{0.8}\ \text{g/cm}^2 \left(\frac{T_i}{4.4\ \text{keV}}\right)^{1.8}, \tag{1}$$

where $\chi_{1\text{-D}} > 1$ defines the ignition threshold.[5] A similar scaling law called ITFX, used on the National Ignition Facility (NIF), gives the probability of ignition as a function of experimental observables.[6,7]

A first approach to infer the areal density from cryogenic DT implosions was to measure the knock-on deuterons and tritons in the colder, dense shell, elastically scattered from the primary neutrons produced in the fusion reaction.[8,9] This technique has an increased uncertainty when the areal density approaches ~200 mg/cm^2 (Ref. 10). Advances in cryogenic implosions, such as using low-adiabat pulses and highly symmetric laser irradiation, have increased the areal density. The higher ρR results in a "leveling off" in the amount of knock-ons that leave the colder, dense shell as a result of the energy loss of the charged particles. An alternative method to infer the areal density in DT cryogenic implosions uses the primary neutrons that elastically scatter off the deuterons and tritons in the dense shell surrounding the hot spot.[1]

The magnetic recoil spectrometer (MRS) was one of the first methods to infer an areal density of >200 mg/cm^2 by measuring the forward-scattered neutron spectrum between 10 to 12 MeV (Ref. 11). This measurement is achieved by placing a plastic foil, either CH or CD, as close as possible to the DT implosion target. The neutrons from the reaction produce recoil protons (or deuterons) that are projected through a focusing magnet. The magnetic field deflects the recoiled protons (deuterons) onto an array of detectors according to their energy. This diagnostic has been successful for areal-density measurements on both OMEGA and the NIF.[12]

Neutron time-of-flight (nTOF) techniques have also been used to measure the areal density on the NIF using the elastically scattered neutron spectrum between 10 and 12 MeV (Ref. 13). These nTOF detectors use a liquid scintillation fluid with special properties to mitigate the long light-afterglow component.[14] Two identical detectors for two separate lines of sight have been calibrated on the OMEGA Laser System before installation on the NIF. The nTOF diagnostics have been successful in measuring the areal density on a large number of NIF cryogenic DT implosions and the results compare favorably with the MRS.

This article reports on a novel nTOF detector that was used for the first time to measure high-resolution, elastically scattered neutron spectra in the 1- to 6-MeV region on cryogenic DT implosions. A well-collimated, 13.4-m line of sight, designed with the aid of the Monte Carlo neutron transport code, and an nTOF detector with low-afterglow liquid scintillator compound were crucial to achieving a high-enough signal to background in the neutron spectrum at these energies. This new diagnostic is able to measure the areal density in the region from 50 to 250 mg/cm^2—typical values achieved in recent experiments where re-scattering of the scattered neutrons was negligible. Future experiments will result in higher areal densities (<1 g/cm^2). Less than 1% of the backscattered neutrons are being re-scattered even at these high areal densities, which will not reduce the accuracy of the areal-density measurements with this diagnostic. Multiple scattering becomes relevant only with areal densities well above 1 g/cm^2. Furthermore, simultane-

ous areal-density measurements from the MRS and the nTOF, which view the target from different directions, will allow for the study of asymmetric implosions on OMEGA.

The ICF neutron energy spectrum of cryogenic DT implosions and the method used to infer the areal density from the elastically scattered neutrons will be described in the next section. The remaining sections will (1) describe the nTOF diagnostic design along with an improved shielded environment with a collimated line of sight that will minimize unwanted neutron scattering; (2) discuss the detector calibration method and the approach used to infer the areal density; and (3) present a summary and a short outlook on future work.

Inferring ρR from the ICF Neutron Energy Spectrum

The primary DT neutrons are generated from the fusion reaction[4]

$$\mathrm{D} + \mathrm{T} \longrightarrow \mathrm{He}^4(3.53\,\mathrm{MeV}) + \mathrm{n}(14.06\,\mathrm{MeV}). \tag{2}$$

A small fraction of the primary DT neutrons elastically scatter off the dense shell consisting of deuterons and tritons:

$$\begin{aligned} \mathrm{n} + \mathrm{D} &\longrightarrow \mathrm{n}'(1.56 - 14.06\,\mathrm{MeV}) + \mathrm{D}'(<12.50\,\mathrm{MeV}), \\ \mathrm{n} + \mathrm{T} &\longrightarrow \mathrm{n}'(3.53 - 14.06\,\mathrm{MeV}) + \mathrm{T}'(<10.53\,\mathrm{MeV}). \end{aligned} \tag{3}$$

Specifically, the number of down-scattered neutrons is given by

$$Y_{\mathrm{n}'} = Y_{\mathrm{n}}(r)\int_0^{\infty}\int_0^{R}\left(\sigma_{\mathrm{d}} n_{\mathrm{d}} + \sigma_{\mathrm{t}} n_{\mathrm{t}}\right)\mathrm{d}r\mathrm{d}t, \tag{4}$$

where $Y_{\mathrm{n}}(r)$ is the quantity of 14.06-MeV neutrons at the radius r, σ_{d} and σ_{t} are the total elastic cross sections for the (n,d) and (n,t) interactions, with n_{d} and n_{t} the fuel ion density distributions. A simple derivation relates the areal density $\langle \rho R \rangle$ to the down-scattered neutrons' fraction[9]

$$\langle \rho R \rangle = 5\frac{m_{\mathrm{p}}}{(\sigma_{\mathrm{d}} + \sigma_{\mathrm{t}})}\frac{Y_{\mathrm{n}'}}{Y_{\mathrm{n}}}\,\mathrm{mg/cm}^2, \tag{5}$$

where m_{p} is the mass of the proton and σ_{d} and σ_{t} are the cross sections for neutron scattering off deuterium and tritium, respectively. The areal density is proportional to total down-scattered neutron fraction $Y_{\mathrm{n}'}$ over the DT primary neutron yield Y_{n}. For average areal densities of <0.3 g/cm^2, typical for experiments on OMEGA, the primary neutrons typically experience no more than a single scatter event while leaving the compressed shell; double scattering is negligible. The kinematic end point of these neutrons scattered from the dense DT shell is 3.53 MeV and 1.56 MeV, for scattering off the triton and deuteron, respectively, as calculated from[15]

$$\frac{E_{\mathrm{n}'}}{E_{\mathrm{n}}} = \frac{4A}{(1+A)^2}\cos^2\theta, \tag{6}$$

where $E_{\mathrm{n}'}$ is the energy of the neutron after scattering, A is the atomic mass of the target nuclei (i.e., D to T), and θ is the recoil angle of the nucleus in the lab frame. The kinematic edge is defined by the value of $E_{\mathrm{n}'}$ for $\theta = 0$, or the point at which maximum energy transfer occurs.

An example of the calculated neutron spectrum for a cryogenic DT implosion with an areal density of 220 mg/cm^2 and a T_{i} of 2.4 keV is shown in Fig. 131.23.

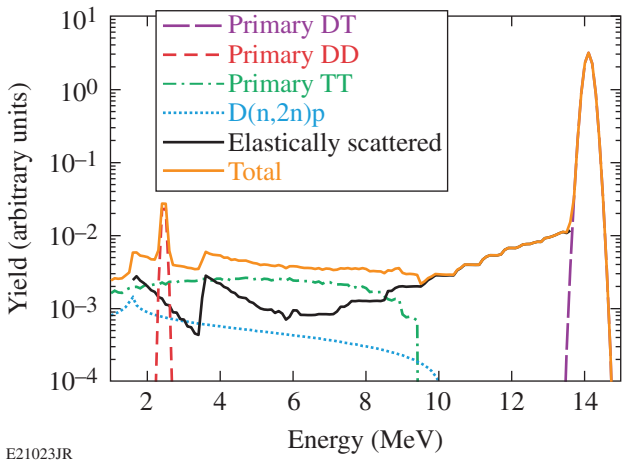

Figure 131.23
The neutron spectrum of a cryogenic DT implosion is generated from 1-D *LILAC* hydrodynamic simulations using the Monte Carlo postprocessor *IRIS*. This spectrum includes the primary DT peak (purple), DD peak (red), and TT neutron feature (green). A fraction (black) of the primary DT neutrons elastically scatter off the dense DT shell. The deuteron breakup reaction (light blue) becomes relevant below 2 MeV. These individual reactions result in the total neutron energy spectrum (orange).

This spectrum was generated using 1-D *LILAC* simulations and post-processed in *IRIS*.[16] The largest contribution to the neutron spectrum comes from the primary D–T fusion reaction at 14.06 MeV. A second primary peak is the D–D fusion reaction at 2.45 MeV followed by the T–T fusion reaction, which is assumed isotropic, and shows a broad energy distribution with a range from 0 to 9.8 MeV (Ref. 17). The elastically scattered neutrons span the entire energy spectrum from 1 to 14.06 MeV.

The deuteron breakup, D(n,2n)p reaction, becomes important below 2 MeV.

The nD and nT elastic cross sections have been measured recently with high accuracy on OMEGA using DT-filled, thin-glass targets.[18] For DT cryogenic implosions, the backscattered neutrons probe the fuel assembly in the 1- to 6-MeV region (150° to 180°).

Setup of the Neutron Time-of-Flight Detector

A time-of-flight spectrum (Fig. 131.24) for a detector at 13.4 m from the target was generated from the neutron energy distribution discussed in the previous section.

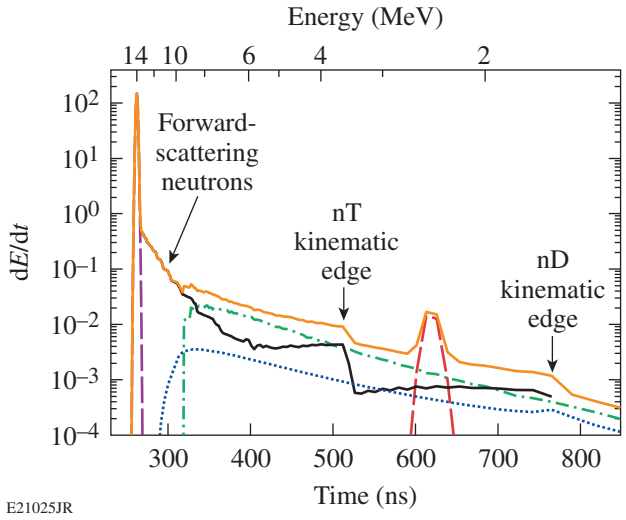

Figure 131.24
A neutron time-of-flight spectrum generated for cryogenic DT implosions on OMEGA with a detector positioned 13.4 m from target chamber center. The primary DT peak (purple), primary DD peak (red), and TT spectrum (green) are generated by fusion reactions. The elastically scattered primary neutrons (black) extend ~10^5 down from the primary DT peak. Below 2 MeV (~700 ns) the deuteron breakup (blue) inelastic reaction becomes relevant. The total neutron spectrum (orange) is the combination of these individual contributions.

The time-of-flight spectrum in Fig. 131.24 illustrate a number of difficulties when trying to measure neutrons over a dynamic range of 10^5 while maintaining sensitivity in the instrument. One issue is the dominant DT peak that accounts for more than 90% of the neutron energy deposited in the detector. Such a large impulse will saturate the photomultiplier tube (PMT) and produce a long light-afterglow component in the scintillator.[13] The lower-energy neutrons in the detector are masked by the afterglow component from the primary peak that is still present from the scintillation process. Another consideration for high-yield DT implosions is the neutron scattering from the target chamber walls and surrounding concrete structures. Three crucial innovations were needed to achieve high-resolution measurements of the neutron energy spectrum.

A gated PMT was used to exclude the primary DT peak from the time-of-flight signal, similar to the detector setup used for fast-ignitor experiments.[13] The microchannel plate (MCP) PMT is gated by applying a positive voltage to the photocathode. The photoelectrons are attracted back toward the photocathode and will not reach the MCP.[19] Once the primary peak has passed, the bias returns to normal and the PMT generates a signal.

Even with the DT peak gated out of the detector, remnants of the scintillation light from the primary DT signal are still evident. To mitigate the long light-afterglow component, advanced scintillating compounds were developed. Oxygenated xylene has been used to reduce the long light-afterglow component by a factor of 10^5 approximately 100 ns after the primary peak.[14]

These modifications led to the construction of a second-generation time-of-flight diagnostic. A computer-aided drawing (CAD) (shown in Fig. 131.25) illustrates the components of the nTOF detector's final design. A significant modification from the first-generation nTOF detector used for the fast-ignitor campaign is a stainless-steel housing lined with gold. The liner is intended to eliminate any possible reaction from the oxygenated xylene that would alter the sensitivity of the detector. The cavity for the nTOF detector is 15 cm in diameter and 5 cm deep. Scintillation

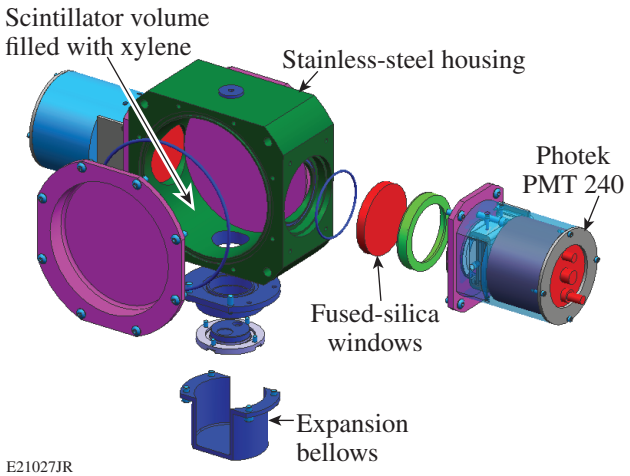

Figure 131.25
A computer-aided design (CAD) of the nTOF detector shows a cavity for the scintillation fluid, the fused-silica windows, and the photomultiplier tube (PMT) mounts. The detector is mounted to the ceiling underneath the Target Bay in a shielded environment to minimize unwanted neutron scattering similar to the setup used in the fast-ignitor experiment.

light from the incident neutrons is viewed through fused-silica windows where the light is coupled to two 40-mm-diam PMT's.

The instrument must be positioned close enough to target chamber center to achieve high neutron statistics but far enough away to interpret the individual components of the energy spectrum. On OMEGA, the maximum distance available for time-of-flight experiments is 13.4 m from the target chamber center. The final necessary modification was to improve the collimation along the line of sight. A Monte Carlo code (MCNP)[20] is used to model the relevant structures in the OMEGA Target Bay and the area underneath the Target Bay. MCNP, developed by the Los Alamos Monte Carlo Group, is used extensively in the nuclear community. This code was cross checked with Geant4 to ensure that the neutron cross sections were in agreement.[21] The simulations showed that the signal to background can be improved by the introduction of a mid-beam collimator. A diagram of the current nTOF detector and mid-beam collimator is shown in Fig. 131.26. The mid-beam collimator has a 60-cm-sq cross section and is ~70 cm in length. It is constructed from high-density polyethylene with a density of ~0.95 g/cm^3. It is mounted on a stand located in the OMEGA Target Bay with semi-permanent mounts. Comparison of data from experiments with and without the mid-beam collimator shows an increase in signal to background by a factor of 2, as shown in Fig. 131.27.

It was determined that a part of the large background was a result of the primary DT neutrons scattering off the target chamber walls. The mid-beam collimator reduced the field of view as seen by the nTOF from the target chamber to provide

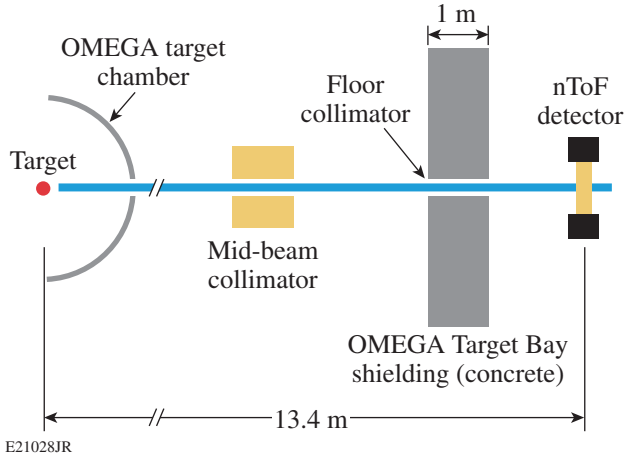

Figure 131.26
A schematic of the target chamber shows the concrete shielding, the nTOF detector's clear line of sight, and the mid-beam collimator. It was determined that the primary DT neutrons scatter off the target chamber walls and produce a large background signal in the nTOF.

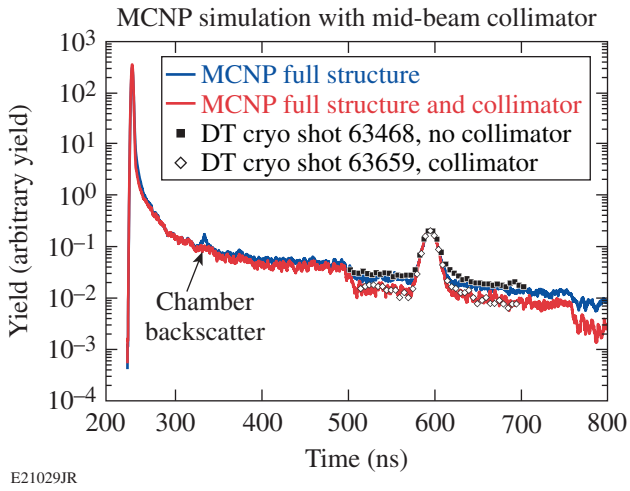

Figure 131.27
Simulations identify the large background resulting from the primary DT neutrons scattering from the target chamber. The models in MCNP included a simulation with (red) and without (blue) a mid-beam collimator. These results were then compared with experimental results (black symbols). The signal to background was in good agreement between simulations and data.

an improved signal to background used to measure the DD and backscattered neutron spectra. A second collimator has been considered for placement inside the target chamber to further reduce neutron scattering from the structures (diagnostics) surrounding the cryogenic target. This will be modeled in MCNP to simulate the effects of this additional collimation needed to further improve the signal to background.

The signals from the PMT's are recorded by a 1-GHz Tektronix DPO-7104 digital oscilloscope. Measurements from recent cryogenic DT experiments are shown in Fig. 131.28. The combination of a gated PMT, an advanced scintillation fluid, and the mid-beam collimator in the clear line of sight made it possible to measure a high-resolution neutron spectrum with good signal to background. The DT peak at ~260 ns is suppressed by the gate. A check of the influence of the gating of PMT's on the nTOF signal was performed by adjusting the timing offset of the gate signals on two nominally identical PMT's. The time-of-flight spectrum indicates that after 50 ns the PMT's are fully recovered.

ρR Measurements Using BackScattered Neutron Yields

The nTOF detector must be calibrated before each use on cryogenic DT campaigns since there is evidence that the scintillating fluid exhibits a depletion of oxygen. A loss of oxygen in the xylene affects the sensitivity of the light-emission process and results in an increased long light-afterglow component. This combination of enhanced sensitivity and longer light decay

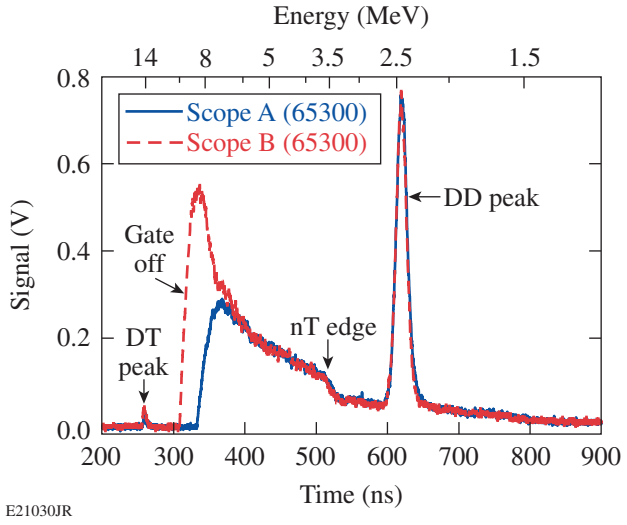

Figure 131.28
To suppress the DT neutron peak, a timing gate is applied to the PMT. The gate recovery has been measured using two PMT 240's, where the time was purposefully offset: PMT A (blue) and PMT B (red). It is clear both PMT's are recovered within 50 ns after the gating is switched off.

will impact the accuracy of the neutron-yield measurement. For this calibration, two D_2-filled targets were imploded with yields that differ by a factor of ~10 to check the linearity of the nTOF detector. A separate detector located in the Target Bay accurately measures the primary neutron yield. Over a six-month period the detector calibration factor changed by ~20%. At this time, it is unclear what causes the xylene to lose the oxygen pressure inside the detector volume.

Recent cryogenic DT implosions have produced neutron yields approaching 1×10^{13} using improved target-positioning procedures and optimized laser pulse shapes on OMEGA.[22] To extract quantitative information from the nTOF signal, the observed spectra are fitted using two of the theoretical components outlined in Fig. 131.24. The first component is the TT spectrum, which is well approximated by a decaying exponential $A \exp(-t/\tau)$ at energies below 6 MeV. The contribution of the TT primary reaction is dependent on the reactivity rate and increases as a function of T_i^4. For this analysis, the overall shape of the spectrum is assumed to be fixed, while the amplitude is scaled from the 1-D simulations where an ion temperature of 2.4 keV was used.

The second component is the down-scattered spectrum that includes both the nT and nD contributions. Since tritium has a half-life of 12.3 years, the fuel D:T ratio changes by ~5% per year. Therefore, it is required to change the nT and nD contributions according to the changing deuterium/tritium fraction in the DT fuel. This scattered neutron contribution is used to infer the areal density in the nTOF detector. The nT kinematic edge is clearly visible and provides a well-defined region for an accurate fit. An additional background is used to account for the remaining neutron scattering from surrounding structures and remnants of scintillator light decay. The background was found to be quite stable over a number of shots spanning several months. The shape of the background is assumed to be a constant exponential decay, where the amplitude is scaled with the primary DT neutron yield.

This method provides a very good fit to the nTOF spectrum using 1-D simulations as a basis. A number of measurement uncertainties must be considered to obtain an estimate on the accuracy of this analysis. The primary DT neutron yield, needed to adjust the background component, is measured to an accuracy of 5% (Ref. 23). The light output from the scintillator is assumed to be proportional to the energy of the incident neutrons. Given the finite thickness of the scintillator, up to 50% of the incident neutrons pass through the scintillator without any interaction. Since the interaction cross section of neutrons with the scintillator material is a function of the neutron energy, a small correction for the changing interaction probability must be applied to obtain a more-accurate description of the light output. Preliminary simulations of this effect using MCNP with the current xylene nTOF detector indicate that the proportionality assumption introduces an error of ~5%. The best fit to nTOF data is obtained by performing minimization of the error sum to optimize the TT and down-scattered components. The error associated with this method is approximately 2% according to a χ^2 analysis. The high accuracy of this fit is due in part to the large number of neutrons measured by the detector in this region. Below 6 MeV, the nTOF detectors measure above 1×10^5 elastically scattered neutrons (typical on OMEGA cryogenic DT implosions), which introduces a statistical error of ~2%. Errors in the nD and nT elastic scattering cross sections also affect these areal-density measurements. Recent measurements improved the accuracy of the differential nD and nT cross sections, especially at a scattering angle of 180°, to ~10% (Ref. 18). Adding these errors in quadrature gives an estimated total error of ~15%.

However, a number of other error sources have not yet been quantified. The shape of the TT neutron spectrum is not yet well known, which introduces some uncertainty in the fit component. A third theoretical component of the neutron energy spectrum, not included in the fit, is the deuteron breakup reaction D(n,2n)p. This nuclear component will affect the fit primarily in the region below 2 MeV (~700 ns) as seen in Fig. 131.29.

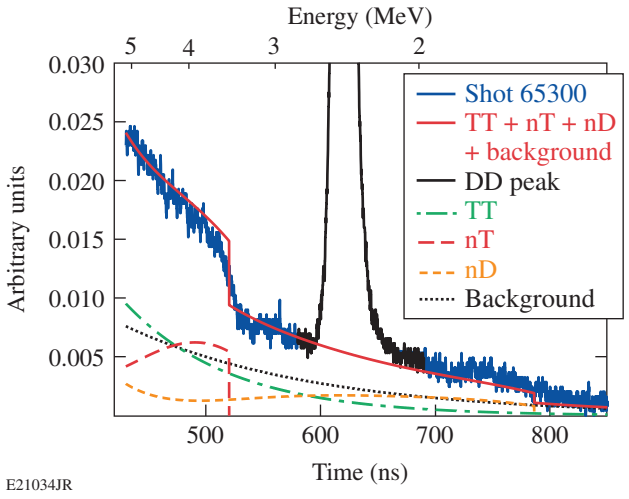

Figure 131.29
Recent nTOF neutron spectra from a DT cryogenic implosion (blue). The DD peak is excluded in this analysis (black). The TT spectrum (green) and the down-scattered component, a combination of the nT and nD spectra (red) are fitted to the experimental data. An additional background component is used that includes any remaining scintillator light decay and neutron scattering (dotted black line). The solid red line illustrates the best fit to this data.

The scattered neutron nTOF diagnostic measured the areal density on a number of recent cryogenic DT implosions on OMEGA. Table 131.V compares the MRS and nTOF data. The comparison between the MRS and nTOF measurements shows good agreement except for some discrepancies in shots 65578 and 65889. The disagreement in the areal density is most likely a result of the target offset and the misfire of a single laser beam causing significant ρR asymmetry. These asymmetries are possible because the MRS and nTOF probe different regions of the shell's areal density.

Table 131.V: Predicted ρR obtained from 1-D simulations compared with experimental results from MRS and nTOF. The values from the MRS and nTOF show good agreement. The large ρR difference between nTOF and MRS seen in shots 65578 and 65889 is most likely a result of a target position offset and a misfire on a single beam.

Shot number	1-D prediction (mg/cm^2)	MRS (mg/cm^2)	nTOF (mg/cm^2)
64668	215	163±33	160±32
64669	235	216±30	200±40
65300	210	162±20	160±32
65576	208	155±17	150±30
65578	215	153±15	100±20
65883	190	182±20	160±32
65884	220	126±25	120±24
65887	223	158±21	130±26
65889	216	197±15	140±28

Summary

High-resolution neutron time-of-flight spectroscopy has been developed at LLE to measure the areal density of OMEGA cryogenic DT implosions. The time-of-flight spectrum of the elastically scattered neutrons is fitted with theoretical spectral components from well-known nuclear processes to infer the areal density. Increased shielding and collimation have significantly reduced the background in nTOF detectors. Initial results indicate the neutron diagnostics (nTOF's) perform very well and have good agreement with the MRS.

A number of improvements are planned for the scattered neutron nTOF system: A new liquid scintillator nTOF detector housing has been designed with a larger scintillator volume and dual PMT's mounted closer to the scintillation fluid than the current design. An additional collimator installed inside the target chamber is under consideration to further reduce the neutron scattering from inside the target chamber. This will be modeled in MCNP to see how much improvement the additional collimation will provide in the signal to background. The increased scintillator volume and better collimation will potentially allow for higher forward- and backscattered neutron statistics with one detector in a single line of sight. For these measurements one of the two PMT's shown in Fig. 131.25 will be replaced with a less-sensitive PMT-140. This PMT-140 will be used to measure the forward-scattered neutrons close to the primary peak. The remaining PMT-240 will measure the lower-energy backscattered neutron spectrum. Additionally, a joint effort between LLNL and LLE is underway to qualify bibenzyl for use in an nTOF detector. Bibenzyl is a new organic scintillator material that shows significantly reduced light-afterglow decay components. Finally, implosion experiments are planned with pure tritium fill to improve the accuracy of the TT fusion neutron energy spectrum.

ACKNOWLEDGMENT

This work was supported by the U.S. Department of Energy Office of Inertial Confinement Fusion under cooperative agreement No. DE-FC52-08NA28302 the University of Rochester, and the New York State Energy Research and Development Authority. The support of DOE constitutes an endorsement by DOE of the views expressed in this article.

REFERENCES

1. V. Yu. Glebov, D. D. Meyerhofer, T. C. Sangster, C. Stoeckl, S. Roberts, C. A. Barrera, J. R. Celeste, C. J. Cerjan, L. S. Dauffy, D. C. Eder, R. L. Griffith, S. W. Haan, B. A. Hammel, S. P. Hatchett, N. Izumi, J. R. Kimbrough, J. A. Koch, O. L. Landen, R. A. Lerche, B. J. MacGowan, M. J. Moran, E. W. Ng, T. W. Phillips, P. M. Song, R. Tommasini, B. K. Young, S. E. Caldwell, G. P. Grim, S. C. Evans, J. M. Mack, T. Sedillo, M. D. Wilke, D. C. Wilson, C. S. Young, D. Casey, J. A. Frenje, C. K. Li, R. D. Petrasso, F. H. Séguin, J. L. Bourgade, L. Disdier, M. Houry, I. Lantuejoul, O. Landoas, G. A. Chandler, G. W. Cooper, R. J. Lepeer, R. E. Olson, C. L. Ruiz, M. A. Sweeney, S. P. Padalino, C. Horsfield, and B. A. Davis, Rev. Sci. Instrum. **77**, 10E715 (2006).

2. C. D. Zhou and R. Betti, Phys. Plasmas **15**, 102707 (2008).

3. T. C. Sangster, R. Betti, R. S. Craxton, J. A. Delettrez, D. H. Edgell, L. M. Elasky, V. Yu. Glebov, V. N. Goncharov, D. R. Harding, D. Jacobs-Perkins, R. Janezic, R. L. Keck, J. P. Knauer, S. J. Loucks, L. D. Lund, F. J. Marshall, R. L. McCrory, P. W. McKenty, D. D. Meyerhofer, P. B. Radha, S. P. Regan, W. Seka, W. T. Shmayda, S. Skupsky, V. A. Smalyuk, J. M. Soures, C. Stoeckl, B. Yaakobi, J. A. Frenje, C. K. Li, R. D. Petrasso, F. H. Séguin, J. D. Moody, J. A. Atherton, B. D. MacGowan, J. D. Kilkenny, T. P. Bernat, and D. S. Montgomery, Phys. Plasmas **14**, 058101 (2007).

4. S. Atzeni and J. Meyer-ter-Vehn, *The Physics of Inertial Fusion: Beam Plasma Interaction, Hydrodynamics, Hot Dense Matter*, International Series of Monographs on Physics (Clarendon Press, Oxford, 2004).

5. R. Betti, P. Y. Chang, B. K. Spears, K. S. Anderson, J. Edwards, M. Fatenejad, J. D. Lindl, R. L. McCrory, R. Nora, and D. Shvarts, Phys. Plasmas **17**, 058102 (2010).

6. S. W. Haan, J. D. Lindl, D. A. Callahan, D. S. Clark, J. D. Salmonson, B. A. Hammel, L. J. Atherton, R. C. Cook, M. J. Edwards, S. Glenzer, A. V. Hamza, S. P. Hatchett, M. C. Herrmann, D. E. Hinkel, D. D. Ho, H. Huang, O. S. Jones, J. Kline, G. Kyrala, O. L. Landen, B. J. MacGowan, M. M. Marinak, D. D. Meyerhofer, J. L. Milovich, K. A. Moreno, E. I. Moses, D. H. Munro, A. Nikroo, R. E. Olson, K. Peterson, S. M. Pollaine, J. E. Ralph, H. F. Robey, B. K. Spears, P. T. Springer, L. J. Suter, C. A. Thomas, R. P. Town, R. Vesey, S. V. Weber, H. L. Wilkens, and D. C Wilson, Phys. Plasmas **18**, 051001 (2011).

7. M. J. Edwards, J. D. Lindl, B. K. Spears, S. V. Weber, L. J. Atherton, D. L. Bleuel, D. K. Bradley, D. A. Callahan, C. J. Cerjan, D. Clark, G. W. Collins, J. E. Fair, R. J. Fortner, S. H. Glenzer, S. W. Haan, B. A. Hammel, A. V. Hamza, S. P. Hatchett, N. Izumi, B. Jacoby, O. S. Jones, J. A. Koch, B. J. Kozioziemski, O. L. Landen, R. Lerche, B. J. MacGowan, A. J. MacKinnon, E. R. Mapoles, M. M. Marinak, M. Moran, E. I. Moses, D. H. Munro, D. H. Schneider, S. M. Sepke, D. A. Shaughnessy, P. T. Springer, R. Tommasini, L. Bernstein, W. Stoeffl, R. Betti, T. R. Boehly, T. C. Sangster, V. Yu. Glebov, P. W. McKenty, S. P. Regan, D. H. Edgell, J. P. Knauer, C. Stoeckl, D. R. Harding, S. Batha, G. Grim, H. W. Herrmann, G. Kyrala, M. Wilke, D. C. Wilson, J. Frenje, R. Petrasso, K. Moreno, H. Huang, K. C. Chen, E. Giraldez, J. D. Kilkenny, M. Mauldin, N. Hein, M. Hoppe, A. Nikroo, and R. J. Leeper, Phys. Plasmas **18**, 051003 (2011).

8. S. Skupsky and S. Kacenjar, J. Appl. Phys. **52**, 2608 (1981).

9. C. K. Li, F. H. Séguin, D. G. Hicks, J. A. Frenje, K. M. Green, S. Kurebayashi, R. D. Petrasso, D. D. Meyerhofer, J. M. Soures, V. Yu. Glebov, R. L. Keck, P. B. Radha, S. Roberts, W. Seka, S. Skupsky, C. Stoeckl, and T. C. Sangster, Phys. Plasmas **8**, 4902 (2001).

10. J. A. Frenje, C. K. Li, F. H. Séguin, D. T. Casey, R. D. Petrasso, T. C. Sangster, R. Betti, V. Yu. Glebov, and D. D. Meyerhofer, Phys. Plasmas **16**, 042704 (2009).

11. J. A. Frenje, D. T. Casey, C. K. Li, J. R. Rygg, F. H. Séguin, R. D. Petrasso, V. Yu. Glebov, D. D. Meyerhofer, T. C. Sangster, S. Hatchett, S. Haan, C. Cerjan, O. Landen, M. Moran, P. Song, D. C. Wilson, and R. J. Leeper, Rev. Sci. Instrum. **79**, 10E502 (2008).

12. J. A. Frenje, D. T. Casey, C. K. Li, F. H. Séguin, R. D. Petrasso, V. Yu. Glebov, P. B. Radha, T. C. Sangster, D. D. Meyerhofer, S. P. Hatchett, S. W. Haan, C. J. Cerjan, O. L. Landen, K. A. Fletcher, and R. J. Leeper, Phys. Plasmas **17**, 056311 (2010).

13. C. Stoeckl, M. Cruz, V. Yu. Glebov, J. P. Knauer, R. Lauck, K. Marshall, C. Mileham, T. C. Sangster, and W. Theobald, Rev. Sci. Instrum. **81**, 10D302 (2010).

14. R. Lauck *et al*., IEEE Trans. Nucl. Sci. **56**, 989 (2009).

15. G. F. Knoll, *Radiation Detection and Measurement*, 3rd ed. (Wiley, New York, 2000).

16. J. Delettrez, R. Epstein, M. C. Richardson, P. A. Jaanimagi, and B. L. Henke, Phys. Rev. A **36**, 3926 (1987); P. B. Radha, J. A. Delettrez, R. Epstein, S. Skupsky, J. M. Soures, S. Cremer, and R. D. Petrasso, Bull. Am. Phys. Soc. **44**, 194 (1999).

17. G. R. Caughlan and W. A. Fowler, At. Data Nucl. Data Tables **40**, 283 (1988).

18. J. A. Frenje, C. K. Li, F. H. Séguin, D. T. Casey, R. D. Petrasso, D. P. McNabb, P. Navratil, S. Quaglioni, T. C. Sangster, V. Yu. Glebov, and D. D. Meyerhofer, Phys. Rev. Lett. **107**, 122502 (2011).

19. Photek Ltd., St. Leonards-on-Sea, East Sussex, TN38 9NS, United Kingdom.

20. Los Alamos Monte Carlo Group, "MCNP-A General Monte Carlo N-Particle Transport Code Version 5," Los Alamos National Laboratory Vols. I-III, April, 2003. Available from Radiation Safety Information Computational Center at Oak Ridge National Laboratory as CCC-740.

21. S. Agostinelli *et al*., Nucl. Instrum. Methods Phys. Res. A 506, 250 (2003).

22. T. C. Sangster, V. N. Goncharov, R. Betti, T. R. Boehly, D. T. Casey, T. J. B. Collins, R. S. Craxton, J. A. Delettrez, D. H. Edgell, R. Epstein, K. A. Fletcher, J. A. Frenje, V. Yu. Glebov, D. R. Harding, S. X. Hu, I. V. Igumenshchev, J. P. Knauer, S. J. Loucks, C. K. Li, J. A. Marozas, F. J. Marshall, R. L. McCrory, P. W. McKenty, D. D. Meyerhofer, P. M. Nilson, S. P. Padalino, R. D. Petrasso, P. B. Radha, S. P. Regan, F. H. Séguin, W. Seka, R. W. Short, D. Shvarts, S. Skupsky, V. A. Smalyuk, J. M. Soures, C. Stoeckl, W. Theobald, and B. Yaakobi, Phys. Plasmas **17**, 056312 (2010).

23. O. Landoas, V. Yu. Glebov, B. Rossé, M. Briat, L. Disdier, T. C. Sangster, T. Duffy, J. G. Marmouget, C. Varignon, X. Ledoux, T. Caillaud, I. Thfoin, and J.-L. Bourgade, Rev. Sci. Instrum. **82**, 073501 (2011).

Experimental Validation of the Two-Plasmon–Decay Common-Wave Process

Direct-drive inertial confinement fusion (ICF) requires multiple overlapping laser beams that can then drive two-plasmon–decay (TPD) instability. TPD creates large-amplitude electron plasma waves in the region near quarter-critical density.[1] These plasma waves can lead to anomalous absorption and hot-electron generation[2,3] that can preheat the fusion fuel and reduce the compression efficiency. Understanding the behavior of TPD is critical to mitigating it in ICF experiments.

TPD instability consists of the decay of an electromagnetic wave into two electron plasma waves.[4,5] Phase matching, energy conservation, and the dispersion relations of the waves limit the instability to a small region near quarter-critical density. Stability calculations of a single-plane electromagnetic wave show that the spatial growth rate of instability is proportional to the quantity IL_n/T_e, where I is the laser-beam intensity, L_n is the plasma density scale length, and T_e is the electron temperature of the plasma.[6,7] When the instability is driven to nonlinear saturation, a broad spectrum of large-amplitude plasma waves is generated.[8] The large electrostatic fields associated with these electron plasma waves can accelerate electrons to high energies (~100 keV) (Ref. 9).

When multiple overlapping laser beams with polarization smoothing were used,[10] the total energy in hot electrons was shown to scale with the overlapped intensity (I_Σ), defined as the sum of the intensity of each beam.[11] This scaling would not be expected if the beams drive the TPD independently, according to the growth rates of the single plane waves. A model is proposed where different laser beams share a common electron wave.[12] As the plasma wave is driven by multiple electromagnetic waves, the TPD growth rate can be larger than when driven by an individual beam. This was observed in nonlinear Zakharov simulations.[8]

This article describes the first experimental validation of the common-wave process [Fig. 131.30(a)], where the total energy in hot electrons was measured to be similar when one or two polarized beams were used at the same overlapped intensity and significantly reduced when four beams with the same overlapped intensity were used. Hot electrons generated by four beams are shown to be similar in total energy to the sum of the hot-electron energies generated by the six possible two-beam interactions [Fig. 131.30(b)]. A theoretical description of the common-wave process shows that multiple laser beams can share an electron-plasma wave in the region bisecting the electromagnetic wave vectors. For two beams, this region defines a plane [Fig. 131.30(a)]; for four beams, it defines a line

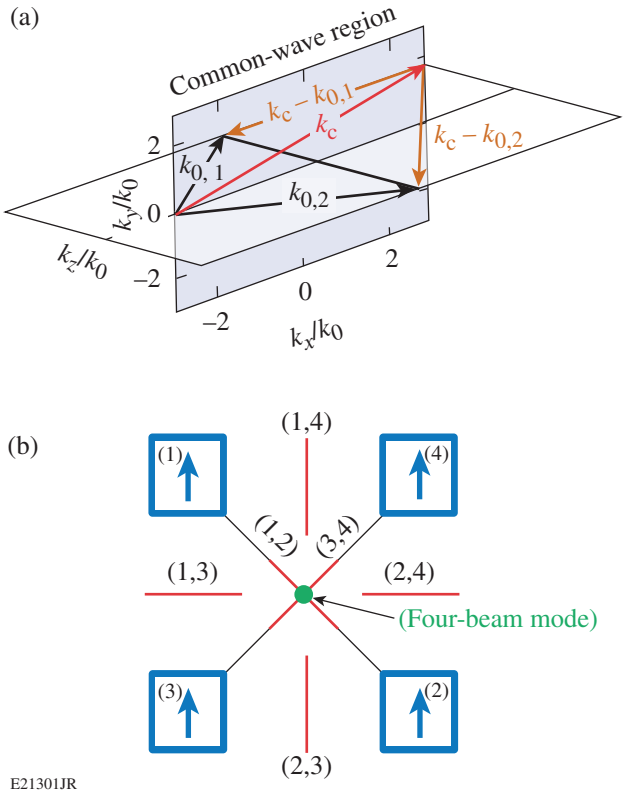

Figure 131.30
(a) Schematic of the common-wave region for two beams. Two laser beams of wave vectors $k_{0,1}$ and $k_{0,2}$ share the common plasma wave k_c located in the bisecting plane, fulfilling the necessary condition $|k_c - k_{0,1}| = |k_c - k_{0,2}|$ independent of the polarizations of the laser beams. (b) Schematic of the seven common-wave regions when four beams were used: six two-beam common-wave planes (red lines) and one four-beam common-wave line (green point).

[Fig. 131.30(b)]. In this region, the temporal growth rate and convective gain of the dominant mode are proportional to the overlapped intensity, a factor that depends on the geometry, the polarization, and the relative intensity of the laser beams.

The experiments were conducted on OMEGA EP,[13] where the four 351-nm beams were polarized vertically and intersected the target at an angle of 23° with respect to the target normal [Fig. 131.30(b)]. The beams were spatially overlapped to within 20 μm and used 2-ns flattop laser pulses that were co-timed to within 50 ps. Two sets of distributed phase plates[10] were used (890-μm diameter for Beams 1 and 2 and 840-μm diameter for Beams 3 and 4) to produce an ~1-mm-diam super-Gaussian intensity distribution profile. A maximum single-beam energy of 2 kJ (2.6 kJ) was used on Beams 1 and 2 (3 and 4), which provided a single-beam $I_{max} = 1.6 \times 10^{14}$ W/cm^2 ($I_{max} = 2.4 \times 10^{14}$ W/cm^2). The relative error in intensities of less than 5% was dominated by the shot-to-shot power measurements on each beam. This resulted in a maximum error of 10% in overlapped intensity.

The laser beams illuminated a 30-μm-thick CH layer deposited on 30 μm of Mo and backed with an additional 30 μm of CH. Hydrodynamic simulations using the two-dimensional (2-D) code *DRACO*[14] indicate that the laser light interacted with the first layer, producing a CH plasma with density and temperature profiles that depend only on the overlapped laser intensity. For the experimental conditions presented here, the hydrodynamic profiles near quarter-critical density reached a steady state after about 1.5 ns. After this time, the calculated quantity $I_{\Sigma,q}L_n/T_e$ varied by less than 10%, where $I_{\Sigma,q}$ is the overlapped intensity at the quarter-critical density. When the overlapped laser intensity was increased from 1.5×10^{14} W/cm^2 to 7×10^{14} W/cm^2, L_n increased from 260 μm to 360 μm, T_e increased from 1.5 keV to 2.5 keV, and, due to absorption, the laser intensity at quarter-critical density was about equal to half of the vacuum intensity; the ratio L_n/T_e was nearly constant (≈160 μm/keV).

Two principal diagnostics were used to determine the amount of laser energy converted to hot electrons: the x-ray spectrometer (XRS)[15–17] and the hard x-ray detector (HXRD).[18] The XRS measured the energy emitted into the Mo K_α emission line $\left(E_{K_\alpha}\right)$ using an absolutely calibrated planar LiF crystal spectrometer that viewed the target from the laser incident side at an angle of 63° from the target normal.[17] Monte Carlo (MC) simulations using the code EGSnrc[19] show that electrons with energies less than 120 keV are stopped in the Mo. The 17.5-keV Mo K_α line was sufficiently energetic so that photoexcitation from the 2.5-keV coronal plasma region did not contribute to the K_α-emission measurement. The relative error in E_{K_α} was less than 5% (Ref. 17).

The HXRD consists of a three-channel scintillator that measures the x-ray radiation generated by hot electrons in the Mo above ~40 keV, ~60 keV, and ~80 keV (Ref. 18). It allows one to estimate the hot-electron temperature using the exponentially decreasing x-ray energy in each channel. The relative error in the measurement of the hot-electron temperature was 20%. MC simulations were used to determine the total hot-electron energy (E_e) given the measured hot-electron temperature (T_{hot}) and the total energy in the K_α emission.[17] The relative error of 25% is dominated by measurement errors. Figure 131.31(a) shows that the dependence of the hot-electron temperature with the total energy in K_α was comparable when one, two, or four beams were used.

Figure 131.31(b) shows that the total laser energy (E_l) converted into hot electrons $\left(f_{hot} = E_e/E_l\right)$ as a function of the overlapped intensity was similar when one or two beams were used in the horizontal, vertical, or diagonal configuration and increased exponentially as a function of the overlapped intensity. These results show that TPD growth was caused by the interplay between the two beams through a common-wave process. If the hot electrons were generated by two independent single-beam processes, each with an intensity of $I_\Sigma/2$, the total hot-electron energy would be the sum of the hot-electron energy generated by each beam. This would be significantly smaller than the hot-electron energy generated by a single beam with I/I_Σ (due to the measured exponential increase of the hot-electron energy with the laser intensity). The fact that the two beams produced a total hot-electron fraction similar to that of a single beam shows that the common-wave process is very efficient.

When comparing the four-beam and single-beam results, Fig. 131.31(b) shows a significant decrease in the hot-electron energy for a given overlapped intensity (up to two orders of magnitude for $I_\Sigma \sim 2 \times 10^{14}$ W/cm^2). This reduction in the four-beam experiments can be explained heuristically on the basis of the two-beam experimental results. The addition of hot-electron fractions measured for six possible two-beam configurations (two horizontal configurations, two vertical configurations, and two diagonal configurations), plotted at twice the overlapped intensity, was consistent with the fraction of hot electrons measured when four beams were employed [see open symbols in Fig. 131.31(b)]. This suggests that the hot electrons generated by four beams were the result of the sum of hot electrons generated by six independent two-beam

interactions; i.e., the hot electrons generated by the interaction between all four beams were not dominant.

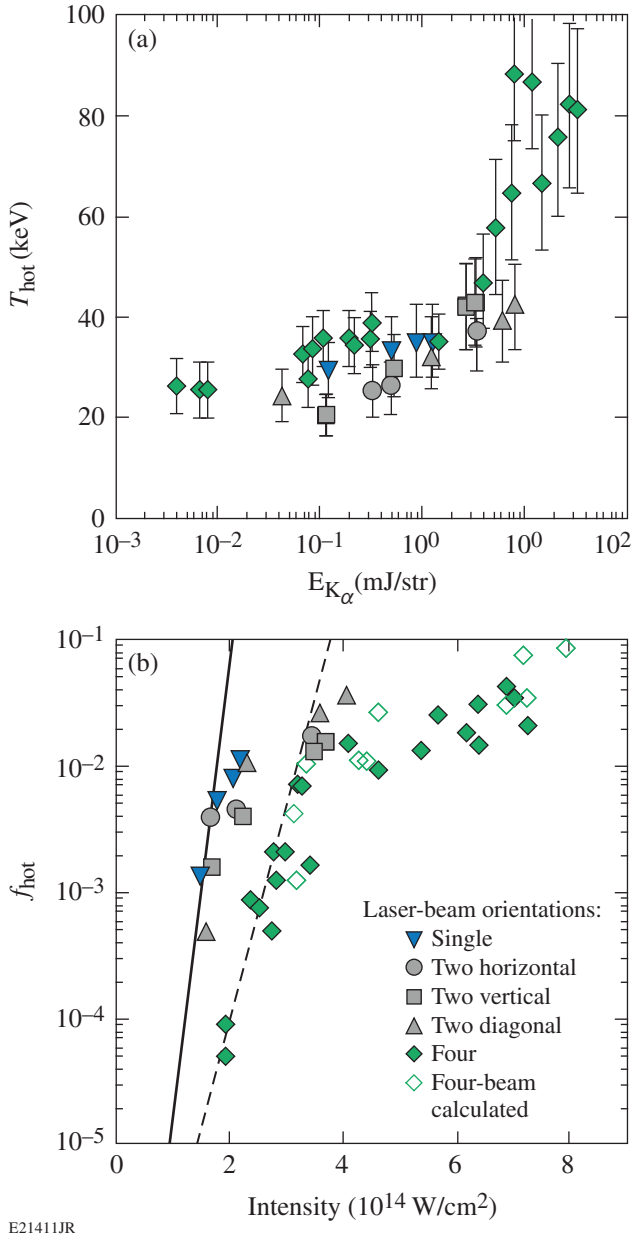

Figure 131.31
(a) The measured hot-electron temperature is plotted as a function of the measured total energy in K_α for the five laser-beam orientations tested. (b) The fraction of laser energy converted to hot electrons (f_{hot}) is plotted as a function of the overlapped intensity. The four-beam hot-electron generation was estimated (open diamonds) by multiplying the measured two-beam total hot-electron energy fraction by 6 and plotting the results at twice the two-beam intensity. The dashed line is a fit to the four-beam data $\left[f_{hot} = 3\times10^{-8}\, e^{\left(8I_\Sigma/2\right)}\right]$. The solid line is scaled from the fit, assuming the four-beam results are dominated by the six two-beam common-wave modes driven at half of the intensity $\left[f_{hot} = 1\times10^{-8}\, e^{\left(8I_\Sigma\right)}\right]$.

The well-known theory of TPD[4,5] is based on the dispersion relation for the two electron plasma waves with frequency and wave vectors $(\omega, \mathbf{k})$ and $(\omega-\omega_0, \mathbf{k}-\mathbf{k}_0)$, where ω_0 and $\mathbf{k}_0$ are the frequency and wave vector of the initial electromagnetic wave, respectively.[4,5] In the case of multiple laser beams driving a common electron plasma wave $(\omega_c, \mathbf{k}_c)$, the dispersion relation is $\omega_c^2 = \omega_{pe}^2 + 3\mathbf{k}_c^2 v_{th,e}^2$ and for the corresponding daughter waves $(\omega_c-\omega_0)^2 = \omega_{pe}^2 + 3(\mathbf{k}_c-\mathbf{k}_{0,i})^2 v_{th,e}^2$, where $v_{th,e}$ is the electron thermal velocity, ω_{pe} is the plasma frequency, and $\mathbf{k}_{0,i}$ (with a norm k_0 independent of i) is the wave vector of beam i. A mathematical definition for the region where a resonant common-wave process exists is determined by satisfying the dispersion relations for all laser beams, cos $(\mathbf{k}_c, \mathbf{k}_{0,i})$ = const, for $i = 1...n$. For a two-beam configuration, this defines a plane in k-space bisecting the wave vectors of the two laser beams [Fig. 131.30(a)]. For more than two laser beams, this condition either restricts the resonant common waves to a line or eliminates them, depending on the laser beam's symmetry. The four-beam growth rate in this experiment is restricted to a line [Fig. 131.30(b)].

The dispersion relation for the common-wave process is derived following the TPD linear theory[4,5] for conditions where the collision frequency is much smaller than the growth rate, satisfied for our experimental parameters:

$$D\left(\omega_c,\gamma,\left|\,\mathbf{k}_c\,\right|\right) = -\sum_i \frac{\gamma_{0,i}^2}{D\left(\omega_c-\omega_0,\gamma,\left|\,\mathbf{k}_c-\mathbf{k}_{0,i}\,\right|\right)},$$

where γ is the temporal growth rate,

$$D\left(\omega,\gamma,\left|\,\mathbf{k}\,\right|\right) = \left\{\left[1-\frac{\omega_{pe}^2}{\omega^2}\left(1+3k^2\lambda_{De}^2\right)\right]\frac{\omega}{2}+i\gamma\right\}$$

is the dispersion relation, and $\lambda_{De} = v_{th,e}/\omega_{pe}$ is the Debye length. The single-beam homogeneous growth rate calculated in the common-wave region $\gamma_{0,i}^2 = \left(\gamma_0^2\right)_{max}^{SB}\cos^2(\alpha_i) f_c \beta_i$, where α_i is the angle between the polarization vector and the common-wave vector,

$$f_c = \left[k_c^2 - \left(\mathbf{k}_c-\mathbf{k}_{0,i}\right)^2 / k_{0,i}\left|\,\mathbf{k}_c-\mathbf{k}_{0,i}\,\right|\right]^2,$$

$\beta_i = I_i/I_\Sigma$, I_i is the intensity of the laser beam i,

$$\left(\gamma_0^2\right)_{max}^{SB} = 2/cn_c m_e\left(k_0/2\right)^2 I_\Sigma$$

is the maximum single-beam homogeneous growth rate squared calculated for the overlapped intensity, c is the light velocity, m_e is the electron mass, $n_c = m_e\omega_0^2/4\pi e^2$ is the critical density, and e is the electron charge. To evaluate the maximum value of the growth rate, the minimum value of $D\left(\omega,\gamma,\left|\mathbf{k}_c-\mathbf{k}_{0,i}\right|\right)$ is determined by ensuring that the dispersion relations for all daughter waves are satisfied. It follows that $D\left(\omega,\gamma,\left|\mathbf{k}_c-\mathbf{k}_{0,i}\right|\right)=i\gamma=\text{const}$ and the resonant common-wave growth rate is given by $\left(\gamma_0^2\right)^{\text{MB}}=\sum_i\gamma_{0,i}^2$. A geometric function is given by normalizing the multiple-beam growth rate squared to the maximum single-beam growth rate squared:

$$\left(\Gamma_0^2\right)^{\text{MB}}=\frac{\left(\gamma_0^2\right)^{\text{MB}}}{\left(\gamma_0^2\right)^{\text{SB}}_{\text{max}}}=f_c\sum\nolimits_i\cos^2\left(\alpha_i\right)\beta_i.$$

The dominant mode is determined by the maximum of the geometric function, which is a geometric factor $f_g=\left(\Gamma_0^2\right)^{\text{SB}}_{\text{max}}$ that depends only on the geometry of the laser beams, their polarizations, and their intensities relative to the overlapped intensity.

Figures 131.32(a) and 131.32(b) show the calculated geometric functions for two beams, $\left(\Gamma_0^2\right)^{2\text{B}}$, polarized perpendicular and parallel to the plane defined by the laser beams ($\mathbf{k}_{0,1}$, $\mathbf{k}_{0,2}$). The geometric functions calculated in k-space are significantly different as a result of the difference in the polarization vectors relative to the common-wave plane, although the geometric factor is similar for the two cases, $\left(\Gamma_0^2\right)^{2\text{B}}_{\text{max}}\sim 1$. The fact that the growth rates are the same explains why the total hot-electron energy is measured to be similar in the horizontal and vertical laser-beam configurations. For the configuration with two horizontal beams [Fig. 131.32(a)], the geometric function in the common-wave planes forms two modified hyperbolas defined by

$$\left(k_y/k_0\right)^2=\left(k_x/k_0\right)\left[\left(k_x/k_0\right)/\cos\left(\theta/2\right)^2-1\right],$$

where θ is the angle between the two laser beams. The maximum value is located in the backward direction ($-\mathbf{k}_x$) for small wave vectors. For the configuration with two vertical beams [Fig. 131.32(b)], the maximum value of the geometric function is located at the intersection $\left(k_y/k_0=0\right)$ of the two hyperbolas of maximum single-beam growth rates (that are in the polarization plane of each beam). The geometric function decreases rapidly with k_y/k_0, corresponding to the rapid decrease in the single-beam growth rates.

Figure 131.32(c) shows the four-beam geometric function $\left(\Gamma_0^2\right)^{4\text{B}}$ plotted along the four-beam common-wave region located along the line bisecting the laser beams [Fig. 131.30(b)]. The maximum value is reached for $k_x/k_0\sim 1.3$

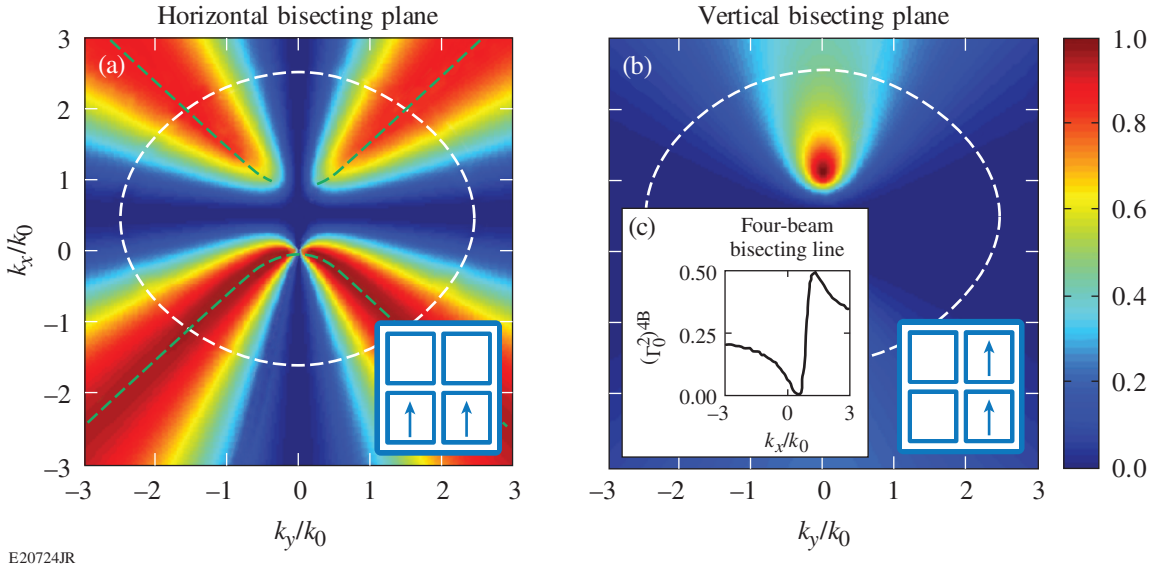

Figure 131.32
Calculation of $\left(\Gamma_0^2\right)^{2\text{B}}$ in the common-wave plane for (a) two beams polarized perpendicular and (b) parallel to the plane ($\mathbf{k}_{0,1}$, $\mathbf{k}_{0,2}$). The dashed white lines correspond to the Landau cutoff $\left[k_{\text{max}}\lambda_{\text{De}}=0.25,\ \text{where}\ k_{\text{max}}=\max\left(k_c,\left|\mathbf{k}_c-\mathbf{k}_{0,i}\right|\right)\right]$ calculated for T_e = 1.6 keV, which defines the maximum wave vector for TPD.[21] The dashed green lines correspond to the two modified hyperbolas of maximum $\left(\Gamma_0^2\right)^{2\text{B}}$. (c) Calculation of $\left(\Gamma_0^2\right)^{4\text{B}}$ along the four-beam common-wave line. $\mathbf{k}_x$ is along the projection of $\mathbf{k}_{0,i}$ in the common-wave region, $\mathbf{k}_y$ is perpendicular to $\mathbf{k}_x$, and k_0 is calculated at quarter-critical density.

and $k_y/k_0 \sim 0.3$, where $\left(\Gamma_0^2\right)_{\max}^{4B} = 0.5$. For the same overlapped intensity, the single-beam and two-beam homogeneous growth rates for the dominant mode are similar: $\left(\Gamma_0^2\right)_{\max}^{2B} = 1$, whereas the four-beam homogeneous growth rate for the dominant mode is decreased by a factor of 2: $\left(\Gamma_0^2\right)_{\max}^{4B} = 0.5$. These calculations support the experimental findings [Fig. 131.31(b)], where the single and two-beam hot-electron fractions are comparable, while the four-beam hot-electron fraction is smaller.

To estimate the common-wave convective gain (in intensity), the maximum common-wave homogeneous growth rate was used in the formalism derived in Refs. 6 and 20,

$$G = \left(16\pi/9\right)\left(v_{\text{th,e}}^2/c^2\right)^{-1} k_0 L\left[\left(\gamma_0^2\right)_{\max}^{\text{MB}}/\omega_0\right]^2.$$

The maximum common-wave gain for each configuration is

$$G_c = 6\times 10^{-2}\,\frac{I_{\Sigma,q} L_n \lambda_0}{T_e}\, f_g,$$

where T_e is in keV, $I_{\Sigma,q}$ is in 10^{14} W/cm^2, and L_n and λ_0 are in microns. For a given laser-beam configuration (relative beam angle and polarization), the common-wave gain is proportional to $I_{\Sigma,q} L_n / T_e$.

Figure 131.33 shows the hot-electron fraction as a function of the calculated common-wave gain for the dominant mode [Eq. (2)]. When there are multiple common-wave regions, the dominant mode corresponds to the maximum common-wave gain. For all laser-beam configurations, except for two diagonal beams, the hot-electron fraction as a function of the gain is similar. For diagonal beams, the calculations underestimate the value of the gain.

In summary, when maintaining an overlapped-laser-beam intensity, the total energy in hot electrons is measured to be similar when using one or two polarized beams and significantly reduced with four polarized beams. In four-beam experiments, the hot-electron energy was shown to be the result of hot electrons generated by the six possible two-beam interactions; i.e., the hot electrons generated by the interaction between all four beams does not dominate. A linear common-wave model is consistent with these observations, where the homogeneous growth rate for the dominant mode was calculated for beams that share a common plasma wave. The model shows that for two beams, the resonant common electron plasma wave was restricted to the plane bisecting the beams. For more than two beams, the resonant common wave was restricted to a line or could not occur. In this region, the homogeneous growth rate and the convective gain are shown to be proportional to the overlapped intensity and a geometric factor that depends on the geometry, the polarization, and the relative intensity of the laser beams. This is consistent with previous experimental results where hot-electron generation was shown to scale with overlapped intensity.[11] For ignition designs, these results suggest that the common-wave process can be reduced by limiting the number of beams that are symmetric to one another or by reducing the geometric factor.

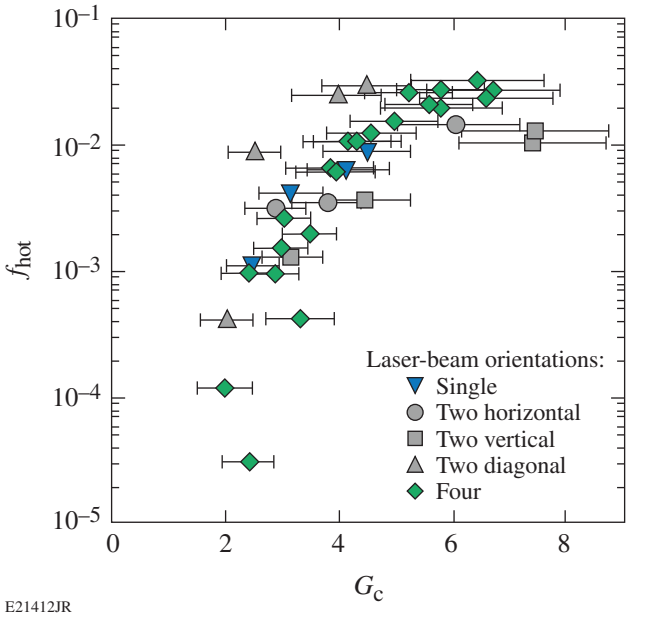

Figure 131.33
The total hot-electron energy divided by the laser energy plotted as a function of the common-wave gain (G_c) for the dominant mode.

ACKNOWLEDGMENT

This work was supported by the U.S. Department of Energy Office of Inertial Confinement Fusion under Cooperative Agreement No. DE-FC52-08NA28302, the University of Rochester, and the New York State Energy Research and Development Authority. The support of DOE does not constitute an endorsement by DOE of the views expressed in this article.

REFERENCES

1. H. A. Baldis and C. J. Walsh, Phys. Rev. Lett. **47**, 1658 (1981).
2. N. A. Ebrahim *et al*., Phys. Rev. Lett. **45**, 1179 (1980).
3. R. L. Keck, L. M. Goldman, M. C. Richardson, W. Seka, and K. Tanaka, Phys. Fluids **27**, 2762 (1984).
4. M. V. Goldman, Ann. Phys. **38**, 117 (1966).

5. C. S. Liu and M. N. Rosenbluth, Phys. Fluids **19**, 967 (1976).

6. M. N. Rosenbluth, Phys. Rev. Lett. **29**, 565 (1972).

7. A. Simon, R. W. Short, E. A. Williams, and T. Dewandre, Phys. Fluids **26**, 3107 (1983).

8. J. F. Myatt, J. Zhang, J. A. Delettrez, A. V. Maximov, R. W. Short, W. Seka, D. H. Edgell, D. F. DuBois, D. A. Russell, and H. X. Vu, Phys. Plasmas **19**, 022707 (2012).

9. D. H. Froula, B. Yaakobi, S. X. Hu, P.-Y. Chang, R. S. Craxton, D. H. Edgell, R. Follett, D. T. Michel, J. F. Myatt, W. Seka, R. W. Short, A. Solodov, and C. Stoeckl, Phys. Rev. Lett. **108**, 165003 (2012).

10. T. J. Kessler, Y. Lin, J. J. Armstrong, and B. Velazquez, in *Laser Coherence Control: Technology and Applications*, edited by H. T. Powell and T. J. Kessler (SPIE, Bellingham, WA, 1993), Vol. 1870, pp. 95–104.

11. C. Stoeckl, R. E. Bahr, B. Yaakobi, W. Seka, S. P. Regan, R. S. Craxton, J. A. Delettrez, R. W. Short, J. Myatt, A. V. Maximov, and H. Baldis, Phys. Rev. Lett. **90**, 235002 (2003).

12. R. W. Short and J. F. Myatt, Bull. Am. Phys. Soc. **56**, 329 (2011).

13. J. H. Kelly, L. J. Waxer, V. Bagnoud, I. A. Begishev, J. Bromage, B. E. Kruschwitz, T. J. Kessler, S. J. Loucks, D. N. Maywar, R. L. McCrory, D. D. Meyerhofer, S. F. B. Morse, J. B. Oliver, A. L. Rigatti, A. W. Schmid, C. Stoeckl, S. Dalton, L. Folnsbee, M. J. Guardalben, R. Jungquist, J. Puth, M. J. Shoup III, D. Weiner, and J. D. Zuegel, J. Phys. IV France **133**, 75 (2006).

14. P. B. Radha, T. J. B. Collins, J. A. Delettrez, Y. Elbaz, R. Epstein, V. Yu. Glebov, V. N. Goncharov, R. L. Keck, J. P. Knauer, J. A. Marozas, F. J. Marshall, R. L. McCrory, P. W. McKenty, D. D. Meyerhofer, S. P. Regan, T. C. Sangster, W. Seka, D. Shvarts, S. Skupsky, Y. Srebro, and C. Stoeckl, Phys. Plasmas **12**, 056307 (2005).

15. B. Yaakobi, C. Stoeckl, T. Boehly, D. D. Meyerhofer, and W. Seka, Phys. Plasmas **7**, 3714 (2000).

16. B. Yaakobi, T. R. Boehly, T. C. Sangster, D. D. Meyerhofer, B. A. Remington, P. G. Allen, S. M. Pollaine, H. E. Lorenzana, K. T. Lorenz, and J. A. Hawreliak, Phys. Plasmas **15**, 062703 (2008).

17. B. Yaakobi, P.-Y. Chang, A. A. Solodov, C. Stoeckl, D. H. Edgell, R. S. Craxton, S. X. Hu, J. F. Myatt, F. J. Marshall, W. Seka, and D. H. Froula, Phys. Plasmas **19**, 012704 (2012).

18. C. Stoeckl, V. Yu. Glebov, D. D. Meyerhofer, W. Seka, B. Yaakobi, R. P. J. Town, and J. D. Zuegel, Rev. Sci. Instrum. **72**, 1197 (2001).

19. I. Kawrakow *et al*., NRC, Ottawa, Canada, NRCC Report PIRS-701 (May 2011).

20. R. Yan, A. V. Maximov, and C. Ren, Phys. Plasmas **17**, 052701 (2010).

21. W. Seka, D. H. Edgell, J. F. Myatt, A. V. Maximov, R. W. Short, V. N. Goncharov, and H. A. Baldis, Phys. Plasmas **16**, 052701 (2009).

A Reflective Optical Transport System for Ultraviolet Thomson Scattering on OMEGA

Introduction

Thomson scattering has become a routine diagnostic in high-energy-density laser–plasma experiments[1–4] for characterizing the electron and ion temperatures by scattering 2ω ($\lambda_{2\omega}$ = 0.527 μm) or 4ω ($\lambda_{4\omega}$ = 0.263 μm) light from ion-acoustic waves.[3,5] Recently the electron density was measured[6] on OMEGA[7] by scattering 2ω light from electron plasma waves, but scattering with a 2ω probe limits these measurements to relatively low densities ($n_e \approx 5 \times 10^{20}$ cm^{-3}).

A reflective optical transport system recently implemented on the OMEGA Thomson-scattering system enables one to diagnose light from 190 nm to 850 nm. Improved spectral sensitivity at lower wavelengths allows for the observation of electron plasma wave scattering using a 4ω probe beam. The spectral range is limited by air attenuation in the UV and photocathode sensitivity in the IR. This extends the peak density from which electron plasma waves can be measured by an order of magnitude ($n_e \approx 2.0 \times 10^{21}$ cm^{-3}) (Fig. 131.34). A high-quality imaging system provides localized measurement of the plasma conditions and reduces the unwanted emission (typically bremsstrahlung and scattering from laser beams other than the probe beam). A localized measurement is obtained by overlapping the image of light scattered from the probe beam (~60-μm diameter) with a 100-μm-diam pinhole located at the entrance of the spectrometer (Fig. 131.35). When accounting for the magnification of the optical transport system (m = 1.4), light is collected from a 60-μm × 70-μm × 70-μm volume (Thomson-scattering volume).

The system consists of a reflective telescope mounted in a ten-inch manipulator (TIM) that collects scattered light and directs it along the TIM-6 line of sight to an instrument cart located approximately 8 m away from the target. A set of Pfund telescopes focus the scattered light into three independently configurable target diagnostics. To measure the ion-acoustic features, a 1-m Czerny–Turner spectrometer (3600 ll/mm grating) is coupled to a Rochester Optical Streak System (ROSS), resulting in a measured spectral resolution of 0.02 nm over a 4-nm spectral range and a pulse-front–limited time resolution of ~200 ps (Ref. 8). A 0.3-m spectrometer (600 ll/mm grating) coupled to a second ROSS is used to measure the electron plasma features. This system has a measured resolution of 0.5 nm over a 90-nm spectral range and a pulse-front–limited

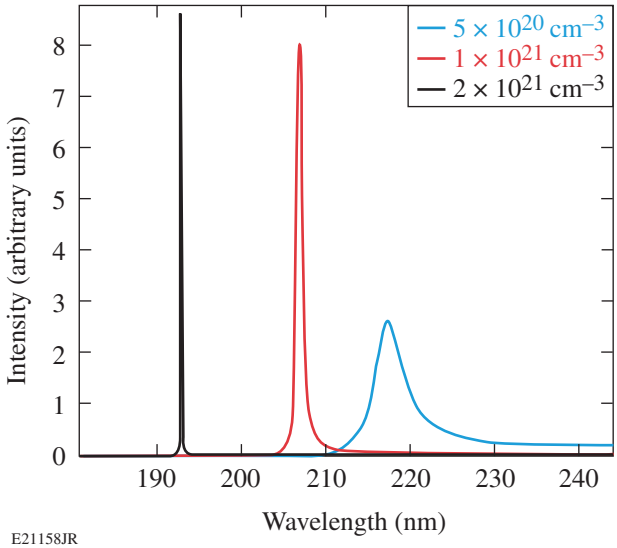

Figure 131.34
A series of calculated Thomson-scattering spectra obtained by assuming a 0.263-μm probe beam is scattered from three densities: 5×10^{20} cm^{-3}, 1×10^{21} cm^{-3}, and 2×10^{21} cm^{-3}. The scattering angle is 60° with an electron temperature of 1.8 keV.

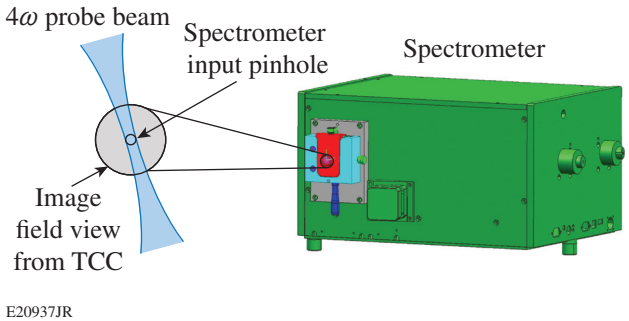

Figure 131.35
The spectrometer entrance slit is replaced with a pinhole assembly. TCC: target chamber center.

time resolution of ~50 ps. An intensified gated charge-coupled–device (CCD) camera captures two-dimensional (2-D) images with a 1.5-mm field of view and a 10-μm spatial resolution in the plasma plane. The minimum gate duration for the camera is 3 ns.

Optical Transport

1. Collection System

The TIM-mounted telescope is based on a Schwarzschild objective that uses two concentric spherical mirrors to provide diffraction-limited imaging across all reflected wavelengths.[9] The telescope was built using an *f*/10 off-axis segment of a traditional *f*/1.25 Schwarzschild objective [Fig. 131.36(a)]. The unobstructed configuration allows one to collect light at a higher *f* number while maintaining the geometry inherent to a Schwarzschild that eliminates third-order aberrations. This allows one to mount the primary and secondary mirrors without a diffraction-inducing support structure common to many reflective objectives. The telescope produces a 19-mm-diam collimated beam.

2. Collimated Transport System

Flat aluminum mirrors are used to direct collected light over an approximately 8-m distance from the OMEGA target chamber to the instrumentation cart. Beamlines for the three separate instruments are produced using uncoated wedge pickoffs or semi-aluminumized beam splitters. Each optical path has provisions to include filtering in the collimated beam to control signal level and spectral throughput.

3. Focusing System

Images are formed for each diagnostic using reflective Pfund telescopes [Fig. 131.36(b)]. Collimated light strikes a flat primary mirror with a central through-hole and is directed toward a concave, spherical secondary mirror. Light reflected off the secondary mirror is focused back through the hole of the primary mirror, allowing one to align the system on its optical axis. The primary mirror through-hole is counter sunk at a 45° angle to prevent clipping of the focusing beam on the rear surface of the mirror.

The minimum through-hole diameter is determined by the required field angle needed to image the entire Thomson-scattered volume at the desired working *f* number. The 1-m and 0.3-m systems use a 5-mm through-hole that provides a 350-μm field of view at target chamber center (TCC) with a magnification of 1.4×. Full coupling of the probe beam's waist can be accomplished with a spectrometer input image of 100 μm. Approximately 7% of the overall signal is lost through the hole in the primary mirror.

Optical Performance

Historically, efforts to observe the electron plasma wave features on OMEGA with a 4ω probe beam have been limited by the performance of the existing optical transport.[10] Previously, scattered light was collected using a fused-silica and calcium-fluoride doublet and focused with a Pfund telescope. The rapidly changing index of refraction of the doublet glasses across the deep UV spectrum introduced an 8-mm focal plane shift between focus at 265 nm and 200 nm [Fig. 131.37(a)]. As a result, the detection efficiency of the system drops significantly at wavelengths below 240 nm [Fig. 131.37(b)]. This is a result of a reduction in the signal intensity as the defocused spot size increases and the reappearance of the central through-hole in the Pfund telescope as a far-field image is presented to the spectrometer.

The reflective system has a 100-μm focal shift from 265 nm to 200 nm. The slight chromatic shift is caused by a 3-mm-thick fused-silica blast window located in front of the Schwarzschild

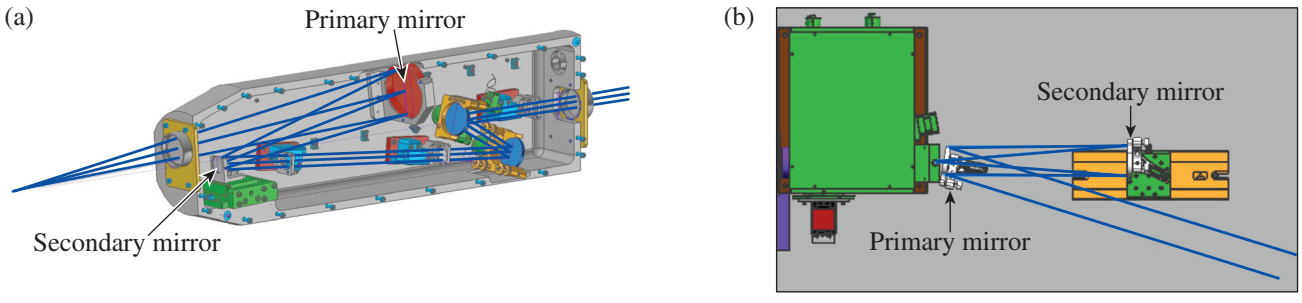

Figure 131.36
(a) An *f*/10 off-axis section of a Schwarzschild objective is used to collect scattered light. (b) A Pfund telescope focuses the scattered light to the diagnostic.

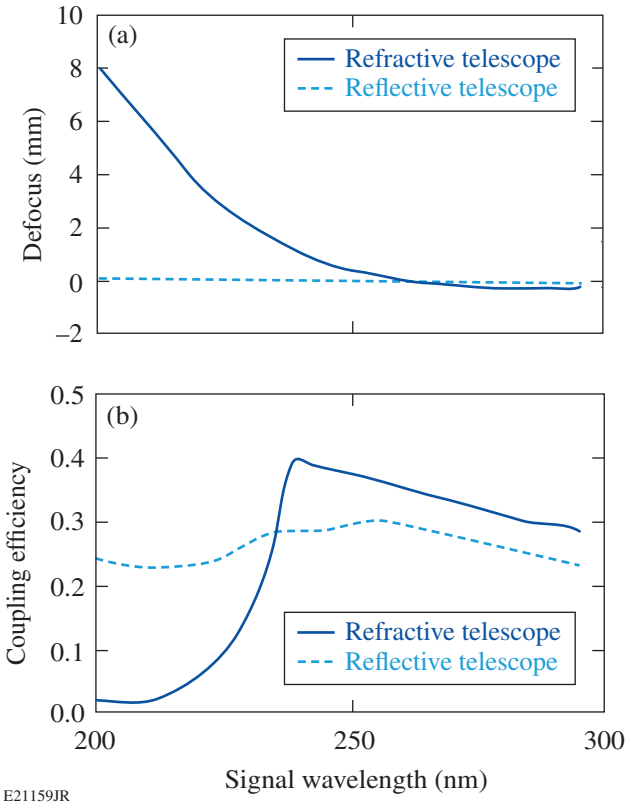

Figure 131.37
(a) Focal shift of the image plane at the spectrometer input for the refractive Thomson-scattering system. (b) Calculated transmission of an on-axis point source through the 100-μm spectrometer pinhole for the refractive system (solid curve) and the reflective system (dashed curve).

objective used to protect the primary mirror from target debris. The maximum transmission of the reflective system is slightly reduced compared to the refractive system because of the addition of four aluminum mirror elements required to collect and steer scattered light from TCC to the instrument cart. Air attenuation of deep UV signals limits the reflective systems transmission to 190 nm.

Summary

A reflective optical transport system has been designed for the Thomson-scattering system on OMEGA to provide suitable performance from 190 nm to 850 nm. This will enable the operator to perform Thomson-scattering measurements of UV light scattered from electron plasma waves.

ACKNOWLEDGMENT

This work was supported by the U.S. Department of Energy Office of Inertial Confinement Fusion under Cooperative Agreement No. DEFC52-08NA28302, the University of Rochester, and the New York State Energy Research and Development Authority. The support of DOE does not constitute an endorsement by DOE of the views expressed in this article.

REFERENCES

1. D. H. Froula, S. H. Glenzer, N. C. Luhmann, and J. Sheffield, *Plasma Scattering of Electromagnetic Radiation: Theory and Measurement Techniques*, 2nd ed. (Academic Press, Burlington, MA, 2011).
2. S. H. Glenzer *et al*., Phys. Rev. Lett. **79**, 1277 (1997).
3. A. J. Mackinnon, S. Shiromizu, G. Antonini, J. Auerbach, K. Haney, D. H. Froula, J. Moody, G. Gregori, C. Constantin, C. Sorce, L. Divol, R. L. Griffith, S. Glenzer, J. Satariano, P. K. Whitman, S. N. Locke, E. L. Miller, R. Huff, K. Thorp, W. Armstrong, W. Bahr, W. Seka, G. Pien, J. Mathers, S. Morse, S. Loucks, and S. Stagnitto, Rev. Sci. Instrum. **75**, 3906 (2004).
4. D. H. Froula, J. S. Ross, L. Divol, N. Meezan, A. J. MacKinnon, R. Wallace, and S. H. Glenzer, Phys. Plasmas **13**, 052704 (2006).
5. D. H. Froula, J. S. Ross, L. Divol, and S. H. Glenzer, Rev. Sci. Instrum. **77**, 10E522 (2006).
6. J. L. Ross, S. H. Glenzer, P. Amendt, R. Berger, L. Divol, N. L. Kugland, O. L. Landen, C. Plechaty, B. Remington, D. Ryutov, W. Rozmus, D. H. Froula, G. Fiksel, C. Sorce, Y. Kuramitsu, T. Morita, Y. Sakawa, H. Takabe, R. P. Drake, M. Grosskopf, C. Kuranz, G. Gregori, J. Meinecke, C. D. Murphy, M. Koenig, A. Pelka, A. Ravasio, T. Vinci, E. Liang, R. Presura, A. Spitkovsky, F. Miniati, and H.-S. Park, Phys. Plasmas **19**, 056501 (2012).
7. J. H. Kelly, L. J. Waxer, V. Bagnoud, I. A. Begishev, J. Bromage, B. E. Kruschwitz, T. J. Kessler, S. J. Loucks, D. N. Maywar, R. L. McCrory, D. D. Meyerhofer, S. F. B. Morse, J. B. Oliver, A. L. Rigatti, A. W. Schmid, C. Stoeckl, S. Dalton, L. Folnsbee, M. J. Guardalben, R. Jungquist, J. Puth, M. J. Shoup III, D. Weiner, and J. D. Zuegel, J. Phys. IV France **133**, 75 (2006).
8. A. Visco, R. P. Drake, D. H. Froula, S. H. Glenzer, and B. B. Pollock, Rev. Sci. Instrum. **79**, 10F545 (2008).
9. M. J. Riedl, *Optical Design Fundamentals for Infrared Systems*, 2nd ed., Tutorial Texts in Optical Engineering, Vol. TT48 (SPIE Press, Bellingham, WA, 2001).
10. J. S. Ross, L. Divol, C. Sorce, D. H. Froula, and S. H. Glenzer, J. Inst. **6**, P08004 (2011).

Laser–Plasma Interactions in Direct-Drive–Ignition Plasmas

Introduction

Two approaches to inertial confinement fusion (ICF)[1] employ megajoule-class laser beams[2,3] to compress a fusion capsule to thermal nuclear burn. For the indirect-drive approach,[4] the laser beams are tightly focused through the laser entrance hole into a radiation cavity (hohlraum) resulting in relatively high single-beam laser intensities ($I_s \sim 10^{15}$ W/cm^2). The beams then propagate through a series of plasmas before converting their energy into soft x-ray radiation at the high-Z hohlraum wall.[5–8] The soft x-ray radiation emitted by the hohlraum illuminates a fusion capsule and the ablated material drives a spherical implosion.[4,9] As the high-intensity laser beams propagate to the hohlraum wall, they encounter millimeter-scale-length plasmas that make them particularly susceptible to laser–plasma instabilities[10] that reduce the x-ray drive. This is in contrast to the direct-drive approach,[11] where laser beams directly illuminate the fusion capsule and it is the overlapped laser beam intensity ($I_{ovr} \sim 10^{15}$ W/cm^2) that launches a series of shocks to compress the nuclear fuel to fusion conditions.[12] As laser beams propagate up the density gradient to the critical surface (Fig. 132.1), they are susceptible to several laser–plasma instabilities that can divert their energy, thereby reducing the hydrodynamic efficiency [$\epsilon = (1/2\, mv^2)/E_{laser}$, where m is the mass of the imploding shell, v is the implosion velocity, and E_{laser} is the total laser energy] or the symmetry of the drive. Direct drive is most susceptible to laser–plasma instabilities that depend on multiple laser beams, as the peak single-beam intensities are relatively low ($I_s \approx 8/NI_{ovr}$, where N is the total number of laser beams illuminating the capsule) and the coronal electron temperatures are high ($T_e \simeq 3.5$ keV). Cross-beam energy transfer (CBET)[13] and two-plasmon decay (TPD)[14] are two such instabilities that are driven by the intensities of multiple laser beams.

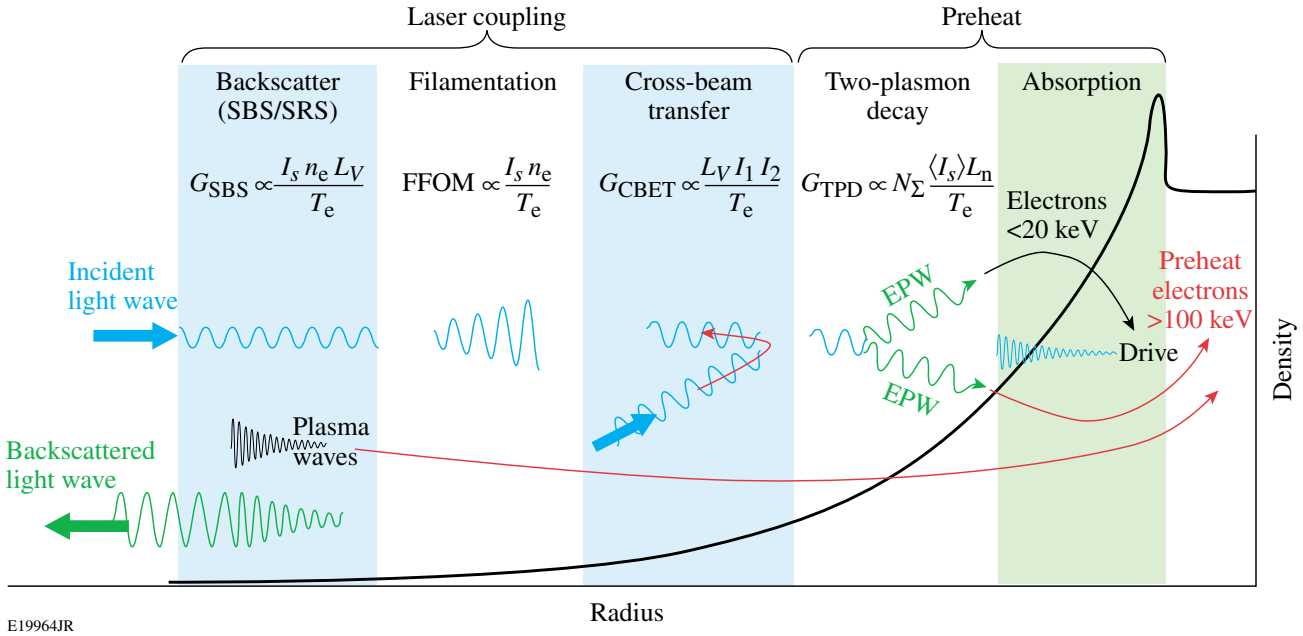

Figure 132.1
Schematic of the direct-drive density profile and potential laser–plasma interactions encountered by incident direct-drive beams. As a result of the relatively low single-beam intensities (I_s), direct-drive experiments are most susceptible to the laser-beam instabilities that are driven by multiple laser beams (e.g., CBET, TPD).

CBET is a mechanism that reduces the hydrodynamic efficiency in high-energy-density laser experiments.[15–19] For direct-drive fusion experiments [Fig. 132.2(a)], CBET was identified by linking discrepancies in the scattered-light spectrum to a lack of energy penetrating to the critical surface.[20] CBET results from large-amplitude ion-acoustic waves [Fig. 132.2(b)] driven by the laser light (k_2) that propagates past the target, seeding stimulated Brillouin scattering[21] along the light from the opposing laser beams (k_1). The enhanced ion-acoustic waves scatter light primarily from the central rays of the incident laser beams to the lower-energy outgoing rays. CBET is driven by the product of the intensity of the crossing beams near the Mach-1 surface.

Experiments focusing on TPD at direct-drive–ignition conditions[22] have shown that the efficiency of hot-electron generation scales with the overlapped laser-beam intensity, and experiments have demonstrated that multiple laser beams can share a common TPD electron plasmon wave.[23,24] The resonant common electron plasma waves are restricted to a region bisecting the laser beams [Fig. 132.2(c)], and the measured efficiency of the hot-electron generation scales rapidly with the maximum convective multibeam (intensity) gain[24,25]

$$G_{\mathrm{MB}} = 2.1\times 10^{-16} N_{\Sigma} f_g \frac{\langle I_{s,\mathrm{q}}\rangle [\mathrm{W/cm}^2] L_{\mathrm{n,q}}[\mu\mathrm{m}]}{T_{\mathrm{e,q}}[\mathrm{keV}]}, \qquad (1)$$

where N_{Σ} is the number of laser beams that share a common angle with the primary electron plasma wave, $\langle I_{s,\mathrm{q}}\rangle$ is the average single-beam intensity, $L_{\mathrm{n,q}}$ is the density scale length, $T_{\mathrm{e,q}}$ is the electron temperature, and q denotes the fact that these parameters are taken at the quarter-critical surface of the laser beams. The factor f_g is determined by the geometry and polarization of the laser beams.[24,25] The geometric factor and the number of symmetric beams are constant for a given configuration, resulting in a common-wave gain proportional to the overlapped laser-beam intensity.

The linear gain calculations provide general guidance for the TPD threshold but the instability is inherently nonlinear. To study the nonlinear behavior of TPD, simulations based on a nonlinear Zakharov model[26] were performed. *ZAK*[27] is a plasma-fluid model that incorporates saturation nonlinearities including density-profile modification,[28] Langmuir wave cavitation,[29] and the generation of ion-acoustic turbulence.[27,30] *ZAK* simulations can describe the growth and nonlinear saturation of the instability but do not include kinetic effects responsible for hot-electron generation. The generalization of the *ZAK* model, *QZAK*,[31–33] accounts for kinetic effects self-consistently in the quasi-linear approximation. The addition of kinetic effects reduces the amplitude of the electron plasma waves for a given $I_{\mathrm{q}} L_{\mathrm{n,q}} / T_{\mathrm{e,q}}$. These models provide a physics-based capability for calculating TPD at ignition conditions and a method for studying different mitigation techniques in this highly nonlinear process.

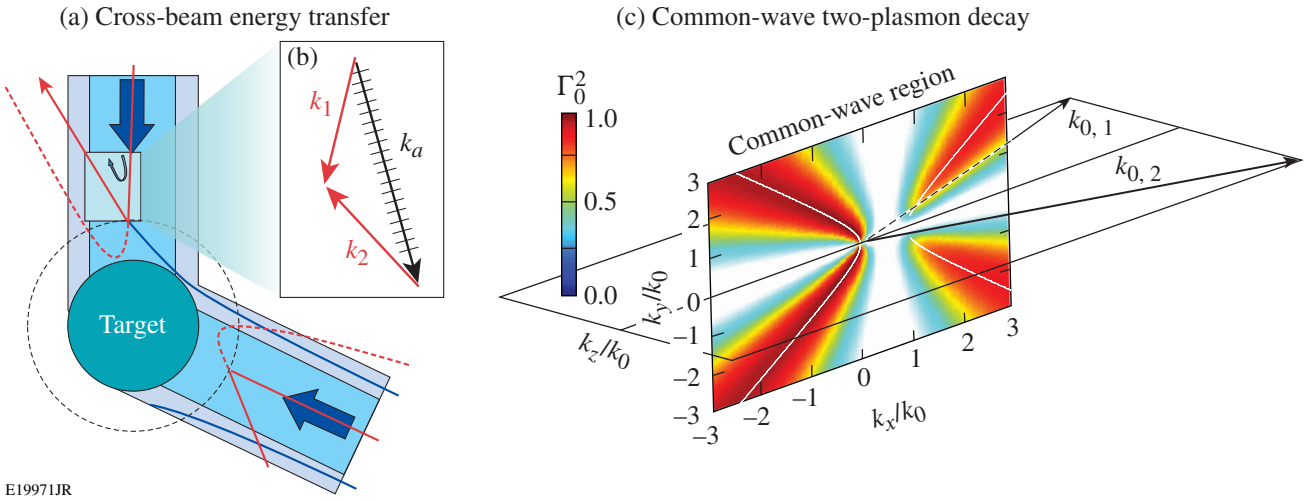

Figure 132.2
(a) Light rays propagating past the target (blue) interact with light rays in the central region of another beam (red). The interacting light rays seed an ion-acoustic wave near the Mach-1 surface (dashed circle). The ion-acoustic wave scatters light before it can penetrate deep into the target (dashed red curves). (b) A wave-vector diagram showing a typical matching condition for CBET. (c) The common-wave TPD growth rate $\left(\Gamma_0^2\right)$ for two OMEGA EP beams that are polarized in the vertical direction (k_y) is plotted in the resonant common-wave region; the common-wave region bisects the laser beams.

Underdense Hydrodynamics

To understand and mitigate the effect of laser–plasma instabilities, it is necessary to characterize the plasma conditions. The laser-intensity threshold for the onset of these instabilities must be taken into account in the design of fusion experiments; small variations in the plasma conditions can greatly impact target performance. Numerous laser–plasma instability studies over the past 20 years have emulated plasma conditions that will be achieved in fusion targets at the National Ignition Facility (NIF).[34–37] Generally, these studies have shown the strong sensitivity of laser–plasma interactions to the exact plasma conditions, highlighting the importance of correctly modeling the underdense plasma. Ultraviolet Thomson scattering provides access to the high densities prevalent in ICF coronal plasmas and is now routinely used as a diagnostic to characterize the electron and ion temperatures.[38–40]

The Thomson-scattering diagnostic on OMEGA employs a 20-J, $\lambda_{4\omega} = 0.26$-μm probe beam.[41] The Thomson-scattered light is collected from a $60 \times 75 \times 75$-mm volume defined by the 60-μm best-focus diameter of the probe beam, the 150-μm-wide spectrometer slit, and the 150-μm-wide streak camera slit.[40,42] The Thomson-scattering diagnostic probes ion-acoustic waves with a wave number $k_a = 2k_{4\omega} \sin(\theta/2)$, where $k_{4\omega} = 2\pi/\lambda_{4\omega}$ and $\theta = 63°$ is the scattering angle.

1. Hydrodynamic Modeling

The direct-drive–implosion experiments are designed using the 1-D hydrodynamics code *LILAC*,[43] which implements a nonlocal heat transport model[44] and a CBET model.[18,19] The CBET model is incorporated into the laser-absorption package, allowing for a self-consistent calculation of laser deposition with CBET. The model considers pairwise interactions of pump light rays with probe light rays and all possible crossings of these rays within the corona plasma. A spatial gain is estimated in the strong damping limit to calculate the energy transfer.

To reproduce the measured laser coupling and the measured hydrodynamic efficiency, both the nonlocal transport and CBET models must be used. The laser coupling is characterized by time-dependent absorption fraction, inferred from scattered-light measurements and the scattered-frequency spectrum.[20] When a flux-limited transport model is used, critical features in the scattering spectrum are not reproduced indicating that the time-dependent coronal conditions have not been simulated correctly. Simulations performed using the nonlocal transport model, but without CBET, drove the implosion too efficiently; the simulated bang time was ~200 ps earlier than measured, which is consistent with the lower shell-trajectory measurements inferred from x-ray self-emission images of the imploding targets.[45]

2. Spherical Geometry

Figure 132.3(a) shows the Thomson-scattering spectra obtained from two shots where 860-μm-diam capsules with 27-μm-thick carbon–hydrogen (CH) walls filled with 10 atm of D_2 gas were driven by a laser pulse consisting of three picket pulses followed by a main drive pulse at $I_{ovr} = 3 \times 10^{14}$ W/cm^2 (Ref. 12). Nearly 0.7 ns after the initial picket illuminated the target, the plasma has expanded to the Thomson-scattering volume located 400 μm from the initial target surface. Two characteristic ion-acoustic features were observed and, to obtain the plasma conditions, the spectra were fit [Fig. 132.3(b)] every 50 ps using a standard theoretical form factor.[46] The light scattered from the ion-acoustic waves was further blue shifted as a result of the outward plasma-flow velocity [Fig. 132.3(d)]; the ion-acoustic wave vectors (k_a) are aligned in the radial direction. The relative amplitude of the ion-acoustic features provides a measure of the drift between the ions and electrons near the phase velocity of the ion-acoustic waves [Fig. 132.3(d)].[46] This drift velocity was caused by the plasma maintaining quasi-neutrality as "fast" heat carrying electrons move outward.

The spectral feature nearest the wavelength of the probe [top feature in Fig. 132.3(a) and expanded in Fig. 132.4(a)] results from light in the wings of the probe beam that is reflected from the plasma; this turning point, located near the 3ω critical surface (the turning point has moved below the 4ω critical density as a result of the glancing incidence of the probe beam), is a result of the 60° angle between the probe beam and the target normal. Figure 132.4(b) shows the calculated spectrum obtained by propagating 4ω light through the simulated plasma conditions. The wavelength shift provides a measure of the changing path length along the probe beam caused by the rapidly changing density[47] and the Doppler shift induced by the moving turning point. The intensity modulation is a result of absorption; between the pickets, the plasma rapidly cools and the probe light is absorbed. These measurements provide a powerful set of criteria to assess the hydrodynamic models used to design direct-drive–fusion experiments and to study laser–plasma instabilities.

3. Planar Geometry

To validate the plasma conditions calculated in planar geometry and used to interpret the two-plasmon–decay results, Thomson-scattering measurements were obtained on OMEGA[48] using the same target platform, pulse shape, and

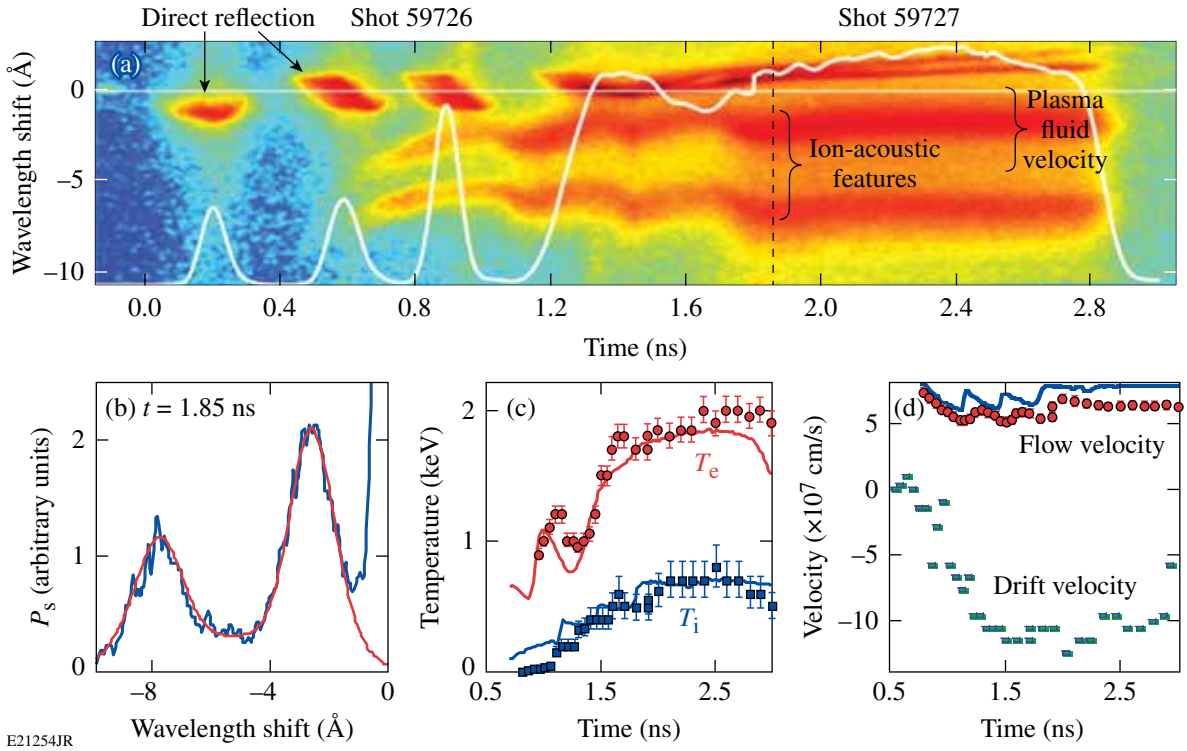

Figure 132.3
(a) The time-resolved Thomson-scattering spectrum obtained from the direct-drive coronal plasma. The pulse shape of the 3ω drive beams is shown (white curve). The Thomson-scattering probe beam was on over nearly the entire record (–0.1 ns to 2.8 ns). (b) The spectrum at 1.85 ns was fit to obtain the electron temperature, flow velocity, and drift velocity. The measured (c) electron temperature and (d) flow and drift velocities are plotted as a function of time. The solid curves are from 1-D hydrodynamic simulations that included nonlocal heat transfer and CBET models.

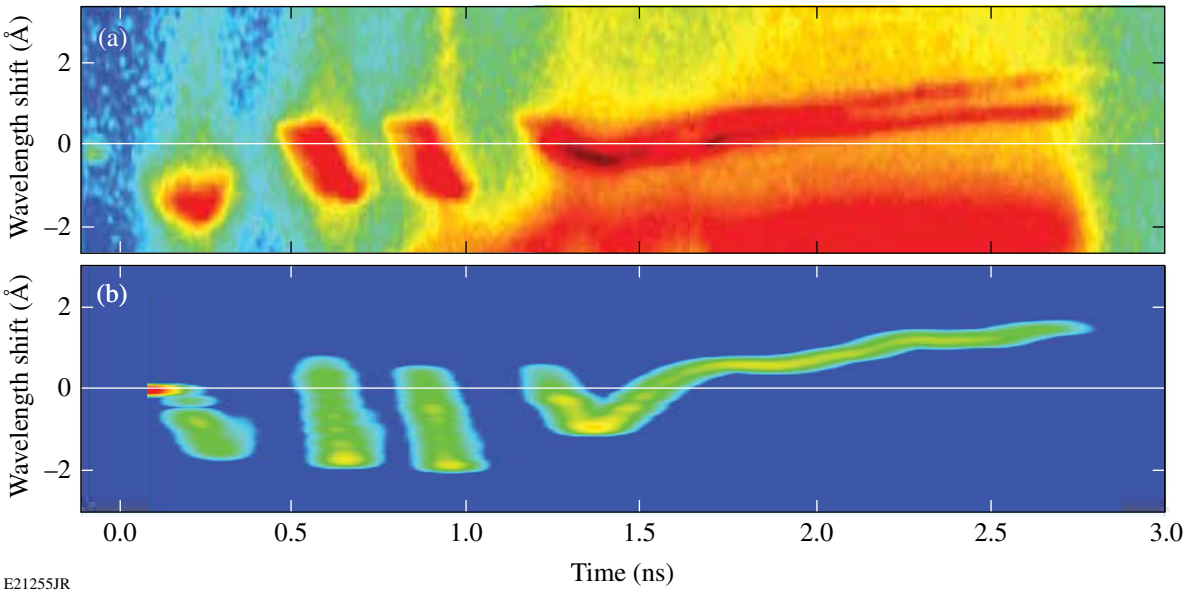

Figure 132.4
(a) The scale from Fig. 132.3(a) was expanded to highlight the spectrum obtained from light reflecting from the target surface. (b) The reflected light was modeled using the simulated plasma conditions.

similar laser beam diameters (490-μm FWHM) as used on the OMEGA EP[49] planar experiments discussed in **Two-Plasmon Decay** (p. 186). The planar targets consist of a 30-μm-thick CH layer deposited on 30-μm-thick molybdenum (Mo). Figure 132.5 shows the electron and ion temperatures as functions of time at the 3ω quarter-critical surface. The wavelength separation is a function of the ion-acoustic sound speed that leads to the direct measure of the electron temperature shown in Fig. 132.3(c). The multiple ion-acoustic modes present in the CH plasma provide an accurate measure of the ion temperature.[50] There is excellent agreement with the 2-D hydrodynamic simulations using the code *DRACO*.[51] Furthermore, the rarefaction wave launched from the CH–Mo interface is observed in the Thomson-scattering spectrum 1.11 ns after the laser beams turn on, which is in agreement with the hydrodynamic simulations. This agreement demonstrates the accuracy of the thermal-conduction model and is a strong indication that the calculated density and temperature profiles are accurate.

Cross-Beam Energy Transfer

1. CBET Experiments

To reduce CBET and increase the implosion velocity in direct-drive experiments, the energy in the rays that bypass the target was reduced by decreasing the radii of the laser beams (R_b) relative to the target radius ($R_t = 430$ μm). Figure 132.6(a) shows that, when the radii of the laser beams are reduced from $R_b/R_t = 1.1$ to 0.75, the measured absorption is increased from 68% to 87% (Ref. 52). This results in an increase in the implosion velocity from 160 to 195 km/s [Fig. 132.6(b)]. Simulations that include both nonlocal heat transport[44] and CBET models[19] developed in the 1-D hydrodynamic code *LILAC* (see **Hydrodynamic Modeling**, p. 183) are in excellent agreement with the measurements shown in Fig. 132.6.

When the CBET model is not included in the simulations, both the absorption and hydrodynamic efficiency increase by ~15% as the tighter focused laser spots direct more energy on target [Fig. 132.6(b)]. This is in contrast to the measured ~35% increase in the hydrodynamic efficiency; a factor of 2 larger than the measured 15% increase in absorption. This enhanced hydrodynamic efficiency is a direct result of reducing CBET, which increases the energy in the central portion of the laser beams, leading to more energy deposited near the critical surface.

Although the hydrodynamic efficiency is significantly increased, reducing the radii of the laser beams with respect to the target radius introduces a nonuniform illumination on the initial target surface [Fig. 132.6(c)], which can lead to low-mode nonuniformities and reduced implosion performance. Figure 132.6(c) shows that the root-mean-square (rms) deviation from the average shell radius (nonuniformities), measured near the ablation front [Fig. 132.6(d)],[45] increased from less than 5 μm to greater than 25 μm as the laser radii were reduced from $R_b/R_t = 1.1$ to 0.5 (Ref. 52).

2. Mitigation of Cross-Beam Energy Transfer

To mitigate CBET and maintain sufficient illumination uniformity in direct-drive implosions, a two-state zooming has been proposed.[53] During the critical time for seeding nonuniformities (laser imprint), before a significant conduction zone is produced, the radii of the laser beams are equal to the target

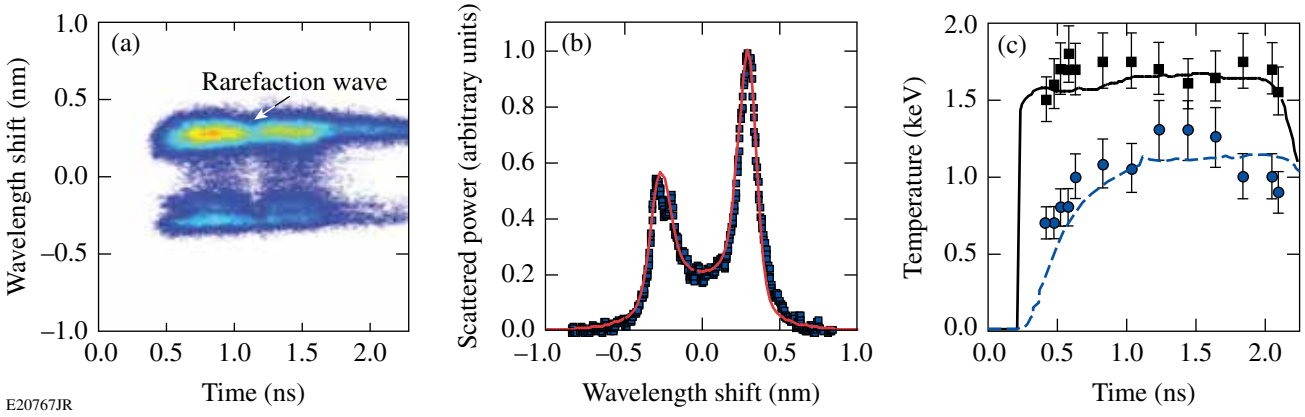

Figure 132.5
(a) The Thomson-scattering spectrum obtained from scattering at the 3ω quarter-critical surface in planar geometry for a drive intensity of $I_{ovr} = 3 \times 10^{14}$ W/cm^2. (b) The spectrum at 0.8 ns is fit to obtain a $T_e = 1.6$ keV and $T_i = 1.0$ keV. (c) The electron (squares) and ion (circles) temperatures are plotted as a function of time and compared with 2-D hydrodynamic modeling.

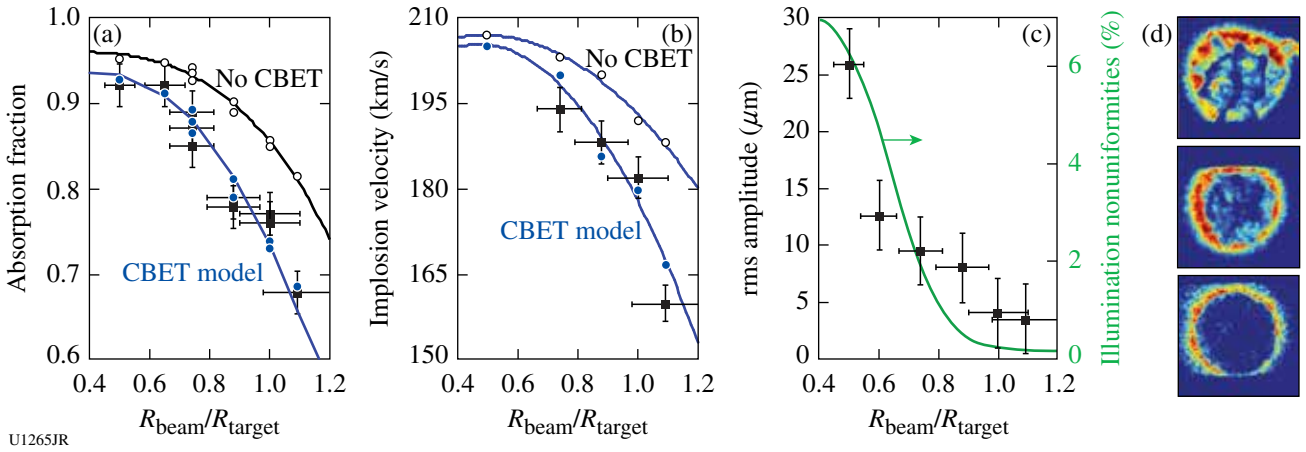

Figure 132.6

(a) The absorbed light, (b) implosion velocity, and (c) rms deviation from the average shell radius (left axis), along with the calculated illumination nonuniformities (right axis) are plotted as functions of the ratio between the laser-beam and target radius. The simulation results that include the CBET model (solid circles) are in excellent agreement with the measurements. Simulations performed without the CBET model (open circles) significantly overestimate the absorbed light and the implosion velocity. (d) X-ray self-emission images are used to determine the nonuniformities at a constant capsule radius of 175 μm; the soft x rays emitted from the ablation surface (outer edge of the imploding shell) were measured for three focus conditions: R_b/R_t = 0.5, 0.75, and 1.0 (from top to bottom).

radius $\left(R_b/R_t = 1.0\right)$, minimizing the laser imprint. Once the plasma has sufficiently expanded, the radii of the laser beams are reduced $\left(R_b/R_t = 0.7\right)$, minimizing CBET. The increase in transverse thermal conduction smooths the low-mode intensity nonuniformities, producing a uniform drive. Initial 2-D hydrodynamic simulations of OMEGA direct-drive experimental conditions indicate that transitioning to smaller laser spots after the picket pulses does not increase the low-mode nonuniformities.[54] The combination of zooming and dynamic bandwidth reduction (removing smoothing by spectral dispersion during the drive[55]) could provide a 30% effective increase in the drive energy for OMEGA direct-drive implosions.

Potential schemes to achieve zooming of the focal spot on target involve modifications to the spatial coherence of the laser that causes broadening in the far field of the laser beams. One method suitable for most high-power laser systems employs a radially varying zoom phase plate (ZPP) and a two-state dynamic near-field profile. The ZPP's central area would produce a large focal spot, while the outer area would produce a smaller focal spot. During the picket pulses, a small-diameter near-field beam propagates through the center region of the ZPP forming a large diameter on-target spot. During the drive pulse, an annulus-shaped near-field profile propagates through the outer region of the ZPP producing a smaller-diameter on-target spot.[56,57]

Two-Plasmon Decay

The large-diameter targets (~3 mm) and moderate overlapped laser intensities ($I_{ovr} \sim 7 \times 10^{14}$ W/cm^2, $I_{s,q} \lesssim 10^{14}$ W/cm^2) proposed for direct-drive–ignition experiments will produce high-temperature ($T_{e,q} \sim 3.5$ keV), long-scale-length ($L_{n,q} \sim 500\ \mu$m) underdense plasmas.[58] Multibeam linear gain calculations [Eq. (1)] and recent results[25] from OMEGA suggest that TPD will be near threshold where details in the exact hydrodynamic conditions and beam pointings may play a significant role in the number of hot electrons produced by TPD. A fraction of the hot electrons produced by two-plasmon decay will be absorbed into the unablated fuel ("preheat"), and may increase the implosion adiabat and reduce the compression efficiency. Typical direct-drive–ignition designs can withstand of the order of 0.1% of the laser energy converted to preheat.[59]

Figure 132.7 shows the results from a series of experiments in planar and spherical geometries that were designed to account for all of the hot electrons generated by TPD.[60] The coupling of these hot electrons to a fusion target (preheat) will be reduced by the electron divergence, the distance between where the electrons are created and where they are absorbed, the energy distribution of the electrons (T_{hot}), and other loss mechanisms. The experiments on OMEGA EP employed a single cone of four beams (23° from the target normal) with ~860-μm FWHM laser spots; the planar experiments on

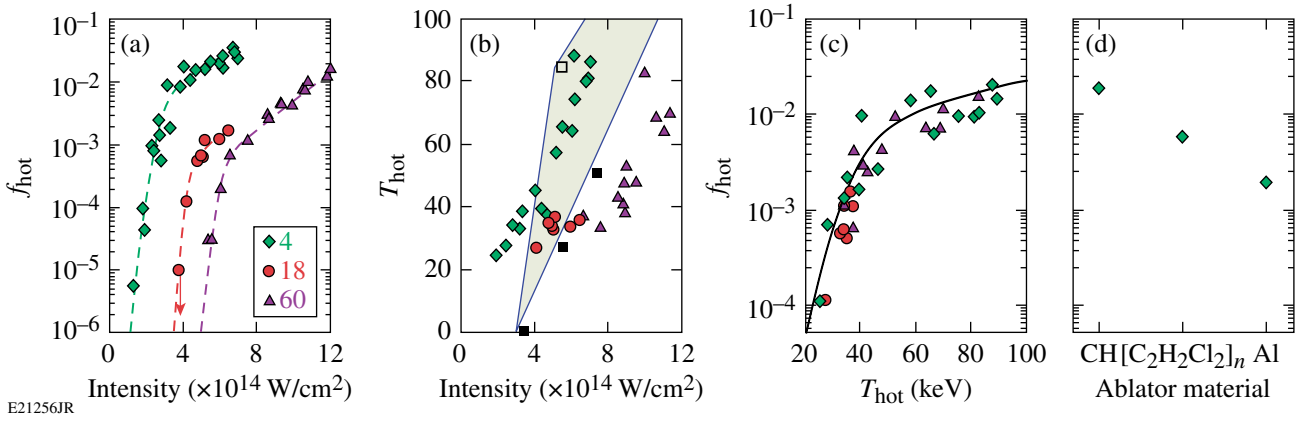

Figure 132.7
(a) The fraction of laser energy converted to hot electrons (f_{hot}) and (b) the hot-electron temperature (T_{hot}) are shown for three beam geometries: four-beam planar (diamonds), 18-beam planar (circles), and 60-beam spherical (triangles) as a function of the vacuum overlapped intensities (I_{ovr}). The hot-electron temperatures calculated by *ZAK* (open squares) and *QZAK* (solid squares) are included for reference. (c) The hot-electron fraction is plotted as a function of the hot-electron temperature for the three target geometries. (d) The f_{hot} measured on the four-beam planar configuration is plotted for a series of ablator materials for a vacuum overlapped intensity of 7×10^{14} W/cm^2.

OMEGA consisted of 18 beams with 710-μm FWHM laser spots in three cones (six at 23°, six at 48°, and six at 60° from the target normal); the spherical experiments used 60 beams and the target diameter was matched to the diameter of the laser spots, where 95% of the laser power illuminates the initial target surface ($R_t = 865$ μm). Each target geometry has its own intensity threshold as a result of the differences in the number of beams that contribute to the common electron plasma wave, scale lengths, electron temperatures, and the geometric factor as indicated in Eq. (1) (see Table 132.I). The hot-electron intensity thresholds shown in Fig. 132.7(a) suggest that the multibeam TPD gain [Eq. (1)] must be greater than $G_{MB} \approx 2$ for a measurable fraction of hot electrons ($f_{hot} \approx 10^{-5}$ is near the detection threshold).

1. Total Hot-Electron Fraction

To study TPD at ignition-relevant plasma conditions, the four ultraviolet (3ω, $\lambda = 0.35$ μm) beams available from OMEGA EP produced the required intensities ($I_{ovr} = 7 \times 10^{14}$ W/cm^2) over a large-diameter laser spot to create 400-μm plasma density scale lengths and $T_e = 2.5$-keV electron temperatures at $n_{cr}/4$. The long-scale-length CH plasma was produced by illuminating a 30-μm-thick CH layer deposited on 30 μm of Mo. The total energy in hot electrons was determined by measuring the K_α yield and the hot-electron temperature.[60]

Figure 132.7(a) shows that the fraction of laser energy converted into hot electrons scales exponentially over nearly three orders of magnitude when the vacuum overlapped intensity is increased from 1.3 to 3×10^{14} W/cm^2 and continues to grow at a slower rate as the intensity is extended to 7×10^{14} W/cm^2 (Ref. 61). The large fraction of laser energy converted into hot electrons along with its observed saturation is a direct consequence of the simultaneous high intensities and long-scale lengths ($L_{n,q} = 400$ μm) in these experiments. Previous TPD studies have shown saturation of the hot-electron generation at 0.1% of the incident laser energy when plotted against the vacuum laser intensity. This apparent saturation and low level of electron generation results from the hydrodynamics; the small laser spots used to produce the highest intensities limited the

Table 132.I: Estimates of the factors used to calculate the common-wave gain at the threshold intensity for each configuration shown.

Configuration	f_g	$N_\Sigma \langle I_{s,q} \rangle$	$L_{n,q}/T_{e,q}$	I_{ovr}^{th}	G_{MB}^{th}
4 beam	0.5	~1/2 I_{ovr}	~170 μm/keV	~2	1.7
18 beam	0.5	~1/4 I_{ovr}	~135 μm/keV	~4	1.4
60 beam	0.5	~1/2 I_{ovr}	~60 μm/keV	~5	1.5

scale length to $L_{n,q} < 200\ \mu$m (Ref. 23). The highest intensity corresponds to a TPD gain larger than those estimated for direct-drive–ignition experiments and the fraction of these electrons that are deposited as preheat in the fuel will be significantly reduced as a result of their divergence and energies.

2. Hot-Electron Temperature (T_{hot})

Figure 132.7(b) shows that, for a given target geometry, the hot-electron temperature scales with the vacuum intensity. The four-beam planar experimental results are compared with the code *ZAK*.[27] While this plasma-fluid model describes the growth and nonlinear saturation of the instability, it does not include kinetic effects responsible for hot-electron generation. An estimate for the hot-electron temperature was instead obtained from the nonlinearly saturated state via the integration of test-electron trajectories in the electrostatic fields associated with the Langmuir turbulence (see Ref. 27 for more details). The solid triangles in Fig. 132.7 show the results of the *QZAK* model where kinetic effects are taken into account self-consistently in the quasi-linear approximation.[62] The addition of kinetic effects lowers the amplitude of the electron plasma waves, reducing the hot-electron temperature for a given $I_q L_{n,q}/T_{e,q}$. The difference between the two model predictions highlights the difficulty in making predictive calculations of a highly turbulent and complex physical system.

Figure 132.7(c) shows the measured correlation, for all three target geometries, between the hot-electron temperature and the fraction of laser energy converted to hot electrons. The fact that each target geometry has its own intensity threshold, even though the hot-electron generation plotted as a function of hot-electron temperature shares a common curve, suggests that the differences in thresholds [Fig. 132.7(b)] result from the laser beam coupling to the TPD instability.[25]

Mitigation of Two-Plasmon Decay

Figure 132.7(d) shows the fraction of hot electrons generated by TPD for various ablator materials measured on OMEGA EP at a vacuum overlapped intensity of 7×10^{14} W/cm^2. Although some of the reduction in the fraction of hot electrons is a result of the changing hydrodynamics (i.e., increased T_e, reduced L_n), recent particle-in-cell simulations indicate a sensitivity of TPD to the electron–ion collisions,[63] and it is plausible that reducing the ion-acoustic wave damping will lead to a reduced TPD saturation level. Previous implosion experiments using silicon dioxide (SiO_2) ablators have observed a significant reduction in the fraction of laser energy converted to hot electrons,[64] and more-recent hydrodynamic studies of direct-drive–implosion designs add Si/Ge doping to the CH ablator to reduce the Rayleigh–Taylor growth.[65,66]

Summary

A series of laser–plasma interaction experiments performed at the Omega Laser Facility have investigated CBET and TPD at direct-drive–ignition conditions. Direct-drive ignition is most susceptible to these multibeam instabilities because the single-beam intensities are low and the electron temperatures in the underdense plasma are high. These studies have led to mitigation strategies for both CBET and TPD; reducing the radii of the laser beams with respect to the target during the main drive minimizes CBET, and varying the ablator material suggests that the hot electrons produced by TPD can be significantly reduced.

ACKNOWLEDGMENT

We acknowledge the OMEGA EP and OMEGA operations teams whose efforts made these results possible. This work was supported by the U.S. Department of Energy Office of Inertial Confinement Fusion under Cooperative Agreement No. DE-FC52-08NA28302, the University of Rochester, and the New York State Energy Research and Development Authority. The support of DOE does not constitute an endorsement by DOE of the views expressed in this article.

REFERENCES

1. J. Nuckolls *et al.*, Nature **239**, 139 (1972).
2. E. I. Moses and C. R. Wuest, Fusion Sci. Technol. **47**, 314 (2005).
3. C. Cavailler, Plasma Phys. Control. Fusion **47**, B389 (2005).
4. J. D. Lindl *et al.*, Phys. Plasmas **11**, 339 (2004).
5. D. H. Froula, L. Divol, R. A. London, R. L. Berger, T. Döppner, N. B. Meezan, J. Ralph, J. S. Ross, L. J. Suter, and S. H. Glenzer, Phys. Plasmas **17**, 056302 (2010).
6. S. H. Glenzer *et al.*, Science **327**, 1228 (2010).
7. W. L. Kruer, *The Physics of Laser–Plasma Interactions*, Frontiers in Physics, Vol. 73, edited by D. Pines (Addison-Wesley, Redwood City, CA, 1988).
8. C. Labaune *et al.*, Plasma Phys. Control. Fusion **46**, B301 (2004).
9. S. H. Glenzer *et al.*, Plasma Phys. Control. Fusion **54**, 045013 (2012).
10. D. H. Froula, L. Divol, N. B. Meezan, S. Dixit, J. D. Moody, P. Neumayer, B. B. Pollock, J. S. Ross, and S. H. Glenzer, Phys. Rev. Lett. **98**, 085001 (2007); D. H. Froula, L. Divol, R. A. London, P. Michel, R. L. Berger, N. B. Meezan, P. Neumayer, J. S. Ross, R. Wallace, and S. H. Glenzer, Phys. Rev. Lett. **100**, 015002 (2008); D. H. Froula, Phys. Rev. Lett. **103**, 045006 (2009).

11. R. L. McCrory, D. D. Meyerhofer, R. Betti, R. S. Craxton, J. A. Delettrez, D. H. Edgell, V. Yu Glebov, V. N. Goncharov, D. R. Harding, D. W. Jacobs-Perkins, J. P. Knauer, F. J. Marshall, P. W. McKenty, P. B. Radha, S. P. Regan, T. C. Sangster, W. Seka, R. W. Short, S. Skupsky, V. A. Smalyuk, J. M. Soures, C. Stoeckl, B. Yaakobi, D. Shvarts, J. A. Frenje, C. K. Li, R. D. Petrasso, and F. H. Séguin, Phys. Plasmas **15**, 055503 (2008).

12. V. N. Goncharov, T. C. Sangster, T. R. Boehly, S. X. Hu, I. V. Igumenshchev, F. J. Marshall, R. L. McCrory, D. D. Meyerhofer, P. B. Radha, W. Seka, S. Skupsky, C. Stoeckl, D. T. Casey, J. A. Frenje, and R. D. Petrasso, Phys. Rev. Lett. **104**, 165001 (2010).

13. C. J. Randall, J. R. Albritton, and J. J. Thomson, Phys. Fluids **24**, 1474 (1981).

14. A. Simon, R. W. Short, E. A. Williams, and T. Dewandre, Phys. Fluids **26**, 3107 (1983).

15. R. K. Kirkwood *et al.*, Phys. Rev. Lett. **76**, 2065 (1996).

16. J. Myatt, A. V. Maximov, W. Seka, R. S. Craxton, and R. W. Short, Phys. Plasmas **11**, 3394 (2004).

17. P. Michel *et al.*, Phys. Rev. Lett. **102**, 025004 (2009).

18. I. V. Igumenshchev, D. H. Edgell, V. N. Goncharov, J. A. Delettrez, A. V. Maximov, J. F. Myatt, W. Seka, A. Shvydky, S. Skupsky, and C. Stoeckl, Phys. Plasmas **17**, 122708 (2010).

19. I. V. Igumenshchev, W. Seka, D. H. Edgell, D. T. Michel, D. H. Froula, V. N. Goncharov, R. S. Craxton, L. Divol, R. Epstein, R. Follett, J. H. Kelly, T. Z. Kosc, A. V. Maximov, R. L. McCrory, D. D. Meyerhofer, P. Michel, J. F. Myatt, T. C. Sangster, A. Shvydky, S. Skupsky, and C. Stoeckl, Phys. Plasmas **19**, 056314 (2012).

20. W. Seka, D. H. Edgell, J. P. Knauer, J. F. Myatt, A. V. Maximov, R. W. Short, T. C. Sangster, C. Stoeckl, R. E. Bahr, R. S. Craxton, J. A. Delettrez, V. N. Goncharov, I. V. Igumenshchev, and D. Shvarts, Phys. Plasmas **15**, 056312 (2008).

21. W. Seka, H. A. Baldis, J. Fuchs, S. P. Regan, D. D. Meyerhofer, C. Stoeckl, B. Yaakobi, R. S. Craxton, and R. W. Short, Phys. Rev. Lett. **89**, 175002 (2002).

22. W. Seka, D. H. Edgell, J. F. Myatt, A. V. Maximov, R. W. Short, V. N. Goncharov, and H. A. Baldis, Phys. Plasmas **16**, 052701 (2009).

23. C. Stoeckl, R. E. Bahr, B. Yaakobi, W. Seka, S. P. Regan, R. S. Craxton, J. A. Delettrez, R. W. Short, J. Myatt, A. V. Maximov, and H. Baldis, Phys. Rev. Lett. **90**, 235002 (2003).

24. D. T. Michel, A. V. Maximov, B. Yaakobi, S. X. Hu, J. F. Myatt, A. A. Solodov, R. W. Short, and D. H. Froula, "Experimental Demonstration of the Two-Plasmon-Decay Common-Wave Process," to be published in Physical Review Letters.

25. D. T. Michel, J. F. Myatt, A. V. Maximov, R. W. Short, J. A. Delettrez, S. X. Hu, I. V. Igumenshchev, W. Seka, A. A. Solodov, C. Stoeckl, B. Yaakobi, J. Zhang, and D. H. Froula, "Measured Multibeam Hot-Electron Intensity Threshold Quantified by a Two-Plasmon–Decay Resonant Common-Wave Gain in Various Experimental Configurations," submitted to Physics of Plasmas.

26. D. F. DuBois, D. A. Russell, and H. A. Rose, Phys. Rev. Lett. **74**, 3983 (1995).

27. J. F. Myatt, J. Zhang, J. A. Delettrez, A. V. Maximov, R. W. Short, W. Seka, D. H. Edgell, D. F. DuBois, D. A. Russell, and H. X. Vu, Phys. Plasmas **19**, 022707 (2012).

28. A. B. Langdon, B. F. Lasinski, and W. L. Kruer, Phys. Rev. Lett. **43**, 133 (1979).

29. G. D. Doolen, D. F. DuBois, and H. A. Rose, Phys. Rev. Lett. **54**, 804 (1985).

30. R. Yan, A. V. Maximov, C. Ren, and F. S. Tsung, Phys. Rev. Lett. **103**, 175002 (2009).

31. H. X. Vu, D. F. Dubois, D. A. Russell, and J. F. Myatt, "Hot-Electron Generation by Cavitating Langmuir Turbulence in the Nonlinear Stage of the Two-Plasmon–Decay Instability," submitted to Physics of Plasmas.

32. H. X. Vu, D. F. Dubois, D. A. Russell, and J. F. Myatt, "Hot-Electron Production and Suprathermal Heat Flux Scaling with Laser Intensity from the Two-Plasmon–Decay Instability," submitted to Physics of Plasmas.

33. J. F. Myatt, H. X. Vu, D. F. DuBois, D. A. Russell, J. Zhang, R. W. Short, A. V. Maximov, W. Seka, and D. H. Edgell, "Mitigation of Two-Plasmon Decay in Direct-Drive Inertial Confinement Fusion Through the Manipulation of Ion-Acoustic and Langmuir Wave Damping," to be submitted to Physics of Plasmas.

34. B. J. MacGowan *et al.*, Phys. Plasmas **3**, 2029 (1996).

35. J. C. Fernández *et al.*, Phys. Plasmas **7**, 3743 (2000).

36. E. Lefebvre *et al.*, Phys. Plasmas **5**, 2701 (1998).

37. D. H. Froula, L. Divol, N. B. Meezan, S. Dixit, P. Neumayer, J. D. Moody, B. B. Pollock, J. S. Ross, L. Suter, and S. H. Glenzer, Phys. Plasmas **14**, 055705 (2007).

38. S. H. Glenzer *et al.*, Rev. Sci. Instrum. **70**, 1089 (1999).

39. J. S. Ross, D. H. Froula, A. J. Mackinnon, C. Sorce, N. Meezan, S. H. Glenzer, W. Armstrong, R. Bahr, R. Huff, and K. Thorp, Rev. Sci. Instrum. **77**, 10E520 (2006).

40. D. H. Froula, J. S. Ross, L. Divol, and S. H. Glenzer, Rev. Sci. Instrum. **77**, 10E522 (2006).

41. A. J. Mackinnon, S. Shiromizu, G. Antonini, J. Auerbach, K. Haney, D. H. Froula, J. Moody, G. Gregori, C. Constantin, C. Sorce, L. Divol, R. L. Griffith, S. Glenzer, J. Satariano, P. K. Whitman, S. N. Locke, E. L. Miller, R. Huff, K. Thorp, W. Armstrong, W. Bahr, W. Seka, G. Pien, J. Mathers, S. Morse, S. Loucks, and S. Stagnitto, Rev. Sci. Instrum. **75**, 3906 (2004).

42. J. Katz, R. Boni, C. Sorce, R. Follett, M. J. Shoup III, and D. H. Froula, Rev. Sci. Instrum. **83**, 10E349 (2012).

43. J. Delettrez, Can. J. Phys. **64**, 932 (1986).

44. V. N. Goncharov, T. C. Sangster, P. B. Radha, R. Betti, T. R. Boehly, T. J. B. Collins, R. S. Craxton, J. A. Delettrez, R. Epstein, V. Yu. Glebov, S. X. Hu, I. V. Igumenshchev, J. P. Knauer, S. J. Loucks, J. A. Marozas, F. J. Marshall, R. L. McCrory, P. W. McKenty, D. D. Meyerhofer, S. P. Regan, W. Seka, S. Skupsky, V. A. Smalyuk, J. M. Soures, C. Stoeckl, D. Shvarts, J. A. Frenje, R. D. Petrasso, C. K. Li, F. Séguin, W. Manheimer, and D. G. Colombant, Phys. Plasmas **15**, 056310 (2008).

45. D. T. Michel, C. Sorce, R. Epstein, N. Whiting, I. V. Igumenshchev, R. Jungquist, and D. H. Froula, Rev. Sci. Instrum. **83**, 10E530 (2012).

46. D. H. Froula, S. H. Glenzer, N. C. Luhmann, and J. Sheffield, *Plasma Scattering of Electromagnetic Radiation: Theory and Measurement Techniques*, 2nd ed. (Academic Press, Burlington, MA, 2011).

47. T. Dewandre, J. R. Albritton, and E. A. Williams, Phys. Fluids **24**, 528 (1981).

48. T. R. Boehly, D. L. Brown, R. S. Craxton, R. L. Keck, J. P. Knauer, J. H. Kelly, T. J. Kessler, S. A. Kumpan, S. J. Loucks, S. A. Letzring, F. J. Marshall, R. L. McCrory, S. F. B. Morse, W. Seka, J. M. Soures, and C. P. Verdon, Opt. Commun. **133**, 495 (1997).

49. J. H. Kelly, L. J. Waxer, V. Bagnoud, I. A. Begishev, J. Bromage, B. E. Kruschwitz, T. J. Kessler, S. J. Loucks, D. N. Maywar, R. L. McCrory, D. D. Meyerhofer, S. F. B. Morse, J. B. Oliver, A. L. Rigatti, A. W. Schmid, C. Stoeckl, S. Dalton, L. Folnsbee, M. J. Guardalben, R. Jungquist, J. Puth, M. J. Shoup III, D. Weiner, and J. D. Zuegel, J. Phys. IV France **133**, 75 (2006).

50. D. H. Froula, J. S. Ross, L. Divol, N. Meezan, A. J. MacKinnon, R. Wallace, and S. H. Glenzer, Phys. Plasmas **13**, 052704 (2006).

51. P. B. Radha, T. J. B. Collins, J. A. Delettrez, Y. Elbaz, R. Epstein, V. Yu. Glebov, V. N. Goncharov, R. L. Keck, J. P. Knauer, J. A. Marozas, F. J. Marshall, R. L. McCrory, P. W. McKenty, D. D. Meyerhofer, S. P. Regan, T. C. Sangster, W. Seka, D. Shvarts, S. Skupsky, Y. Srebro, and C. Stoeckl, Phys. Plasmas **12**, 056307 (2005).

52. D. H. Froula, I. V. Igumenshchev, D. T. Michel, D. H. Edgell, R. Follett, V. Yu. Glebov, V. N. Goncharov, J. Kwiatkowski, F. J. Marshall, P. B. Radha, W. Seka, C. Sorce, S. Stagnitto, C. Stoeckl, and T. C. Sangster, Phys. Rev. Lett. **108**, 125003 (2012).

53. P. W. McKenty, R. S. Craxton, A. Shvydky, F. J. Marshall, J. A. Marozas, S. Skupsky, D. D. Meyerhofer, and R. L. McCrory, Bull. Am. Phys. Soc. **56**, 341 (2011).

54. I. V. Igumenshchev, D. H. Edgell, D. H. Froula, V. N. Goncharov, T. J. Kessler, F. J. Marshall, R. L. McCrory, P. W. McKenty, D. D. Meyerhofer, D. T. Michel, T. C. Sangster, W. Seka, and S. Skupsky, "Improved Performance in Direct-Drive Implosions Using Beam Zooming," to be submitted to Physical Review Letters.

55. T. J. B. Collins, J. A. Marozas, K. S. Anderson, R. Betti, R. S. Craxton, J. A. Delettrez, V. N. Goncharov, D. R. Harding, F. J. Marshall, R. L. McCrory, D. D. Meyerhofer, P. W. McKenty, P. B. Radha, A. Shvydky, S. Skupsky, and J. D. Zuegel, Phys. Plasmas **19**, 056308 (2012).

56. I. V. Igumenshchev, D. H. Froula, D. H. Edgell, V. N. Goncharov, T. J. Kessler, F. J. Marshall, R. L. McCrory, P. W. McKenty, D. D. Meyerhofer, D. T. Michel, T. C. Sangster, W. Seka, and S. Skupsky, "Laser Beam Zooming to Mitigate Cross-Beam Energy Losses in Direct-Drive Implosions," to be submitted to Physical Review Letters.

57. D. H. Froula, I. V. Igumenshchev, A. Shvydky, J. H. Kelly, J. D. Zuegel, E. Hill, and V. N. Goncharov, "Mitigation of Cross-Beam Energy Transfer: Implicaitons of Two-State Optical Zooming on OMEGA," to be submitted to Plasma Physics and Controlled Fusion.

58. P. W. McKenty, V. N. Goncharov, R. P. J. Town, S. Skupsky, R. Betti, and R. L. McCrory, Phys. Plasmas **8**, 2315 (2001).

59. *LLE Review Quarterly Report* **79**, 121, Laboratory for Laser Energetics, University of Rochester, Rochester, NY, LLE Document No. DOE/SF/19460-317, NTIS Order No. DE2002762802 (1999).

60. B. Yaakobi, P.-Y. Chang, A. A. Solodov, C. Stoeckl, D. H. Edgell, R. S. Craxton, S. X. Hu, J. F. Myatt, F. J. Marshall, W. Seka, and D. H. Froula, Phys. Plasmas **19**, 012704 (2012).

61. D. H. Froula, B. Yaakobi, S. X. Hu, P.-Y. Chang, R. S. Craxton, D. H. Edgell, R. Follett, D. T. Michel, J. F. Myatt, W. Seka, R. W. Short, A. Solodov, and C. Stoeckl, Phys. Rev. Lett. **108**, 165003 (2012).

62. K. Y. Sanbonmatsu *et al.*, Phys. Rev. Lett. **82**, 932 (1999).

63. R. Yan, C. Ren, J. Li, A. V. Maximov, W. B. Mori, Z. M. Sheng, and F. S. Tsung, Phys. Rev. Lett. **108**, 175002 (2012).

64. V. A. Smalyuk, R. Betti, J. A. Delettrez, V. Yu. Glebov, D. D. Meyerhofer, P. B. Radha, S. P. Regan, T. C. Sangster, J. Sanz, W. Seka, C. Stoeckl, B. Yaakobi, J. A. Frenje, C. K. Li, R. D. Petrasso, and F. H. Séguin, Phys. Rev. Lett. **104**, 165002 (2010).

65. S. X. Hu, G. Fiksel, V. N. Goncharov, S. Skupsky, D. D. Meyerhofer, and V. A. Smalyuk, Phys. Rev. Lett. **108**, 195003 (2012).

66. G. Fiksel, S. X. Hu, V. N. Goncharov, D. D. Meyerhofer, T. C. Sangster, V. A. Smalyuk, B. Yaakobi, M. J. Bonino, and R. Jungquist, Phys. Plasmas **19**, 062704 (2012).

Stress-Radiation–Induced Swelling in Plastic Capsules

Introduction

Unique and distinctive features on the inner surface of plastic capsules used in deuterium–tritium (DT) inertial confinement fusion (ICF) experiments on OMEGA[1] were observed when the capsules were permeation filled to provide cryogenic ignition-scale targets. The features were not observed when deuterium (D_2) was substituted for DT nor were they observed in similar targets filled at the National Ignition Facility (NIF) with DT through a narrow fill tube (<10-μm inner diameter) (Ref. 2). The size and number of these features did not change when the capsules were warmed above 40 K. A capsule warmed to 300 K without rupturing was recovered and inspected using electron microscopy. The features were smaller than 100 nm high and are not expected to impair the hydrodynamic stability during the implosion.[3] Despite their small size, the features are sufficiently noticeable that their origin and magnitude should be understood and eliminated if possible.

The likely cause of these features was deduced through a process of elimination: the features were not present before the capsules were filled with DT and appeared once the targets were cold (19 K) and filled with DT. These features did not grow in size or number after they were first observed; they possessed a sizeable footprint (>20-μm diameter) and were less than 100 nm high. No pore structure or voids (>20 nm, the detection limit) were observed in or below the features, and no blisters were formed by subsurface pressurized voids. The best explanation for their origin is that they arise from the radiation dose imparted to the plastic, combined with the stresses experienced by the capsules during gas permeation and/or transfer of the capsule at cryogenic temperatures (25 to 40 K). While it is well known that β-radiation ruptures carbon–carbon and carbon–hydrogen bonds to generate volatile species,[4] it is postulated that at very high doses and while under stress, the high density of $C_xH_y^*$ radicals and dissolved deuterium–tritium gas present in the polymer structure may recombine to form a material with a lower density in localized areas. This would cause volumetric swelling, and buckling would be more likely to occur at the inner surface because that region receives the highest dose. This would be a soft-matter analogue to stress–corrosion behavior in metals where a combination of stress and a corrosive environment accelerates chemical changes. This article describes the observed features, the radiation doses, and stress levels that the capsule experiences when it is processed to produce a cryogenic DT target.

Observed Defects

All the targets discussed here were provided by General Atomics and processed through the OMEGA Cryogenic Target Handling System using permeation-filling, cooling, and transporting protocols that are well established.[5] Figure 132.8(a) shows a DT-filled target (0.86-mm outer diameter; 10-μm plastic wall; 95-μm ice layer) at 19.5 K with several distinctive features, two of which are the topic of this article. These features were subsequently identified to be on the inner surface of the plastic wall. Figure 132.8(b) shows that same target at 227 K with the features in the same location possessing the same shape, indicating that the features were not condensed gas that had formed on the capsule. Features with similar shapes and in similar numbers (1 to 5) were observed in most but not all of the DT-filled targets.

Attempts to recover DT-filled cryogenic targets from the cryostat had limited success; all the targets except one exploded as the target warmed and the DT evaporated. In this instance the rate of temperature (and therefore pressure) rise was slower than the rate at which gas permeated out of the capsule so that the burst pressure was not exceeded. The capsule was examined optically and then fractured to image the inner surface with electron microscopy.

Figure 132.9 shows electron microscopy images of the features on the inner surface. Two separate features were imaged using backscattered-electron [Figs. 132.9(a) and 132.9(c)] and secondary-electron [Figs. 132.9(b) and 132.9(d)] modes of operation. The backscattered signal arises from incident electrons elastically scattered off atoms at the surface and is more sensitive to the elemental composition of the surface than is the signal obtained from secondary electrons. Images from the backscattered signal show greater contrast between the

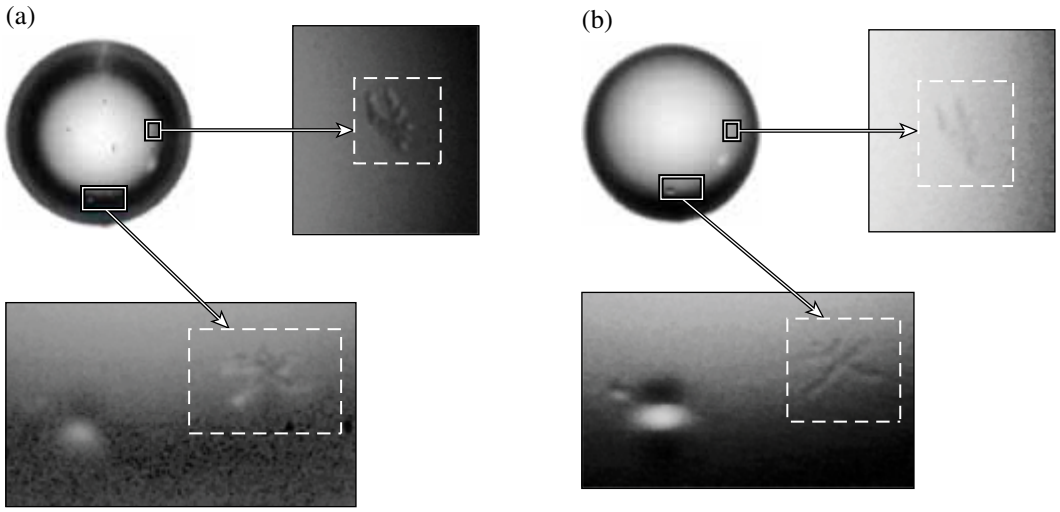

Figure 132.8
A DT-filled target is shown with two distinctive features at (a) 19.5 K and (b) 227 K. Both images were acquired while the target was inside the moving cryostat and were imaged using the existing shadowgraphy optical system. The insets show the features magnified digitally.

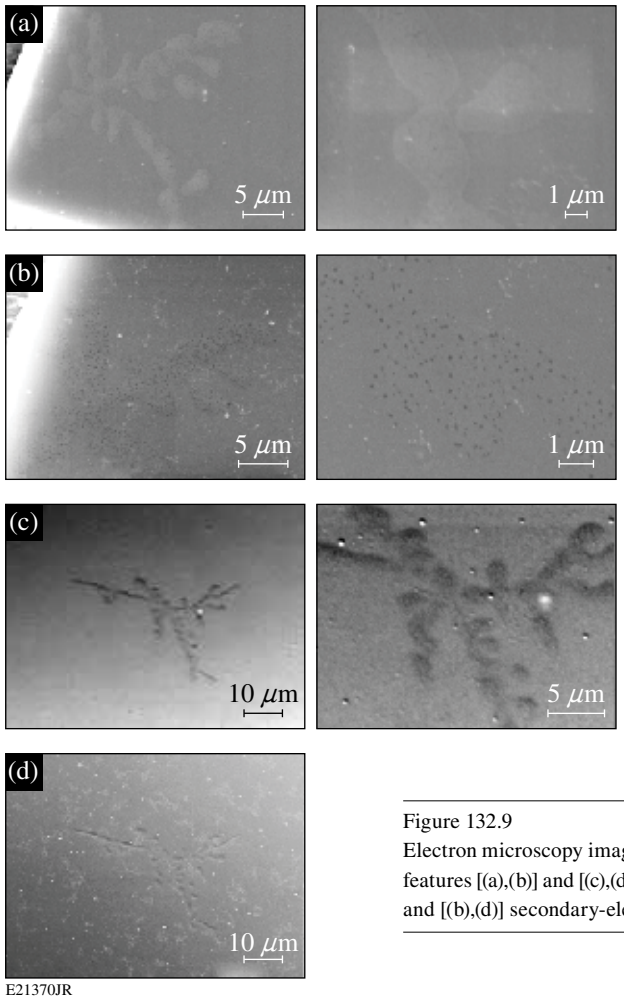

features and the plastic shell than could be obtained from the secondary-electron signal, suggesting that the feature could be associated with a difference in the elemental composition of the material; for example, a difference in the ratio of carbon to hydrogen atoms.

Viewing these features at an oblique angle (Fig. 132.10) provided topographic information: the two-dimensional (2-D) pattern seen in Figs. 132.8 and 132.9 is seen as a series of small domes less than 0.1 μm high when the surface is imaged from an angle of less than 50° to the surface. Imaging the edge of the shell wall at the location where the fracture intersects the dome features revealed no deep-level porosity or void structure [Figs. 132.10(a) and 132.10(b)]. No porosity was observed beneath the dome when a 0.5- × 0.5-μm-sq–shaped, 0.2-μm-deep depression was etched into the dome by repeatedly rastering the electron beam across the surface [Fig. 132.10(b)].

Figure 132.9
Electron microscopy images of the inner surface of the plastic shell recovered from the moving cryostat. Two features [(a),(b)] and [(c),(d)] were imaged and each image was acquired in both [(a),(c)] backscatter signal mode and [(b),(d)] secondary-electron mode. The insets show the features at higher magnifications.

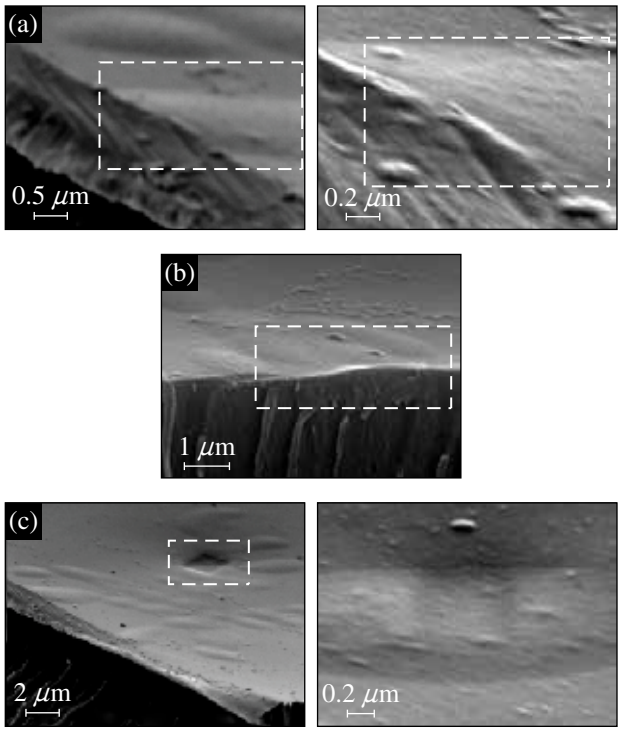

E21371JR

Figure 132.10
The secondary-electron images of the features taken at oblique angles. [(a),(b)] Images are of cross sections through the plastic wall and two domed features (highlighted in the box). The areas highlighted by the rectangular boxes are the regions where the domes intersect the fractured edge of the plastic capsule. (c) A square indentation (denoted by the rectangular box) was etched into the plastic and imaged to see if subsurface porosity was present (it was not).

Radiation Dose and Damage to the Plastic Capsule

Tritium has a half-life of 12.3 years and decays into ^{3}He, releasing an electron with a mean energy of 5.7 keV and a maximum energy of 18.6 keV (Ref. 6). The electron loses energy due to ionization and excitation as it propagates through a medium according to Bethe's relationship:[7]

$$dE/dx = 2\pi e^4 nZ\left[\ln\left(E/I\right)/E\right],$$

where E is the kinetic energy of the electron at position x, n is the number density, Z is the atomic number, and I is the average ionization and excitation energy of the absorber. The effect is that the electron flux to the plastic wall is, to the first order, independent of the DT-gas pressure: electron generation and self-absorption are equally proportional to the tritium density, so increasing the tritium density decreases the shell thickness of tritium near the capsule wall that generates the electron flux that strikes the plastic. The penetration range of the mean and the maximum electron energies in DT and plastic are shown in Table 132.II.

Calculating the dose to the plastic wall assumes that the attenuation of the electron energy is linear with distance. The electron flux (ϕ) to a surface is

$$\phi = \left(1/6\right)\int_0^R \left(1 - x/R\right)\lambda n\,dx,$$

where x is the distance traveled normal to the plastic surface, R is the range of the electron, n is the tritium number density, λ is the probability of tritium atom decay, and the dose (D) is

$$D = E\phi/\rho_m R_m = En\left[\lambda/\left(\rho_m R_m\right)\right]R_T/4,$$

where m is the mass of the absorbing region, ρ_m is the density of the region, R_m is the range in the absorbing region, and R_T is the average range of a 5.7-keV electron in the tritium gas.[8]

The plastic capsules experienced a dose of 259 Mrad during the 17.3 h required to permeation fill the target to 700 bar and the 16.3 h to cool the target to 26 K [Fig. 132.11(a)]. The plastic experienced an additional dose of 136 Mrad during the subsequent 34 h required to form and characterize the ice layer [Fig. 132.11(b)]. Increasing the time to fill the capsule to provide a thicker ice layer, or to permeate through a thinner plastic wall increased the dose to the plastic proportionally. A

Table 132.II: Electron ranges in relevant material.

Material	Density (g/cm^3)	Range for 5.7-keV electrons (μm)	Range for 18.6-keV electrons (μm)
DT (1 bar)	0.000223	2786	35571
DT (10 bar)	0.00223	280	3557
DT (50 bar)	0.0115	57	711
DT (700 bar)	0.156	4	50
DT (ice at 19.7 K)	0.25	2.3	29
Plastic	1.06	0.4	5

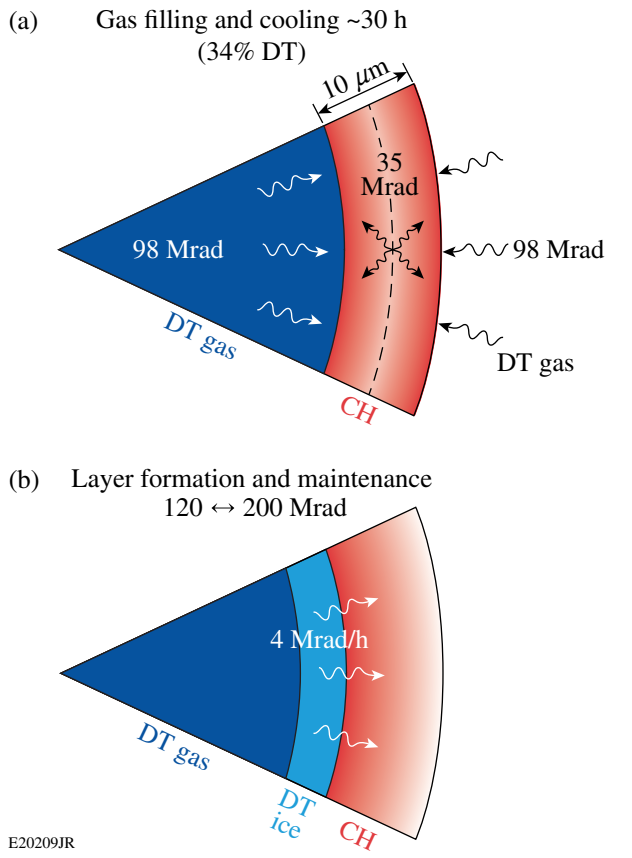

Figure 132.11
A schematic showing the electron dose to the plastic surface from (a) the gas inside and outside the capsule and the gas dissolved in the plastic during the permeation and cooling phase, and (b) the gas/liquid/ice inside the capsule during the layer formation and target storage period before the target is imploded.

portion of this dose was delivered to the plastic from the tritium dissolved in the plastic wall. This dose was

$$D = n\left(1/\rho\right)\lambda E,$$

where n is the concentration of tritium atoms in the material, ρ is the material density, and E is the mean β energy that varied during the pressure ramp as the amount of DT dissolved in the plastic is ~10% of the surrounding gas density. The solubility of deuterium in the plastic was not known; however, it may be estimated from the known solubility of hydrogen in polymers with comparable densities and elemental composition: neoprene has a solubility of 0.014 scc/cc-atm, corresponding to a dose of 35 Mrad for the 30-h–duration filling and cooling process.

Features attributed to tritium damage were present when the target was first observed after filling. No additional features developed while the ice layer was formed and until the target was imploded (up to 3 weeks). This suggests that a radiation dose alone is not a sufficient condition for the formation of features, but the absence of these features in D_2-filled shells indicates that it is a necessary condition.

These calculations are a conservative estimate since they assume an average electron energy of 5.7 keV, whereas the actual energy distribution is non-Gaussian and is skewed to higher energy values.

Stresses that Develop During Permeation Filling and Cryogenic Transport

The process of filling targets by permeation, cooling them, and transporting them from the permeation cell to individual moving cryostats subjects the capsules to compressive and tensile stress that approaches the limits for the plastic material (~60 MPa).

DT is permeated into the capsule at 295 K over a 24-h duration and subjects the capsules to a constant compressive stress. The magnitude of the compressive stress is limited by the buckling pressure of the shell, which is ~0.3 to 1 MPa for capsules with the dimensions used here (wall thickness was 5 or 10 μm) (Ref. 9). These stress levels are a worst-case instantaneous load averaged over the entire shell wall and the time-averaged compressive stress is ~0.2 MPa. Compressive stresses greater than 1 MPa could arise from near-instantaneous pressure spikes that occur as a result of isolated events (such as compressibility changes in the hydraulic fluid or rapid volume changes associated with valves closing) over a time interval that is shorter than the measurement duration of the pressure sensor (~2 s). Further, regions of the plastic wall that deviate from perfect circularity could experience approachably higher localized stress as the compressive hoop stress becomes increasingly a shear stress depending on the deviation from circularity.

Cooling the target from 300 K to 26 K (to recover the gas inside the pressure vessel but outside the capsule) takes 18 h and subjects the capsule to a maximum burst pressure of 0.8 bar (Ref. 10), equivalent to a tensile stress of 0.081 MPa (Fig. 132.12). As the target approaches 26 K, a compressive load forms (~0.1 MPa) on the capsule wall. This buckle pressure is an unavoidable consequence of the construction of the equipment that requires the pressure vessel to be sealed with a valve at 300 K (to avoid leakage), and the lower density of the warm gas near the valve results in a higher gas pressure outside the capsule than inside it. Removing the DT gas surrounding the capsule removes the compressive stress in the

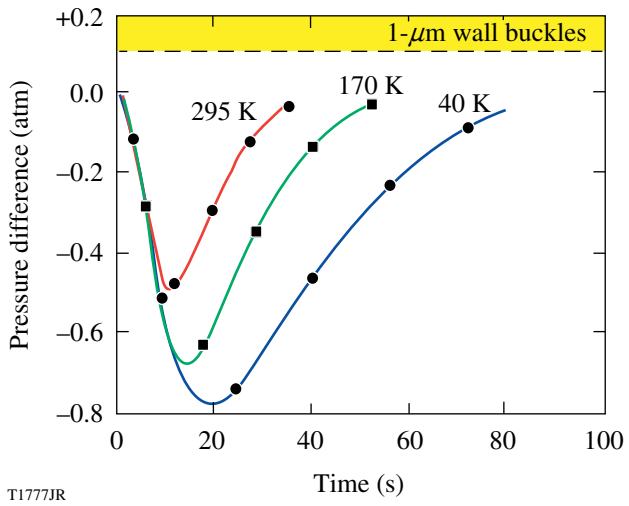

Figure 132.12
Time-dependent average burst pressure exerted on the plastic capsule wall when it was cooled by 1 K. The three curves show the effort of the 1-K temperature step at three separate temperatures: 295 K, 170 K, and 40 K.

plastic and replaces it with a 0.16-MPa tensile stress, resulting from the vapor pressure of liquid DT inside the capsule. A prolonged cyclic stress in the plastic that varies between compressive and tensile is a consequence of these permeation and cooling operations.

Once the capsule has the desired DT inventory, there is a constant heat source inside the capsule from β decay (up to 9 μW) and a heat-exchange gas cools the target. The pressure of the gas must be greater than 100 Pa for cooling to be most effective. The temperature of the capsule (and therefore the pressure in the capsule) depends on the temperature of the boundary (the permeation cell or cryostat) and the distance between the capsule and the boundary. Capsules are maintained below 19 K inside the permeation cell and at an external pressure of 250 Pa (helium). Transferring capsules to the moving cryostat is the process that induces the greatest known stress in the capsule wall, which approaches, and in some cases exceeds, the ultimate yield strength of the plastic. This occurs because the cooling process is inefficient [the helium cooling gas pressure in the cryostat is low (7 Pa), and the distance between the capsule and the cold surface is large (>15 cm)] and the process is lengthy. The capsule begins the transfer process at ~16 K and has taken up to 45 min to be inserted into the moving cryostat and cooled back to 19 K. The calculated rate of increase in the pressure inside the capsule during this process is shown in Fig. 132.13. This calculation includes the temperature-dependent heat capacity, heat-of-fusion, and heat-of-evaporation of DT. Figure 132.14 shows a target that overheated and ruptured during a transfer process that took too long to complete; a portion of the plastic shell is missing and features in the plastic wall appear similar to those imaged with the electron microscope.

One experiment that demonstrated the importance of stress on the formation of the features was to include a capsule with a

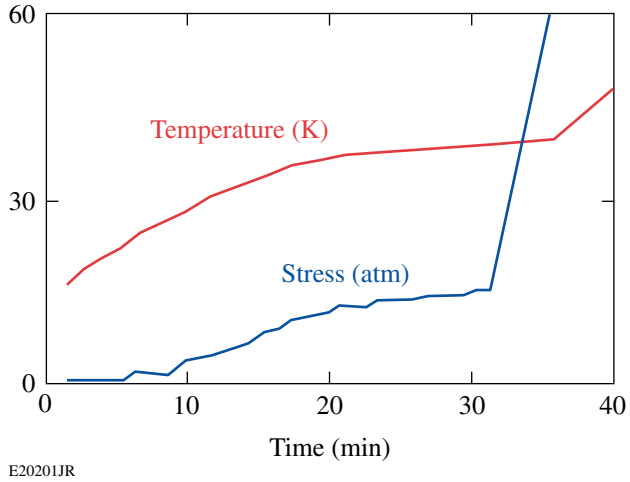

Figure 132.13
Calculated rise in temperature and pressure of a DT target when it was transferred from the permeation cell to the moving cryostat inside the Fill/Transfer Cryostat. β decay is the sole heat source.

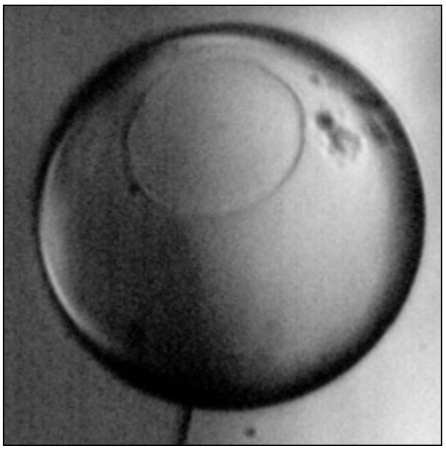

Figure 132.14
Image of a ruptured target inside the moving cryostat that overheated during transfer. A circular portion of the capsule is missing. Note the presence of a sizeable feature near the rupture area that is similar to the features identified as domes in the target (Fig. 132.8) that was recovered.

hole in it with other intact capsules in a fill cycle. This subjected all the capsules to the same radiation dose but the capsule with the hole did not experience the stresses experienced by the other capsules during the permeation, cooling, and transport phases. No evidence of these features was observed in the capsule containing the hole.

Improvements in the equipment and process used to transfer targets to the moving cryostat decreased the time required for the transfer and allowed for a higher helium gas pressure to be used in the moving cryostat. This substantially reduced the number of defects in the capsules.

Radiation-Relevant Properties and Behavior of ICF Capsules

Plastic capsules for ICF experiments are made using a vapor-phase, glow-discharge polymerization process where hydrocarbon radicals are formed in a low-temperature plasma and deposited on a mandrel that is subsequently removed.[11] The carbon-to-deuterium atomic-percent ratio is 0.53:0.47. The fraction and distribution of carbon–hydrogen and carbon–carbon single, double, and triple bonds throughout the capsule wall are stochastic. The polymer cannot be characterized by a molecular weight and the material is better defined as an amorphous hydrocarbon structure where on average one carbon atom is bonded to at least two other carbon atoms to form the structural backbone, and one carbon is bonded to two or three deuterium atoms to form branching side chains. No information regarding the radiation toughness of this material is available, although the material may be expected to have slightly higher radiation toughness than materials with comparable elemental ratios (such as polystyrene) because of the higher carbon-to-deuterium ratio and greater fraction of carbon–carbon double and triple bonds. It is speculated that the regions of the plastic wall that exhibit the domed features possess a locally higher fraction of species that are more likely to experience a density change when the chemical bonds are broken and subsequently rearranged.

Radiation damage from β electrons will rupture carbon–carbon and carbon–deuterium bonds (bond energies are 3.3 eV/bond and 3.9 eV/bond, respectively) at a high rate given the 5.7-keV mean energy of the electrons and flux of 7.4×10^9 electrons/s, which equates to 10^{13} bond ruptures per second. The majority of the bonds subsequently reform; however, carbon atoms may reform with neighboring carbon atoms rather than the ones from which they separated (possibly making double or triple bonds), or they may bond with nearby deuterium atoms formed in the D–T → D + ^{3}He + e$^-$ (5.7-keV) dissociation process. Should sufficient changes occur in a localized region of the capsule wall, the density and mechanical properties of the area will be altered. The behavior of an alternative plastic material with an estimated lower radiation toughness [poly(α-methyl)styrene (PAMS)] based on its structure was tested by filling a comparably dimensioned PAMS capsule with DT. (Capsules made from PAMS and glow-discharge polymerizations are the only ones available for testing and neither material has known radiation toughness values.) A feature larger than those typically observed in standard GDP (glow-discharge plasma) shells was observed in the PAMS capsule (Fig. 132.15).

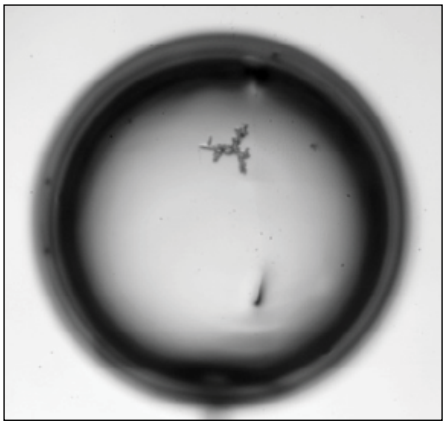

E21373JR

Figure 132.15
Image of a feature in a PAMS [poly(α-methyl)styrene] shell that was filled with DT along with standard GDP (glow-discharge plasma) shells.

Conclusion

Domed-shaped defects with large footprints (>20 μm) and small heights (<0.1 μm) were observed on the inside surface of plastic ICF shells that were permeation filled with DT and cooled to form ignition-scale targets. These features were not present on targets that were processed similarly and filled with D_2 instead of DT nor were they present on targets filled through a fill tube. A combination of high-radiation doses and stress levels inside the plastic wall were required for their formation. It is unclear which stage of the permeation filling, cooling, and transfer steps was responsible for their formation; however, it is clear that these features do not propagate in size or number once the ice layer has formed. There was no evidence of any porosity in these features nor were these features a result of blistering. These observations, combined with data from backscatter- and secondary-electron microscopy, suggest that the scission and reformation of carbon–carbon and carbon–hydrogen bonds may cause a localized decrease in the density of the material

that is manifested as a small-scale swelling. Other possible causes are not precluded, although no other mechanism has been identified that is consistent with all the data.

ACKNOWLEDGMENT

Electron microscopy of the tritium-contaminated plastic capsule was performed by General Atomics using dedicated equipment configured for handling radiation-exposed materials. We thank Abbas Nikroo and David Wall for their support.

This work was supported by the U.S. Department of Energy Office of Inertial Confinement Fusion under Cooperative Agreement No. DE-FC52-08NA28302, the University of Rochester, and the New York State Energy Research and Development Authority. The support of DOE does not constitute an endorsement by DOE of the views expressed in this article.

REFERENCES

1. V. N. Goncharov, T. C. Sangster, T. R. Boehly, S. X. Hu, I. V. Igumenshchev, F. J. Marshall, R. L. McCrory, D. D. Meyerhofer, P. B. Radha, W. Seka, S. Skupsky, C. Stoeckl, D. T. Casey, J. A. Frenje, and R. D. Petrasso, Phys. Rev. Lett. **104**, 165001 (2010).

2. E. Mapoles, Lawrence Livermore National Laboratory, private communication (2011).

3. T. J. B. Collins, J. A. Marozas, K. S. Anderson, R. Betti, R. S. Craxton, J. A. Delettrez, V. N. Goncharov, D. R. Harding, F. J. Marshall, R. L. McCrory, D. D. Meyerhofer, P. W. McKenty, P. B. Radha, A. Shvydky, S. Skupsky, and J. D. Zuegel, Phys. Plasmas **19**, 056308 (2012).

4. E. A. Evans, *Tritium and Its Compounds*, 2nd ed. (Wiley, New York, 1974).

5. D. R. Harding, T. C. Sangster, D. D. Meyerhofer, P. W. McKenty, L. D. Lund, L. Elasky, M. D. Wittman, W. Seka, S. J. Loucks, R. Janezic, T. H. Hinterman, D. H. Edgell, D. Jacobs-Perkins, and R. Q. Gram, Fusion Sci. Technol. **48**, 1299 (2005).

6. K. C. Jordan, B. C. Blanke, and W. A. Dudley, J. Inorg. Nucl. Chem. **29**, 2129 (1967).

7. G. F. Knoll, *Radiation Detection and Measurement*, 3rd ed. (Wiley, New York, 2000).

8. Canadian Fusion Fuels Technology Project, Ontario, Canada, CFFTP Report I-9219 (1992).

9. A. Nikroo *et al.*, Fusion Sci. Technol. **45**, 229 (2004).

10. E. L. Alfonso, R. Q. Gram, and D. R. Harding, Fusion Sci. Technol. **45**, 218 (2004).

11. S. A. Letts *et al.*, Fusion Technol. **28**, 1797 (1995).

Time-Resolved Carrier Dynamics in Si-on-Glass Absorbers for Photovoltaic Cells

The first amorphous silicon (a-Si) photovoltaic (PV) solar cell was fabricated in 1974 (Ref. 1). By the 1980s, commercial a-Si modules were limited to about 5% efficiency[2] because of a light-induced degradation called the Staebler–Wronski (SW) effect, which diminishes the efficiency of a-Si cells over time due to the creation of recombination centers.[3,4] While the impact of the SW effect could be minimized by reducing the intrinsic absorber thickness to below 250 nm, this also limited the conversion efficiency. Therefore, double-junction cells, such as a-Si–a-Si (Refs. 5 and 6) or a-Si–a-SiGe (Ref. 7), were the obvious path around the above limitations. Independently, the successful growth of microcrystalline silicon (mc-Si), a viable absorber material, was made possible by improvements in gas purification and the implementation of very high frequency (VHF) discharges. As a result, the commercialization thrust of thin-film Si PV cells has been focused on the a-Si–mc-Si tandem.[8] Recently reported stabilized efficiencies of a-Si–mc-Si tandem cells have been as high as 11.9% as a result of cell-design optimization and the use of light-management techniques throughout the device stack.[9] Further improvements, however, require better control of the growth process of the a-Si and mc-Si films to enhance their electron-hole recombination time, via reduced defect formation,[10] improved grain-boundary passivation, and minimized unwanted contaminants.[11] While the empirical approach to determining the optimized deposition is preferred, it would be time consuming and cost prohibitive to use the actual completed cell characterization and analysis as a feedback mechanism. In this work, we demonstrate that a time-resolved, optical pump–probe technique provides an effective means for determining the nonequilibrium carrier dynamics for feedback on the Si growth process. We have collected a large family of normalized reflectivity change ($\Delta T/T$) waveforms of various a-Si and mc-Si films, deposited under different conditions, to determine the optimum deposition parameter space.

The basic structure of a thin-film Si tandem cell, designed in a superstrate geometry on a transparent conductive oxide (TCO)–coated glass, is shown schematically in Fig. 132.16 (Ref. 12). Presently, the most common is low-iron, soda-lime float glass with a fluorinated tin oxide as a TCO material

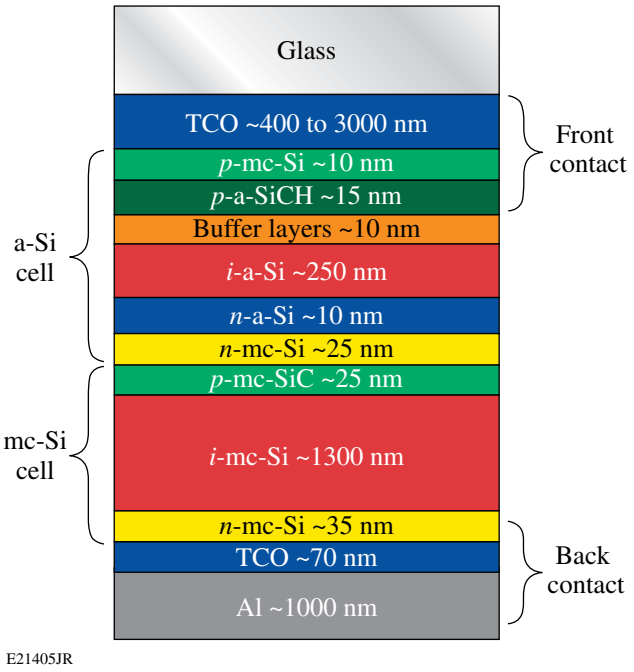

Figure 132.16
Schematic showing the layer structure of a typical Si tandem cell.

applied in-line on the float-glass process by atmospheric pressure chemical vapor deposition (APCVD).[13] In addition, other materials, such as boron-doped, aluminum-doped, or gallium-doped zinc oxide coatings, are utilized in the Si tandem PV cells. Both the a-Si cell and the mc-Si cell are *p-i-n* structures and drift-type devices with highly doped *p* and *n* layers to set up a built-in field. Therefore, for the *i* region, the a-Si and mc-Si materials with the best-possible electron lifetime and mobility are required to ensure an efficient drift under the built-in field of the *p* and *n* contacts, particularly for the a-Si film characterization by a very low hole mobility.[14]

Two sets of Si-on-glass samples were deposited for this study, and the growth conditions, band gap E_G, and optical properties (complex index of refraction; *n* and *k*) are listed in Table 132.III. The first set ("S" samples) was deposited using a plasma-enhanced CVD method, and the fabricated films

Table 132.III: Deposition conditions and measured index and band gap of a-Si films used in this study. The doping type, deposition conditions [hydrogen dilution ratio, radio frequency (rf) power, and pressure], and measured index and bandgap are listed.

		Deposition conditions				Spectroscopic ellipsometry measurements at 632 nm		
Sample	Type	Ratio $\left(H_2/SiH_4\right)$	rf power (W)	Pressure (mtorr)	Thickness (nm)	E_G (eV)	n	k
H032811S1	p	0.75	15	300	251.8	1.773	3.181	0.022
H032811S2	n	0.75	15	350	521.6	1.671	3.586	0.051
B032811S3	i	0.25	15	375	455.7	1.705	3.730	0.044
B032811S4	i	5	20	1000	342.4	1.680	3.864	0.057
B032811P3	i	5	20	1000	390.3	1.676	3.910	0.058
B032811P4	i	10	50	1000	506.9	1.818	3.651	0.015
B032811P5	i	1	15	1000	291.3	1.650	3.850	0.066

were primarily p-type SiCH and n-type a-Si films. Of notable interest, sample H032811S1 was deposited with a CH_4/SiH_4 ratio of 0.85 and a BF_3/SiH_4 ratio of 1. The "P" samples were deposited by the CVD method with no dopants. Intrinsic Si films grown by this system actually produced better solar cells with lower free-carrier concentration in the i layer. The film thickness and optical properties were determined by measuring the fringe fitting with an n and k analyzer and spectroscopic ellipsometry. The samples were 250 to 500 nm thick. Fits were performed by first fixing the optical model and surface roughness and getting thickness to fit, then fitting the material model, and finally the surface roughness. This method was required to overcome the instability inherent in the n and k fitting routines. Spectroscopic ellipsometry was performed using a commercial ellipsometer, and the data were fitted with JV's DeltaPsi2 software.[15] The a-Si was fit with the Jellison model,[16] and the mc-Si was fit as a crystalline Si using the standard JV's built-in model. Measurements were performed at a 70° angle over an energy range of 1.5 to 6.0 eV.

The carrier lifetime of our femtosecond pump–probe spectroscopy was characterized in a two-color setup using an optical system analog similar to that used by Zhang *et al.*[17] The pump beam had a 400-nm wavelength and an 800-nm probe. Special care was taken to ensure proper alignment of the beams to avoid any beam "walking" since, contrary to most femtosecond pump–probe experiments, we were interested not only in the early, fastest time evolution of the photoresponse, but also in the long relaxation tail. The latter was required in order to properly resolve the Shockley–Read–Hall recombination process,[18,19] and, correspondingly, our delay stage had a traveling range of over 30 cm. A large family of normalized transmissivity change ($\Delta T/T$) waveforms was measured at room temperature. Each sample was tested at least three times at three different spots in order to average any film inhomogeneities. All collected transients had the same general shape and consisted of a pump-pulse–limited rising edge and a bi-exponential decay. An example, in this particular case a recorder for the S3 sample, is shown in Fig. 132.17. Based on our phenomenological fitting, the initial fast relaxation was ascribed to electron–optical phonon cooling of highly excited electrons with the corresponding characteristic time constant τ_{cool} varying from 2.4 ps and 25.7 ps for the S1 and S3 samples, respectively, to 79.2 ps for the P3 sample. We interpret the subsequent relatively slow relaxation as the Shockley–Read–Hall recombination with

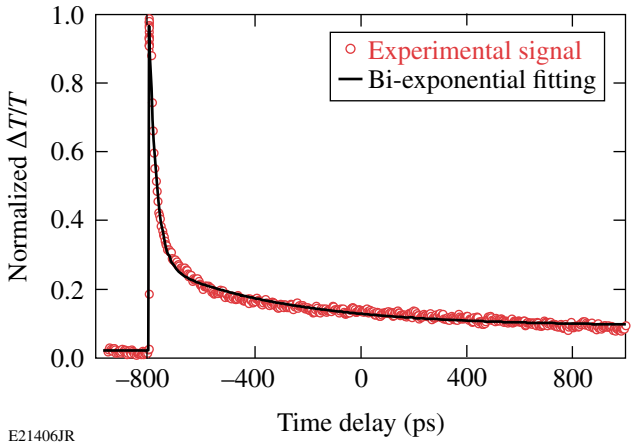

Figure 132.17
An experimental, normalized $\Delta T/T$ transient of the sample H032811S3 and a fit consisting of an error (erfc) function (rising edge) and bi-exponential relaxation (falling part).

the recombination time τ_{rec} varying from 76.4 ps and 490.5 ps for the S1 and S3 samples, respectively, to 954 ps for the P3 sample. As a result, we can see that both τ_{cool} and τ_{rec} vary substantially with the Si deposition process, with the P-type samples exhibiting the longest and most-desired τ_{rec} values.

Although the above phenomenological model provided direct indication of the desired growth conditions for maximized electron lifetime in Si PV absorbers, it did not provide physical insight into the actual carrier relaxation dynamics. It is well known that in a-Si and mc-Si materials, trapping centers strongly influence the carrier dynamics of the material.[20–22] The early trapping model for a-Si was proposed by Tiedje *et al.* based on drift-mobility measurements.[23] The underlying concept for the model consists of a continuum of energy states instead of a discrete set. In a perfect crystal, the valence and conduction band gap edge energies are well defined. In disordered semiconductors, however, the distribution of energy states begins with transport states occupying the energy levels of the material, i.e., the conduction and valence bands. This distribution continues into the energy gap as trap states. These states form a so-called band tail, and their distribution decreases exponentially near the band edge. The widths of these exponential distributions for both the conduction and valence band tails are asymmetrical. In fact, for a-Si, the width of the valence band tail is roughly twice that of the conduction tail.[24,25] For a-Si, the above model has been confirmed through electron photoemission[26,27] and optical absorption[28] measurements.

Jepsen *et al.*[29] proposed a dynamical model that involves shallow trap sites in the band gap to reproduce the transient photoresponse of carriers in optically excited and pulsed THz-probed mc-Si wafers. A schematic of the proposed relaxation process is illustrated in Fig. 132.18. After absorption of a femtosecond laser pulse, the excited electrons achieve the quasi-equilibrium Fermi distribution very rapidly (within ~10 fs). Next, they lose their energy via relaxing toward the bottom of the conduction band through the electron–optical phonon interaction. After that, electrons are very likely to be trapped by the band-tail sites near the conduction-band edge. However, after all these traps are filled, the remaining photoexcited electrons are forced to directly decay to the valence band through the nonradiative electron-hole recombination, i.e., the Shockley–Read–Hall process. Independently, over time, the trapped electrons can also be released to the valence band by recombination on a time scale that cannot be distinguished from the across-the-band gap recombination time τ_{rec}. Mathematically, the above scenario corresponds to a set of linear rate equations for concentrations of photoexcited electrons (N_{hot}),

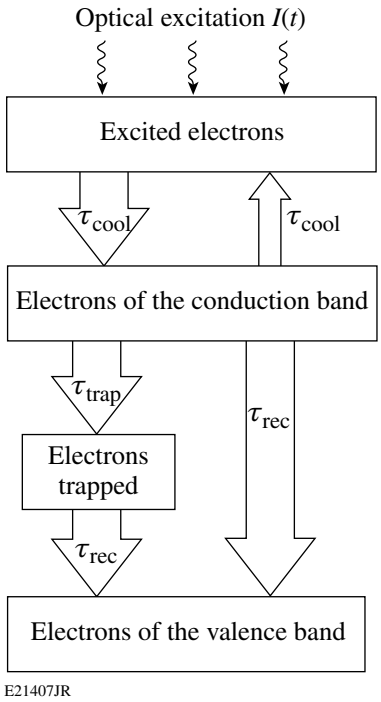

Figure 132.18
Schematic diagram of the dynamics of the carrier relaxation process for a-Si.

electrons at the bottom of the conduction band (N_{con}), and trap states N_{trap}, listed below:

$$\frac{dN_{hot}}{dt} = I(t) - \frac{N_{hot} - N_{con}}{\tau_{cool}}, \tag{1}$$

$$\frac{dN_{con}}{dt} = \frac{N_{hot} - N_{con}}{\tau_{cool}} - \left(\frac{1}{\tau_{trap}} + \frac{1}{\tau_{rec}}\right)N_{con}, \tag{2}$$

$$\frac{dN_{trap}}{dt} = \frac{N_{con}}{\tau_{trap}} - \frac{N_{trap} - N_{trap,e}}{\tau_{rec}}, \tag{3}$$

$$\tau_{trap} = \frac{\tau_{trap,max}}{1 - N_{trap}/N_{trap,max}}, \tag{4}$$

where $I(t)$ is the optical pump-pulse intensity and is assumed to be Gaussian with a width of 100 fs, τ_{trap} is the trap lifetime, and $N_{trap,e}$ is the final concentration of electrons in the trap sites. We stress that τ_{trap} actually depends on a function of the number of available trap sites and their individual lifetimes and is given by Eq. (4), with the $N_{trap,max}$ and $\tau_{trap,max}$ representing the maximum concentration of trap sites in the sample and the

longest trapping time, respectively. As compared to the equations introduced in Ref. 22, we added an extra term in Eq. (1) that is responsible for the re-exciting of some of the cooling electrons by nonequilibrium optic phonons.

Figure 132.19 shows experimental $\Delta T/T$ transients (red circles) and corresponding, simulated temporal evolutions for N_{hot} (dashed blue line), N_{con} (solid green line), and N_{trap} (solid black line) densities for four selected samples, namely, S1, S3, P5, and P3. First of all, we note that in each case the overall relaxation dynamics of photoexcited carriers, N_{hot}, fits the experimental data extremely well. At the same time, there is a considerable difference in the behavior of concentrations of trapped electrons, N_{trap}, among the various samples, providing crucial information on the difference in the density of trap sites and their trapping efficiency in samples fabricated using various methods. Figures 132.19(a) and 132.19(b) show that in both cases (samples S1 and S3), the densities of trapped electrons are large and the trapping is clearly very efficient and effective; for the S1 sample, it reaches approximately 90% with the direct across-the-band gap recombination channel, N_{con}, representing just the background. For the S3 samples, the proportions are less dramatic, even though most of the photoexcited electrons are trapped. For these samples, traps are filled fast and remain occupied (N_{trap} almost constant) at the end of our >1-ns-wide observation window. We believe that, actually, $\tau_{trap,max}$ for these a-Si samples is very likely to be longer than the pulse repetition time of our laser (~13 ns) and in our experiments the traps are being emptied by the next incoming ultraviolet (400-nm) pump pulse. In contrast to the S-type samples, for the P5 sample [Fig. 132.19(c)], the density of trapped electrons is low, while for the P3 sample [Fig. 132.19(d)], it can be neglected. Especially in this latter case, the hot carrier dynamics N_{con} is clearly governed by the

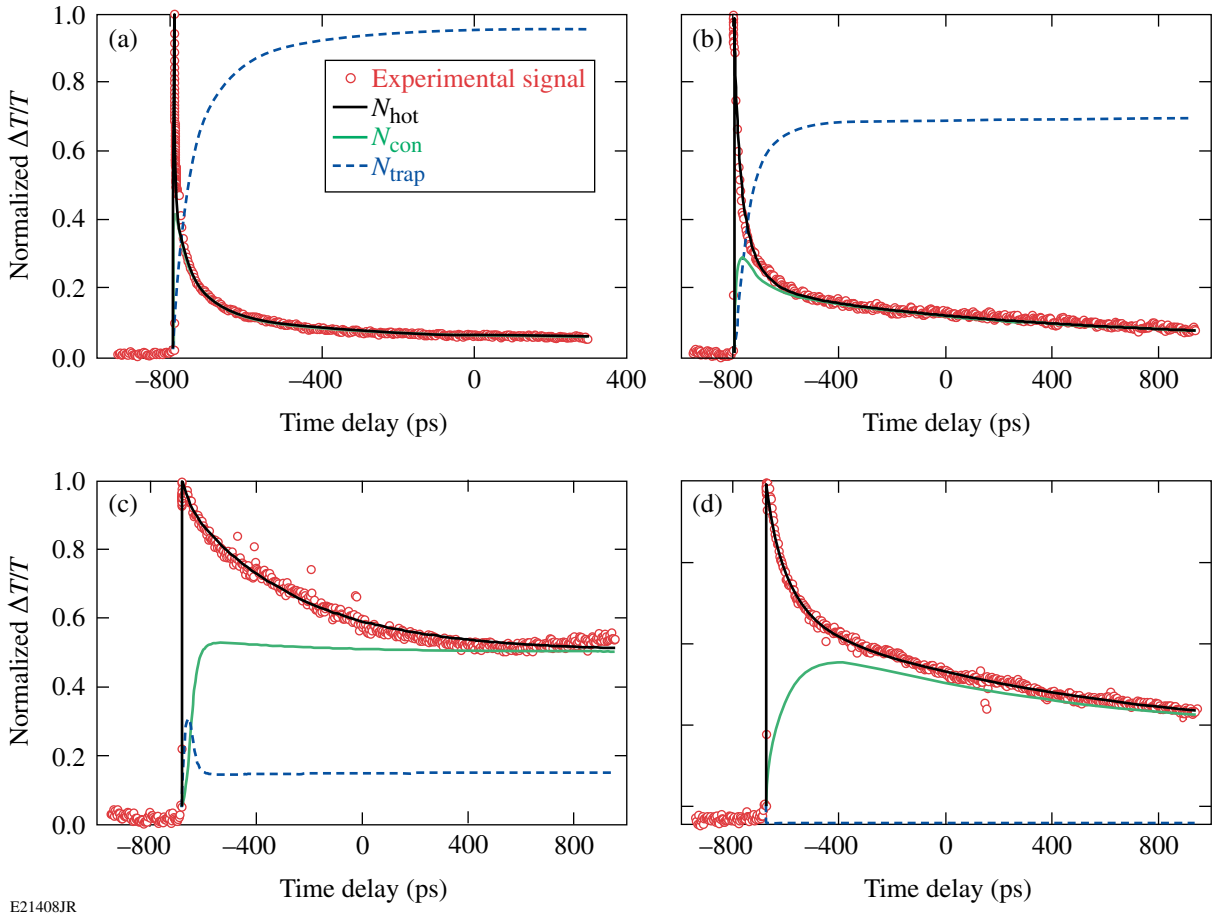

Figure 132.19
Experimental, normalized $\Delta T/T$ transients of the samples (a) H032811S1, (b) H032811S3, (c) B032811P5, and (d) B032811P3 and the corresponding simulation results based on Eqs. (1)–(4).

electron-hole recombination process, resulting in the longest value of the experimental τ_{rec} time.

The film growth conditions presented in Table 132.III corroborate with our observations. Sample H032811S1 is *p* type; therefore, its trap density is expected to be very large. The other three samples are intrinsic films with no doping; therefore, the number of trap sites should be lower. Samples B032811P5 and B032811P3 were fabricated using a growth apparatus in which the hydrogen dilution was increased as compared to the growth with the S-type samples. Since increasing hydrogen dilution shifts the material deposition from a-Si to mc-Si, we can conclude that the trap site's density has been significantly reduced in mc-Si specimens.

Finally, our S4 sample represents a very interesting case, as shown in Fig. 132.20. In this case, a significant portion of electrons is initially trapped; however, the trap lifetime is shorter than our measurement window. Therefore, we observe that at longer times, traps start to release electrons that, subsequently, "drop" to the valence band through the recombination process.

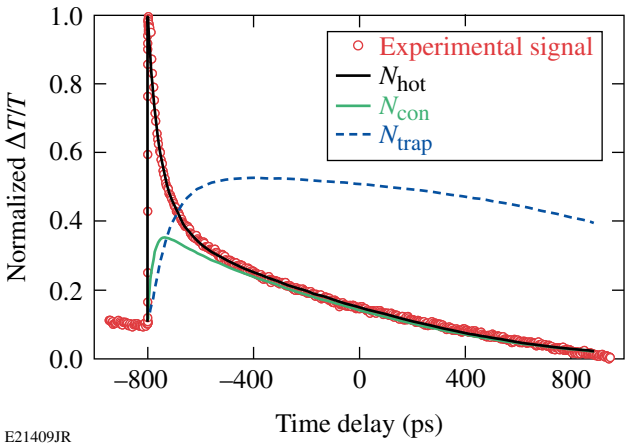

Figure 132.20
Experimental, normalized $\Delta T/T$ transients of the sample H032811S4 and the corresponding simulation results based on Eqs. (1)–(4).

Our femtosecond spectroscopy pump–probe experimental studies and subsequent simulations have proved that shallow trap sites in the band-tail states play a very important role in the relaxation of excited carriers in both a-Si and mc-Si samples. The relaxation dynamics reflects the trap-site densities and trapping lifetime in the samples, providing much-needed feedback on the control of wafer growth conditions. The latter is a crucial element for designing and optimizing new generations of Si-absorber–based PV solar cells with higher efficiencies.

ACKNOWLEDGMENT

This work is supported in part by the Corning, Inc., grant to the University of Rochester and by the New York State NYSTAR grant to the University of Rochester Center for Emerging and Innovative Sciences. J. Serafini acknowledges support from the Frank Horton Graduate Fellowship Program at the University of Rochester's Laboratory for Laser Energetics, funded by the U.S. Department of Energy Office of Inertial Confinement Fusion under Cooperative Agreement No. DE-FC52-08NA28302 and the New York State Energy Research and Development Authority. The support of NYSTAR and DOE does not constitute their endorsement of the views expressed in this article.

REFERENCES

1. D. E. Calson, U.S. Patent No. 4,064,521 (20 December 1977).
2. D. E. Carlson *et al.*, J. Mater. Res. **13**, 2754 (1998).
3. D. L. Staebler and C. R. Wronski, Appl. Phys. Lett. **31**, 292 (1977).
4. P. Stradins, Sol. Energy Mater. Sol. Cells **78**, 349 (2003).
5. R. Platz *et al.*, Sol. Energy Mater. Sol. Cells **46**, 157 (1997).
6. B. Rech, C. Beneking, and H. Wagner, Sol. Energy Mater. Sol. Cells **41/42**, 475 (1996).
7. E. Maruyama *et al.*, Sol. Energy Mater. Sol. Cells **74**, 339 (2002).
9. J. Bailat *et al.*, in *25th European Photovoltaic Solar Energy Conference and Exhibition* (Valencia, Spain, 2010), pp. 2720–2723.
10. P. Torres *et al.*, in *13th European Photovoltaic Solar Energy Conference*, edited by W. Freiesleben *et al.* (Nice, France, 1995), pp. 1638–1641.
11. U. Kroll *et al.*, J. Vac. Sci. Technol. A **13**, 2742 (1995).
12. J. Müller *et al.*, Sol. Energy **77**, 917 (2004).
13. C. Beneking *et al.*, Thin Solid Films **351**, 241 (1999).
14. R. Brenot *et al.*, Thin Solid Films **383**, 53 (2001).
15. DeltaPsi2 ©2006, HORIBA Jobin Yvon, Inc., Edison, NJ 08820-3012.
16. G. E. Jellison, Jr., M. F. Chisholm, and S. M. Gorbatkin, Appl. Phys. Lett. **62**, 3348 (1993).
17. J. Zhang, A. Belousov, J. Karpiński, B. Batlogg, G. Wicks, and R. Sobolewski, J. Appl. Phys. **110**, 113112 (2011).
18. R. N. Hall, Phys. Rev. **87**, 387 (1952).
19. W. Shockley and W. T. Read, Jr., Phys. Rev. **87**, 835 (1952).
20. S. Brehme *et al.*, Mater. Sci. Eng. B **69–70**, 232 (2000).
21. W. Fuhs, P. Kanschat, and K. Lips, J. Vac. Sci. Technol. B **18**, 1792 (2000).
22. E. A. Schiff, J. Phys.:Condens. Matter **16**, S5265 (2004).

23. T. Tiedje *et al.*, Phys. Rev. Lett. **46**, 1425 (1981).

24. X. Deng and E. A. Schiff, in *Handbook of Photovoltaic Science and Engineering*, edited by A. Luque and S. Hegedus (Wiley, Chichester, England, 2003), Chap. 12, pp. 505–566.

25. Q. Gu *et al.*, Phys. Rev. B **52**, 5695 (1995).

26. L. Ley, J. Non-Cryst. Solids **114**, 238 (1989).

27. W. B. Jackson *et al.*, Phys. Rev. B **31**, 5187 (1985).

28. G. D. Cody *et al.*, Phys. Rev. Lett. **47**, 1480 (1981).

29. P. Uhd Jepsen *et al.*, Appl. Phys. Lett. **79**, 1291 (2001).

Proton Emission from Cone-in-Shell Fast-Ignition Experiments at the Omega Laser Facility

Introduction

The fast-ignition concept[1,2] has been described thoroughly in literature as one alternative to direct-drive hot-spot ignition. In this scheme a high-energy, high-intensity (10^{15} W/cm^2) laser is used to compress a cold shell containing fusion fuel to high areal densities ($\rho R \sim 1$ g/cm^2). A short-pulse, ultrahigh-intensity laser (10^{19} W/cm^2) is then used to generate megavolt electrons to heat the core of the dense fuel assembly in a time that is short compared to hydrodynamic time scales. The use of two independent laser drivers to compress the fuel assembly and subsequently heat the core allows for higher target gains, in principle, for the same amount of driver energy. This is because high fuel-areal-density cores can be assembled with slow implosion velocities and ignition is achieved by efficiently coupling the short-pulse beam energy to the dense core.[1] In comparison to conventional hot-spot ignition, the symmetry requirement of the fuel assembly in fast ignition is not as stringent; this relaxes the illumination uniformity and power-balance constraints of the driver.

The success of this approach relies on the effective energy coupling between the short-pulse laser and the pre-assembled dense fuel. A high coupling efficiency (CE) depends on the generation of hot electrons and their transport and energy deposition to the dense fuel core. A potential problem is that the generation of energetic electrons will also inevitably accelerate ions. Any energy coupling to ions is a direct-loss channel that must be examined.

The acceleration of ions, and in particular protons, by electrostatic sheath fields set up by hot electrons generated by laser–plasma interaction (LPI) has been observed in both direct-drive[3] and indirect-drive[4] configurations with high-intensity (~10^{14}-W/cm^2) long-pulse beams. Protons and heavier ions produced by ultra-intense (~10^{18} to 10^{19} W/cm^2) short-pulse laser–plasma interactions have also been studied extensively using flat-foil and cone targets. In short-pulse scenarios, laser-to-proton energy conversion efficiency, angular emission of protons from flat-foil targets, focused emission of proton beams, and effects of plasma scale length on proton acceleration have been studied.[5–7] Proton measurements have also been used, in conjunction with ion expansion models,[8–10] to infer the temperature of the LPI-generated hot-electron distribution that accelerates these protons.[11,12]

This article presents the first measurements of fast protons in surrogate cone-in-shell fast-ignitor experiments conducted at the Omega Laser Facility.[13,14] In these experiments, a short-pulse laser was focused into gold cones to generate hot electrons and subsequently heat a pre-assembled dense D_2 core, with the aim to increase the DD-neutron yield by raising the ion temperature.[15] For these experiments, the neutron-yield enhancement caused by core heating has been measured to be a factor of ~4, corresponding to a CE of 3.5% (Ref. 15).

In the context of proton acceleration, these experiments differ from previous work with cone targets and short-pulse lasers in that protons have been used here as a diagnostic tool to (1) assess effectiveness of fast-ignitor coupling to the dense core and (2) determine the energy coupling to protons, a loss mechanism in fast-ignition experiments.

The following sections provide an overview of the experimental setup and charged-particle diagnostics used to measure proton spectra; present proton spectra and maximum energies; discuss where and how the protons are generated; and relate how protons are used to infer the hot-electron temperature for these experiments. The article concludes with a summary of results.

Experiments

The experiments were performed at LLE using both the OMEGA (long-pulse) and OMEGA EP (short-pulse) lasers. OMEGA is a 60-beam neodymium-glass laser capable of focusing 30 kJ of frequency-tripled light at a wavelength of 351 nm to on-target intensities greater than 10^{15} W/cm^2. OMEGA EP consists of four beams, two of which are short pulse, each capable of delivering 1 kJ of 1053-nm light in 10 ps, while the other two are long pulse. In these experiments,[15] 54 OMEGA beams delivering 18 kJ of UV light to the capsule were used to compress the target along a low adiabat ($\alpha \approx 1.5$), which

was achieved using a short single picket, followed by a main drive pulse with a duration of approximately 2.7 ns. A single short-pulse (~10-ps), Gaussian-shaped OMEGA EP beam was then brought to focus inside the OMEGA target chamber. At best focus, 80% of the beam energy was contained within a diameter of approximately 50 μm, resulting in a maximum, beam-averaged on-target intensity of $\approx 6 \times 10^{18}$ W/cm^2. For these experiments, the OMEGA EP power and energy contrast were of the order of 10^6 and 10^4, respectively.[15] Details on the targets can also be found in Ref. 15. In summary, the targets for these experiments were re-entrant gold cones inside 40-μm-thick, deuterated-plastic (CD) shells with a nominal diameter of 870 μm. The cones were either 1.2 or 1.8 mm in length and had an opening half-angle of 17°. The cone tips were flat with a variable tip thickness (5 to 15 μm) and a tip diameter of 10 μm. The cone walls were 10 μm thick inside the shell and 50 μm thick outside. The shells were not gas filled, leaving only the CD shell and the ablated material from it to undergo fusion.

Proton energy spectra were measured using both magnet-based charged-particle spectrometers (CPS1 and CPS2) and wedged-range-filter (WRF) spectrometers.[16] These instruments utilize CR-39 solid-state nuclear track detectors (SSNTD's), which are known to provide information about the energy and species of the detected charged particles.[16] It has been shown recently, however, that there exists CR-39 piece-to-piece variability in its response to charged particles.[17] Therefore, CR-39 alone cannot be used to accurately measure charged-particle spectra and must be paired with an additional particle dispersion mechanism. In addition, CR-39 is immune to electromagnetic pulse and, to some extent, to x rays, making it ideal for short-pulse experiments such as those presented here.

The CPS's feature a 0.1-mm slit and a 7.6-kG magnet to disperse charged particles onto CR-39 detectors. These spectrometers are capable of measuring proton energy spectra in the range of 200 keV to 30 MeV. The low-energy limit is set by filtering (directly in front of the CR-39), which is required to mitigate a very large flux of low-energy charged particles that would otherwise scatter within the diagnostic and saturate the detector. The high-energy limit is set by the magnet dispersion and detector arrangement. The CPS systems are fixed to the OMEGA target chamber at two different polar angles, as shown in Fig. 132.21. In practice, the exponential energy spectra of short-pulse accelerated protons result in a large on-detector proton fluence at lower energies. This may cause saturation of the CR-39 detector at these energies, effectively raising the low-energy limit of this diagnostic. It is worth noting that the CPS cannot resolve heavy ions because of the degeneracy between charge state, mass, and energy that exists for magnetic spectrometers.[16] Filters constructed of mylar and aluminum are overlaid on the CR-39 to filter out these ions. Furthermore, any energetic heavy ions that penetrate the filters are separated from protons on the basis of the contrast and diameter of the tracks they leave on the CR-39.

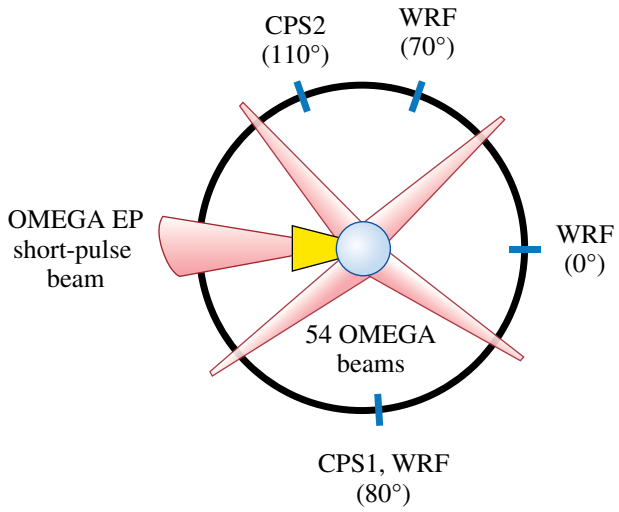

Figure 132.21
Schematic of the experimental setup. The charged-particle spectrometers (CPS1 and CPS2) and wedged-range-filter (WRF) spectrometers positioned at different azimuthal angle were used in these experiments. The coordinate system is defined such that the pole (0°) corresponds to the direction of the short-pulse laser. The OMEGA beams were used to first compress the CD shell, after which the short-pulse OMEGA EP beam was used to produce energetic electrons to heat the deuterium fuel.

The WRF spectrometers use CR-39 overlaid with a piece of wedge-shaped zirconia ceramic (ZrO_2), in which the minimum particle energy required to penetrate the wedge varies along the thickness (dispersion) direction. Since the zirconia wedge cannot be made thinner than 40 μm, the low-energy instrument cutoff for measurement of protons is approximately 3 to 4 MeV. The WRF's are compact (5 cm across) spectrometers that are ideal in probing the implosion at several locations. Several (either three or five) WRF modules, each consisting of two WRF's, were used at a single measurement location to obtain good statistics. Figure 132.21 shows the azimuthal projection of these spectrometers in the OMEGA target chamber relative to the short-pulse beam and target. The coordinate system is defined such that the pole (0°) corresponds to the direction of the short-pulse laser.

The WRF spectrometers were the primary proton diagnostic. They were fielded on nearly every shot, while the CPS was fielded on a handful of shots to corroborate the WRF measurements and provide additional details of the spectrum at energies below the WRF low-energy cutoff. The spectrometers were pointed to the target chamber center, which coincides with the center of the spherical shell. The spectrometers also subtend small solid angles (1 μsr for the CPS and 100 μsr for the WRF). As a result, they measured protons accelerated normal to the CD shell surface for each of the locations shown in Fig. 132.21. In addition, when fielded at 70° and 80°, the spectrometers measured protons accelerated nearly normal to the cone surface since that surface is nearly parallel to the spectrometer aperture because of the 17° cone opening half-angle.

Proton Spectra and Maximum Energies

A typical proton energy spectrum from integrated experiments, acquired using CPS1 (OMEGA shot 56971), is shown in Fig. 132.22. Alongside this spectrum is the proton spectrum for a neutron reference implosion (OMEGA shot 56976), where a similar target was imploded using the same long-pulse configuration (~20 kJ, 54 OMEGA beams) without any short-pulse core heating. It has been well established that long-pulse LPI generates protons up to ~1 MeV (Refs. 3 and 18), consistent with the data shown from the reference implosion. Nearly all of the observed energetic protons, however, arise from short-pulse LPI. These spectra exhibit a high-energy cutoff corresponding to the maximum path-integrated electric fields seen by the ions.

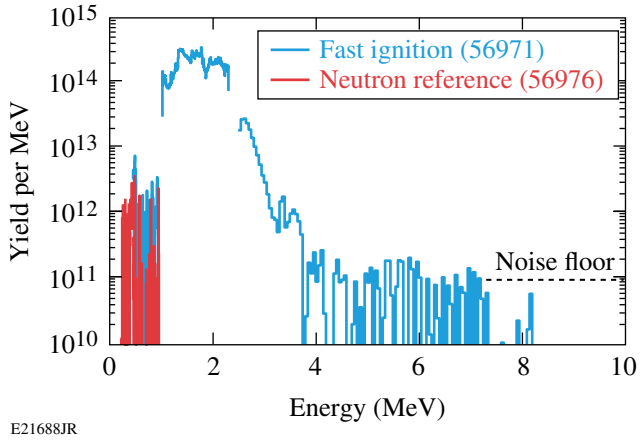

Figure 132.22
Proton spectra measured with CPS1 (80°) on fast-ignition experiments and neutron reference experiments. In both cases, a gold cone-in-shell target was compressed using 54 OMEGA beams (~20 kJ) and a low-adiabat laser drive. For the fast-ignition case, the OMEGA EP short-pulse laser was fired, at peak compression of the target, to generate hot electrons and heat the dense core. These energy spectra were background subtracted, although some residual background is observed in the 4- to 7-MeV range. The gaps in the spectrum at ~1 MeV and ~2.3 MeV are due to the instrument.

Proton energy spectra were measured down to approximately 200 keV using the CPS. As proton emission was anisotropic, it was difficult to precisely measure the total energy lost to protons. On the basis of measurements such as the one shown in Fig. 132.22, we estimate that the total energy carried by these protons is typically of the order of 10 J, or just about 1% of the incident short-pulse laser energy. This number can be compared to the previously inferred 20% coupling efficiency of short-pulse laser energy to hot electrons.[19] Therefore, approximately 5% of the short-pulse laser energy coupled to hot electrons is lost to the acceleration of ions.

The fact that the observed ions were protons (and not deuterons or heavier ions) was confirmed by simultaneous charged-particle measurements using CPS and WRF spectrometers. Since the CPS's use magnetic fields for ion dispersion, it can be shown that the inferred energy of an ion depends inversely on the assumed ion mass.[16] Therefore, the CPS-inferred energy of a deuteron mistakenly identified as a proton will be twice as large as the actual particle's energy. The WRF's have an opposite energy-mass dependence, whereby the inferred energy of a deuteron mistakenly identified as a proton will be lower than the actual particle's energy. It is therefore possible to constrain the particle species using these measurement techniques on the same shot and same polar angle. In particular, CPS1 and the WRF's measure particles at the same polar angle (80°) but different azimuthal angles.

Since the target is composed of a CD shell and Au cone, these protons originate predominantly from hydrocarbon contaminants on the surface of the target. The implications are that the protons do not significantly interact or scatter with the compressed shell. The cone-in-shell target conditions at the time when the short-pulse laser interacts with the cone are schematically illustrated in Fig. 132.23, which shows the cone, the compressed D_2 core (~50-μm diameter), the blowoff plasma surrounding the core, the generated hot electrons, and the accelerated surface protons. The relative timing between the short-pulse laser and the start of the long-pulse compression lasers was varied from shot to shot, but it is typically 3 ns. At this point in time, the blowoff plasma from the ablated shell has expanded for this same amount of time at the ion sound speed $\left(c_s \equiv \sqrt{T/m_i}\right)$, resulting in a characteristic scale length of about 400 μm to 1 mm for typical coronal temperatures of ~2 keV. The blowoff plasma scale length is therefore comparable to the length of the cone, and it is expected that the

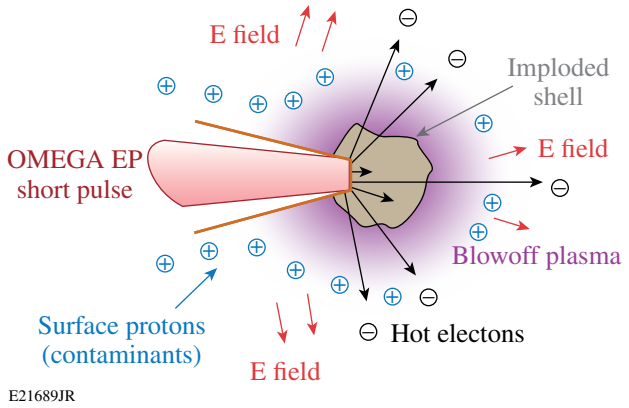

Figure 132.23
Schematic of the target conditions when the short-pulse OMEGA EP laser interacts with the cone tip. The CD shell has been compressed to a diameter of ~50 μm and is surrounded by blowoff plasma from the ablated shell (~1-mm scale length). Interaction of the short-pulse laser with the cone generates hot electrons that accelerate surface-contaminant protons from the ablated plasma.

protons from the target are accelerated in the presence of this long-scale-length plasma.

The maximum proton energy for each shot is of interest since it scales directly with the temperature of short-pulse–generated hot electrons.[20,21] Direct measurements of the maximum energy can therefore be used to qualitatively infer how the hot-electron temperature varies with experimental parameters. The maximum proton energy was measured at various locations around the implosion using the compact WRF spectrometers on several shots (Fig. 132.24). These data incorporate measurements from gold cones with 5-μm-, 10-μm-, and 15-μm-thick tips and 10-μm tip diameters. The data obtained in the direction transverse to the short-pulse beam (80° and 70°) scale with intensity. A χ^2 analysis of the data indicates that these data fit a normalized ponderomotive scaling ($\propto I^{1/2}$) at both 80° (reduced $\chi^2 = 0.96$) and 70° (reduced $\chi^2 = 0.71$). This is further confirmation that these protons are accelerated by short-pulse–generated hot electrons. In addition, since the maximum energies scale with intensity as expected from theory, these protons can be used to estimate a hot-electron temperature, albeit with some caveats (see **Inferred Hot-Electron Temperature**, p. 209).

In contrast to the transverse direction, the maximum energies of forward-going protons (0°) show neither such scaling nor a dependence on cone-tip thickness. In addition, the maximum energies of forward-going protons are lower compared to the transverse-going protons. This is consistent with simulations, which indicate that for these experiments, the hot electrons are emitted in two lobes with half-angles of 57° (with a minimum

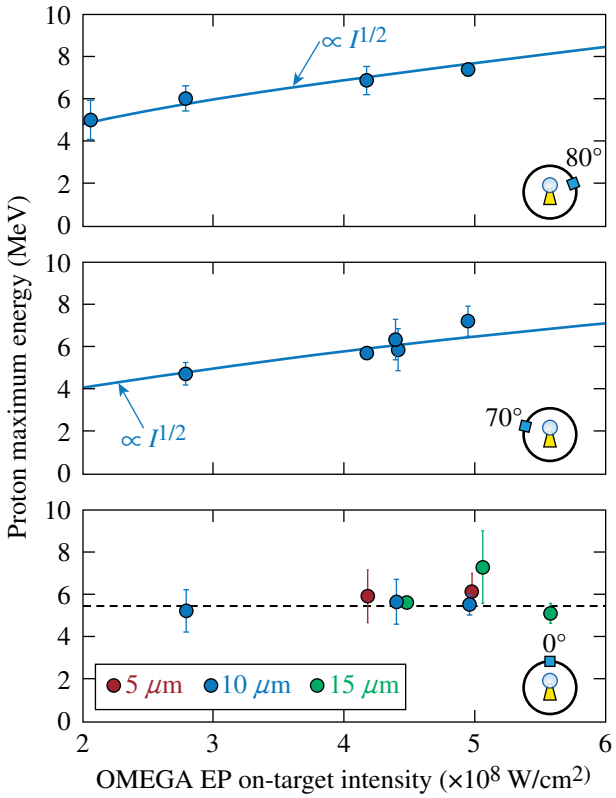

Figure 132.24
Maximum proton energies measured by WRF spectrometers at 80°, 70°, and 0° with respect to the forward short-pulse beam direction. The data points shown are averages over many WRF measurements at one location. The error bars (within 95% confidence limits) were computed from the standard deviation of these multiple measurements. At both 80° and 70°, the data show reasonable agreement with the known ponderomotive hot-electron scaling. The maximum proton energies for the forward beam direction (0°) show neither scaling with intensity nor dependence on cone-tip thickness.

in the forward direction).[22] In this case, it is expected that fewer and less-energetic protons would be observed in the forward direction even when the cone tip is intact, which is consistent with these observations.

In addition, forward-going protons are accelerated by hot electrons that have interacted with the compressed core and lost a significant amount of energy (Fig. 132.23). Some of the slower electrons are even ranged out in the core. The inferred electron temperatures and ρR of the compressed shell (~150 mg/cm^2) are consistent with this notion, as discussed further in **Inferred Hot-Electron Temperature**, p. 209. As a result, the distribution of forward-going electrons has a lower maximum energy and empty regions in velocity space, thereby reducing the energies of forward-going protons relative to transverse protons.

Several WRF's were used to obtain the average maximum proton energies at each location. The standard deviations of these measurements were used to compute the error bars (within 95% confidence limits) shown in Fig. 132.24. Since the spatial separation between adjacent WRF's is of the order of several centimeters, the observed uncertainties in the data arise from both the absolute measurement uncertainty of each WRF (~200 to 300 keV) and possible spatial variations in the maximum energy. For the case of forward-going protons, the uncertainties are as large as ±2 MeV, which is larger than the absolute measurement uncertainty of the WRF spectrometers. Therefore, we conclude that there are real spatial modulations of the maximum proton energy for forward-going protons. These observed larger spatial variations could be the reason why the scaling with intensity is not readily apparent. Furthermore, these variations are consistent with the presence of a stochastic process, such as hot electrons scattering in the compressed shell. For these reasons, it is difficult to infer a hot-electron temperature from forward-going protons, as additional physics must be unfolded from the proton measurement, and we defer to only transverse-going protons when inferring hot-electron temperatures in **Inferred Hot-Electron Temperature**, p. 209.

Source of the Protons

There is evidence that the observed protons are accelerated from the cone walls rather than from the cone tip, where the laser interacts with the cone. The data presented throughout this article consist primarily of cones 1.2 mm in length, with 10-μm or 40-μm tip diameters and variable tip thicknesses. On a few shots, cones with a length of 1.8 mm (but otherwise identical) were also shot. A comparison of 1.2-mm and 1.8-mm cones showed that the proton yields scale with the square of cone length (and therefore the surface area of the cone, for a fixed cone-opening angle). This suggests that the protons are accelerated from the entire surface of the cone rather than from the tip alone. Since charged-particle spectra were not available for these shots, proton yields could not be directly measured. Instead, relative proton yields were inferred from the neutron time-of-flight (nTOF) data in Fig. 132.25, which shows the raw signals from the nTOF liquid scintillator.[23] For these two shots, the nTOF settings, laser drive, and target parameters were identical with the exception of the cone length. The x-ray flash, which occurs when the short-pulse beam hits the cone, and the 2.45-MeV DD-neutron signals are characteristic of these implosions, as shown in Fig. 132.25. In between these signals are a number of smaller peaks associated with neutrons from (p,n) reactions in the surrounding material. Their arrival time is generally consistent with the maximum energies of the protons

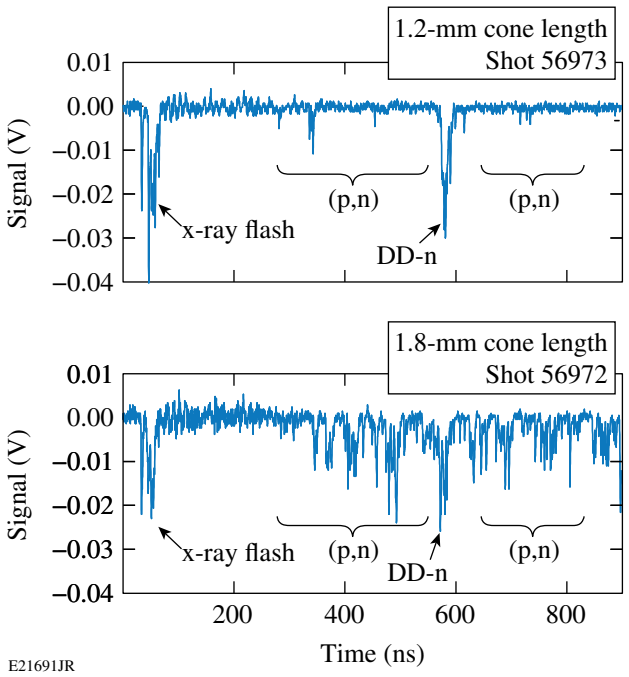

Figure 132.25
Neutron time-of-flight signal (Channel 2), showing the x-ray flash, 2.45-MeV DD-n signal, and neutrons from (p,n). For these two shots, all laser and target parameters were identical with the exception of the cone length, which was 50% greater, corresponding to 2.25× more surface area. The ratio of the total (p,n) signal of these two cone lengths is ~2 to 3, roughly proportional to the ratio of the cone surface areas. This suggests that the protons are emitted over the entire cone surface as opposed to just the tip alone.

shown in **Proton Spectra and Maximum Energies** (p. 206). The integral of these signals from the proton-arrival time (e.g., ~300 ns for 7.5-MeV protons) through 900 ns (excluding the DD-n peak) was computed for three shots: two with 1.2-mm cones and one with a 1.8-mm cone. The ratio of the integrals between the 1.2- and 1.8-mm cones' data were found to be 2.0±0.5 and 3.0±0.3, respectively. These ratios are comparable to the increase in surface area of the two cones (an increase of 2.25×). Since the number of (p,n) neutrons and, therefore, fast protons scale with the area of the cone, it is likely that they are accelerated over the entire surface of the cone.

Throughout the course of these experiments, the timing between the long-pulse OMEGA and short-pulse OMEGA EP beams was varied to find the optimal timing of the OMEGA EP beam for maximum core heating and yield. Optimal timing corresponds to core heating at peak compression of the cold, dense core.[15] For effective coupling of the short-pulse laser energy to the dense core, the cone tip must be intact when the

short-pulse laser is fired. Shock waves launched into the fuel during compression by the long-pulse OMEGA lasers will eventually reach the cone tip, break through, and leave the tip physically destroyed.[15] In this scenario, we expect poor hot-electron production, and, therefore, less-energetic protons. The cone tip was intact for the data shown in Fig. 132.24. For two shots, the timing between OMEGA and OMEGA EP was such that the tip was broken when the short pulse arrived at the tip. Figure 132.26 shows data taken at 80° using CPS1, alongside data from WRF's (80°) and CPS2 (110°). The CPS1 data are generally in excellent agreement with the WRF data. This is expected since these instruments are at the same polar angle. The two shots where the tip was broken are indicated by the open circles; WRF's were not fielded at 80° for these shots. The maximum proton energies were significantly lower (~40%) at 80° and 70° (not shown) when the tip was not intact.

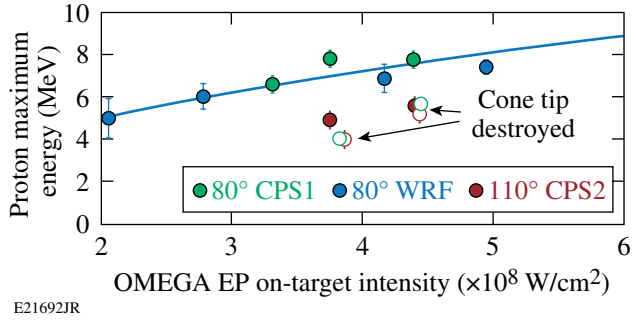

Figure 132.26
Maximum proton energies measured by CPS1, CPS2, and WRF's. The different CPS1 and WRF measurements (at 80°) show good agreement with one another, despite the fact that they sample different azimuthal angles. The solid line is a fit to the data ($\propto I^{1/2}$, with reduced $\chi^2 = 0.72$). The maximum energies of the transverse protons depend on whether the cone tip is intact when the OMEGA EP short-pulse laser arrives at the tip. When not intact (open circles), the maximum energy of the transverse protons (and therefore the fields that accelerate them) are smaller and similar to measurements and large angles (110°), as shown by the CPS2 measurement.

Since the acceleration of transverse-going protons upstream of the cone tip is affected by the presence of the tip, these data suggest that return currents associated with the initial hot-electron production could be responsible for the acceleration of these protons. We speculate that destruction of the tip affects the formation of return currents and could mitigate proton acceleration.

The drastic effect of the cone tip's destruction on electron production and subsequent proton acceleration was not observed in the forward direction, as shown in Fig. 132.27. For two shots, the 10-μm-thick cone tip was shocked before the

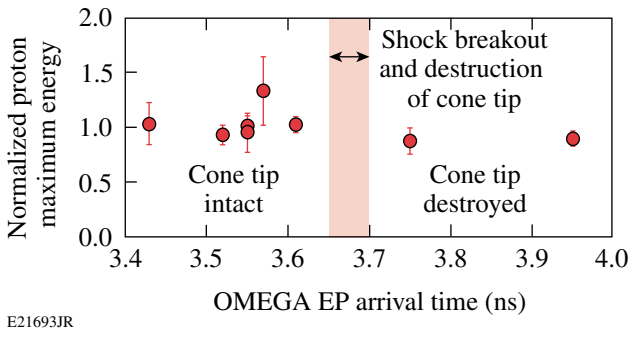

Figure 132.27
Maximum energies of forward-going protons as a function of the OMEGA EP arrival time at the cone tip relative to the start of the long-pulse drive. For comparison, the maximum energies were normalized to the mean of the data shown. Forward-going protons show no significant dependence on whether the cone tip is intact when the OMEGA EP short-pulse laser arrives at the cone tip. The shock-breakout time at the cone tip, which depends on cone-tip thickness, occurs between 3.65 ns and 3.7 ns, as shown schematically.

short pulse arrived at the cone tip. The previously measured shock-breakout time,[15] which varies with tip thickness, is indicated in Fig. 132.27. Therefore, neither the presence of the cone tip nor the thickness of the tip (per Fig. 132.24) affects the acceleration in the forward direction.

Inferred Hot-Electron Temperature

It has been suggested that the presence of a significant preformed plasma inside the cone can lead to filamentation and self-focusing of the short-pulse laser, leading to higher hot-electron temperatures.[15,24] In particular, simulations suggest that for these experiments, a preformed plasma with a scale length of 100 μm is present within the cone at the arrival time of the short-pulse OMEGA EP laser. The large preformed plasma, if present, is due to the laser prepulse that arises from amplified spontaneous emission (ASE). The prepulse is characterized by the laser contrast, defined as the amplitude ratio of the main drive to the prepulse.

Hotter electron temperatures, due to either self-focusing or another physical mechanism, result in more-energetic electrons that would not stop in the core as intended, thereby lowering the overall CE. The average ρR for spherical implosions with comparable laser and target parameters has been previously measured to be approximately 150 mg/cm^2 (Ref. 25). Given this dense core, electrons generated on one side near the cone tip would need energies of 500 keV to penetrate and escape the core, thereby accelerating surface ions in the forward direction. Therefore, we require temperatures of a few hundred kilo-electron volts, which are the expected temperatures in these experiments given the on-target intensities and the ponderomo-

tive scaling.[24] Using the proton data presented in this work, we can place a lower bound on the initial hot-electron temperature to see whether the electrons are hotter than expected from the ponderomotive scaling. The hot-electron temperature is inferred using a plasma expansion model, which links the temperature of an initial hot-electron distribution to the proton maximum energies measured here (80°). In particular, $E_M = \alpha T_H$ (Ref. 21), where α depends on the expansion model.[8–10,26] In general, α has a logarithmic dependence on the hot-electron density (n_0) and the laser pulse duration. The expansion process can be described as isothermal, adiabatic, or two phase, as described shortly. The choice of an appropriate model depends only on the relative time scales of the laser-pulse duration (τ_L) and the transit time of electrons through the target (τ_e) (Ref. 9). For these experiments, $\tau_L \sim 20\ \tau_e$. Therefore, during the first part of the laser pulse, the cone tip is completely populated with hot electrons generated from the preformed plasma on the inside of the cone. For the remainder of the pulse duration, the laser maintains the temperature of these electrons. After the pulse turns off, the electrons expand adiabatically, giving their energy to the ions. A one-dimensional (1-D) fluid model has been previously used to describe this process. This so-called two-phase fluid model[9,26] treats the laser as a source term that acts to maintain a steady temperature during the pulse (isothermal expansion) and then conserves energy between electrons, ions, and the accelerating field thereafter (adiabatic expansion).

The two-phase model relates the hot-electron temperature to the maximum proton energy by the relation

$$T_H = E_M \times \left[2.5 + 0.92 \ln\left(\omega_{pi}\tau_L\right)\right]^{-1}, \qquad (1)$$

where T_H, E_M, ω_{pi}, and τ_L are the hot-electron temperature, maximum proton energy, ion plasma frequency [$\omega_{pi} \equiv (n_{e0}e^2/m_p\varepsilon_0)^{1/2}$], and the laser-pulse duration, respectively. This formula was interpolated from numerical simulations[26] and applies for $\omega_{pi}\tau_L$ in the range of 5 to 100. The maximum energies and laser-pulse duration were measured for each shot, while the plasma frequency was estimated. To estimate n_{e0} and therefore ω_{pi}, we used a variation of a known method.[11] First, we determined the number of hot electrons generated by the short-pulse laser. Recent experiments on OMEGA EP showed that the laser-energy conversion efficiency to hot electrons is 20% for such kilojoule-class short-pulse lasers,[19] and is independent of the laser intensity. The number of hot electrons is then found by dividing the energy converted to hot electrons by the average energy of the electrons, as given by the hot-electron temperature. For the experiments presented in this work, we estimate (self-consistently, from the results of this calculation) that N_e is about 10^{14} to 10^{15}. Next, we obtained the volume by taking the product of the surface area of the cone and the characteristic scale length along the expansion dimension, given by $\approx c \times \tau_L$. The hot-electron density is then just the ratio of the number of hot electrons to volume. Since the plasma frequency ultimately depends on the hot-electron temperature through the density, Eq. (1) is transcendental and must be solved numerically.

It is important to recognize that the density computed here ($n_{e0} \sim 10^{17}$ cm^{-3}) is an overestimate. As discussed in **Source of the Protons** (p. 208), these protons are accelerated from the surfaces of the cone, possibly by hot-electron return currents. In the calculation, we assumed that the hot-electron density is uniform, which is generally not the case. We expect the hot-electron densities to be lower upstream of the cone tip, where the ions are accelerated. In addition, if the protons are indeed accelerated by hot-electron return currents, we expect these currents to be colder and less dense than the initial forward current. From Eq. (1), it is evident that for a given maximum proton energy, an upper bound on n_{e0}, and therefore on ω_{pi}, corresponds to a *minimum* inferred hot-electron temperature.

Even though these ion expansion models apply primarily to thin-foil experiments,[11,12] they can be used in the context of this work. A major distinction, however, between thin-foil experiments and those presented here must be considered to allow for a correct interpretation of the data taken in this work. The scale length of the ion front where the protons are accelerated is very different in these experiments. The two-phase model used here assumes that the initial scale length of this front is small in comparison to the hot-electron Debye length. While this is true for typical thin-foil experiments with short-pulse lasers, in our case the scale length of the blowoff plasma in front of the cone is ~400 μm to 1 mm due to the long-pulse laser's interaction with the capsule. The effective scale length seen by the accelerating protons is roughly of this order, whereas the hot-electron Debye length is ~20 μm. In this case, the maximum proton energy scales inversely with the initial density scale length at the ion front;[27] therefore, the proton energies shown in Fig. 132.24 are significantly lower than that expected by the model. To quantify this difference to some extent, it has been shown that the addition of a 100-μm-scale-length plasma at the ion expansion front (in a scale length otherwise dominated by the much smaller hot-electron Debye length), reduced the observed maximum proton energies by about 4× (Ref. 27). Therefore, in applying the expansion model to these experiments, it is expected that the actual temperatures are much higher than the temperature inferred using the model.

We used protons at 80° to infer the hot-electron temperature. For each shot, Eq. (1) was solved numerically for the minimum inferred hot-electron temperature, shown in Fig. 132.28. The error bars correspond to the uncertainty of the maximum proton energy measurement. The ponderomotive vacuum scaling (for the case of negligible pre-plasma) is shown alongside these data. The minimum inferred temperatures are factors of 2 to 3 higher than the vacuum scaling. If this inferred increase in temperature is due entirely to laser self-focusing in the pre-plasma, this result corresponds to a 3 to 10× enhancement of the incident laser intensity.

It is worth noting that OMEGA EP is known to produce maximum proton energies that are higher in comparison to those of other laser systems.[28] In particular, it has been shown that for a fixed laser intensity (~2 to 8×10^{18} W/cm^2), the maximum proton energy increases as the pulse duration is increased from 1 ps to 10 ps (Ref. 29). Observations indicate that the maximum proton energy increases faster with the laser-pulse duration than models [for example, Eq. (1)] predict. At present, there is no explanation for this observation. We speculate that the effect itself could be caused by hotter electron temperatures (for instance, enhanced absorption or hot-electron refluxing) for longer pulses (10 ps) or by additional physics of the ion acceleration process that is not incorporated into the models at this point. In the context of this work, the effect of the former would be to reinforce our argument about enhanced temperatures. The effect of the latter, if present, would be to compete with the effect of the initial scale length on maximum energies; if taken into account, it would act to lower the minimum temperatures inferred in this work.

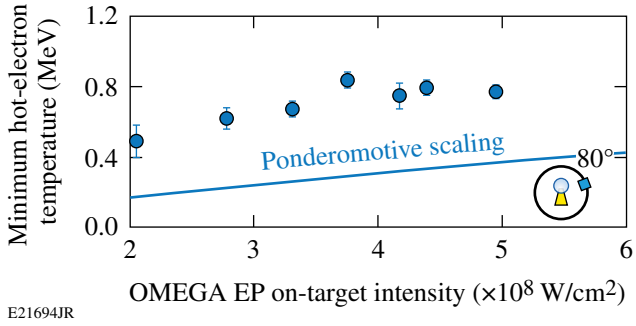

Figure 132.28
Proton-inferred hot-electron temperatures as a function of the incident short-pulse laser intensity. These temperatures are an underestimate and therefore represent the minimum initial hot-electron temperature. Shown alongside the data is the ponderomotive prediction of the hot-electron temperature for the case of negligible preformed plasma inside the cone. These inferred temperatures are 2× to 3× higher than expected.

Conclusion

This work has for the first time characterized the energy loss to fast protons in cone-in-shell fast-ignitor experiments. We estimate that of the order of 10 J, or 1% of the short-pulse laser energy, is lost to fast protons. It has been shown that these protons are accelerated from the entire surface of the cone, rather than from the cone tip alone. Since these protons are accelerated far upstream from where the short-pulse laser interacts with the tip, one possibility is that they are accelerated by hot-electron return currents. This notion is further corroborated by the fact that proton acceleration depends on the integrity of the cone tip.

Finally, these protons have been used to estimate a lower bound on the initial hot-electron temperature. These minimum, proton-inferred hot-electron temperatures (500 to 900 keV) are hotter than predicted from the ponderomotive scaling by factors of 2 to 3. If the enhancement of the hot-electron temperature is due entirely to laser self-focusing, this result corresponds to a minimum enhancement of 3× to 10× the incident laser intensity.

ACKNOWLEDGMENT

This work was supported in part by the Fusion Science Center (Rochester Sub Award PO No. 415023-G), National Laser Users' Facility (DOE Award No. DE-NA0000877), U.S. DOE (Grant No. DE-FG52-09NA29553), Laboratory for Laser Energetics (LLE) (No. 414090-G), and Lawrence Livermore National Laboratory (No. B580243).

REFERENCES

1. N. G. Basov, S. Yu. Gus'kov, and L. P. Feokistov, J. Sov. Laser Res. **13**, 396 (1992).
2. M. Tabak *et al.*, Phys. Plasmas **1**, 1626 (1994).
3. D. G. Hicks, C. K. Li, F. H. Séguin, J. D. Schnittman, A. K. Ram, J. A. Frenje, R. D. Petrasso, J. M. Soures, D. D. Meyerhofer, S. Roberts, C. Sorce, C. Stoeckl, T. C. Sangster, and T. W. Phillips, Phys. Plasmas **8**, 606 (2001).
4. A. B. Zylstra *et al.*, Phys. Plasmas **19**, 042707 (2012).
5. P. McKenna *et al.*, Phil. Trans. R. Soc. A **364**, 711 (2006).
6. S. S. Bulanov *et al.*, Phys. Rev. E **78**, 026412 (2008).
7. K. A. Flippo *et al.*, Phys. Plasmas **15**, 056709 (2008).
8. P. Mora, Phys. Rev. Lett. **90**, 185002 (2003).
9. P. Mora, Phys. Rev. E **72**, 056401 (2005).
10. P. Mora, Phys. Plasmas **12**, 112102 (2005).
11. J. Fuchs *et al.*, Nat. Phys. **2**, 48 (2006).

12. L. Robson *et al.*, Nat. Phys. **3**, 58 (2007).

13. T. R. Boehly, D. L. Brown, R. S. Craxton, R. L. Keck, J. P. Knauer, J. H. Kelly, T. J. Kessler, S. A. Kumpan, S. J. Loucks, S. A. Letzring, F. J. Marshall, R. L. McCrory, S. F. B. Morse, W. Seka, J. M. Soures, and C. P. Verdon, Opt. Commun. **133**, 495 (1997).

14. L. J. Waxer, D. N. Maywar, J. H. Kelly, T. J. Kessler, B. E. Kruschwitz, S. J. Loucks, R. L. McCrory, D. D. Meyerhofer, S. F. B. Morse, C. Stoeckl, and J. D. Zuegel, Opt. Photonics News **16**, 30 (2005).

15. W. Theobald, A. A. Solodov, C. Stoeckl, K. S. Anderson, R. Betti, T. R. Boehly, R. S. Craxton, J. A. Delettrez, C. Dorrer, J. A. Frenje, V. Yu. Glebov, H. Habara, K. A. Tanaka, J. P. Knauer, R. Lauck, F. J. Marshall, K. L. Marshall, D. D. Meyerhofer, P. M. Nilson, P. K. Patel, H. Chen, T. C. Sangster, W. Seka, N. Sinenian, T. Ma, F. N. Beg, E. Giraldez, and R. B. Stephens, Phys. Plasmas **18**, 056305 (2011).

16. F. H. Séguin, J. A. Frenje, C. K. Li, D. G. Hicks, S. Kurebayashi, J. R. Rygg, B.-E. Schwartz, R. D. Petrasso, S. Roberts, J. M. Soures, D. D. Meyerhofer, T. C. Sangster, J. P. Knauer, C. Sorce, V. Yu. Glebov, C. Stoeckl, T. W. Phillips, R. J. Leeper, K. Fletcher, and S. Padalino, Rev. Sci. Instrum. **74**, 975 (2003).

17. N. Sinenian *et al.*, Rev. Sci. Instrum. **82**, 103303 (2011).

18. D. G. Hicks, C. K. Li, F. H. Séguin, A. K. Ram, J. A. Frenje, R. D. Petrasso, J. M. Soures, V. Yu. Glebov, D. D. Meyerhofer, S. Roberts, C. Sorce, C. Stöckl, T. C. Sangster, and T. W. Phillips, Phys. Plasmas **7**, 5106 (2000).

19. P. M. Nilson, A. A. Solodov, J. F. Myatt, W. Theobald, P. A. Jaanimagi, L. Gao, C. Stoeckl, R. S. Craxton, J. A. Delettrez, B. Yaakobi, J. D. Zuegel, B. E. Kruschwitz, C. Dorrer, J. H. Kelly, K. U. Akli, P. K. Patel, A. J. Mackinnon, R. Betti, T. C. Sangster, and D. D. Meyerhofer, Phys. Rev. Lett. **105**, 235001 (2010).

20. S. P. Hatchett, C. G. Brown, T. E. Cowan, E. A. Henry, J. S. Johnson, M. H. Key, J. A. Koch, A. B. Langdon, B. F. Lasinski, R. W. Lee, A. J. MacKinnon, D. M. Pennington, M. D. Perry, T. W. Phillips, M. Roth, T. C. Sangster, M. S. Singh, R. A. Snavely, M. A. Stoyer, S. C. Wilks, and K. Yasuike, Phys. Plasmas **7**, 2076 (2000).

21. S. C. Wilks *et al.*, Phys. Plasmas **8**, 542 (2001).

22. J. Li, J. Davies, C. Ren, A. Solodov, W. Theobald, J. Tonge, and W. Mori, Bull. Am. Phys. Soc. **56**, 222 (2011).

23. C. Stoeckl, M. Cruz, V. Yu. Glebov, J. P. Knauer, R. Lauck, K. Marshall, C. Mileham, T. C. Sangster, and W. Theobald, Rev. Sci. Instrum. **81**, 10D302 (2010).

24. A. A. Solodov, K. S. Anderson, R. Betti, V. Gotcheva, J. F. Myatt, J. A. Delettrez, S. Skupsky, W. Theobald, and C. Stoeckl, Phys. Plasmas **16**, 056309 (2009).

25. C. D. Zhou, W. Theobald, R. Betti, P. B. Radha, V. A. Smalyuk, D. Shvarts, V. Yu. Glebov, C. Stoeckl, K. S. Anderson, D. D. Meyerhofer, T. C. Sangster, C. K. Li, R. D. Petrasso, J. A. Frenje, and F. H. Séguin, Phys. Rev. Lett. **98**, 025004 (2007).

26. P. Mora, in *Asian Summer School on Laser Plasma Acceleration and Radiation*, edited by Z.-M. Sheng and J. Zhang (AIP, New York, 2007), Vol. 920, pp. 98–117.

27. A. J. Mackinnon *et al.*, Phys. Rev. Lett. **86**, 1769 (2001).

28. K. Flippo, T. Bartal, F. Beg, S. Chawla, J. Cobble, S. Gaillard, D. Hey, A. MacKinnon, A. MacPhee, P. Nilson, D. Offermann, S. Le Pape, and M. J. Schmitt, J. Phys., Conf. Ser. **244**, 022033 (2010).

29. L. Gao, P. M. Nilson, W. Theobald, C. Stoeckl, C. Dorrer, T. C. Sangster, D. D. Meyerhofer, L. Willingale, and K. M. Krushelnick, Bull. Am. Phys. Soc. **55**, 377 (2010).

The Fourth Omega Laser Facility Users' Group Workshop

Introduction

A capacity gathering of 115 researchers from over 25 universities and laboratories and 9 countries met at the Laboratory for Laser Energetics (LLE) for the Fourth Omega Laser Facility Users' Group (OLUG) Workshop. The purpose of the 2.5-day workshop was to facilitate communications and exchanges among individual Omega users and between users and the LLE management; to present ongoing and proposed research; to encourage research opportunities and collaborations that could be undertaken at the Omega Laser Facility and in a complementary fashion at other facilities [such as the National Ignition Facility (NIF) or the Laboratoire pour l'Utilisation des Lasers Intenses (LULI)]; to provide an opportunity for students, postdoctoral fellows, and young researchers to present their research in an informal setting; and to provide feedback to LLE management from the users about ways to improve the facility and future experimental campaigns. The interactions were wide ranging and lively, as illustrated in the accompanying photographs.

OLUG consists of 304 members from 33 universities and 25 centers and national laboratories; their names and affiliations can be found at **www.lle.rochester.edu/media/about/documents/OLUGMEMBERS.pdf**. OLUG is by far the largest users' group in the world in the field of high-energy-density (HED) physics and certainly one of the most active.

During the first two mornings of the workshop, seven science and facility talks were presented. The facility talks proved especially useful for those not familiar with the art and complexities of performing experiments at the Omega Laser Facility. But since the facility is constantly changing and improving, even experienced users significantly benefited from these updates. The overview science talks, given by leading world authorities, described the breadth and excitement of HED science undertaken at the Omega Laser Facility.

Approximately 50 students and postdoctoral fellows participated in the workshop; 42 of these participants were supported

U1458JR

Figure 132.29
A capacity gathering of 115 researchers from 25 universities and laboratories around the world participated in this year's workshop. OLUG has 304 members who come from 33 universities and 25 laboratories, making it by far the largest users' group in the world in high-energy-density physics. The next annual OLUG Workshop will occur on 24–26 April 2013.

U1459JR

Figure 132.30
Nearly all of the 50 students and postdoctoral fellows who attended made poster presentations; 42 of these attendees received travel assistance from an NNSA grant. Travel assistance has already been arranged for the 2013 workshop. The workshop places tremendous emphasis on the participation and involvement of young researchers.

by travel grants from the National Nuclear Security Administration (NNSA). The content of their presentations ranged from target fabrication to simulating aspects of supernovae; the presentations generated spirited discussions, probing questions, and friendly suggestions. In total, there were 75 contributed posters, including 11 that focused on the Omega Facility. The invited and facility presentations, as well as OLUG's Findings and Recommendations, can be found at **www.lle.rochester.edu/about/omega_laser_users_group.php**.

An important function of the workshop was to develop a set of findings and recommendations to help set future priorities for the Omega Laser Facility. These findings were grouped into four areas: 60-beam OMEGA, OMEGA EP, general facility improvements, and accessibility of OMEGA operational information. These categories comprise a report to be given to the Omega Facility management. Twenty presentations were made by researchers deeply involved in HED science. LLE management uses these recommendations as a guide for making decisions about Omega Laser Facility operations, priorities, and future changes. In addition, the status of these OLUG findings and recommendations were updated and reviewed at a satellite evening meeting during the 2012 APS–DPP Conference. They will also form the grist for the forthcoming workshop.

One highlight of the workshop, as in past workshops, was a panel of students and postdoctoral fellows who discussed their experiences at the Omega Laser Facility and their thoughts and recommendations on facility improvements. The engaging discussions that were sparked by this forum resulted in student/postdoctoral recommendations for the facility.

Another important event at the end of the workshop was a panel of experts who gave an overview of the HED opportunities at national laboratories, universities, and LLE itself. These discussions are very useful for young researchers who may not know all the capabilities and HED research occurring at these different institutions.

U1460JR

Figure 132.31
Registration for OLUG 2012 was a busy time. MIT's seven Ph.D. students worked the registration desk, demonstrating that they are capable of doing more than just physics!

Finally, one of the important decisions made at the workshop was the selection of 24–26 April 2013 as the date of the next users' workshop. Plans are already well underway for this event.

The photographs on the following pages provide a representative sampling of the workshop's talks, interactions, and ambience.


U1461JR

Figure 132.32
University of Rochester Provost Ralph Kuncl (above), along with LLE Director Dr. Robert L. McCrory (not shown), welcomed and thanked the OLUG members for their active involvement in helping to guide and formulate the priorities and activities of the Omega Laser Facility.

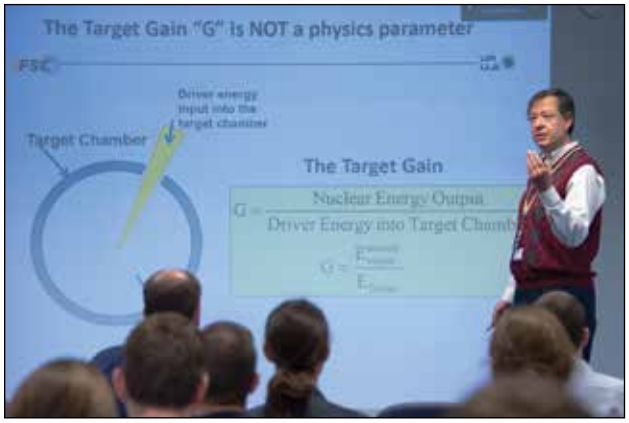

U1462JR

Figure 132.33
Invited presentations of OLUG 2012 were made by world-class physicists, such as LLE's Riccardo Betti, who talked about frontier research in inertial confinement fusion (ICF) and, more generally, in HED physics.


U1463JR

Figure 132.34
General Atomics' Joe Kilkenny, head of NIF diagnostics, presented many examples of the critical role that OMEGA and OLUG play in developing and fielding essential NIF diagnostics and platforms.


U1464JR

Figure 132.35
Nino Landen [Lawrence Livermore National Laboratory (LLNL)] presented two talks: one highlighting the National Ignition Campaign's (NIC's) scientific progress and challenges; the other regarding the HED opportunities available at the Jupiter facility, in which a wider but smaller-scale spectrum of research was described.

U1465JR

Figure 132.36
Hans Herrmann also presented two talks: one on gamma-ray spectroscopy at the Omega Laser Facility and the NIF; the other on the broader HED activities at Los Alamos National Laboratory. Hans is one of the leaders in the nascent field of plasma nuclear science.

U1466JR

Figure 132.37
During the workshop's numerous question and discussion sessions, animated and spirited discussions were the norm. Here LLNL postdoctoral fellow Nathan Kugland humorously (but seriously) raises a technical issue of widespread concern that impacts many OLUG members (i.e., imaging detectors for multi-MeV protons).

U1467JR

Figure 132.38
During three different poster sessions, 75 posters were presented, the majority by students and postdoctoral fellows.

The 11 "Facility" posters (available online), many addressing findings and recommendations of OLUG, were widely lauded by the users. "Incredibly useful" was the universal sentiment for this session.

Another critical finding and recommendation of OLUG was the appointment of a key technical contact with whom the users can interact to help implement their complex experiments.

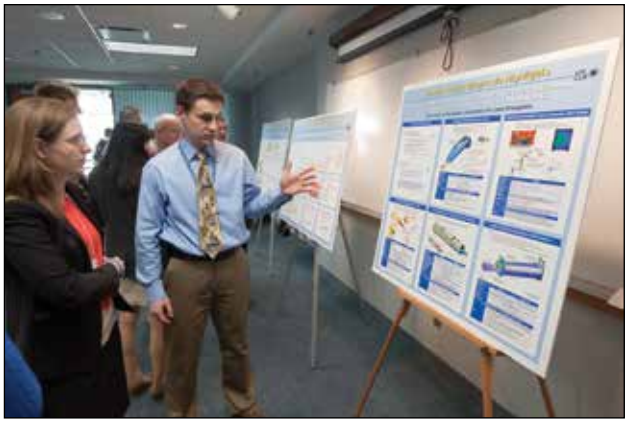

U1468JR

Figure 132.39
Chuck Sorce, shown here talking with Carolyn Kuranz of the University of Michigan, was subsequently appointed head of the Experimental Support Group with a staff to address this issue. OLUG thanks LLE for such responsiveness.


U1469JR

Figure 132.40
The student/postdoc panel and town meeting is one of OLUG's most important sessions, highlighting many of the challenges faced by young researchers at the Omega Laser Facility and elsewhere. Their findings and recommendations often highlight infrastructure and operational issues, many of which have been addressed by LLE.


U1471JR

Figure 132.42
Princeton Physics Laboratory's Ken Hill presented, in a Findings and Recommendations session, a unique concept and proposal for an OMEGA high-resolution x-ray imaging spectrometer. OLUG recommends that we actively pursue further exploration and development of Dr. Hill's promising concept.


U1470JR

Figure 132.41
Rutherford-Appleton Laboratory's Peter Norreys chaired a session on findings and recommendations. Here he shares a light moment during Tammy Ma's presentation on the student/postdoc findings and recommendations. Tammy, a LLNL postdoctoral fellow, chairs that group.


U1472JR

Figure 132.43
One of OLUG's 2011 Findings and Recommendations focused on the development of a robust magnetized HEDLP platform. LLE's Gennady Fiksel (right) and Professor Peter Norreys of Rutherford Appleton Laboratory (left) talked about these recent implementations, which OLUG found truly impressive! Thank you, LLE and Gennady!


U1473JR

Figure 132.44
In a session chaired by University of Nevada's Roberto Mancini (left), DOE technical manager Lois Buitano praised the OLUG/LLE working relationship: "This is an excellent model" for all NNSA facilities.

Questions Addressed in the General Workshop Sessions

What new avenues of research should we be pursuing at the Omega Laser Facility?

What facility improvements, large or small, can improve current research and help us pursue science at the cutting edge?

How can the administrative organization and the infrastructure at LLE better support ongoing and groundbreaking research?

What additional platforms/experiments/diagnostics might advantageously be built and coordinated, e.g., between OMEGA and the NIF, and/or between OMEGA and Trident or Jupiter?

The next Omega Laser Users' Group Workshop will be held at LLE on 24–26 April 2013.

ACKNOWLEDGMENT

This Omega Laser Facility Users' Workshop is made possible in part by the generous support of the National Nuclear Security Administration for travel expenses of students and postdoctoral fellows; by the Office of Fusion Energy Sciences for support of general workshop costs; by the Fusion Science Center; by the MIT/Plasma Science and Fusion Center; and by the Laboratory for Laser Energetics for the use and availability of critical resources and support. In addition, OLUG especially thanks LLE Director Dr. Robert L. McCrory and the LLE management and technical staff for their responsiveness to OLUG's findings and recommendations and for providing a superb and dynamic HED facility in which to conduct state-of-the-art experiments. For capturing through his lens the workshop ambiance, OLUG thanks Eugene Kowaluk. R. D. Petrasso is the editor for this Proceeding.


U1474JR

Figure 132.45
The banquet at the Meliora on the University of Rochester's campus offered workshop attendees a wonderful opportunity for socializing and good cuisine.

LLE's Summer High School Research Program

During the summer of 2012, 16 students from Rochester-area high schools participated in the Laboratory for Laser Energetics' Summer High School Research Program. The goal of this program is to excite a group of high school students about careers in the areas of science and technology by exposing them to research in a state-of-the-art environment. Too often, students are exposed to "research" only through classroom laboratories, which have prescribed procedures and predictable results. In LLE's summer program, the students experience many of the trials, tribulations, and rewards of scientific research. By participating in research in a real environment, the students often become more excited about careers in science and technology. In addition, LLE gains from the contributions of the many highly talented students who are attracted to the program.

The students spent most of their time working on their individual research projects with members of LLE's technical staff. The projects were related to current research activities at LLE and covered a broad range of areas of interest including experimental concept development and diagnostics modeling, computational modeling of implosion physics, materials science, laser system development and diagnostics, isotope separation, and database development (see Table 132.IV).

The students attended weekly seminars on technical topics associated with LLE's research. Topics this year included laser physics, fusion, holography, nonlinear optics, shape memory polymers, electronic paper, and scientific ethics. The students also received safety training, learned how to give scientific presentations, and were introduced to LLE's resources, especially the computational facilities.

The program culminated on 29 August with the "High School Student Summer Research Symposium," at which the students presented the results of their research to an audience including parents, teachers, and LLE staff. The students' written reports will be made available on the LLE Website and bound into a permanent record of their work that can be cited in scientific publications.

Two hundred and ninety-seven high school students have now participated in the program since it began in 1989. This year's students were selected from over 60 applicants.

At the symposium LLE presented its 16th annual William D. Ryan Inspirational Teacher Award to Ms. Sage Miller, a mathematics and computer science teacher at Webster Schroeder and Webster Thomas High Schools. This award is presented to a teacher who motivated one of the participants in LLE's Summer High School Research Program to study science, mathematics, or technology and includes a $1000 cash prize. Teachers are nominated by alumni of the summer program. Ms. Miller was nominated by Troy Thomas and Avery Gnolek, participants in the 2011 program, both of whom credit her for their decisions to major in computer science. Troy wrote, "I get most inspired by the way Ms. Miller teaches computer science…I had not realized how intricate and complex this subject was, and I now know that I will definitely study this in college…Ms. Miller is completely responsible for this decision as she showed me the true nature of computer science, and inspired me to pursue this more closely as a possible career option." Avery wrote, "As my math teacher Ms. Miller inspires many of her students and also displays a passion for teaching…She went out of her way to help students succeed, even when it used her own time…She would frequently meet after school with students to help them make up missed work or understand topics better…Her enthusiasm and attitude made class both informative and enjoyable…I believe that I would have never chosen such a career path had it not been for Ms. Miller's teaching and assistance." Ms. Miller also received strong support from Mr. Joe Pustulka, principal of Webster Schroeder High School, who described her as "a wonderful math and computer science teacher" who "is very devoted to her students, and is well respected and admired by her colleagues."

Table 132.IV: High School Students and Projects—Summer 2012.

Name	High School	Supervisor	Project Title
Emily Armstrong	Mercy	M. Barczys, B. E. Kruschwitz	Wavefront Measurements of High-Power UV Lasers with a Hartmann Sensor
Virginia Boy	East Rochester	R. W. Kidder	Integrating Semantic Technology with Legacy Databases
Christa Caggiano	Victor	K. L. Marshall, C. Dorrer	Fabrication of Radial Polarization Converters with Photo-aligned Liquid Crystals
Ian Gabalski	Webster Thomas	P. B. Radha	Polar-Drive Target Designs for Early Experiments on the National Ignition Facility
Mary Kate Hanchett	Fairport	W. T. Shmayda	Oxygen Uptake Using a Nickel Catalyst
Aaron Jo	Victor	W. T. Shmayda, N. Redden	Hydrogen Isotope Separation Using Gas Chromatography
Alec Kirkley	Pittsford Sutherland	G. Fiksel	Magnetic-Field Penetration into a Conducting Hohlraum
Evan Lustick	Canandaigua Academy	R. S. Craxton, M. D. Wittman	Modeling Density Change Inside a Cryogenic Target Using a Fabry–Perot Interferometer: A Feasibility Study
Aimee Owens	Home School	T. Z. Kosc, S. D. Jacobs	Performance Degradation of OMEGA Liquid Crystal Polarizers
Jesse Pan	Webster Thomas	S. X. Hu	Examination of Opacity Effects in Inertial Confinement Fusion Implosions
Mitchell Perry	Brighton	J. Qiao	Deformable-Grating Design Evaluation and Optimization for Large-Aperture Pulse-Compressor Systems
Raz Rivlis	Brighton	R. Boni	Optical Modeling and Analysis of a High-Throughput and High-Temporal-Bandwidth Spectrometer
Lucas Shadler	West Irondequoit	W. D. Bittle	Prediction of Getter Bed Regeneration Intervals Through Absolute Humidity and Flow Rate
Julia Tucker	Brighton	R. Epstein	The Dependence of Plasma Ionization Equilibrium on Electron and Radiation Temperatures
Jack Valinsky	Brighton	W. R. Donaldson, D. H. Froula	Electronic Analysis of Pulse Propagation Through an X-Ray Framing Camera
Charles Wan	Penfield	K. L. Marshall	Dynamic Mechanical Analysis of Cryogenic Target Materials

FY12 Laser Facility Report

During FY12, the Omega Laser Facility conducted 1494 target shots on OMEGA and 426 target shots on OMEGA EP for a total of 1920 target shots (see Tables 132.V and 132.VI). OMEGA averaged 11.2 target shots per operating day with Availability and Experimental Effectiveness averages for FY12 of 94.2% and 96.7%, respectively.

OMEGA EP was operated extensively in FY12 for a variety of internal and external users. A total of 356 target shots were taken in the OMEGA EP target chamber and 70 joint target shots were taken in the OMEGA target chamber. OMEGA EP averaged 6.1 target shots per operating day with Availability and Experimental Effectiveness averages for FY12 of 88.0% and 95.5%, respectively.

Table 132.V: OMEGA Laser System target shot summary for FY12.

Laboratory	Planned Number of Target Shots	Actual Number of Target Shots	NIC	Shots in Support of NIC	Non-NIC
AWE	10	12	0	0	12
CEA	35	43	0	0	43
CRASH	20	18	0	0	18
LANL	200	244	361	0	183
LBS	170	202	0	0	202
LLE	347	411	13	398	0
LLNL	300	335	116	8	211
NLUF	172	215	0	0	215
SNL	10	14	14	0	0
Total	1264	1494	204	406	884

Table 132.VI: OMEGA EP Laser System target shot summary for FY12.

Laboratory	Planned Number of Target Shots	Actual Number of Target Shots	NIC	Shots in Support of NIC	Non-NIC
LBS	45	71	0	0	71
LLE	120	172	0	172	0
LLNL	105	121	39	0	82
NLUF	55	62	0	0	62
Total	325	426	39	172	215

Highlights of achievements in FY12 include the following:

Multi-FM Beam Smoothing on OMEGA EP

A one-dimensional smoothing by spectral dispersion (SSD) demonstration system using multiple modulation frequencies (multi-FM 1-D SSD) was commissioned on one long-pulse beamline of OMEGA EP. The modified OMEGA EP beamline has supported experiments to validate this novel beam-smoothing capability prior to implementation at the National Ignition Facility (NIF) to enable polar-drive ignition. The fiber-laser–based seed-pulse system design greatly increases the laser pulse–shaping flexibility and is compatible with the NIF front-end laser design. Multi-FM SSD modulation is selectively applied to portions of the laser pulse required for polar-drive ignition on the NIF. The output seed pulse is injected into the NIF preamplifier module (PAM) with a custom SSD grating inserted into the PAM's multipass amplifier section. The dispersion of the SSD grating was selected to cleanly propagate the dispersed SSD bandwidth through the spatial-filter pinholes in the system while providing the required focal-spot smoothing performance. A series of equivalent-target-plane measurements was conducted that confirmed the expected time-integrated smoothing of the focal spot when combined with a distributed phase plate (DPP).

Equivalent-Target-Plane Diagnostics on OMEGA EP

An equivalent-target-plane (ETP) diagnostic has been activated on Beamline 4 to characterize the UV laser pulse spot on target through DPP's. The UV diagnostic package receives a sample of the laser pulse after frequency conversion. A mount has been added to install a DPP into this diagnostic arm. A far-field camera is configured to observe the entire intensity profile in low-resolution mode with 1-μrad/pixel resolution and also features a fine-resolution mode to study details of the speckle pattern with 0.3 μrad/pixel.

OMEGA EP Short-Pulse Contrast Improvement

The primary source for prepulse in the OMEGA EP short-pulse laser has historically been the amplified stimulated emission (ASE) in the optical parametric amplifiers. In FY12, the seed oscillators were upgraded to include an ultrafast optical parametric amplifier (UOPA) prior to the pulse stretcher. With this equipment, the seed energy into the next stage of amplification is increased, allowing a redistribution of the system gain to realize reduced ASE. This upgrade resulted in an improvement in the short-pulse (SP) contrast of over two orders of magnitude. (See Fig. 132.46 for representative short-pulse contrast measurements before and after this upgrade.)

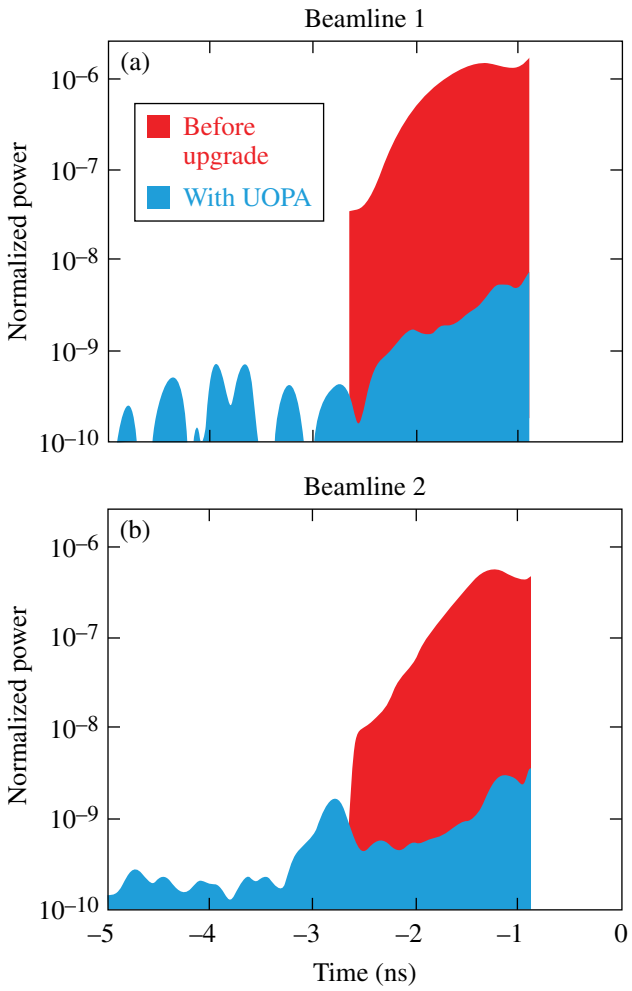

Figure 132.46
Short-pulse contrast measurements from Beamlines 1 and 2. The red curves show previously normal contrast results. The blue curves are characteristic of contrast measurements after the UOPA upgrade. On-shot power contrasts higher than 10^9 at best compression have been measured, translating into intensity contrasts higher than 10^{10}.

OMEGA EP Spatial Profile Improvements on Beamlines 3 and 4

Programmable spatial light modulators (PSLIM's) have been installed and activated in the front ends of Beamlines 3 and 4. The PSLIM system consists of a spatial light modulator installed at an image plane. The spatial light modulator applies a phase term in a 2-D array to the beam such that a prescribed amount of energy is removed at the next spatial filter in the system. A dedicated wavefront sensor (employing a novel routine for calculating the spatial profile) is used to provide feedback and achieve the desired near field without adversely affecting the wavefront.

OMEGA Ultraviolet Pulse-Shape-Measurement Capabilities

A precision ultraviolet pulse (PUVP) shape measurement diagnostic has been commissioned on the OMEGA laser to improve the resolution of pulse-shape measurements. The PUVP is a streak camera with 6-ps resolution that is free-space coupled to Beamlines 47, 57, and 67. This is twice the resolution offered by the fastest sweep speed of the P-510 streak cameras. This diagnostic also offers longer sweep speeds to ensure data collection when the beamline timings are requested to be within 13-ns separation.

A 33-ns sweep speed was added to complement existing 6-ns and 20-ns options on the P-510 timing diagnostic for all six clusters. The extended acquisition duration gives new capability to capture reference fiducials when large timing offsets are employed on individual beams or between multiple drivers. The longer sweep speed was specifically tailored to provide improved timing analysis for several campaigns that routinely employ such offsets. Standard automated analysis gives a reported timing accuracy of 350 ps and a precision of 100 ps. Additional manual processing can be performed to further improve these results when necessary.

4ω Probe Laser System

The source laser for the 4ω probe diagnostic has been installed and activated in the OMEGA EP Target Bay. This system produces a 10-ps pulse of 263-nm light, which will be used to investigate laser–plasma interactions in the OMEGA EP target chamber. The seed laser is a mode-locked oscillator that is synchronized to the short-pulse lasers by the hardware timing system to less than 5 ps. The pulse is stretched to a length of 10 ps and amplified by two stages of regenerative amplifiers before being frequency quadrupled. The energy at the target interaction (currently >20 mJ available) will exceed the background UV in the diagnostic systems. A shadowgraphy and schlieren diagnostic package is under construction to accurately

characterize the plasma densities based on the refracted light from the source.

Thomson-Scattering Spectrometer System on OMEGA

The Thomson-scattering spectrometer diagnostic has proven to be a valuable resource for characterizing the electron and ion temperatures during a target interaction. During FY12, the Thomson-scattering spectrometer system was upgraded to improve the resolution, increase the signal to noise, and add functionality. In this diagnostic, the scattered light from a probe beam is collected by an improved optical system in TIM-6 and relayed to diagnostic tables where an ion-acoustic wave spectrometer, electron plasma wave spectrometer, and the new two-plasmon-decay imager reside. Both of the spectrometers have a resolution of 20 lp/mm (increased from 7 lp/mm).

Experimental Operations and Diagnostics

In FY12, 26 new target diagnostics were commissioned on OMEGA and 8 on OMEGA EP. These included a suite of TIM-based scattered-energy calorimeters, the SXS crystal spectrometer for x-ray streak cameras, the first of the new PJX-2 streak cameras, a new high-speed video target viewing system, and an additional x-ray pinhole camera. The streaked optical pyrometer diagnostic measures the time-resolved laser-driven shocks on OMEGA. This system has been upgraded with a ROSS streak camera system and improved optical relay for higher resolution in increased signal strength. As in previous years, many of the new instruments were developed by or in collaboration with other laboratories, including LLNL, LANL, CEA, and General Atomics.

Experimental facility improvements included the introduction of an image plate scanning capability on OMEGA, the addition of a second image plate scanner on OMEGA EP, and the commissioning of a set of fully integrated TIM-based target positioning systems on both OMEGA and OMEGA EP. Two of the OMEGA TIM's were retrofit with new EMI-resistant, OMEGA EP–type control systems, and updated TIM vacuum system operating software was installed on both OMEGA and OMEGA EP.

National Laser Users' Facility and External Users' Programs

Under the facility governance plan that was implemented in FY08 to formalize the scheduling of the Omega Laser Facility as an National Nuclear Security Administration (NNSA) User Facility, Omega Facility shots are allocated by campaign. The majority (67.6%) of the FY12 target shots were allocated to the National Ignition Campaign (NIC) conducted by integrated teams from the national laboratories and LLE and to the high-energy-density campaigns conducted by teams led by scientists from the national laboratories.

Nearly 29% of the facility shots in FY12 were allocated to basic science experiments. Half of these were dedicated to university basic science under the National Laser Users' Facility (NLUF) Program, and the remaining shots were allotted to the Laboratory Basic Science (LBS) Program, comprising peer-reviewed basic science experiments conducted by the national laboratories and by LLE including the Fusion Science Center (FSC).

The Omega Facility is also being used for several campaigns by teams from the Commissariat à l'Énergie Atomique (CEA) of France and the Atomic Weapons Establishment (AWE) of the United Kingdom. These programs are conducted at the facility on the basis of special agreements put in place by DOE/NNSA and participating institutions.

The facility users during this year included 11 collaborative teams participating in the NLUF Program; 12 teams led by Lawrence Livermore National Laboratory (LLNL) and LLE scientists participating in the LBS Program; many collaborative teams from the national laboratories conducting experiments for the NIC; investigators from LLNL and Los Alamos National Laboratory (LANL) conducting experiments for high-energy-density-physics programs; and scientists and engineers from CEA, AWE, and the Center for Radiative Shock Hydrodynamics (CRASH) of the University of Michigan.

In this section, we briefly review all the external user activity on OMEGA during FY12.

FY12 NLUF Program

In FY12, the Department of Energy (DOE) issued a solicitation for NLUF grants for the period FY13–FY14. A record of 23 proposals were submitted to DOE for the NLUF FY13–FY14 program. An independent DOE Technical Evaluation Panel reviewed the proposals on 11 July 2012 and recommended that 11 proposals receive DOE funding and 28 days of shot time on OMEGA in each of FY13 and FY14. Table 132.VII lists the successful NLUF proposals for FY13–FY14.

FY12 was the second of a two-year period of performance for the NLUF projects approved for the FY11–FY12 funding and OMEGA shots. Eleven NLUF projects were allotted Omega Laser Facility shot time and conducted a total of 277 target shots at the facility. This work is summarized in this section.

Systematic Study of Fast-Electron Transport in Imploded Plasmas

Principal Investigators: F. N. Beg (University of California, San Diego) and M. S. Wei (General Atomics)
Co-investigators: R. B. Stephens (General Atomics); H. Sawada, C. McGuffey, and B. Qiao (UCSD); A. A. Solodov, W. Theobald, C. Stoeckl, J. A. Delettrez, and R. Betti (LLE); M. H. Key, P. Patel, and H. McLean (LLNL); and T. Yabuuchi and H. Habara (Osaka University)
Lead Graduate Student: L. C. Jarrott (UCSD)

Understanding fast-electron generation inside the cone and its subsequent transport into hot dense plasmas is crucial to the success of the cone-guided fast-ignition (FI) scheme of inertial confinement fusion. The goal of the University of California, San Diego (UCSD) NLUF project is to investigate the coupling efficiency and spatial energy deposition of fast electrons into an imploded CH/CD shell attached to a re-entrant gold cone target in joint OMEGA and OMEGA EP experiments. The Au cone has a 34° opening angle, 10-μm inner tip diameter, 15-μm cone-tip thickness, with 44-μm offset distance from the tip to the shell center, while the CH/CD shell has an 870-μm outer

Table 132.VII: NLUF proposals approved for shots at the Omega Laser Facility for FY13–FY14.

Principal Investigator	Institution	Project Title
F. N. Beg	University of California, San Diego	Systematic Study of Fast-Electron Energy Deposition in Imploded Plasmas with Enhanced OMEGA EP Laser Contrast and Intensity
R. P. Drake	University of Michigan	Experimental Astrophysics on the OMEGA Laser
T. Duffy	Princeton University	Dynamic Compression of Earth and Planetary Materials Using OMEGA
W. Fox	University of New Hampshire	Dynamics and Instabilities of Magnetic Reconnection Current Sheets in High-Energy-Density Plasmas
P. Hartigan	Rice University	Astrophysical Dynamics in the Laboratory: Mach Stems and Magnetized Shocks
R. Jeanloz	University of California, Berkeley	Journey to the Center of Jupiter, Recreating Jupiter's Core on OMEGA
H. Ji	Princeton University	Study of Particle Acceleration and Fine-Scale Structures of Collisionless Magnetic Reconnection Driven by High-Energy Petawatt Lasers
B. Qiao	University of California, San Diego	Dynamics of High-Energy Proton Beam Focusing and Transition into Solid Targets of Different Materials
R. D. Petrasso	Massachusetts Institute of Technology	Studies of Laboratory Astrophysics, Inertial Confinement Fusion, and High-Energy-Density Physics with Nuclear Diagnostics
A. Spitkovsky	Princeton University	Generation of Collisionless Shocks in Laser-Produced Plasmas
R. B. Stephens	General Atomics	Investigation of the Dependence of Fast-Electron Generation and Transport on Laser Pulse Length and Plasma Materials

diameter consisting of a 15-μm-thick outer CH ablator and a 23-μm-thick inner CD layer. A Cu dopant (at ~1% atomic number density of CD) is added to the CD layer of the shell, which allows one to characterize the fast electrons' transport via their induced Cu K-shell fluorescence radiation. The CH ablator prevents direct heating of the CD layer by the OMEGA driver beam and also reduces the neutron background from the corona plasmas. In this experiment, 54 (with a total energy of ~18 kJ) of the 60 OMEGA beams with a low-adiabat pulse shape [LA241701P with smoothing by spectral dispersion (SSD) off] were used to compress the shell. The 10-ps OMEGA EP backlighter beam (BL2) was tightly focused at the inner cone tip with various time delays relative to the OMEGA driver. The primary diagnostics were a monochromatic spherical crystal imager (SCI) (centered at 8048 eV with 6-eV bandwidth) to image the Cu K_α emission and a zinc Von Hamos (ZVH) x-ray spectrometer tuned to measure the Cu K-shell and ionic line emission spectrum. Several other diagnostics including broadband x-ray imaging diagnostics such as pinhole cameras and Kirkpatrick–Baez (KB) microscopes, neutron time-of-flight detectors, and a multichannel magnetic electron spectrometer were also employed. Figure 132.47 shows the target and diagnostic setup for the experiment.

In this second-year (FY12) NLUF experiment, with the improvement made to the SCI diagnostic that was newly implemented on the OMEGA chamber in FY11 for the first-year NLUF experiment, we have obtained for the first time clear images of fast electrons' spatial energy deposition in the imploded plasmas. Figure 132.48 depicts the background-subtracted SCI images showing that the OMEGA EP beam produced fast-electron–induced Cu K_α emission. The images show the imploded shell's center region from three joint shots with the OMEGA EP beam at ~500-J energy injected at three different time delays (i.e., 3.65 ns, 3.75 ns, and 3.85 ns) relative to the OMEGA driver. These SCI images clearly show that fast electrons penetrated through the cone (wall and tip) into the compressed shell, producing strong Cu K_α emission from the region of the imploded high-density plasmas. The observed decreasing fluorescence emission spot size in the SCI images with increasing OMEGA EP time delay is consistent with the simulated density profiles of the imploded shell at the

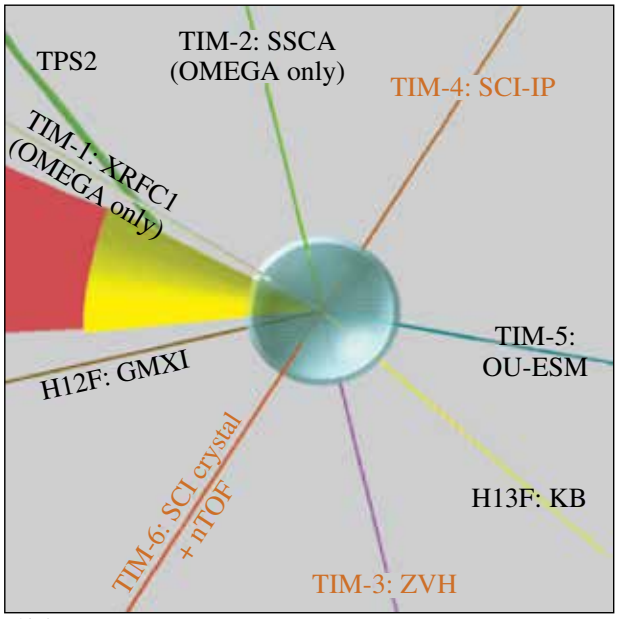

Figure 132.47
VisRad view of the cone-in-shell target and diagnostics layout. Primary diagnostics for this experiment were the SCI and ZVH for Cu K-shell measurements, OU-ESM (multichannel magnetic spectrometer) for electron spectra, and nTOF (LaCave) for neutron measurement.

corresponding implosion time in the 2-D radiation–hydrodynamic modeling results (also shown in Fig. 132.48) using the *DRACO* code. It should be pointed out that the peak emission from the dense shell outside the side cone wall is ~100 μm farther away from the cone tip, which can be caused by the pre-plasma filling of the cone as a result of the intrinsic 3-ns-long prepulse with an energy of ~20 mJ prior to the main pulse. It was also observed that the Cu K_α emission was reduced in the hot region of the core in front of the cone tip, which can be explained by the reduced collection efficiency of the SCI due to the shifting and broadening of the Cu K_α spectral line at plasma temperatures increasing above the order of 150 eV. The ZVH spectrometer provided spatially integrated Cu K_α-yield measurements. As seen in Fig. 132.49, the total Cu K_α yield (due to both OMEGA EP–produced MeV fast electrons and OMEGA driver–produced superthermal electrons with an energy of 20 to 30 keV) increased significantly (up to 60%) in the joint shots compared to the OMEGA-only implosion shots as a result of fast electrons propagating into the high-density plasma. Fast-electron energy coupling to the compressed core was found to increase with the OMEGA EP beam energy injected into the cone up to the time the cone tip broke out by the implosion-driven shocks. It is worth noting that at the latest delay, 3.85 ns, the yield decreased because the cone filled

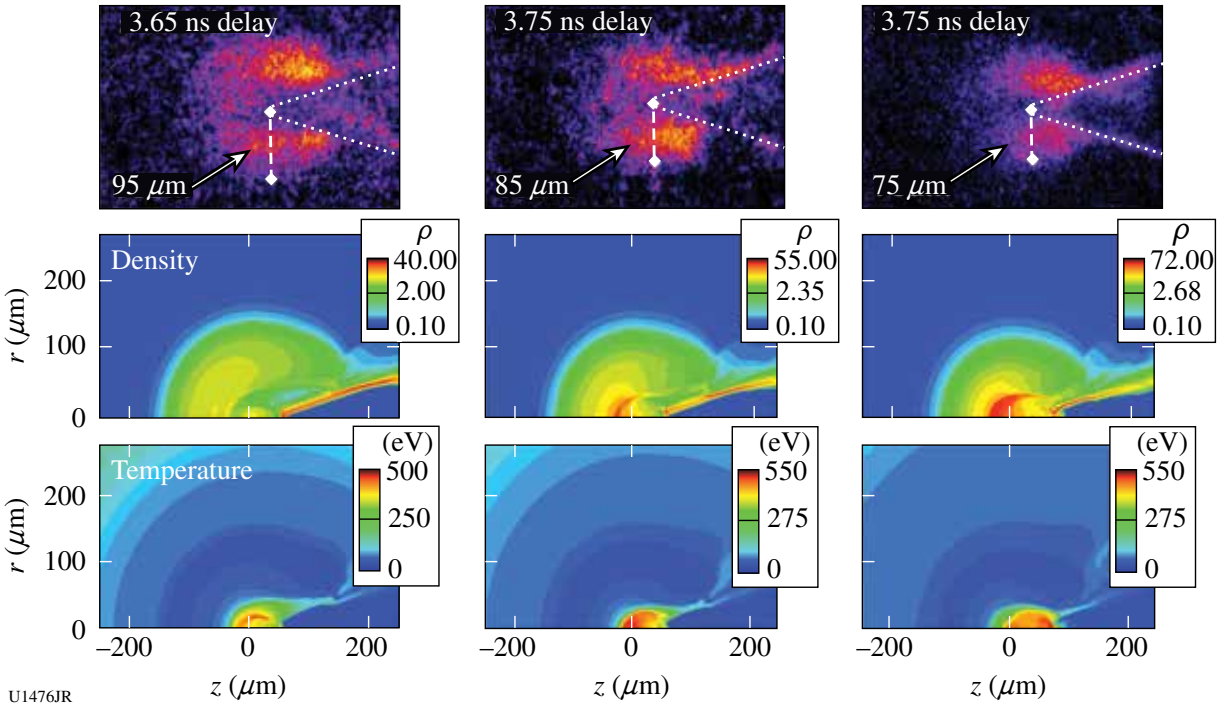

Figure 132.48
(Top) Cu K_α images show the emission from the vicinity of the cone tip at various delays with the OMEGA EP beam energy at ~500 J. The dotted lines are added to visualize the cone position, and the dashed lines show the estimated emission spot radius. The middle and bottom plots are the calculated mass density (in units of g/cm^3) and temperature (eV) maps from the *DRACO* simulations above.

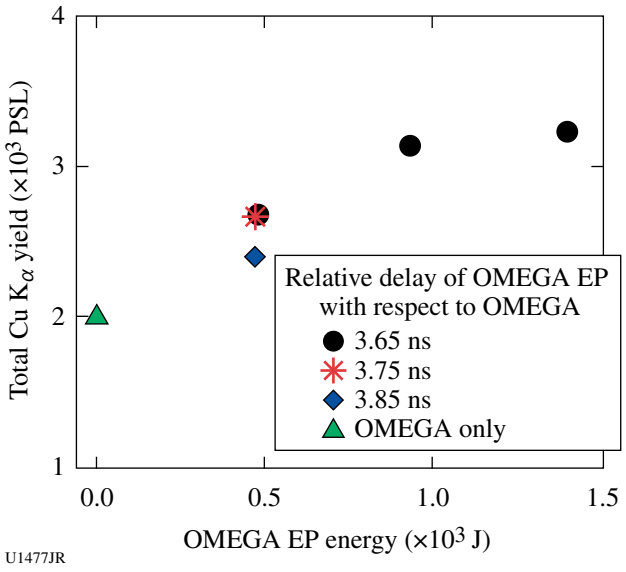

Figure 132.49
Total Cu K_α yield from the joint shots and OMEGA-only shots showing increasing yield with increasing OMEGA EP energy. Also note the significant reduction in Cu K_α yield at 3.85 ns for the OMEGA EP delay corresponding to after the cone-tip breakout by the implosion.

with plasma after the implosion-driven shock destroyed the cone tip—consistent with the *DRACO*-simulation prediction.

In summary, the FY12 UCSD-led NLUF fast-electron transport experiment with cone-in-shell (with Cu doping) targets has made the first direct measurements of the spatial energy deposition of fast electrons into an imploded high-density plasma core in the cone-guided FI configuration. The Cu fluorescence images show a clear signature of fast electrons heating the high-density plasma core and an increase in fast-electron energy coupling with OMEGA EP beam energy. Further work is in progress to combine these measurements with simulations to deconvolve the quantitative spatial information of fast-electron distribution, core plasma density, and temperature.

Experimental Astrophysics on the OMEGA Laser
Principal Investigator: R. P. Drake (University of Michigan)
Co-investigators: B. Loupias and E. Falize (CEA); J. Holloway, C. Kuranz, P. Keiter, and K. Powell (University of Michigan); T. R. Boehly and D. H. Froula (LLE); T. Plewa (Florida State University); and B. A. Remington, S. Ross, H.-S. Park, and S. H. Glenzer (LLNL)

Recreating aspects of astrophysical phenomena on OMEGA provides the ability to quantitatively test observations and models in an experimental setting and is a long-term goal of our research there. The OMEGA laser makes this feasible due to the very high-energy-density (>10-MBar) conditions it can create in millimeter-scale areas. This project includes various experiments exploring either the contribution of hydrodynamic instabilities to the structure in astrophysical systems such as supernovae or the dynamics of radiative shock waves. Here we discuss a continuation of successful campaigns at LLE that investigate the contribution of radiative shock waves to the evolving dynamics of binary star-accretion disk systems in which they reside.

Radiative shock waves produce shocked matter so hot that it radiates away most of its thermal energy. This radiation causes variable structure to develop depending on the optical properties of the material on either side of the shock. In an attempt to control these properties and understand the shock-front emission, this experiment produces an accelerating plasma flow into vacuum that becomes strongly shocked when the flow is impeded. We study the three-dimensional shock structure and the developing dynamics around it using stereoscopic x-ray radiography.

The experiments on OMEGA employ a laser configuration of ten UV beams with a 1-ns square pulse. They are focused on the 10-μm plastic ablator whose opposite face is coated with 5 μm of Sn. The beams deposit a total energy of ~4.5 kJ, giving an average irradiance of $\sim 1.2 \times 10^{15}$ W/cm^2. After an ablative shock breaks out of the rear of the foil, the Sn plasma will expand, cool, and accelerate down the evacuated target cylinder at an average velocity of the order of 150 km/s. About 4 mm from the laser drive surface, the Sn ejecta impact a 100-μm-thick, cold Al foil. In response, a reverse shock develops in the flow. The traditional "upstream" velocity in the shocked system is defined by the Sn flow, which is fast enough that the reverse shock will reach temperatures of a few hundred eV. As it radiatively cools, a thin dense layer of Sn will form, showing compressions much above the adiabatic limit of about 4. Additional sets of four OMEGA laser beams each irradiate zinc foils on orthogonally placed backlit pinhole targets for 1 ns, creating the x-ray sources used to radiograph the reverse shock onto film and image plates. Figure 132.50 shows a pair of images from a single experimental target shot, taken ~34 ns after the drive laser pulse was turned off.

Ramp Compression for Studying Equations of State, Phase Transformations, and Kinetics on OMEGA
Principal Investigator: T. Duffy (Princeton)
Co-investigators: R. Smith, J. H. Eggert, J. Hawreliak, C. Bolme, and D. Braun (LLNL); and T. R. Boehly (LLE)

The aim of this campaign was to measure powder diffraction of MgO under ramp compression. We used the PXRDIP diagnostic

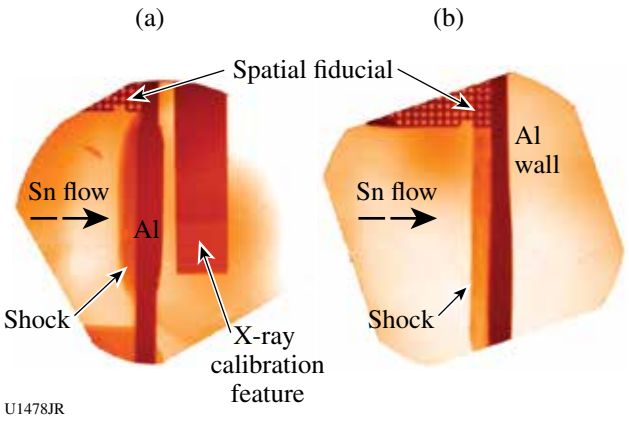

Figure 132.50
Orthogonal x-ray radiographs of a radiative reverse shock in a Sn plasma. The Al obstacle in the collision region of the experiment is 1 mm × 2 mm × 100 μm. (a) The rebounding flow from the 1-mm side, in which we see the shock wave as well as the flow moving above and below it. (b) The orthogonal view along the 2-mm Al edge where it and the reverse shock span the field of view of the diagnostic. Both radiographs were taken at the same time.

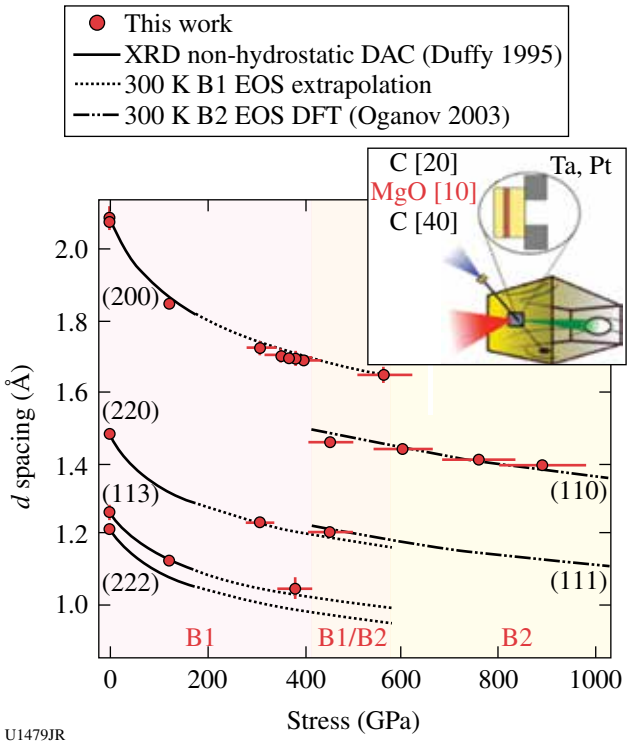

Figure 132.51
Measured d spacing of ramp-compressed MgO. The red dots indicate our experimental data and the black curves indicate our data compared with data from the literature.[1] Below 400 GPa our data indicate that the B1 phase of MgO is the stable one. Above 600 GPa a new solid phase is observed and is consistent with the B2 phase.[2]

reported in the inset of Fig. 132.51 to perform the experiments. Four OMEGA beams were focused on the main target (H7) to drive and compress the MgO powder (sandwiched between two diamonds) and up to ten beams were focused on a Fe or Cu backlighter (H2) to generate x-ray emission for diffraction measurements. We used a 3.5-ns ramp (rm3501) followed by a 1-ns square pulse (sg1018) to drive the main target and a 1-ns square to drive the backlighter. The active shock breakout [velocity interferometer for any reflector (VISAR)] was used to estimate the pressure by measuring the free-surface velocity of the diamond.

MgO was ramp compressed to about 900 GPa and diffraction patterns were recorded. The measured d spacings are shown in Fig. 132.51 as a function of the applied stress. Below 400 GPa, our data (red dots) are in good agreement with static compression experiments (black line)[1] and their extrapolation to higher pressure (black dashed line). The clear discontinuity observed between 400 and 600 GPa is the first experimental evidence for the occurrence of a phase transition in solid MgO. Analysis of the diffraction data shows that the observed solid–solid transformation is consistent with the expected B1–B2 transition[2] (from the six-fold–coordinated NaCl structure to the eight-fold–coordinated CsCl structure).

Detailed In-Situ *Diagnostics of Higher-Z Shocks: Angularly Resolved Quasi-Elastic XRTS of Shocked Al Using 18-keV X Rays*

Principal Investigator: L. Fletcher (University of California, Berkeley)

Co-investigators: T. Ma, A. Pak, H. J. Lee, T. Döppner, C. Fortmann, O. L. Landen, S. H. Glenzer, and R. Falcone (LLNL)

Molybdenum He$_\alpha$ (18-keV) x rays have been used to probe Al foils that have been compressed using both single and double (counter-propagating) shocks in a forward, small-angle scattering platform with very high angular precision.

In this experiment two scattering platforms, demonstrated in Fig. 132.52, have been used. In one configuration [Fig. 132.52(a)], 125-μm-thick Al targets were shock compressed up to 3.5× solid density using nine beams with a total energy of 4.5 kJ using stacked 1-ns pulses. In the second configuration [Fig. 132.52(b)], 200-μm-thick Al targets were shock compressed, under a counter-propagating shock geometry, up to 7× solid density using 18 beams (nine stacked 1-ns pulses on each side), resulting in a total energy of 9 kJ delivered to the Al foil. Both experiments used SG4 distributed phase plates to achieve a smooth 800-μm focal spot, yielding a total

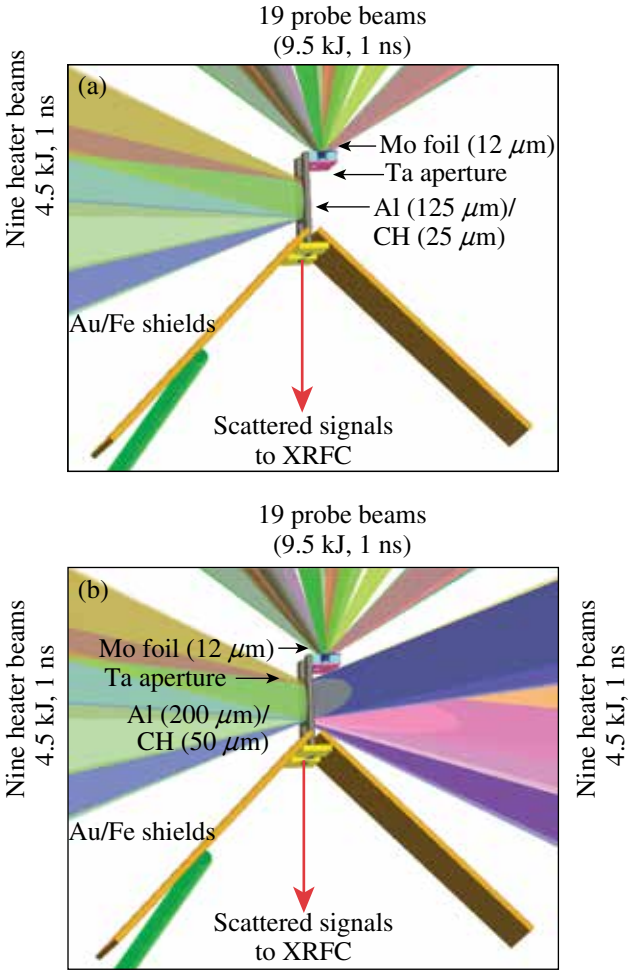

Figure 132.52
The experimental setup for HiZShk-12A. (a) A 125-μm-thick Al target and beam configuration; (b) a 200-μm-thick Al target and beam configuration; (c) a photo of the Al scattering target.

drive intensity of 3×10^{14} W/cm^2 on each irradiated surface. Nineteen beams were incident on a thin Mo foil to generate Mo He$_\alpha$ x rays at 17.9 keV used to probe the compressed targets.

Figure 132.53 shows the predicted shift of the calculated elastic x-ray scattering amplitudes to higher wave numbers with increased density. Therefore, for higher densities, the mean separation between ions decreases while the wave number k increases, making it possible to observe the structure's peak shift. The width and shape of the angularly resolved scattering feature can provide additional information on temperature and the ionization state. By directly measuring the frequency-integrated, quasi-elastic contribution to the dynamic structure factor using angularly resolved x-ray Thomson scattering (XRTS), it is possible to infer the electron densities, electron temperatures, and ionization states of double- and single-shocked Al foils with one experimental platform. Our initial analysis of the scattered data demonstrates good agreement with the predicted quasi-elastic contribution.

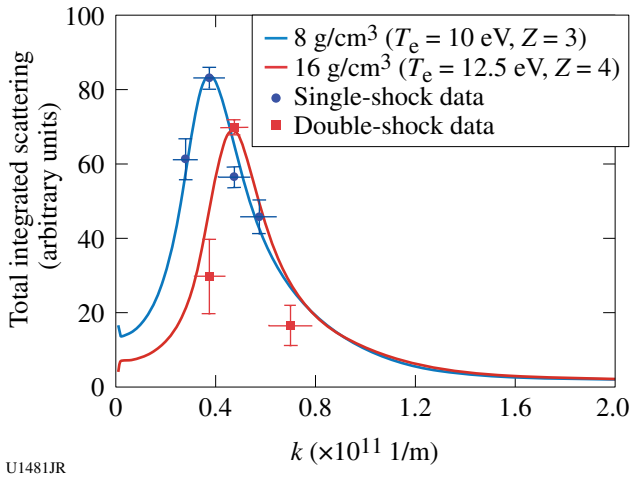

Figure 132.53
Preliminary data analysis shows the total integrated signal of the scattering data as a function of k, following the trends predicted by the SOCP or OCP models using the frequency-integrated, quasi-elastic contribution to the dynamic structure factor of single-shocked (ρ = 8 g/cm^3) and double-shocked (ρ = 16 g/cm^3) aluminum.

Measuring the Compression of Multishocked CH Ablators Using X-Ray Scattering

Principal Investigator: L. Fletcher (University of California, Berkeley)
Co-investigators: A. Kritcher, A. Pak, T. Ma, T. Döppner, C. Fortmann, R. W. Lee, J. J. Lee, O. L. Landen, R. W. Falcone, and S. H. Glenzer (LLNL)

We have performed measurements of the electron densities, electron temperatures, and ionization states of spherically compressed multishocked CH capsules by using spectrally resolved x-ray Thomson scattering. Forty-five beams (13.5 kJ at 300 J/beam incident on a CH shell) compress the 70-μm-thick CH shell above solid-mass density using a laser pulse shape comprised of three precisely timed coalescing shocks. Separately, a laser-produced, high-energy zinc He_α x-ray source at 9 keV, delayed approximately 200 ps to 800 ps in time after maximum compression (full shock coalescence), is used to probe the plasma under a noncollective 135° scattering geometry.

Figure 132.54 shows a schematic of the experimental configuration and the target geometry. In addition, hydrodynamic simulations performed with Helios [Fig. 132.54(c)] demonstrate the possibility of compressing 70-μm-thick CH ablators up to 8.75 g/cm^3 using three co-propagating coalescing shocks. A mass density of approximately 8× the initial solid density (ρ_{CH} = 1.1 g/cm^3) can be achieved using a pulse shape [Fig. 132.54(c)] with three timed steps of 1 ns, 1.5 ns, and 500 ps in duration along with precisely controlled amplitudes of 0.67 TW, 6.85 TW, and 15.5 TW, respectively. Figure 132.54(c) shows the measured radii of the CH shell superimposed on radiation–hydrodynamic simulations of the shell mass density as a function of time and shell radius. In the figure, t = 0 ns indicates the start of the drive beams and t = 3 ns indicates when the laser pulse has turned off. The simulations predict peak compression at the end of the 3-ns-long laser drive, at which time laser-produced x rays are used to probe the plasma by varying the delay between the drive laser beams (used to heat the CH capsule) and the probe laser beams incident on a Zn foil (used to produce high-energy zinc He_α x rays).

The best fits to theoretical spectra shown in Fig. 132.55 allow one to infer the temperature, electron density, and ionization state of shock-compressed CH. The changing shape of the Compton feature with respect to time, as seen in Fig. 132.55, shows that the electron density and the electron temperature change with shock propagation. The Compton feature at each time of 3.4 ns, 3.5 ns, 3.6 ns, and 3.8 ns represents the response

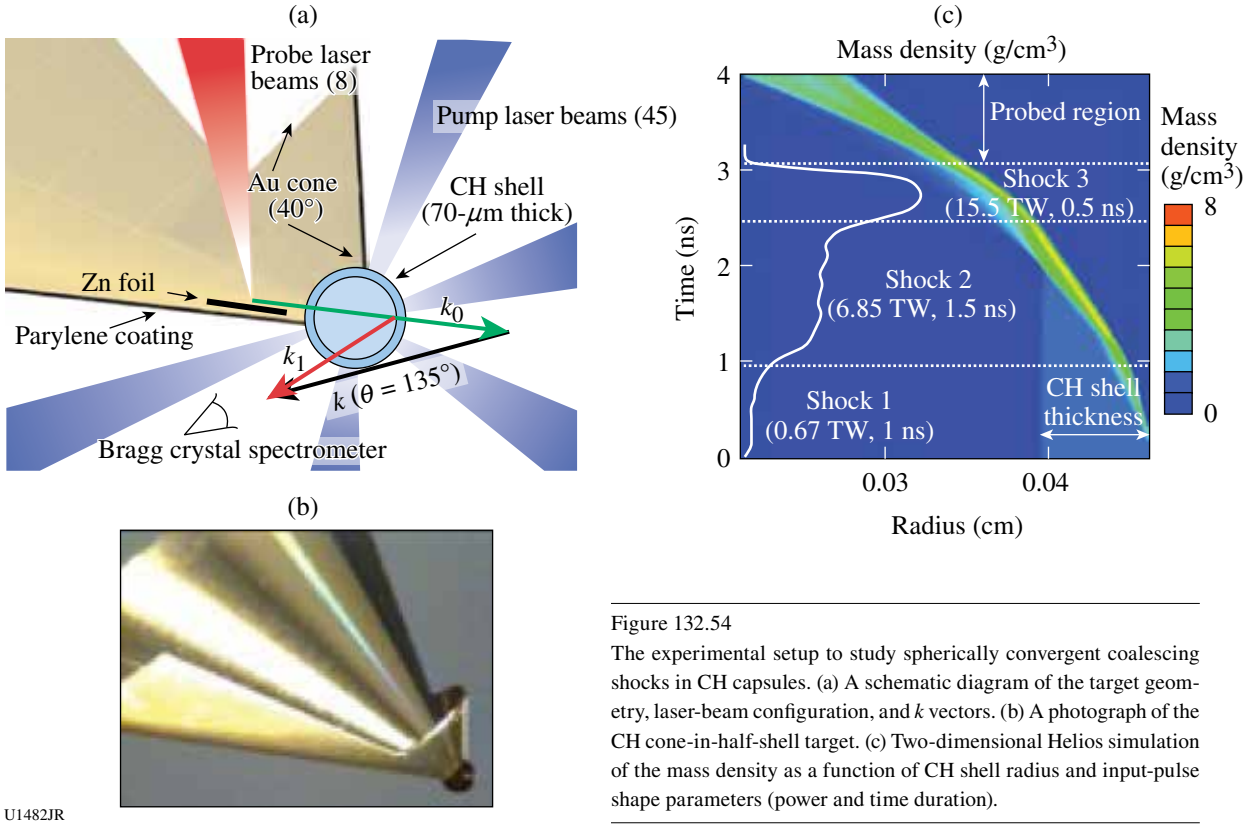

Figure 132.54
The experimental setup to study spherically convergent coalescing shocks in CH capsules. (a) A schematic diagram of the target geometry, laser-beam configuration, and k vectors. (b) A photograph of the CH cone-in-half-shell target. (c) Two-dimensional Helios simulation of the mass density as a function of CH shell radius and input-pulse shape parameters (power and time duration).

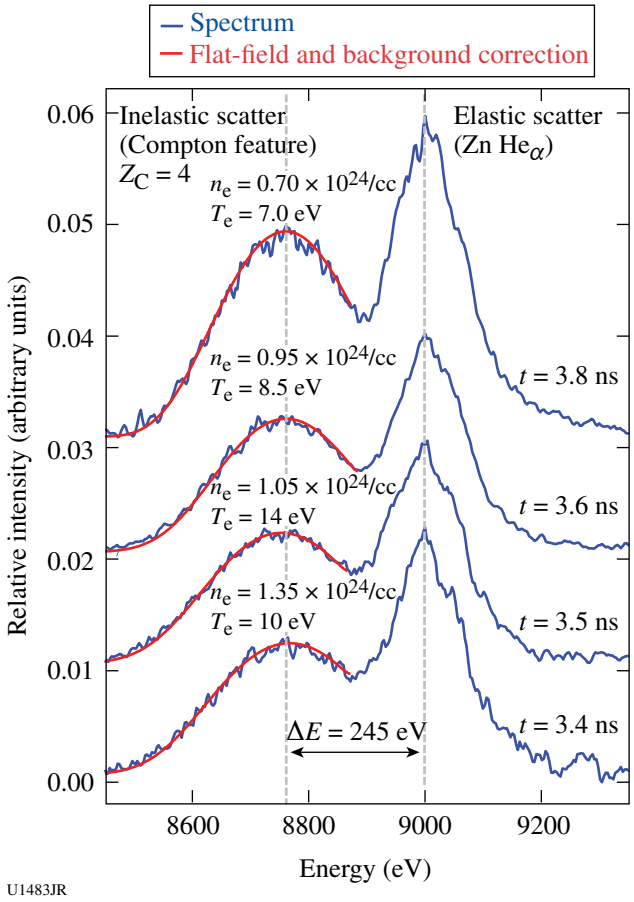

Figure 132.55
Thomson-scattering curve fit analysis. Measured scattered spectra (blue) and best fit (red) to the Compton x-ray scatter features from multishocked CH ablators at t = 3.4 ns, 3.5 ns, 3.6 ns, and 3.8 ns, yielding n_e, T_e, and Z.

of the compressed state during shock coalescence. Our analysis, which provides a full characterization of the heating process, will enable us to completely describe the time-dependent hydrodynamic evolution of shock-compressed CH capsules. It can also be used as a platform to study current equation-of-state models of CH under similar extreme conditions.

Clumpy Environments and Interacting Shock Waves: Realistic Laboratory Analogs of Astrophysical Flows
Principal Investigator: P. Hartigan (Rice University)
Co-investigators: J. Foster and P. Rosen (AWE); K. Yirak, B. Wilde, and M. Douglas (LANL); D. Martinez (LLNL); A. Frank (Rochester); and B. Blue (General Atomics)

Motivated by recent astrophysical images from the Hubble Space Telescope (HST) that were taken as part of a previous NLUF program, our focus in the past year has been to recreate laboratory analogs of some of the shock structures present in jets from young stars. Hot spots appear at the intersection points of overlapping shocks in the HST images, and it is possible that these represent transient normal shocks known as Mach stems. In the laboratory, one can study Mach stems when a strong shock wave moves along a surface. Mach stems may either grow, remain static, or vanish, depending on the intersection angle between the shock front and the surface. Our goals have been to quantify how easily Mach stems form and how fragile they are once formed.

In the last year we have been fielding a suite of experiments that control the angle of interaction between a shock wave and a reflecting surface. We do this by altering the shape of a cone embedded in foam into which we drive a strong shock front. One goal has been to study hysteresis, a phenomenon that allows a Mach stem, once formed, to persist even when the interaction angle decreases below the critical angle for formation. Another project has been to embed irregularities in the surface of the cone to determine how rough surfaces disrupt the growth and survival of Mach stems. We are also quantifying effects of preheating and ablation of the surface by radiation in the shock. A third goal has been to develop a second test bed that involves gas targets to study a system with a lower value (down to about 1.2) at gamma, the specific heat ratio. Theoretical work predicts that critical angles depend on gamma, and we will be testing that prediction. In the astrophysical case, the shock radiates and effectively lowers gamma, so it is important to understand how the system behaves when gamma deviates from the typical value of 5/3.

Examples of data from experiments fielded in the last year appear in Figs. 132.56–132.58. At the end of the campaign, we will have enough data taken at different delay times and with differently shaped cones to be able to measure growth rates for Mach stems under a variety of conditions and compare these results with predictions from simulations. These experiments are being designed using the LANL hydrocode *RAGE*. On the most-recent shot day we experimented with a design for the low-gamma gas targets that produced the expected behavior, but the image contrast was not sufficient to accurately measure Mach-stem sizes. After a modest redesign, we are ready to attempt this again with the next set of shots, where we will continue to fill out the parameter space of angles and delay times, as well as quantify the effects of preheating.

On the astrophysical side, we have discovered a way to image irradiated interfaces in regions of massive star formation. The technique involves taking narrowband images of fluoresced molecular hydrogen at near-infrared wavelengths

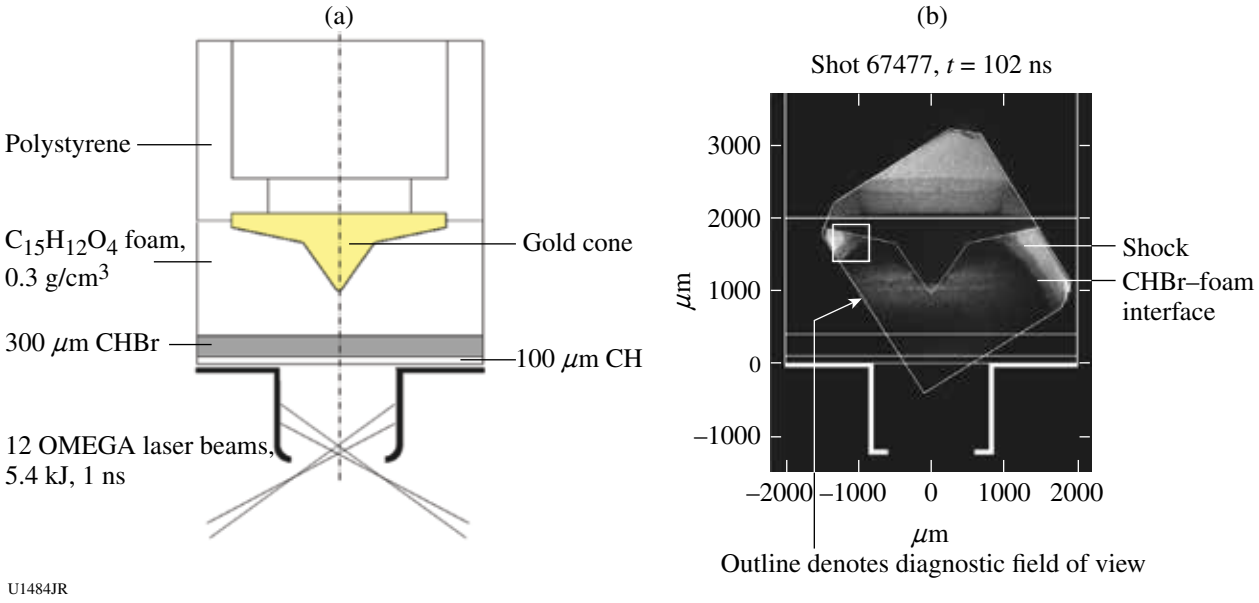

Figure 132.56
(a) Experiment to investigate hysteresis in the development of the Mach stem generated by reflection of a shock at the surface of a gold cone embedded in hydrocarbon foam. Radiation from a laser-heated hohlraum results in ablation of a CH and CHBr pusher that then drives a shock into foam containing the gold cone. (b) The experiment is diagnosed using point-projection backlighting radiography. The small, 500-μm-sq region (surrounded by a white line) identifies the position of the Mach stem, shown in detail in Fig. 132.57. The profile of the gold cone is chosen to provide a specific trajectory of the angle of the incident shock at the cone's surface, as a function of time and radial position.

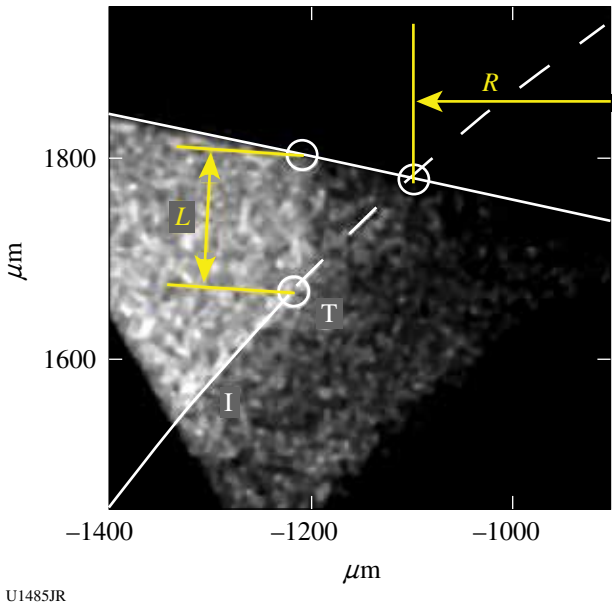

Figure 132.57
Detail taken from Fig. 132.56 showing the incident shock (I) and triple point (T). Metrics of the experiment are the length (L) of the Mach stem, and the radial position (R) at which the incident shock meets the surface of the cone. The 30-μm-diam white circles identify the triple point and the points at which the Mach stem and the extrapolation of the incident shock meet the surface of the cone.

and subtracting off a suitable continuum image. The result shows where molecular clouds absorb ultraviolet radiation and allows us to observe any radiation-driven instability that may be present. It is impossible to do this observation directly at ultraviolet wavelengths because ambient dust causes the entire region to be opaque. An example of such an image, also used on the cover of the 2012 annual report of the NNSA Stewardship Science Academic Alliance program, appears in Fig. 132.59. Observations such as these provide a wonderful opportunity to study the physics of ablated interfaces, a subject of great interest in the laboratory as well.

Results from this work have appeared in several major journals, including High Energy Density Physics and the Astrophysical Journal. A status report on the Mach-stem work, including an analysis of the growth-rate information obtained thus far, was given by co-investigator K. Yirak at the most-recent HEDLA meeting, and a paper is in press to High Energy Density Physics. Additional papers on shock waves overrunning clumps (J. Foster *et al.*, in preparation) and irradiated interfaces (P. Hartigan *et al.*, High Energy Density Physics in press; P. Hartigan *et al.*, Astrophysical Journal in preparation) are forthcoming.

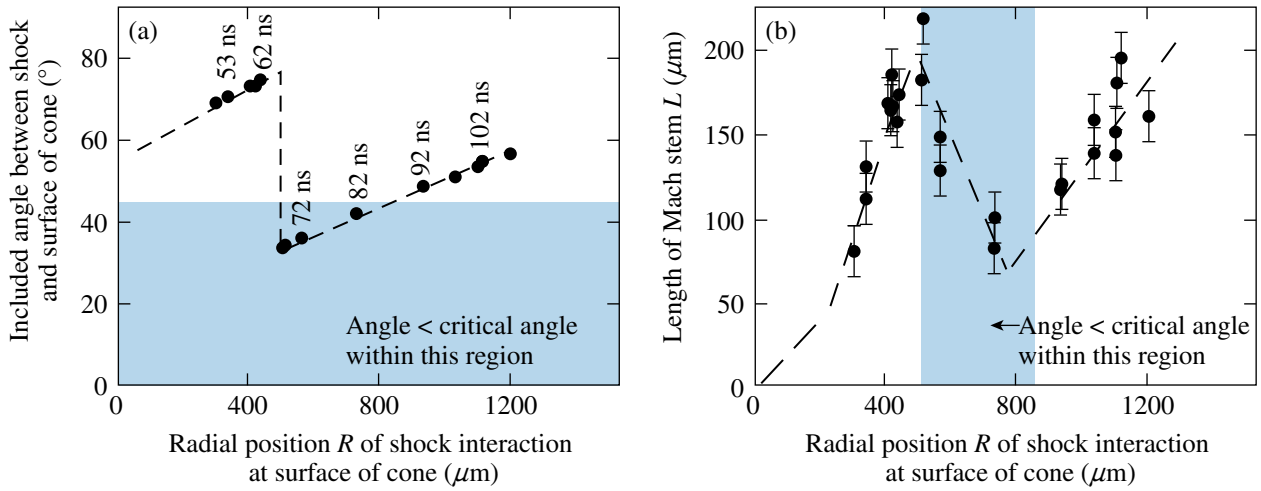

Figure 132.58
(a) Included angle between the incident shock and the surface of the cone and (b) length of Mach stem, both as functions of the radial position of the interaction of the incident shock with the reflecting surface. The growth, destruction, and later re-growth of the Mach stem are evident.

Figure 132.59
A color composite (red = H2, green = HI, blue = OIII) of a small portion of the Carina star formation region. The image reveals spectacular structures that arise when radiation from massive stars interacts with molecular globules that harbor newborn stars.

Recreating Planetary Core Conditions on OMEGA

Principal Investigator: R. Jeanloz (University of California, Berkeley)
Co-investigators: P. Loubeyre (CEA); J. H. Eggert, D. G. Hicks, and G. W. Collins (LLNL); and T. R. Boehly (LLE)

We have extended the determination of the equation of state of dense fluid hydrogen by measuring the Hugoniot of D_2 precompressed in a diamond anvil cell to 6 GPa. We have also collected an extended pressure–density–temperature data set on hydrogen–helium mixtures precompressed to 4 GPa. Two He concentrations have been studied: 20 mol.% He and 50 mol.% He. A strong difference is observed between the shock temperature curves of these two concentrations. As illustrated in Fig. 132.60,

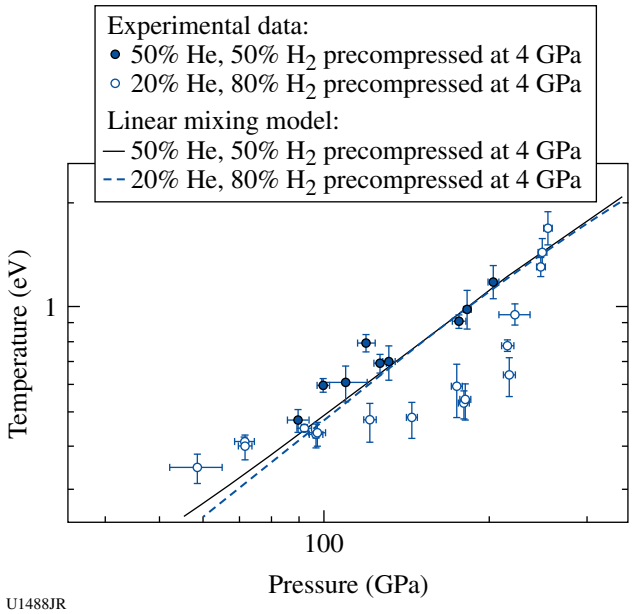

Figure 132.60
In FY12, the OMEGA laser was used to study hydrogen–helium mixtures at planet-core conditions. The H_2, D_2, and H_2–He shock pressure and density were inferred by shock-velocity measurements impedance matched to a quartz standard. The temperature along the Hugoniot data for two different helium contents (20 mol.% He: open symbols; 50 mol.% He: solid symbols) provide evidence for demixing at 20 mol.% He by a drop of the temperature below the expected linear-mixing behavior that describes well the 50-mol.%-He mixture.

for a 20-mol.% He mixture, a strong *relative-cooling* effect is observed, whereas for 50 mol.%, the ideal mixing behavior is followed. We interpret this *relative-cooling* effect as the signature of the phase separation along the shock Hugoniot between 100 and 250 GPa. This result is important because it provides the first experimental evidence for a longstanding theoretical prediction that warm dense H–He fluid mixtures can undergo *unmixing*. This has direct astrophysical implications: a helium-rich phase may separate from hydrogen inside giant planets (so-called "helium rain"). This *differentiation* process releases gravitational energy that is thought to have greatly influenced the evolution of Saturn relative to Jupiter.

Investigation of Hydrodynamic Stability and Shock Dynamics in OMEGA Direct-Drive Implosions Using Spectrally Resolved Imaging

Principal Investigator: R. C. Mancini (University of Nevada, Reno) and R. Tommasini (LLNL)
Co-investigators: J. A. Delettrez, S. P. Regan, and W. Theobald (LLE)

The multimonochromatic (MMI) x-ray imager instrument records arrays of spectrally resolved images whose interpretation and analysis have created a new era for x-ray spectroscopy of inertial confinement fusion plasmas. The MMI data are based on spectrally, spatially, and time-resolved x-ray images because of the emission and/or absorption of radiation by a tracer element added to the plasma. The instrument combines pinhole-array imaging with the dispersion of a Bragg multilayer mirror and the time resolution provided by a framing (gated) camera detector. The MMI data are rich in information and its processing permits the extraction of narrow and broad images as well as space-integrated and space-resolved spectra.[3] The simultaneous and self-consistent analysis of sets of spatially resolved spectra observed along quasi-orthogonal directions has led to the demonstration of a new type of tomography, i.e., *polychromatic tomography*, which, unlike standard tomography, relies on data recorded along a limited number of lines-of-sight (LOS) but employs the information encoded in multiple wavelengths.[4] In this project, we apply spectrally resolved imaging to investigate the hydrodynamic stability and shock dynamics of low-adiabat, direct-drive implosions on OMEGA. In low-adiabat implosions, a nearly isentropic compression is launched by a shaped laser pulse drive that starts from a low intensity, gradually leading to a high intensity. By minimizing preheat, higher compressions are achieved in low-adiabat implosions compared to high-adiabat implosions, therefore making fundamental studies on the stability of low-adiabat implosions relevant to high-energy-density-plasma hydrodynamics and, in particular, inertial confinement fusion. Furthermore, benchmarking of hydrodynamic codes with data from well-characterized implosions is important since these codes are also used to model and design low-adiabat cryogenic implosions and advanced ignition concepts.

The experiments on OMEGA consist of spherical implosions where the 60 OMEGA laser beams symmetrically illuminate a spherical shell filled with deuterium gas. The plastic shell has a 0.5-μm-thick, plastic tracer layer doped with Ti at the 6% (atomic) level of concentration and initially located on the inner surface of the shell. Three identical MMI instruments fielded on TIM-3, TIM-4, and TIM-5 of the OMEGA chamber are used to record the x-ray signal of this spectroscopic tracer. Figures 132.61–132.63 illustrate some of the data processing and analysis results.

Figure 132.61 shows gated narrowband images reconstructed from spectrally resolved image data recorded in frame 1 of OMEGA shot 62086 with the MMI instrument mounted on TIM-3. In addition to the narrowband image based on the Ti Ly$_\alpha$ line transition ($1s$–$2p$, $h\nu$ = 4979 eV), an x-ray image of the same bandwidth based on the nearby continuum is also displayed. The fact that MMI data afford the extraction of images based on spectral signatures of the tracer, and the nearby continuum is important since it permits the removal of the underlying continuum from the line transition image and, therefore, produces a better approximation to the image due to just the line emission of the tracer; this image is also included in Fig. 132.61. In turn, the intensity distribution observed on the line emission image allows us to track the spatial localization of the tracer originally placed on the inner surface of the shell. Since in a perfectly stable, one-dimensional spherical implosion the tracer remains on the inner surface of the shell (i.e., core–shell boundary), the observation of the actual spatial distribution of tracer in the core (through its line emission) provides information about the stability and mixing of the implosion. In this regard, Fig. 132.62 displays the time evolution of the Ti Ly$_\alpha$ line emissivity radial profiles in the core obtained from Abel inversion of angle-averaged narrowband images from data of the same OMEGA shot and TIM shown in Fig. 132.61. Results from two frames, i.e., frames 1 and 3, are shown that are characteristic of early and late times through the collapse of the implosion. The separation in time between frames 1 and 3 is approximately 200 ps. Early in time the tracer emission is localized away from the core center. Later in time, the tracer emission is seen to peak at the center of the core.

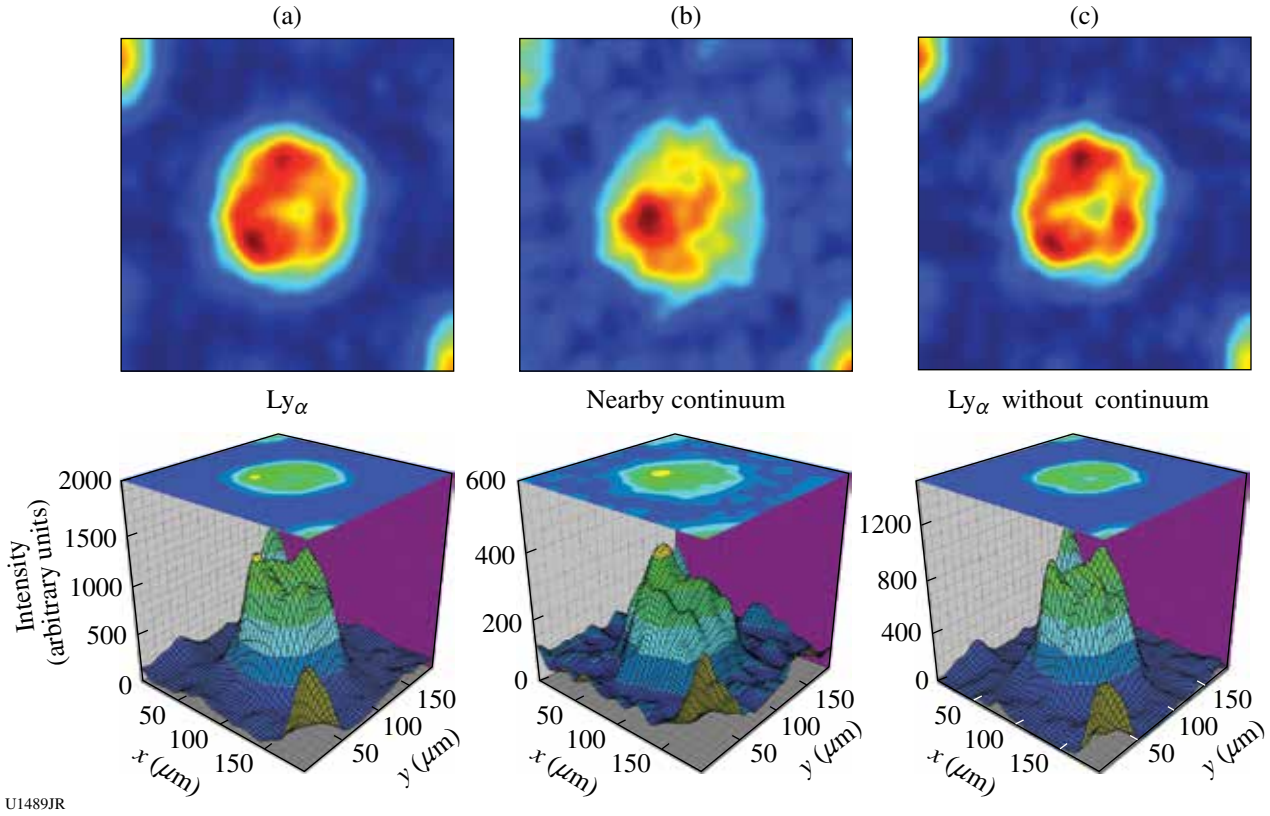

Figure 132.61
Gated narrowband images reconstructed from spectrally resolved image data recorded in frame 1 of OMEGA shot 62086 with the MMI instrument mounted on TIM-3. (a) Intensity map and surface plot of the Ti Ly$_\alpha$ image; (b) intensity map and surface plot of the nearby continuum image; (c) intensity map and surface plot of the Ly$_\alpha$ with the continuum removed.

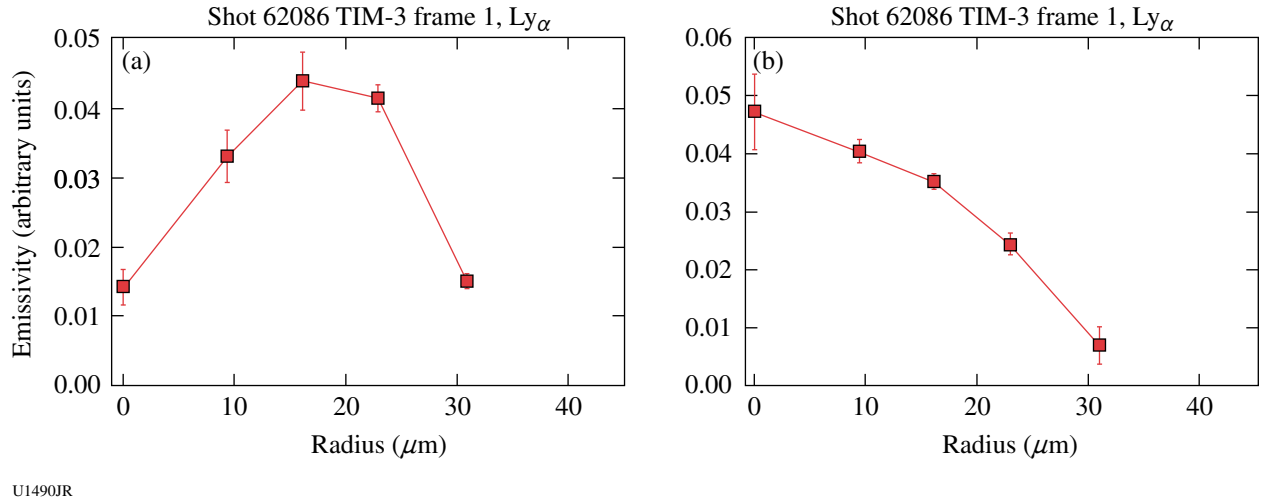

Figure 132.62
Time evolution of the Ti Ly$_\alpha$ line emissivity radial profiles in the core obtained from Abel inversion of angle-averaged narrowband images recorded on OMEGA shot 62086 with the MMI instrument mounted on TIM-3. (a) Early-in-time emissivity profile based on image data recorded in frame 1. (b) Later-in-time emissivity profile based on image data recorded in frame 3. The separation in time between frames 1 and 3 is ~200 ps.

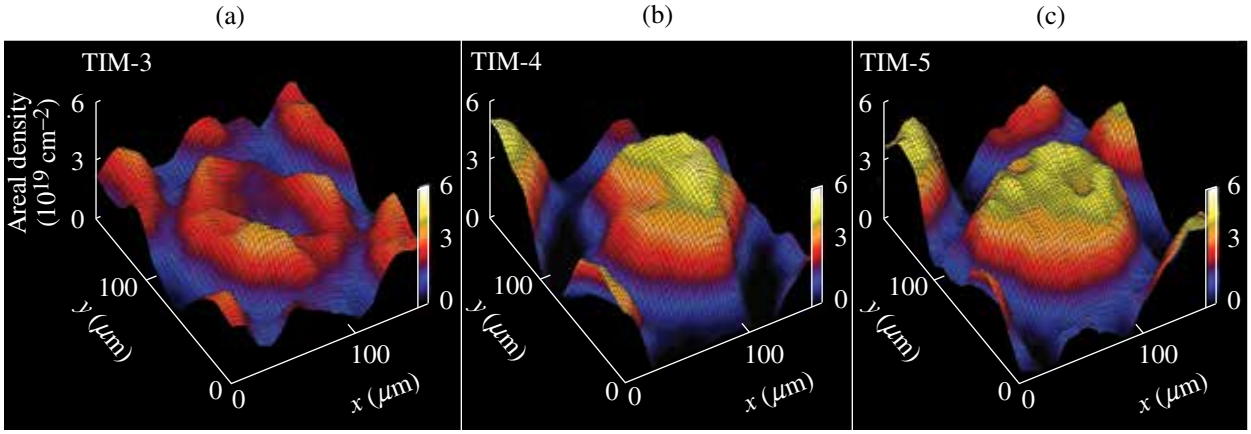

Figure 132.63
Areal-density surface plots extracted from the absorption signature of a Ti-doped tracer layer embedded in the plastic shell, initially located 3 μm from the shell's inner surface. The data were recorded on OMEGA shot 49953 with three identical MMI instruments mounted on TIM-3, TIM-4, and TIM-5. The x and y axes' ranges of the surface plots are from 0 μm to 160 μm, and the z-axis range is from 0 Ti-atoms/cm^2 to 8×10^{19} Ti-atoms/cm^2, or ~45 mg/cm^2 of plastic areal density. This areal density is due to only the compressed plastic of the Ti-doped tracer layer.

Another important aspect of the stability and symmetry of the implosion is the uniformity of the compression of the (unablated) shell confining the implosion core. In this connection, Fig. 132.63 shows areal-density surface plots extracted from the absorption signature of a Ti-doped plastic tracer layer embedded in the plastic shell, 1 μm thick with a 2% atomic concentration level and initially located 3 μm from the shell's inner surface. In this case, the absorption is due to 1s–2p line transitions in F- through He-like Ti ions that are backlit by continuum radiation coming from the hot spot in the core. The photon-energy range of these transitions spans the range from 4450 eV to 4750 eV. The data were recorded in OMEGA shot 49953 with three identical MMI instruments mounted on TIM-3, TIM-4, and TIM-5. We emphasize that this areal density is due to only the compressed plastic of the Ti-doped tracer layer and not the entire compressed shell. We also note that the areal-density maps are extracted in two different ways and checked against each other for consistency: on the one hand, from ratios of images based on the (attenuated) absorption feature and the (unattenuated) nearby continuum; on the other hand, from the analysis of sets of spatially resolved absorption spectra. The results displayed in Fig. 132.63 clearly show the modulations in areal density along a given LOS as well as the differences along different LOS. These results provide information about the stability and symmetry of the implosion.

Charged-Particle Probing of Inertial Confinement Fusion Implosions and High-Energy-Density Plasmas

Principal Investigators: R. D. Petrasso and C. K. Li (MIT)
Co-investigators: F. H. Séguin and J. A. Frenje (MIT); T. C. Sangster, V. Yu. Glebov, D. D. Meyerhofer, and R. Betti (LLE); and O. L. Landen (LLNL)

In FY12 MIT work included a wide range of experiments applying proton radiography, charged-particle spectrometry, and neutron spectrometry methods developed by MIT and collaborators to the study of high-energy-density physics (HEDP) and inertial confinement fusion (ICF) plasmas. Eighteen NLUF-related papers were published in FY12,[5–22] including four papers in Physical Review Letters,[5,10–12] and there were many invited talks and contributed talks at conferences. Our NLUF experiments also provided unique research opportunities in HEDP for eight MIT graduate students, who will use (or have already used) resultant data in major parts of their theses, and for several undergraduates.

Topics studied on the OMEGA[23] and OMEGA EP[24] lasers included the imaging, identification, and measurement of electric and magnetic fields generated in direct- and indirect-drive ICF plasmas[9,12,13,17,19,21] and other laser-generated plasmas;[7,9,10] Rayleigh–Taylor[7,10] and other[12,13] instabilities; the characterization of ICF capsule implosions;[8,11,13] ions accelerated by laser–plasma interactions;[6,8] plasma nuclear science;[5] and diagnostic development.[14–20,22] The work successfully addressed basic physics issues and issues directly relevant to the future success of ignition experiments at the National Ignition Facility (NIF) as well as general issues of importance to HEDP and the physics of fields generated by laser–plasma interactions.

As described in Physical Review Letters[10] and illustrated in Fig. 132.64, monoenergetic, charged-particle radiography[17,25] was used to make the first measurements of magnetic fields generated by Rayleigh–Taylor (RT) instabilities.[10] Experiments were performed using laser-irradiated plastic (CH) foils with pre-imposed surface perturbations to stimulate the instability at a known spatial wavelength. Path-integrated field measurements were compared directly with benchmarked hydrodynamic simulations, and it was shown that diffusion processes were necessary to explain the observations.[10] Figure 132.64(a) illustrates that RT-induced fields are generated near the ablation front, where local resistivity is high; therefore, magnetic fields of the measured strength, shown in Fig. 132.64(b), will have a minimal impact on thermal heat conduction. This evidence demonstrated for the first time that RT-induced magnetic fields do *not* significantly reduce heat conduction in directly driven targets until perturbation growth reaches the hotter, more-conductive region near the critical surface.[7]

Work described in Physical Review Letters[12] and illustrated in Fig. 132.65 provided novel physics insight into the effects of hohlraum fill gas on x-ray–driven implosions. The first time-gated proton radiography showing spatial structure and temporal evolution of fields and plasma in the hohlraum interior demonstrated that fill gas compresses wall blowoff, inhibits plasma jet formation, and impedes plasma stagnation. The important roles of spontaneously generated electric and magnetic fields in the hohlraum dynamics and capsule implosion were demonstrated. Interpenetration of blowoff and fill gas occurs as a result of the classical RT instability as the lighter, decelerating ionized fill gas pushes against the heavier, expanding gold wall blowoff. The results will have an important impact on the ongoing ignition experiments on the NIF.

Two other papers in Physical Review Letters[5,11] described important studies of basic nuclear physics and ICF dynamics. Neutron spectrometry was used to diagnose implosions of deuterium–tritium (DT)-gas–filled capsules on OMEGA. The neutron spectrum from the T(t,2n)^{4}He (*tt*) reaction was measured[5] and used to study the *tt* reaction in thermonuclear plasmas at low reactant center-of-mass (c.m.) energies. When compared to accelerator experiments at higher c.m. energies

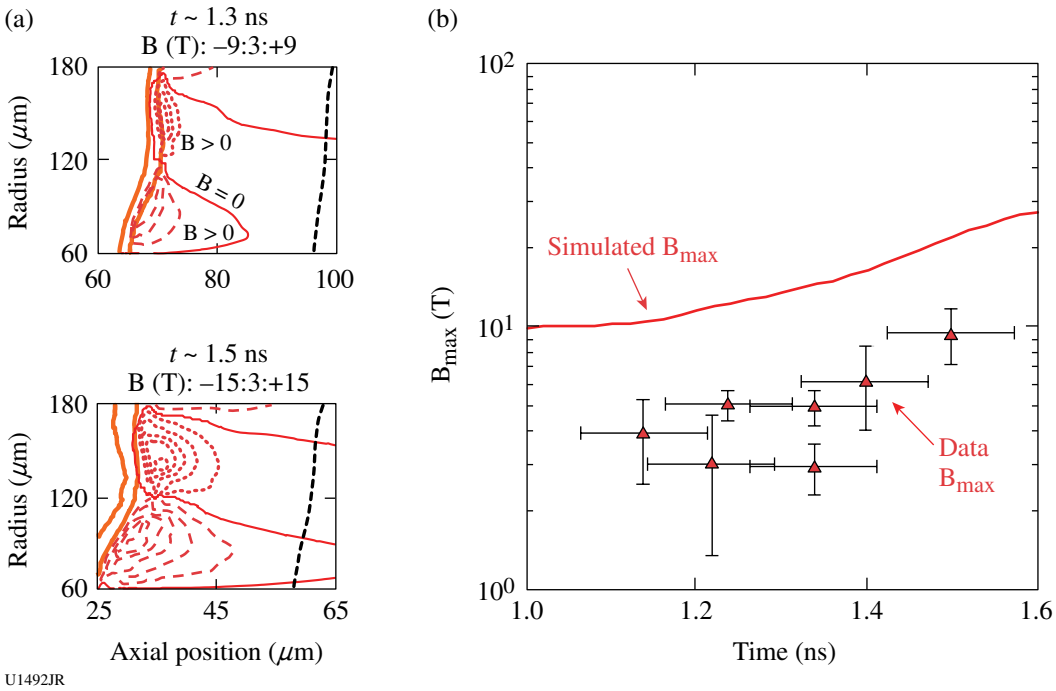

Figure 132.64
(a) Contour plots of magnetic fields from hydrodynamic simulations of a growing Rayleigh–Taylor instability in a laser-driven plastic foil that had machined grooves with a wavelength of 120 μm (thick solid orange). The times corresponding to the two plots are 1.3 and 1.5 ns during a 2-ns laser pulse. Magnetic-field contour levels are identified at the top of each plot and contours are indicated as follows: negative (into page) (red dots); positive (out of page) (red dashes); and zero contour (thin red solid line). Maximum field strength is clearly shown to occur near the ablation front, far from the hotter critical surface (short black dashes). (b) Comparison of measured and simulated peak magnetic fields. The factor of ~2 discrepancy is due to exclusion of collisional terms (diffusion) in the model. For more information, see Refs. 7 and 10.

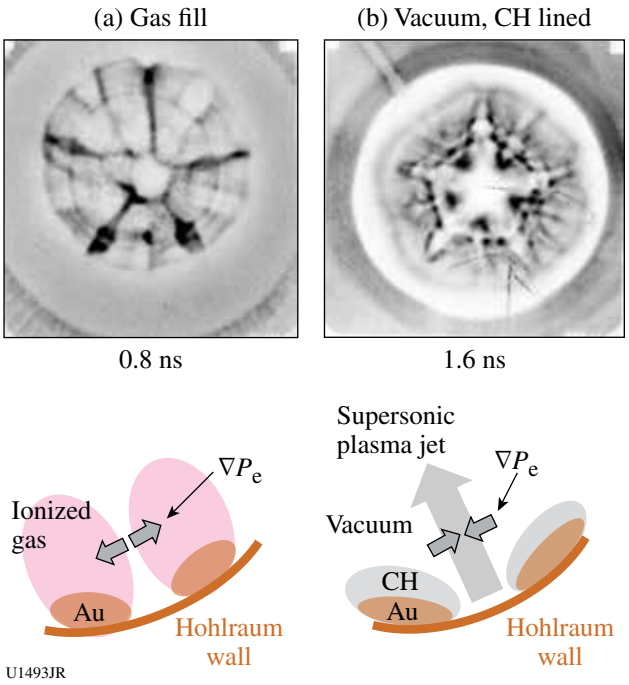

Figure 132.65
Some differences between plasma behavior in laser-driven hohlraums (a) with gas fill and (b) without gas fill but with a CH liner, shown by proton radiography images. The images were recorded during indirect-drive ICF experiments, looking down the hohlraum axis from a CR-39 detector toward a monoenergetic, 15-MeV proton backlighter. The proton fluence distributions in these images show a proton surplus in the regions between pairs of expanding plasma plumes in (a) a gas-filled, Au hohlraum but a proton deficit in (b) a CH-lined, vacuum Au hohlraum, indicating opposing directions of the self-generated electric fields as illustrated schematically by the corresponding cartoons. For details, see Ref. 12.

(above 100 keV), the results indicate an energy-dependent n + ^{5}He reaction channel branching ratio not previously recognized. In addition, D(d,p)T (*dd*) and T(t, 2n)^{4}He (*tt*) reaction yields were measured and compared[11] with those of the D(t,n)^{4}He (*dt*) reaction yield. Absolute spectral measurements of *dd* protons and *tt* neutrons were measured. It was concluded that the *dd* yield is anomalously low and the *tt* yield is anomalously high relative to the *dt* yield, an observation that we conjecture to be caused by a stratification of the fuel in the implosion core. This effect may be present in ignition experiments planned on the NIF.

Collisionless Shocks in Laboratory High-Energy-Density Plasmas

Principal Investigator: A. Spitkovsky (Princeton)
Co-investigators: L. Gargate (Princeton); H.-S. Park, B. A. Remington, S. Pollaine, and D. Ryutov (LLNL); J. P. Knauer, G. Fiksel, and R. Betti (LLE); Y. Sakawa, T. Ide, T. Kato, Y. Kuramitsu, T. Morita, and H. Takabe (Osaka University); T. Bell (University of Oxford); M. Koenig and A. Ravasio (Ecole Polytechnique); and E. Liang (Rice University)

This NLUF program studies the creation of collisionless shocks in counter-propagating laser-produced plasmas. Collisionless shocks are of great importance in astrophysical and space plasmas and occur when the mean free path to Coulomb collisions is large compared to the size of the shock transition. The shock is then mediated by collective plasma effects as the result of the interaction between plasma particles and the self-generated electromagnetic fields. Collisionless plasma conditions can now be created on OMEGA and OMEGA EP, where the laser-driven plasmas propagate at speeds of ~1000 km/s and densities of ~10^{18} to 10^{19} cm^{-3}. The experiments in this program collide two streams of high-speed plasma and study the formation of shocks as a function of an externally applied magnetic field that is generated by a set of Helmholtz coils at the interaction region (Fig. 132.66). The theoretical expectation is that at low external fields the shock is mediated by the filamentation (Weibel) instability, while at higher fields magnetic reflection of ions will form the shock. These regimes are representative of the conditions encountered in a range of astrophysical environments, including supernova remnant shocks and solar wind shocks. The experiments on OMEGA are testing these shock-formation mechanisms and addressing the open questions of astrophysical collisionless shock physics such as the presence of particle acceleration and the mechanisms of magnetic-field amplification in shocks.

In FY12, we performed shock experiments in a joint OMEGA/OMEGA EP shot day on 24 April 2012. In this experiment, we used the OMEGA laser to initiate two ablated plasma

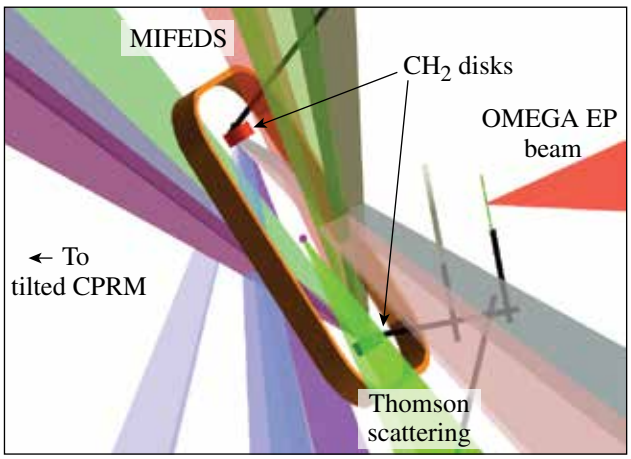

Figure 132.66
Diagram of the experimental setup for NLUF MagShock-12a.

flows from CH foils. OMEGA EP was used to provide a short pulse for proton radiography of the interaction region. The new configuration of the magnetic coil was fielded (fabricated by G. Fiksel's group at LLE). The new design used a single coil, which delivered a higher peak magnetic field of 5 T (compared to 1 T in 2011). The diagnostics included Thomson scattering and proton radiography (delivered by a short pulse from OMEGA EP). We moved the radiochromic film pack (CPRM) closer to the target to obtain a wider field of view than in 2011. We performed seven shots (five joint) and are very thankful to the facility for providing outstanding support during this challenging experiment.

We studied the Thomson signal and proton images as a function of the external magnetic field and tried several time offsets for diagnostics to build a time series. The Thomson signal was fairly insensitive to the magnetic field. The proton signal showed characteristic filamentation that we observed in 2011. It is important that this signal is reproducible. The field had a moderate effect on the early time signal [Figs. 132.67(a) and 132.68(a)]. Analysis of later snapshots (5 ns) is still continuing and requires additional shots to completely fill out the time series. This will be performed in 2013.

We modeled the proton signal using particle-in-cell (PIC) simulations. We concentrated on the unmagnetized 3-D PIC simulations of interpenetrating flows, tracing orbits of test protons through the simulation domain to accumulate proton images. The results (Fig. 132.69) show that we can reproduce main features of the interaction–turbulent ripples with horizon-

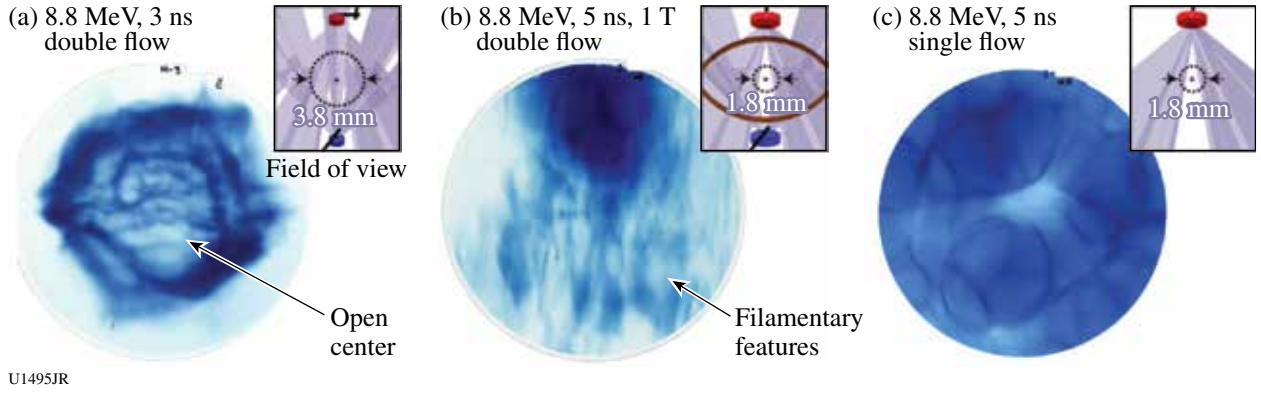

Figure 132.67
Proton images of plasma flows with little or no external magnetic field. (a) 3-ns counter-streaming flows, (b) 5-ns counter-streaming flows, and (c) 5-ns single-plasma flow. Insets: experimental configuration and proton-image field of view.

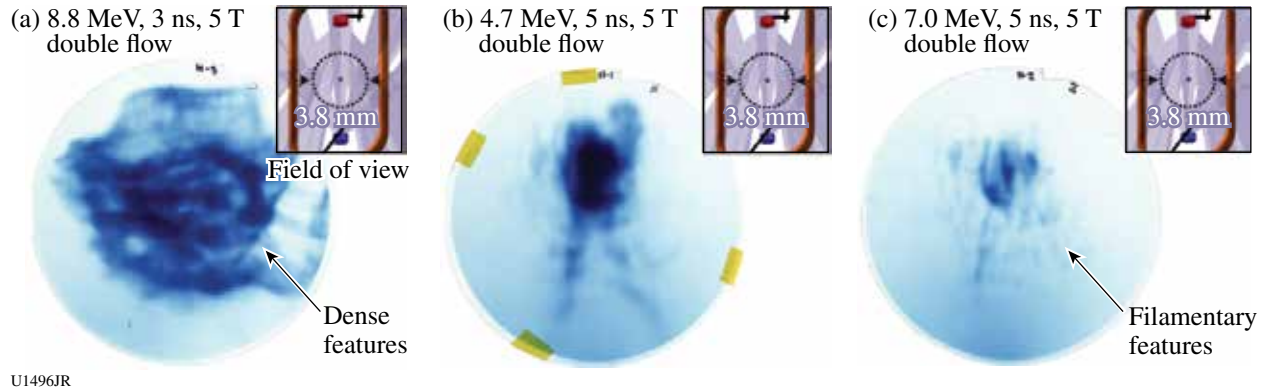

Figure 132.68
Proton images of counter-streaming plasma flows with a moderately strong external B field of 5 T. Both foils are illuminated. (a) 3 ns with 8.8-MeV protons, (b) 5 ns with 4.7-MeV protons, and (c) 5 ns with 7.0-MeV protons. Insets: experimental configuration and proton-image field of view.

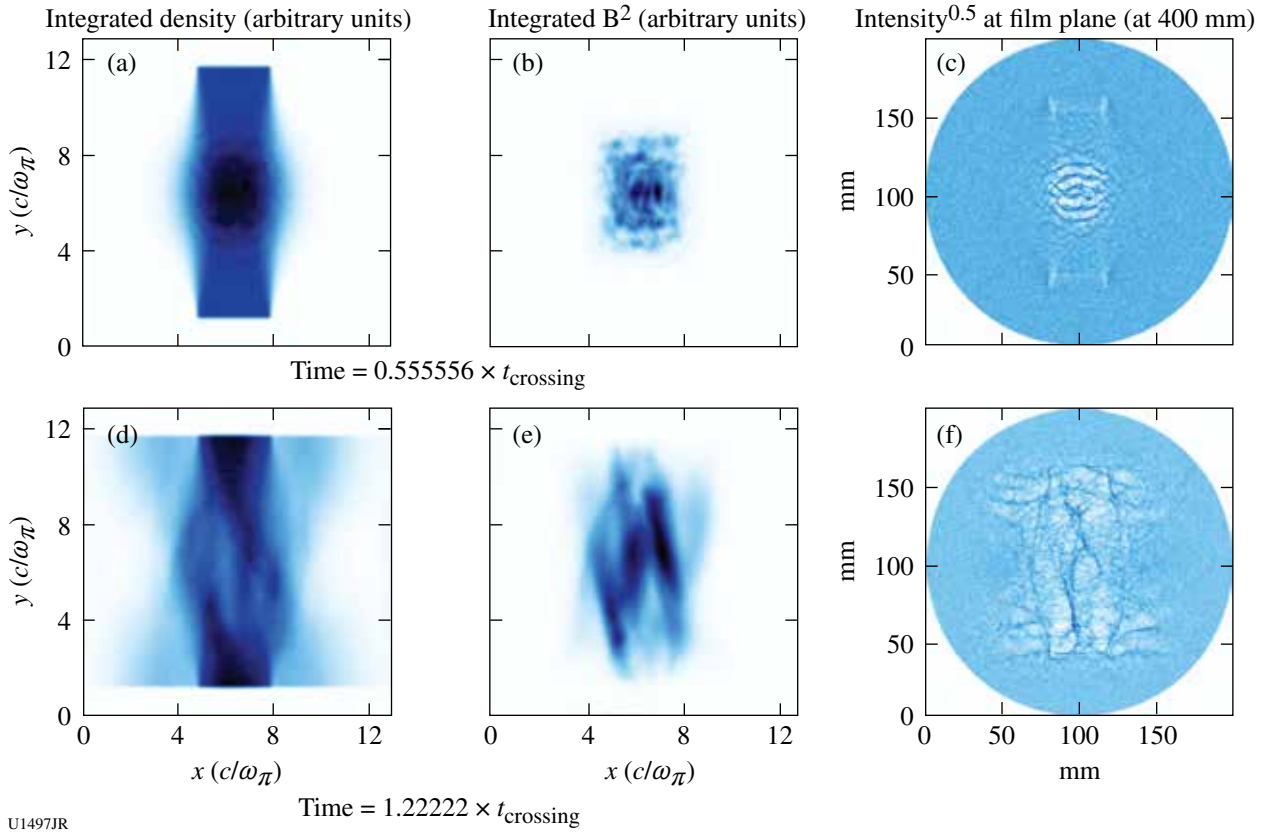

Figure 132.69
Simulated proton imaging using PIC simulations. Plasmas collide along the *y* axis. [(a),(d)] Time evolution of the integrated density and [(b),(e)] magnetic-energy profiles. [(c),(f)] Simulated proton imaging signal as collected on the film plate 400 mm from the proton source. These images show horizontal and bubble-like features at early times and filamentary features at late times. The field of view in (c) is 2× larger than in (f).

tal features at early times and longitudinal filaments at later times. The ripples are caused by electrostatic fields that are created in the first moments of collision, while the later filaments are driven by the magnetic field from the Weibel instability. We are currently exploring how the flow parameters can be better approximated in the simulation and checking whether any of the structures observed in the experiment are a result of electrostatic shocks.

We developed a suite of post-processing diagnostics for the PIC simulation code that allows us to calculate Thomson and radiography signals based on the full distribution function from the simulations. Preliminary analysis of the data and PIC simulations indicates that the next experiment in this program in FY12 will require stronger magnetic fields. The design work on increasing the magnetized inertial fusion energy delivery system (MIFEDS) magnetic fields is currently underway, and we expect another increase by a factor of 2 after the upgrade of MIFEDS.

This NLUF research has been reported in three peer-reviewed publications,[26–28] five invited papers,[29–33] and one contributed paper.[34]

Investigation of Laser-to-Electron Energy Coupling Dependence on Laser Pulse Duration and Materials Composition

Principal Investigators: M. S. Wei and R. B. Stephens (General Atomics)
Co-investigators: F. N. Beg, R. Mishra, H. Sawada, L. C. Jarrott, and J. Peebles (University of California, San Diego); H. McLean and P. Patel (LLNL); W. Theobald and C. Stoeckl (LLE); and Y. Sentoku (University of Nevada, Reno)
Lead graduate student: A. Sorokovikova (University of California, San Diego)

Efficient conversion of laser energy to fast electrons (1 to 3 MeV) and their subsequent energy transport to the compressed fuel are extremely important for the success of fast ignition.

Energy coupling is controlled by the nature of the plasma (i.e., density profile, ionization, etc.) at the laser–plasma-interaction (LPI) interface and the dynamic response of the transport material, which both evolve with time, therefore dependent on laser pulse length. For full-scale fast ignition, the high-intensity ignitor pulse duration will be of the order of 10 ps. So far, most of the electron source and transport studies have been limited to subpicosecond pulses with energies ~100 J. The goal of the General Atomics NLUF project is to extend such investigation to fast-ignition (FI)–relevant pulse durations using the high-energy (>1-kJ) OMEGA EP laser. In this second-year NLUF experiment in FY12, our study is focused on the effect of the laser pulse length on LPI and fast-electron source generation and the transport by systematically varying laser pulse duration from 0.7 ps up to 10 ps at a constant laser intensity and using identical multilayered planar-foil targets. Figure 132.70 shows the schematics of the target and experimental setup on the OMEGA EP laser. The planar multilayered foil targets consist of an Al substrate with a Cu x-ray tracer layer (20 μm thick) buried ~100 μm below the front surface and a large, thick (5-mm × 5-mm × 1-mm) conductive carbon layer at the back to minimize fast-electron refluxing. The OMEGA EP backlighter beam was normally incident onto the front target surface. The beam was tightly focused with a spot radius of ~20 μm within which contained 80% of the laser energy. The experiment was performed with identical targets at the same laser intensity ($I_{peak} \sim 2 \times 10^{19}$ W/cm^2) for three different laser pulse lengths, i.e., 0.7 ps, 3 ps, and 10 ps, with main pulse energies of 100 to 150 J, 400 J, and 1500 J, and prepulse energies of 5 mJ, 16 mJ, and 110 mJ, respectively. Fast electrons were characterized by the induced K-shell fluorescence from the Cu tracer layer and high-energy bremsstrahlung x rays from the whole target. Two-dimensional Cu K_α spot and the total K_α yield were measured with a spherical quartz crystal imager (SCI) and a calibrated x-ray spectrometer using a highly oriented pyrolytic graphite (HOPG) diffraction crystal, and the high-energy bremsstrahlung spectrum was monitored at two angles behind the targets with two fixed-port bremsstrahlung MeV x-ray spectrometers (BMXS), which were recently implemented in the OMEGA EP chamber by the PI and project team.

The measured bremsstrahlung spectrum data suggest a hotter energy distribution in the 10-ps interaction case. Figure 132.71 shows the inferred fast-electron temperature from the Monte Carlo modeling analysis fitting a synthetic electron energy distribution (one temperature exponential) to the measured bremsstrahlung spectrum. The slope temperature increased by a factor of 2, i.e., ~1.5 MeV in 10-ps LPI compared to 0.7 MeV in the 0.7-ps case. The 2-D Cu K_α images (Fig. 132.72) showed a large change in LPI-produced electron-beam spatial distribution with increasing laser pulse duration. The fast-electron beam evolved from a single beam with a beam spot size of about 160 μm in a subpicosecond interaction into multiple narrow (~70-μm) filaments over a 10-ps pulse dura-

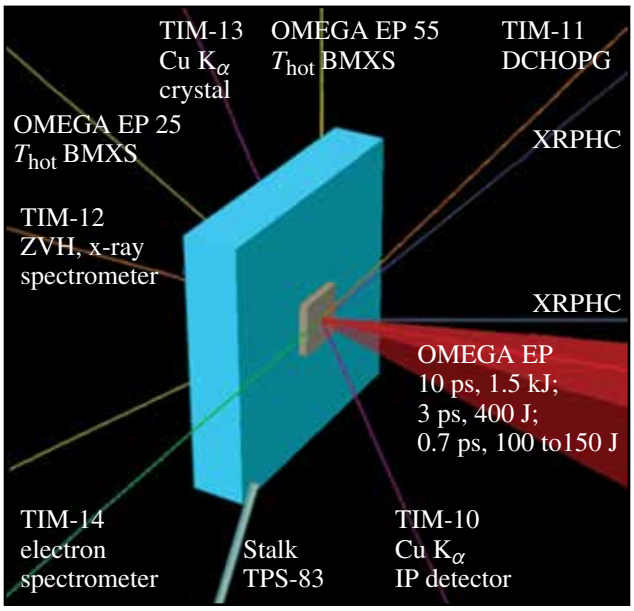

U1498JR

Figure 132.70
Schematic of the experimental setup.

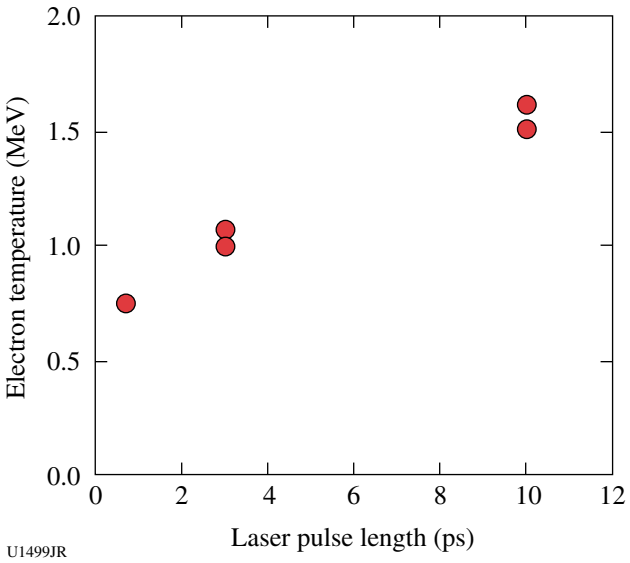

U1499JR

Figure 132.71
Inferred fast-electrons' energy spectrum slope temperature from the measured bremsstrahlung spectrum data.

tion. The very large angular separation (~45°) between these distinct filaments in the 10-ps case is quite unusual, indicating a significant deviation of energy flow directions from the original laser propagation axis. The observed new phenomena such as hotter energy distributions and multiple widely separated filaments can be caused by the presence of an extended pre-plasma in the 10-ps case. It is well known that LPI in a longer pre-plasma can produce fast electrons with a hotter electron spectrum as the result of stochastic heating. Extended pre-plasmas can also result in strong nonlinear LPI processes such as filamentation, hole boring, and hosing instabilities, which can develop over a longer pulse duration leading to the formation of widely separated electron-beam filaments. Preliminary collisional particle-in-cell (PIC) simulations to examine LPI and fast-electron generation over 2 ps using the PICLS (PIC simulations for large-scale plasmas) code have suggested that these widely separated electron filaments could be initiated by the filamented and self-focused laser beam [Fig. 132.73(a)] in the long-scale-length pre-plasma, injecting electrons into solid plasmas at particular angles. These electron filaments could be further pinched by self-generated resistive magnetic fields inside the high-density plasmas as shown in Figs. 132.73(b)

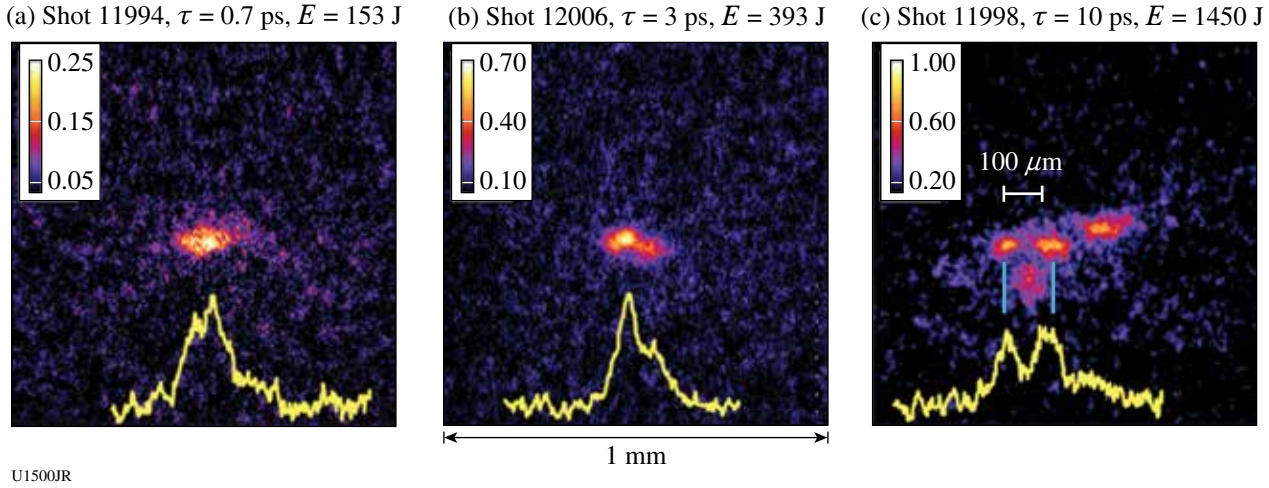

Figure 132.72
Cu K_α fluorescence images showing a fast-electron beam cross section ~100 μm below the generating point using a laser pulse of (a) 0.7 ps, 153 J, (b) 3 ps, 393 J, and (c) 10 ps, 1450 J in the OMEGA EP experiment. All images are to the same spatial scale and compressed vertically because of the view angle. The yellow lines at the bottom of each image are plots of the pixel intensity along a horizontal line through the points.

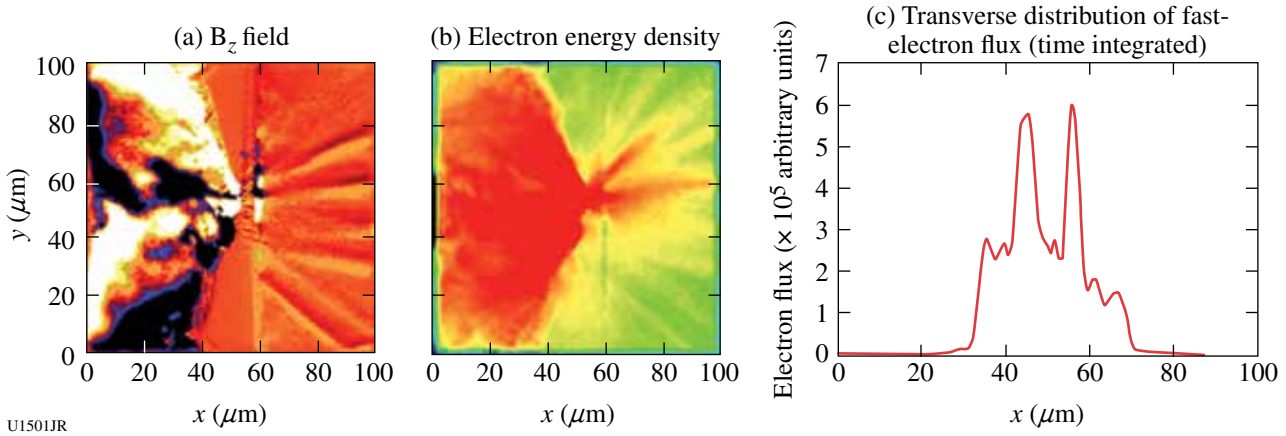

Figure 132.73
Preliminary 2-D PIC modeling results of LPI and fast-electron generation over a 2-ps pulse duration. The semi-infinite high-intensity laser with a focal-spot size of 30 μm rises to peak intensity (10^{20} W/cm^2) in 330 fs and stays constant. The target is a planar Al slab with a pre-plasma (8-μm density scale length) in front of the solid Al. (a) Quasi-static azimuthal B_z field; (b) electron energy density at 2 ps; and (c) the transverse profile of the time-integrated fast-electron flux taken in a 2-μm-thick, 100-μm-wide sampling box at x = 65 μm.

and 132.73(c). Although this simulation was performed with a much higher laser intensity, the pre-plasma scale length is of a similar order as that in our experiment and the observed phenomena may be applicable to the observed electron filaments in our experiment. Simulations with the realistic laser and pre-plasma parameters are underway, which will examine the dependence of beam filaments on pre-plasma scale length and pulse duration.

In summary, the FY12 GA-led NLUF experiment has systematically investigated the dynamics of the LPI-produced fast-electron source generation and transport from subpicosecond to over 10-ps pulse durations. We observed formation of multiple electron filaments in LPI with a longer scale length of pre-plasma over 10 ps. Future experiments using the newly available ultrahigh-contrast OMEGA EP pulses are planned to further examine the LPI and electron-beam dynamics in an initially pre-plasma free condition to help identify the roles of the pre-plasma and pulse length on the laser filaments and resistive beam filamentation.

Intense Laser Interactions with Low-Density Plasma Using OMEGA EP

Principal Investigator: L. Willingale, C. Zulick, A. G. R. Thomas, A. Maksimchuk, and K. Krushelnick (University of Michigan); P. M. Nilson, R. S. Craxton, C. Stoeckl, V. Yu. Glebov, and T. C. Sangster (LLE); H. Chen (LLNL); J. Cobble (LANL); and P. Norreys (RAL)

The study of high-intensity laser interactions with low-density plasma is of interest to many phenomena such as channeling,[35] electron and ion acceleration, and neutron and x-ray production. The focus of the low-density plasma campaign this year has been to investigate electron acceleration and neutron production. To generate an underdense target, a long-pulse beam (2.5 ns, ~1200 J in an 800-μm-diam focal spot) is used to create a plasma plume from a plastic-foil target. The main interaction beam is then focused into the plasma plume, with the laser propagating parallel to the target surface so that it sees an approximately Gaussian density profile (2-D *SAGE* modeling estimates the plasma-density profile).

Electron spectra along the laser axis were measured using the electron positron proton spectrometer (EPPS). High-energy electrons with an effective beam temperature many times greater than the ponderomotive potential were measured under several different laser pulse-length and energy conditions. Since the channels are almost completely cavitated at OMEGA EP laser intensities, a plasma wakefield cannot be responsible for the electron acceleration. Instead, particle-in-cell simulations indicate that a direct laser acceleration (DLA) mechanism is responsible.[36] For the electrons to be accelerated via DLA, they must be injected into the cavitated channel with some initial momentum. Based on proton probe data showing the channel formation, periodic modulations are observed at the channel wall [Fig. 132.74(d)], which are consistent with surface wave formation. Particle-in-cell simulations indicate the surface waves can act as the required injection mechanism for DLA.[37]

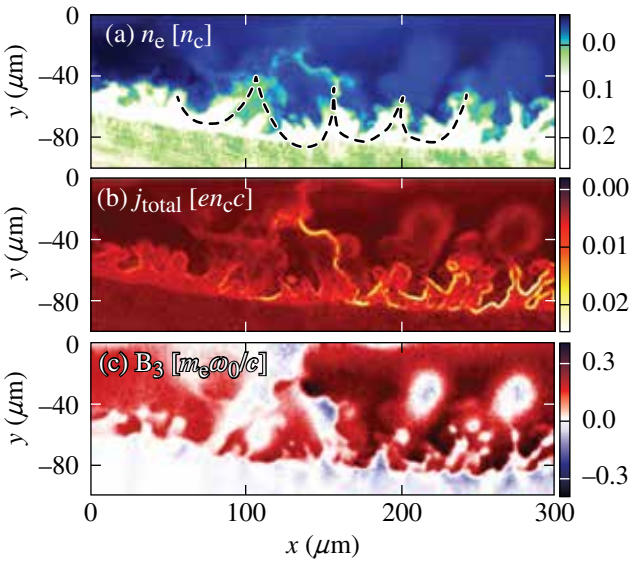

(d) Experimental proton probe image of the channel

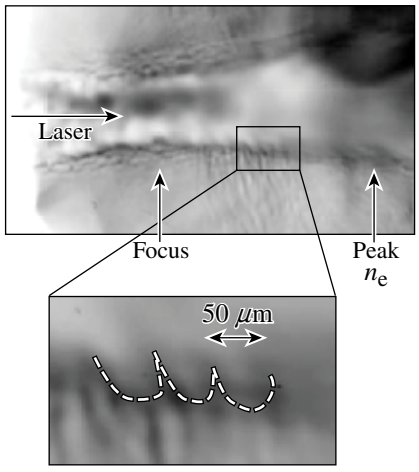

U1502JR

Figure 132.74
Particle-in-cell simulation data showing the modulations in the channel wall region in (a) electron density, (b) the total current, and (c) the transverse magnetic field. (d) Experimental proton probe image of the channel wall illustrating the periodic modulations.

Figures 132.74(a)–132.74(c) show simulation data illustrating the surface wave modulation that has been driven in the channel walls. High-temperature electron spectra are also observed in the simulations.

The shape of the neutron spectra from underdense plasma interactions can enable us to estimate the ion heating within the channel.[38] For the neutron-production experiment, deuterated polyethylene (CD_2) targets were used instead of the regular CH_2 targets. To measure the neutrons, a time-of-flight scintillator diagnostic that was gated using a microchannel plate to reduce the signal from the prompt gamma flash. Simultaneously, the transverse ion spectrum was measured using the Thomson parabola ion spectrometer (TPIE). Figure 132.75(a) shows an example of a time-of-flight trace and indicates the main features. Figure 132.75(b) shows the uncalibrated neutron spectra comparing the signal from CH and CD plasma at the same plasma density and under the same laser conditions. The residual signal from the prompt γ flash means that it is not possible to measure neutrons with energies >12 MeV. A plasma density scan was also performed and indicated higher neutron yield for higher plasma density as would be expected [shown in Fig. 132.75(c)]. Analysis is underway to address calibration and saturation effects for the neutron diagnostic so that comparison with the measured ion spectra and qualitative conclusions can be made.

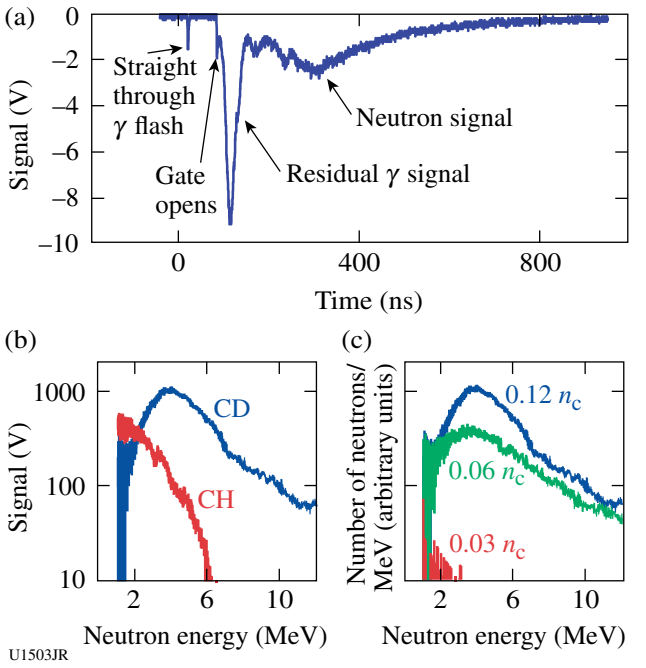

Figure 132.75
(a) Time-of-flight trace showing the main features of the signal. Uncalibrated, preliminary neutron spectra comparing (b) CH with CD plasma shots and (c) different peak CD plasma density shots.

The authors gratefully acknowledge the *OSIRIS* consortium for the use of the *OSIRIS* 2.0 code.

FY12 Laboratory Basic Science Programs

In FY12, LLE issued a solicitation for LBS proposals to be conducted in FY13. A total of 32 proposals were submitted. An independent review committee reviewed the proposals and recommended that 16 proposals receive 28 shot days at the Omega Laser Facility in FY13. Table 132.VIII lists the successful LBS proposals.

Fifteen LBS projects were allotted Omega Facility shot time and conducted a total of 273 target shots at the facility in FY12. This work is summarized in this section.

Measurements of the Viscosity of Shock-Compressed Fluids: Studies of Water and Silica

Principal Investigators: P. M. Celliers and M. A. Barrios (LLNL)

This is the second in a series of experiments that aims to demonstrate a method for determining the viscosity of a high-pressure fluid created by the propagation of a strong shock front through an initially transparent sample. The measurement technique is based on observing the evolution of a spectrum of perturbations imposed on a multi-Mbar shock front passing through the sample material. The viscosity of the liquid state just behind the shock front is expected to influence the decay rate of the perturbations as the shock front propagates; detailed measurements of the perturbation state can be compared with calculations to assess the viscosity. The sample under study is liquid silica (SiO_2), produced by propagating the shock through samples of either alpha-quartz or fused silica. The viscosity of high-pressure liquid silica has obvious geophysical relevance, and measurements in the Mbar domain are impossible with conventional methods. An earlier campaign in 2010 examined the shock response to a perturbation spectrum that was generated by an etched array of shallow pits a few microns deep and 10 μm in diameter that were created on the sample surface at the interface with the ablator. The 2012 campaigns examined the response to a random distribution of surface perturbations generated by roughening the silica surface with a grinding technique. Initial experiments in October 2011 used the active shock breakout (ASBO)/streaked optical pyrometer (SOP) to perform hohlraum drive characterization measurements in preparation

Table 132.VIII: Approved FY13 LBS proposals.

Principal Investigator	Affiliation	Project Title
P. M. Celliers	LLNL	Equation of State and Optical Properties of Dense Silica: Shock Study of Coesite and Stishovite
H. Chen	LLNL	Exploring Pair Plasma and Their Applications Using OMEGA EP
J. R. Davies	LLE	Fast-Electron Control with Magnetic Field in Hohlraum
J. H. Eggert	LLNL	HED Condensed Matter: Magnesium and Aluminum
G. Fiksel	LLE	Magnetic Reconnection and Particle Energization in High-Energy-Density Plasmas in the Presence of an External Magnetic Field
G. Fiksel	LLE	Magnetized ICF Implosions on OMEGA
R. F. Heeter	LLNL	"Gattling Gun" Long-Duration Radiation Sources on OMEGA EP for Sustained-Drive Hydrodynamics and Low-Density Atomic Physics Applications on OMEGA EP and the NIF
B. R. Maddox	LLNL	Direct Measurements of Dislocation-Based Plastic Flow in Quasi-Isentropically Compressed bcc Metals
H.-S. Park	LLNL	Astrophysical Collisionless Shock Generation by Laser-Driven Experiments
P. K. Patel	LLNL	Areal-Density Measurements of Cone-in-Shell Implosions Using Compton Radiography for Fast Ignition
Y. Ping	LLNL	Long-Term Dynamics of Hole Boring and Target Heating at Fast-Ignition-Relevant Conditions
S. P. Regan	LLE	Collective X-Ray Scattering from Shocked Liquid Deuterium
J. R. Rygg	LLNL	Extreme Chemistry, Equation of State, and Optical Properties of Dense Water at Terapascal Pressure
A. A. Solodov	LLE	Fast-Ignition Integrated Experiments with Low-Z Cone-Tip Targets
C. Stoeckl	LLNL	Spectroscopy of Neutrons Generated Through Nuclear Reactions with Light Ions in Short-Pulse Laser-Interaction Experiments
W. Theobald	LLE	Laser Channeling in Long-Scale-Length, Overdense Plasmas

for the rippled shock measurements carried out in May 2012. The second campaign in May used the OMEGA high-resolution velocimeter (OHRV) to observe the velocity perturbations directly on the surface of the reflecting shock front.

The shocks were driven using a hohlraum coupled to a 50-μm poly(methylmethacrylate) (PMMA) ablator followed by the sample. As the shock passed through this interface, the perturbations were transferred to the shock front, which were detected and measured quantitatively by the OHRV. An example of a 2-D velocity spectrum recorded on these experiments is shown in Fig. 132.76. Examples of averaged velocity spectra for ~170-GPa shocks driven into fused silica are shown in Fig. 132.77, along with model calculations of the expected velocity spectra assuming a viscosity of 35 poise. The model calculations employ an analytical expression derived by Miller and Ahrens.[39] Detailed analysis of these data is at a preliminary stage; the goal is to fit the data set to the analytical model in order to estimate the viscosity. Initial indications suggest that the viscosity is in the range of a few poise to tens of poise.

Exploring Pair Plasma and Its Applications Using OMEGA and OMEGA EP

Principal Investigator: H. Chen (LLNL)

In FY12, an LLNL/LLE team performed a Laboratory Basic Science (LBS) experiment on OMEGA EP to study positron production during high-intensity laser interactions with high-Z targets. This experiment was a follow-up on to those of 2010 and 2011. In the previous experiments, a record number of positrons were produced using the 1-kJ, 10-ps OMEGA EP backlighter interacting with a 1-mm-thick Au target.[40] It was deduced that a non-neutral pair plasma was made in those shots.[41] In FY11, the laser energy was extended to 1400 J for the backlighter beam, and a seemingly faster increase in positron number was observed once the laser energy exceeded 1 kJ. In

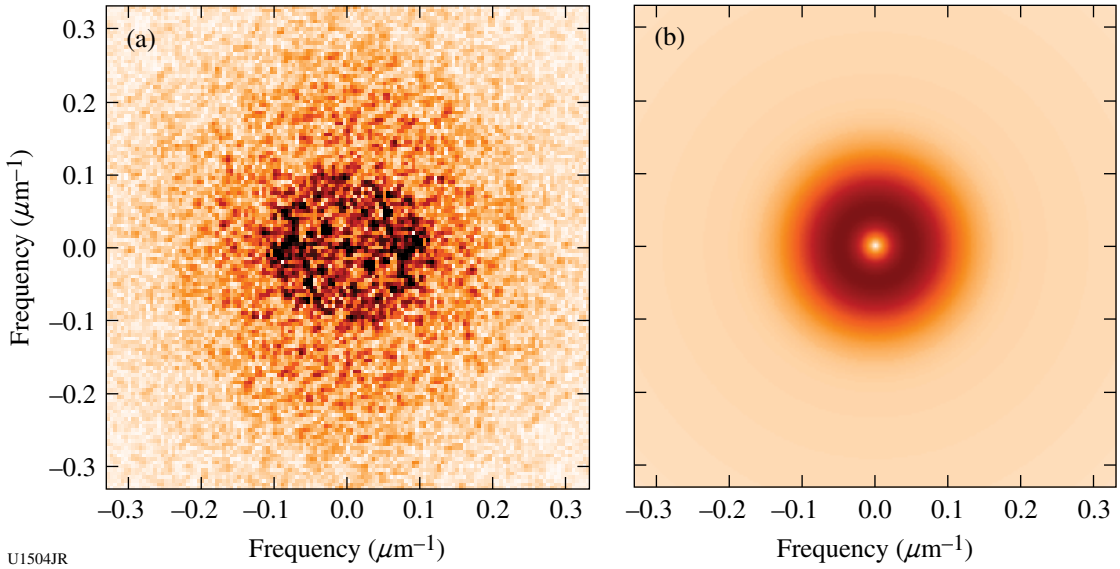

Figure 132.76
(a) An example of a 2-D velocity spectrum on a rippled shock front generated at a roughened interface between a PMMA ablator and a fused-silica sample recorded 650 ps after the passage of the shock through the interface (shot 66008). The gray scale is proportional to mode amplitude. (b) A velocity spectrum computed for similar conditions as in the experiment using the analytical expression provided in Ref. 39.

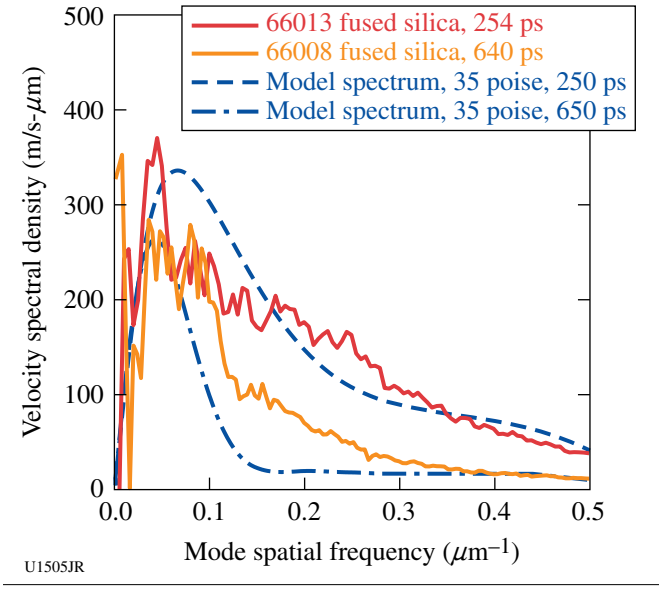

Figure 132.77
Averaged velocity spectra for ~170-GPa shocks in fused silica recorded at 250 ps and 650 ps after passing through the interface, compared with calculations of the expected spectra assuming 35-poise viscosity. More precise fits to the model are in progress.

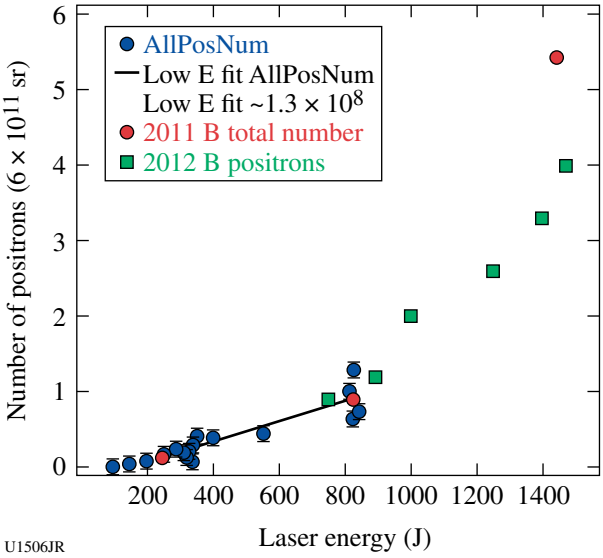

Figure 132.78
Positron yield is nonlinear at higher laser energies (green squares) in 2012B, confirming the conclusion from previous OMEGA EP experiments.

FY12, we carried out systematic experiments to confirm this finding. The preliminary results are shown in Figs. 132.78 and 132.79. At a higher laser-contrast condition (10^9 versus 10^7 in FY11), the positron scaling remains "nonlinear" at laser energies greater than 1000 J. The effect of laser contrast to fast electrons and positrons was also observed. Further data analysis is in progress to evaluate the laser–electron conversion efficiency as a result of enhanced contrast. Positron research extends over diverse fields ranging from particle physics and astrophysics to medical application. This often requires the production of

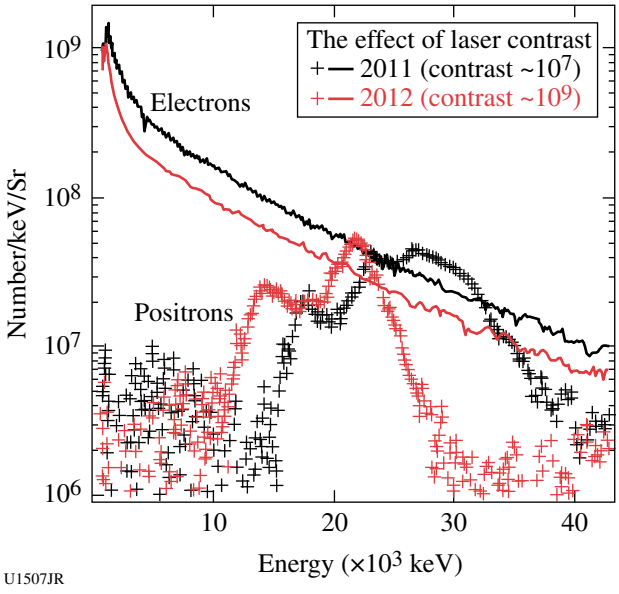

Figure 132.79
Fewer electrons were made in 2012B apparently due to a higher contrast laser condition, resulting in fewer and lower-energy positrons.

large numbers of positrons on a short time scale, which has been difficult to supply. The new OMEGA EP results could alter the direction of the quest to establish a laser-produced positron source for research in these fields.

Magnetic-Field Compression in Spherical Implosions on OMEGA

Principal Investigators: G. Fiksel, M. Hohenberger, J. P. Knauer, and P.-Y. Chang (LLE); R. Betti, K. S. Anderson, and J. R. Davies (FSC/LLE); and F. H. Séguin (MIT)

Project objective: The main goal of the experiments was to measure the compressed magnetic field in spherically imploded targets embedded in an externally generated seed field. These experiments will establish the scientific basis for magnetizing high-energy-density (HED) plasmas and enhancing the performance of inertial fusion implosions through the use of magnetic fields.

Experimental setup: The experimental setup is illustrated in Fig. 132.80. A spherical CH target is embedded in a seed magnetic field generated by a single-loop coil powered by the magnetized inertial fusion energy delivery system (MIFEDS) generator. The target is then imploded by 40 OMEGA beams with a square 1-ns pulse at maximum power. The shell is filled with 5 atm of deuterium gas. The shell's outer diameter is 860 μm, and the shell's thickness is 24 μm. The compressed magnetic field will be measured by the proton radiography

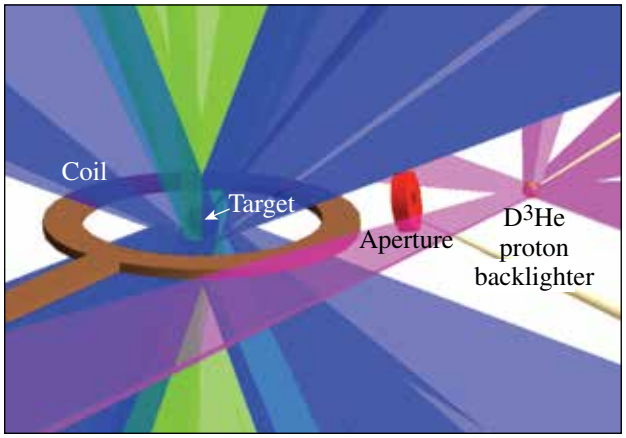

Figure 132.80
Experimental setup to measure magnetic-field compression.

technique. The 14.7-MeV fusion protons, used to radiograph the compressed core and field, are produced by the D + ^{3}He fusion reactions from an imploding glass microballoon filled with an 18-atm D^{3}He gas mix. The implosion of the proton backlighter is driven by ten OMEGA beams. The protons are recorded on a CR-39 nuclear track detector stack that allows for both spatial and energy resolution (via the track diameter) of the particles incident on the surface. The backlighter implosion can be timed so the backlighter proton beam passes through the target at the desired time of peak compression (e.g., "bang" time).

Preliminary results and future plans: Despite good laser performance and excellent MIFEDS operations, the obtained proton radiography images did not indicate the presence of deflected fast protons. After analyzing the results, a conclusion was made that the fast-proton fluence was too low and because the compressed magnetized spot has a diameter of less than 20 μm, the number of deflected protons was low as well, comparable to the background noise level of the CR39 detectors. In future experiments we plan to use fast protons generated from the interaction of OMEGA EP with a thin metal foil. The OMEGA EP–generated fast-proton fluence is at least three orders of magnitude higher than that from the D^{3}He source.

Magnetic Reconnection in High-Energy-Density Plasmas in the Presence of an External Magnetic Field

Principal Investigators: G. Fiksel and P. M. Nilson (LLE); and W. Fox and A. Bhattacharjee (University of New Hampshire)

Project objectives: The primary goals for the magnetic-reconnection experiments are to (1) demonstrate that an

extended reconnection current sheet can be formed in the gap between two laser-irradiated foils by the collision of the high-conductivity blowoff plasmas, (2) show that this interaction can be well diagnosed using proton radiography and x-ray imaging, and (3) observe basic properties of the reconnection, such as inflow and outflow rates, the geometry of the current sheet, and the magnitude of the magnetic field in the current sheet.

Experimental setup: Figure 132.81 shows a simplified diagram of the experiment on OMEGA EP. The experiment was carried out in close collaboration with the computational plasma physics group at the University of New Hampshire. This group has recently conducted particle simulations of reconnection in LLE and Rutherford (UK) laser-driven reconnection experiments.

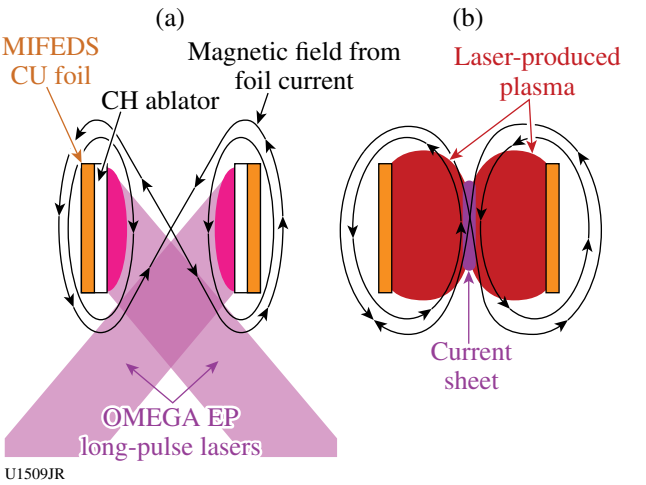

Figure 132.81
A simplified diagram of the proposed reconnection experiments. (a) Laser-driven plasma blowoff drives the collision of two magnetized plasma flows and reconnection of the (b) seed magnetic fields from the MIFEDS current generator.

For the first series of shots (5 September 2012) the magnetic coils were not energized. The main goal of that experiment was to establish proper parameters of the drive lasers and investigate the dynamics of the colliding plasmas with the proton radiography diagnostic. The actual experimental setup is shown in Fig. 132.82.

Preliminary results and future plans: One of the proton images of the colliding plasma interface is shown in Fig. 132.83. The result indicates the presence of a long-lived, self-organized structure similar to what was recently described in a Nature Physics publication.[26] A new series of experiments on characterization of the reconnection magnetic field and particle energization is planned.

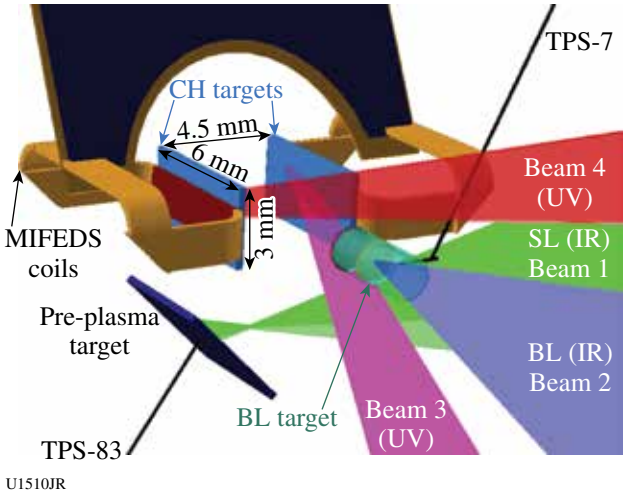

Figure 132.82
The experimental setup showing MIFEDS coils with the support structure and the attached CH targets. The colliding plasmas are generated with 1.8-kJ, 2-ns OMEGA EP Beams 3 and 4. The proton backlighter beam is generated by the 800-J, 10-ps OMEGA EP Beam 2. The protons are detected with a radiochromic film (RCF)-based detector situated 8 cm away from the target. Also shown is a target for prefilling the intercoil region with pre-plasma.

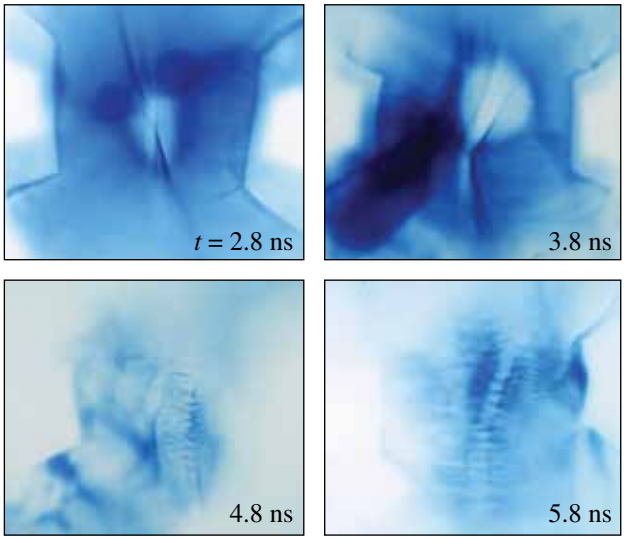

Figure 132.83
A series of images of the colliding plasmas obtained with the proton radiography diagnostic.

Measurements of Linear, Nonlinear, and Turbulent Mixing Regimes in Kelvin–Helmholtz Instability in the Subsonic Regime

Principal Investigators: O. A. Hurricane and V. A. Smalyuk (LLNL)

A Kelvin–Helmholtz (KH) growth experiment was performed using a platform successfully developed in earlier OMEGA experiments.[42–44] Figure 132.84 shows a target schematic that consists of a plastic ablator and a shock tube. In the shock tube the interface between low-density foam and high-density plastic was either flat or had pre-imposed sinusoidal modulation at a 400-μm wavelength and a 30-μm amplitude, as in previous experiments. The central part of the plastic target contained a layer of I-doped CH to increase the contrast to 5-keV backlighter x rays. The ablator of the target was directly driven with laser light, producing a strong shock that propagated through the target. The shock produced a velocity gradient at the interface between foam and plastic. This velocity difference between two materials resulted in the KH growth of the surface modulations. The density of foam was 100 mg/cm^3. Previous experiments detected a mixing layer development caused by the growth of 3-D, short-scale modulations in addition to pre-imposed, 2-D, 400-μm-wavelength modulations. New experiments performed with flat CH–foam interfaces were aimed at measurements of 3-D turbulent mixing since in previous experiments the growth of large 400-μm-wavelength modulations could have modified the growth of 3-D, short-scale modulations.

Figure 132.85 shows the experimental data. Figures 132.85(a) and 132.85(b) present flat-interface data at 35 ns and 75 ns, respectively. Figure 132.85(c) shows data with 2-D pre-imposed modulation at 75 ns, taken to confirm evolution measured in previous experiments. The shock traveled from left to right, so the modulations at the left-hand side of the image had more time to grow than the modulations at the right-hand side. The

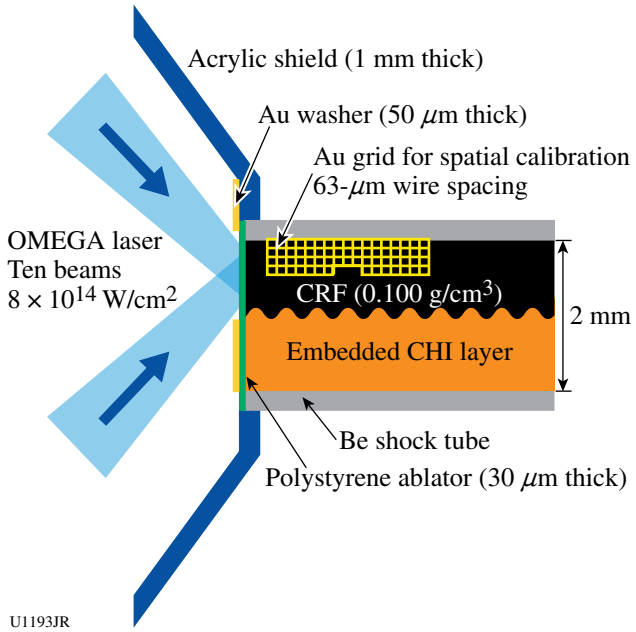

Figure 132.84
Experimental configuration. The interface between lower-density CRF foam and higher-density I-doped plastic was either flat or had a pre-imposed 2-D modulation with a 400-μm wavelength, as in previous experiments. The surface roughness at the interface had a rms amplitude of 100 nm. The density of the CRF foam was 100 mg/cm^3.

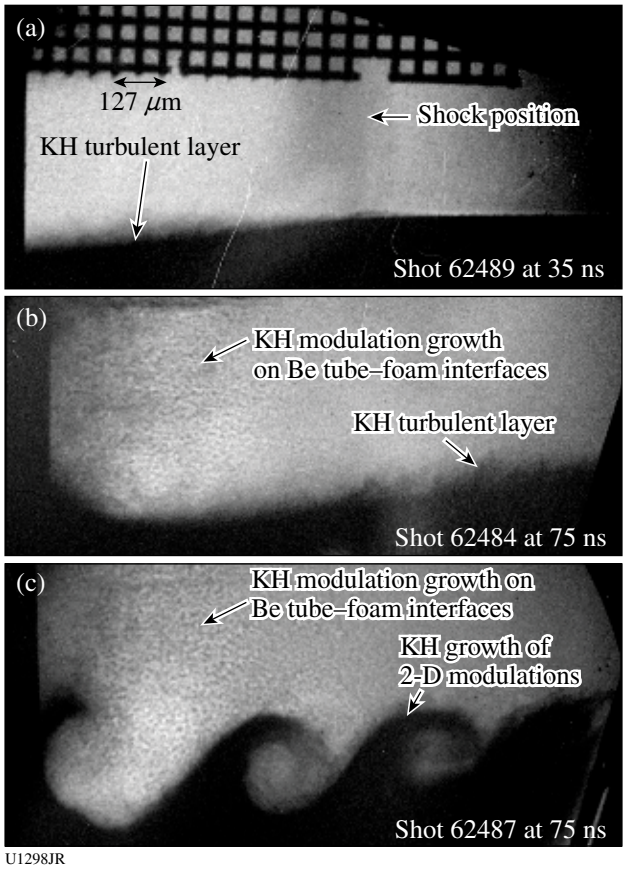

Figure 132.85
X-ray radiographs of KH growth with a flat CHI–foam interface were taken at (a) 35 ns, (b) 75 ns, and (c) with an interface having a 2-D modulation at 75 ns. The areas on the right-hand side of the images experienced less KH growth than the areas on the left-hand side.

light color in the image corresponds to foam material, while the dark color corresponds to plastic. A mixing layer developed behind the shock front, as expected since the Reynolds number was high in this experiment, Re ~ 1×10^6. The mix width was ~60 μm at ~700 μm behind the shock front, inferred from the measured image at 35 ns, close to mix-model predictions. Growth of 2-D pre-imposed modulations [Fig. 132.85(c)] was similar to previous experiments, confirming the repeatability of the drive. In addition, growth of 3-D modulations at the Be tube–foam interfaces was also detected, as shown in both 75-ns images. These experimental data are used to develop and validate mix models that are based on post-processing of hydrodynamic simulations.[45–47]

Nuclear-Atomic–Plasma Interactions in Laser-Produced Plasmas (NEEC and NEET)

Principal Investigator: A. L. Kritcher (LLNL)

Plasma coupling to nuclei in high-energy-density plasmas, or nuclear–plasma physics, is a cutting-edge field that traverses the areas of nuclear physics, plasma physics, and atomic physics. Nuclear–plasma interactions occur in hot and dense plasmas such as inertial confinement fusion environments and astrophysical bodies. The effect of high-energy-density-plasma (HEDP) environments on astrophysical nucleosynthesis, the formation of heavy elements from pre-existing nucleons in astrophysical plasmas, is expected to play a significant role.[48] Nuclei in stellar plasmas reach a thermal population of low-lying excited nuclear states from photoexcitation, free electrons in the plasma (NEEC),[49–52] excitation from atomic transitions (NEET),[53–55] and inelastic electron scattering in the dense plasma. In these experiments at the Omega facility, we investigate the NEEC process in underdense plasmas by illuminating mini hot hohlraums (400 or 600 μm in diameter) with ~15 kJ of laser light (Fig. 132.86).

The goal of these first experiments was to identify the plasma conditions of hot Tm hohlraums with spectral line emission analysis and optical Thomson scattering, measure the energy and time-resolved atomic emission background, investigate this experimental platform to study nuclear lifetime shortening in hot plasmas, and determine the possibility to investigate nuclear–plasma interactions. We collected high-quality data and are in the process of analyzing the results. Future campaigns will continue to measure plasma conditions of hot hohlraums and investigate nuclear–plasma interactions in HEDP plasma environments. We will also field additional isotopes in this configuration.

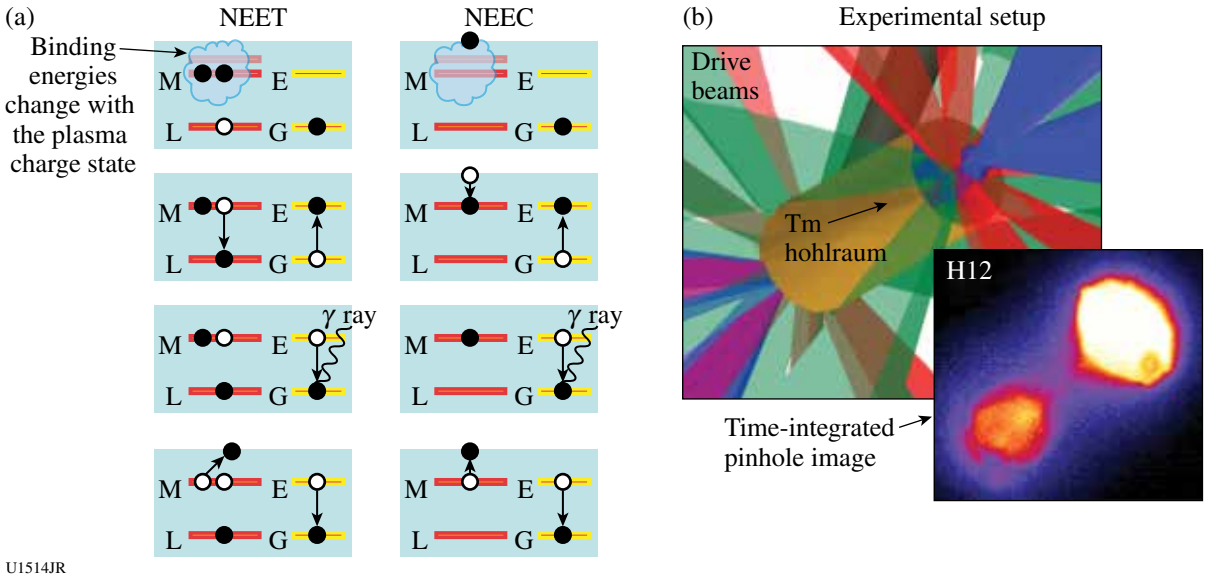

Figure 132.86

(a) Schematic of the NEET and NEEC processes. The red levels on the left-hand side denote the atomic shells; the yellow levels on the right-hand side denote the nuclear excited and ground states. First, the nucleus in the ground state and atomic shell vacancies are present (and/or free electrons are present). Electrons either transition or are captured into atomic states and the nucleus becomes excited. The nucleus radioactively decays by γ-ray emission or internal conversion. (b) A schematic of the experimental configuration. Tm hohlraums, 400 and 600 μm in diameter, are illuminated by 40 drive beams with a total of 15 to 20 kJ.

Astrophysical Collisionless Shock Generation by Laser-Driven Laboratory Experiments on OMEGA and OMEGA EP

Principal Investigators: N. Kugland, S. Ross, and H.-S. Park (LLNL)

The goal of this experiment is to study astrophysical collisionless shocks with counter-streaming plasmas from high-power lasers. Astrophysical "collisionless" shocks form via plasma instabilities and self-generated magnetic fields. Laboratory experiments at large laser facilities can achieve the conditions necessary for the formation of collisionless shocks and will provide a unique avenue for studying the nonlinear physics of shock waves. We are performing a series of experiments on the OMEGA and OMEGA EP lasers in which collisionless shock conditions will be generated by the two high-speed plasma flows resulting from the laser ablation of solid targets using 10 kJ to 20 kJ of laser energy. The experiments will aim to answer several questions of relevance to collisionless shock physics: the importance of the electromagnetic filamentation (Weibel) instability in shock formation, the self-generation of magnetic fields in shock collisions, the influence of external magnetic fields on shock formation, and the signatures of particle acceleration in shocks.

Our second year of OMEGA EP experiments (EP-ACSEL-12A and EP-ACSEL-12B) continued proton imaging to visualize the electromagnetic fields produced by two counter-streaming plasmas. As shown in Fig. 132.87, these plasmas were made by two UV beams that irradiated plastic or carbon drive targets with 2200 J (per target) in 3 ns. These interpenetrating plasmas were then probed from the side by short-pulse laser-generated protons.

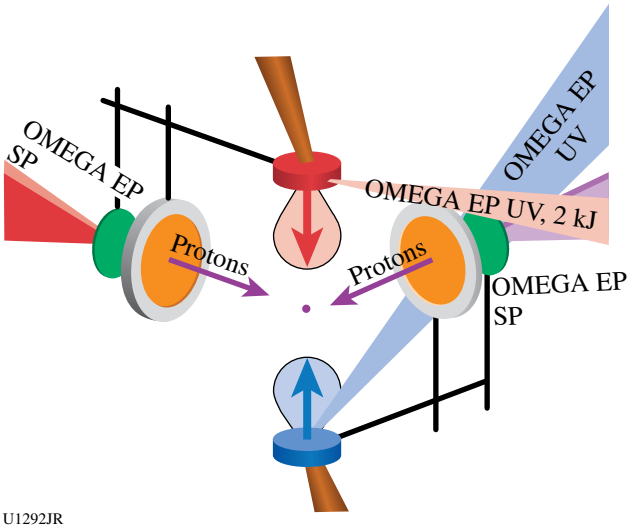

Figure 132.87
EP-ACSEL experimental setup.

EP-ACSEL-12A confirmed the presence of the large self-organized fields first observed in our FY11 OMEGA EP shots. These surprising structures, formed by a yet unexplained mechanism, are much larger than the intrinsic plasma spatial scales and persist for much longer than the plasma kinetic time scales. Now in press in Nature Physics[26] as a cover figure article, this finding provides a new way to understand how electromagnetic order emerges from chaos in the cosmos, such as in the plasma flows that emerge from young stars.

EP-ACSEL-12B explored the sensitivity of these self-organized fields to changes in the laser-drive conditions and target type. Figure 132.88 shows the dramatic difference in the fields that develop in counter-streaming CH_2 flows (a hydrogenated multi-species plasma), and pure C plasmas. The C flows develop much less turbulence. We are currently exploring the origin of these features using basic plasma theories and numeric simulations.

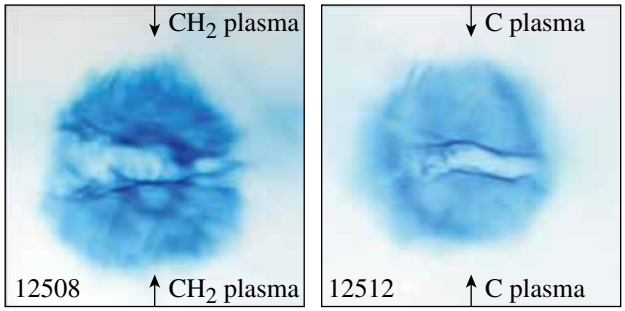

Figure 132.88
Proton images of the counter-streaming plasmas from the collisionless shock experiments of July 2012.

The results have been presented at many conferences.[56–59] Seven papers[26–28,59–62] have been published and additional papers are in preparation.[63–65]

The ACSEL-12A/B on OMEGA-60 campaigns focused on characterizing plasma conditions in the interaction region of two high-velocity plasma flows. The target geometry is similar to previous ACSEL campaigns with two foil targets separated by 8 mm. The targets are heated with 5 kJ of laser energy per foil, producing high-velocity plasma blowoff. The target material is pure carbon, CH_2, or beryllium. Thomson scattering is then used to measure the plasma conditions. High-quality data

were obtained, providing plasma parameters that have never before been measured, as seen in Fig. 132.89.

The electron temperature and density are measured from the electron feature; then the ion feature can be used to measure the ion temperature and flow velocity. The ion temperature is shown in Fig. 132.90 for all three target materials. The ion temperatures were similar for the targets containing carbon and significantly lower for the beryllium target. A detailed understanding of the counter-streaming heating mechanism is currently being developed.

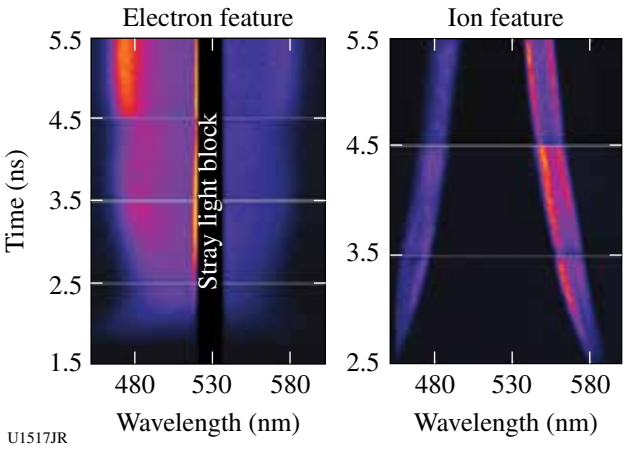

Figure 132.89
Thomson-scattered light from the plasma is measured on a series of carbon target shots.

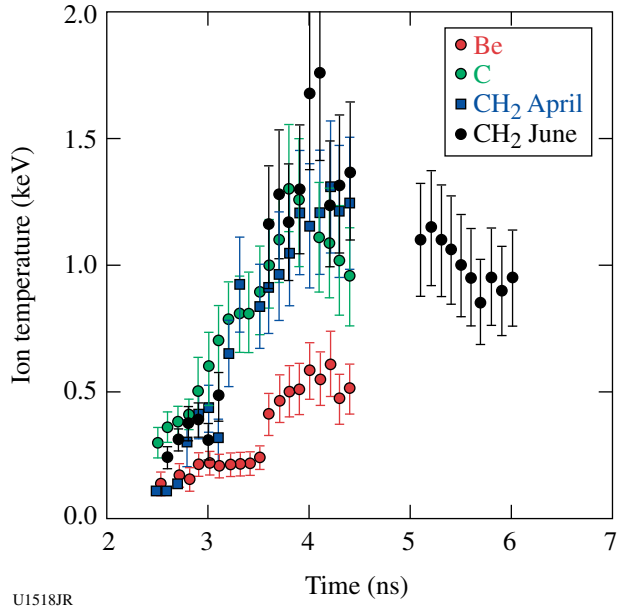

Figure 132.90
Compilation of ion temperatures of counter-streaming plasmas from different target materials of Be, carbon, and CH_2. The differences are important to understanding the collisionless shock-creation regime.

Our work and collaboration produced numerous invited talks and high-profile papers including Nature Physics (cover figure),[26] Physics of Plasmas (highlight research), and Review of Scientific Instruments (invited article).

Dislocations and Twinning at High Pressures and Strain Rate on bcc Metals

Principal Investigators: B. R. Maddox, A. Comley, and C. Wehrenberg (LLNL)

In TaRDiff-2012 our goal was to study twinning and dislocation motion in shock-compressed tantalum. The experimental configuration used the broadband x-ray diffraction diagnostic on TIM-4 as the primary diagnostic for studying twinning. Alternatively, a recovery tube was fielded on TIM-1, to allow for the study of recovered micro-indented samples. Samples were driven using a 1-ns square pulse with laser energy in the 15- to 65-J range. High-quality diffraction data were obtained and Ta samples were successfully recovered. Initial analysis did not show driven diffraction signal for the (110) Ta samples, which were expected to show larger amounts of twinning. However, high-contrast–driven Laue spots were observed for (100) oriented Ta crystals, and these data were used in Ta strength measurements. Recovered Ta samples will be examined by a transmission electron microscope (TEM) to measure the dislocation motion originating from the micro-indents.

Thermonuclear Reactions in Stellar Plasmas and High-Resolution Measurements of Three-Body Breakup in Isobaric Analogue Reactions

Principal Investigators: D. P. McNabb (LLNL); R. D. Petrasso (MIT); and T. C. Sangster (LLE)

The starting point for this project was to design a series of direct-drive, exploding-pusher implosions to measure particle production spectra for the $T(t,2n)^4He$ fusion reaction. The $T(t,2n)^4He$ reaction is important for NIF diagnostics and is the charge-symmetric reaction to $^3He(^3He,2p)^4He$—a key reaction in the solar proton–proton chain. Our initial goal is to compare these results with those predicted by nuclear theory calculations to gain insight into the reaction mechanism. We will be measuring the neutrons with an improved neutron time-of-flight (nTOF) detector system, with the magnetic recoil spectrometer optimized for lower-energy neutrons and high resolution, and different activation systems. The Thomson parabola ion

energy (TPIE) analyzer has also been optimized to attempt to measure the continuum alpha particle spectrum in addition to the emitted neutrons. Due to difficulties getting capsules filled with high-purity tritium, the shot day was deferred until Q1FY13. There is a renewed interest in these experiments on OMEGA given the recent high-quality TT symcap nTOF data obtained on the NIF and the discrepancy between these neutron spectral measurements and previous experiments. In addition to fielding the TPIE spectrometer, the OMEGA measurements are expected to take place at a higher temperature than the new NIF data.

Compton Radiography Fast Ignition (CRFI) Campaign

Principal Investigators: P. Patel (LLNL) and H. Sawada (University of California, San Diego)

Co-investigators: C. D. Chen, R. Tommasini, H. S. McLean, and M. H. Key (LLNL); L. C. Jarrott and F. N. Beg (University of California, San Diego); W. Theobald, A. A. Solodov, J. A. Delettrez, V. Yu. Glebov, and C. Stoeckl (LLE); and M. S. Wei and R. B. Stephens (General Atomics)

The goal of the Compton radiography fast ignition (CRFI) campaign is to measure the 2-D areal-density map of an imploded cone-in-shell target using a high-energy bremsstrahlung x-ray backlighter. In cone-guided fast ignition, the formation of a high-density compressed core near the cone tip is critical for efficient fast-electron core heating. The areal density, core shape, and standoff distance from the cone tip provide important parameters for experimentally estimating the energy coupling of an ignition laser to the core. In our joint OMEGA experimental campaign, a 40-μm-thick deuterated carbon (CD) shell was imploded by 54 18-kJ OMEGA beams with a low-adiabat shaped drive pulse. A backlighter target consisting of a 10-μm-diam Au wire embedded on a 300-μm × 300-μm CH foil was irradiated with a 250- to 1500-J, 10-ps OMEGA EP beam in a 100-μm focal spot to produce high-energy bremsstrahlung x rays. The hard x rays with an energy greater than 20 to 30 keV transmitting through CD plasmas were dominated by Compton scattering and the mass attenuation coefficient was weakly sensitive to the plasma density. The bremsstrahlung spectrum and spatial resolution were estimated to be an ~160-keV x-ray slope and 7-μm half width at half maximum (HWHM), respectively, from a radiograph of a 200-mm-diam solid tungsten sphere using 10-ps, 250-J OMEGA EP beam energy. Figure 132.91 shows the radiographic images of an imploded cone-in-shell target at 4.0 ns from the start of the drive pulse with an OMEGA EP energy of 1.5 kJ. Figures 132.91(a) and 132.91(b) show the same image but in different color scales. A preliminary analysis shows a

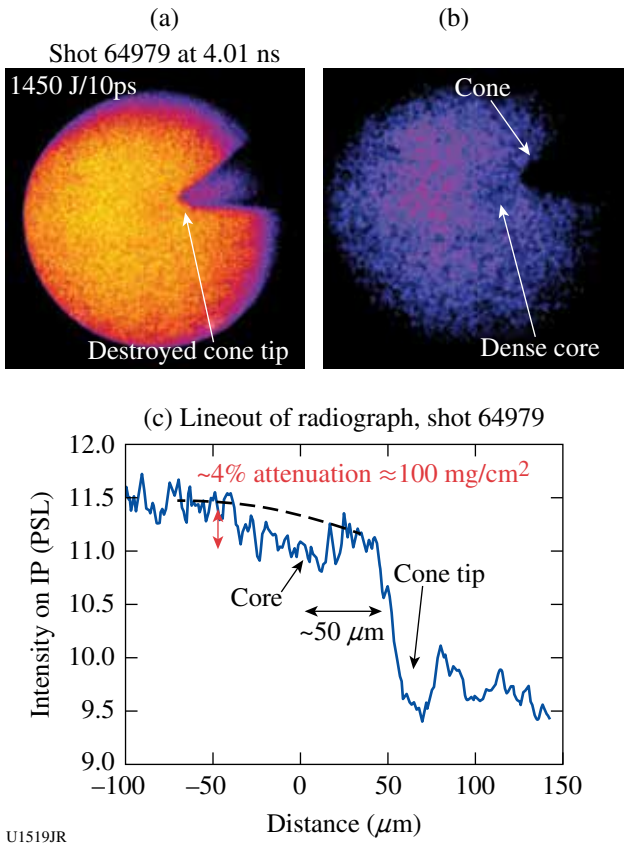

Figure 132.91
[(a) and (b)] Radiographic images of an imploded cone-in-shell target 4.0 ns from the start of the drive pulse. (c) Analysis of images to deduce areal density and standoff distance.

peak areal density of ~100 mg/cm^2 and a standoff distance of ~50 μm as shown in Fig. 132.91(c). Further analysis is underway to estimate the core size and errors caused by uncertainties in the backlighter spectrum and source size. The inferred areal density from the radiographic images will be compared to a 2-D radiation–hydrodynamic *DRACO* simulation to validate the simulation results.

Probing Shocked Liquid H, H/He, CH_4, N_2, and NH_3 with Inelastic X-Ray Scattering and Shock-Velocity Measurements: Toward the Equation of State of Planetary Interiors

Principal Investigator: S. P. Regan (LLE)

The Fermi-degenerate plasma conditions created in liquid deuterium by a laser-ablation–driven shock wave were probed with noncollective, spectrally resolved, inelastic x-ray Thomson scattering (XRTS) employing Cl Ly$_\alpha$ line emission at 2.96 keV (Ref. 66). These first XRTS measurements of the microscopic

properties of shocked deuterium show an inferred spatially averaged electron temperature of 8±5 eV, an electron density of 2.2 (±0.5) × 10^{23} cm^{-3}, and an ionization of 0.8 (−0.25, +0.15). Two-dimensional hydrodynamic simulations using equation-of-state (EOS) models suited for the extreme parameters occurring in inertial confinement fusion research and planetary interiors are consistent with the experimental results.

The scattered spectrum of the Cl Ly$_\alpha$ emission taken at t = 5 ns with a 250-μm slit in the scattering channel is shown in Fig. 132.92(a). The measurement taken without the slit is shown in Fig. 132.92(b), and the incident spectrum is shown in Fig. 132.92(c). The observed noise in the measured scattered x-ray spectrum is consistent with the estimated signal level. The incident spectrum is measured by irradiating a parylene D foil target on a separate laser shot. The scattered spectrum has a strong Rayleigh peak around 2960 eV and a Compton-downshifted feature. Scattered x-ray spectra were calculated using the x-ray scattering (XRS) code, which uses the finite-temperature random-phase approximation with static local field corrections to obtain the spectral shape of the inelastic (Compton) feature caused by scattering from free electrons.[67] The elastic scattering intensity strongly depends on the degree of ion–ion correlations in the plasma via the structure factor S_{ii} (Ref. 68). To constrain the value for S_{ii}, density functional theory molecular dynamics (DFT-MD) simulations were performed using the Vienna *ab initio* simulation package (VASP).[69,70] The simulations indicate weak ionic correlations for the conditions similar to the average of the plasma probed. This means the ion–ion structure factor S_{ii} at the relevant scattering wave number is close to unity for most of the conditions probed. With this information, the elastic scattering feature can be used to constrain the temperature and the ionization degree of the system. Structure factors close to unity are also found for the unshocked deuterium liquid. In addition to Doppler broadening, the width and position of the inelastic feature depend on the density for $\alpha_s \sim 1$. This fact allows us to bracket the electron density and estimate the ionization charge based on the initial mass density of the sample. The simulated scattering spectra computed using XRS provided the best fit to the spectrum measured with the slit for the following plasma conditions: T_e = 8±5 eV, $Z \sim 0.8$ (−0.25, +0.15), and n_e = 2.2 (±0.5) × 10^{23} cm^{-3}. The *DRACO* simulations are in close agreement with the experimental results. These plasma conditions were repeatable on a subsequent laser shot. The plasma conditions inferred from the spectrally resolved x-ray spectrum recorded without the slit in the x-ray scattering channel are lower with T_e = 3±2 eV, $Z \sim 0.6 \pm 0.2$, and n_e = 2.0 (±0.5) × 10^{23} cm^{-3}. The lower plasma pressure created by the lower-intensity portion of the laser drive causes bowing of the shock front (see Fig. 131.7 in Ref. 66). When the slit is placed in the scattering channel, the x rays scattered from this underdriven portion of the target are blocked from the detector. This leads to higher inferred values of T_e, Z, and n_e, which is more representative of the uniformly shocked region.

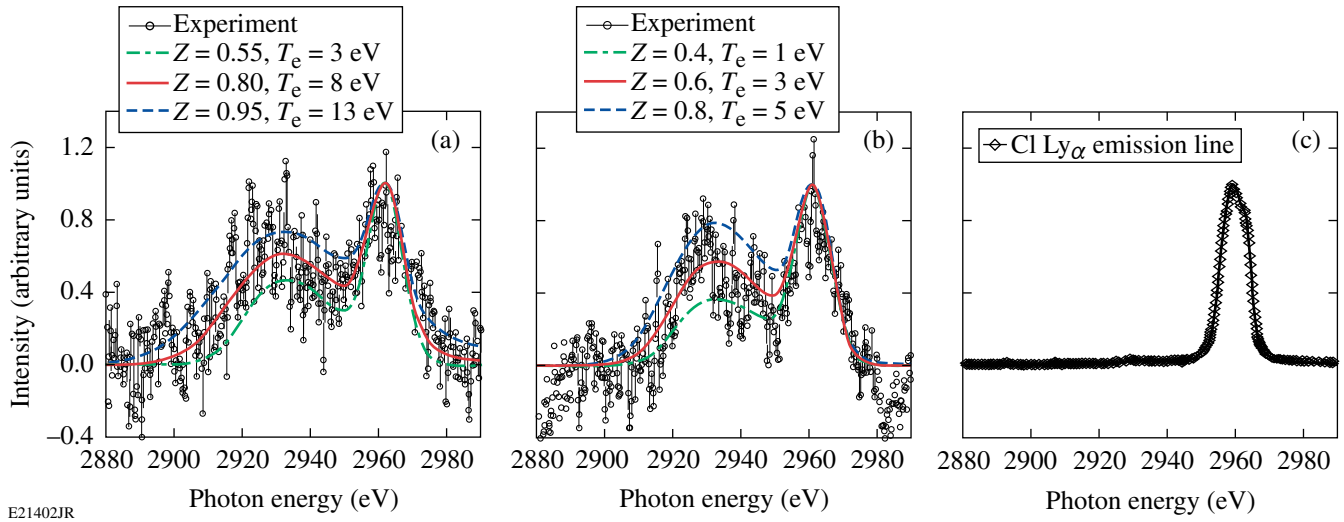

Figure 132.92
Measurement of (a) Cl Ly$_\alpha$ emission scattered from shocked liquid deuterium with a 250-μm slit in the scattering channel and simulated scattering spectra, (b) Cl Ly$_\alpha$ emission scattered from shocked liquid deuterium without a 250-μm slit in the scattering channel and simulated scattering spectra, (c) Cl Ly$_\alpha$ emission incident on the shocked liquid deuterium. The inferred plasma conditions in (a) are T_e = 8±5 eV, $Z \sim 0.8$ (−0.25, +0.15), and n_e = 2.2 (±0.5) × 10^{23} cm^{-3} and in (b) are T_e = 3±2 eV, $Z \sim 0.6 \pm 0.2$, and n_e = 2.0 (±0.5) × 10^{23} cm^{-3}.

Unlike previous velocity spectrometer for any reflector (VISAR) measurements, the x-ray scattering experimental platform offers the considerable advantage of probing off-Hugoniot states. This experimental result is a significant step toward achieving accurate measurements of all thermodynamic variables needed to provide stringent tests of EOS models, which would require at least three thermodynamic variables like pressure, mass density, and temperature.

Extreme Chemistry of Precompressed Nitrogen

Principal Investigator: J. R. Rygg (LLNL)

Experimental measurement of the N_2 Hugoniot was extended to 850 GPa by launching shocks into N_2 samples precompressed in diamond anvil cells to ~2 GPa (see Fig. 132.93). VISAR and streaked optical pyrometry (SOP) measurements of the N_2 shock front in comparison to concomitant measurements in quartz were used to infer pressure, density, reflectance, and temperature of shocked N_2. Compressibility, optical reflectivity, and temperature measurements show that N_2 undergoes a complex dissociation–polymerization transition, in good agreement with first principle calculations.

Measurements of the Ablative Richtmyer–Meshkov Instability in the Nonlinear Regime

Principal Investigator: V. A. Smalyuk (LLNL)

Figure 132.94 shows a schematic of the experimental setup for the nonlinear Richtmyer–Meshkov (RM) instability experiments on OMEGA. Planar CH targets (15, 30, and 50 μm thick) were driven with three UV beams using a 6-ns square pulse shape, a total energy of ~0.7 kJ, and a laser intensity of ~5×10^{13} W/cm^2. Initial target modulations were imposed by laser imprinting using a beam with a special 2-D phase plate with a modulation wavelength of ~70 μm. The timing of this beam was advanced by ~200 ps, relative to other drive beams that have regular SG4 distributed phase plates (DPP's). Figure 132.95 shows laser-beam images with an SG4 DPP [Fig. 132.95(a)] and a special 2-D DPP [Fig. 132.95(b)]. Growth of target modu-

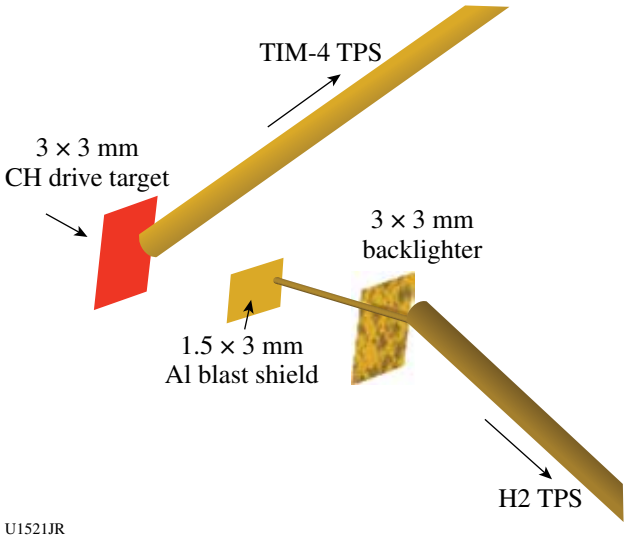

Figure 132.94
Experimental setup.

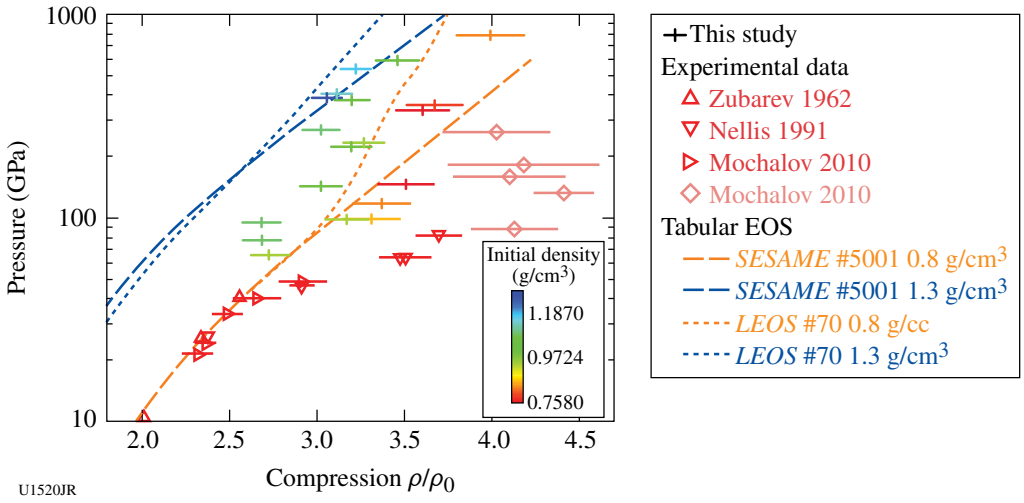

Figure 132.93
In FY12, the OMEGA laser was used to extend the N_2 Hugoniot from 100 to 850 GPa (crosses). The N_2 shock pressure and density were inferred by shock-velocity measurements impedance matched to a quartz standard.

lations was measured with x-ray radiography using uranium (~1.3-keV), samarium (~1.8-keV), and tantalum (~2.2-keV) backlighters on a framing camera with 10-μm spatial resolution and 80-ps temporal resolution. The backlighter targets were driven with a 2-ns square pulse shape and an intensity of ~3×10^{14} W/cm^2 using seven additional UV beams. Figure 132.96 shows an example of a measured image at 1.1 ns (near the end of the RM phase) taken with a 50-μm-thick CH foil and tantalum backlighter. Evolution of 2-D broadband modulations was observed in the RM phase for all target types during a shock transit time before the onset of acceleration and subsequent RT growth. Figure 132.97 summarizes the areal-density evolution of 2-D modulation at a wavelength of 70 μm for the 30- and 50-μm-thick foils and compares data with predictions of the 2-D hydrocode *DRACO*. The vertical dashed lines show expected times of the end of the RM phase and the beginning of the RT phase for these types of foils. Blue data points and curves correspond to 30-μm-thick foils, while black curves and data points correspond to 50-μm-thick foils. Areal-density modulations grow throughout the RM phase, and their evolution is similar to code predictions, validating the simulations.

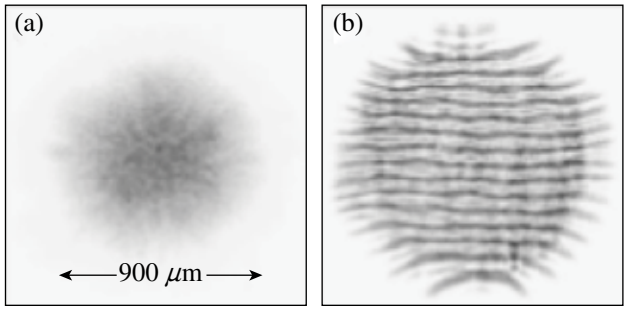

U1522JR

Figure 132.95
Laser-beam images with (a) regular SG4 DPP and (b) special 2-D DPP.

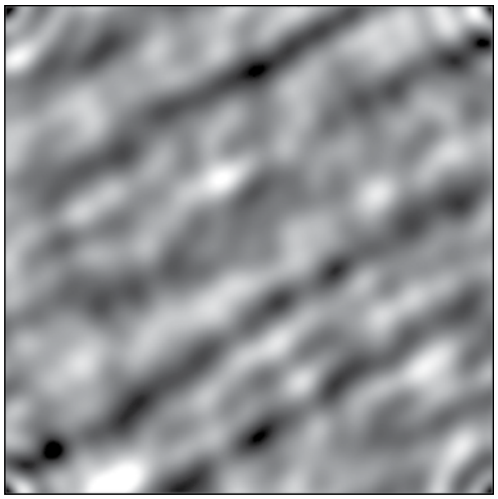

U1523JR

Figure 132.96
X-ray images of 2-D broadband modulations near the end the Richtmyer–Meshkov instability growth phase measured in 50-μm-thick CH targets.

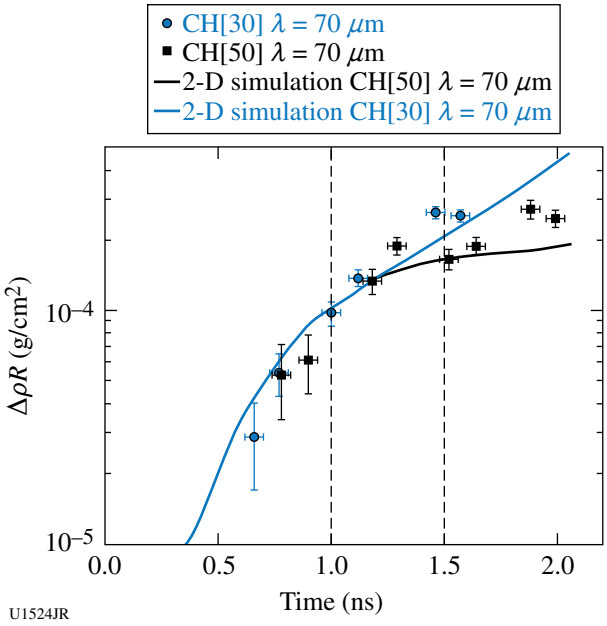

U1524JR

Figure 132.97
Evolution of 2-D areal-density modulations at a wavelength of 70 μm measured in 30-μm-thick foils (blue circles) and in 50-μm-thick foils (black squares). Solid curves correspond to 2-D *DRACO* simulations, while vertical dashed lines correspond to times of the end of the RM phase and beginning of the RT phase in 30-μm-thick foils (blue curves) and 50-μm-thick foils (black curves).

Spectroscopy of Neutrons Generated Through Nuclear Reactions with Light Ions in Short-Pulse Laser Interaction Experiments

Principal Investigators: C. Stoeckl, V. Yu. Glebov, and T. C. Sangster (LLE)

The experimental objective of this project is to study nuclear reactions in light ions by measuring the spectrum of neutrons generated in short-pulse laser interaction experiments and compare them with simulated spectra based on the published cross sections.

Planar targets are irradiated with one short-pulse beam focused at the target's front surface. Charged particles from the back side of the target create neutrons and charged particles through nuclear reactions in a second converter target placed closely behind the primary interaction target. The spectrum of the neutrons generated in the converter target is measured using a scintillator/photomultiplier–based neutron time-of-flight (nTOF) detector. Charged-particle detectors are used to measure the spectra of the primary particles.

In FY12 three new nTOF detectors were installed on OMEGA EP (see Fig. 132.98). One in the laser forward direction on port 82, one at 90° to the laser on port 90, and one in the laser backward direction on port 73. Each of these detectors is heavily shielded with lead and gated to suppress the signal from the prompt hard x rays generated in the laser–plasma interaction processes on the primary target.

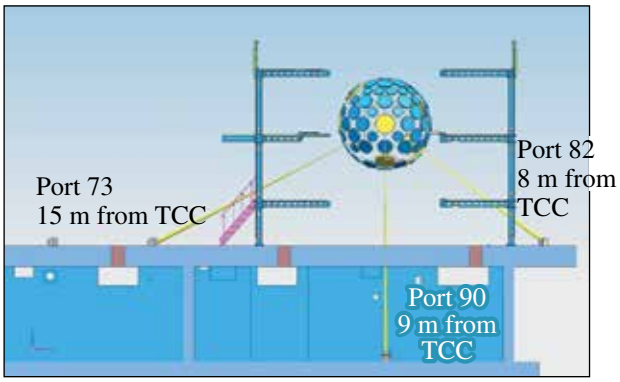

Figure 132.98
Location map of the three neutron detectors installed in FY12.

In FY12 one shot day (19 September) was available for experiments. Copper foils were used as primary targets to generate protons and irradiated with 10- and 100-ps OMEGA EP pulses and energies of up to 2.0 kJ. A container target was developed to place ~100 mg of LiD inside a stainless-steel container ~2.5 cm behind the primary target. High-quality nTOF spectra were recorded on all detectors for all shots during the day. Figure 132.99 shows data from all three detectors.

No specific spectral features like DT fusion neutrons are visible in the recorded data. The analysis of this data is ongoing. The current working hypothesis is that the measured neutron spectrum is dominated by p–n reactions in the LiD container and the target chamber. Efforts to reduce this background are currently under consideration.

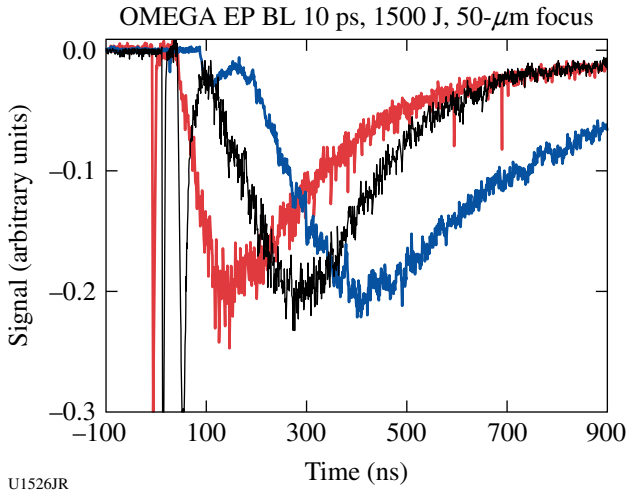

Figure 132.99
Neutron time-of-flight data from the detectors in ports 82 (red), 90 (black), and 73 (blue). The first peak in the data corresponds to the arrival of the prompt hard x rays. Gating suppresses this peak by at least five orders of magnitude.

Integrated Fast-Ignition Experiments

Principal Investigators: W. Theobald and A. A. Solodov (LLE)
Co-investigators: C. Stoeckl, R. Epstein, V. Yu. Glebov, G. Fiksel, S. Ivancic, F. J. Marshall, G. McKiernan, C. Mileham, P. M. Nilson, and T. C. Sangster (LLE); L. C. Jarrott and F. N. Beg (University of California, San Diego); E. Giraldez, R. B. Stephens, and M. S. Wei (General Atomics); H. McLean (LLNL); H. Sawada (University of Nevada, Reno); H. Habara (ILE); and J. J. Santos (CELIA)

Integrated fast-ignition experiments with cone-in-shell targets on OMEGA have demonstrated ~3.5% coupling efficiency of short-pulse laser energy into a compressed target.[71] The goals of this Laboratory Basic Science (LBS) proposal were to study the short-pulse laser/fast-electron coupling efficiency using an improved OMEGA EP laser and to validate the 2-D radiation–hydrodynamic modeling predictions of a new aluminum cone-tip target design with a backlighter experiment. The new target design has been modeled with detailed hydrodynamic simulations. Figure 132.100 shows a *DRACO*[72] simulation of the cone-in-shell target with an aluminum block mounted in front of a gold cone for different times during the implosion. This design is more resilient against the strong shock from the implosion than a previous design with a gold-only cone.[71] Shock breakout is predicted to be delayed by ~80 ps in the new target design. Figure 132.100(c) shows that the interior of the cone volume is free of plasma up to the time when the shock breaks through. A new backlighter platform has been developed

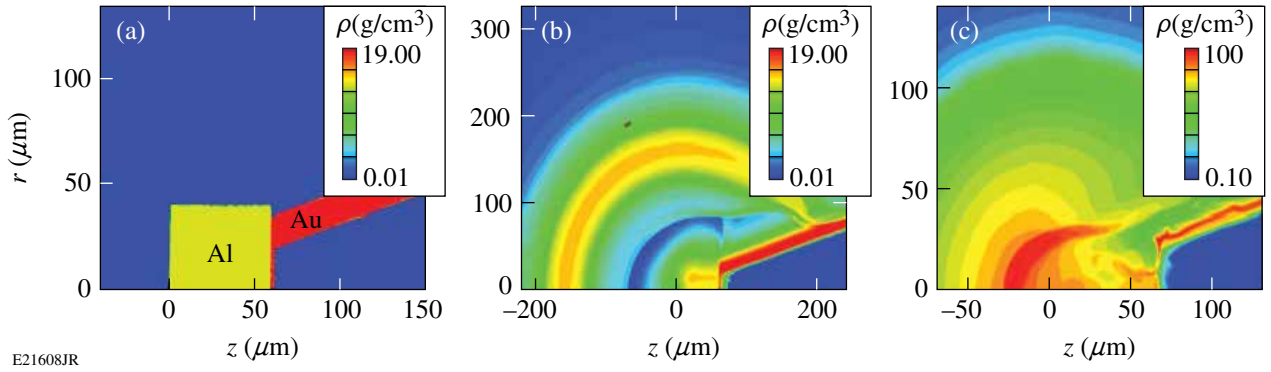

Figure 132.100
Two-dimensional hydrodynamic *DRACO*[72] simulation of a new cone-in-shell target design. (a) Detail of the target tip showing the gold cone with an aluminum tip. (b) Imploding shell before peak compression at 3.25 ns. Simulations predict thermal expansion of the cone material due to radiation preheat. The aluminum tip expands faster than the gold material. (c) Density map at 3.87 ns (~0.19 ns before peak compression) showing better shock resilience of this design than the previous[71] Au cone tip target.

and was tested during the first shot day in FY12 to characterize the fuel assembly of cone-in-shell targets close to peak compression and to validate the 2-D radiation–hydrodynamic modeling predictions. This was done with flash radiography[73] using a monochromatic 8.05-keV x-ray source that radiographed the target that was imploded by 54 OMEGA beams. A thin Cu foil was irradiated by the 1.5-kJ, 10-ps OMEGA EP short-pulse laser and generated a bright Cu K_α backlighter source. The laser was defocused to an ~20-μm spot that provided an intensity of ~5×10^{17} W/cm^2. The fast electrons refluxed in the Cu foil and generated K_α radiation over the ~1-mm foil, which provided an ideal area backlighter source. A spherical Bragg crystal located on the opposite side of the target imaged the implosions onto an image plate detector.[74] Figure 132.101 shows measured images of the implosion at various times around peak compression over a time range of ~0.4 ns and over a region of 500 μm × 500 μm. Note that each image was taken with a different shot. Figure 132.101(a) shows an image of an undriven target, where the Al tip is clearly visible and less opaque than the gold cone. The false color scheme represents the measured optical density. The frame in Fig. 132.101(b) shows an implosion at 3.75 ns after the start of the drive pulse. The fuel starts to assemble in front of the tip and the Al tip is compressed in the radial and longitudinal directions to a higher density. The following frames were taken at successively later times: Fig. 132.101(c) at 3.82 ns, Fig. 132.101(d) at 3.93 ns, Fig. 132.101(e) at 4.05 ns, and Fig. 132.101(f) at 4.15 ns. At later times the Al tip is more deformed and eventually completely destroyed and the fuel assembly reaches higher density. The radiographs show how the implosion destroys and pushes back the cone tip. Peak compression was reached close to the time of the frame in Fig. 132.101(e), while the last frame was

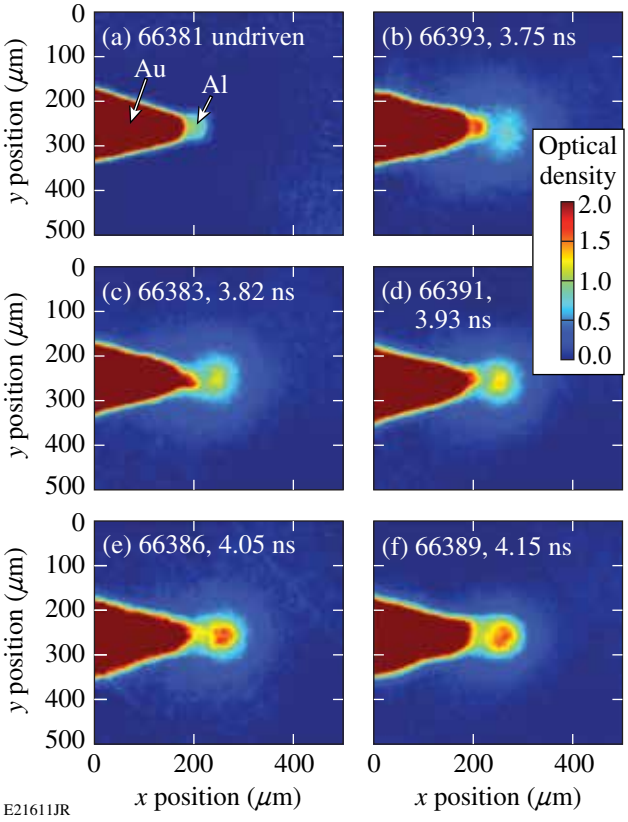

Figure 132.101
(a) Radiography images of an undriven target and imploded cone-in-shell targets at various stages of the implosion: (b) 3.75 ns, (c) 3.82 ns, (d) 3.93 ns, (e) 4.05 ns, and (f) 4.15 ns after the start of the UV drive laser pulse.

after peak compression. The measured time of peak compression (~4.10±0.05 ns) compares well to the time (4.06 ns) predicted from 2-D *DRACO* simulations. The measured peak

areal density is 330±50 mg/cm^3 using a calculated average mass absorption coefficient from the *DRACO* simulation along the line of sight. The predicted peak value of 360 mg/cm^3 shows that the measured value is close to the 2-D prediction. Interleaved with joint shots, the shock-breakout measurements were performed with OMEGA-only beams. The measured shock-breakout time agrees with the predicted breakout time within ~60 ps. The experiments confirm the improved shock resilience of the target. The second shot day at the end of FY12 studied the fast-electron coupling of the new target. The OMEGA EP laser was significantly improved with a smaller focus (R_{80} = 15 μm), a higher energy (1.35 kJ), and a higher contrast (~0.5-mJ prepulse energy). Compared to the previous experiment,[71] the average intensity increased about four times to $\sim 2 \times 10^{19}$ W/cm^2. The laser contrast was sufficiently high so that no significant pre-plasma formation is expected. The data of the integrated experiment are still being analyzed.

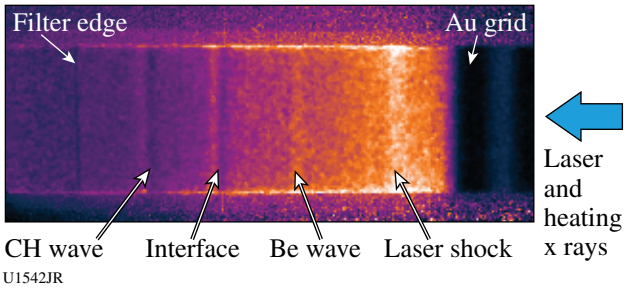

Figure 132.102
A radiograph of the heated CH/Be target. The delay between the heater and the backlighter was 5 ns. The laser beams and heating x rays were incident from the right side. Three fringes show up in the image: the middle fringe representing the interface and two side fringes corresponding to the waves propagating in CH and Be, respectively. The shock driven by the laser, traveling from right to left, is also visible.

FY12 LLNL OMEGA Experimental Programs

In FY12, LLNL conducted several campaigns on the OMEGA and OMEGA EP lasers, as well as campaigns that jointly used the OMEGA and OMEGA EP beams. Overall, LLNL led 335 target shots involving OMEGA and 121 target shots involving OMEGA EP. Approximately 38% of the total number of shots (124 OMEGA shots and 39 OMEGA EP shots) supported the National Ignition Campaign (NIC). The remaining 211 OMEGA shots and 82 OMEGA EP shots were dedicated to experiments for high-energy-density (HED) physics.

National Ignition Campaign Experiments

Thermal Conductivity Study of CH/Be and CH/D_2 Interfaces by Refraction-Enhanced X-Ray Radiography

Principal Investigator: Y. Ping
Co-investigators: O. L. Landen, J. A. Koch, R. Wallace, and G. W. Collins

The Atwood#12A&B campaigns are based on the technique of time-resolved, refraction-enhanced x-ray radiography that was successfully demonstrated in FY11. The evolution of the density profile at a cylindrical CH/Be interface isochorically heated by Ag L-band radiation has been measured to infer the thermal conductivity under inertial confinement fusion (ICF)-relevant conditions. In addition to observing the density evolution caused by thermal conduction, a counter-propagating shock wave and rarefaction wave were also observed as shown in Fig. 132.102. The velocities of these waves were measured simultaneously, providing constraints on the temperature after heating. Preliminary analysis of the data and hydrodynamic simulations shows that the thermal conductivity is higher than most models predict. The measurements of the CH/D_2 interface in cryogenic targets were complicated by leaking in the cryo cells, limited rotation movement, and condensation on the backlighter, which significantly reduced the brightness. A list of potential improvements has been provided to LLE for future experiments with cryogenic targets.

High-Resolution Measurements of Velocity Nonuniformities Created by Microscopic Perturbations in NIF Ablator Materials

Principal Investigator: P. M. Celliers
Co-investigator: M. A. Barrios

In May 2012, a full day was dedicated to the CAPSEED campaign. This campaign is a continuation of earlier campaigns that studied the performance of National Ignition Facility (NIF) ablators. The latest capsule designs using glow-discharge–polymer (GDP) ablators for the NIC currently employ Si doping layers as preheat shielding for the fuel; the earlier NIC designs employed Ge-doping layers. In response to this design change, most of the CAPSEED-12A campaign was devoted to assessing the performance of the newer Si-doped design (as compared to the previous Ge-doped designs). Results from this campaign (see Fig. 132.103) show that the performance of the Si-doped material matches that of the Ge-doped material.

Three additional shots were devoted to studying double-shocked nanocrystalline diamond [or "high-density carbon" (HDC)]. In current capsule designs employing diamond ablators, the initial shock strength is sufficient to only partially melt the capsule. Shock strengths much higher than this will set the fuel adiabat higher than the design goal of current designs.

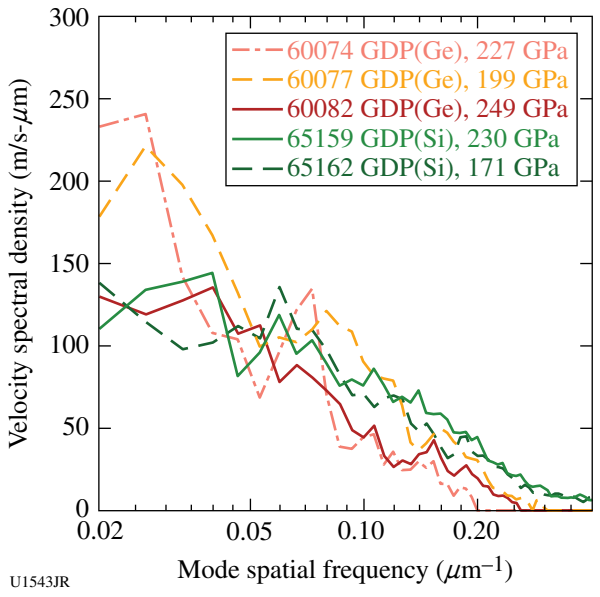

Figure 132.103
Velocity-fluctuation spectra measured for Ge-doped GDP in 2011 (shots 60074, 60077, and 60082) and Si-doped GDP in 2012 (shots 65159 and 65162). The velocity spectra for all cases appear to be equivalent within the range of statistical fluctuations.

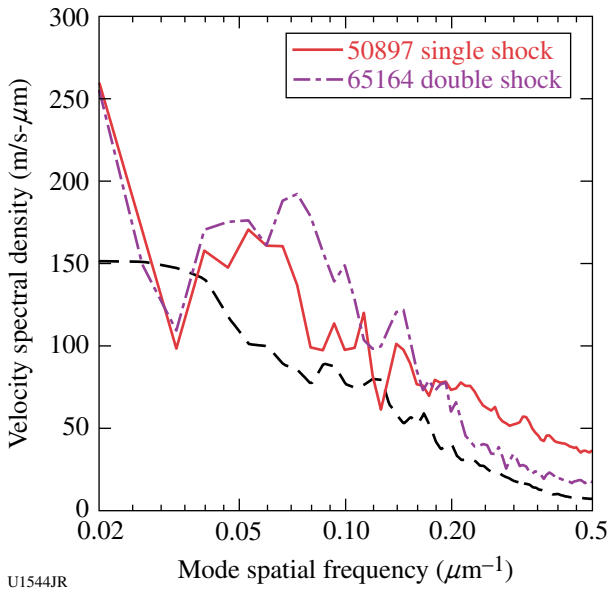

Figure 132.104
Velocity-fluctuation spectra measured for single-shocked and double-shocked HDC ablators. The black dashed curve represents the noise floor of the measurement (which is higher than for the measurements in Fig. 132.103). The fluctuation levels behind the second shock appear comparable to those behind the first shock.

Velocity fluctuations on the first (leading) shock are known to diminish significantly when the shock melting starts. The purpose of the double-shock test is to see whether the second and third shocks that follow in the compression sequence accumulate further velocity fluctuations, owing to the mixed-phase state of the diamond ablator following passage of the first shock. An initial double-shock test performed during the CAPSEED-12A campaign suggests (Fig. 132.104) that subsequent shocks appear to have similar fluctuation levels as the initial shock. Further tests are needed to extend the data set.

Measuring the Adiabatic Index of Polystyrene Using Counter-Propagating Shocks and X-Ray Thomson Scattering

Principal Investigator: A. Pak
Co-investigators: T. Ma, L. Fletcher, T. Döppner, and S. H. Glenzer

The adiabatic index of a material γ is an important quantity in determining a material's equation of state (EOS), which describes the response in density and temperature of a material to a change in pressure (such as that created by a strong shock). Understanding the EOS of polystyrene, a material similar to the NIF ablator, at high densities (>4× solid) and at temperatures of several eV, is of interest since it may inform the design and performance of current implosion experiments. In the CH-HeatCap campaign on OMEGA, the electron density, temperature, and charge state of shocked polystyrene (CH) were directly measured with x-ray Thomson scattering (XRTS). Using the Hugoniot relationships for a single strong shock, γ can be experimentally determined by measuring the mass density of the shocked material. Additionally, the use of colliding shocks in this experiment allowed for γ to be measured at higher mass densities and temperatures than could be obtained using a single shock.

Figure 132.105(a) shows the experimental setup, in which six drive beams on each side drove counter-propagating shock waves into an initially 200-μm-thick polystyrene foil. The drive beams were each 1 ns long and delayed with respect to one another to create an ~3-ns-long pulse with an 800-μm spot diameter at an intensity of $\sim 1 \times 10^{14}$ W/cm^2. An additional eight co-timed laser beams with a 1-ns pulse width and a focused intensity of $\sim 1 \times 10^{15}$ W/cm^2 created a probe of zinc He$_\alpha$ x rays. The x rays scattered through the shocked CH and to the ZSPEC crystal spectrometer onto the framing-camera detector. The timing of the probe with respect to the drive was varied to probe the CH before, during, and after shock collision.

Figures 132.105(b) and 132.105(c) show the scattering spectrum at two different times: just before and after shock collision,

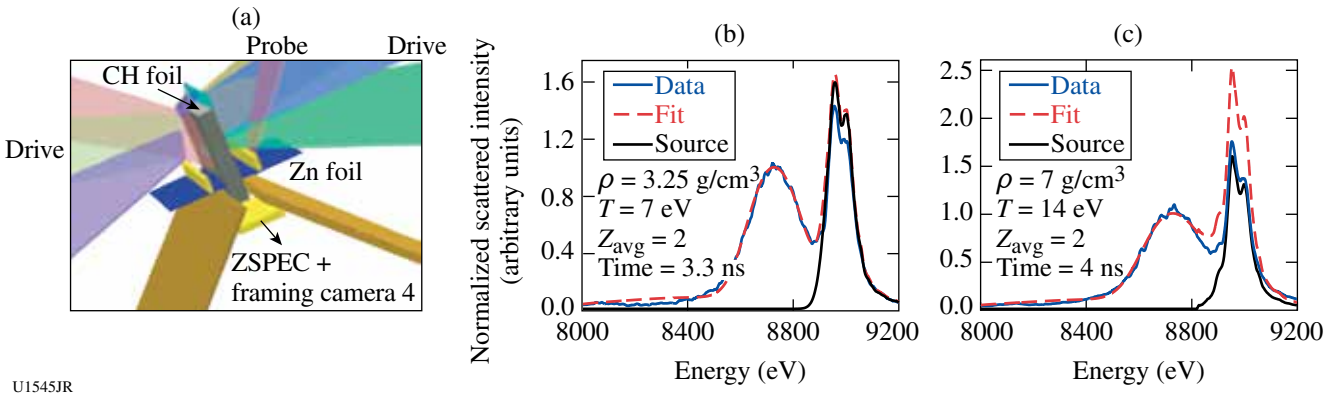

Figure 132.105
(a) Experimental setup. Two drive bundles compress the CH foil, while a probe bundle creates a burst of Zn He_α x rays that scatter through the target. Scattered x rays are collected via ZSPEC onto a framing camera detector in TIM-3. The normalized source and scattered x-ray intensity versus energy are shown (b) before and (c) after shock collision, respectively.

respectively. An increase in the width of the lower-energy, downshifted Compton feature indicates an increase in the material's electron density. Initial fits of the data indicate that a single shock density of 3.25±0.5 g/cm^3 and a 7±0.5 g/cm^3 density after shock collision have been reached. From this preliminary data analysis, the γ measured at the single- and double-shock density is 1.7 to 2.1 and 1.57 to 2.36, respectively. Additional data analysis is in progress.

In a second set of experiments, this time using OMEGA EP, a new experimental platform was developed to pursue similar physics. This year a total of four shot days in the BeXRTS and CH HeatCap campaigns were spent developing an experimental platform utilizing counter-propagating shocks and XRTS on OMEGA EP. One unique property of this class of experiments is that they allow for the adiabatic index γ of warm dense matter (WDM) to be directly measured. Additionally, counter-propagating shocks allow for materials to be compressed to higher densities and temperatures than single-shock experiments can create. A direct measurement of the γ of a material at densities and temperatures relevant to conditions existing in the ablator of NIF implosion experiments will contribute to the understanding, selection, and performance in ablator materials.

The experimental setup is shown in Fig. 132.106(a). In these preliminary experiments, a $200 \times 1000 \times 1400$-$\mu$m polystyrene (CH) foil was driven symmetrically from two sides by separate laser beams. Each drive beam had an ~351-nm wavelength, a 4-ns temporal width, and an average on-target intensity of ~1×10^{13} W/cm^2. Strong shocks, one from each of the two drive beams, counter-propagate with respect to one another and collide at the center of the CH foil. Two additional 1-ns-long UV laser beams are focused onto a zinc foil to create an

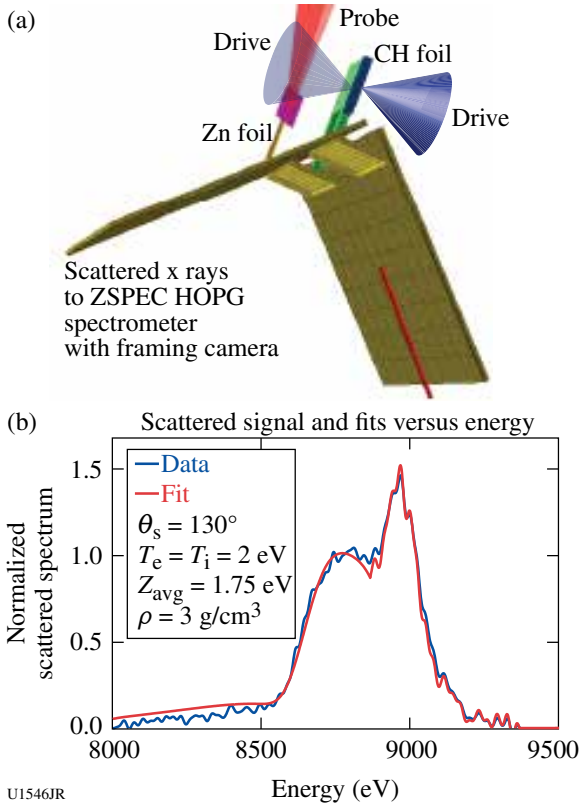

Figure 132.106
(a) The experimental setup for the XRTS OMEGA EP colliding-shock campaign. The CH foil is driven from the top and bottom by separate 4-ns-long UV laser beams with $I_0 \sim 1 \times 10^{13}$ W/cm^2. The counter-propagating shocks are diagnosed using Zn He_α x rays created from one or two probe UV laser beams. The scattered x rays travel through a target aperture to the ZSPEC highly oriented pyrolytic graphite (HOPG) crystal spectrometer and onto a framing camera. (b) An example of the measured scattered x-ray signal plotted versus energy taken 4.5 ns from the start of the laser drive. The fit of the scattered signal (red line) indicates that $\rho = 3$ g/cm^3, $T = 2$ eV, and $Z_{avg} = 1.75$ eV.

x-ray probe pulse. The Zn He_α x rays scatter from the shock-compressed CH foil through a gold aperture in the bottom of the target to the HOPG ZSPEC crystal spectrometer and onto a framing-camera detector that records the scattering signal over ~500 ps. Figure 132.106(b) shows an XRTS spectrum obtained at 4.5 ns after the laser drive had begun. The initial fit is in good agreement with predicted values for the density, temperature, and charge state from 2-D *HYDRA* simulations at this time. Additional analysis of the data is ongoing at this time.

Ablator Opacity Measurements

Principal Investigator: R. F. Heeter
Co-investigators: A. Graf, G. V. Brown, C. Mauche, R. E. Marrs, and B. Wilson

A new effort was initiated in FY12 to validate models of x-ray absorption and re-emission of capsule ablator materials, including germanium, silicon, and glow-discharge–polymer (GDP) plastic, over x-ray energies and material conditions typical of inertial confinement ablation plasmas. Experiments were undertaken using two platforms: First, the high-energy-density (HED) hohlraum-based opacity platform on OMEGA was used to assess the transmission opacity of Si, Ge, and GDP samples in LTE (local thermodynamic equilibrium) at T = 100 eV at densities around 0.03 g/cm^3. The second platform was launched in FY12 on OMEGA EP using dual short-pulse backlighters to measure the x-ray transmission of buried silicon layers embedded in plastic samples. This newer OMEGA EP technique is able to achieve both higher densities and higher temperatures than the OMEGA technique, but it requires tuning to achieve uniform sample conditions.

Sample data from the initial OMEGA experiments are shown in Fig. 132.107. For both Si and Ge samples, the transmission data for the spectral band from 250 to 1500 eV came in below the expected transmission calculated with standard opacity models using the plasma conditions predicted by 2-D radiation–hydrodynamic simulations. These plastic-tamped samples appear to be cooler and denser than expected, indicating either slower ablation and heating than predicted or a substantial error in the opacity models.

In late FY12, a series of follow-up shots were completed, including a tuned-up target design and independent characterization of the plasma conditions. Those data are currently being analyzed. Additional platform improvements, focused on reducing the noise in the transmission measurements, were implemented for beryllium-tamped, Si-doped GDP (plastic) opacity shots taken in early FY13.

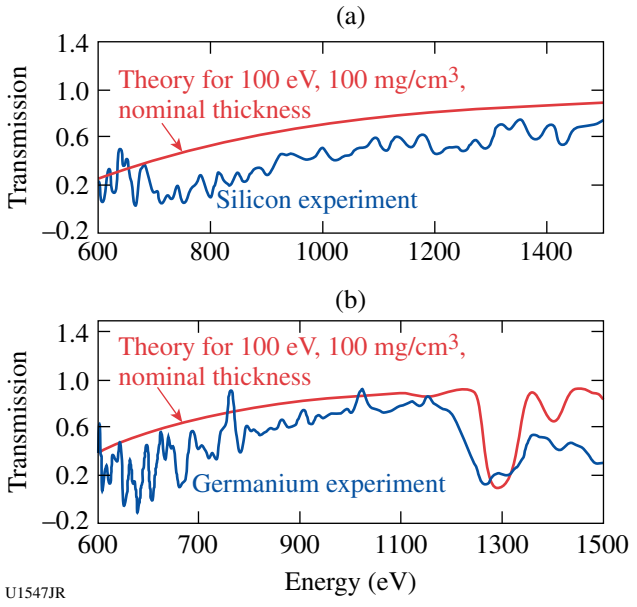

Figure 132.107
Initial results from (a) silicon and (b) germanium transmission experiments on OMEGA with comparison to expected transmissions.

Meanwhile, success was also achieved in obtaining dual-axis transmission spectra for silicon samples. In this new platform, up to two of the OMEGA EP UV beams are used to heat a CH-tamped Si foil with up to 200 J delivered in a Gaussian pulse shape with 100-ps FWHM (full-width-at-half-maximum). Peak sample temperatures of up to 400 eV are inferred from the time-integrated emission spectra of the embedded Si foil. Shortly after the UV heating pulse, a 10-ps IR laser drives a Zn wire backlighter, producing a bright continuum x-ray source with 16-ps FWHM duration and roughly 20-μm source size. This backlighter probes the expanding silicon plasma edge-on, measuring the sample expansion to yield the plasma density, and measuring the ionization state via absorption spectroscopy to provide information on the sample temperature. A second 10-ps continuum backlighter, synchronized to within 30 ps of the first, probes the sample face-on, delivering precise transmission spectral data for the measured temperature and density. Initial transmission measurements were completed in FY12 and are now being compared with theory.

Furthermore, by choosing a relatively thin tamper layer thickness, it is possible to tailor nonuniform density profiles and study the density of specific charge states as a function of position in an expanding ablated plasma. A sample of the latter data is shown in Fig. 132.108. In this case, 100 J of UV laser energy, arriving from the upper side of the image, heated the sample for 100 ps. The image was recorded roughly 400 ps

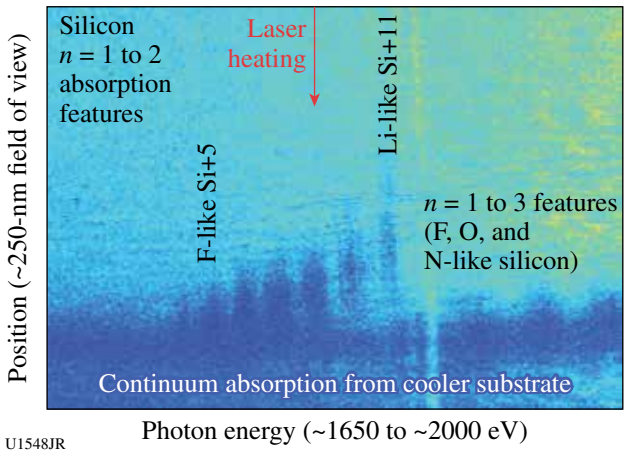

Figure 132.108
Space-resolved absorption spectrum obtained on OMEGA EP using edge-on broadband radiography of a silicon foil deposited on a carbon substrate and overcoated with a thin CH tamper layer.

after peak drive, during the cooling of the silicon plasma. The n = 1 to 2 absorption features of multiple ionization states of silicon are visible on the left (lower-energy) side of the spectrum, with additional n = 1 to n = 3 features on the right (higher-energy) side. The data show that 400 ps after peak sample drive, lithium-like Si persists on the low-density, laser-heated side of the plasma, while the various charge states of L-shell ions (Be- through F-like) are observed deeper into the plasma at higher density. The typical density at the location of the L-shell features is about 0.1 g/cm^3. The laser appears to not have fully heated the carbon substrate and perhaps some of the silicon, so continuum absorption from the rear of the sample is also visible. This technique is now being applied to study x-ray–ablated, silicon-doped GDP ablator plasmas in FY13.

Multipump Stimulated Raman Scattering

Principal Investigator: R. Kirkwood

The second campaign in this series was carried out to investigate the cooperative interaction of multiple beams in a cone to drive stimulated Raman scattering (SRS). The experiments used exploding-CH foil targets preheated by 11 heater beams to create a symmetric density profile. A normally incident seed beam was focused on the back side of the foil where it could produce SRS backscatter with a total power waveform as shown in the "seed beam only" case in Fig. 132.109. When (in a separate experiment) the seed beam was intersected by a cone of two to six pump beams that were pointed to cross the seed on the front side of the foil (where the density and temperature would allow further re-amplification of the SRS), a significant enhancement in the scattered power was observed. The

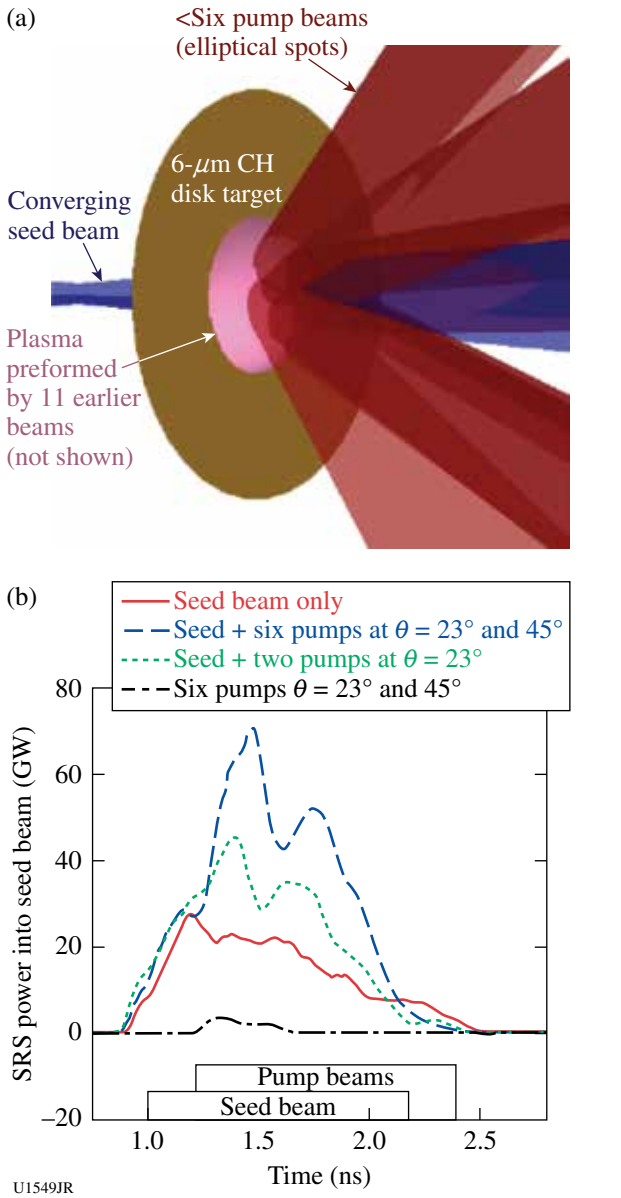

Figure 132.109
The geometry and measured SRS backscatter of a seed beam in the presence of different numbers of pump beams, from the SRS multipump experiments.

enhanced level of power was seen to increase with the number of pumps as expected from models of SRS re-amplification, and the total peak SRS was significantly greater than the sum of the SRS observed in both "seed only" and "six pumps" cases, as also shown in the figure. The overall increase in SRS with all beams cannot be explained by the simulated change in absorption by the plasma due to the pump beams and has the magnitude expected for SRS re-amplification. The experiment has provided an important benchmark for models of multibeam stimulated Raman scattering from ignition experiments.

Comparison of Plastic and High-Density Carbon Ablator Performance

Principal Investigator: S. Ross

The HDCEnerg-12A campaign successfully compared high-density carbon (HDC) and CH ablator performance. A series of OMEGA experiments with three distinct pulse shapes were used to investigate HDC and CH performance. The pulse shapes were designed to deliver different drive pressures during the foot of the laser pulse. The pulses delivered foot pressures ranging from ~1.7 Mb (LA234002) to ~7.5 Mb (LA190801) with an intermediate pressure of ~3.6 Mb (LA232301). The capsules were filled with either 40 atm or 20 atm of deuterium. The measured neutron yield is shown in Fig. 132.110.

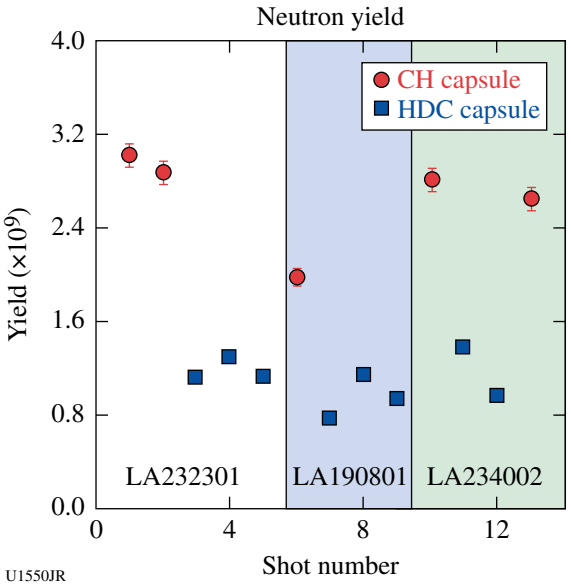

Figure 132.110
The measured neutron yield for different capsule materials and pulse shapes.

The HDC capsules showed very similar neutron yields for all three pulse shapes. This is evidence that the capsule's compression and performance are independent of the pressure in the laser foot for pressures ranging from 1.7 Mb to 7.5 Mb. The difference in HDC and CH yields are expected because of differences in capsule thickness. These results are being used to design future HDC experiments.

Shock Release of ICF-Relevant Materials

Principal Investigator: D. E. Fratanduono

Inertial confinement fusion (ICF) capsule implosions are driven by four shock waves. The strength and timing of each shock are controlled to maintain a low adiabat. High-pressure (>1-Mbar) equation-of-state (EOS) experiments on ICF ablators have been primarily limited to Hugoniot measurements. These experiments focus on developing a technique to measure the release isentropes of ICF-relevant materials in order to better constrain the EOS of ICF-relevant materials.

Experiments are performed at the Omega Laser Facility. Target design consists of a glow-discharge polymer (GDP, an ICF ablator), and a thin (~50-nm) silicon nitride film separated by a vacuum or gas-filled gap (~250 μm) as shown in Fig. 132.111. A strong shock (>250 GPa) is generated in the GDP ablator. When the shock breaks out of the sample and into vacuum, it releases and isentropically expands as it propagates across the gap. When the strong shock in the GDP enters the gas-filled void, a weak shock is generated and propagates across the gap. By measuring the shock state of the gas, a point on the GDP release isentrope is determined. The released material stagnates on the silicon nitride. The velocity of the silicon nitride is measured using a velocity interferometer system for any reflector (VISAR). Using the measured velocity profile, a momentum balance technique is employed to extract information regarding the release isentrope.

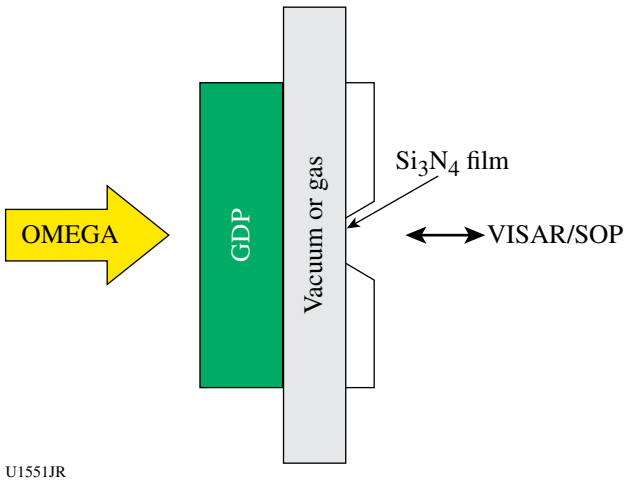

Figure 132.111
Target design.

The vacuum results indicate that the velocity of the leading edge of the release isentrope is traveling ~30% faster than predicted by the LEOS tables. This behavior has been observed on CH, GDP, and diamond. These results are shown in Fig. 132.112. The gas (methane)-filled results are consistent with Hugoniots generated from LEOS tables. However, the data at lower-pressure shock states are inconsistent with the vacuum measurements. Further experiments are being performed to examine this discrepancy. We are in the process of designing

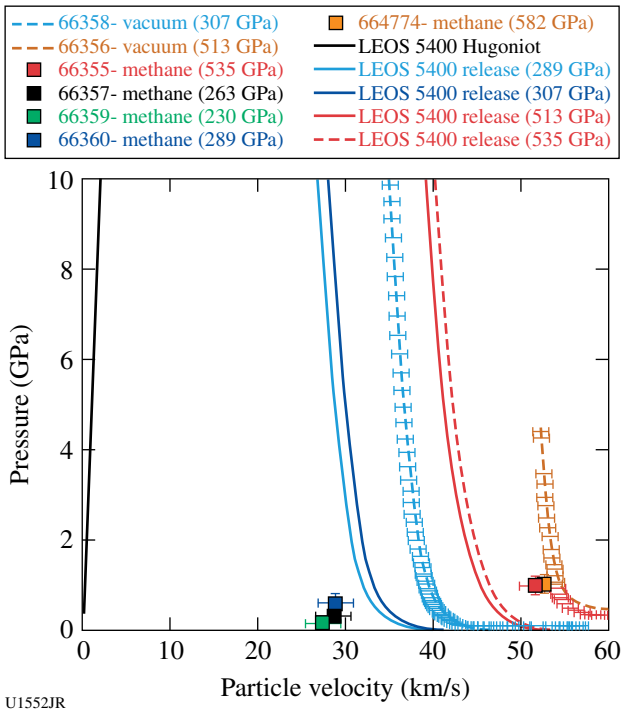

Figure 132.112
Glow-discharge–polymer release isentropes.

targets to measure the release of D_2 ice into low-density D_2 gas. Using this technique, we may be able to determine species separation for DT.

High-Energy-Density Experiments

1. Material Dynamics and Equation of State

Tantalum Rayleigh–Taylor Experiments

Principal Investigators: H.-S. Park and C. Plechaty

The focus of the ICETaRT campaign was to study Ta material strength at high pressure (>1 Mbar) and high strain rates (10^6 to 10^8 s^{-1}). To achieve these conditions in the experiment while keeping the temperature of the Ta sample well below melting, a reservoir and vacuum gap[75] configuration was employed to produce a quasi-isentropic pressure drive (see Fig. 132.113). The plasma drive was produced by ablating a hohlraum with 40 OMEGA beams to deposit a total energy of 20 kJ. Attached to the side of the hohlraum was an ablator/reservoir and a physics package, which were separated by a vacuum gap to produce ramped drive conditions onto the physics package.

The physics package consisted of a CH heat shield placed on a Ta sample. Sinusoidal perturbations were imposed on the

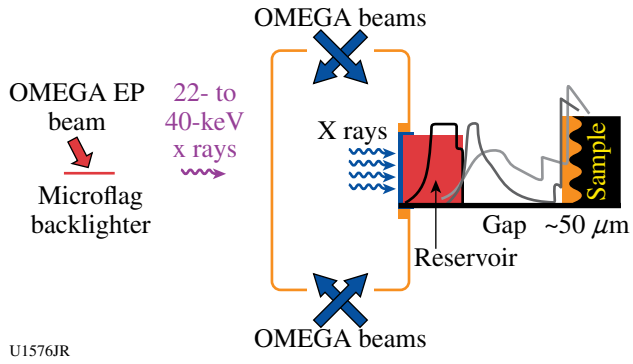

Figure 132.113
Experimental configuration employed for OMEGA EP joint shots. OMEGA beams deposited energy into the hohlraum, producing a plasma drive. Face-on high-energy radiography was employed on the rippled Ta sample by using a short-pulse OMEGA EP beam to ablate an Ag backlighter. For OMEGA shots, the rippled Ta sample was replaced by a VISAR witness sample to characterize the plasma drive.

surface of the Ta. As the plasma from the reservoir crosses the gap and stagnates on the sample package, the Ta ripples undergo an effective acceleration from the stagnating plasma drive. This acceleration actuates Rayleigh–Taylor (RT) growth of the pre-imposed sinusoidal pattern. Since the Ta material strength acts to suppress the amount of RT growth, measuring the RT ripple amplitude gives a measure of the material strength.[75–77] To measure the perturbation amplitude, face-on high-energy (22-keV Ag K_α) radiography was employed using an OMEGA EP short-pulse beam. We needed the OMEGA EP beam to employ a high-energy backlighter (22 keV) to probe the high-Z tantalum material. The amount of backlighter transmission through the ripples is governed by the quantity $\rho\Delta Z$, where ρ is the density of the driven ripples and ΔZ is the amplitude. The RT growth factor (GF) is determined by measuring the driven $\rho\Delta Z$:[75,78]

$$\mathrm{GF} = \frac{(\rho\Delta Z)_{\mathrm{driven}}}{(\rho_0 \Delta Z_0)_{\mathrm{undriven}}\,\mathrm{gMTF}}, \tag{1}$$

where ρ_0 and ρZ_0 are the initial density and ripple amplitude (determined from pre-shot metrology) and the MTF is the modulation transfer function, which characterizes the frequency response of the system and is measured by using a knife edge. To determine the properties of the plasma drive, separate shots without the backlighter were performed by replacing the physics package with a witness sample and taking VISAR measurements.

The FY12 ICETaRT campaign employed the experimental setup discussed above to study several aspects of Ta material

strength. The first topic studied was the Ta material failure threshold. In previous experiments, we observed (Fig. 132.114) that as the relative growth increased, defined as the ratio between the ripple amplitude and the Ta sample thickness, the measured relative growth deviated from that predicted by the multiscale model.[79] To study the threshold where the relative growth measured in the experiment deviates from that predicted by the multiscale model, or measure the threshold where failure occurs, a three-amplitude pattern was employed. The Ta sample was split into three regions, each with a 50-μm wavelength, but with a different amplitude—namely, 1.0, 2.0, and 3.5 μm. We found that failure occurred as the relative growth in experiment exceeded ~20%.

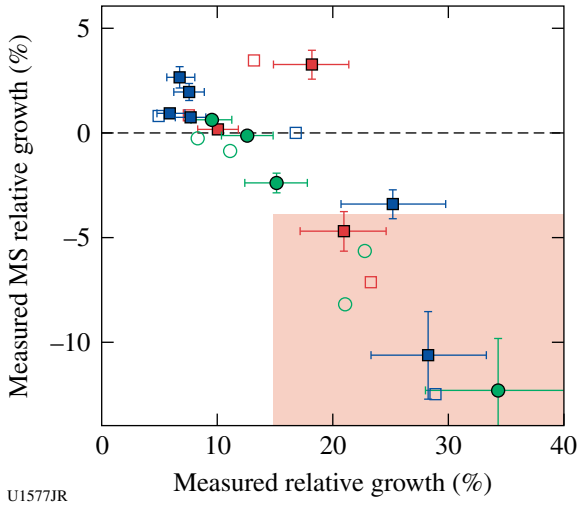

Figure 132.114
Plot of measured relative growth (RG) versus the deviation of the measured relative growth from that predicted by the multiscale (MS) model. The colored box in the lower right-hand corner denotes where the absolute value of this difference becomes >4%. This is defined as failure.

The second topic studied was a comparative material strength study between Ta [100] and Ta [111] crystal orientations. In previous studies[80] the target samples were predominantly in the [111] orientation. In the multiscale model, crystal orientation can affect material strength via the Taylor factor. To understand the effect of crystal orientation on the material strength, we placed the two samples side by side and compared the ripple growth for a given shot (see Fig. 132.115). Initial results from just a few shots suggest that the difference in the growth factor between these two crystal orientations is too small to be measured within our error bars of ~18%.

Lastly, the final topic of study undertaken in the FY12 ICETaRT campaign was the study of a new multimode configuration (Fig. 132.116). A superposition of two different sinusoidal ripple patterns was imposed on the Ta sample. The two modes employed had the same amplitude (1.85 μm) but different wavelengths (75 and 112 μm, respectively) and phases (210° and 24°, respectively). The purpose of this study was twofold. The first purpose was to study the coupling of RT growth between the modes. For example, the growth of the designed modes with wave vectors k_1 and k_2 induced growth at $|k_1 \pm k_2|$, $2k_1$, and $2k_2$. The exact details of the coupling are not fully understood. Second, by using multiple modes, the multimode configuration can be used to produce simultaneous Rayleigh–Taylor (RT) measurements, with corresponding strengths. A detailed analysis of this data is currently underway.

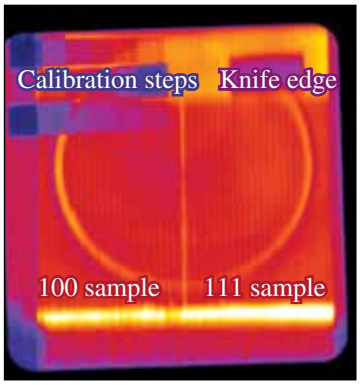

Figure 132.115
Radiography image of [100] and [111] target configuration. The 100 sample is on the left, and the 111 sample is on the right. The calibration steps are employed to relate the backlighter transmission to a specific value of $\rho\Delta Z$. The knife edge is used to determine the MTF. The circular structure in the middle is a hole in the hohlraum and indicates where the plasma drive can stagnate onto the sample, driving RT ripple growth.

Iron Rayleigh–Taylor Experiments
Principal Investigator: C. Plechaty

The ICEIronRT campaign focused on the study of iron material strength at high pressures and strain rates when a phase transition occurs at lower pressures (~100 kbar). The goal was to understand the strength parameter difference at high pressure when a phase transition occurs from the α-to-ε phase at a lower pressure level.

For ICEIronRT, we employed a quasi-isentropic plasma drive produced by a reservoir–gap–sample configuration.[76] A newly designed 6% BrCH reservoir was employed to achieve pressures up to ~1.5 Mbar. In the experiment, 40 OMEGA beams (with a total energy of 20 kJ) were employed to ablate a hohlraum with a side-mounted reservoir–gap–sample pack-

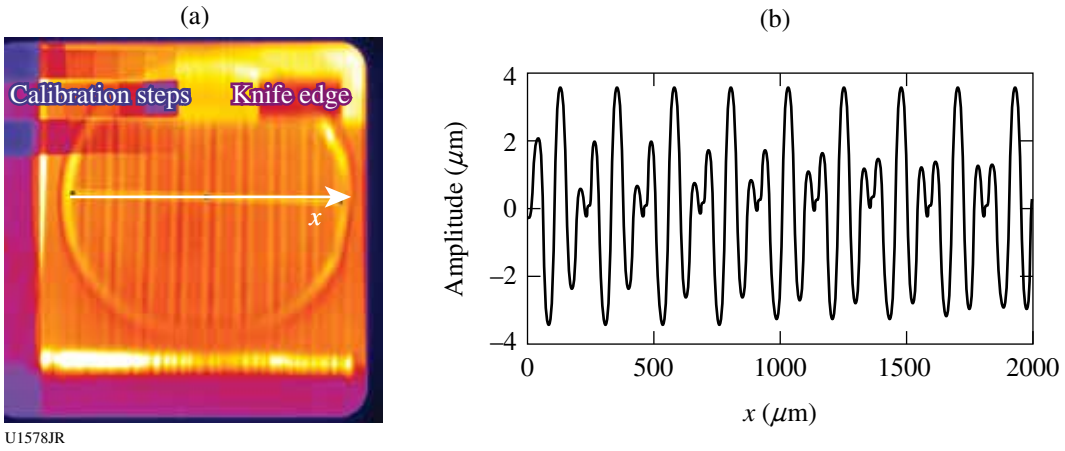

Figure 132.116
(a) The radiography image obtained for this multimode configuration; (b) an ideal plot of the ripple structure for $0 < x < 2000$ μm.

age in order to produce a plasma drive. As the plasma drive crossed the vacuum gap, it stagnated onto the Fe sample with an imposed sinusoidal pattern on the surface. The stagnation of the plasma drive onto the Fe sample drives Rayleigh–Taylor (RT) growth of the ripples where the observed RT growth rate is dependent on the strength.

To obtain the quantities listed in Eq. (1), $\rho_0\Delta Z_0$ was derived from pre-shot Veeco measurements and the MTF was measured using a knife edge (Fig. 132.117). To measure $\rho\Delta Z$ for the driven sample, face-on high-energy (22-keV) radiography was employed using an Ag microflag backlighter ($200 \times 200 \times 5$ μm). A short-pulse (100-ps) OMEGA EP beam was employed to ablate the backlighter with a 1.0-kJ pulse delivered with a given time delay in respect to the OMEGA drive beams. To resolve the ripple growth, the thinnest side of the backlighter was aligned along the direction of the ripples.

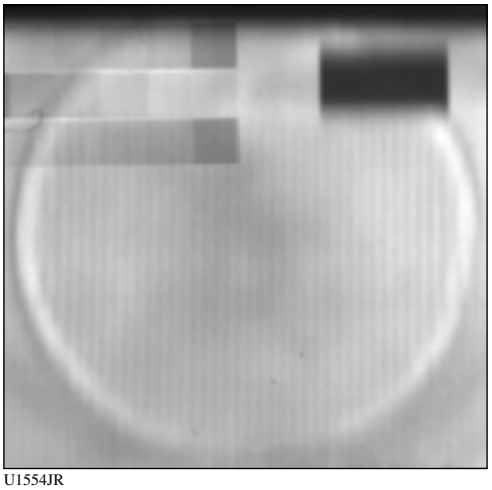

Figure 132.117
A radiograph for shot 67210 (60-ns delay). The iron calibration steps, located in the upper left-hand corner, are used to relate the backlighter transmission to a specific value of $\rho\Delta Z$. The knife edge located in the upper right-hand corner is used to measure the MTF. The circular feature in the middle of the image indicates the region of driven ripple growth.

In addition to joint OMEGA EP shots, OMEGA-only shots were performed to determine the properties of the plasma drive. In these shots, the Fe sample was replaced with a witness sample and VISAR measurements were performed.

Figure 132.118 compares the undriven ripple $\rho_0\Delta Z_0$ and the driven ripple $\rho\Delta Z$. As shown, $\rho\Delta Z > \rho_0\Delta Z_0$, indicating that the driven ripples have undergone RT growth. The GF, calculated

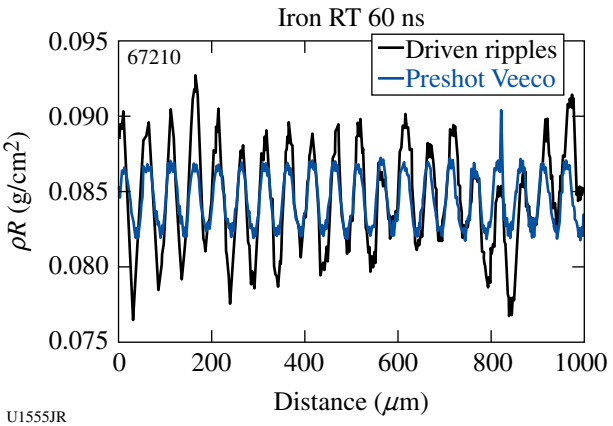

Figure 132.118
Comparison of the pre-shot values of $\rho_0\Delta Z_0$ and the shot values of $\rho\Delta Z$ for a 60-ns delay between the OMEGA drive and OMEGA EP backlighter beams.

with Eq. (1), is shown in Fig. 132.119 with error bars of ~±50%. An initial analysis indicates that the iron material strength is higher than that predicted using a hybrid α-to-ε phase-transiting Preston–Tonks–Wallace (PTW) strength model[81] calculated using our experimental condition of ~1.5-Mbar pressure and strain rate >10^6 s^{-1}.

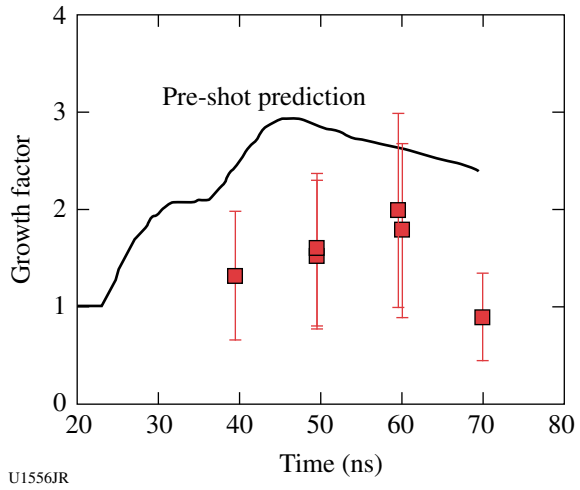

Figure 132.119
Comparison between the GF (with error bars of 50%) and the GF prediction obtained from a hybrid α-to-ε transition PTW model.

Double-Pulse Radiography Development

Principal Investigator: C. Plechaty

Laser-driven, high-energy (>22-keV) x-ray radiography has been employed as a diagnostic tool in many different types of high-energy-density (HED) experiments with applications ranging from material strength studies[75,78,82,83] to capsule implosion experiments. In FY12, the DBLPULSE campaign focused on the development of a new multiframe radiography technique that takes advantage of the multiple beams available at state-of-the-art laser facilities such as Omega and the NIF. This concept is of particular importance to the NIF and HED programs since it will yield twice the amount of data per shot.

Experiments were performed on OMEGA EP using two short-pulse (100-ps, 100-μm spot size) beams to independently ablate two 300 × 300 × 10-μm foils (Cu and Ag) placed 1.2 mm apart (Fig. 132.120). In the experiment a 1-kJ beam was employed to ablate the Cu backlighter. After delayed time t, the Ag backlighter target was irradiated by a 1.5-kJ beam. The performance of the two time-delayed x-ray pulses were tested by radiographing a Au grid pattern placed 10.3 mm from the foils. To obtain two distinct images of the grid pattern, a collimator was employed. The collimator consisted of a 1-mm-thick Au disk, with two tapered holes to act as pinholes for each backlighter. The surface of the collimator was placed 3.2 mm from the center of the foils. The angle of the holes was chosen such that two distinct and spatially separate images were produced at the location of the image plate (IP), placed ~500 mm from the foils.

To characterize the frequency response of the system, we employed a Au grid pattern that consisted of several orthogonal mesh elements, each with different spatial scales. The Au grid had 10-, 20-, 30-, 40-, and 80-μm mesh features, aligned along the horizontal and vertical axes of the grid. The Cu and Ag foils were mounted orthogonal to each other and the IP such that each backlighter would produce a 1-D orthogonal x-ray source aligned along either the vertical or horizontal axis of

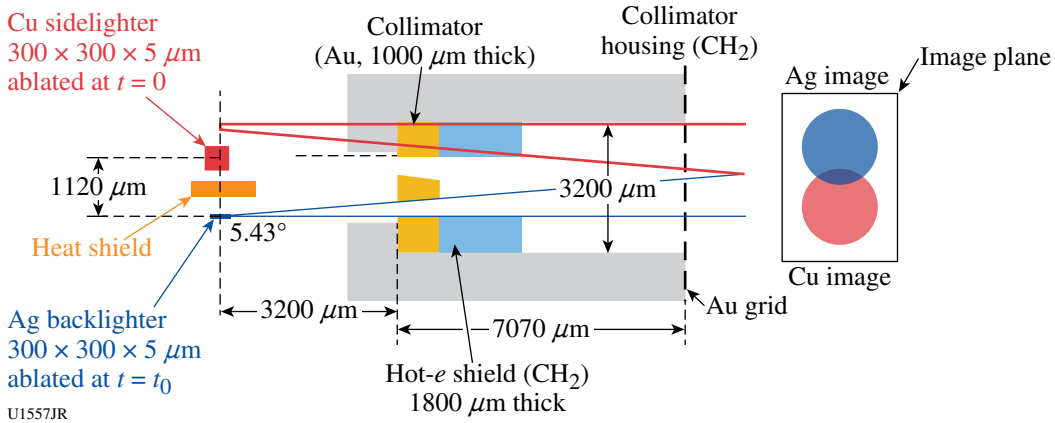

Figure 132.120
Schematic of experimental setup. X rays from the two independently ablated backlighter foils pass through a collimator assembly. This produces two temporally and spatially independent images of an Au grid on an image plate.

the Au grid. The IP was placed far enough away so that two spatially distinct images were captured.

To protect the second backlighter target from the hydrodynamic expansion and x-ray emission from the first backlighter, a heat shield was placed between the foils on a separate target positioner.

Radiography images captured using this configuration are shown in Fig. 132.121. In Figs. 132.121(a)–132.121(c), the heat shield employed was a 1000 × 1000 × 200-μm-thick CH heat shield. At $t = 0$ ns [Fig. 132.121(a)] the 10-, 20-, 30-, and 80-μm features are clearly visible in the Cu (top) image. In the Ag (bottom) image, the 10- and 30-μm features are observed, while the other features are located out of the instrument field of view. At $t = 5$ ns [Fig. 132.121(b)], the image produced by the delayed backlighter is observed to degrade; only the 30-μm features are visible. This trend continues when $t = 20$ ns [Fig. 132.121(c)], where the Ag backlighter resolution has degraded enough so that the grid features are not observed.

An explanation for the reduction in the image quality can be found by examining the time-integrated x-ray pinhole camera (XRPHC) images (Fig. 132.122). As shown by Fig. 132.122, the Ag backlighter x-ray source size becomes notably larger for the $t = 20$ ns case [Fig. 132.122(c)] when compared to the $t = 0$ ns case [Fig. 132.122(b)], causing the delayed image quality to degrade.

Since the CH heat shield employed for the images captured in Figs. 132.121(a)– 132.121(c) is transparent to laser backscatter and x-ray emission from the $t = 0$ ns backlighter, it was replaced by a 1000 × 1000 × 50-μm Au heat shield [Fig. 132.121(d)]. When employing this heat shield design, the resolution of the delayed backlighter only slightly increases. Employing an even thicker Au heat shield (1000 × 1000 × 200 μm) does not yield better system resolution.

Since the 50-μm-thick and 200-μm-thick Au heat shields prevent a significant portion of the low-energy x-ray emission from the Cu backlighter from reaching the Ag backlighter, the observed preheating of the Ag backlighter is likely caused by radiating plasma expansion. As the Cu backlighter is ablated, the resulting plasma expands past the heat shield and radiates. This causes the Ag backlighter to be preheated, producing plasma and increasing the x-ray source size once the backlighter is ablated. A future study will investigate this effect.

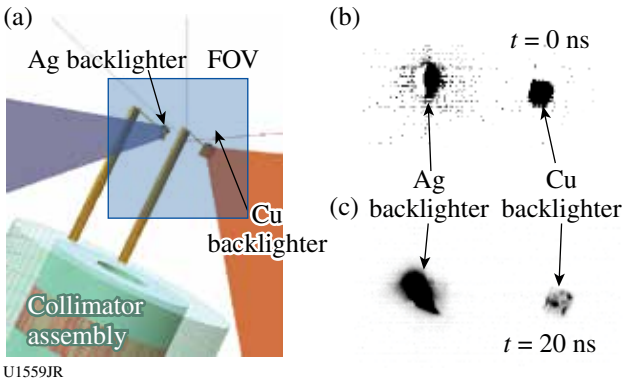

Figure 132.122
XRPHC images. (a) Image geometry showing the Cu beam and backlighter (on the right) and the Ag beam and backlighter (on the left). The field of view (FOV) for the XRPHC images is shown. The captured time-integrated images are shown in (b) for the case of $t = 0$ ns and (c) for the case of $t = 20$ ns.

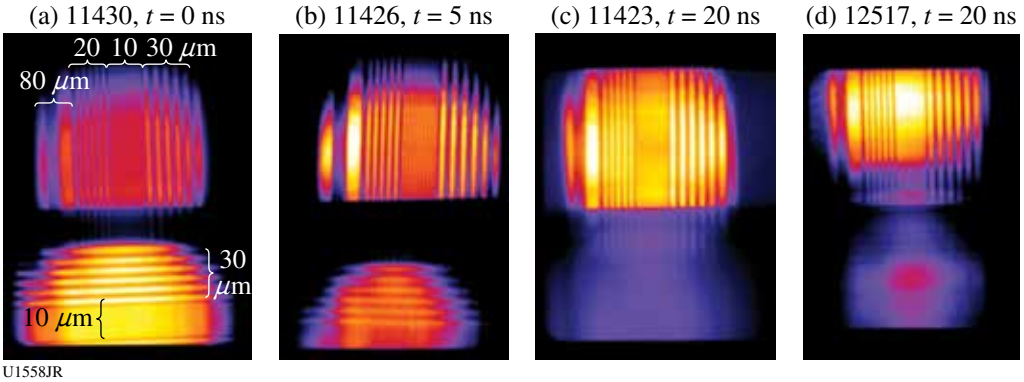

Figure 132.121
Images obtained with the HERIE. In these images, the top image was produced by the Cu backlighter, which is always taken at $t = 0$ ns. The bottom image was produced by the Ag backlighter, which ablates the foil at the time shown. [(a)–(c)] A 1000 × 1000 × 200-μm-thick CH heat shield was employed; (d) a 1000 × 1000 × 50-μm-thick Au heat shield was employed.

Diffraction Studies on Shocked Tantalum

Principal Investigators: B. Maddox, A. Comley, and C. Wehrenberg

Three distinct experiments were conducted to study the behavior of shocked and ramp-loaded tantalum.

StrDiff-12A: The goals of the StrDiff-12A campaign were to observe twin formation in single-crystal Ta shocked along the [110] direction, obtain large-pinhole diffraction for a quantitative temperature analysis of shocked Ta, extend out previous measurements of the lattice anisotropy of Ta shocked along [100] to lower peak pressure, verify our simulations using a stepped diamond drive target, and test a glueless target for future studies of shock- and ramp-compressed Ta. The experiment used the broadband x-ray diffraction diagnostic (BBXRD) on TIM-4 as the primary diffraction diagnostic, as well as the tilted VISAR. Crystal samples were driven using a single beam (Beam 18) with an SG8 phase plate. The x rays for diffraction were produced by an imploded CH shell driven by 44 beams with SG4 phase plates. All beams used a 1-ns square pulse. We achieved 12 shots and obtained excellent data. Due to the initial crystal sample quality of the Ta [110] samples, we were unable to observe any useful driven diffraction patterns for Ta shocked along [110] and, therefore, observed no twinning. However, all other experimental goals were met. In this campaign, we recorded our highest-quality Laue diffraction pattern to date, detecting up to seven compressed diffraction spots on a single side of the BBXRD detector (shown in Fig. 132.123).

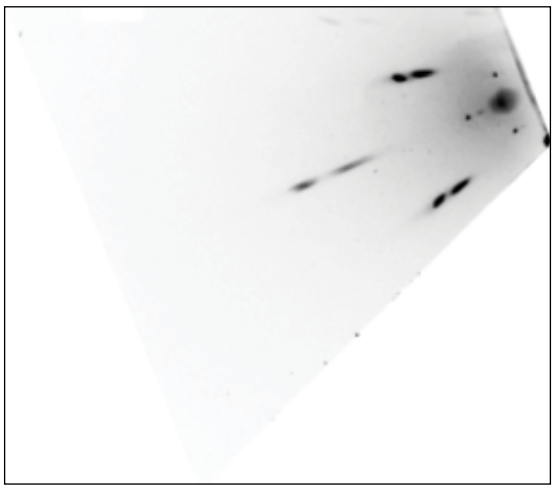

U1560JR

Figure 132.123
Example of high-quality Laue diffraction recorded from Ta single-crystal shock compressed to ~0.5 Mbar along the [100] direction.

ShkLaue-2012: In ShkLaue-2012 our goal was to extend previously successful strength measurements of shocked Ta using *in-situ* Laue diffraction to ramped-loading conditions, allowing us to compare our measurements to Rayleigh–Taylor strength experiments with similar strain rates. As in previous ShkLaue campaigns, the BBXRD diagnostic was used to record Laue diffraction data, giving a direct measurement of lattice anisotropy and shear strength of the material. A reservoir drive was developed in which a directly driven brominated-CH reservoir releases across a gap and creates a ramped stagnation shock on the Ta sample. A new glueless target design was also developed for this campaign, in which the Ta samples were kept on the MgO substrate and the substrate was polished down to the desired thickness. This design allowed us to record high-quality VISAR data simultaneously with Laue diffraction data. Initial analysis shows that the reservoir drive was successful in creating the ramped drive, which demonstrated highly repeatable behavior. High-contrast diffraction data were recorded for a range of drive times and show a range of lattice anisotropy ratios.

EP-TaBragg-2012: In EP-TaBragg-2012 our goal was to study shock-compressed Ta using *in-situ* Bragg diffraction, building on the successful BraggDiff-2011 campaign. The experimental configuration used the Lawrence Livermore diffraction imager as the primary diagnostic on TIM-13. Samples were driven using two defocused beams with a 10-ns pulse, while a short-pulse beam was used to drive a silver backlighter to create the high-energy x rays. There were a few issues in adjusting the drive-backlighter relative timing, producing an imbalance in the signal strength in either the driven or static diffraction signal in the initial shots. This issue was solved by comparing VISAR data with previous campaigns, resulting in a 0.5-ns shift from previous experiments. The data quality obtained was excellent and, combined with BraggDiff-2011 data, provides a range of pressures for Ta strength measurements.

Ta X-Ray Diffraction

Principal Investigators: A. Lazicki, J. H. Eggert, and J. R. Rygg

In FY12 powder x-ray diffraction experiments (Fig. 132.124) on solid ramp-compressed tantalum yielded additional data points confirming a high-pressure phase transition near 300 GPa (Fig. 132.125). The structure was determined to be consistent with a predicted simple hexagonal (ω) phase.[84,85] During the shot day, we ramp compressed Ta and Fe samples to pressures above 10 Mbar. The technical difficulties encountered while trying to measure x-ray diffraction at these high pressures

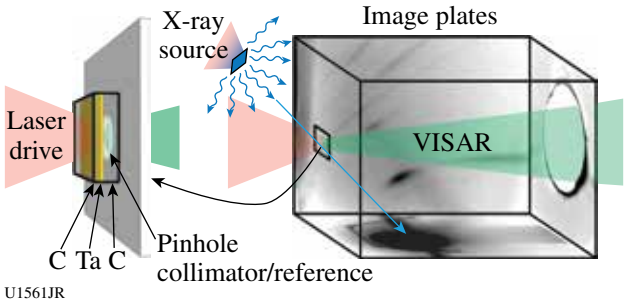

Figure 132.124
X-ray diffraction experimental setup. The target consisted of a 4-μm foil of Ta sandwiched between single-crystal diamond plates. The x-ray source was laser-excited He_α radiation from Fe or Cu thin foils. X rays diffracted off of the Ta sample were scattered onto the inner surfaces of a box lined with image plates, yielding crystal structure and volume. Target rear-surface velocities were detected using VISAR, yielding pressure.

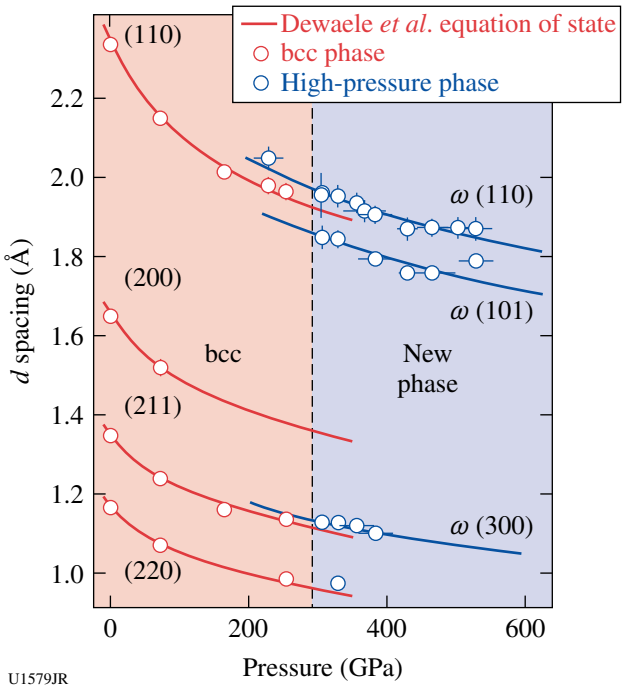

Figure 132.125
Shift of the d spacings of x-ray diffraction peaks under pressure showing evidence of a new phase at 300 GPa.

have provided critical feedback for our design of terapascal-range x-ray diffraction experiments on the NIF.

Hydrogen Equation of State

Principal Investigators: A. Lazicki, M. Millot, J. R. Rygg, and J. H. Eggert

The purpose of this study was to look for pressure-induced chemistry in deuterium by electron doping from an added ~5% of xenon, evidenced by the effects on the Hugoniot and the reflectivity, compared to pure deuterium. Gas mixtures were precompressed to fluid deuterium density in a diamond anvil cell prior to shock compression. Measurements (Fig. 132.126) reveal a Hugoniot shifted to higher density but not to the extent predicted by a simple linear mixing model, indicating chemical interaction between the species. There is, however, some uncertainty in the concentrations of gas captured in the diamond cells, so the conclusion awaits further experiments. Because of difficulties in sample preparation, some of the shots were devoted instead to the measurement of the Hugoniot of the hydrogen compound lithium hydride (Fig. 132.127), precompressed to 5 to 9 kbar in a diamond anvil cell. Results will aid in refinement of equation-of-state models.

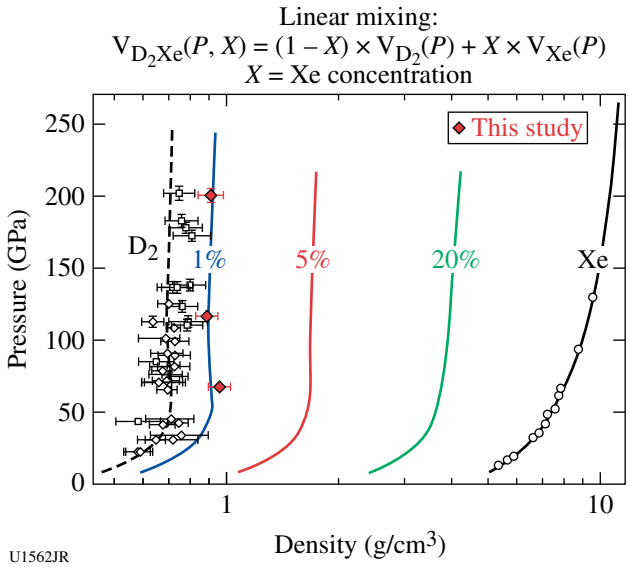

Figure 132.126
Hugoniot of D_2 (Ref. 86) and Xe (Ref. 87) compared with the data from this study. Curves predicting the behavior the mixture are based on the linear mixing model.

XAFS Study of Ramp-Compressed Fe, Ta, and Mo

Principal Investigator: Y. Ping
Co-investigators: F. Coppari, D. G. Hicks, D. E. Fratanduono, S. Hamel, J. H. Eggert, J. R. Rygg, R. F. Smith, D. C. Swift, and G. W. Collins (LLNL); B. Yaakobi and T. R. Boehly (LLE)

Extended x-ray absorption fine structure (EXAFS) measurements of dynamically compressed iron have been performed on OMEGA using an implosion backlighter. Iron is compressed in the solid state to 560 GPa (5.6 Mbar), the highest solid-state pressure for iron explored in the laboratory (Fig. 132.128). EXAFS measurements provide simultaneous density, tem-

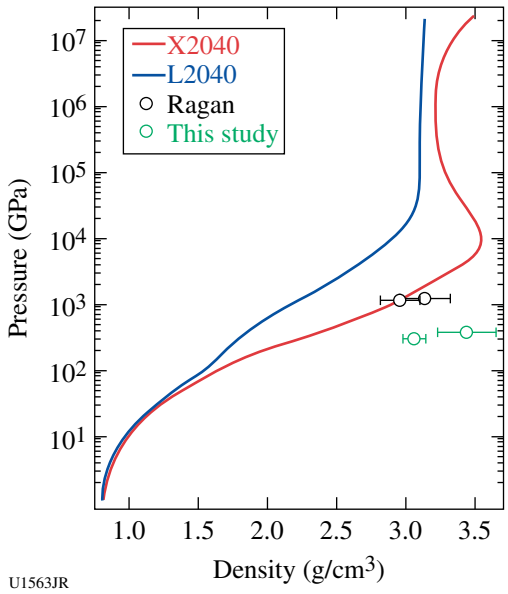

Figure 132.127
Hugoniot of LiH from EOS models, compared to experimental data.[88] The data shown from this study are for LiH precompressed to ~6.5 kbar.

perature, and local-structure data for compressed iron in this new regime—the first such data for constraining solid-state theory and evolution models for many newly discovered extra-solar terrestrial planets. The data show that the close-packed structure of iron is stable up to 560 GPa, the temperature at peak compression is significantly higher than expected from pure compressive work, and the strength of iron is many times greater than expected from lower-pressure data.[89]

Based on the success of EXAFS measurements of iron, we have extended this platform to study L edges of Ta and Mo. Data on Mo at ambient conditions, 2 Mbar, and 3 Mbar have been obtained, and EXAFS of undriven Ta has been observed for the first time on OMEGA. The last campaign in September 2012 demonstrated 2× enhancement in backlighter brightness and 4× enhancement in the spectrometer efficiency, making it possible to do single-shot EXAFS measurements of driven Ta in FY13.

Tin Melt

Principal Investigator: A. Lazicki

Campaigns investigating the high-pressure solid crystal structure and probing the melting curve of tin have continued in FY12, extending the measured diffraction up to 720 GPa (Fig. 132.129), and potentially yielding information about the melting curve up to 300 GPa (Fig. 132.130). The new x-ray diffraction data provide further evidence for a high-pressure, high-temperature phase transition near 200 GPa. The structure of this new phase differs from the hexagonal close-packed structure that arises near 200 GPa at ambient temperature.[90] We propose the simple hexagonal omega phase as a likely crystal structure for this new phase. The particle velocity histories of shock-melted and ramp-compressed tin show a plateau consistent with changing sound velocities at a phase transition such as recrys-

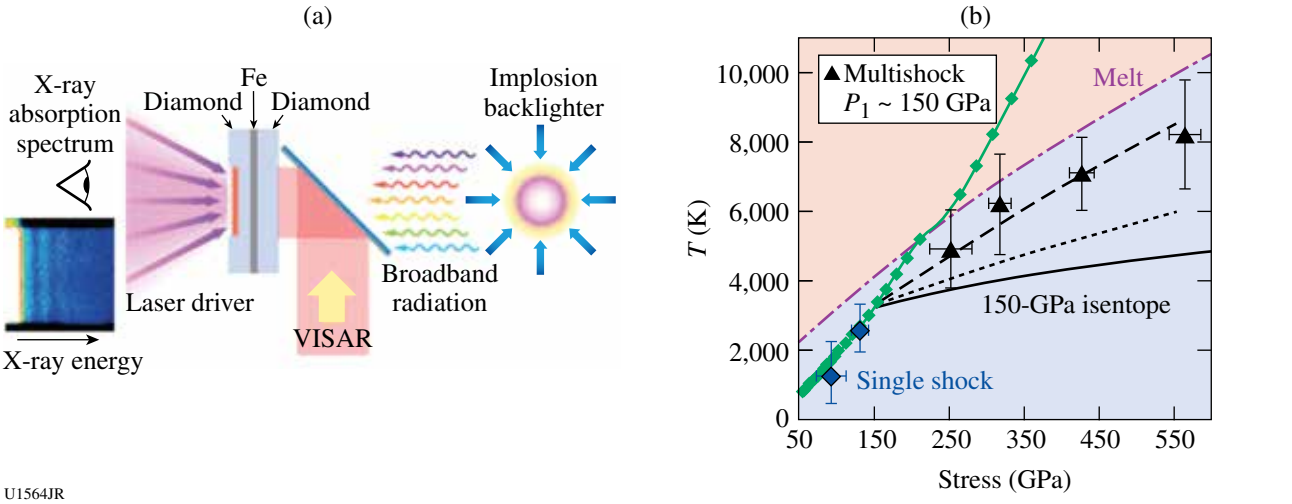

Figure 132.128
(a) Experimental schematic. The raw image of a typical x-ray absorption spectrum is displayed at the lower left corner, showing the intensity modulations above the K edge. (b) Temperature inferred from EXAFS data as a function of stress for the shock + ramp data with an initial shock of 150 GPa. The single-shock data are also shown (blue diamonds). The melting curve (dashed–dotted lines) and the Hugoniot (green solid lines with squares) are plotted for comparison. Also shown are isentropes (solid lines), isentropes with the temperature increase calculated using static strength Y_{sta} (dotted lines), and dynamic strength $Y_{dyn} = 3Y_{sta}$ (dashed lines).

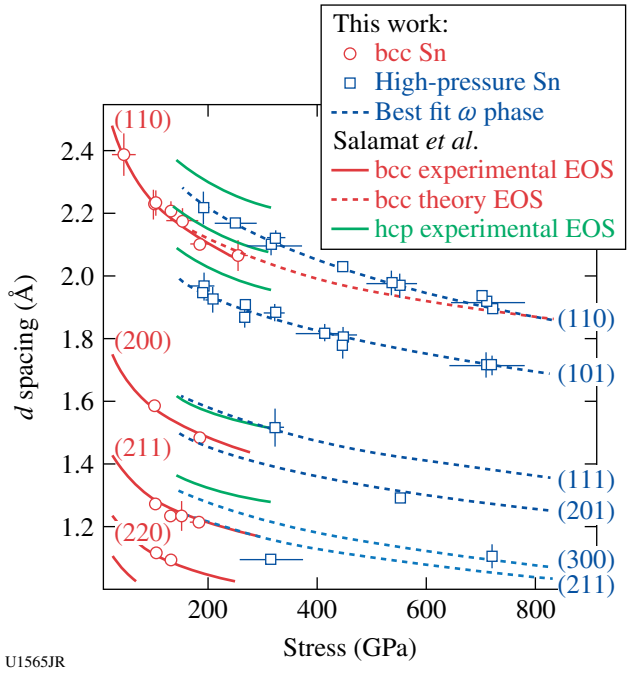

Figure 132.129
The *d* spacing of observed peaks, compared with known isothermal equation of state and phase transition from static experiments.[90,92,93] Our observed high-pressure *d* spacings fit a simple hexagonal (ω) phase. The line weight is proportional to the expected relative peak intensity.

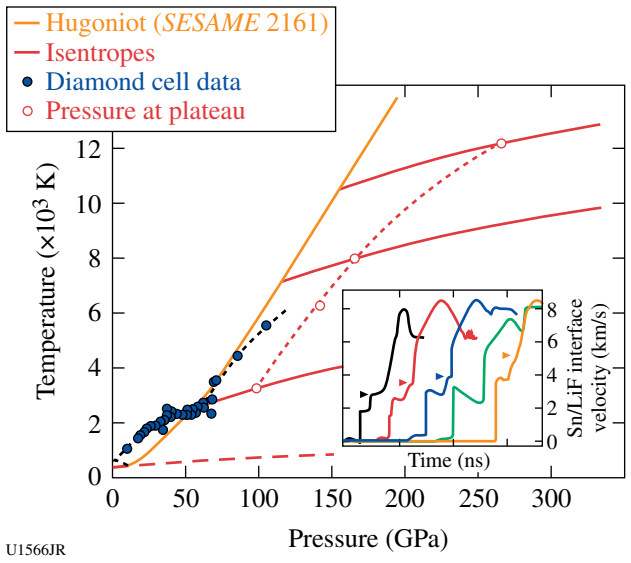

Figure 132.130
Melting curve of tin with new data from this study, determined from the pressure at which a plateau is seen in the ramp-compression wave profile (shown in the inset). Paths in phase space are approximated as shown, with the temperatures associated with the principle Hugoniot and subsequent ramp-compression pathways (modeled as isentropes) determined from the *SESAME* 2161 table.

tallization. Assuming recrystallization, a preliminary analysis shows the melting temperature rising steeply with pressure, in qualitative agreement with recent diamond anvil cell results.[91]

Gigabar Equation of State

Principal Investigator: J. Hawreliak

High-pressure equation-of-state (EOS) experiments using convergent compression of a solid spherical target have a geometric advantage over conventional planar techniques, in which a constant ablation pressure causes the propagating shock to maintain a constant pressure, because in the converging case the shock will increase in strength as it approaches the sphere's center. This approach makes it possible to achieve shock pressures >100 Mbar at the Omega Laser Facility. These experiments use *in-situ* gated radiography to measure the propagating shock speed and density. We will apply the Hugoniot relations to determine the pressure based on the measure shock front speed and density:

$$P = \rho_0 u_s^2 \left(1 - \frac{\rho_0}{\rho}\right)$$

$$\frac{\delta P}{P} = \sqrt{\left(\frac{2\delta u_s}{u_s}\right)^2 + \left[\left(\frac{\rho_0}{\rho - \rho_0}\right)\frac{\delta\rho}{\rho}\right]^2}, \qquad (2)$$

where ρ_0 is the initial density and δu_s, $\delta\rho$, and δP are the associated uncertainties in the shock speed, density, and pressure, respectively. Figure 132.131 is an example of a single frame

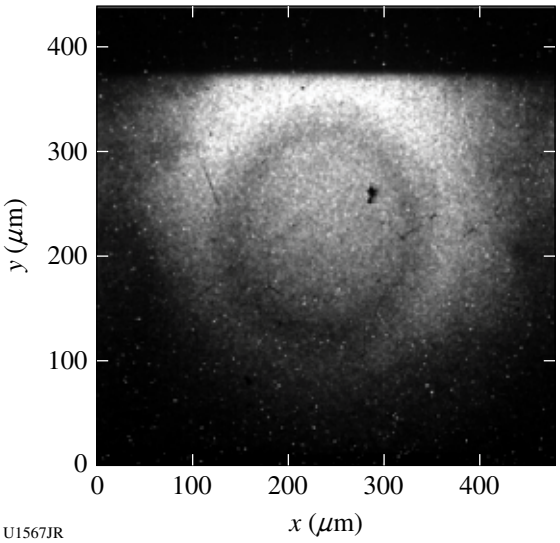

Figure 132.131
Gated 2-D radiograph from a shock propagating through a solid sphere, demonstrating a key capability needed for high-pressure equation-of-state measurements.

from a radiograph image from which the density profile can be inferred.

Equation of State for Foams Using OMEGA EP

Principal Investigator: J. Hawreliak

The equation of state (EOS) of porous materials is of great interest in high-energy-density (HED) science because it allows conventional shock techniques to achieve different thermodynamic end states than the principal Hugoniot. Figure 132.132 is an example of the pressure–density space of shock-compressed quartz for a range of different initial densities. For the low-density foam materials, where the final density is below the ambient density of the base material, the pressure is dominated by the thermal pressure caused by compressing the voids in the material. Many carbon-based foams are opaque, unlike transparent foams where the shock front becomes reflective at high pressures and velocity can be measured directly. The opaque materials require an x-ray technique to view the shock. We are developing an *in-situ* radiograph technique to make Hugoniot EOS measurements of shock-compressed opaque low-density foams. We had success using a chlorinated plastic (PVC) area backlighter for 50-mg/cm^3 carbon resorcinol foam (CRF).

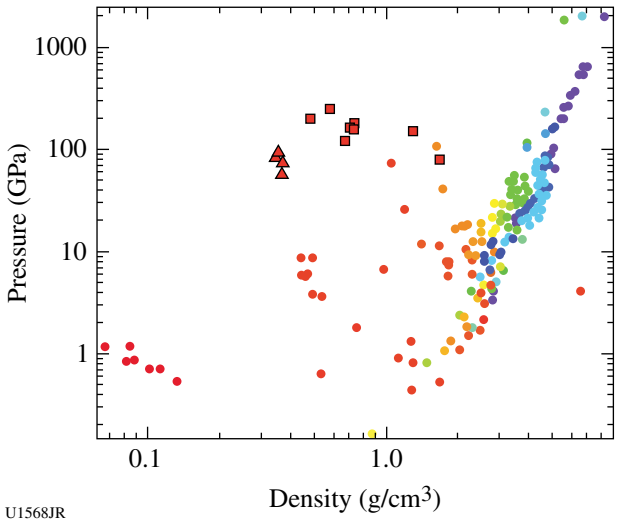

Figure 132.132
Pressure-density space of shock-compressed quartz foams.

Advanced X-Ray Diffraction Techniques

Principal Investigator: J. Hawreliak

Since the discovery of x rays by Rontgen over a century ago, x-ray diagnostic techniques have been used to examine the macroscopic structure of samples through radiography, the atomic structure of materials through x-ray diffraction (XRD), and electronic structure of atoms through x-ray spectroscopy. X-ray diffraction has been one of the most widely used techniques to determine a material's atomic structure. It has recently been applied to dynamic experiments where a shock or ramped pressure wave is applied to a material and then x rays are flashed in a pump–probe experiment to examine the atomic structure as the pressure wave propagates. An effort is currently underway to achieve ultrahigh pressure on laser systems using dynamic compression; in concert with this effort is the development of new advanced XRD techniques that will enable one to structurally probe the material at high pressure. This campaign was the first implementation of a technique that uses a Soller slit-like array of grids to provide limited line of sight of the detector. Figure 132.133 shows the effective geometric shielding the Soller slits provide and a sample image of the x-ray source, which is limited to a small portion of the image plate. This is part of an ongoing development project.

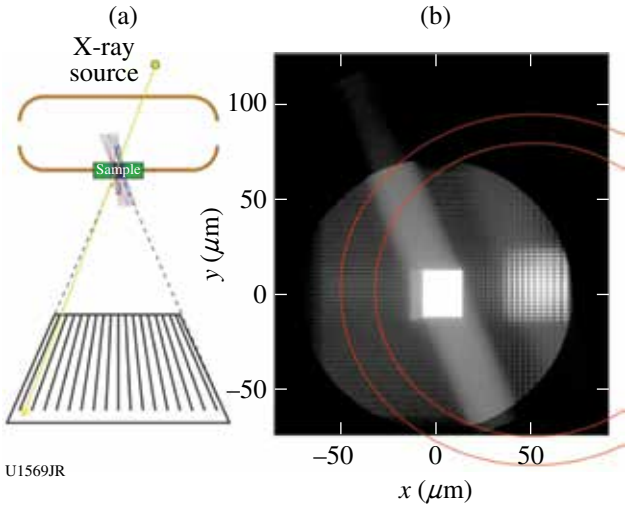

Figure 132.133
Initial data from the new Soller slit diffraction diagnostic.

2. Radiation Transport

Heated Wall

Principal Investigator: K. Baker

The heated-wall campaign measured radiation transport in a geometry that enabled the heat wave to propagate as if there were no wall loss. This was accomplished by placing a thin CRF annulus around a low-density, 30-mg/cm^3, SiO_2 cylindrical foam. One end of the SiO_2 foam and the outer surface of the CRF annulus were heated by the radiation environment inside a hohlraum driven by 15 OMEGA beams. The thickness of the CRF annulus was chosen such that the time-dependent position

as a function of Z of the supersonic heat wave propagating down the SiO_2 cylindrical foam would match the time and Z position of the subsonic heat wave traveling radially inward through the CRF annulus and reaching the SiO_2 foam from the side. In this manner the front of the supersonic heat wave traveling along the z axis of the SiO_2 foam did not see a significant radial disparity in radiation temperature and consequently propagated as if it were being driven in a 1-D geometry.

The heated-wall campaign used the SXI/SSC-A (an imaging x-ray streak camera) diagnostic to measure the uniformity and breakout time of the supersonic heat wave from the rear of the SiO_2 foam. The diagnostic measured breakout times consistent with simulations, including a delayed breakout of the heat wave as the density increased in the SiO_2 foam. Two control experiments were performed: one with a gold disk covering the front of the SiO_2 foam to block radiation from entering the SiO_2 foam along the z axis; and a second in which the CRF tube was replaced with gold to prevent radiation from entering the SiO_2 foam from the radial direction. The shot with a cylindrical block showed no evidence of a heat wave reaching the end of the SiO_2 foam; the shots with a gold annulus to block radial transport of the hohlraum x rays into the SiO_2 foam showed a delayed signal that was significantly weaker and significantly shorter temporal emission as compared to the two heated-wall shots.

Crystal Window

Principal Investigator: B. Maddox

The CrystalWindow-12A campaign was designed to test fused silica as a VISAR window up to pressures exceeding 50 Mbar (5 TPa). Quartz had been shown to be an excellent high-pressure VISAR window at ultrahigh pressure. Although quartz blanks at low shock pressures, the shock wave in the quartz becomes reflective at higher shock pressures and can be used to measure the shock velocity transmitting into the quartz crystal. Fused silica is a noncrystalline form of silicon dioxide (SiO_2), the crystalline form being quartz. Due to the amorphous nature of fused silica, it can be polished readily making it an ideal window material for state-of-the-art experiments on the NIF that require nonplanar VISAR witness windows. The CrystalWindow-12A campaign used the 15 H7 Cones 2 and 3 beams to drive a scale-one halfraum to 190 eV. To collect the VISAR signal, the aluminum-coated VISAR samples were attached to the open end of the halfraum and mounted on a 2.65-mm-diam gold washer with a 0.4-mm central aperture. A 2-mm-diam, 2-mm-long gold tube was also mounted on the VISAR side of the target to shield the VISAR optics from any scattered light from the drive laser. Figure 132.134(a) depicts a photo of the completed target. Two thicknesses of aluminum were tested (50 μm and 70 μm) to study any blanking caused by preheating in the 50-μm-thick Al samples. Additionally, two samples were fitted with reference quartz windows for comparison. Figure 132.134(b) shows VISAR traces for 70-μm Al/quartz and 70-μm Al/fused-silica window targets. The decaying velocity seen here represents the ultrahigh-pressure shock wave traveling through the quartz and fused silica. The data obtained in this campaign confirmed that fused silica works well as a VISAR window at a peak shock pressure of

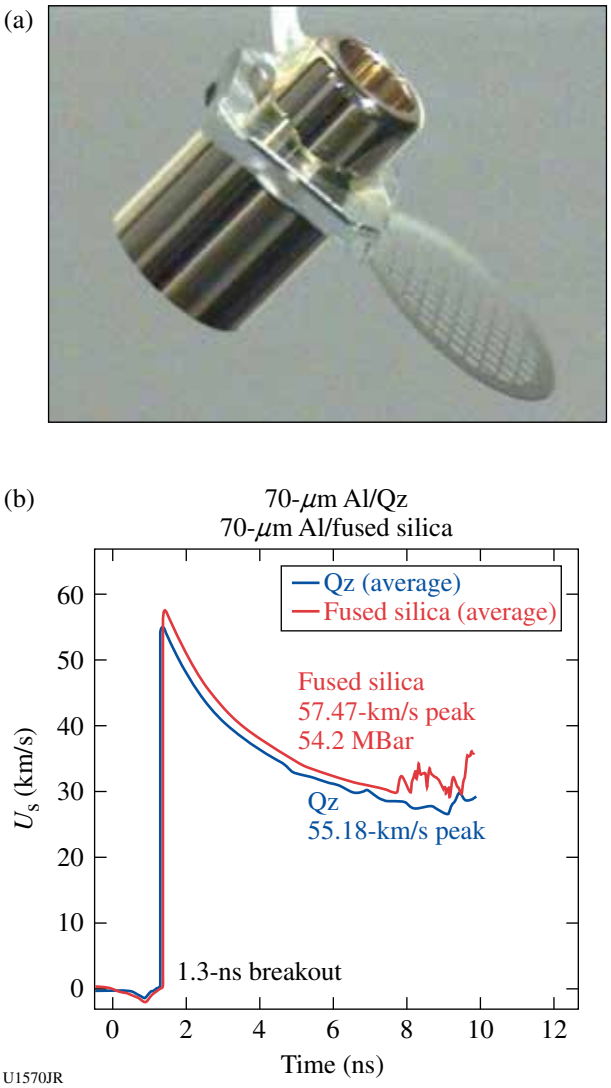

Figure 132.134
(a) CrystalWindow-12A target used to verify fused silica as a VISAR window and shock witness material to >50 Mbar. (b) VISAR data confirming that fused silica works well as a VISAR window at a peak pressure of 54.2 Mbar. The velocity versus time trace represents the shock wave traveling through the fused-silica and quartz (Q_2) windows.

54.2 Mbar with little to no blanking using a 70-μm Al ablator. Some blanking was seen in the 50-μm aluminum ablator targets, likely related to x-ray preheat.

3. High-Temperature Plasma Opacity

High-Temperature Plasma Opacity Experiments on OMEGA and OMEGA EP

Principal Investigator: R. F. Heeter
Co-investigators: A. Graf, G. V. Brown, C. Mauche, and R. E. Marrs

LLNL's high-energy-density (HED) opacity research on OMEGA in FY12 had three main directions: First, the MBOP-12 campaign followed up on physics questions from the very successful 2009–2011 Ti opacity shots, where the observed Ti continuum opacity and one to three line opacity regions did not match code expectations. New data obtained with a modified hohlraum design indicated that up to that 50% higher sample temperature was achieved.

The second campaign, NLTE-Dynamics-12, continued previous work on the non-LTE x-ray emission properties of hot high-Z plasmas as found in hohlraums at the laser-driven "hot spots." Uranium was chosen as the sample material because of its use on ignition and other shots on the NIF and also the paucity of experimental data. Shots performed in FY12 extended earlier work on uranium emission to 2× lower intensity (material temperature) and the data are now being compared with simulations.

The third research direction was the EPOp-12 series, which substantially upgraded the novel short-pulse "absorption-emission" opacity platform developed on OMEGA EP in FY10–FY11. The new platform uses a sample driven with up to 200 J via 100-ps FWHM Gaussian UV laser pulses using two of the "long-pulse" beams on OMEGA EP. The two short-pulse beams deliver up to 1500 J in 10 ps to a pair of continuum x-ray backlighters that probe the plasma after some delay. Figure 132.135 shows the first face-on transmission spectrum obtained from this new platform using a silicon sample and a probe beam delayed about 300 ps. Multiple L-shell charge states are observed in absorption. Self-emission from helium- and hydrogen-like silicon (produced prior to the backlighter probe but recorded on the time-integrated detector) is also observed. The presence of the Be-like and Li-like ions implies that this new platform achieves temperatures similar to those observed with the single-backlighter platform and titanium samples in FY11.

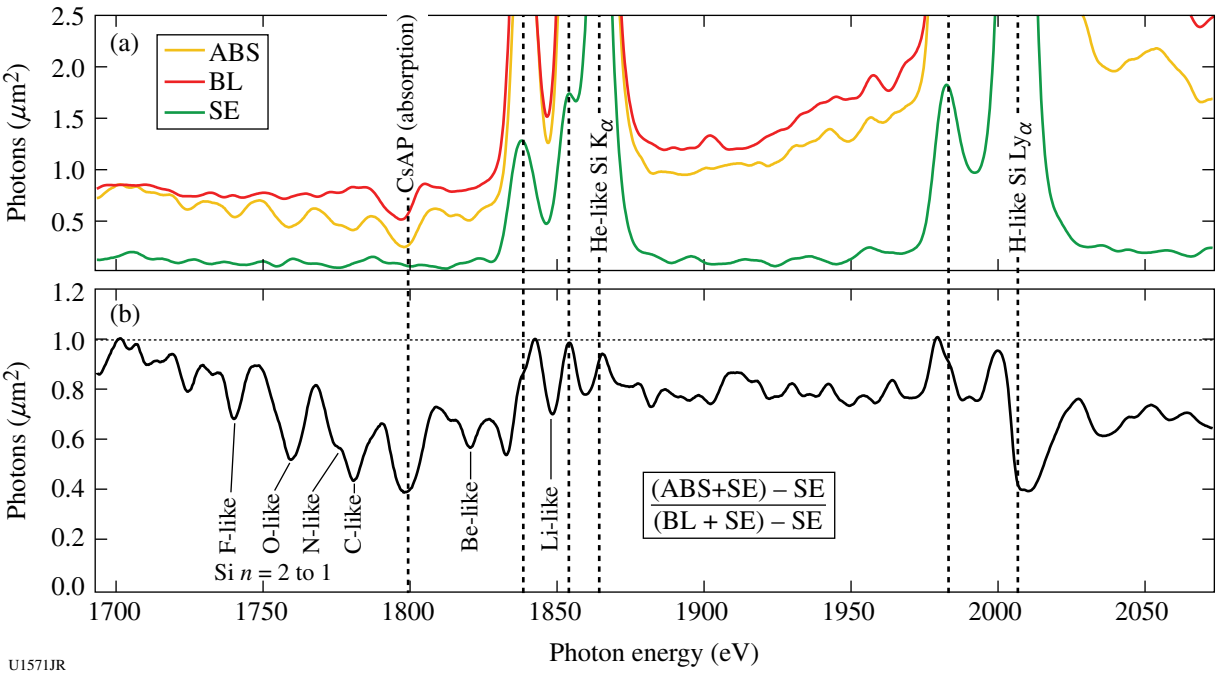

Figure 132.135
Initial silicon opacity spectra from OMEGA EP. (a) Backlighter, sample absorption, and sample self-emission spectra recorded on Biomax film; (b) sample transmission.

4. Burn Physics

Non-LTE Transport and Nuclear Lifetimes
Principal Investigator: A. Kritcher

Plasma coupling to nuclei in high-energy-density plasmas, or *nuclear–plasma* physics, is a cutting-edge field that traverses the areas of nuclear physics, plasma physics, and atomic physics. Nuclear–plasma interactions occur in hot dense plasmas such as inertial confinement fusion (ICF) environments and astrophysical bodies. The effect of high-energy-density–plasma (HEDP) environments on astrophysical nucleosynthesis—the formation of heavy elements from pre-existing nucleons in astrophysical plasmas—is expected to play a significant role.[48] Nuclei in stellar plasmas reach a thermal population of low-lying excited nuclear states from photoexcitation, free electrons in the plasma (NEEC),[49–52] excitation from atomic transitions (NEET),[53–55] and inelastic electron scattering in the dense plasma. In these experiments at the Omega Laser Facility we investigate the NEEC process in underdense plasmas by illuminating mini hot hohlraums (400 or 600 μm in diameter) with ~15 kJ of laser light.

The goal of these first experiments was to identify the plasma conditions of hot Tm hohlraums with spectral line emission analysis and optical Thomson scattering, measure the energy and time-resolved atomic emission background, investigate this experimental platform to study nuclear lifetime shortening in hot plasmas, and determine the possibility of investigating nuclear–plasma interactions on OMEGA. In these first experiments we have collected high-quality data and are in the process of analyzing the results. Future campaigns will continue to measure plasma conditions of hot hohlraums and investigate nuclear–plasma interactions in HEDP plasma environments. We will also field additional isotopes in this configuration.

5. Hydrodynamics

Short-Pulse, UV Backlighting Development for the NIF
Principal Investigator: V. A. Smalyuk

High-energy-density complex hydrodynamics experiments on the NIF require short-pulse backlighting capability. Experiments on OMEGA EP tested the short-pulse, UV beam backlighting concept for the NIF. Four OMEGA EP beams were focused onto 10-μm-thick Ag wires, mounted on 300 × 300-μm-sq, 10-μm-thick polyimide foils to mimic the illumination conditions of one quad on the NIF. The total laser energy was ~400 J with an ~100-ps Gaussian pulse shape, a peak laser intensity of ~3×10^{16} W/cm^2, and a mispointing of <50-μm rms. Three beams were co-timed while the fourth beam was advanced up to 300 ps from the co-timed beams to maximize the x-ray backlighter signal. Results were compared with ~1.2-kJ short-pulse (~100-ps) IR beam backlighting with the same Ag-wire targets, driven at an intensity of ~1×10^{17} W/cm^2. Figure 132.136 shows a measured image of the target, created with Ag-wire backlighting on an image plate using a high-energy radiography imager for EP (HERIE) diagnostic located 50 cm from target chamber center on OMEGA EP. The configuration consists of a Au grid to determine magnification, a 100-μm-thick Au plate to determine resolution, and seven Cu steps with 18-μm thickness between adjacent steps to determine contrast and sensitivity. Areas inside and outside the Au plate were also used to measure noise. Figure 132.137 shows the change in the intensity across the Cu step wedge. The 300-ps advance produced the brightest signal, while a 150-ps advance produced nominally the same results as all four beams co-timed. The ~20-μm spatial resolution was similar to IR-beam experiments, while the signal was ~100× lower. The short-pulse UV backlighting might be feasible for complex hydrodynamics experiments on the NIF if hohlraum and backlighter x-ray backgrounds do not exceed ~10 PSL (photostimulated luminescence) on the image plate at 50 cm from the NIF target chamber center.

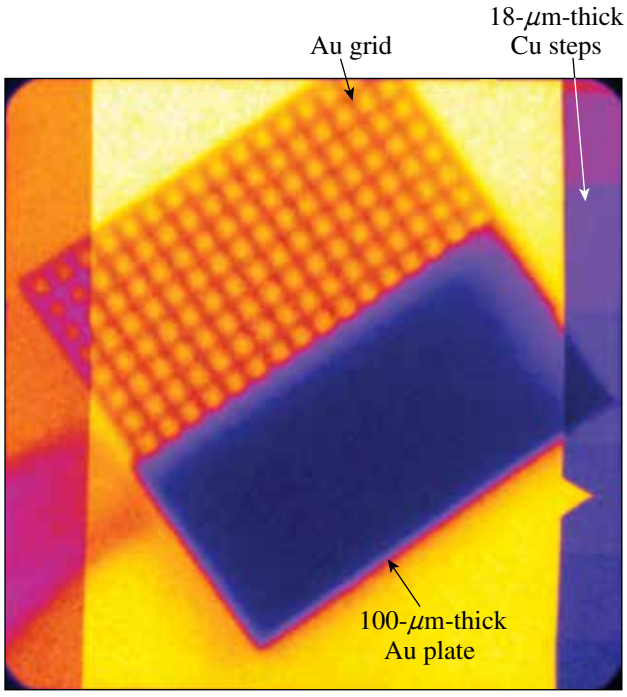

Figure 132.136
X-ray radiograph of the target consisting of an Au grid, a 100-μm-thick Au plate, and seven 17-μm-thick Cu steps.

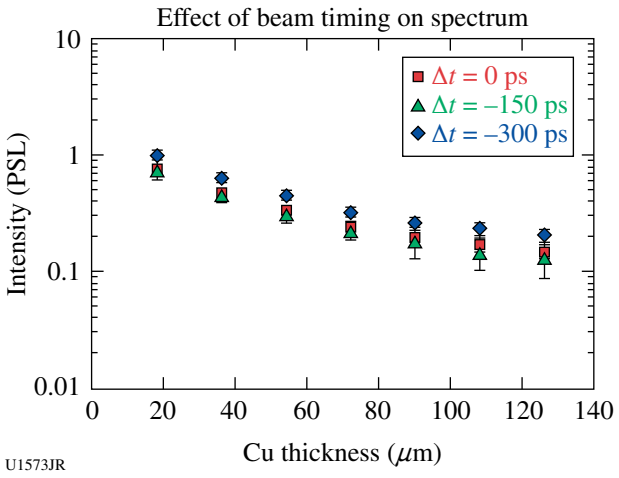

Figure 132.137
Intensity across the step wedge shows relative differences in backlighter emission. A 300-ps advance in beam timing shows a small increase in signal. Uncertainties illustrate shot-to-shot variation.

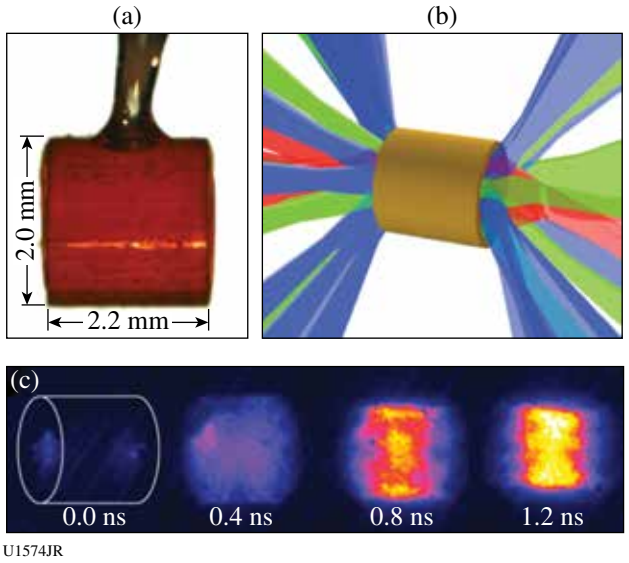

Figure 132.138
(a) Photograph of a cylindrical aerogel target held inside a thin plastic tube. (b) Irradiation structure from 40 OMEGA beams. (c) Example of x-ray emission images at different times relative to the beginning of the interaction.

6. X-Ray Source Development and Application

X-Ray Source Development with Nanostructured Materials

Principal Investigator: R. Patterson

Progress in the fabrication of new metallic aerogels for x-ray generation[94] led to a campaign for optimizing titanium x-ray sources, as illustrated in Fig. 132.138. Experiments were conducted in FY12 by the X-Ray Source Development team in collaboration with the Defense Threat Reduction Agency and researchers from Commissariat à l'Énergie Atomique (CEA). In the FY12 shots, when irradiated by 40 OMEGA beams, Ti-doped aerogels (4 mg/cm^3, 4 at. % of Ti) made by a wet-chemistry process yielded only a 0.7% laser-to-x-ray conversion efficiency (CE) in the x-ray band between 4.6 and 5 keV, which is significantly lower than the previous record of 3% CE (Ref. 95). However, in this campaign novel aerogels were measured to provide a 5.5% CE in the same energy range. These new targets were made by coating SiO_2 aerogel templates with TiO_2. They are of similar ultralow density (4 mg/cm^3) but reach a higher Ti concentration (22 at. %).

Current analysis is focused on precise understanding of the x-ray spectra, which will bring interesting new insights to our understanding of the heating of these targets. Analysis will also cover the heating dynamics[96,97] and yield optimization of these targets using hydrodynamic simulations. The objective is to design future targets by optimizing the Ti concentration and aerogel pore size, which are now controllable.

Solar Cell Electrostatic Discharge

Principal Investigator: R. Patterson

During FY12, the X-Ray Source Development team, in collaboration with the Naval Research Laboratory and the Defense Threat Reduction Agency, conducted a series of experiments to examine the effects of x-ray loading on solar cells. Our tests were broken into two parts: We first evaluated the ability of the Omega facility to produce a laboratory environment suitable for conducting electrostatic discharge experiments on solar cells; then we subsequently conducted the first tests of active solar cell arrays. For each of these experiments, Fe- or Ge-based targets positioned at the center of the target chamber were irradiated with ~20 kJ in a 1-ns square pulse. The XRSA Langmuir Probe Diagnostic (XLPD) or a modification including active solar cells was positioned a few tens of cm from the target.

Building on initial tests in the previous year, we deployed XLPD configured as an array of eight cylindrical Langmuir probes [Fig. 132.139(a)] on 29 February 2012 to observe the arrival of the source plasma. Time-of-flight measurements resulted in an observed velocity of ~16±2 cm/μs for the leading edge of the source plasma.[98] Based on these measurements, we concluded that the OMEGA target chamber is suitable for conducting electrostatic discharge experiments on solar cells, provided that the cells are positioned sufficiently far from the target.

On 12 September 2012 we did indeed place an array of two solar cells along with four standard XLPD probes [Fig. 132.139(b)] a minimum of 40 cm from target chamber center to examine the response of these cells to the x-ray and plasma environment produced from Ge-aerogel targets. Figure 132.140 shows the prompt x-ray response of the probes as well as the solar cells. In addition, the Langmuir probes show signals consistent with sheath formation in the first 200 ns, followed by the arrival of charged particles from the target. While our analysis of the solar cell data is ongoing, the data are consistent with an electrostatic discharge, perhaps caused by current flowing to ground through the dense plasma formed from the ablation of the XLPD cassette itself. In future experiments, we will insulate the solar cells from the chassis in order to test the potential arc formation between cells.

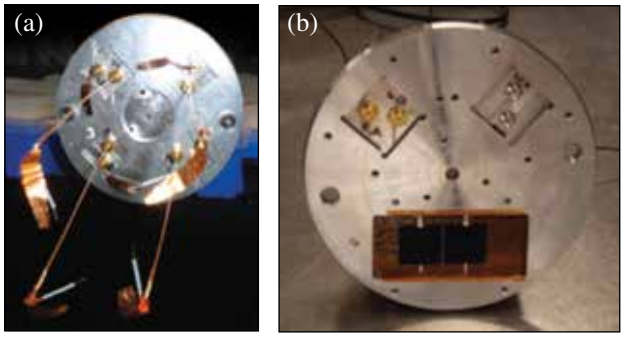

U1575JR

Figure 132.139
(a) An XLPD cassette with four pairs of Langmuir probes. Each pair is composed of one 2.5-cm and one 20-cm probe. (b) Modification of XLPD to include an active solar cell array. Two 2 × 2-cm Ge triple-junction solar cells are biased up to 100 V and can be fielded with up to two pairs of standard XLPD Langmuir probes.

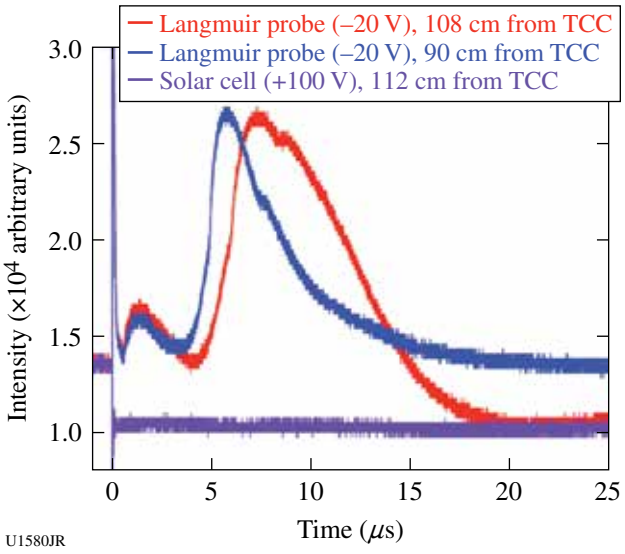

U1580JR

Figure 132.140
Initial results from the solar cell discharge experiments. Signals from two ion-collecting probes are shown in addition to the signal recorded from a solar cell biased at 100 V.

ACKNOWLEDGMENT

This work was performed under the auspices of the U.S. Department of Energy by Lawrence Livermore National Laboratory under Contract DE-AC52-07NA27344.

FY12 LANL Experimental Campaigns—Overview

In FY12, Los Alamos National Laboratory (LANL) executed 244 total shots on OMEGA. LANL experiments contributed to the National Ignition campaign (NIC) in the following ways:

- Measured the x-ray ablative Richtmyer–Meshkov growth of isolated defects on plastic ablators
- Studied branching ratios in DT fusion plasmas
- Continued neutron imaging and radchem scintillator development for the NIF

High-energy-density (HED) campaigns included

- Study of shear in a counter-propagating flow geometry and reshock-driven turbulent mixing
- Backlit defect implosion experiments to study the effect of trench defect and polar drive
- Measurement of the effect of capsule asymmetries on neutron yield and ion temperature
- Imaging x-ray Thomson-scattering platform development for dense plasmas and warm dense matter equation of state (EOS)
- Measurement of a supersonic radiation wave and foam aerogel EOS

CHaRM

The CH ablative Richtmyer–Meshkov (CHaRM) campaign had two shot days in FY12. The goal of these experiments was to measure the oscillation frequency of small perturbations on CH ablators driven by the x-ray–ablation Richtmyer–Meshkov effect. With this knowledge we would have a better understanding of how isolated defects behave during the first shock transit stage of a NIF ignition attempt, which could then provide methods for minimizing perturbations at the onset of Rayleigh–Taylor.

Our experiments used 15 beams inside large Au half-hohlraums, which were staggered in time to produce a 7.5-ns radiation drive with a radiation temperature of 70 eV (see Fig. 132.141). Targets with 2-D arrays of 5-μm-tall, 17-μm FWHM Gaussian bumps were attached over the opposite laser entrance hole with the defects facing inside the halfraum. During the experiment the bump arrays were backlit with Y and Ta backlighters (~2.2-keV emission) and imaged at 37× magnification into an x-ray framing camera.

Radiation–hydrodynamics simulations running with EOS tables for CH predict that these small bumps decay for our experimental conditions as shown in Fig. 132.142 (green curve). The trend in our data supports this prediction even though the data lie somewhat above the simulation curve, which we think is due to either systematic errors in the data analysis or errors in the models. Nevertheless, this decay in amplitude occurs at a rate that is much slower than under direct-drive conditions measured at Naval Research Laboratory (NRL). This has to do with the differences in absorption, transport, and ablation mechanisms between x-ray and laser drives. Under our conditions only very narrow bumps (<20 μm) exhibited this decay while wider bumps (>30 μm, FY11 data) only saturated.

Shear

In FY12 the Shear campaign focused on developing a counter-propagating flow platform for studying shear-driven turbulent mixing. These experiments use Be tubes containing

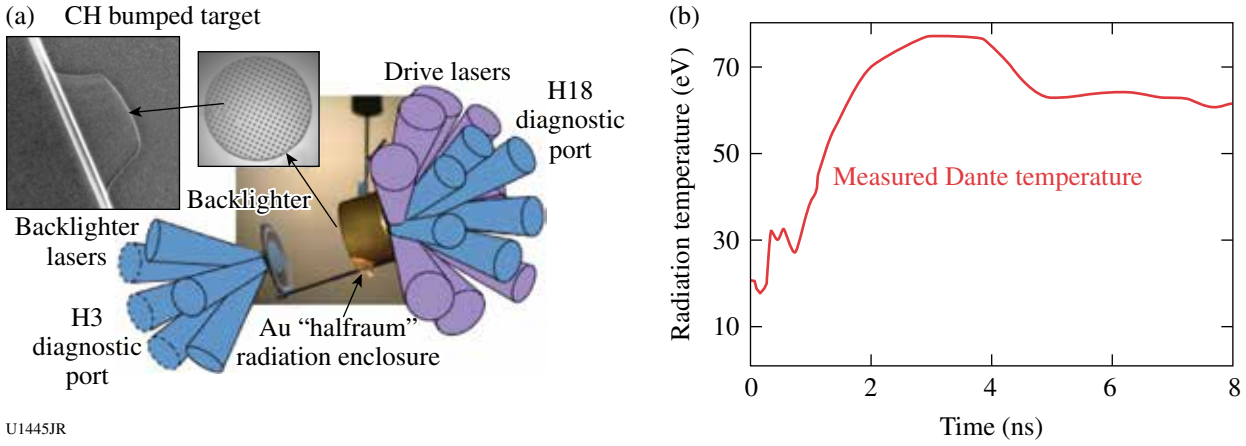

Figure 132.141
(a) Schematic of the CHaRM platform where a Au halfraum is heated to 70 eV, driving an ablation front into an array of isolated Gaussian bump defects. (b) Bumps are radiographed along the axis of the halfraum.

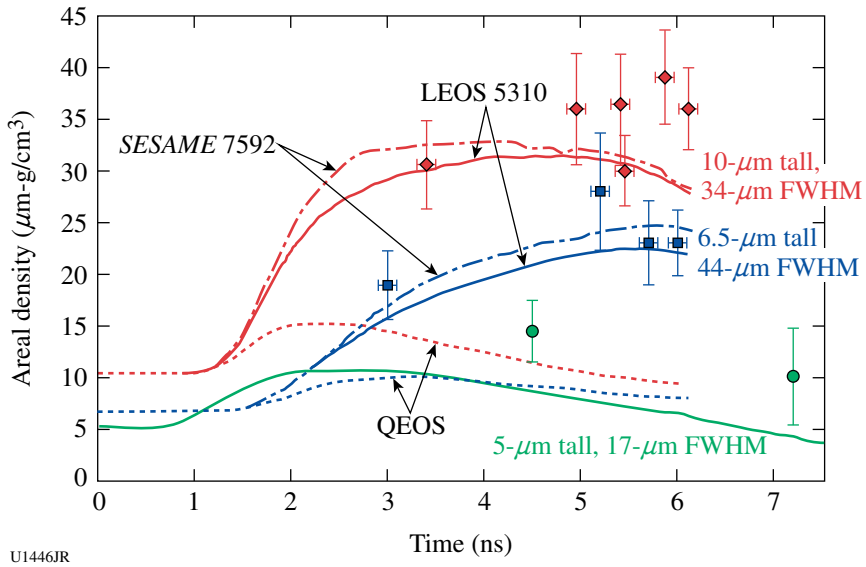

Figure 132.142
Summary of long drive duration data showing the saturation of bumps with >30-μm width and ablative RM decay for those with widths <20 μm.

low-density CH foam semi-cylinders separated by Al tracer layers. The counter-propagating flow is created by inserting Au "plugs" in front of each foam semi-cylinder at opposite ends to hold back the shock in each foam at one end (see Fig. 132.143). With the plugs in place, the Be tube ends are irradiated with 10^{15}-W/cm^2 laser intensity to initiate the counter-propagating flow. When the shocks cross, they establish a shear layer in the Al, which then grows due to turbulent mixing.

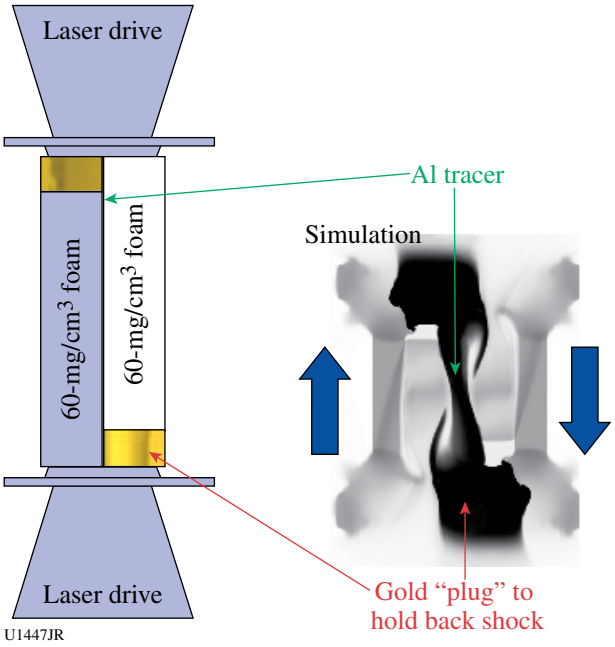

Figure 132.143
Geometry for a counter-flowing shear platform. Simulations with the Besnard–Harlow–Rauenzahn (BHR) mix model are also shown.

Over the course of the year, we improved the target design by extending the length of the Al tracer so that shocks from one end could not penetrate into the adjacent foam. This created a longer-duration, cleaner shear flow for studying the turbulence. We used x-ray radiography along two orthogonal lines of sight (edge-on and plan view of the tracer layer) to image the evolving turbulent structure at >20× magnification. In the edge-on view (see Fig. 132.144) the growing mix layer was imaged at times from 6 to 16 ns and in relatively good agreement with the LANL Besnard–Harlow–Rauenzahn (BHR) turbulent mix model. The same data times were used (on the same shot) for the plan view radiography, which appears to show a transition to turbulence around the 10-ns point where 3-D structures begin to form out of the initially homogeneous flow.

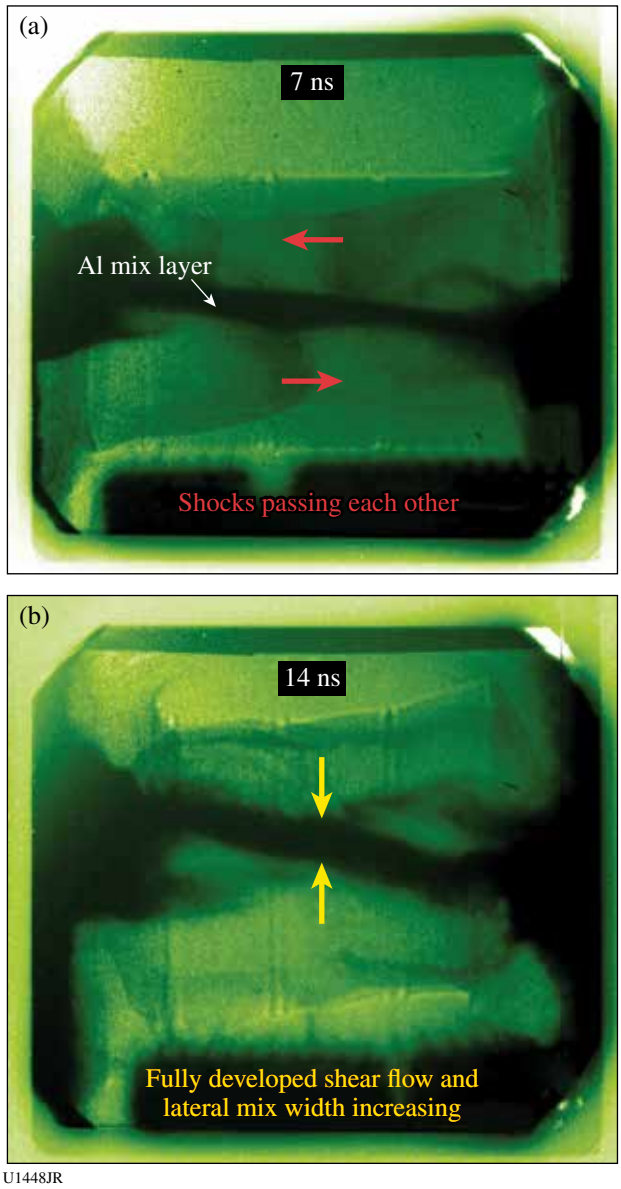

Figure 132.144
Radiographs at two different times showing development of counter-flowing shear and mixing.

ABEX

In laser-driven implosions, of importance to inertial confinement fusion and stockpile stewardship, the cold shell is known to mix into imploding nuclear fuel. Yet there are no direct observations of just where, and at what rate, shell material migrates into the fuel. In June 2012 experiments at the Omega Laser Facility, LANL's ABEX (asymmetric burn experiment) campaign, in collaboration with Prof. Roberto Mancini's University of Nevada, Reno group, has made advances toward providing time-resolved images of shell mix into fuel. Emission from titanium dopant in the shell is used to make quasi-

monochromatic images. Temperature, and ultimately a crude estimate of chord-integrated titanium, has been extracted (see Fig. 132.145). Three such separate views, each at multiple times, were obtained during each shot.

A capsule with pre-imposed perturbations (Fig. 132.146) showed images similar to those obtained with perfect spheres—but to just what depth the Ti has penetrated remains ambiguous. The team is now focused on advanced analysis and refinement of the target design to address the longstanding absence of mix images in laser-driven implosions.

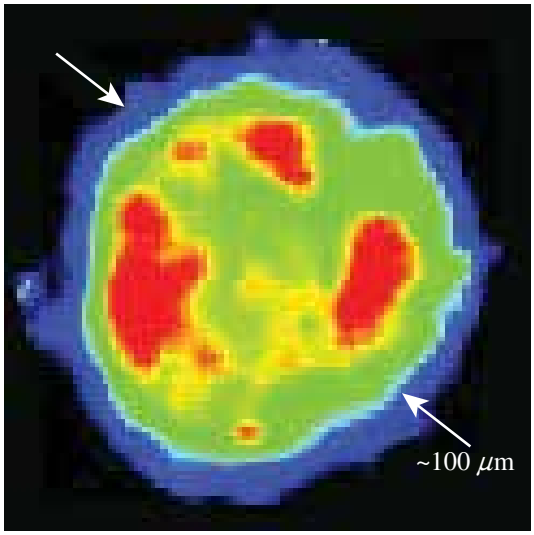

U1449JR

Figure 132.145
Ti originally in the shell has mixed into the fuel (typical false-color map is used, i.e., red corresponds to an increased signal).

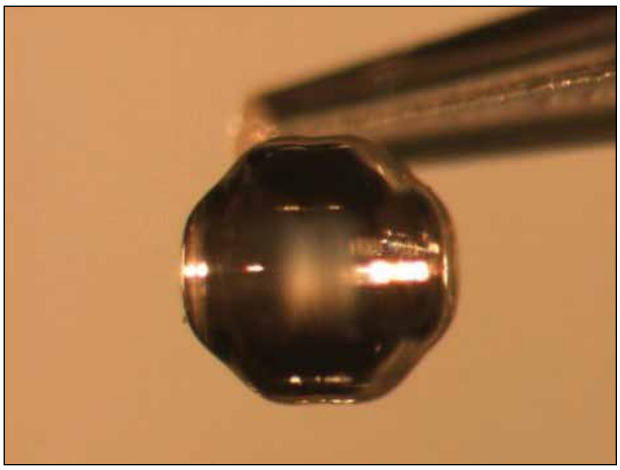

U1450JR

Figure 132.146
Photograph of a machined PAMS mandrel with ±10-mm-amplitude perturbation. The axis of symmetry is horizontal in this photograph.

RadChem

On 6 August 2012, the LANL Prompt Radchem Development team successfully tested new assay system designs on the OMEGA laser. Prompt radiochemical signatures generated in high-energy-density experiments provide insight into a variety of physical phenomena including late-time hydrodynamic performance of the implosion as well as particle stopping within the plasma. These signatures are created through charged- and neutral-particle nuclear interactions within the imploded capsule materials. Often the resulting radioactive products undergo beta decay with end-point kinetic energies approaching 14 MeV and half-lives as short as 20 ms. The short half-lives necessitate deploying an assay system within the target chamber that will withstand the harsh, prompt radiation environment but will readily assay the high end-point energy beta decays that immediately follow. Furthermore, the detector must have minimal sensitivity to the flux generated by background sources.

During the August campaign, the LANL-based team fielded a new four-element scintillator telescope to measure beta decay from various elements with different end-point energies ranging from 3 MeV up to 14 MeV and half-lives from 20 ms to several minutes. Figure 132.147 illustrates the strategy employed by the detector. The red curves represent the electron spectrum expected from decays of ^{16}N and ^{9,10}B. The colored vertical lines approximately represent the threshold sensitivity of the individual elements within the telescope detector, e.g., the first element will register hits from electrons above ~1 MeV, the second above ~2 MeV, etc. By requiring a coincidence between the elements of the telescope detector, not only is the background flux outside the solid angle of the detector acceptance reduced, but a threshold cut is placed on the electrons depositing energy within the telescope.

To test these concepts, the detector was fielded in the OMEGA target chamber during a set of high-yield implosions of DT-filled glass and plastic capsules. Activation targets, including a polytetrafluoroethylene (Teflon) puck, were located in front of the telescope yielding the data shown in Fig. 132.148. Figure 132.148(a) shows the coincidence rate of the first two scintillator elements shortly after a shot. A fit to the distribution clearly shows half-life contributions from ^{16}N and ^{19}O decays, as expected from ^{19}F(n,α) ^{16}N, and ^{19}F(n,p)^{19}O reactions. Figure 132.148(b) shows the coincidence rate using the first three elements, thereby requiring a ~5-MeV threshold. This higher threshold eliminates the ^{19}O contribution and significantly

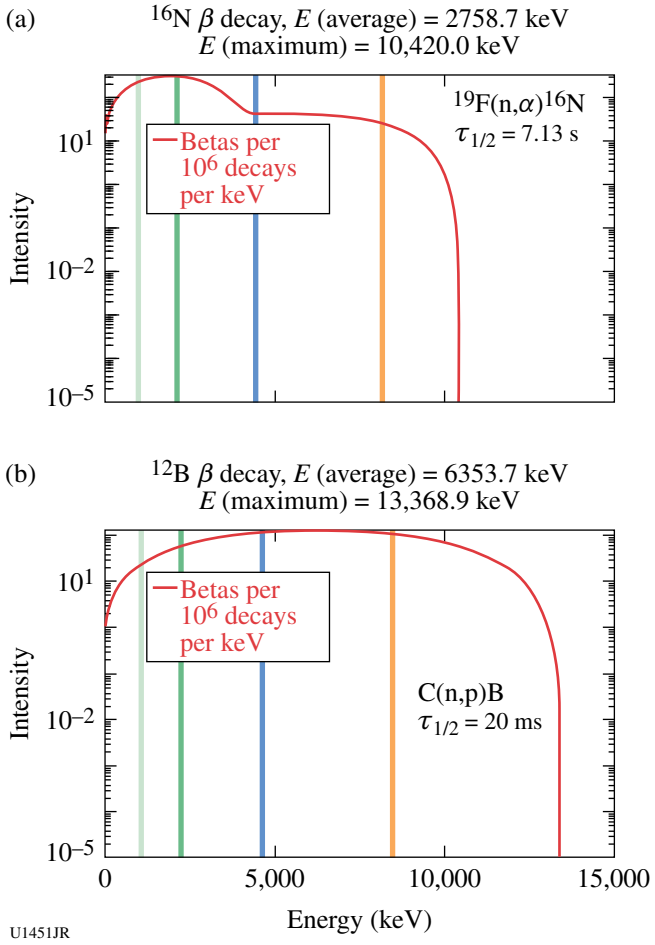

Figure 132.147
Beta-decay spectrum with approximate detector element thresholds. (a) ^{16}N beta spectrum and (b) ^{9,10}B beta spectrum.

reduces the ^{16}N to the lower-intensity, higher-energy decay. The fit shown in Fig. 132.148(b), using an exponential and no background, gives a half-life measurement of $\tau_{1/2}(^{16}\text{N})$ = 7.11±0.14 s, in excellent agreement with the published value of 7.13 s.

In future experiments planned at the Omega Facility, the telescope will be moved closer to the imploding capsule to test the robustness of the detector to prompt radiation, as well as to provide the opportunity for other activation measurements.

DPEOS

The purpose of the DPEOS project is to measure the EOS of material in the warm dense matter regime. To accomplish this, we are developing an experimental platform to do this at the Omega Facility. Our experimental platform uses the OMEGA laser to drive a very strong shock into an aluminum or graphite sample. The shock is then released into a 0.2-g/cm^3 aerogel foam that is used as a pressure standard. A shock-breakout measurement is used to determine the shock velocity and pressure in the foam. We have also developed an imaging x-ray Thomson spectrometer to measure Compton-scattered x rays from the released sample. This information can be used to determine the temperature and density of the released material, providing the necessary measurements to determine the EOS.

Our experimental plan for FY12 was to test and measure the shock and release conditions produced in the aluminum sample, get our new imaging x-ray Thomson spectrometer (IXTS) approved, test its operation, and obtain the first x-ray scattering measurements of WDM aluminum and/or carbon.

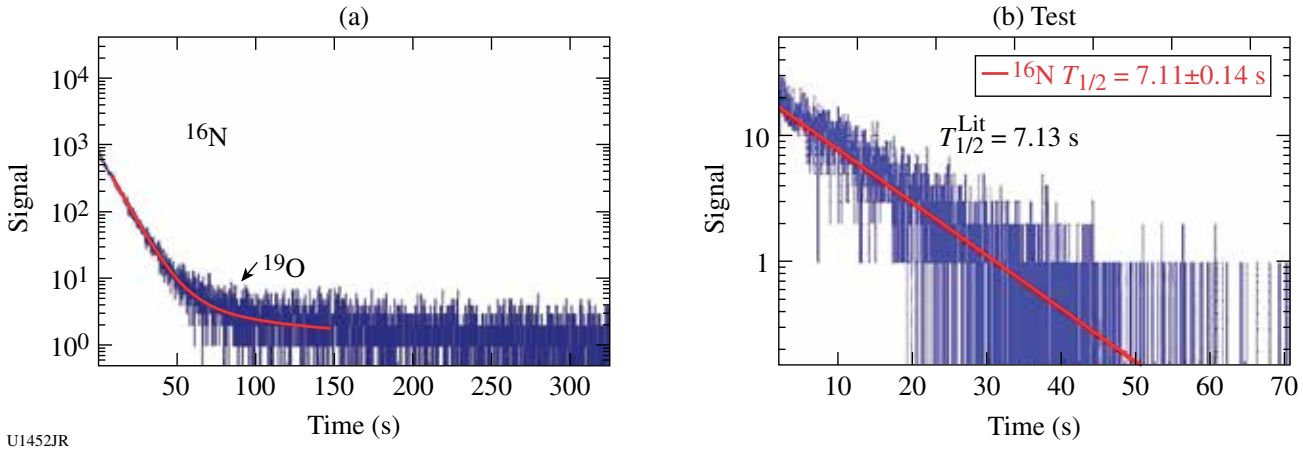

Figure 132.148
Prompt decay data from a high-yield OMEGA implosion. (a) Two-element coincidence rate and (b) three-element coincidence rate.

We were successful in reaching these goals. We completed a total of 24 shots in two days on OMEGA. On the first day, we successfully fielded the IXTS for the first time and obtained scattering data. However, our signals were contaminated by background x-ray signals from our x-ray backlighter. Our shielding and target design were improved for the second shot day in August, and we obtained our first detailed x-ray scattering measurements from warm dense matter carbon. These measurements enabled us to determine the temperature of the shock and released carbon. In addition, we verified the shock conditions for both carbon and aluminum, which were consistent with our previous measurements. An example of the IXTS data we obtained is shown in Fig. 132.149. This figure contains the analyzed x-ray scattering signal along with a series of fits to the data. Two shot days are planned for FY13 in which we will perfect our target design to obtain better signal to noise for this data and in addition will carry out x-ray radiography measurements to pin down the density of the material. This will provide a complete EOS measurement for these warm dense matter conditions and be used to test EOS models in this regime.

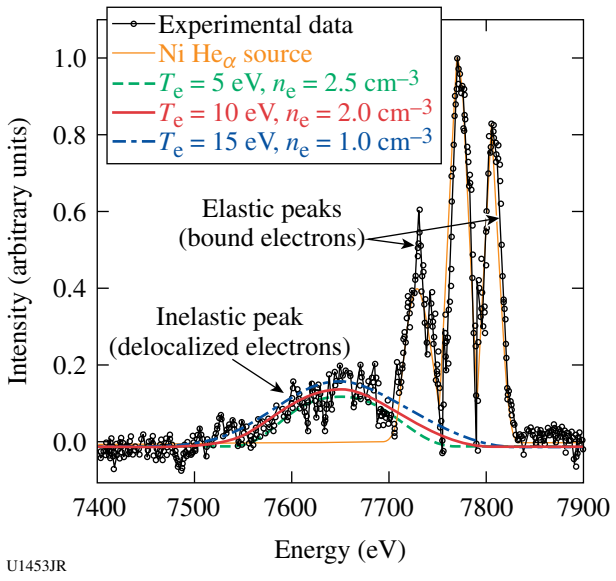

Figure 132.149
X-ray Thomson-scattering measurements from shock and a released warm dense matter graphite target. The elastic peaks correspond to scattering from bound electrons while the inelastic peak is due to scattering from free electrons. The measurements indicate a temperature of ~10 eV and density near 2 g/cm^{-3}.

NIF-5

The purpose of the NIF-5 project is to test both diagnostics and physics ideas that are important for facilitating our understanding of important radiation flow experiments being carried out on the NIF. In the past, this project has focused significantly on diagnostic development and testing and experimental platform development. This fiscal year we changed the focus of the project to address an important physics issue for these experiments, namely the EOS of the foams used in these experiments. Foams sometimes exhibit significantly different material behavior than normal materials, both in their response to shocks and in their relatively high specific heats at moderate energy density.

To address these concerns, we carried out two days of experiments and a total of 28 shots on OMEGA in FY12. These experiments built on the platform development of other shock physics experiments on OMEGA, including target geometries and diagnostics. This immediately enabled us to be relatively successful. Our specific purpose for these experiments was to measure the temperature of shocked aerogel foam in the few-Mbar range. The foam would have an initial density of 0.2 g/cm^{-3}, which has the advantage that the principal Hugoniot for this foam is well known, requiring only a measurement of the shock velocity to determine the state. We were very successful obtaining both good shock-velocity measurements and streaked optical pyrometer (SOP) measurements for a wide range of pressures. A brief analysis of the shock velocity and SOP data is given in Fig. 132.150. We found that the temperature dependence on the shock velocity was weak for a wide range of shock velocities, indicating a very high specific heat and also indicating the

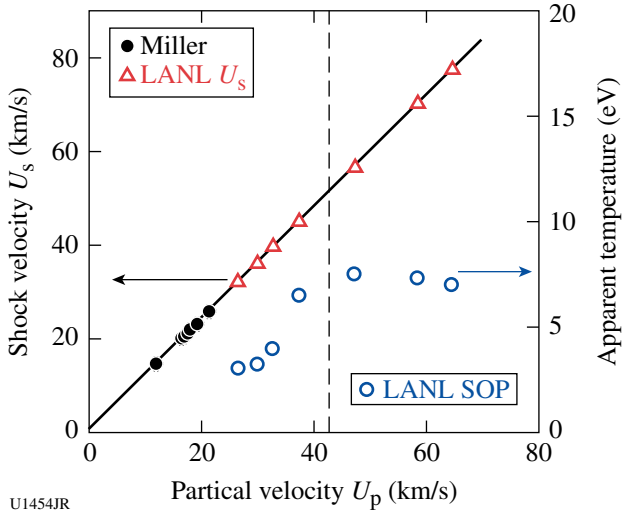

Figure 132.150
Temperature and shock-velocity measurements for 0.2-g/cm^{-3} aerogel foam targets. The straight line fit is based on Hugoniot measurements for this foam and the vertical dashed line corresponds to a pressure of ~4.4 Mbar.

important energy density range where ionization and dissociation occur. We also see a saturation of the SOP temperature at higher shock pressures. We believe either a limitation of the diagnostic or more likely radiative heating at the shock front is confusing the measurement. Since the two shot days were quite close together, few modifications were made to the target design, so this effect could not really be further investigated. We expect to learn more about this effect through a series of double-shock experiments to be carried out in FY13.

DTRat

On 9 August 2012, LANL's ICF Gamma Ray Physics team conducted ongoing DT Ratio Campaign experiments on OMEGA. Y. Kim and H. Herrmann led the collaborative effort including participation from LLNL, AWE, MIT, Colorado School of Mines, Cornell, and LLE. The capsules consisted of D^3He, $^3He^3He$, and DT fills for the primary purpose of characterizing the D^3He γ-ray spectrum. D^3He γ-ray measurements have been used by Kim *et al.*[99] as a cross-calibration for the recently published DT gamma-to-neutron branching ratio (BR) inference under the assumption that ^5He from DT and mirror nucleus ^5Li from D^3He generate virtually identical γ-ray spectra. This shot day was intended to test this assumption.

Figure 132.151 shows preliminary data taken by the gas Cherenkov detector (GCD) during a Cherenkov threshold scan indicating that, as expected, the primary peak from D–^{3}He fusion gammas decreases with an increasing energy threshold. More-quantitative analysis is awaiting the results of CR-39–based proton-yield measurements. One interesting feature, however, is what appears to be a secondary peak (~0.2 ns) that is not reduced as readily by thresholding, implying that it is from photons of higher energy than the 16.6 MeV D–^{3}He fusion gammas. The peak remains when the capsules contain no D (i.e., ^{3}He–^{3}He implosions). Since there is no expectation of a fusion gamma from the unbound and therefore extremely short-lived ^{6}Be, the current speculation is that this peak is the result of extremely high energy laser–plasma instability (LPI) x rays (>20 MeV) coming from the two-plasmon instability. This mechanism is known to be amplified for thin-walled glass capsules in which fusion bang time occurs before the end of the laser pulse. Over the past two years we have observed that this secondary peak becomes more pronounced with capsule thinness. It is now clear that this secondary peak must be accounted for when measuring the D–^{3}He gamma yield and cross-calibrating D–T γ/n BR to D–^{3}He γ/p BR. Doing so will result in making the cross-calibrated BR value more consistent with the previously determined absolute BR value published in Y. H. Kim *et al.*[100] This discovery may also lead to greater insight into LPI mechanisms leading to ultrahot electrons having deleterious effects on ignition.

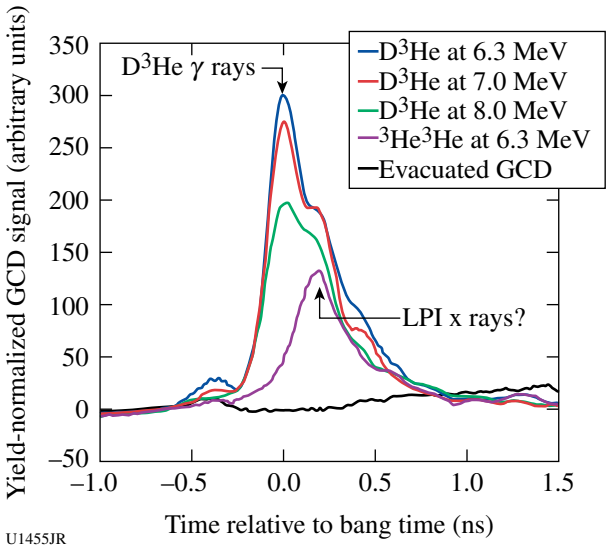

Figure 132.151
Data from the GCD showing fusion gamma decreasing with an increasing energy threshold.

DIME

The DIME campaign had two shot days in 2012 on OMEGA. On the first of the shot day, we used symmetric 60-beam illumination with ~800-μm-spot phase-plate smoothing for 1 ns to drive spherical implosions. The objective was to measure the mix depth of an embedded Ti layer (1% by atom) in the spherical capsule wall. The variable was the separation of the 2-μm impurity layer from the inner wall of the 435-μm-radius capsule for the ten targets. The embedded depth was 0.0, 1.4, 3.0, or 4.8 μm. The 19-μm wall thickness was sufficient to prevent burnthrough by the laser drive. Therefore, we collected data for the 4π mix. A first look at normalized data is shown in Fig. 132.152.

Neutron yield data were provided by V. Yu. Glebov (LLE). B. Yaakobi (LLE) facilitated the spectral analysis of the Ti K_α absorption feature and Ti line emission from the x-ray spectrographic data. One calculates the ρR of Ti from the transmission T of the continuum at 4.5 keV: $\rho R = -\ln T/\sigma$, where σ is the x-ray attenuation coefficient (cm^2/gm) of cold Ti. The line emission of Ti, heated by mix with the hot deuterium fill gas, peaks at zero depth and damps quickly with burial depth, thereby corroborating this picture of mix. The curved lines are to "guide the eye." The anticorrelation between yield and the Ti spectral data, which indicates a mix depth of ~1.5 μm, is consistent with expectations. A similar campaign, identical in

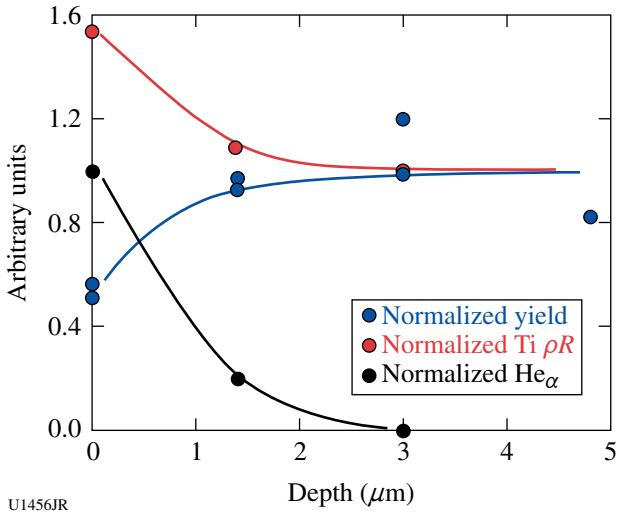

Figure 132.152
Correlation of mix parameters for the 60-beam drive.

every respect for targets, was executed for polar direct drive (PDD) later in the year. The objective for this campaign was to assess how PDD altered the mix depth and the spatial variations inherent with PDD. Steps in the inner CH wall layer were smaller. Data analysis is pending.

Colliding Shock

The LANL Colliding Shock Campaign had nearly 30 shots on OMEGA in November 2011 and March and July 2012. Radiographs of the colliding shocks were obtained on two cameras looking on orthogonal axes and at 2-ns delays with respect to each other. Excellent quality images were obtained, and a series of three are shown in Fig. 132.153 from 6, 12, and 18 ns. The experimental target shown in the top of Fig. 132.153 consists of a Be tube filled with foam and a 20-μm Ti foil tracer on one side. The target is driven from both ends (with a slight delay to the beam opposed to the foil). At 6 ns the foil is just beginning to be driven into the foam; at 12 ns the foil has propagated into the foam and is just meeting the oncoming shock; and at 18 ns it has been recompressed and stalled by the counter-propagating shock passing through it. The Be tube and shocks are visible in the radiographs as faint outlines perturbed by the propagating shock at the walls and in the foam. At 18 ns the tube is almost completely unrecognizable. The information from the turbulent mixing of the Ti layer in the reshocked area is contained in the width of the Ti layer. This width can be compared to our BHR-2 mix model in hydrodynamic simulations to understand how turbulence can affect the mixing of materials at material boundaries.

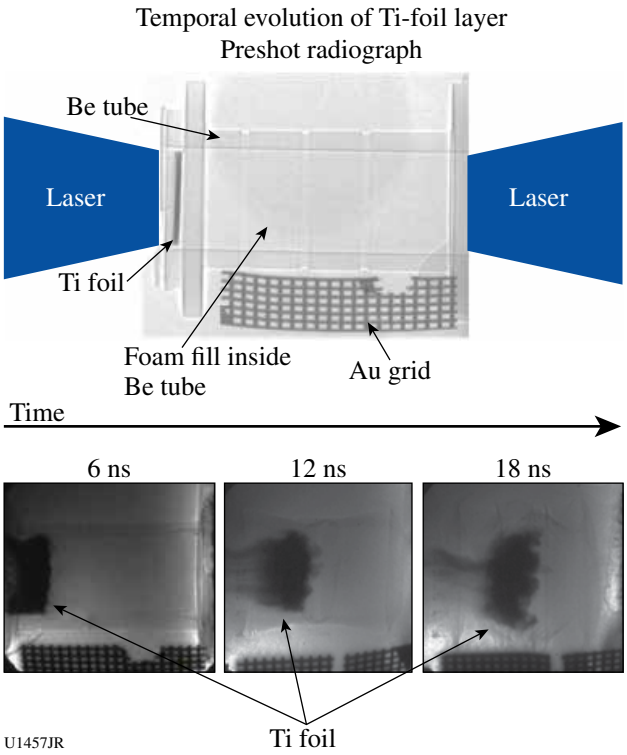

Figure 132.153
The temporal evolution of a 20-μm Ti tracer foil inside a Be shock tube filled with foam. The laser pushes a shock into the tube from both ends, with a resultant recompression and stall of the shocked layer.

FY12 CEA Experiments at the Omega Laser Facility

CEA Vulnerability Diagnostics on OMEGA

Vulnerability is a key point for plasma diagnostic design in megajoule-class lasers: hardened diagnostics must preserve their nominal performances for neutron yields up at least to 10^{17}. Since the DT shots at the Omega Laser Facility reproduce the perturbing source expected during the first 100 ns on megajoule-class laser facilities like Laser Mégajoule (LMJ) or the National Ignition Facility (NIF), this facility can be used to study the survivability of diagnostic elements such as optical relays or optical analyzers.

A standard imaging system, consisting of a fiber bundle, a light amplifier, and a cooled charge-coupled–device (CCD) camera, has been exposed to high neutron yield shots 5 m from target chamber center (TCC) (see Fig. 132.154). The level of nuclear background generated at the Omega Laser Facility leads to visible effects on the recording device that can be quantified thanks to masks positioned between the various optical interfaces. As a result (Fig. 132.155), the increasing background level of the recording device has been clearly

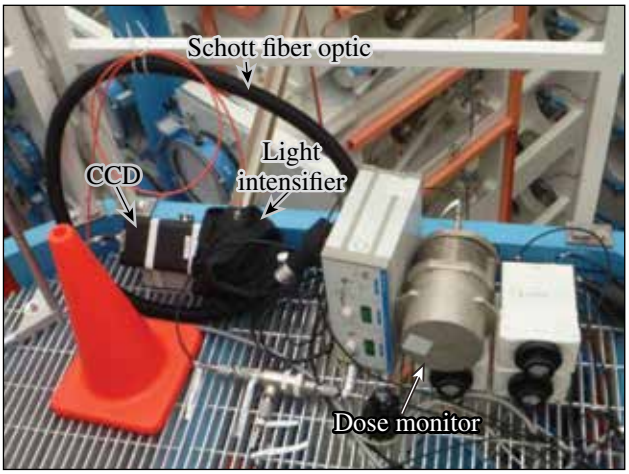

U1530JR

Figure 132.154
Experimental setup.

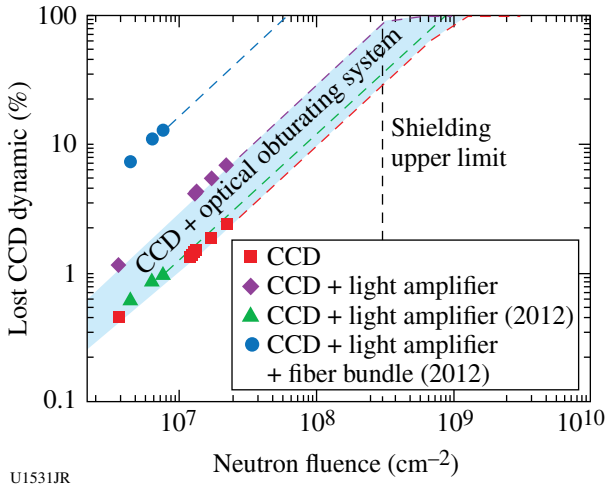

U1531JR

Figure 132.155
Parasitic signal intensity converted into the CCD dynamic range reduction.

observed: the dynamic range reduction appears to be directly proportional to the neutron fluence. The extreme sensitivity of the fiber bundle has been checked and extrapolation to NIF or LMJ radiative constraints leads us to expect a complete failure of the diagnostic. As a conclusion, such an optical relay must be avoided in a hardened diagnostic architecture.

A new mitigation technique to improve the radiation tolerance of a CMOS image sensor used in plasma diagnostics has been tested. It consists of resetting the charges generated by the incoming particles and then shortly after start to record a second image of a decaying scintillator, free of neutron impacted pixels. Such a scheme, based on the use of a custom global reset (GR) functionality designed by the Institut Supérieur de l'Aéraunotique et de l'Espace (ISAE), University of Toulouse is illustrated in the timing diagrams in Fig. 132.156.

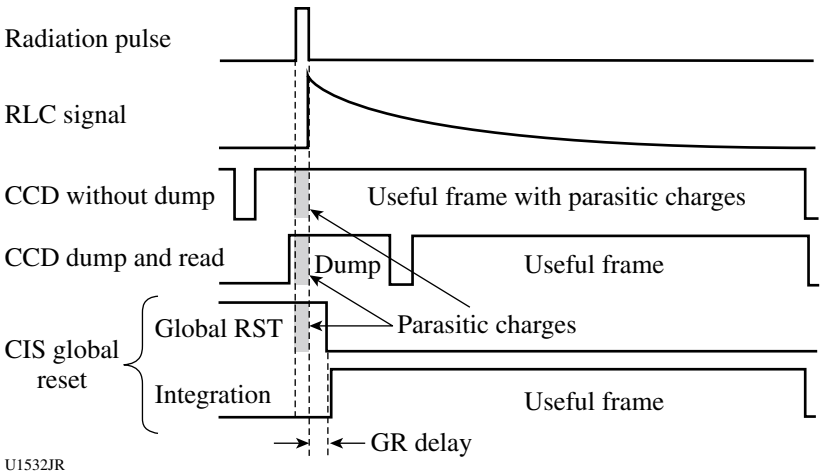

U1532JR

Figure 132.156
Timing diagrams illustrating the standard CCD readout operation, the dump and read technique, and the proposed CIS global reset technique.

A dedicated radiation-hardened test bench has been developed to simulate a plasma diagnostic and has been exposed to neutron yields produced by OMEGA DT shots.[101] The useful signal is generated by a pulsed UV light-emitting diode (LED) synchronized with bang time to excite a long decay-time scintillator. A test pattern has been placed after the radiation-to-light convertor (RLC) to validate that the sensor properly acquires the useful signal. As a first result, the GR reset mode significantly reduces the transient perturbation (parasitic white pixels) without degradation of the image quality (Fig. 132.157). Nevertheless, there is still a small number of remaining disturbed pixels in the image taken with the GR mode. Monte Carlo simulations show that some delayed high-energy particles impinge the sensor after the GR dump phase and create these perturbations during the image acquisition.

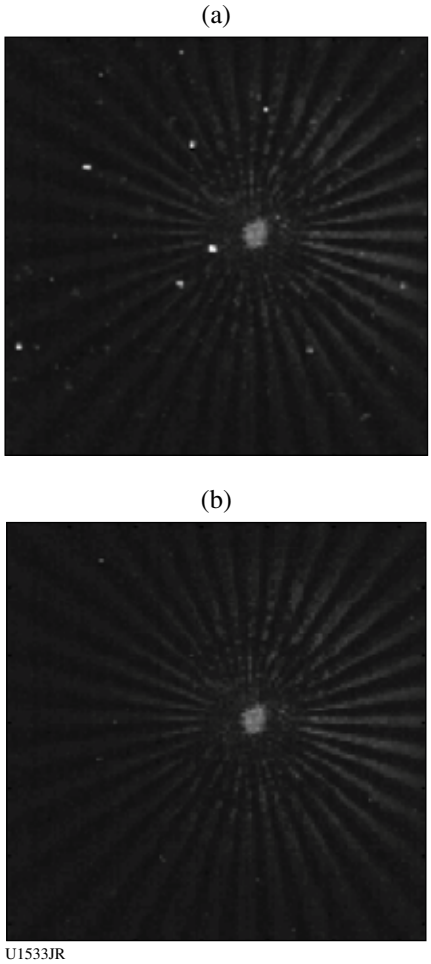

Figure 132.157
RLC and test pattern image captured during a laser shot. (a) Image acquired with the standard timing diagram (no GR) and (b) image acquired with the GR fast dump phase.

High-Resolution Imaging at LLE for CEA Shots

An extended high-resolution x-ray imager (EHRXI) was successfully implemented on OMEGA in May 2012 for the CEA "preheat" campaign. This diagnostic consists of an x-ray microscope and a charge-injection–device (CID) camera. The microscope is a two toroidal mirror pseudo-Wolter microscope. EHRXI is the extended version of an already existing diagnostic, the high-resolution x-ray imager (HRXI). We have replaced its mirrors with similar ones yet coated with a non-periodic multilayer coating that extends their reflectivity up to 12 keV at a grazing angle of 0.6°. The overall layout of the EHRXI is shown in Fig. 132.158.

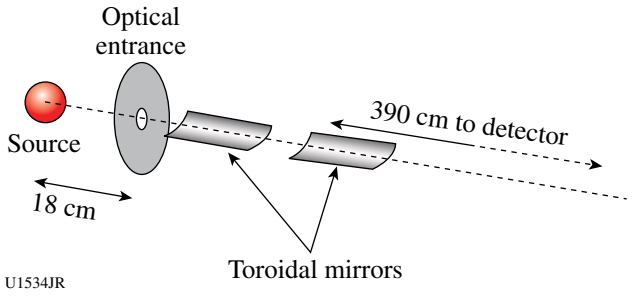

Figure 132.158
Schematic showing the layout of the EHRXI diagnostic.

The design of the microscope allows it to obtain a resolution of 4 μm in a 1-mm-diam field of view. This resolution was measured on a low-energy Riber x-ray generator at CEA.[102]

The goal of the experiment led at LLE was to observe the preheating of a metallic sample on a cavity laser entrance hole (LEH) using radiography while the cavity is being shot. The purpose of the EHRXI was to get a precise image of the Ti backlighting x-ray source. The EHRXI was aimed at the center of the backlighting source, with an angle of 56° regarding the back normal vector of that source. It was placed 30 cm from the backlighter. The microscope entrance was filtered with 75 μm of vanadium to get the spectrum presented Fig. 132.159. The CID camera was placed in a dedicated holder at the back of a ten-inch manipulator (TIM-1) as shown Fig. 132.160.

The target used for the experiment is presented in Fig. 132.161(a). The radiography target is the black disk in the foreground. Figure 132.161(b) shows an image of a shot recorded by the EHRXI. The expected x-ray source size was 200×300 μm and the measured size is 230×300 μm. The results are, therefore, in good agreement with the expectations.

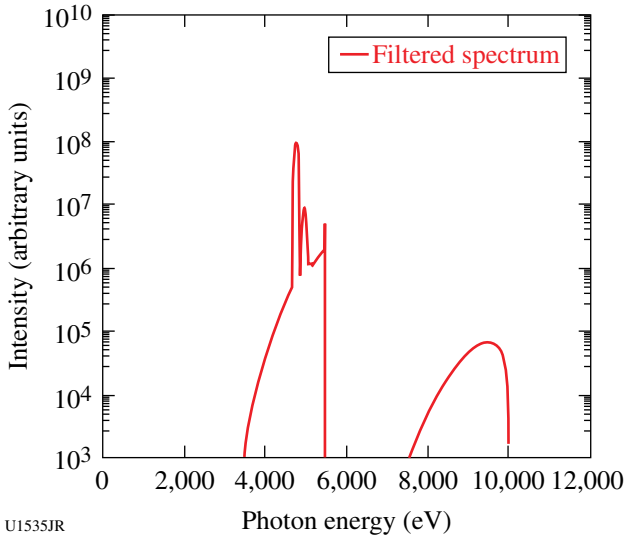

Figure 132.159
Emission spectrum filtered with 75 μm of vanadium.

Figure 132.160
Photo of the EHRXI in TIM-1; the CID camera holder sits at the back of the TIM.

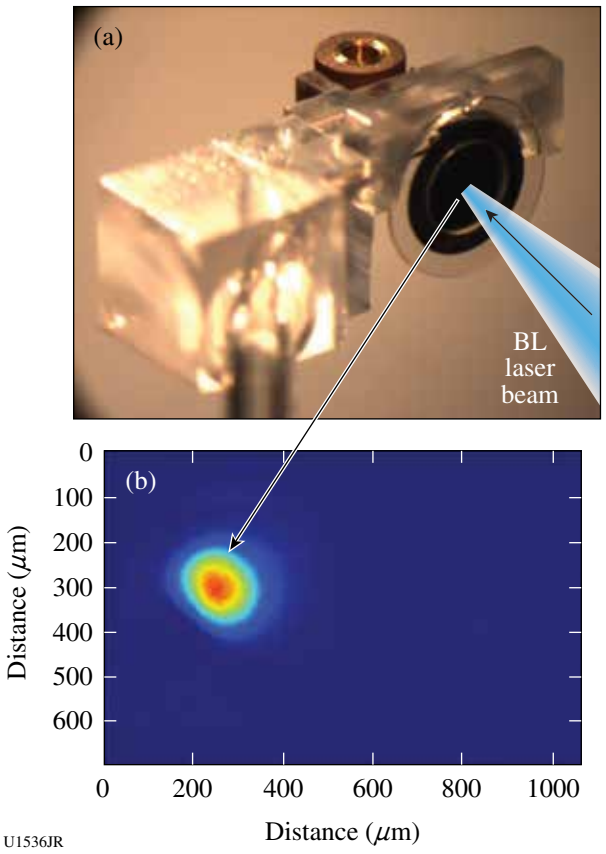

Figure 132.161
(a) Target photo taken on the EHRXI line-of sight. (b) An EHRXI image of the backlighting source of the preheat campaign.

The image is post-treated to remove the charge injection device (CID) noise and the anamorphosis caused by the angle of the line of sight. In conclusion, the EHRXI implementation on OMEGA was a success and it proved to be a versatile, easy-to-use diagnostic.

X-Ray Crystal Spectrometers (XCCS)

Two x-ray crystal spectrometers in the TIM have been built by CEA. The first one is the XCCS-CID (Fig. 132.162). It is time integrated. It features three channels with an imaging slit (magnification 3), a blast shield, filters, a cylindrical crystal, and detection is performed by a CID detector. The distance of the CID to target chamber center (TCC) is 1055 mm. The second one is XCCS-FC (Fig. 132.163). It features four channels with an imaging slit (magnification 3), filters, a cylindrical crystal, and detection is performed by a framing camera (FC). Two adjacent channels share the same 20-mm-width crystal. The distance of the framing camera to TCC is 701 mm. Both spectrometers can accommodate crystals on spacers and shims with a fixed angle ranging from 7.5° to 35° inside a large box.

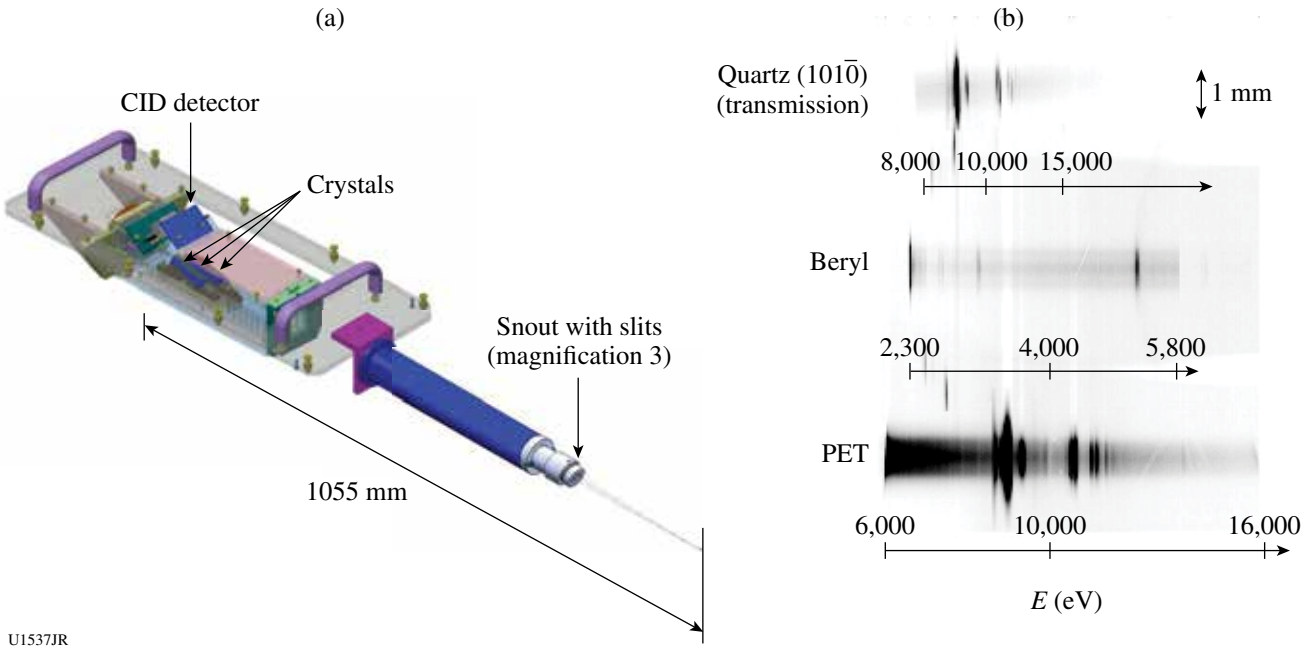

Figure 132.162
(a) Schematic of the XCCS-CID; (b) Zn spectrum recorded on shot 62653.

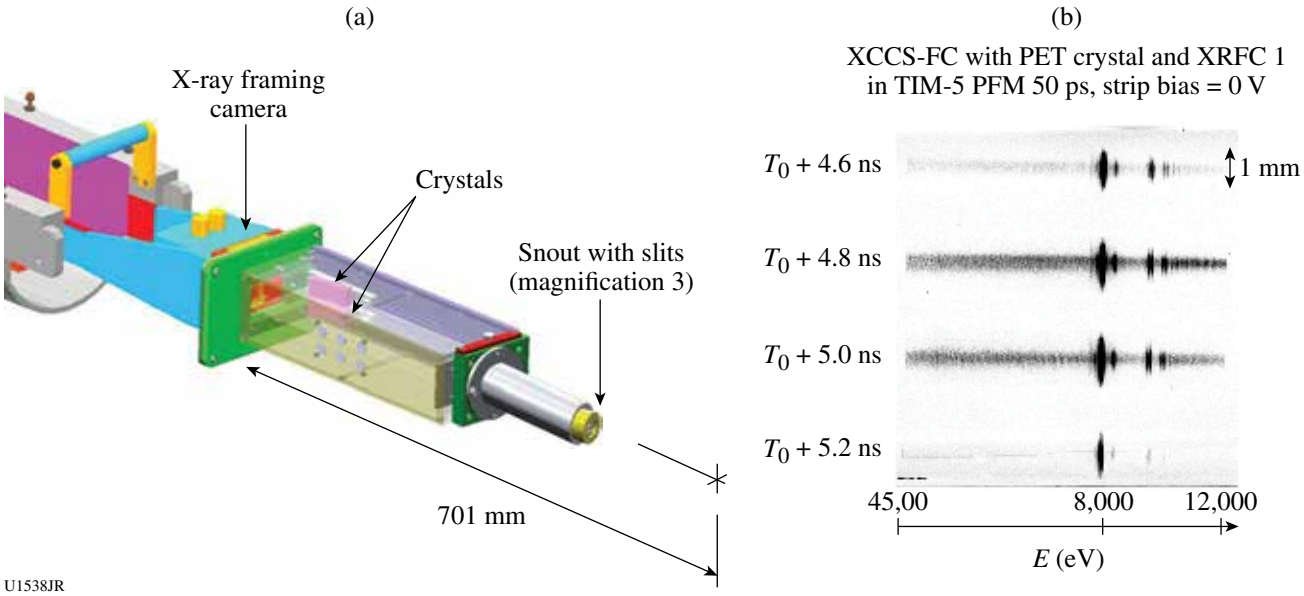

Figure 132.163
(a) Schematic of the XCCS-FC; (b) Ni spectrum obtained on shot 67454.

With the available crystals, configurations covering 1.5 to 15 keV can be achieved.

CEA Rugby Implosions and Convergent Ablation Experiments on OMEGA

CEA is pursuing indirect-drive–implosion experiments on OMEGA using rugby-shaped hohlraums in preparation for early implosion on the Laser Mégajoule (LMJ). It has been previously demonstrated that an increased x-ray drive (+18% in flux) was achieved with a vacuum rugby-shaped hohlraum in comparison with a cylinder.[103] These results were confirmed and even enhanced in the case of gas-filled hohlraums.The question of the precise wall shape of the rugby hohlraum has been addressed recently[104] and it was demonstrated that elliptically shaped hohlraums [see Fig. 132.164(a)] are more efficient than spherically shaped hohlraums. There is less wall hydrodynamic motion and less absorption for the LMJ inner cone, providing a better control of time-dependent symmetry swings. The goal of one experiment was, therefore, to characterize energetics and capsule implosion in elliptical hohlraums compared to rugby- and cylinder-shaped hohlraums during last year's shots.

The round core image acquired on an implosion performed in a gas-filled elliptical hohlraum confirms our capability to control the symmetry in this new hohlraum geometry [see Fig. 132.164(b)].

The increased x-ray drive in rugby measured with Dante was confirmed by enhanced nuclear performances and more ablated mass.[103] It is nevertheless important to perform convergent ablation measurements[105] to assess the implosion velocity—a key metric for ignition performance. ConA experiments with gas-filled rugby hohlraums were, therefore, shot for the first time. The schematic of the experimental configuration is shown in Fig. 132.165(a). A time-resolved 1-D streaked radiography is

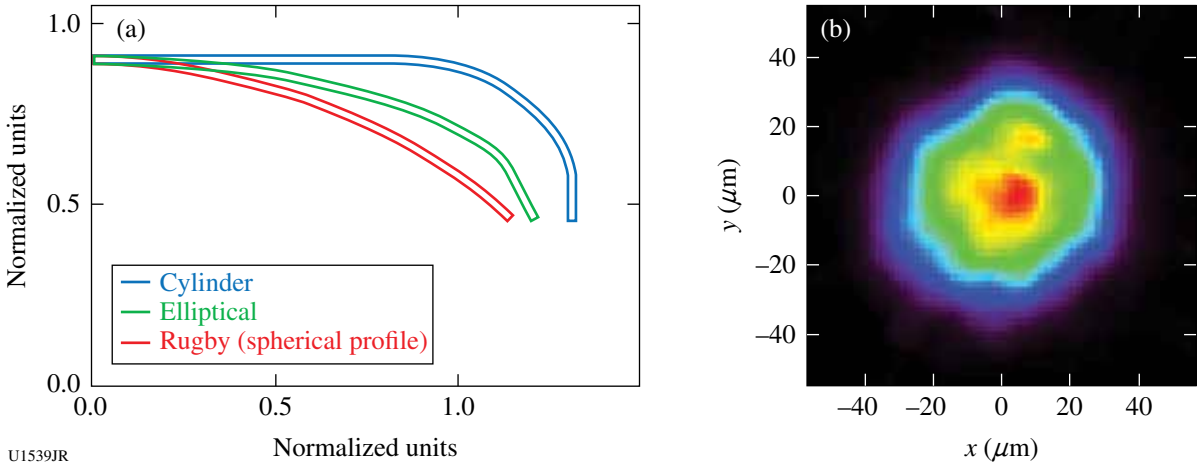

Figure 132.164
(a) Shaped-hohlraum profiles and (b) an x-ray core image for a D_2 implosion performed in an elliptically shaped hohlraum.

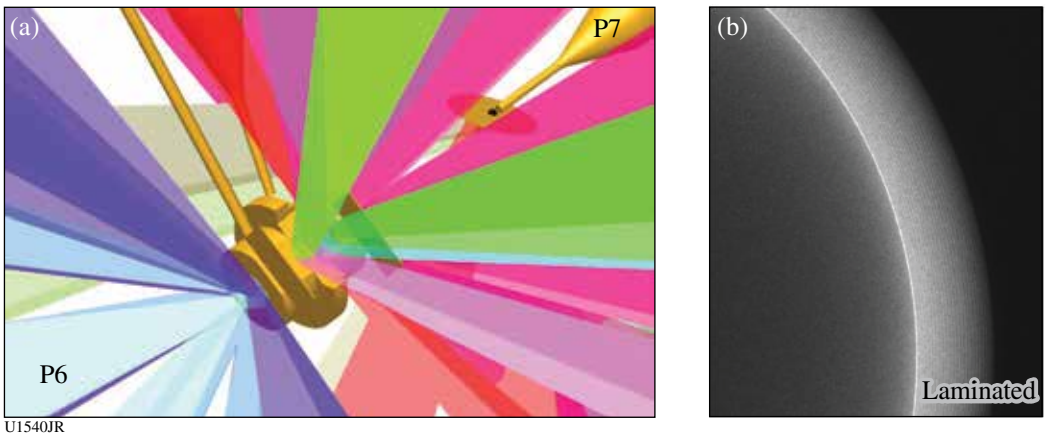

Figure 132.165
(a) Experimental configuration along P6/P7. The streaked implosion radiography is performed toward H14, perpendicular to the hohlraum axis. (b) A typical laminated capsule.

acquired with SSC A in the direction perpendicular to the hohlraum axis, whereas a 2-D time-resolved radiography is acquired at the same time along the hohlraum axis on an x-ray framing camera. These experiments were also aimed at comparing the implosion performance of a uniformly doped and laminated ablator.[106] A laminated ablator consists of thin alternate layers of undoped and germanium-doped CH. Figure 132.165(b) presents a pre-shot radiography of a laminated capsule, on which the thin layers of doped and undoped material are clearly visible. It has been experimentally demonstrated in planar geometry that laminated ablators could mitigate Rayleigh–Taylor growth at the ablation front.[107]

A typical backlight implosion is shown on Fig. 132.166(a). The limb of the shell is well defined and its position could be extracted from the radiography. Preliminary data comparing uniformly doped and laminated capsule trajectory do not indicate discrepancies for the implosion. This corroborates the trajectory measurements already acquired for planar samples.[107]

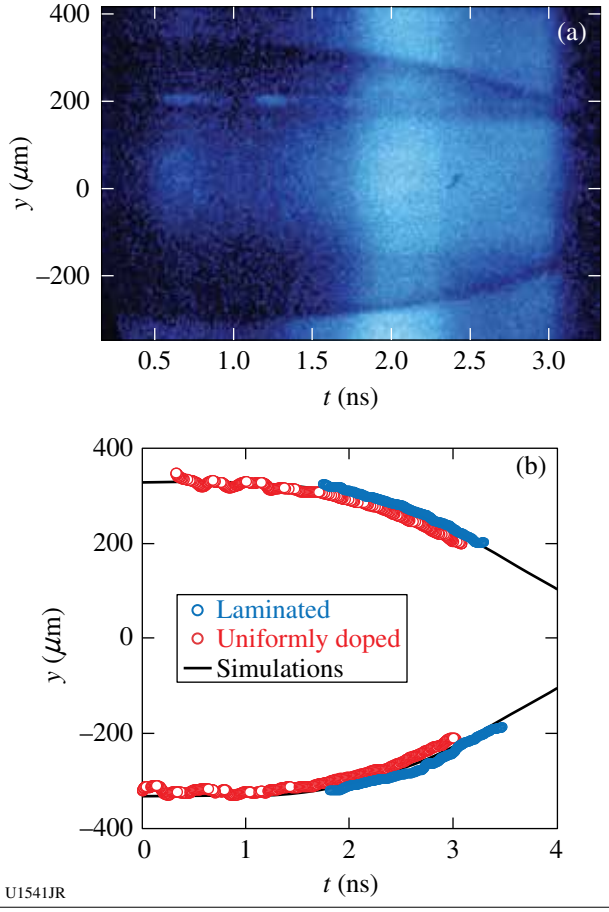

Figure 132.166
(a) Typical streaked radiography acquired on a gas-filled rugby implosion. (b) Comparison of capsule trajectory for laminated and uniformly doped ablators.

FY12 AWE OMEGA EP and OMEGA Experimental Programs

ShkLaue-12A

Principal Investigator: A. J. Comley (AWE)

In the ShkLaue-12A campaign, we made a first attempt to diagnose ramp-compressed, single-crystal tantalum [100] using our established broadband x-ray ("white light") Laue diffraction platform. This platform utilizes an implosion capsule backlighter (980-μm outer diameter, with a 10-μm-thick CH wall) driven by 30 beams [each beam contained 500 J in a 1-ns square pulse and SG4 distributed phase plate (DPP)] to generate a smoothly varying and broadband spectrum of x rays from a "point" source. VISAR (velocity interferometer system for any reflector) is also employed simultaneously with the x-ray diffraction technique.

The target design is shown in Fig. 132.167. Three beams were employed (each ~200 J in a 3.7-ns square pulse and SG8 DPP) to produce a shock in the BrCH reservoir. Upon shock breakout, the reservoir material crosses the gap and stagnates near the sample (which is protected from direct heating by a CH heat shield), such that a smoothly increasing ramp-compression drive is produced, with a peak pressure of ~100 GPa. X-ray diffraction and VISAR data were obtained successfully (Fig. 132.168). Analysis of the diffraction patterns, in which we see a clear signature from the driven tantalum sample, is currently undergoing detailed analysis in conjunction with information obtained from VISAR.

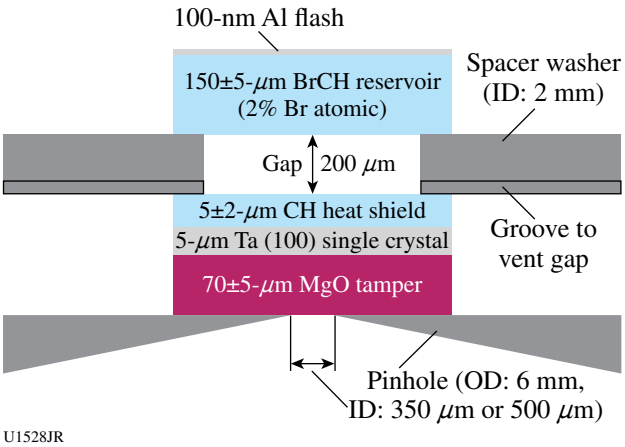

Figure 132.167
ShkLaue-12A ramp-compression target design.

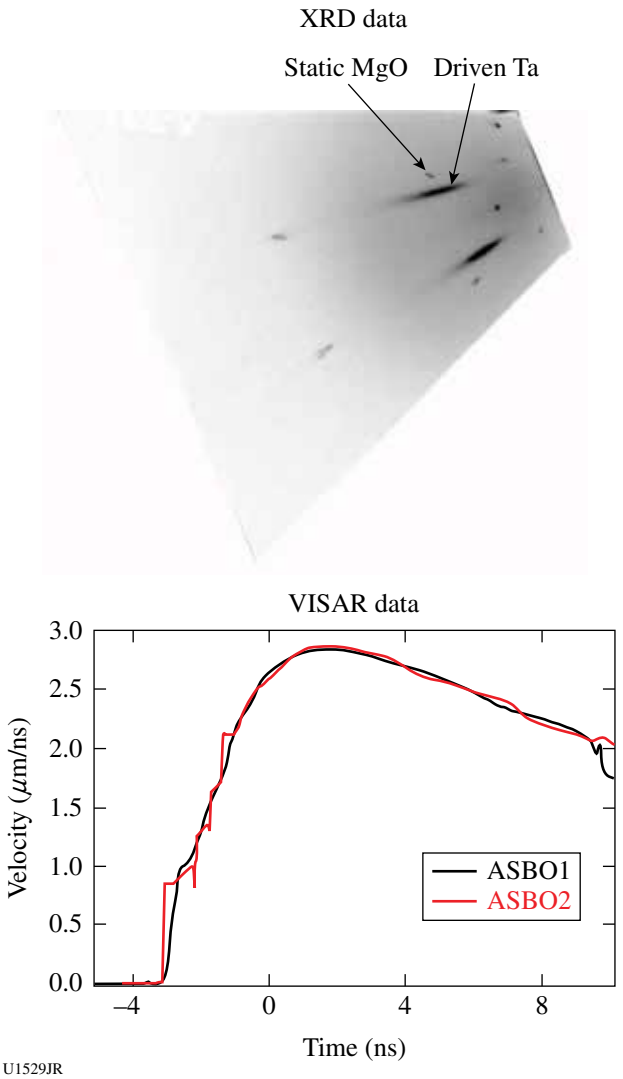

Figure 132.168
(a) The x-ray diffraction (XRD) pattern contains characteristic spots, each of which can be attributed to either the tantalum or MgO layers in the target package and to specific crystallographic lattice planes. (b) VISAR records the compression history of the sample.

REFERENCES

1. T. S. Duffy, R. J. Hemley, and H. Mao, Phys. Rev. Lett. **74**, 1371 (1995).

2. A. R. Organov, M. J. Gillian, and G. D. Price, J. Phys. Chem. **118**, 10,174 (2003).

3. T. Nagayama, R. C. Mancini, R. Florido, R. Tommasini, J. A. Koch, J. A. Delettrez, S. P. Regan, and V. A. Smalyuk, J. Appl. Phys. **109**, 093303 (2011).

4. T. Nagayama, R. C. Mancini, R. Florido, D. Mayes, R. Tommasini, J. A. Koch, J. A. Delettrez, S. P. Regan, and V. A. Smalyuk, Phys. Plasmas **19**, 082705 (2012).

5. D. T. Casey, J. A. Frenje, M. Gatu Johnson, M. J.-E. Manuel, N. Sinenian, A. B. Zylstra, F. H. Séguin, C. K. Li, R. D. Petrasso, V. Yu. Glebov, P. B. Radha, D. D. Meyerhofer, T. C. Sangster, D. P. McNabb, P. A. Amendt, R. N. Boyd, S. P. Hatchett, S. Quaglioni, J. R. Rygg, I. J. Thompson, A. D. Bacher, H. W. Herrmann, and Y. H. Kim, Phys. Rev. Lett. **109**, 025003 (2012).

6. N. Sinenian, G. Fiksel, J. A. Frenje, C. G. Freeman, M. J.-E. Manuel, D. T. Casey, P. M. Nilson, C. Stoeckl, W. Theobald, D. D. Meyerhofer, and R. D. Petrasso, Phys. Plasmas **19**, 093118 (2012).

7. M. J.-E. Manuel, C. K. Li, F. H. Séguin, J. A. Frenje, D. T. Casey, R. D. Petrasso, S. X. Hu, R. Betti, J. D. Hager, D. D. Meyerhofer, and V. Smalyuk, Phys. Plasmas **19**, 082710 (2012).

8. N. Sinenian, A. B. Zylstra, M. J. E. Manuel, H. G. Rinderknecht, J. A. Frenje, F. H. Seguin, C. K. Li, R. D. Petrasso, V. Goncharov, J. Delettrez, I. V. Igumenshchev, D. H. Froula, C. Stoeckl, T. C. Sangster, D. D. Meyerhofer, J. A. Cobble, and D. G. Hicks, Appl. Phys. Lett. **101**, 114102 (2012).

9. M. J.-E. Manuel *et al.*, Appl. Phys. Lett. **100**, 203505 (2012).

10. M. J.-E. Manuel, C. K. Li, F. H. Séguin, J. Frenje, D. T. Casey, R. D. Petrasso, S. X. Hu, R. Betti, J. D. Hager, D. D. Meyerhofer, and V. A. Smalyuk, Phys. Rev. Lett. **108**, 255006 (2012).

11. D. T. Casey, J. A. Frenje, M. Gatu Johnson, M. J.-E. Manuel, H. G. Rinderknecht, N. Sinenian, F. H. Séguin, C. K. Li, R. D. Petrasso, P. B. Radha, J. A. Delettrez, V. Yu. Glebov, D. D. Meyerhofer, T. C. Sangster, D. P. McNabb, P. A. Amendt, R. N. Boyd, J. R. Rygg, H. W. Herrmann, Y. H. Kim, and A. D. Bacher, Phys. Rev. Lett. **108**, 075002 (2012).

12. C. K. Li, F. H. Séguin, J. A. Frenje, M. J. Rosenberg, H. G. Rinderknecht, A. B. Zylstra, R. D. Petrasso, P. A. Amendt, O. L. Landen, A. J. Mackinnon, R. P. J. Town, S. C. Wilks, R. Betti, D. D. Meyerhofer, J. M. Soures, J. Hund, J. D. Kilkenny, and A. Nikroo, Phys. Rev. Lett. **108**, 025001 (2012).

13. F. H. Séguin, C. K. Li, M. J.-E. Manuel, H. G. Rinderknecht, N. Sinenian, J. A. Frenje, J. R. Rygg, D. G. Hicks, R. D. Petrasso, J. Delettrez, R. Betti, F. J. Marshall, and V. A. Smalyuk, Phys. Plasmas **19**, 012701 (2012).

14. N. Sinenian *et al.*, "A Multithreaded Modular Software Toolkit for Control of Complex Experiments," to be published in Computing in Science and Engineering.

15. D. T. Casey, J. A. Frenje, M. Gatu Johnson, F. H. Séguin, C. K. Li, R. D. Petrasso, V. Yu. Glebov, J. Katz, J. P. Knauer, D. D. Meyerhofer, T. C. Sangster, R. M. Bionta, D. L. Bleuel, T. Döppner, S. Glenzer, E. Hartouni, S. P. Hatchett, S. Le Pape, T. Ma, A. MacKinnon, M. A. Mckernan, M. Moran, E. Moses, H.-S. Park, J. Ralph, B. A. Remington, V. Smalyuk, C. B. Yeamans, J. Kline, G. Kyrala, G. A. Chandler, R. J. Leeper, C. L. Ruiz, G. W. Cooper, A. J. Nelson, K. Fletcher, J. Kilkenny, M. Farrell, D. Jasion, and R. Paguio, Rev. Sci. Instrum. **83**, 10D912 (2010).

16. F. H. Séguin, N. Sinenian, M. Rosenberg, A. Zylstra, M. J. E. Manuel, H. Sio, C. Waugh, H. G. Rinderknecht, M. Gatu Johnson, J. Frenje, C. K. Li, R. Petrasso, T. C. Sangster, and S. Roberts, Rev. Sci. Instrum. **83**, 10D908 (2012).

17. M. J.-E. Manuel *et al.*, Rev. Sci. Instrum. **83**, 063506 (2012).

18. N. Sinenian *et al.*, Rev. Sci. Instrum. **83**, 043502 (2012).

19. A. Zylstra, C. K. Li, H. G. Rinderknecht, F. H. Séguin, R. D. Petrasso, C. Stoeckl, D. D. Meyerhofer, P. Nilson, T. C. Sangster, S. Le Pape, A. Mackinnon, and P. Patel, Rev. Sci. Instrum. **83**, 013511 (2012).

20. A. B. Zylstra *et al.*, Nucl. Instrum. Methods Phys. Res. A **681**, 84 (2012).

21. M. Hohenberger, P.-Y. Chang, G. Fiksel, J. P. Knauer, R. Betti, F. J. Marshall, D. D. Meyerhofer, F. H. Séguin, and R. D. Petrasso, Phys. Plasmas **19**, 056306 (2012).

22. N. Sinenian *et al.*, Rev. Sci. Instrum. **82**, 103303 (2011).

23. T. R. Boehly, D. L. Brown, R. S. Craxton, R. L. Keck, J. P. Knauer, J. H. Kelly, T. J. Kessler, S. A. Kumpan, S. J. Loucks, S. A. Letzring, F. J. Marshall, R. L. McCrory, S. F. B. Morse, W. Seka, J. M. Soures, and C. P. Verdon, Opt. Commun. **133**, 495 (1997).

24. L. J. Waxer, D. N. Maywar, J. H. Kelly, T. J. Kessler, B. E. Kruschwitz, S. J. Loucks, R. L. McCrory, D. D. Meyerhofer, S. F. B. Morse, C. Stoeckl, and J. D. Zuegel, Opt. Photonics News **16**, 30 (2005).

25. C. K. Li, F. H. Séguin, J. A. Frenje, J. R. Rygg, R. D. Petrasso, R. P. J. Town, P. A. Amendt, S. P. Hatchett, O. L. Landen, A. J. Mackinnon, P. K. Patel, V. Smalyuk, J. P. Knauer, T. C. Sangster, and C. Stoeckl, Rev. Sci. Instrum. **77**, 10E725 (2006).

26. N. L. Kugland, D. D. Ryutov, P. Y. Chang, R. P. Drake, G. Fiksel, D. H. Froula, S. H. Glenzer, G. Gregori, M. Grosskopf, M. Koenig, Y. Kuramitsu, C. Kuranz, M. C. Levy, E. Liang, J. Meinecke, F. Miniati, T. Morita, A. Pelka, C. Plechaty, R. Presura, A. Ravasio, B. A. Remington, B. Reville, J. S. Ross, Y. Sakawa, A. Spitkovsky, H. Takabe, and H. S. Park, Nat. Phys. **8**, 809 (2012).

27. J. S. Ross, S. H. Glenzer, P. Amendt, R. Berger, L. Divol, N. L. Kugland, O. L. Landen, C. Plechaty, B. Remington, D. Ryutov, W. Rozmus, D. H. Froula, G. Fiksel, C. Sorce, Y. Kuramitsu, T. Morita, Y. Sakawa, H. Takabe, R. P. Drake, M. Grosskopf, C. Kuranz, G. Gregori, J. Meinecke, C. D. Murphy, M. Koenig, A. Pelka, A. Ravasio, T. Vinci, E. Liang, R. Presura, A. Spitkovsky, F. Miniati, and H.-S. Park, Phys. Plasmas **19**, 056501 (2012).

28. H.-S. Park, D. D. Ryutov, J. S. Ross, N. L. Kugland, S. H. Glenzer, C. Plechaty, S. M. Pollaine, B. A. Remington, A. Spitkovsky, L. Gargate, G. Gregori, A. Bell, C. Murphy, Y. Sakawa, Y. Kuramitsu, T. Morita, H. Takabe, D. H. Froula, G. Fiksel, F. Miniati, M. Koenig, A. Ravasio, A. Pelka, E. Liang, N. Woolsey, C. C. Kuranz, R. P. Drake, and M. J. Grosskopf, High Energy Density Phys. **8**, 38 (2012).

29. A. Spitkovsky, presented at the Colloquium at Northwestern University, Evanston, IL, February 2012.

30. A. Spitkovsky, presented at the 9th International Conference on High Energy Density Laboratory Astrophysics, Tallahassee, FL, 30 April–4 May 2012.

31. A. Spitkovsky, presented at the Twenty-Second International Conference on Numerical Simulations of Plasmas (ICNSP 2011), Long Branch, NJ, 7–9 September 2011.

32. A. Spitkovsky, presented at the Center for Magnetic Self-Organization (CMSO) General Meeting, Durham, NH, 17–20 October 2011.

33. J. Ross, Bull. Am. Phys. Soc. **56**, 282 (2011).

34. M. Grosskopf *et al.*, presented at High Energy Density Laboratory Astrophysics, Tallahassee, FL, 30 April–4 May 2012.

35. L. Willingale, P. M. Nilson, A. G. R. Thomas, J. Cobble, R. S. Craxton, A. Maksimchuk, P. A. Norreys, T. C. Sangster, R. H. H. Scott, C. Stoeckl, C. Zulick, and K. Krushelnick, Phys. Rev. Lett. **106**, 105002 (2011).

36. S. P. D. Mangles *et al.*, Phys. Rev. Lett. **94**, 245001 (2005).

37. N. Naseri, S. G. Bochkarev, and W. Rozmus, Phys. Plasmas **17**, 033107 (2010).

38. S. Fritzler *et al.*, Phys. Rev. Lett. **89**, 165004 (2002).

39. G. H. Miller and T. J. Ahrens, Rev. Mod. Phys. **63**, 919 (1991), Eq. (127).

40. H. Chen, S. C. Wilks, D. D. Meyerhofer, J. Bonlie, C. D. Chen, S. N. Chen, C. Courtois, L. Elberson, G. Gregori, W. Kruer, O. Landoas, J. Mithen, J. Myatt, C. D. Murphy, P. Nilson, D. Price, M. Schneider, R. Shepherd, C. Stoeckl, M. Tabak, R. Tommasini, and P. Beiersdorfer, Phys. Rev. Lett. **105**, 015003 (2010).

41. H. Chen, D. D. Meyerhofer, S. C. Wilks, R. Cauble, F. Dollar, K. Falk, G. Gregori, A. Hazi, E. I. Moses, C. D. Murphy, J. Myatt, J. Park, J. Seely, R. Shepherd, A. Spitkovsky, C. Stoeckl, C. I. Szabo, R. Tommasini, C. Zulick, and P. Beirsdorfer, High Energy Density Phys. **7**, 225 (2011).

42. O. A. Hurricane, High Energy Density Phys. **4**, 97 (2008).

43. E. C. Harding *et al.*, Phys. Rev. Lett. **103**, 045005 (2009).

44. O. A. Hurricane *et al.*, Phys. Plasmas **16**, 056305 (2009).

45. V. A. Smalyuk *et al.*, Phys. Plasmas **19**, 092702 (2012).

46. K. S. Raman *et al.*, Phys. Plasmas **19**, 092112 (2012).

47. O. A. Hurricane *et al.*, Phys. Rev. Lett. **109**, 155004 (2012).

48. Z. Y. Bao *et al.*, At. Data Nucl. Data Tables **76**, 70 (2000).

49. N. Cue, J.-C. Poizat, and J. Remillieux, Europhys. Lett. **8**, 19 (1989).

50. A. Pálffy *et al.*, Phys. Lett. B **661**, 330 (2008).

51. A. Pálffy, W. Scheid, and Z. Harman, Phys. Rev. A **73**, 012715 (2006).

52. M. R. Harston and J. F. Chemin, Phys. Rev. C **59**, 2462 (1999).

53. M. Morita and K. Otozai, Hyperfine Interact. **2**, 418 (1976).

54. S. Kishimoto *et al.*, Nucl. Phys. A **748**, 3 (2005).

55. M. R. Harston and J. J. Carroll, Laser Phys. **14**, 1452 (2004).

56. N. L. Kugland, presented at the 9th International Conference on High Energy Density Laboratory Astrophysics, Tallahassee, FL, 30 April–4 May 2012.

57. H.-S. Park, N. L. Kugland, J. S. Ross, B. A. Remington, C. Plechaty, D. D. Ryutov, A. Spitkovsky, G. Gregori, A. Bell, J. Meinecke, C. Murphy, Y. Sakawa, Y. Kuramitsu, H. Takabe, D. H. Froula, G. Fiksel, F. Miniati, M. Koenig, A. Ravasio, E. Liang, N. Woolsey, R. P. Drake, C. Kuranz, M. Grosskopf, and R. Presura, presented at the 9th International Conference on High Energy Density Laboratory Astrophysics, Tallahassee, FL, 30 April–4 May 2012.

58. D. D. Ryutov *et al.*, presented at the 9th International Conference on High Energy Density Laboratory Astrophysics, Tallahassee, FL, 30 April–4 May 2012.

59. J. S. Ross *et al.*, Rev. Sci. Instrum. **83**, 10E323 (2012).

60. N. L. Kugland *et al.*, Rev. Sci. Instrum. **83**, 101301 (2012).

61. D. D. Ryutov *et al.*, Plasma Phys. Control. Fusion **54**, 105021 (2012).

62. D. D. Ryutov *et al.*, Phys. Plasmas **19**, 074501 (2012).

63. D. D. Ryutov *et al.*, Phys. Plasmas **18**, 104504 (2011).

64. N. L. Kugland *et al.*, "Visualizing Electromagnetic Fields in Laser-Produced Counter-Streaming Plasma Experiments for Collisionless Shock Laboratory Astrophysics," to be submitted to Physics of Plasmas.

65. M. J. Grosskopf, R. P. Drake, C. C. Kuranz, E. M. Rutter, J. S. Ross, N. L. Kugland, S. Pollaine, B. A. Remington, D. D. Ryutov, A. Spitkovsky, L. Gargate, G. Gregori, A. Bell, C. D. Murphy, J. Meinecke, B. Reville, Y. Sakawa, Y. Kuramitsu, H. Takabe, D. H. Froula, G. Fiksel, F. Miniati, M. Koenig, A. Ravasio, E. Liang, N. Woolsey, and H.-S. Park, "Simulation of Laser-Driven, Ablated Flows in Collisionless Shock Experiments on OMEGA and the NIF," submitted to High Energy Density Physics.

66. S. P. Regan, K. Falk, G. Gregori, P. B. Radha, S. X. Hu, T. R. Boehly, B. J. B. Crowley, S. H. Glenzer, O. L. Landen, D. O. Gericke, T. Doeppner, D. D. Meyerhofer, C. D. Murphy, T. C. Sangster, and J. Vorberger, "Inelastic X-Ray Scattering from Shocked Liquid Deuterium," to be published in Physical Review Letters; *LLE Review Quarterly Report* **131**, 143, Laboratory for Laser Energetics, University of Rochester, Rochester, NY, LLE Document No. DOE/NA/28302-1064 (2012); *LLE Review Quarterly Report* **130**, 72, Laboratory for Laser Energetics, University of Rochester, Rochester, NY, LLE Document No. DOE/NA/28302-1058 (2012).

67. G. Gregori *et al.*, High Energy Density Phys. **3**, 99 (2007).

68. E. García Saiz *et al.*, Nat. Phys. **4**, 940 (2008).

69. G. Kresse and J. Furthmüller, Phys. Rev. B **54**, 11169 (1996).

70. J. Vorberger *et al.*, Phys. Rev. B **75**, 024206 (2007).

71. W. Theobald, A. A. Solodov, C. Stoeckl, K. S. Anderson, R. Betti, T. R. Boehly, R. S. Craxton, J. A. Delettrez, C. Dorrer, J. A. Frenje, V. Yu. Glebov, H. Habara, K. A. Tanaka, J. P. Knauer, R. Lauck, F. J. Marshall, K. L. Marshall, D. D. Meyerhofer, P. M. Nilson, P. K. Patel, H. Chen, T. C. Sangster, W. Seka, N. Sinenian, T. Ma, F. N. Beg, E. Giraldez, and R. B. Stephens, Phys. Plasmas **18**, 056305 (2011).

72. P. B. Radha, T. J. B. Collins, J. A. Delettrez, Y. Elbaz, R. Epstein, V. Yu. Glebov, V. N. Goncharov, R. L. Keck, J. P. Knauer, J. A. Marozas, F. J. Marshall, R. L. McCrory, P. W. McKenty, D. D. Meyerhofer, S. P. Regan, T. C. Sangster, W. Seka, D. Shvarts, S. Skupsky, Y. Srebro, and C. Stoeckl, Phys. Plasmas **12**, 056307 (2005).

73. J. A. King, K. Akli, B. Zhang, R. R. Freeman, M. H. Key, C. D. Chen, S. P. Hatchett, J. A. Koch, A. J. MacKinnon, P. K. Patel, R. Snavely, R. P. J. Town, M. Borghesi, L. Romagnani, M. Zepf, T. Cowan, H. Habara, R. Kodama, Y. Toyama, S. Karsch, K. Lancaster, C. Murphy, P. Norreys, R. Stephens, and C. Stoeckl, Appl. Phys. Lett. **86**, 191501 (2005).

74. C. Stoeckl, J. A. Delettrez, R. Epstein, G. Fiksel, D. Guy, M. Hohenberger, R. K. Jungquist, C. Mileham, P. M. Nilson, T. C. Sangster, M. J. Shoup III, and W. Theobald, Rev. Sci. Instrum. **83**, 10E501 (2012).

75. H.-S. Park *et al.*, Phys. Rev. Lett. **104**, 135504 (2010).

76. J. F. Barnes *et al.*, J. Appl. Phys. **45**, 727 (1974).

77. H.-S. Park *et al.*, Phys. Plasmas **17**, 056314 (2010).

78. H.-S. Park *et al.*, AIP Conf. Proc. **1426**, 1371 (2012).

79. N. R. Barton *et al.*, J. Appl. Phys. **109**, 073501 (2011).

80. B. Remington *et al.*, AIP Conf. Proc. **1426**, 1375 (2012).

81. J. L. Belof *et al.*, AIP Conf. Proc. **1426**, 1521 (2012).

82. J. Edwards *et al.*, Phys. Rev. Lett. **92**, 075002 (2004).

83. H.-S. Park, D. M. Chambers, H.-K. Chung, R. J. Clarke, R. Eagleton, E. Giraldez, T. Goldsack, R. Heathcote, N. Izumi, M. H. Key, J. A. King, J. A. Koch, O. L. Landen, A. Nikroo, P. K. Patel, D. F. Price, B. A. Remington, H. F. Robey, R. A. Snavely, D. A. Steinman, R. B. Stephens, C. Stoeckl, M. Storm, M. Tabak, W. Theobald, R. P. J. Town, J. E. Wickersham, and B. B. Zhang, Phys. Plasmas **13**, 056309 (2006).

84. L. Burakovsky *et al.*, Phys. Rev. Lett. **104**, 255702 (2010).

85. A. Dewaele, P. Loubeyre, and M. Mezouar, Phys. Rev. B **70**, 094112 (2004).

86. D. G. Hicks, T. R. Boehly, P. M. Celliers, J. H. Eggert, S. J. Moon, D. D. Meyerhofer, and G. W. Collins, Phys. Rev. B **79**, 014112 (2009); M. D. Knudson *et al.*, Phys. Rev. B **69**, 144209 (2004).

87. S. Root *et al.*, Phys. Rev. Lett. **105**, 085501 (2010).

88. C. E. Ragan III *et al.*, Los Alamos National Laboratory, Los Alamos, NM, LA-UR-83-2081 (1983).

89. Y. Ping, D. G. Hicks, B. Yaakobi, F. Coppari, D. E. Fratanduono, S. Hamel, J. H. Eggert, J. R. Rygg, R. F. Smith, T. R. Boehly, and G. W. Collins, "EXAFS Study of Iron Ramp-Compressed up to 560 GPa," submitted to Physical Review Letters.

90. A. Salamat *et al.*, Phys. Rev. B **84**, 140104 (2011).

91. R. Briggs *et al.*, J. Phys.: Conf. Ser. **377**, 012035 (2012).

92. B. Schwager *et al.*, J. Chem. Phys. **133**, 084501 (2010); S. T. Weir *et al.*, J. Appl. Phys. **111**, 123529 (2012).

93. S. Desgreniers, Y. K. Vohra, and A. L. Ruoff, Phys. Rev. B **39**, 10359 (1989).

94. F. Pérez *et al.*, Phys. Plasmas **19**, 083101 (2012).

95. K. B. Fournier *et al.*, Phys. Rev. Lett. **92**, 165005 (2004).

96. C. Constantin *et al.*, Phys. Plasmas **12**, 063104 (2005).

97. M. Tanabe *et al.*, High Energy Density Phys. **6**, 89 (2010).

98. J. R. Patterson *et al.*, Rev. Sci. Instrum. **83**, 10D725 (2012).

99. Y. Kim, J. M. Mack, H. W. Herrmann, C. S. Young, G. M. Hale, S. Caldwell, N. M. Hoffman, S. C. Evans, T. J. Sedillo, A. McEvoy, J. Langenbrunner, H. H. Hsu, M. A. Huff, S. Batha, C. J. Horsfield, M. S. Rubery, W. J. Garbett, W. Stoeffl, E. Grafil, L. Bernstein, J. A. Church, D. B. Sayre, M. J. Rosenberg, C. Waugh, H. G. Rinderknecht, M. Gatu Johnson, A. B. Zylstra, J. A. Frenje, D. T. Casey, R. D. Petrasso, E. K. Miller, V. Yu Glebov, C. Stoeckl, and T. C. Sangster, Phys. Plasmas **19**, 056313 (2012).

100. Y. Kim, J. M. Mack, H. W. Herrmann, C. S. Young, G. M. Hale, S. Caldwell, N. M. Hoffman, S. C. Evans, T. J. Sedillo, A. McEvoy, J. Langenbrunner, H. H. Hsu, M. A. Huff, S. Batha, C. J. Horsfield, M. S. Rubery, W. J. Garbett, W. Stoeffl, E. Grafil, L. Bernstein, J. A. Church, D. B. Sayre, M. J. Rosenberg, C. Waugh, H. G. Rinderknecht, M. Gatu Johnson, A. B. Zylstra, J. A. Frenje, D. T. Casey, R. D. Petrasso, E. K. Miller, V. Yu Glebov, C. Stoeckl, and T. C. Sangster, Phys. Rev. C **85**, 061601 (2012).

101. V. Goiffon *et al.*, Electron. Lett. **48**, 1338 (2012).

102. D. Dennetiere, P. Audebert, R. Bahr, S. Bole, J. L. Bourgade, B. Brannon, F. Girard, G. Pien, and Ph. Troussel, in *Target Diagnostics Physics and Engineering for Inertial Confinement Fusion*, edited by P. Bell and P. Grim (SPIE, Bellingham, WA, 2012), Vol. 8505, p. 85050G.

103. F. Philippe, A. Casner, T. Caillaud, O. Landoas, M. C. Monteil, S. Liberatore, H. S. Park, P. Amendt, H. Robey, C. Sorce, C. K. Li, F. Seguin, M. Rosenberg, R. Petrasso, V. Glebov, and C. Stoeckl, Phys. Rev. Lett. **104**, 035004 (2010).

104. S. Laffite and P. Loiseau, Phys. Plasmas **17**, 102704 (2010).

105. D. G. Hicks, B. K. Spears, D. G. Braun, R. E. Olson, C. M. Sorce, P. M. Celliers, G. W. Collins, and O. L. Landen, Phys. Plasmas **17**, 102703 (2010).

106. L. Masse, Phys. Rev. Lett. **98**, 245001 (2007).

107. L. Masse *et al.*, Phys. Rev. E **83**, 055401(R) (2011).

Publications and Conference Presentations

Publications

M. A. Barrios, T. R. Boehly, D. G. Hicks, D. E. Fratanduono, J. H. Eggert, G. W. Collins, and D. D. Meyerhofer, "Precision Equation-of-State Measurements on National Ignition Facility Ablator Materials from 1 to 12 Mbar Using Laser-Driven Shock Waves," J. Appl. Phys. **111**, 093515 (2012).

J. Bromage, C. Dorrer, and R. K. Jungquist, "Temporal Contrast Degradation at the Focus of Ultrafast Pulses from High-Frequency Spectral Phase Modulation," J. Opt. Soc. Am. B **29**, 051125 (2012).

J. Bromage, C. Dorrer, M. Millecchia, J. Bunkenburg, R. Jungquist, and J. D. Zuegel, "A Front End for Ultra-Intense OPCPA," in *Light at Extreme Intensities 2011, AIP Conf. Proc. 1462*, edited by K. Osvay, P. Dombi, J. A. Fulop, and K. Varju (American Institute of Physics, New York, 2012), pp. 74–77.

S. H. Chen and S. K.-H. Wei, "Modification of the Stokes–Einstein Equation with a Semiempirical Microfriction Factor for Correlation of Tracer Diffusivities in Organic Solvents," Ind. Eng. Chem. Res. **50**, 12,304 (2011).

T. J. B. Collins, J. A. Marozas, R. L. McCrory, P. B. Radha, D. R. Harding, P. W. McKenty, R. S. Craxton, A. Shvydky, V. N. Goncharov, S. Skupsky, and J. D. Zuegel, R. Betti, F. J. Marshall, J. A. Delettrez, K. S. Anderson, and D. D. Meyerhofer, "A Polar-Drive–Ignition Design for the National Ignition Facility," Phys. Plasmas **19**, 056308 (2012).

W. R. Donaldson, C. Zhao, L. Ji, R. G. Roides, K. Miller, and B. Beeman, "A Single-Shot, Multiwavelength Electro-Optic Data-Acquisition System for ICF Applications," Rev. Sci. Instrum. **83**, 10D726 (2012).

C. Dorrer, S. K.-H. Wei, P. Leung, M. Vargas, K. Wegman, J. Boulé, Z. Zhao, K. L. Marshall, and S. H. Chen, "High-Damage-Threshold Static Laser Beam Shaping Using Optically Patterned Liquid-Crystal Devices," Opt. Lett. **36**, 4035 (2011).

D. H. Edgell, D. K. Bradley, E. J. Bond, S. Burns, D. A. Callahan, J. Celeste, M. J. Eckart, V. Yu. Glebov, D. S. Hey, G. Lacaille, J. D. Kilkenny, J. Kimbrough, A. J. Mackinnon, J. Magoon, J. Parker, T. C. Sangster, M. J. Shoup III, C. Stoeckl, T. Thomas, and A. MacPhee, "South Pole Bang-Time Diagnostic on the National Ignition Facility," Rev. Sci. Instrum. **83**, 10E119 (2012).

K. Falk, S. P. Regan, J. Vorberger, M. A. Barrios, T. R. Boehly, D. E. Fratanduono, S. H. Glenzer, D. G. Hicks, S. X. Hu, C. D. Murphy, P. B. Radha, S. Rothman, A. P. Jephcoat, J. S. Wark, D. O. Gericke, and G. Gregori, "Self-Consistent Measurement of the Equation of State of Liquid Deuterium," High Energy Density Phys. **8**, 76 (2012).

G. Fiksel, S. X. Hu, V. N. Goncharov, D. D. Meyerhofer, T. C. Sangster, V. A. Smalyuk, B. Yaakobi, M. J. Bonino, and R. Jungquist, "Experimental Reduction of Laser Imprinting and Rayleigh–Taylor Growth in Spherically Compressed, Medium-Z–Doped Plastic Targets," Phys. Plasmas **19**, 062704 (2012).

G. Fiksel, F. J. Marshall, C. Mileham, and C. Stoeckl, "Note: Spatial Resolution of Fuji BAS-TR and BAS-SR Imaging Plates," Rev. Sci. Instrum. **83**, 086103 (2012).

C. J. Forrest, V. Yu. Glebov, V. N. Goncharov, A. Pruyne, J. P. Knauer, P. B. Radha, M. Romanofsky, T. C. Sangster, M. J. Shoup III, C. Stoeckl, D. T. Casey, M. Gatu-Johnson, and S. Gardner, "High-Resolution Spectroscopy Used to Measure ICF Neutron Spectra on OMEGA," Rev. Sci. Instrum. **83**, 10D919 (2012).

D. E. Fratanduono, J. H. Eggert, T. R. Boehly, M. A. Barrios, D. D. Meyerhofer, B. J. Jensen, and G. W. Collins, "Index of Refraction of Shock-Released Materials," J. Appl. Phys. **110**, 083509 (2011).

D. H. Froula, R. Boni, M. Bedzyk, R. Brown, R. S. Craxton, T. Duffy, F. Ehrne, S. Ivancic, R. Jungquist, N. Kugland,

J. Puth, R. G. Roides, M. C. Rushford, W. Seka, M. J. Shoup III, W. Theobald, and D. Weiner, "Optical Diagnostic Suite (Schlieren, Interferometry, and Grid-Image Refractometry) on OMEGA EP Using a 10-ps, 263-nm Probe Beam," Rev. Sci. Instrum. **83**, 10E523 (2012).

D. H. Froula, I. V. Igumenshchev, D. T. Michel, D. H. Edgell, R. Follett, V. Yu. Glebov, V. N. Goncharov, J. Kwiatkowski, F. J. Marshall, P. B. Radha, W. Seka, C. Sorce, S. Stagnitto, C. Stoeckl, and T. C. Sangster, "Increasing Hydrodynamic Efficiency by Reducing Cross-Beam Energy Transfer in Direct-Drive-Implosion Experiments," Phys. Rev. Lett. **108**, 125003 (2012).

D. H. Froula, B. Yaakobi, S. X. Hu, P.-Y. Chang, R. S. Craxton, D. H. Edgell, R. Follett, D. T. Michel, J. F. Myatt, W. Seka, R. W. Short, A. A. Solodov, and C. Stoeckl, "Saturation of the Two-Plasmon Decay Instability in Long-Scale-Length Plasmas Relevant to Direct-Drive Inertial Confinement Fusion," Phys. Rev. Lett. **108**, 165003 (2012).

L. Gao, P. M. Nilson, I. V. Igumenshchev, S. X. Hu, J. R. Davies, C. Stoeckl, M. G. Haines, D. H. Froula, R. Betti, and D. D. Meyerhofer, "Magnetic-Field Generation by Rayleigh–Taylor Instability in Laser-Driven Planar Plastic Targets," Phys. Rev. Lett. **109**, 115001 (2012).

V. Yu. Glebov, C. Forrest, J. P. Knauer, A. Pruyne, M. Romanofsky, T. C. Sangster, M. J. Shoup III, C. Stoeckl, J. A. Caggiano, M. L. Carman, T. J. Clancy, R. Hatarik, J.McNaney, and N. P. Zautseva, "Testing a New NIF Neutron Time-of-Flight Detector with a Bibenzyl Scintillator on OMEGA," Rev. Sci. Instrum. **83**, 10D309 (2012).

R. Q. Gram, A. She, R. S. Craxton, and D. R. Harding, "Thermal Conductivity of Solid Deuterium by the 3ω Method," J. Appl. Phys. **112**, 033504 (2012).

M. Guziewicz, W. Słysz, M. Borysiewicz, R. Kruszka, Z. Sidor, M. Juchniewicz, K. Golaszewska, J. Z. Domagała, W. Rzodkiewicz, J. Ratajczak, J. Bar, M. Węgrzecki, and R. Sobolewski, "Technology of Ultrathin NbN and NbTiN Films for Superconducting Photodetectors," Acta Phys. Pol A **120**, A76 (2011).

J. D. Hager, V. A. Smalyuk, S. X. Hu, J. P. Knauer, D. D. Meyerhofer, and T. C. Sangster, "Study of Rayleigh–Taylor Growth in Directly Driven Cryogenic Deuterium Targets," Phys. Plasmas **19**, 072707 (2012).

M. Hohenberger, P.-Y. Chang, G. Fiksel, J. P. Knauer, D. D. Meyerhofer, R. Betti, F. J. Marshall, F. H. Séguin, and R. D. Petrasso, "Inertial Confinement Fusion Implosions with Imposed Magnetic Field Compression Using the OMEGA Laser," Phys. Plasmas **19**, 056306 (2012).

S. X. Hu, G. Fiksel, V. N. Goncharov, S. Skupsky, D. D. Meyerhofer, and V. A. Smalyuk, "Mitigating Laser Imprint in Direct-Drive Inertial Confinement Fusion Implosions with High-Z Dopants," Phys. Rev. Lett. **108**, 195003 (2012).

S. X. Hu, V. N. Goncharov, and S. Skupsky, "Burning Plasmas with Ultrashort Soft-X-Ray Flashing," Phys. Plasmas **19**, 072703 (2012).

S. X. Hu, B. Militzer, V. N. Goncharov, and S. Skupsky, "First-Principles Equation-of-State Table of Deuterium for Inertial Confinement Fusion Applications," Phys. Rev. B **84**, 224109 (2011).

I. V. Igumenshchev, W. Seka, D. H. Edgell, D. T. Michel, D. H. Froula, V. N. Goncharov, R. S. Craxton, L. Divol, R. Epstein, R. Follett, J. H. Kelly, T. Z. Kosc, A. V. Maximov, R. L. McCrory, D. D. Meyerhofer, P. Michel, J. F. Myatt, T. C. Sangster, A. Shvydky, S. Skupsky, and C. Stoeckl, "Crossed-Beam Energy Transfer in Direct-Drive Implosions," Phys. Plasmas **19**, 056314 (2012).

I. Íñiguez-de-la-Torre, S. Purohit, V. Kaushal, M. Margala, M. Gong, R. Sobolewski, D. Wolpert, P. Ampadu, T. González, and J. Mateos, "Exploring Digital Logic Design Using Ballistic Deflection Transistors Through Monte Carlo Simulations," IEEE Trans. Nanotech. **10**, 1337 (2011).

I. Iñiguez-de-la-Torre, H. Rodilla, J. Mateos, T. González, H. Irie, and R. Sobolewski, "Monte Carlo Studies of the Intrinsic Time-Domain Response of Nanoscale Three-Branch Junctions," J. Appl. Phys. **111**, 084511 (2012).

J. Katz, R. Boni, M. J. Shoup III, R. Follett, and D. H. Froula, "A Reflective Optical Transport System for Ultraviolet Thomson Scattering from Electron Plasma Waves on OMEGA," Rev. Sci. Instrum. **83**, 10E349 (2012).

B. E. Kruschwitz, S.-W. Bahk, J. Bromage, M. D. Moore, and D. Irwin, "Accurate Target-Plane Focal-Spot Characterization in High-Energy Laser Systems Using Phase Retrieval," Opt. Express **20**, 20,874 (2012).

T. Y.-H. Lee, Q. Wang, J. U. Wallace, and S. H. Chen, "Temporal Stability of Blue Phosphorescent Organic Light-Emitting Diodes Affected by Thermal Annealing of Emitting Layers," J. Mater. Chem. **22**, 23,175 (2012).

K. A. Marsh, C. E. Clayton, C. Joshi, W. Lu, W. B. Mori, A. Pak, L. O. Silva, N. Lemos, R. A. Fonseca, S. de Freitas Martins, F. Albert, T. Doeppner, C. Filip, D. Froula, S. H. Glenzer, D. Price, J. Ralph, and B. B. Pollock, "Laser Wakefield Accelerator Beyond 1 GeV Using Ionization Induced Injection," in the *Proceedings of the Particle Acceleration Conference* (IEEE, New York, 2011), pp. 707–711.

F. J. Marshall, "Compact Kirkpatrick–Baez Microscope Mirrors for Imaging Laser–Plasma X-Ray Emission," Rev. Sci. Instrum. **83**, 10E518 (2012).

K. Mehrotra, H. P. Howard, S. D. Jacobs, and J. C. Lambropoulos, "Nanoindentation of High-Aspect Ratio Pillar Structures on Optical Multilayer Dielectric Diffraction Gratings," AIP Advances **1**, 042179 (2011).

D. T. Michel, C. Sorce, R. Epstein, N. Whiting, I. V. Igumenshchev, R. Jungquist, and D. H. Froula, "Shell-Trajectory Measurements from Direct-Drive Experiments," Rev. Sci. Instrum. **83**, 10E530 (2012).

M. Mikulics, J. Zhang, J. Serafini, R. Adam, D. Grützmacher, and R. Sobolewski, "Subpicosecond Electron-Hole Recombination Time and Terahertz-Bandwidth Photoresponse in Freestanding GaAs Epitaxial Mesoscopic Structures," Appl. Phys. Lett. **101**, 031111 (2012).

M. Millecchia, S. P. Regan, R. E. Bahr, M. Romanofsky, and C. Sorce, "Streaked X-Ray Spectrometer Having a Discrete Selection of Bragg Geometries for Omega," Rev. Sci. Instrum. **83**, 10E107 (2012).

J. F. Myatt, J. Zhang, J. A. Delettrez, A. V. Maximov, R. W. Short, W. Seka, D. H. Edgell, D. F. DuBois, D. A. Russell, and H. X. Vu, "The Dynamics of Hot-Electron Heating in Direct-Drive-Implosion Experiments Caused by Two-Plasmon-Decay Instability," Phys. Plasmas **19**, 022707 (2012).

P. M. Nilson, J. R. Davies, W. Theobald, P. A. Jaanimagi, C. Mileham, R. K. Jungquist, C. Stoeckl, I. A. Begishev, A. A. Solodov, J. F. Myatt, J. D. Zuegel, T. C. Sangster, R. Betti, and D. D. Meyerhofer, "Time-Resolved Measurements of Hot-Electron Equilibration Dynamics in High-Intensity Laser Interactions with Thin-Foil Solid Targets," Phys. Rev. Lett. **108**, 085002 (2012).

A. V. Okishev, "Highly Efficient Room-Temperature Yb:YAG Ceramic Laser and Regenerative Amplifier," Opt. Lett. **37**, 1199 (2012).

A. V. Okishev, C. Dorrer, Y. Fisher, and M. Pavia, "A Multi-wavelength, Variable-Pulse-Width, Diode-Pumped Laser System," in *Solid State Lasers XXI: Technology and Devices*, edited by W. A. Clarkson and R. K. Shori (SPIE, Bellingham, WA, 2012), Vol. 8235, Paper 82350Y.

J. B. Oliver, P. Kupinski, A. L. Rigatti, A. W. Schmid, J. C. Lambropoulos, S. Papernov, A. Kozlov, S. Smith, and R. D. Hand, "Stress Compensation in Hafnia/Silica Optical Coatings by Inclusion of Alumina Layers," Opt. Express **20**, 16,596 (2012).

B. B. Pollock, G. R. Tynan, F. Albert, C. Filip, S. H. Glenzer, J. Meinecke, A. Pak, J. E. Ralph, C. E. Clayton, C. Joshi, K. A. Marsh, J. Shaw, K. L. Herpoldt, and D. H. Froula, "The Effects of a Density Mismatch in a Two-Stage LWFA," in the *Proceedings of the Particle Acceleration Conference* (IEEE, New York, 2011), pp. 1421–1423.

P. B. Radha, J. A. Marozas, F. J. Marshall, A. Shvydky, T. J. B. Collins, V. N. Goncharov, R. L. McCrory, P. W. McKenty, D. D. Meyerhofer, T. C. Sangster, and S. Skupsky, "OMEGA Polar-Drive Target Designs," Phys. Plasmas **19**, 082704 (2012).

S. P. Regan, R. Epstein, B. A. Hammel, L. J. Suter, J. Ralph, H. Scott, M. A. Barrios, D. K. Bradley, D. A. Callahan, C. J. Cerjan, G. W. Collins, S. N. Dixit, T. Doeppner, M. J. Edwards, D. R. Farley, S. Glenn, S. H. Glenzer, I. E. Golovkin, S. W. Haan, A. Hamza, D. G. Hicks, N. Izumi, J. D. Kilkenny, J. L. Kline, G. A. Kyrala, O. L. Landen, T. Ma, J. J. MacFarlane, R. C. Mancini, R. L. McCrory, N. B. Meezan, D. D. Meyerhofer, A. Nikroo, K. J. Peterson, T. C. Sangster, P. Springer, and R. P. J. Town, "Hot-Spot Mix in Ignition-Scale Implosions on the NIF," Phys. Plasmas **19**, 056307 (2012).

S. P. Regan, R. Epstein, B. A. Hammel, L. J. Suter, J. Ralph, H. Scott, M. A. Barrios, D. K. Bradley, D. A. Callahan, G. W. Collins, S. N. Dixit, M. J. Edwards, D. R. Farley, S. H. Glenzer, I. E. Golovkin, S. W. Haan, A. Hamza, D. G. Hicks, N. Izumi, J. D. Kilkenny, J. L. Kline, G. A. Kyrala, O. L. Landen,

T. Ma, J. J. MacFarlane, A. J. MacKinnon, R. C. Mancini, F. J. Marshall, R. L. McCrory, N. B. Meezan, D. D. Meyerhofer, A. Nikroo, K. J. Peterson, T. C. Sangster, P. Springer, and R. P. J. Town, "Diagnosing Implosions at the National Ignition Facility with X-Ray Spectroscopy," in *The 17th International Conference on Atomic Processes in Plasmas (ICAPiP), AIP Conf. Proc. 1438*, edited by K. Aggarwal, and F. Shearer (American Institute of Physics, New York, 2012), pp. 49–54.

J. E. Schoenly, W. Seka, J. D. B. Featherstone, and P. Rechmann, "Near-UV Laser Treatment of Extrinsic Dental Enamel Stains," Lasers Surg. Med. **44**, 339 (2012).

C. Stoeckl, J. A. Delettrez, R. Epstein, G. Fiksel, D. Guy, M. Hohenberger, R. K. Jungquist, C. Mileham, P. M. Nilson, T. C. Sangster, M. J. Shoup III, and W. Theobald, "Soft X-Ray Backlighting of Direct-Drive Implosions Using a Spherical Crystal Imager on OMEGA," Rev. Sci. Instrum. **83**, 10E501 (2012).

C. Stoeckl, G. Fiksel, D. Guy, C. Mileham, P. M. Nilson, T. C. Sangster, M. J. Shoup III, and W. Theobald, "A Spherical Crystal Imager for OMEGA EP," Rev. Sci. Instrum. **83**, 033107 (2012).

A. Trajkovska Petkoska and S. D. Jacobs, "The Manufacture, Characterization and Manipulation of Polymer Cholesteric Liquid Crystal Flakes and Their Possible Applications," J. Mater. Sci. Eng. A **2**, 137 (2012).

A. J. Visco, R. P. Drake, S. H. Glenzer, T. Döppner, G. Gregori, D. H. Froula, and M. J. Grosskopf, "Measurement of Radiative Shock Properties by X-Ray Thomson Scattering," Phys. Rev. Lett. **108**, 145001 (2012).

B. Yaakobi, P.-Y. Chang, A. Solodov, C. Stoeckl, D. H. Edgell, R. S. Craxton, S. X. Hu, J. F. Myatt, F. J. Marshall, W. Seka, and D. H. Froula, "Fast-Electron Generation in Long-Scale-Length Plasmas," Phys. Plasmas **19**, 012704 (2012).

J.-H. Yang, R. S. Craxton, and M. G. Haines, "Explicit General Solutions to Relativistic Electron Dynamics in Plane-Wave Electromagnetic Fields and Simulations of Ponderomotive Acceleration," Plasma Phys. Control. Fusion **53**, 125006 (2011).

J. Zhang, A. Belousov, J. Karpiński, B. Batlogg, and R. Sobolewski, "Time-Resolved Femtosecond Optical Characterization of Multi-Photon Absorption in High-Pressure-Grown $Al_{0.86}Ga_{0.14}N$ Single Crystals," J. Appl. Phys. **110**, 113112 (2011).

OMEGA External Users' Publications

T. Caillaud, O. Landoas, M. Briat, S. Kime, B. Rossé, I. Thfoin, J. L. Bourgade, L. Disdier, V. Yu. Glebov, F. J. Marshall, and T. C. Sangster, "Development of the Large Neutron Imaging System for Inertial Confinement Fusion Experiments," Rev. Sci. Instrum. **83**, 033502 (2012).

D. A. Callahan, N. B. Meezan, S. H. Glenzer, A. J. MacKinnon, L. R. Benedetti, D. K. Bradley, J. R. Celeste, P. M. Celliers, S. N. Dixit, T. Döppner, E. G. Dzentitis, S. Glenn, S. W. Haan, C. A. Haynam, D. G. Hicks, D. E. Hinkel, O. S. Jones, O. L. Landen, R. A. London, A. G. MacPhee, P. A. Michel, J. D. Moody, J. E. Ralph, H. F. Robey, M. D. Rosen, M. B. Schneider, D. J. Strozzi, L. J. Suter, R. P. J. Town, K. Widmann, E. A. Williams, M. J. Edwards, B. J. MacGowan, J. D. Lindl, L. J. Atherton, G. A. Kyrala, J. L. Kline, R. E. Olson, D. Edgell, S. P. Regan, A. Nikroo, H. Wilkins, J. D. Kilkenny, and A. S. Moore, "The Velocity Campaign for Ignition on NIF," Phys. Plasmas **19**, 056305 (2012) (invited).

D. T. Casey, J. A. Frenje, M. Gatu Johnson, M. J.-E. Manuel, H. G. Rinderknecht, N. Sinenian, F. H. Séguin, C. K. Li, R. D. Petrasso, P. B. Radha, J. A. Delettrez, V. Yu. Glebov, D. D. Meyerhofer, T. C. Sangster, D. P. McNabb, P. A. Amendt, R. N. Boyd, J. R. Rygg, H. W. Herrmann, Y. H. Kim, and A. D. Bacher, "Evidence for Stratification of Deuterium-Tritium Fuel in Inertial Confinement Fusion Implosions," Phys. Rev. Lett. **108**, 075002 (2012).

D. T. Casey, J. A. Frenje, M. Gatu Johnson, M. J.-E. Manuel, N. Sinenian, A. B. Zylstra, F. H. Séguin, C. K. Li, R. D. Petrasso, V. Yu. Glebov, P. B. Radha, D. D. Meyerhofer, T. C. Sangster, D. P. McNabb, P. A. Amendt, R. N. Boyd, S. P. Hatchett, S. Quaglioni, J. R. Rygg, I. J. Thomson, A. D. Bacher, H. W. Herrmann, and Y. H. Kim, "Measurements of the $T(t,2n)^4He$ Neutron Spectrum at Low Reactant Energies from Inertial Confinement Implosions," Phys. Rev. Lett. **109**, 025003 (2012).

M. Chini, B. Zhao, H. Wang, Y. Cheng, S. X. Hu, and Z. Chang, "Subcycle ac Stark Shift or Helium Excited States Probed with Isolated Attosecond Pulses," Phys. Rev. Lett. **109**, 073601 (2012).

J. M. N. Djiokap, S. X. Hu, W.-C. Jiang, L.-Y. Peng, and A. F. Starace, "Enhanced Asymmetry in Few-Cycle Attosecond Pulse Ionization of He in the Vicinity of Autoionizing," New J. Phys. **14**, 095010 (2012).

E. S. Dodd, J. F. Benage, G. A. Kyrala, D. C. Wilson, F. J. Wysocki, W. Seka, V. Yu. Glebov, C. Stoeckl, and J. A. Frenje, "The Effects of Laser Absorption on Direct-Drive Capsule Experiments on OMEGA," Phys. Plasmas **19**, 042703 (2012).

S. H. Glenzer, D. A. Callahan, A. J. MacKinnon, J. L. Kline, G. Grim, E. T. Alger, R. L. Berger, L. A. Bernstein, R. Betti, D. L. Bleuel, T. R. Boehly, D. K. Bradley, S. C. Burkhart, R. Burr, J. A. Caggiano, C. Castro, D. T. Casey, C. Choate, D. S. Clark, P. Celliers, C. J. Cerjan, G. W. Collins, E. L. Dewald, P. DiNicola, J. M. DiNicola, L. Divol, S. Dixit, T. Döppner, R. Dylla-Spears, E. Dzenitis, M. Eckart, G. Erbert, D. Farley, J. Fair, D. Fittinghoff, M. Frank, L. J. A. Frenje, S. Friedrich, M. Gatu Johnson, C. Gibson, E. Giraldez, V. Glebov, S. Glenn, N. Guler, S. W. Haan, B. J. Haid, B. A. Hammel, A. V. Hamza, C. A. Haynam, G. M. Hestand, M. Hermann, H. W. Hermann, D. G. Hicks, D. E. Hinkel, J. P. Holder, D. M. Holunda, J. B. Horner, W. W. Hsing, H. Huang, N. Izumi, M. Jackson, O. S. Jones, D. H. Kalantar, R. Kauffman, J. D. Kilkenny, R. K. Kirkwood, J. Klingmann, T. Kohut, J. P. Knauer, J. A. Koch, B. Kozioziemki, G. A. Kyrala, A. L. Kritcher, J. Kroll, K. La Fortune, L. Lagin, O. L. Landen, D. W. Larson, D. LaTray, R. J. Leeper, S. Le Pape, J. D. Lindl, R. Lowe-Webb, T. Ma, J. McNaney, A. G. MacPhee, T. N. Malsbury, E. Mapoles, C. D. Marshall, N. B. Maazan, F. Merrill, P. Michel, J. D. Moody, A. S. Moore, M. Moran, K. A. Moreno, D. H. Munro, B. R. Nathan, A. Nikroo, R. E. Olson, C. D. Orth, A. E. Pak, P. K. Patel, T. Parham, R. Petrasso, J. E. Ralph, H. Rinderknecht, S. P. Regan, H. F. Robey, J. S. Ross, M. D. Rosen, R. Sacks, J. D. Salmonson, R. Saunders, J. Sater, C. Sangster, M. B. Schneider, F. H. Séguin, M. J. Shaw, B. K. Spears, P. T. Springer, W. Stoeffl, L. J. Suter, C. A. Thomas, R. Tommasini, R. P. J. Town, C. Walters, S. Weaver, S. V. Weber, P. J. Wegner, P. K. Whitman, K. Widmann, C. C. Widmayer, C. H. Wilde, D. C. Wilson, B. Van Wonterghem, B. J. MacGowan, L. J. Atherton, M. J. Edwards, and E. I. Moses, "Cryogenic Thermonuclear Fuel Implosions on the National Ignition Facility," Phys. Plasmas **19**, 056318 (2012) (invited).

S. H. Glenzer, B. K. Spears, M. J. Edwards, E. T. Alger, R. L. Berger, D. L. Bleuel, D. K. Bradley, J. A. Caggiano, D. A. Callahan, C. Castro, D. T. Casey, C. Choate, D. S. Clark, C. J. Cerjan, G. W. Collins, E. L. Dewald, J.-M. G. Di Nicola, P. Di Nicola, L. Divol, S. N. Dixit, T. Döppner, R. Dylla-Spears, E. G. Dzenitis, J. E. Fair, L. J. A. Frenje, M. Gatu Johnson, E. Giraldez, V. Glebov, S. M. Glenn, S. W. Haan, B. A. Hammel, S. P. Hatchett II, C. A. Haynam, R. F. Heeter, G. M. Heestand, H. W. Herrmann, D. G. Hicks, D. M. Holunga, J. B. Horner, H. Huang, N. Izumi, O. S. Jones, D. H. Kalantar, J. D. Kilkenny, R. K. Kirkwood, J. L. Kline, J. P. Knauer, B. Kozioziemski, A. L. Kritcher, J. J. Kroll, G. A. Kyrala, K. N. LaFortune, O. L. Landen, D. L. Larson, R. J. Leeper, S. Le Pape, J. D. Lindl, T. Ma, A. J. Mackinnon, A. G. MacPhee, E. Mapoles, P. W. McKenty, N. B. Meezan, P. Michel, J. L. Milovich, J. D. Moody, A. S. Moore, M. Moran, K. A. Moreno, D. H. Munro, B. R. Nathan, A. Nikroo, R. E. Olson, C. D. Orth, A. Pak, P. K. Patel, T. Parham, R. Petrasso, J. E. Ralph, H. Rinderknecht, S. P. Regan, H. F. Robey, J. S. Ross, J. D. Salmonson, C. Sangster, J. Sater, M. B. Schneider, F. H. Séguin, M. J. Shaw, M. J. Shoup, P. T. Springer, W. Stoeffl, L. J. Suter, C. A. Thomas, R. P. J. Town, C. Walters, S. V. Weber, P. J. Wegner, C. Widmayer, P. K. Whitman, K. Widmann, D. C. Wilson, B. M. Van Wonterghem, B. J. MacGowan, L. J. Atherton, and E. I. Moses, "First Implosion Experiments with Cryogenic Thermonuclear Fuel on the National Ignition Facility," Plasma Phys. Control. Fusion **54**, 045013 (2012).

A. J. Harvey-Thomson, S. V. Lebedev, S. Patankar, S. N. Bland, G. Burdiak, J. P. Chittenden, A. Colaitis, P. De Grouchy, H. W. Doyle, G. N. Hall, E. Khoory, M. Hohenberger, L. Pickworth, F. Suzuki-Vidal, R. A. Smith, J. Skidmore, L. Suttle, and G. F. Swadling, "Optical Thomson Scattering Measurements of Plasma Parameters in the Ablation Stage of Wire Array *Z* Pinches," Phys. Rev. Lett. **108**, 145002 (2012).

A. J. Harvey-Thompson, S. V. Lebedev, S. Patankar, S. N. Bland, G. Burdiak, J. P. Chittenden, A. Colaitis, P. De Grouchy, G. N. Hall, E. Khoory, M. Hohenberger, L. Pickworth, F. Suzuki-Vidal, R. A. Smith, J. Skidmore, L. Suttle, and G. F. Swadling, "Optical Thomson Scattering Measurements of Cylindrical Wire Array Parameters," Phys. Plasmas **19**, 056303 (2012).

O. S. Jones, C. J. Cerjan, M. M. Marinak, J. L. Milovich, H. F. Robey, P. T. Springer, L. R. Benedetti, D. L. Bleuel, E. J. Bond, D. K. Bradley, D. A. Callahan, J. A. Caggiano, P. M. Celliers,

D. S. Clark, S. M. Dixit, T. Döppner, R. J. Dylla-Spears, E. G. Dzentitis, D. R. Farley, S. M. Glenn, S. H. Glenzer, S. W. Haan, B. J. Haid, C. A. Haynam, D. G. Hicks, B. J. Kozioziemski, K. N. LaFortune, O. L. Landen, E. R. Mapoles, A. J. MacKinnon, J. M. McNaney, N. B. Meezan, P. A. Michel, J. D. Moody, M. J. Moran, D. H. Munro, M. V. Patel, T. G. Parham, J. D. Sater, S. M. Sepke, B. K. Spears, R. P. J. Town, S. V. Weber, K. Widmann, C. C. Widmayer, E. A. Williams, L. J. Atherton, M. J. Edwards, J. D. Lindl, B. J. MacGowan, L. J. Suter, R. E. Olson, H. W. Hermann, J. L. Kline, G. A. Kyrala, D. C. Wilson, J. Frenje, T. R. Boehly, V. Glebov, J. P. Knauer, A. Nikroo, H. Wilkens, and J. D. Kilkenny, "A High-Resolution Integrated Model of the National Ignition Campaign Cryogenic Layered Experiments," Phys. Plasmas **19**, 056315 (2012) (invited).

Y. Kim, J. M. Mack, H. W. Herrmann, C. S. Young, G. M. Hale, S. Caldwell, N. M. Hoffman, S. C. Evans, T. J. Sedillo, A. McEvoy, J. Langenbrunner, H. H. Hsu, M. A. Huff, S. Batha, C. J. Horsfield, M. S. Rubery, W. J. Garbett, W. Stoeffl, E. Grafil, L. Bernstein, J. A. Church, D. B. Sayre, M. J. Rosenberg, C. Waugh, H. G. Rinderknecht, M. Gatu Johnson, A. B. Zylstra, J. A. Frenje, D. T. Casey, R. D. Petrasso, E. K. Miller, V. Yu. Glebov, C. Stoeckl, and T. C. Sangster, "D-T Gamma-to-Neutron Branching Ratio Determined from Inertial Confinement Fusion Plasmas," Phys. Plasmas **19**, 056313 (2012) (invited).

Y. Kim, J. M. Mack, H. W. Herrmann, C. S. Young, G. M. Hale, S. Caldwell, N. M. Hoffman, S. C. Evans, T. J. Sedillo, A. McEvoy, J. Langenbrunner, H. H. Hsu, M A. Huff, S. Batha, C. J. Horsfield, M. S. Rubery, W. J. Garbett, W. Stoeffl, E Grafil, L. Bernstein, J. A. Church, D. B. Sayre, M. J. Rosenberg, C. Waugh, H. G. Rinderknecht, M. Gatu Johnson, A. B. Zylstra, J. A. Frenje, D. T. Casey, R. D. Petrasso, E. K. Miller, V. Yu. Glebov, C. Stoeckl, and T. C. Sangster, "Determination of the Deuterium-Tritium Branching Ratio Based on Inertial Confinement Fusion Implosions," Phys. Rev. C **85**, 061601(R) (2012).

C. K. Li, F. H. Séguin, J. A. Frenje, M. J. Rosenberg, H. G. Rinderknecht, A. B. Zylstra, R. D. Petrasso, P. A. Amendt, O. L. Landen, A. J. Mackinnon, R. P. J. Town, S. C. Wilks, R. Betti, D. D. Meyerhofer, J. M. Soures, J. Hund, J. D. Kilkenny, and A. Nikroo, "Impeding Hohlraum Plasma Stagnation in Inertial-Confinement Fusion," Phys. Rev. Lett. **108**, 025001 (2012).

A. J. Mackinnon, J. L. Kline, S. N. Dixit, S. H. Glenzer, M. J. Edwards, D. A. Callahan, N. B. Meezan, S. W. Haan, J. D. Kilkenny, T. Döppner, D. R. Farley, J. D. Moody, J. E. Ralph, B. J. MacGowan, O. L. Landen, H. F. Robey, T. R. Boehly, P. M. Celliers, J. H. Eggert, K. Krauter, G. Frieders, G. F. Ross, D. G. Hicks, R. E. Olson, S. V. Weber, B. K. Spears, J. D. Salmonsen, P. Michel, L. Divol, B. Hammel, C. A. Thomas, D. S. Clark, O. S. Jones, P. T. Springer, C. J. Cerjan, G. W. Collins, V. Y. Glebov, J. P. Knauer, C. Sangster, C. Stoeckl, P. McKenty, J. M. McNaney, R. J. Leeper, C. L. Ruiz, G. W. Cooper, A. G. Nelson, G. G. A. Chandler, K. D. Hahn, M. J. Moran, M. B. Schneider, N. E. Palmer, R. M. Bionta, E. P. Hartouni, S. LePape, P. K. Patel, N. Izumi, R. Tommasini, E. J. Bond, J. A. Caggiano, R. Hatarik, G. P. Grim, F. E. Merrill, D. N. Fittinghoff, N. Guler, O. Drury, D. C. Wilson, H. W. Herrmann, W. Stoeffl, D. T. Casey, M. G. Johnson, J. A. Frenje, R. D. Petrasso, A. Zylestra, H. Rinderknecht, D. H. Kalantar, J. M. Dzenitis, P. Di Nicola, D. C. Eder, W. H. Courdin, G. Gururangan, S. C. Burkhart, S. Friedrich, D. L. Blueuel, L. A. Bernstein, M. J. Eckart, D. H. Munro, S. P. Hatchett, A. G. Macphee, D. H. Edgell, D. K. Bradley, P. M. Bell, S. M. Glenn, N. Simanovskaia, M. A. Barrios, R. Benedetti, G. A. Kyrala, R. P. J. Town, E. L. Dewald, J. L. Milovich, K. Widmann, A. S. Moore, G. LaCaille, S. P. Regan, L. J. Suter, B. Felker, R. C. Ashabranner, M. C. Jackson, R. Prasad, M. J. Richardson, T. R. Kohut, P. S. Datte, G. W. Krauter, J. J. Klingman, R. F. Burr, T. A. Land, M. R. Hermann, D. A. Latray, R. L. Saunders, S. Weaver, S. J. Cohen, L. Berzins, S. G. Brass, E. S. Palma, R. R. Lowe-Webb, G. N. McHalle, P. A. Arnold, L. J. Lagin, C. D. Marshall, G. K. Brunton, D. G. Mathisen, R. D. Wood, J. R. Cox, R. B. Ehrlich, K. M. Knittel, M. W. Bowers, R. A. Zacharias, B. K. Young, J. P. Holder, J. R. Kimbrough, T. Ma, K. N. La Fortune, C. C. Widmayer, M. J. Shaw, G. V. Erbert, K. S. Jancaitis, J. M. DiNicola, C. Orth, G. Heestand, R. Kirkwood, C. Haynam, P. J. Wegner, P. K. Whitman, A. Hamza, E. G. Dzenitis, R. J. Wallace, S. D. Bhandakar, T. G. Parham, R. Dylla-Spears, E. R. Mapoles, B. J. Kozioziemski, J. D. Sater, C. F. Walters, B. J. Haid, J. Fair, A. Nikroo, E. Giraldez, K. Moreno, B. Vanwonterghem, R. L. Kauffman, S. Batha, D. W. Larson, R. J. Fortner, D. H. Schneider, J. D. Lindl, R. W. Patterson, L. J. Atherton, and E. I. Moses, "Assembly of High-Areal-Density Deuterium-Tritium Fuel from Indirectly Driven Cryogenic Implosions," Phys. Rev. Lett. **108**, 215005 (2012).

M. J.-E. Manuel, C. K. Li, F. H. Séguin, J. Frenje, D. T. Casey, R. D. Petrasso, S. X. Hu, R. Betti, J. D. Hager, D. D. Meyerhofer, and V. A. Smalyuk, "First Measurements of Rayleigh-Taylor-Induced Magnetic Fields in Laser-Produced Plasmas," Phys. Rev. Lett. **108**, 255006 (2012).

H.-S. Park, D. D. Ryutov, J. S. Ross, N. L. Kugland, S. H. Glenzer, C. Plechaty, S. M. Pollaine, B. A. Remington, A. Spitkovsky, L. Gargate, G. Gregori, A. Bell, C. Murphy, Y. Sakawa, Y. Kuramitsu, T. Morita, H. Takabe, D. H. Froula, G. Fiksel, F. Miniati, M. Koenig, A. Ravasio, A. Pelka, E. Liang, N. Woolsey, C. C. Kuranz, R. P. Drake, and M. J. Grosskopf, "Studying Astrophysical Collisionless Shocks with Counterstreaming Plasmas from High Power Lasers," High Energy Density Phys. **8**, 38 (2012).

H. G. Rinderknecht, M. Gatu Johnson, A. B. Zylstra, N. Sinenian, M. J. Rosenberg, J. A. Frenje, C. J. Waugh, C. K. Li, F. H. Séguin, R. D. Petrasso, J. R. Rygg, J. R. Kimbrough, A. MacPhee, G. W. Collins, D. Hicks, A. Mackinnon, P. Bell, R. Bionta, T. Clancy, R. Zacharias, T. Döppner, H.-S. Park, S. LePape, O. Landen, N. Meezan, E. I. Moses, V. U. Glebov, C. Stoeckl, T. C. Sangster, R. Olson, J. Kline, and J. Kilkenny, "A Novel Particle Time of Flight Diagnostic for Measurements of Shock- and Compression-Bang Times in D^3He and DT Implosions at the NIF," Rev. Sci. Instrum. **83**, 10D902 (2012).

H. F. Robey, T. R. Boehly, P. M. Celliers, J. H. Eggert, D. Hicks, R. F. Smith, R. Collins, M. W. Bowers, K. G. Krauter, P. S. Datte, D. H. Munro, J. L. Milovich, O. S. Jones, P. A. Michel, C. A. Thomas, R. E. Olson, S. Pollaine, R. P. J. Town, S. Haan, D. Callahan, D. Clark, J. Edwards, J. L. Kline, S. Dixit, M. B. Schneider, E. L. Dewald, K. Wildmann, J. D. Moody, T. Döppner, H. B. Radousky, A. Throop, D. Kalantar, P. DiNicola, A. Nikroo, J. J. Kroll, A. V. Hamza, J. B. Horner, S. D. Bhandarkar, E. Dzenitis, E. Alger, E. Giraldez, C. Castro, K. Moreno, C. Haynam, K. N. LaFortune, C. Widmayer, M. Shaw, K. Jancaitis, T. Parham, D. M. Holunga, C. F. Walters, B. Haid, E. R. Mapoles, J. Sater, C. R. Gibson, T. Malsbury, J. Fair, D. Trummer, K. R. Coffee, B. Burr, L. V. Berzins, C. Choate, S. J. Brereton, S. Azevedo, H. Chandrasekaran, D. C. Eder, N. D. Masters, A. C. Fisher, P. A. Sterne, B. K. Young, O. L. Landen, B. M. Van Wonterghem, B. J. MacGowan, J. Atherton, J. D. Lindl, D. D. Meyerhofer, and E. Moses, "Shock Timing Experiments on the National Ignition Facility: Initial Results and Comparison with Simulation," Phys. Plasmas **19**, 042706 (2012).

H. F. Robey, P. M. Celliers, J. L. Kline, A. J. Mackinnon, T. R. Boehly, O. L. Landen, J. H. Eggert, D. Hicks, S. Le Pape, D. R. Farley, M. W. Bowers, K. G. Krauter, D. H. Munro, O. S. Jones, J. L. Milovich, D. Clark, B. K. Spears, R. P. J. Town, S. W. Haan, S. Dixit, M. B. Schneider, E. L. Dewald, K. Wodmann, J. D. Moody, T. D. Döppner, H. B. Radousky, A. Nikroo, J. J. Kroll, A. V. Hamza, J. B. Horner, S. D. Bhandarkar, E. Dzenitis, E. Alger, E. Giraldez, C. Castro, K. Moreno, C. Haynam, K. N. LaFortune, C. Widmayer, M. Shaw, K. Jancaitis, T. Parham, D. M. Holunga, C. F. Walters, B. Haid, T. Malsbury, D. Trummer, K. R. Coffee, B. Burr, L. V. Berzins, C. Choate, S. J. Brereton, S. Azevedo, H. Chandrasekaran, S. Glenzer, C. Caggiano, J. P. Knauer, J. A. Frenje, D. T. Casey, M. Gatu Johnson, F. H. Séguin, B. K. Young, M. J. Edwards, B. M. Van Wonterghem, J. Kilkenny, B. J. MacGowan, J. Atherton, J. D. Lindl, D. D. Meyerhofer, and E. I. Moses, "Precision Shock Tuning on the National Ignition Facility," Phys. Rev. Lett. **108**, 215004 (2012).

J. S. Ross, S. H. Glenzer, P. Amendt, R. Berger, L. Divol, N. L. Kugland, O. L. Landen, C. Plechaty, B. Remington, D. Ryutov, W. Rozmus, D. H. Froula, G. Fiksel, C. Sorce, Y. Kuramitsu, T. Morita, Y. Sakawa, H. Takabe, R. P. Drake, M. Grosskopf, C. Kuranz, G. Gregori, J. Meinecke, C. D. Murphy, M. Koenig, A. Pelka, A. Ravasio, T. Vinci, E. Liang, R. Presura, A. Spitkovsky, F. Miniati, and H.-S. Park, "Characterizing Counter-Streaming Interpenetrating Plasmas Relevant to Astrophysical Collisionless Shocks," Phys. Plasmas **19**, 056501 (2012) (invited).

F. H. Séguin, C. K. Li, M. J.-E. Manuel, H. G. Rinderknecht, N. Sinenian, J. A. Frenje, J. R. Rygg, D. G. Hicks, R. D. Petrasso, J. Delettrez, R. Betti, F. J. Marshall, and V. A. Smalyuk, "Time Evolution of Filamentation and Self-Generated Fields in the Coronae of Directly Driven Inertial-Confinement Fusion Capsules," Phys. Plasmas **19**, 012701 (2012).

L. Willingale, P. M. Nilson, A. G. R. Thomas, J. Cobble, R. S. Craxton, A. Maksinchuk, P. A. Norreys, T. C. Sangster, R. H. H. Scott, C. Stoeckl, C. Zulick, and K. Krushelnick, "Proton Probe Imaging of Fields Within a Laser-Generated Plasma Channel," IEEE Trans. Plasma Sci. **39**, 2616 (2011).

D. C. Wilson, P. S. Ebey, T. C. Sangster, W. T. Shmayda, V. Yu. Glebov, and R. A. Lerche, "Atomic Mix in Directly Driven Inertial Confinement Implosions," Phys. Plasmas **18**, 112707 (2011).

A. B. Zylstra, J. A. Frenje, F. H. Séguin, M. J. Rosenberg, H. G. Rinderknecht, M. Gatu Johnson, D. T. Casey, N. Sinenian, M. J.-E. Manuel, C. J. Waugh, H. W. Sio, C. K. Li, R. D. Petrasso, S. Friedrich, K. Knittel, R. Bionta, M. McKernan, D. Callahan, G. W. Collins, E. Dewald, T. Döppner, M. J. Edwards, S. Glenzer, D. G. Hicks, O. L. Landen, R. London, A. Mackinnon, N. Meezan, R. R. Prasad, J. Ralph, M. Richardson, J. R. Rygg,

S. Sepke, S. Weber, R. Zacharias, E. Moses, J. Kilkenny, A. Nikroo, T. C. Sangster, V. Glebov, C. Stoeckl, R. Olson, R. J. Leeper, J. Kline, G. Kyrala, and D. Wilson, "Charged-Particle Spectroscopy for Diagnosing Shock ρR and Strength in NIF Implosions," Rev. Sci. Instrum. **83**, 10D901 (2012).

A. B. Zylystra, C. K. Li, H. G. Rinderknecht, F. H. Séguin, R. D. Petrasso, C. Stoeckl, D. D. Meyerhofer, P. Nilson, T. C. Sangster, S. Le Pape, A. Mackinnon, and P. Patel, "Using High-Intensity Laser-Generated Energetic Protons to Radiograph Directly Driven Implosions," Rev. Sci. Instrum. **83**, 013511 (2012).

Conference Presentations

The following presentations were made at the 8th International Laser Operations Workshop, Aldermaston, U.K., 4–6 October 2011:

D. Canning, S. F. B. Morse, J. Qiao, T. Nguyen, B. E. Kruschwitz, and A. Kalb, "OMEGA EP Grating Compressor Chamber Operations."

B. E. Kruschwitz, M. D. Moore, and R. Jungquist, "OMEGA EP Focal-Spot Improvement Activities."

S. F. B. Morse, "A Polar-Drive-Irradiation Platform for NIF is Being Developed Using OMEGA."

J. Puth, "Omega Facility Status and Performance."

S. J. Stagnitto, J. Kwiatkowski, S. F. B. Morse, M. Labuzeta, and V. Guiliano, "Characterizing Debris-Shield Transmission Degradation and Estimating On-Target Energy."

G. Fiksel, A. Bhattacharjee, W. Fox, R. Betti, P.-Y. Chang, M. Hohenberger, and P. M. Nilson, "Studies of Magnetized and HED Plasmas—Recent Results and Future Plans," presented at the Center for Magnetized Self-Organization Meeting, Durham, NH, 17–20 October 2011.

S. Friedrich, T. J. Clancy, M. J. Eckart, M. J. Shoup III, T. Buczek, and V. Yu. Glebov, "High-Speed Diamond Detectors for Fast-Neutron Analysis of Inertial Confinement Fusion," presented at the IEEE Nuclear Science Symposium, Valencia, Spain, 23–29 October 2011.

J. H. Kelly, "The Optics of Inertial Confinement Fusion," presented at The Institute of Optics Colloquium, Rochester, NY, 31 October 2011.

J. Bromage, C. Dorrer, M. Millecchia, J. Bunkenburg, R. K. Jungquist, and J. D. Zuegel, "A Front End for Ultra-Intense OPCPA," presented at Light at Extreme Intensities, Szeged, Hungary, 14–18 November 2011.

The following presentations were made at the 53rd Annual Meeting of the APS Division of Plasma Physics, Salt Lake City, UT, 14–18 November 2011:

K. S. Anderson, R. Betti, P. W. McKenty, T. J. B. Collins, R. S. Craxton, J. A. Marozas, R. Nora, S. Skupsky, and L. J. Perkins, "Simulations of Shock-Ignition Targets for the NIF."

T. R. Boehly, V. N. Goncharov, W. Seka, S. X. Hu, J. A. Marozas, D. D. Meyerhofer, P. M. Celliers, D. G. Hicks, M. A. Barrios, D. E. Fratanduono, G. W. Collins, "Multiple Spherically Converging Shock Waves in Liquid Deuterium."

P.-Y. Chang, G. Fiksel, M. Hohenberger, J. P. Knauer, R. Betti, F. H. Séguin, C. K. Li, M. E. Manuel, and R. D. Petrasso, "Experiments and Simulations of Laser-Driven Magnetized ICF Targets on OMEGA."

T. J. B. Collins, J. A. Marozas, K. S. Anderson, R. Betti, R. S. Craxton, J. A. Delettrez, V. N. Goncharov, D. R. Harding, F. J. Marshall, R. L. McCrory, D. D. Meyerhofer, P. W. McKenty, P. B. Radha, A. Shvydky, S. Skupsky, J. D. Zuegel, "A Polar-Drive–Ignition Design for the National Ignition Facility" (invited).

R. S. Craxton, P. W. McKenty, E. J. Bond, S. Le Pape, A. J. MacKinnon, P. A. Michel, and J. D. Moody, "Three-Dimensional Distributions of Scattered Light in NIF 'Exploding-Pusher' Polar-Drive Experiments."

J. A. Delettrez, W. Seka, D. H. Froula, and T. J. B. Collins, "Three-Dimensional Numerical Investigation of Oblique Laser Irradiation of Planar Targets."

D. H. Edgell, J. Magoon, T. C. Sangster, M. J. Shoup III, F. J. Marshall, C. Stoeckl, V. Yu. Glebov, A. MacPhee, G. Krauter, S. Burns, J. Celeste, M. J. Eckart, J. R. Kimbrough, J. D. Kilkenny, G. Lacaille, N. B. Meezan, J. Parker, Z. Sober, and M. Thayne, "First Results from the South Pole Bang Time (SPBT) Diagnostic on the NIF."

R. Epstein, S. P. Regan, F. J. Marshall, T. C. Sangster, S. W. Hamlin, R. L. McCrory, D. D. Meyerhofer, B. A. Hammel, L. J. Suter, H. Scott, M. A. Barrios, D. A. Callahan, N. Izumi, N. B. Meezan, I. E. Golovkin, J. J. MacFarlane, R. C. Mancini, and K. J. Peterson, "Analysis of Diagnostic X-Ray Spectra of Implosions at the National Ignition Facility."

G. Fiksel, P.-Y. Chang, M. Hohenberger, J. P. Knauer, F. J. Marshall, D. D. Meyerhofer, R. Betti, F. H. Séguin, and R. D. Petrasso, "Fusion-Yield Enhancement in Magnetized Laser-Driven Implosions."

C. J. Forrest, V. Yu. Glebov, V. N. Goncharov, J. P. Knauer, D. D. Meyerhofer, P. B. Radha, T. C. Sangster, and C. Stoeckl, "Measurement of the Areal Density (ρR) Using nT Elastic Backscattering on OMEGA."

D. E. Fratanduono, M. A. Barrios, T. R. Boehly, D. D. Meyerhofer, J. H. Eggert, D. G. Hicks, R. F. Smith, D. Braun, P. M. Celliers, and G. W. Collins, "Refractive Index of Lithium Fluoride Ramp Compressed to 800 GPa" (invited).

D. H. Froula, I. V. Igumenshchev, D. T. Michel, C. Sorce, R. Follett, D. H. Edgell, W. Seka, and V. N. Goncharov, "Measurements of an Increased Neutron Yield with Reduced CBET."

L. Gao, P. M. Nilson, I. V. Igumenshchev, S. X. Hu, C. Stoeckl, D. H. Froula, and D. D. Meyerhofer, "Magnetic-Field Generation in Planar Plastic Targets on OMEGA EP."

V. Yu. Glebov, C. Stoeckl, T. C. Sangster, C. Forrest, J. P. Knauer, V. N. Goncharov, and P. B. Radha, "Measurements of DD Neutron Yield and Ion Temperature in DT Implosions on OMEGA."

V. N. Goncharov, T. C. Sangster, R. Epstein, S. X. Hu, I. V. Igumenshchev, D. H. Froula, R. L. McCrory, D. D. Meyerhofer, P. B. Radha, W. Seka, S. Skupsky, and C. Stoeckl, "Cryogenic Deuterium–Tritium Implosions on OMEGA."

M. Hohenberger, P.-Y. Chang, G. Fiksel, J. P. Knauer, D. D. Meyerhofer, R. Betti, F. J. Marshall, F. H. Séguin, and R. D. Petrasso, "Inertial Confinement Fusion Implosions with Seeded Magnetic Fields on OMEGA" (invited).

S. X. Hu, G. Fiksel, V. N. Goncharov, S. Skupsky, and V. A. Smalyuk, "Analysis of Laser-Imprinting Reduction in Spherical-RT Experiments with Si-/Ge-Doped Plastic Targets."

I. V. Igumenshchev, W. Seka, D. H. Edgell, D. H. Froula, V. N. Goncharov, R. S. Craxton, L. Divol, R. Follett, J. H. Kelly, T. Z. Kosc, D. T. Michel, P. Michel, R. L. McCrory, A. V. Maximov, D. D. Meyerhofer, J. F. Myatt, T. C. Sangster, A. Shvydky, S. Skupsky, and C. Stoeckl, "Crossed-Beam Energy Transfer in Direct-Drive Implosions" (invited).

S. Ivancic, W. Theobald, C. Stoeckl, P. M. Nilson, T. C. Sangster, D. D. Meyerhofer, S. X. Hu, and L. Willingale, "Initial Channeling of a Kilojoule-Class Laser in Long-Scale-Length Plasmas."

J. P. Knauer, V. Yu. Glebov, D. D. Meyerhofer, T. C. Sangster, C. Stoeckl, E. J. Bond, J. A. Caggiano, T. J. Clancy, M. J. Eckart, S. Friedrich, R. Hatarik, R. A. Lerche, A. J. Mackinnon, J. M. McNaney, M. J. Moran, D. H. Munro, S. J. Padalino, and J. D. Kilkenny, "Neutron Spectra Measured with Time-of-Flight Detectors on the National Ignition Facility."

J. A. Marozas, T. J. B. Collins, D. H. Edgell, I. V. Igumenshchev, and J. F. Myatt, "Two-Dimensional Analysis of Crossed-Beam Energy Transfer (CBET) in Direct-Drive ICF Target Implosions."

F. J. Marshall, P. B. Radha, R. Epstein, V. Yu. Glebov, J. A. Frenje, C. K. Li, R. D. Petrasso, and F. H. Séguin, "High-Convergence-Ratio Polar-Drive Experiments on OMEGA."

A. V. Maximov, J. F. Myatt, R. W. Short, I. V. Igumenshchev, D. H. Edgell, and W. Seka, "Energy Transfer Between Crossing Laser Beams in the Plasmas of Direct-Drive ICF."

P. W. McKenty, R. S. Craxton, F. J. Marshall, A. Shvydky, R. Epstein, A. M. Cok, J. A. Marozas, T. J. B. Collins, S. Skupsky, C. Stoeckl, T. C. Sangster, M. J. Bonino, R. Janezic, D. R. Harding, W. T. Shmayda, S. F. B. Morse, D. D. Meyerhofer, and R. L. McCrory, "Numerical Evaluation of Subtangential Focusing in OMEGA Target Implosions."

D. D. Meyerhofer, S.-W. Bahk, J. Bromage, C. Dorrer, J. H. Kelly, B. E. Kruschwitz, S. J. Loucks, R. L. McCrory, S. F. B. Morse, J. Qiao, C. Stoeckl, L. J. Waxer, and J. D. Zuegel, "Status of the OMEGA EP Laser System."

D. T. Michel, B. Yaakobi, S. X. Hu, R. W. Short, J. F. Myatt, C. Stoeckl, D. H. Edgell, W. Seka, V. N. Goncharov, and D. H. Froula, "Measurements of Hot Electrons Produced by Two-Plasmon Decay in Near Direct-Drive–Ignition Plasma Conditions."

J. F. Myatt, J. Zhang, A. V. Maximov, R. W. Short, D. F. DuBois, D. A. Russell, and H. X. Vu, "A Self-Consistent Quasilinear Model for the Two-Plasmon-Decay Instability in Inhomogeneous Plasmas."

R. Nora, R. Betti, K. S. Anderson, W. Theobald, A. Casner, M. Lafon, X. Ribeyre, and G. Schurtz, "Cryogenic Shock-Ignition Target Designs for OMEGA."

P. B. Radha, F. J. Marshall, T. R. Boehly, T. J. B. Collins, R. S. Craxton, R. Epstein, V. N. Goncharov, J. A. Marozas, R. L. McCrory, D. D. Meyerhofer, A. Shvydky, S. Skupsky, J. A. Frenje, and R. D. Petrasso, "Polar-Drive Designs for OMEGA."

S. P. Regan, R. Epstein, B. A. Hammel, L. J. Suter, J. Ralph, H. Scott, M. A. Barrios, D. K. Bradley, D. A. Callahan, C. J. Cerjan, G. W. Collins, S. N. Dixit, T. Doeppner, M. J. Edwards, D. R. Farley, S. Glenn, S. H. Glenzer, I. E. Golovkin, S. W. Haan, A. Hamza, D. G. Hicks, N. Izumi, J. D. Kilkenny, J. L. Kline, G. A. Kyrala, O. L. Landen, T. Ma, J. J. MacFarlane, R. C. Mancini, R. L. McCrory, N. B. Meezan, D. D. Meyerhofer, A. Nikroo, K. J. Peterson, T. C. Sangster, P. Springer, and R. P. J. Town, "Hot-Spot Mix in Ignition-Scale Implosions at the National Ignition Facility" (invited).

T. C. Sangster, W. T. Shmayda, V. Versteeg, D. R. Harding, R. Janezic, V. N. Goncharov, D. H. Edgell, D. H. Froula, V. Yu. Glebov, S. X. Hu, F. J. Marshall, R. L. McCrory, P. W. McKenty, D. D. Meyerhofer, J. F. Myatt, P. B. Radha, W. Seka, C. Stoeckl, B. Yaakobi, J. A. Frenje, M. Gatu-Johnson, and R. D. Petrasso, "Cryogenic-DT-Implosion Performance with Improved Target-Surface Quality."

W. Seka, I. V. Igumenshchev, D. H. Froula, D. H. Edgell, J. F. Myatt, R. W. Short, V. N. Goncharov, and A. V. Maximov, "Absorption by the Two-Plasmon-Decay Instability in Direct-Drive Implosions."

R. W. Short and J. F. Myatt, "Convective Multibeam Two-Plasmon Decay for Spherical and Planar Irradiation Geometries."

A. Shvydky, P. W. McKenty, M. Hohenberger, G. Fiksel, T. J. B. Collins, J. A. Marozas, J. D. Zuegel, and T. C. Sangster, "Preparing for OMEGA EP Validation of 1-D Multi-FM SSD for the NIF."

A. A. Solodov, K. S. Anderson, A. Shvydky, W. Theobald, R. Betti, J. F. Myatt, and C. Stoeckl, "Simulations of Implosion Core Heating for Integrated Cone-in-Shell Fast-Ignition Experiments on OMEGA."

A. Sorokovikova, M. S. Wei, R. B. Stephens, J. Jaquez, R. Nishra, H. Sawada, W. Theobald, P. Patel, H. McLean, Y. Sentoku, and F. N. Beg, "Study of Dependence of Fast Electron Transport on Target Material Using the 10 ps, 1.5 kJ Omega EP Laser."

C. Stoeckl, P. B. Radha, R. E. Bahr, J. A. Delettrez, D. H. Edgell, V. Yu. Glebov, V. N. Goncharov, I. V. Igumenshchev, T. C. Sangster, W. Seka, J. A. Frenje, and R. D. Petrasso, "Preheat Studies Using Low-Adiabat Plastic-Shell Implosions with Triple-Picket Pulses on OMEGA."

W. Theobald, M. Hohenberger, S. X. Hu, K. S. Anderson, R. Betti, T. R. Boehly, A. Casner, D. H. Edgell, D. E. Fratanduono, M. Lafon, D. D. Meyerhofer, R. Nora, X. Ribeyre, T. C. Sangster, G. Schurtz, W. Seka, C. Stoeckl, B. Yaakobi, "High-Intensity Shock-Ignition Experiments in Planar Geometry."

R. Yan, A. V. Maximov, C. Ren, and F. S. Tsung, "Energetic-Electron Generation in Two-Plasmon-Decay Instabilities in Inertial Confinement Fusion."

The following presentations were made at the International Collaboration on High Energy Density Science Workshop, Kanazawa, Japan, 25−29 November 2011:

T. R. Boehly, D. E. Fratanduono, M. A. Barrios, D. D. Meyerhofer, J. H. Eggert, D. G. Hicks, R. F. Smith, D. Braun, P. M. Celliers, and G. W. Collins, "Refractive-Index Measurements of LiF Ramp Compressed to 800 GPa."

T. R. Boehly, V. N. Goncharov, W. Seka, S. X. Hu, J. A. Marozas, D. D. Meyerhofer, P. M. Celliers, D. G. Hicks, M. A. Barrios, D. E. Fratanduono, and G. W. Collins, "Radiative Precursors and Temperature Measurements in Shock Deuterium."

R. L. McCrory, "LLE's Perspective on FY13–FY18 Planning," ICF Executives Meeting, Albuquerque, NM, 18 January 2012.

A. V. Okishev, C. Dorrer, Y. Fisher, and M. Pavia, "A Multiwavelength, Variable-Pulse-Width, Diode-Pumped Laser System," Solid State Lasers XXI: Technology and Devices, San Francisco, CA, 21–26 January 2012.

The following presentations were made at the MAGLIF Workshop, Albuquerque, NM, 5–8 February 2012:

G. Fiksel, P.-Y. Chang, M. Hohenberger, J. P. Knauer, F. J. Marshall, D. D. Meyerhofer, R. Betti, F. H. Séguin, and R. D. Petrasso, "Effect of Magnetic Fields on Neutron Emission from ICF Implosions."

J. P. Knauer, P.-Y. Chang, M. Hohenberger, G. Fiksel, F. J. Marshall, D. D. Meyerhofer, R. Betti, F. H. Séguin, and R. D. Petrasso, "Compressing Magnetic Fields with High-Energy Lasers."

J. D. Hager, J. P. Knauer, V. A. Smalyuk, T. J. B. Collins, J. A. Delettrez, S. X. Hu, D. D. Meyerhofer, and T. C. Sangster, "Rayleigh–Taylor Measurements in Planar Targets with CH and SiO_2 Ablators on OMEGA," NIF User Group Meeting, Livermore, CA, 12–15 February 2012.

J. M. Soures, "High-Energy-Density-Physics Research at the Omega Laser Facility," 2012 Stewardship Science Academic Alliances Symposium, Washington, DC, 22–23 February 2012.

The following presentations were made at the 2012 Materials Research Society Spring Meeting and Exhibit, San Francisco, CA, 9–13 April 2012:

K. Mehrotra, H. P. Howard, S. D. Jacobs, and J. C. Lambropoulos, "Mechanical Characterization of 'Blister' Defects on Optical Oxide Multilayers Using Nanoindentation."

K. Mehrotra, H. P. Howard, S. D. Jacobs, and J. C. Lambropoulos, "Nanoindentation Probing of High-Aspect-Ratio Pillar Structures on Optical Multilayer Dielectric Diffraction Gratings."

The following presentations were made at the Omega Laser Facility Users Group Workshop, Rochester, NY, 25–27 April 2012:

D. Canning, "Omega EP Facility Update and Progress on OLUG Recommendations."

G. Fiksel, P.-Y. Chang, M. Hohenberger, R. Betti, M. J. Shoup III, C. Taylor, T. Duffy, D. Lonobile, and W. Bittle, "Developing Magnetic Platforms for Inertial Confinement Fusion and Basic High-Energy-Density Science."

D. H. Froula, R. Boni, M. Bedzyk, R. Brown, R. S. Craxton, T. Duffy, F. Ehrne, S. Ivancic, R. Jungquist, N. Kugland, J. Puth, R. G. Roides, M. C. Rushford, W. Seka, M. J. Shoup III, W. Theobald, and D. Weiner, "Optical Diagnostic Suite (Schlieren, Interferometry, and Grid Refractometry) on OMEGA EP Using a 10-ps, 263-nm Probe Beam."

R. Jungquist, "Laser Retroreflected and Reflected Light Management."

J. Katz, R. Boni, D. Froula, G. Gates, A. Nauss, J. Szczepanski, M. Shoup, and T. Agliata, "OMEGA Thomson-Scattering System Upgrade."

J. Kwiatkowski, S. Stagnitto, S. F. B. Morse, M. Labuzeta, and V. Guiliano, "Characterizing Debris-Shield Transmission Degradation and Estimating On-Target Energy."

S. F. B Morse, "Omega Facility Updates: Progress on OLUG Recommendations."

G. Pien and J. Puth, "Omega Experimental Systems Performance and Improvements Since OLUG 2011."

S. P. Regan, G. Gregori, P. B. Radha, S. X. Hu, T. R. Boehly, B. Crowley, S. H. Glenzer, O. L. Landen, D. O. Gericke, T. Doeppner, D. D. Meyerhofer, C. D. Murphy, T. C. Sangster, and J. Vorberger, "X-Ray Thomson Scattering: An Incisive Probe for Warm, Dense Matter."

W. T. Shmayda, "Isotope Separation System and Gas Chromatograph Support Non-Standard Fills."

C. Sorce, M. Millecchia, D. Mastrosimone, A. Sorce, J. Katz, S. Ingraham, A. Pruyne, R. Bahr, D. Hassett, and D. Guy, "Omega Facility Diagnostic Highlights."

S. Stagnitto, W. R. Donaldson, E. Hill, M. Labuzeta, and M. Millecchia, "OMEGA Performance Metrics and Status Update on OLUG Recommendations."

C. Stoeckl, G. Fiksel, R. Jungquist, P. M. Nilson, and W. Theobald, "Spherical Crystal X-Ray Imaging for OMEGA and OMEGA EP."

The following presentations were made at the 19th Topical Conference on High-Temperature Plasma Diagnostics, Monterey, CA, 6–10 May 2012:

M. A. Barrios, A. MacPhee, S. P. Regan, J. Kimbrough, S. R. Nagel, L. R. Benedetti, S. F. Khan, D. Bradley, P. Bell, D. H. Edgell, and G. W. Collins, "X-Ray Bang-Time Measurements at the National Ignition Facility (NIF) Using a Polar Diamond Detector."

W. R. Donaldson, C. Zhao, L. Ji, R. G. Roides, K. Miller, and B. Beeman, "A Single-Shot, Multiwavelength Electro-Optic Data-Acquisition System for ICF Applications" (invited).

D. H. Edgell, A. MacPhee, D. K. Bradley, E. Bond, S. Burns, J. Celeste, M. J. Eckart, V. Yu. Glebov, D. S. Hey, G. Lacaille, J. D. Kilkenny, J. R. Kimbrough, A. J. Mackinnon, J. Magoon, J. Parker, T. C. Sangster, M. J. Shoup III, C. Stoeckl, and T. Thomas, "South Pole Bang-Time Diagnostic on the NIF."

C. J. Forrest, V. Yu. Glebov, V. N. Goncharov, A. Pruyne, J. P. Knauer, P. B. Radha, M. Romanofsky, T. C. Sangster, M. J. Shoup III, C. Stoeckl, D. T. Casey, M. Gatu-Johnson, and S. Gardner, "High-Resolution Spectroscopy Used to Measure ICF Neutron Spectra on OMEGA."

D. H. Froula, R. Boni, M. Bedzyk, R. Brown, R. S. Craxton, T. Duffy, F. Ehrne, S. Ivancic, R. Jungquist, N. Kugland, J. Puth, R. G. Roides, M. C. Rushford, W. Seka, M. J. Shoup III, W. Theobald, and D. Weiner, "Optical Diagnostic Suite (Schlieren, Interferometry, and Grid-Image Refractometry) on OMEGA EP Using a 10-ps, 263-nm Probe Beam."

V. Yu. Glebov, C. Forrest, J. P. Knauer, A. Pruyne, M. Romanofsky, T. C. Sangster, M. J. Shoup III, C. Stoeckl, J. A. Caggiano, M. L. Carman, T. J. Clancy, R. Hatarik, J. McNaney, and N. P. Zautseva, "Testing a New NIF Neutron Time-of-Flight Detector with a Bibenzyl Scintillator on OMEGA."

J. Katz, R. Boni, M. J. Shoup III, R. Follett, and D. H Froula, "A Reflective Optical Transport for Streaked Thomson Scattering and Gated Imaging on OMEGA."

J. P. Knauer, V. Yu. Glebov, C. Forrest, C. Stoeckl, T. C. Sangster, D. D. Meyerhofer, J. A. Caggiano, M. J. Moran, R. Hatarik, J. M. McNaney, S. Friedrich, E. J. Bond, M. J. Eckart, S. J. Padalino, and J. D. Kilkenny, "Neutron Spectra from 1 to 15 MeV Measured with Time-of-Flight Detectors at the National Ignition Facility."

F. J. Marshall, "Compact Kirkpatrick–Baez Microscope Mirrors for Imaging Laser–Plasma X-Ray Emission."

D. T. Michel, C. Sorce, R. Epstein, N. Whiting, I. V. Igumenshchev, R. Jungquist, and D. H. Froula, "Shell-Trajectory Measurements from Direct-Drive Experiments."

M. Millecchia, S. P. Regan, C. Sorce, R. E. Bahr, C. M. Romanofsky, and "Streaked X-Ray Spectrometer (SXS) Having a Discrete Selection of Bragg Geometries for Omega."

P. M. Nilson, C. Stoeckl, G. Fiksel, P. A. Jaanimagi, C. Mileham, W. Theobald, J. R. Davies, J. F. Myatt, A. A. Solodov, D. H.

Froula, R. Betti, and D. D. Meyerhofer, "Streaked X-Ray Imaging of Ultrafast Ionization Waves Inside a Metal."

C. Stoeckl, J. A. Delettrez, G. Fiksel, D. Guy, R. Jungquist, C. Mileham, P. M. Nilson, T. C. Sangster, M. J. Shoup III, and W. Theobald, "Soft X-Ray Backlighting of Direct-Drive Implosions Using a Spherical Crystal Imager on OMEGA."

The following presentations were made at CLEO 2012, San Jose, CA, 6–11 May 2012:

J. Bromage, C. Dorrer, and R. K. Jungquist, "Temporal Contrast Degradation at the Focus of Ultrashort Pulses from High-Frequency Spectral Phase Noise."

J. Bromage, C. Dorrer, M. Millecchia, J. Bunkenburg, R. Jungquist, and J. D. Zuegel, "A Front End for Ultra-Intense OPCPA."

J. Bromage, M. Millecchia, J. Bunkenburg, R. K. Jungquist, C. Dorrer, and J. D. Zuegel, "A Cylindrical Öffner Stretcher for Reduced Chromatic Aberrations and Improved Temporal Contrast."

C. Dorrer, "Broadband Operation of High-Damage-Threshold Phase and Polarization Binary Beam Shapers."

C. Dorrer, A. V. Okishev, R. G. Roides, R. Cuffney, W. Bittle, and J. D. Zuegel, "Fiber Front End for an OMEGA EP Demonstration of Beam-Smoothing Techniques for NIF Polar-Drive Ignition."

J. Qiao, P. A. Jaanimagi, R. Boni, J. Bromage, and E. Hill, "Beam-Homogenization and Space-Charge–Broadening Calibration for Accurately Measuring High-Intensity Laser Pulses Using a High-Speed Streak Camera."

M. Statt, M. Vargas, J. B. Oliver, S. H. Chen, K. L. Marshall, and C. Dorrer, "High-Damage-Threshold Components for Radially and Azimuthally Polarized Beam Generation."

R. Xin and J. D. Zuegel, "A Negative-Feedback-Stabilization System for an All-Fiber Regenerative Amplifier."

The following presentations were made at the 20th Target Fabrication Meeting, Santa Fe, NM, 20–24 May 2012:

Z. Bei, G. Randall, T. B. Jones, and D. R. Harding, "Implementation of Dielectrophoretic Droplet Centering in a Miniaturized Centering Cell for ICF Foam Capsule."

M. J. Bonino, F. J. Marshall, D. H. Froula, S. P. Regan, D. Turner, D. R. Harding, S. G. Noyes, J. Fooks, and E. Giraldez, "Overview of the Requirements and Construction of Targets for Experiments on OMEGA and OMEGA EP."

R. Q. Gram, D. R. Harding, and T. B. Jones, "Dielectrophoresis of Liquid Deuterium for IFE Target Filling."

D. R. Harding, M. D. Wittman, and D. H. Edgell, "Considerations and Requirements for Providing Cryogenic Targets for Direct-Drive Inertial Fusion Implosions at the National Ignition Facility."

W. T. Shmayda, D. R. Harding, M. J. Bonino, V. Versteeg, A. Greenwood, and M. Farrel, "Mitigating Defects on Cryotargets."

D. Turner, M. J. Bonino, D. R. Harding, S. G. Noyes, and B. Rice, "Properties and Performance of Target Mounts for Cryogenic Experiments on OMEGA."

S. X. Hu, V. N. Goncharov, S. Skupsky, L. A. Collins, M. J. N. Dijokap, A. F. Starace, and B. I. Schneider, "Probing Ultrafast Processes in Intense Laser–Matter Interactions," presented at the 43rd Annual APS Division of Atomic, Molecular, and Optical Physics Meeting, Anaheim, CA, 4–8 June 2012.

The following presentations were made at the OSA Topical Meeting on Optical Fabrication and Testing, Monterey, CA, 24–28 June 2012:

H. P. Howard, J. C. Lambropoulos, and S. D. Jacobs, "Dependence of Thermal Stresses on Substrate Thickness During Wet Processing of Large Coated Optics."

J.C. Lambropoulos, K. Mehrotra, H. P. Howard, and S. D. Jacobs, "Glass Ductility and Fracture at the 50- to 100-nm Scale."

The following presentations were made at the 42nd Annual Anomalous Absorption Conference, Key West, FL, 25–29 June 2012:

D. H. Edgell, P. B. Radha, D. H. Froula, V. N. Goncharov, I. V. Igumenshchev, J. F. Myatt, and W. Seka, "Mitigation of Cross-Beam Energy Transfer in Polar-Drive Implosions."

R. K. Follett, D. T. Michel, J. F. Myatt, S. X. Hu, B. Yaakobi, and D. H. Froula, "Thomson-Scattering Measurements of Ion-Acoustic Wave Amplitudes Driven by the Two-Plasmon Decay."

D. H. Froula, I. V. Igumenshchev, D. T. Michel, D. H. Edgell, R. Follett, V. Yu. Glebov, V. N. Goncharov, J. Marozas, P. B. Radha, W. Seka, C. Sorce, and C. Stoeckl, "Mitigation of Cross-Beam Energy Transfer in Direct-Drive Plasmas."

L. Gao, P. M. Nilson, I. V. Igumenshchev, J. R. Davies, S. X. Hu, C. Stoeckl, M. G. Haines, D. H. Froula, R. Betti, and D. D. Meyerhofer, "Magnetohydrodynamic Effects in Ablatively Driven High-Energy-Density System Experiments."

S. X. Hu, D. H. Edgell, D. H. Froula, V. N. Goncharov, D. T. Michel, S. Skupsky, and B. Yaakobi, "Analyses of Long-Scale-Length Plasma Experiments with Different Ablator Materials on the OMEGA EP Laser System."

A. V. Maximov, J. F Myatt, R. W Short, I. V. Igumenshchev, D. H. Edgell, and W. Seka, "Interaction of Multiple Laser Beams via Common Waves and Beam Energy Transfer."

D. T. Michel, A. V. Maximov, B. Yaakobi, S. X. Hu, J. F. Myatt, A. A. Solodov, R. W. Short, and D. H. Froula, "Experimental Validation of the Two-Plasmon-Decay Common-Wave Process."

J. F. Myatt, J. Zhang, V. N. Goncharov, A. V. Maximov, R. W. Short, D. F. DuBois, D. A. Russell, and H. X. Vu, "The Mitigating Effect of Wave Dissipation on Hot-Electron Generation Caused by the Two-Plasmon Decay in Inhomogeneous Plasmas."

D. A. Russell, H. X. Vu, D. F. DuBois, and J. F. Myatt, "Two-Plasmon-Decay Turbulence Driven by the Shared-Wave Triad of Two Crossed Beams."

W. Seka, D. H. Edgell, D. H. Froula, J. Katz, J. F. Myatt, J. Zhang, R. W. Short, T. D. Michel, A. V. Maximov, and V. N. Goncharov, "Half-Integer Harmonic Images and Spectra Point Toward Localized, Multibeam Two-Plasmon Decay."

R. W. Short, J. Myatt, A. Maximov, T. Michel, and D. Froula, "The Effects of Beam Polarization on Convective and Absolute Two-Plasmon-Decay Driven by Multiple Laser Beams."

A. A. Solodov, K. S. Anderson, W. Theobald, A. Shvydky, R. Betti, J. F. Myatt, and C. Stoeckl, "Simulations of Cone-in-Shell Targets for Integrated Fast-Ignition Experiments on OMEGA."

H. X. Vu, D. Russell, D. F. DuBois, and J. F. Myatt, "Hot-Electron Generation by 'Cavitating' Langmuir Turbulence in the Nonlinear Stage of the Two Plasmon Decay Instability."

A. V. Okishev, C. Dorrer, B. E. Kruschwitz, J. H. Kelly, E. Hill, A. Consentino, G. Balonek, J. A. Marozas, M. Hohenberger, A. Shvydky, R. G. Roides, R. Cuffney, W. Bittle, and J. D. Zuegel, "Multifrequency Smoothing by Spectral Dispersion on OMEGA EP for NIF Polar-Drive Implosions," presented at Laser Optics 2012, St. Petersburg, Russia, 25–29 June 2012 (invited).

The following presentations were made at the European Physical Society 2012 Conference, Stockholm, Sweden, 2–6 July 2012:

D. H. Froula, D. T. Michel, R. S. Craxton, D. H. Edgell, R. Follett, V. Yu. Glebov, V. N. Goncharov, S. X. Hu, I. V. Igumenshchev, F. J. Marshall, J. F. Myatt, P. B. Radha, T. C. Sangster, W. Seka, R. W. Short, A. A. Solodov, C. Stoeckl, and B. Yaakobi, "Direct-Drive Laser–Plasma Interaction Experiments."

M. LaFon, X. Ribeyre, G. Schurtz, A. Casner, W. Theobald, R. Nora, M. Hohenberger, K. S. Anderson, R. Betti, C. Stoeckl,

and D. D. Meyerhofer, "Hydrodynamic Modeling for Shock-Ignition Implosions and Simulations for Experiments on OMEGA."

The following presentations were made at the Optics and Photonics 2012, San Diego, CA, 12–16 August 2012:

B. Beeman, A. G. MacPhee, J. R. Kimbrough, G. A. Lacaille, M. A. Barrios, J. Emig, J. R. Hunter, E. K. Miller, and W. R. Donaldson, "Mach-Zehnder Modulator Performance Using the Comet Laser Facility and Implications for Use on NIF."

K. L. Marshall, C. Dorrer, M. Vargas, A. Gnolek, M. Statt, and S.-H. Chen, "Photoaligned Liquid Crystal Devices for High-Peak-Power Laser Applications."

C. Mileham, C. Stoeckl, W. Theobald, G. Fiksel, D. Guy, R. K. Jungquist, P. M. Nilson, T. C. Sangster, and M. J. Shoup III, "Crystal Imager Development at the Laboratory for Laser Energetics."

K. L. Marshall, A. Schulz, J. Lee, M. Rutan, E. Jones, G. Mitchell, C. Smith, and A. L. Rigatti, "Chemically Modified Organosilane Optical Coatings and Their Applications in High-Peak-Power Lasers," presented at the 244th American Chemical Society Fall 2012 National Meeting, Philadelphia, PA, 19–23 August 2012.

The following presentations were made at the International Committee on Ultra-High Intensity Lasers, Mamaia, Romania, 16–21 September 2012:

S.-W. Bahk, I. A. Begishev, and J. D. Zuegel, "An Anamorphically Imaged, Programmable Beam-Shaping System for High-Power Lasers."

J. Bromage, J. B. Oliver, C. Dorrer, and J. D. Zuegel, "Optical Coatings for Ultra-Intense OPCPA Systems."

C. Dorrer, "Characterization of Highly Dispersive Components Using Direct Instantaneous Frequency Measurements."

C. Dorrer, K. L. Marshall, S. H. Horn, M. Vargas, M. Statt, C. Caggiano, S. K.-H. Wei, J. B. Oliver, P. Leung, K. Wegman, J. Boulé, and Z. Zhao, "High-Damage-Threshold Beam Shaping Using Optically Patterned Liquid Crystal Devices."

H. P. Howard, A. F. Aiello, J. G. Dressler, N. R. Edwards, T. J. Kessler, A. A. Kozlov, S. LaDelia, J. B. Oliver, S. Papernov, A. L. Rigatti, A. W. Schmid, C. C. Smith, B. N. Taylor, and S. D. Jacobs, "An Improved Cleaning Method to Enhance the Damage Threshold of MLD Gratings."

J. Qiao, P. A. Jaanimagi, R. Boni, J. Bromage, and E. Hill, "Uniform Illumination and Space-Charge–Broadening Calibration for Accurate Short-Pulse Measurement Using a High-Speed Streak Camera."

J. Qiao, A. Kalb, Z. De Santis, and J. Papa, "Design and Analysis of a Meter-Scale Deformable Multilayer-Dielectric-Grating–Based Compressor for Kilojoule, Petawatt Laser Systems."

J. D. Zuegel, I. A. Begishev, J. Bromage, S.-W. Bahk, C. Dorrer, R. B. Brannon, and D. D. Meyerhofer, "Design and Status of an Energy Upgrade to the Multi-Terawatt Laser at the University of Rochester's Laboratory for Laser Energetics."

S. Papernov, E. Shin, T. Murray, A. W. Schmid, and J. B. Oliver, "355-nm Absorption in HfO_2 and SiO_2 Monolayers with Embedded Hf Nanoclusters Studied Using Photothermal Heterodyne Imaging," presented at Laser Damage, Boulder, CO, 23–26 September 2012.